18th EAWE PhD Seminar

2-4 November 2022
Bruges, Belgium

Book of Proceedings

Edited by:

Angelo Goethals

Benoit Foloppe

Dominik Fallais

Francois Trigaux

Ivandito Herdayanditya

Nandar Hlaing

Thomas de Kerf

Thuy-hai Nguyen

Younes Oudich

Corresponding email:
phairywind@gmail.com

PhairywinD
Belgian Offshore PhD Expertise

eawe
european academy of wind energy

Hosted and organized by:

PhairywinD
Belgian Offshore PhD Expertise

eawe
european academy of wind energy

Sponsored by:

economie
FPS Economy, S.M.E.s, Self-employed and Energy

DEME

ZF

otary
OFFSHORE ENERGY

BOP
BELGIAN OFFSHORE PLATFORM

PARK WIND

24SEA
MONITORING OFFSHORE STRUCTURES

IMDC

RelyOn Nutec
360° Safety

eBO

Coastal & Ocean Basin
Ostend

Table of contents

Cover page **1**

Sponsor page **2**

Wind farms and wakes **1**

A Simple and Robust Algorithm to Determine Wake Interactions, Pepper Benjamin [et al.] 1

Actuator Line Model development in Nek5000 for wind turbine wake simulation in Large Eddy Simulation, Gillyns Emmanuel [et al.] 6

Aeroelastic simulations of wind turbines in an atmospheric boundary layer using a flexible actuator curve method, Trigaux Francois [et al.] 8

An open-source operational dynamic wake modelingframework, Lejeune Maxime [et al.] 12

Application of the wake identification via thresholding to wake characterization and lidar retrieval, Krutova Maria [et al.] 16

Calibrating the actuator line model in the large eddy simulation solver YALES2, Parinam Anand [et al.] 20

Comparison of generalized actuator disk and actuator line wind turbine models for varying atmospheric conditions, Kale Baris [et al.] 24

Coupling an atmospheric perturbation model to a wake-merging method to include meso-scale perturbations, Devesse Koen [et al.] 28

Coupling of a dynamic wake model with WRF: a case study of the Belgian wind farms, Foloppe Benoit [et al.] 30

Development of a load surrogate model based on rotor-equivalent inflow quantities, Guilloré Adrien [et al.] 32

Development of filtering method for LiDAR measurements that retain the turbine wake information, Pinilla Sebastian 36

Dynamic wake mitigation control: towards better understanding of wake physics using high-resolution large-eddy simulations, Coquelet Marion [et al.] 39

Effect of data assimilation of local observations in WRF on the predictability of atmospheric variables for offshore wind energy applications, Ivanova Tsvetelina [et al.] 43

Finite wind-farm operations in conventionally neutral boundary layers using a large-eddy simulation framework, Lanzilao Luca [et al.] 47

Identifying Turbulent Inflow Time Scales Beneficial for Wake Recovery, Hodgson Emily Louise [et al.] 51

Investigation of the Impact of Hub Height Optimization for Two Interacting Onshore Wind Farms, Kütükçü Gökay [et al.] 54

Mesoscale modelling of offshore wind farm wakes over the North Sea for different turbine densities., Borgers Ruben [et al.] 58

Modelling of ice throw from wind turbines: a case study, Janovski Kim [et al.] . . 62

Multi-rate integration techniques in wind farm LES using actuator line method, Ntrelia Konstantina [et al.] 66

Simulating Large Wind Farms with the Lattice Boltzmann Method, Korb Henry [et al.] 69

Study of wave effects on the wind turbine aerodynamics with large-eddy simulation in sigma coordinates, Ning Xu [et al.] 71

Wind field reconstruction with LIDAR measurements, Marini Rebeca [et al.] . . 74

convective atmospheric boundary layer using LES, Vigny Ulysse [et al.] 78

wind turbuine wake study considering the influence of atmospheric stability using lattice Boltzmann method, Wang Ziwen [et al.] 82

Wind resources, turbulence and acoustics **87**

A study on the performance of two ship-based profiling wind lidars under different motion scenarios in extreme cold climate, Malekmohammadi Shokoufeh [et al.] . 87

Advanced numerical modeling of the interaction between trees and the local wind climate, Pabst Helen Alina [et al.] 92

Characterization of the effect of inflow turbulence on vortex shedding engineering models parameters using Large Eddy Simulations, Fernandez-Aldama Ricardo [et al.] 95

Climate Change Impact on the Offshore Wind Energy over the North Sea and the Irish Sea, Susini Stefano [et al.] 99

Effect of free-stream turbulence on the performance of a simplified wind turbine: a wind-tunnel study, Dumanoir Mylène [et al.] 103

Further characteristics of the atmospheric turbulent wind: Periods of constant wind speed and waiting times between gusts, Moreno Daniela [et al.] 107

GIS-based inverse Sound Propagation Modelling, Arends Henning [et al.] 111

Mesoscale structure of typhoons for wind energy applications, Müller Sara [et al.] 114

Mesoscale variability in wind speed, a study for the Kattegat (Denmark, Sweden), Neirynck Jérôme [et al.] 118

Noise Source Identification on a Diffuser-Augmented Wind Turbine Using Ffowcs Williams–Hawkings Analogy, Freire-Guimaraes J. Manoel [et al.] 122

Simulating spatio-temporal varying waves using a WRF-LES-IBM system, Hamzeloo Sima [et al.] 126

Statistical characteristics of turbulent wind inflow obtained from WRF-LES simulations for the SWiFT test site, Elagamy Mohanad [et al.] 127

Uncertainties of long-term wind speed predictions for site assessment tasks, Borowski Johanna [et al.] 135

Turbine technology and control **138**

A Force Partitioned Approach for Numerical Analysis of Vortex-Induced Vibrations on Wind Turbine Towers, Vimalkumar Shyam [et al.] 138

A Self-Similarity scaling for Integral Boundary Layer analysis of Vortex Generators, Sahoo Abhratej 142

Active Trailing Edge Flap on a 4.3 MW wind turbine: characterization and aeroelastic modeling of a pneumatic flap actuator, Gamberini Andrea 150

Comparison of different wind farm control strategies in a quasi-static closed-loop control framework, Sood Ishaan [et al.] 153

Decentralized Q-learning for Wind Farm Control under Dynamic Conditions, Bizon Monroc Claire [et al.] 156

Dynamic modelling of wind farms for closed-loop control applications, Liew Jaime 160

FE Model Validation and Progressive Damage Analysis of a 5-m Composite Wind Turbine Blade under Monotonic Loading, Muyan Can [et al.] 164

Mitigating leading edge erosion in wind farms through optimal erosion-safe mode control, Visbech Jens 166

Modeling of wind energy systems under non-axial inflow conditions and the effect of low Reynolds number, Afanasieva Nadiia 169

Numerical simulations for active power control of wind farms, Tamaro Simone [et al.] 173

On a nonlinear, objective coupling element in a director-based finite element formulation for structural modelling of wind energy turbines, Märtins David [et al.]175

Electrical conversion, energy system and wind power-to-X 177

Advance Generative Model for Scenario Generation of Wind Power Distributions With Hight Granularity, Hosseini Ahmad 177

Comparison of Hybrid Wind Power Plant Sizing Optimization Methods, Assaad Charbel [et al.] 180

Increasing the Magnetic Permeability of Wind Turbine Generator Air-gaps, Hall Fergus [et al.] 186

Machine Learning-based Methodologies for Grid Compliance Assessment of Wind Turbines and Farms, Gomes Guerreiro Gabriel Miguel [et al.] 190

Model-based Control and Operation of Large-Scale Water Electrolyser Plants for Optimal Integration into Modern Power Systems, Riofrio Jonathan [et al.] 193

Offshore Wind Farm Power Prediction For Security of Supply Assessment Using a Unique Machine Learning Proxy, Nguyen Thuy-Hai [et al.] 196

Stability enhancement of weakly-connected offshore wind power plants by wind turbines with grid-forming converter control, Ghimire Sulav [et al.] 200

Wind Farm and Hydrogen Storage Co-location System for Frequency Response Provision in the UK, Skellern Shanay [et al.] 202

Production, O&M, decommissioning and lifetime extension **206**

Characterisation of fatigue life and short fatigue crack growth for welds used in offshore turbine monopile, Saeed Hasan [et al.] 206

Circular Supply Chain Management for the German Wind Energy Industry, Kramer Kathrin Julia 211

I spy with my little eye, or: estimating offshore wind farm installation times utilizing satellite data, Sander Aljoscha 215

Leading edge erosion of wind turbine blades, lifetime and roughness modelling for coatings, Tempelis Antonios 218

Predicting the Mechanical Performance of Composite Materials and Sub-components for Wind Turbine Blades Through Manufacturing Modelling, Jørgensen Jesper Kjær221

Rolling horizon based adjustable maintenance management: A case study of a 3-MW wind turbine, Li Mingxin [et al.] 224

Runup under Waves and Current to Improve Offshore Wind Marine Operations, Herdayanditya Ivandito [et al.] 228

Reliability, monitoring and sensing technology **232**

A Novel Approach for Constructing Health Indicators for Degrading Wind Turbine Components, Eftekhari Milani Ali [et al.] 232

Budget constrained modelling for the reliability assessment of offshore wind substructures under accidental impact events, Moran Jonathan 242

Fleet-wide model updating and virtual sensing for fatigue monitoring of offshore wind turbines, Fallais Dominik [et al.] 248

Grey-box modeling for data-based structural health monitoring, Möller Sören [et al.] 250

Higher-Order Cyclostationary approaches for Fault Detection of Wind Turbines Gearboxes, Nitti Marcello [et al.] 254

Interpretation of offshore wind management policies identified via partially observable Markov decision processes, Hlaing Nandar [et al.] 261

Long-term damage effect of low-frequency loads of offshore wind turbines using SHM data, Sadeghi Negin [et al.] 267

Model Updating for damage localisation and quantification using a deterministic optimiser and a damage distribution function, Dierksen Niklas [et al.] 272

Monitoring blade leading edge erosion with Graph Neural Networks and aerodynamic data, Duthé Gregory [et al.] 276

Optical imaging methods to detect corrosion in offshore wind turbines, De Kerf Thomas 280

System Structural Reliability Modelling for Offshore Wind Welded Connections, Mishael Jose [et al.] 283

Temperature Influence on Structural Health Monitoring Systems, Bartels Jan-Hauke [et al.] 287

Wind Turbine Blade Defect Detection using Fibre Bragg Grating Distributed Sensing, Sihivahana Sarma Aananthalakshmy 291

Support structures and geotechnics **295**

A Numerical Investigation on the Pitting Corrosion in Offshore Wind Turbine Sub-structures, Mehri Sofiani Farid [et al.] 295

Analysis of discrepancy between modelled and measured natural eigenfrequencies of offshore wind turbines, Winkler Kristof 300

Current and wave patterns in the nearfield of an offshore jacket structure, Wynants Mareile [et al.] 303

Development of Bluff Body Benchmark at high Reynolds numbers, Breitkopf Sophie [et al.] 307

Development of a database of offshore substructures for evaluating and prognosing the design quality of the structures using machine learning methods, Qian Han . 311

Geological considerations for offshore wind foundations at "Sørlige Nordsjø II", Norwegian North Sea, Petrie Hannah [et al.] 315

Numerical study on the effect of pitting corrosion on the fatigue strength degradation of offshore wind turbine sub-structures using a short crack model, Elahi Seyed Ahmad [et al.] 319

Sensitivity of Monopile Response to Scour: a laboratory case study, Fernandes De Oliveira Junior Adelmo [et al.] 323

The Effect of Varying Soil Properties on the Probability of Unsatisfactory Performance of Offshore Monopile Foundations, Orakci Olgu [et al.] 326

Floating wind turbines **328**

Design Optimization of Multi-used Components for Floating Offshore Wind Turbine Substructures, Benifla Victor [et al.] 328

Development of a methodology for the analysis of tip vortices in floating horizontal axis wind turbines, Cioni Stefano [et al.] 333

Experimental campaign of a floating offshore wind turbine: Preliminary results, Pimenta Francisco [et al.] 337

Multi-fidelity simulation of floating offshore wind turbine aerodynamics: are current tools ready for future challenges?, Papi Francesco [et al.] 338

Simulation models for the analysis of floating wind turbine wakes: a comparison between the Actuator Line and the Actuator Disk Models, Pagamonci Leonardo [et al.] 342

Wind tunnel investigation of the wake of a model floating wind turbine under imposed surge motion, Messmer Thomas [et al.] 345

Wind tunnel study of the wake meandering of a floating wind turbines by a porous disk, Hubert Antonin [et al.] 348

Emerging technologies and special sessions **351**

Analysis of stresses in a wind turbine composite adhesive using CT Scans and Deep Learning., Khan A. Wasay 351

High fidelity fluid-structure interaction simulation of a multi-megawatt airborne wind energy reference system in cross-wind flight, Pynaert Niels 355

Modelling and control of Airborne Wind Energy Systems using lifting line/surface aerodynamics, Crismer Jean-Baptiste [et al.] 358

Multi-objective substructure generation, Panagiotou Emmanouil 362

Multidisciplinary Design, Analysis and Optimization of fixed wing Airborne Wind Energy Systems, Trevisi Filippo 366

Legal aspects **370**

Congestion management in an interconnected offshore grid, Angelo Goethals . . 371

Minimizing light pollution from wind turbines lighting, Yakushina Yana 371

Economic and policy **377**

A levelized cost of energy analysis of changing global commodity markets and the impact on floating offshore wind, White Craig [et al.] 377

An integrated decision support system for offshore wind farm site selection in the Baltic Sea, Barzehkar Mojtaba [et al.] 383

Feasibility study for floating offshore wind in the Arabian Gulf, Donnelly Orla [et al.] 390

Ecological aspects **394**

Combined life cycle impact and cost assessment of wind energy generation in large-scale offshore wind farms, Kainz Samuel 394

Other topics **401**

CFD model of a wind tunnel: making a digital twin, Mishra Rishabh [et al.] . . . 401

Description of the methodology for quantifying geometrically non-linear cross-sectional deformations of rotor blades, Gebauer Julia [et al.] 406

Experimental investigation of failure mechanism in cross-ply curved composite laminates under transverse loading, Cevik Ahmet [et al.] 408

Numerical investigation of impact-induced damage progression in composite wind turbine blade structures, Batmaz Onur Ali [et al.] 411

On the use of the Actuator Line Method to simulate the performance of twin Darrieus turbines, Mohamed Omar [et al.] 414

Wind farms and wakes

18th EAWE PhD Seminar on Wind Energy
2-4 November 2022
Bruges, Belgium

A Simple and Robust Algorithm to Determine Wake Interactions

Benjamin Pepper[a], **Prof. William Leithead**[a], and **Dr. Luis Recalde Camacho**[a]

[a]University of Strathclyde, 204 George Street, Glasgow, G1 1XW, UK

E-mail: benjamin.pepper@strath.ac.uk

Keywords: Wind turbine anomaly detection, wake interactions, wind turbine control

1 Introduction

In a wind farm, the wakes of upwind turbines may impinge upon turbines downwind. This typically has negative consequences for the turbine in the wake, such as decreased energy capture and increased, unbalanced loads. It is important, therefore, to be able to detect whether a wake is incident on a rotor. The presence of a wake on a rotor can be inferred from signatures in the wind field at the rotor. In previous work, it has been established that the effective wind field, averaged over the radial direction, can be expressed as

$$U(\theta,t) = \bar{U} + U_p(t) + \sum_{n=1}^{\infty} \left[\big(a_n + U_{an}(t)\big)\sin(n\theta) + \big(b_n + U_{bn}(t)\big)\cos(n\theta) \right] \tag{1}$$

where θ is the rotor azimuth angle; $\bar{U}$ is the mean wind speed; $U_p(t)$, $U_{an}(t)$, and $U_{bn}(t)$ represent stochastic processes; and a_n and b_n represent the deterministic components of the wind field [1, 2]. Since a wake is a deterministic component, it may be possible to detect its presence using the a_n and b_n amplitudes. In the set of a_n and b_n elements, the most important are a_1 and b_1 which account for vertical and horizontal variations in the wind field, respectively. In [2], an Extended Kalman Filter approach is used to estimate a_1 and b_1, but the method is unsuitable for implementing in a controller due to its complexity. In this project, a simpler alternative for calculating a_1 and b_1 is explored.

The simulations in this project were carried out in *DNV-GL Bladed* on the Supergen 5MW exemplar turbine, which is a 3-bladed, horizontal-axis machine with variable-speed, pitch-regulated control. The turbulence intensity and ground roughness height across all simulations are 10% and 1 mm, respectively.

2 Estimation of $\bar{U} + U_p(t)$

2.1 Aerodynamic torque

From Newton's second law, a simple equation of motion for the rotor can be written as

$$J\frac{d\Omega}{dt} = Q_a - NQ_e - B\Omega \tag{2}$$

where J is the moment of inertia of the rotor, Ω is the rotor angular speed, Q_a is the aerodynamic torque, N is the gearbox ratio, Q_e is the generator torque, and B is a damping coefficient [3]. The aerodynamic torque can also be expressed as

$$Q_a = \frac{1}{2}\rho U_Q^2 \pi R^3 C_Q(\lambda,\beta) \tag{3}$$

where ρ is the density of air, U_Q is the upstream wind speed, R is the rotor radius, λ is the tip speed ratio, β is the pitch angle, and C_Q is the torque coefficient. In equation 3, it is important to note that the upstream wind field is uniform.

2.2 Effective wind speed for the rotor

To calculate the effective wind speed for the rotor, it is first of all helpful to define the non-analytical function $H_Q(\lambda,\beta)$ as

$$H_Q(\lambda,\beta) = \frac{Q_a}{\Omega^2} = \frac{1}{2}\rho\pi\lambda^{-2}R^5 C_Q(\lambda,\beta) \tag{4}$$

By inverting equation 4, it is possible to derive a look-up table for $\lambda(H_Q,\beta)$. Given that Q_a has been calculated and Ω and β are available, the $\lambda(H_Q,\beta)$ look-up table allows the tip speed ratio to be calculated. Once the tip speed ratio is known, it is straightforward to compute the upstream wind speed using

$$U_Q = \frac{\Omega R}{\lambda} \tag{5}$$

U_Q is an estimate of the upstream wind speed which imparts the same aerodynamic torque on the rotor as the full wind field. It represents an averaging of the wind field over the rotor, and is thus an effective wind speed.

2.3 Estimation of $\bar{U} + U_p(t)$

For a simulation with a mean wind speed of 14 m/s, figure 1 shows the power spectrum density (PSD) of U_Q. Two peaks can be considered significant from causing step increases in the cumulative sum curve. The peak at 3.80 rad/s can be identified as the 3P passing frequency, while the peak at 23.9 rad/s is a structural frequency of the turbine.

In equation 1, $\bar{U}$ is the mean wind speed and $U_p(t)$ represents an averaging over the rotor disc of the stochastic processes such as turbulence. It is possible to estimate $\bar{U} + U_p(t)$ by removing the spectral spectral peaks from the PSD of U_Q. A popular and effective approach for removing a spectral peak is applying a notch filter. The standard form for a notch filter is

$$F(s) = \frac{s^2 + 2\alpha\eta\omega_0 s + \omega_0^2}{s^2 + 2\eta\omega_0 s + \omega_0^2} \tag{6}$$

where ω_0 is the frequency to be attenuated, and α and η are tuning parameters. The structural frequency in figure 1 does not depend on rotor speed, and therefore a notch filter with $\omega_0 = 23.9$ rad/s can be used across all operating conditions. The frequency of the 3P peak, however, is proportional to the rotor speed. As the operating conditions vary, ω_0 must also vary to track the 3P peak. This makes the notch filter in the form of equation 6 difficult to implement. A solution to this problem is to apply a notch filter in the domain of the rotor azimuth angle, θ. In this case, the notch filter for an nP passing frequency takes the form

$$\bar{F}(\bar{s}) = \frac{\bar{s}^2 + 2\alpha\eta\bar{\omega}_n\bar{s} + \bar{\omega}_n^2}{\bar{s}^2 + 2\eta\bar{\omega}_n\bar{s} + \bar{\omega}_n^2} \tag{7}$$

where $\bar{\omega}_n = \text{n}$ and $\bar{s}$ is the operator representing differentiation with respect to θ. Importantly, in this domain the frequency to be attenuated, $\bar{\omega}_n$, does not depend on rotor speed. The action of both filters on U_Q is shown in figure 1. For equation 6, it was found that setting $\alpha = 0.01$ and $\eta = 1$ removes the step in the cumulative curve at 23.9 rad/s. Meanwhile, having $\bar{\omega}_n = 3$, $\alpha = 0.1$ and $\eta = 0.4$ in equation 7 removes the 3P peak.

3 Estimation of a_1 and b_1

3.1 Effective wind speed for a blade

The effective wind speed for aerodynamic torque represents an average of the wind field over the three blades of the rotor. When extracting key attributes of the wind field, it is also useful to have the wind speed experienced by a single blade. This is captured by the effective wind speed for the out-of-plane blade root bending moment (BRBM), M_y. Similarly to the aerodynamic torque, the out-of-plane BRBM can be expressed as

$$M_y = \frac{1}{2}\rho U_M^2 \pi R^3 C_{M_y}(\lambda,\beta) \tag{8}$$

where C_{M_y} is the out-of-plane BRBM coefficient and U_M is the upstream wind speed which induces the same bending moment as the full wind field.

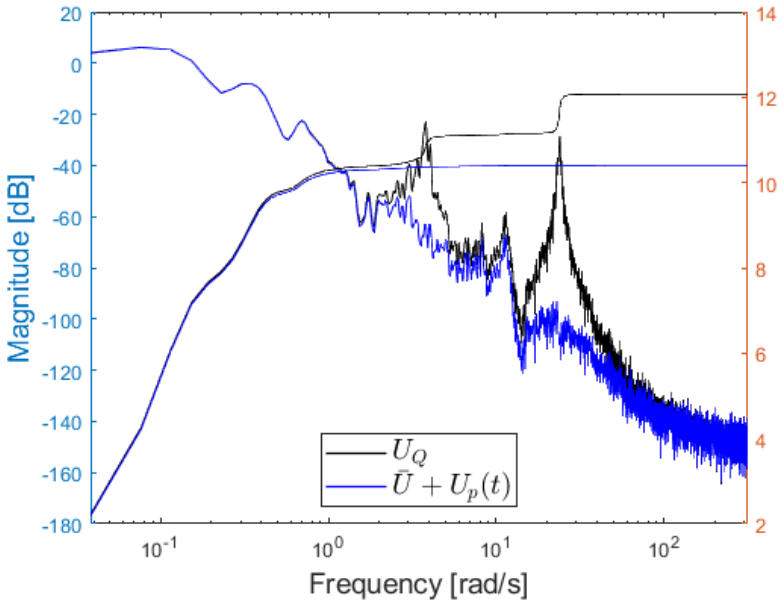


Figure 1: The PSD of $\bar{U} + U_p(t)$ is estimated by applying notch filters to the 3P and structural frequency peaks of U_Q.

As in section 2.2, a function $H_{M_y}(\lambda, \beta)$ is defined as

$$H_{M_y}(\lambda, \beta) = \frac{M_y}{\Omega^2} = \frac{1}{2}\rho\pi\lambda^{-2}R^5 C_{M_y}(\lambda, \beta) \tag{9}$$

This equation can be inverted to obtain a look-up table of $\lambda(H_{M_y}, \beta)$. In contrast to section 2.2, where Q_a is calculated from an equation of motion, M_y would be available on the turbine from a direct measurement. The tip speed ratio can be calculated from the $\lambda(H_{M_y}, \beta)$ look-up table, and then the upstream wind speed can be obtained from the definition of tip speed ratio.

3.2 nP deterministic components

From equation 1, the nP deterministic components of wind speed are $a_n \sin(n\theta)$ and $b_n \cos(n\theta)$ for $n \in \mathbf{Z}^+$. The amplitudes a_n and b_n can be calculated as

$$a_n(\Theta) = \frac{\pi^{-1}}{N_{2\pi}(\Theta)} \int_0^{\Theta} \sin(n\theta) U(\theta) d\theta \tag{10a}$$

$$b_n(\Theta) = \frac{\pi^{-1}}{N_{2\pi}(\Theta)} \int_0^{\Theta} \cos(n\theta) U(\theta) d\theta \tag{10b}$$

where $N_{2\pi}(\Theta) = \Theta/2\pi$ and $U(\theta)$ represents an averaging of the wind field over the radial direction. In this report, the effective wind speed for a blade is used (i.e., $U(\theta) = U_M(\theta)$).

3.3 Estimation of a_1 and b_1

If the wind field were symmetric about the tower axis, then it would be expected that $b_1 = 0$ m/s. If, however, a wake were overlapping with part of the rotor, then it would be expected that $|b_1| > 0$ m/s. While b_1 relates to lateral variations in the wind field, a_1 relates to vertical variations. It is expected that $a_1 > 0$ for most wind fields because wind shear ensures that the wind speed increases with height.

For a simulation with a mean wind speed of 14 m/s, a_1 and b_1 are presented in figure 2. a_1 tends to 1.48 m/s as time increases, which is greater than zero as expected. Meanwhile, b_1 tends to 0.73 m/s. This non-zero value of b_1 suggests that the wind field is asymmetric about the tower axis, which is not the case in this simulation. The cause of b_1 being non-zero is a phase lag between M_y and U_M induced by the blade dynamics.

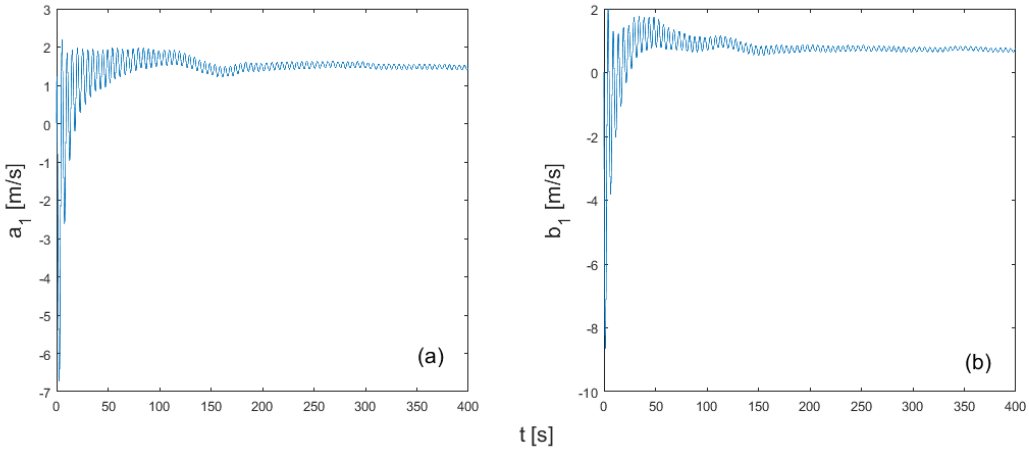


Figure 2: The deterministic components a_1 and b_1 tend to 1.48 m/s and 0.73 m/s as time increases in (a) and (b), respectively. It is expected that $a_1 > 0$ because of vertical wind shear, while a phase delay gives rise to a non-zero value of b_1.

4 Conclusions and future work

Standard turbine measurements (e.g., rotor speed and pitch angle) can be used with turbine coefficients to derive effective wind speeds. With the effective wind speed for a blade, it is possible to compute the nP deterministic components of the effective wind field. These components provide insight into the structure of the wind field, and therefore may be able to detect whether a wake is present on a rotor.

In this report, the 1P deterministic components across a range of mean wind speeds simulated in *DNV-GL Bladed* are presented. The values obtained for the amplitude of the lateral component, b_1, are non-negative. In the absence of a wake or lateral shear, as is the case in the simulations, this reflects a phase lag between the measured blade bending moment and the aerodynamic moment acting on the blade.

Unfortunately, no simulations with wakes have been tested in this project. Consequently, the ability of the 1P deterministic components to register a wake and the extent of its overlap on a rotor has not been tested. This would be among the first tasks of future work. Calculating higher order deterministic components would allow the extent of wake interactions to be determined with greater resolution. Therefore, this would be another suitable task for future work. Other tasks could include accounting for the phase delay which gives rise to non-zero values of b_1, and investigating whether the nP deterministic components are able to distinguish between wakes and other deterministic horizontal variations in the wind field such as lateral shear.

References

[1] M. L. Gala Santos. Aerodynamics and wind-field models for wind turbine control. 2018.

[2] S. Hur, L. Recalde-Camacho, and W. Leithead. Detection and compensation of anomalous conditions in a wind turbine. *Energy*, 124:74–86, 2017.

[3] W. Leithead and B. Connor. Control of variable speed wind turbines: dynamic models. *International Journal of Control*, 73(13):1173–1188, 2000.

18th EAWE PhD Seminar on Wind Energy
2-4 November 2022
Bruges, Belgium

Actuator Line Model development in Nek5000 for wind turbine wake simulation in Large Eddy Simulation

Emmanuel Gillyns[a,b] and **Sophia Buckingham**[b]

[a]Institute of Mechanics, Materials and Civil Engineering (IMMC), Université Catholique de Louvain (UCLouvain)
[b]Environmental and Applied Fluid Dynamics, von Karman Institute for Fluid Dynamics (VKI)

E-mail: emmanuel.gillyns@vki.ac.be

Keywords: Actuator Line, ALM, wind turbine wake, LES, spectral element, Nek5000

Understanding the wind turbine wake, and its effect on structures such as electrical cables and/or buildings is crucial for improving the implementation of wind turbines in urban areas. Simulating such behavior can provide deep insight to this issue and improve our current knowledge around this growing energy producing system. Such wake can easily extend to 10 times the swept diameter, with most recent ones reaching 180 m. At the scales involved, high accuracy both spatially and temporarily are required, which requires the use of Large Eddy Simulation (LES). Unfortunately, the computational cost of a resolving the geometry of each blade is beyond today's computational power, and will most likely stay this way for years to come. Most of the computational cost comes from resolving the geometry of the blades, whether it is wall-resolved (wrLES) or wall-modelled (wmLES). The present work will demonstrate a technique for reducing significantly this cost by replacing each blade with the equivalent forces of lift and drag on a coarse grid. This modelling is known as an Actuator Line Model (ALM) [4].

The code of choice here is Nek5000, a high order spectral element CFD code. It is chosen in this framework for its efficiency and highly scalability, which will become essential with large computational domain. The reduced cost per degree of freedom, and fast convergence that it provides as compared to other finite difference codes, makes is the ideal choice here.

The Actuator Line Model (ALM) consists in reproducing the reaction force from the blades on the inflow along the blade line in a coarse grid. At each timestep, the three velocity component are sampled along a line representing the moving blade. The local inflow and angle of attack in each part of the blade is used, together with the known airfoil, to obtain the force of lift and drag. These forces are then redistributed on the coarse grid, as added force to the momentum equation, to mimic the presence of the blade. The present work improves on previous works [1, 2] by proposing an alternative distribution of the forces. Most implementations use a set number of points along the line to distribute the forces on a 3D Gaussian sphere. In the regions of high gradient in the radial direction, this method is not capable of capturing good resolution without a fine grid and a high number of points along the line. The present implementation solves this issue by spreading the forces only on a 2D Gaussian plane normal to the radial direction. No points along the line is required here, equivalent to an infinite number of points in this direction. This is able to capture much better regions such as the hub, as shown in Figure 1, without compromising on the computational cost of a finer grid. For numerical stability, a local spread at the tip is applied in the radial direction. The tip spread used here is similar to the other implementations to obtain a comparable result. This adjustable spread at the tip allows a variable resolution in this region, based on the mesh resolution used.

To evaluate the quality of the present implementation, a comparison with 4 other codes is given from [3]. In Figure 1, the reader can identify how this ALM in the 7th order spectral element method of Nek5000 compares to codes spanning from 2nd order finite difference to 4th order finite difference and pseudo-spectral.

As a result, the present implementation matches well with other similar ones, which ensures that the methodology is correct. The improved resolution at the hub is well captured, and especially visible at the streamwise distances from 0D to 3D (where D is the rotor diameter).

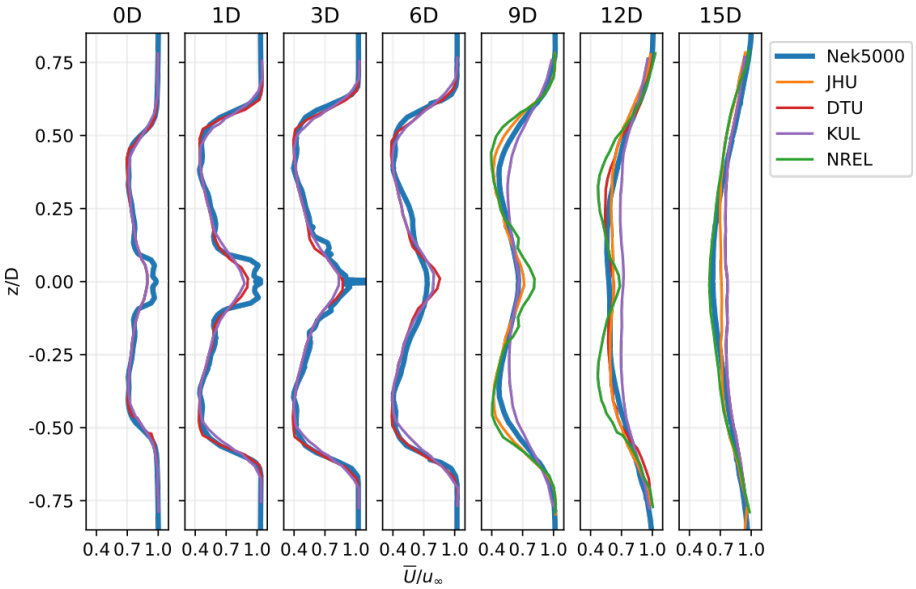


Figure 1: Mean velocity deficit comparison

Acknowledgements

This work is supported by a von Karman PhD grant.

References

[1] W. Jin. Numerical simulation of wind turbine wakes based on actuator line method in nek5000. Master's thesis, KTH Mechanics, 1 2013.

[2] E. Kleusberg. Wind turbine simulations. Master's thesis, KTH Mechanics, 5 2017.

[3] L. A. Martínez-Tossas, M. J. Churchfield, A. E. Yilmaz, H. Sarlak, P. L. Johnson, J. N. Sørensen, J. Meyers, and C. Meneveau. Comparison of four large-eddy simulation research codes and effects of model coefficient and inflow turbulence in actuator-line-based wind turbine modeling. *Journal of Renewable and Sustainable Energy*, 10(3):033301, may 2018.

[4] J. N. Sorensen and W. Z. Shen. Numerical modeling of wind turbine wakes. *Journal of Fluids Engineering*, 124(2):393–399, may 2002.

18th EAWE PhD Seminar on Wind Energy
2-4 November 2022
Bruges, Belgium

Aeroelastic simulations of wind turbines in an atmospheric boundary layer using a flexible actuator curve method

F. Trigaux[a], **P. Chatelain**[a], and **G. Winckelmans**[a]

[a]Institute of Mechanics, Materials and Civil Engineering (iMMC), Université catholique de Louvain (UCLouvain), 1348 Louvain-la-Neuve, Belgium

E-mail: francois.trigaux@uclouvain.be

Keywords: Aeroelaticity, Actuator line model, Large Eddy Simulation

1 Context

The primary objective of recent wind turbine designs is to maximize the power that it can extract from the wind. The easiest way to reach this goal is to increase the rotor diameter. However, an important constrain is the mass of the blade, that directly impacts the blade lifespan due to the centrifugal and gravitational loads. To overcome this constrain, the blades are nowadays manufactured using lightweight composite materials and are consequently more flexible.

The increased structural flexibility raises the question of the aeroelastic effects that can occur on a wind turbine blade. The study of those effects is made difficult as they arise from fundamentally unsteady loads, due to the blade rotation in a sheared flow and the atmospheric turbulence. To improve the future blade design, it is essential that those effects are well understood, especially in realistic atmospheric conditions.

The objective of this study is to present a flexible actuator curve model. This model is then used to simulate one or multiple wind turbines in an atmospheric boundary layer. The unsteady deformations of the blade are discussed, as well as the impact of the increased flexibility on the loads and power.

2 Methodology: a flexible actuator curve method

The Large Eddy Simulation (LES) of turbulent flows is considered. The incompressible Navier-Stokes equations supplemented by a subgrid scale model are solved using an in-house developed HPC and fourth-order finite differences code [1, 2]. A flexible actuator curve method is added to represent the effect of a wind turbine. The actuator curve method is an extension of the actuator line method to curved blades. It allows to compute and distribute the aerodynamic forces on a parametric curve instead of on a line [3]. The accuracy of the classical actuator line is also improved. In fact, the actuactor line methods requires that the aerodynamic forces are distributed on the mesh using a smoothing function. In the classical method, this smoothing function is a 3D isotropic Gaussian kernel. Yet, it has been shown that spreading the loads in the spanwise direction leads to an overprediction of the aerodynamic forces, especially near the blade tip [4]. Several studies have therefore been conducted to add a tip correction that removes the effect of the mollification a posteriori [5, 6]. However, in this case, a smoothing function without spanwise mollification is used directly. The actuator curve distributes the forces in a plane perpendicular to the curve, as depicted on Figure 1. A 2D Gaussian kernel is used

$$\eta_{2D} = \frac{1}{\pi\sigma^2} \exp\left(-\frac{d^2}{\sigma^2}\right).$$

where d is the distance to the control point in the plane and σ the width of the Gaussian. This approach improves the accuracy of the actuator curve method without the need for an additional tip correction.

The actuator curve is coupled to a one-dimensional beam model. Here, the Euler-Bernoulli classical beam theory (EBBT) is used. This simplified theory is sufficient to represent the considered NREL-5MW blade because the latter does not have bend-twist coupling, and it is unlikely to undergo significantly large displacements for

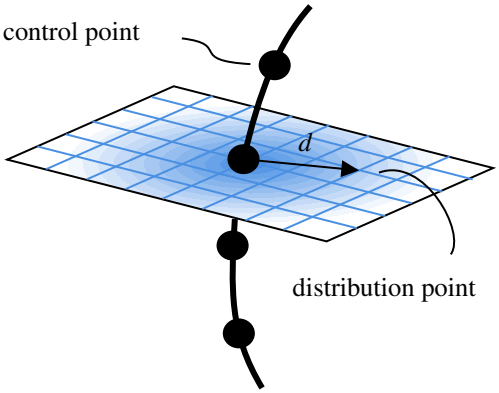


Figure 1: Schematic of the 2D distribution using a template plane perpendicular to the curve and with Gaussian weights.

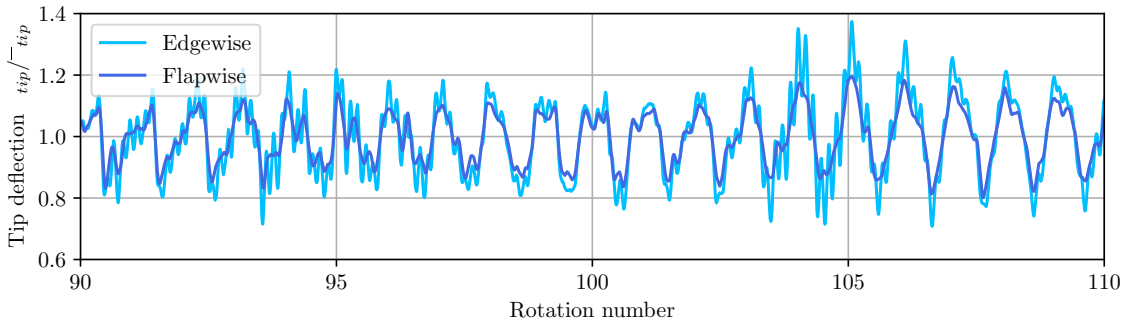


Figure 2: Instantaneous edgewise and flapwise blade tip deflections, each normalized by its mean deflection. $\bar{u}_t ip = 3.47$ m in the flapwise direction, -0.40 m in the edgewise direction.

typical load cases. The EBBT equations are solved using a finite element method, here 3rd order beam elements. A second order Newmark scheme is used for the transient analysis. The coupling between the flow and the structural solver is carried using a 2nd order improved staggered scheme [7].

3 Results

In this section, the case of the NREL-5MW wind turbine in a realistic atmospheric boundary layer (ABL) is considered. The turbine rotates at a constant speed of 10.29 rpm with an mean inflow speed at hub height of 9 m/s. The simulation is run for 110 rotations, corresponding to $\simeq$ 640 s. In the following, a rigid and a flexible rotor are therefore compared in realistic turbulent wind conditions.

We first observe the blade tip displacement for a subset of rotations on Figure 2. The deflections present a strong periodicity at the frequency of the blade rotation. This is due to the cyclic aerodynamic loads arising from the mean wind shear. Additional deflections at higher and lower frequencies can also be observed, due to the turbulent fluctuations. Those additional deflections are also more important in the edgewise direction, which seems to indicate that the latter is less aerodynamically damped than the flapwise one. An analysis of the power spectral densities of the displacement (not shown here) has indicated that there is indeed a peak of displacement at this first eigenfrequency in the edgewise direction.

An interesting effect of the flexibility is also to modify the phase of the power with regard to the blade rotation angle. In fact, Figure 3 shows that even though the mean power is not virtually not affected by the flexibility, its variation during one rotation is shifted by $\simeq 15^o$. Moreover, the amplitude of the variation is also decreased in the case of flexibility due to higher compliance of the blade.

A case with two wind turbines in a row is also presented, as depicted on Figure 4. In this case, the second wind turbine experiences lower mean loads, but much more fluctuations due to the turbulent nature of the wake. There-

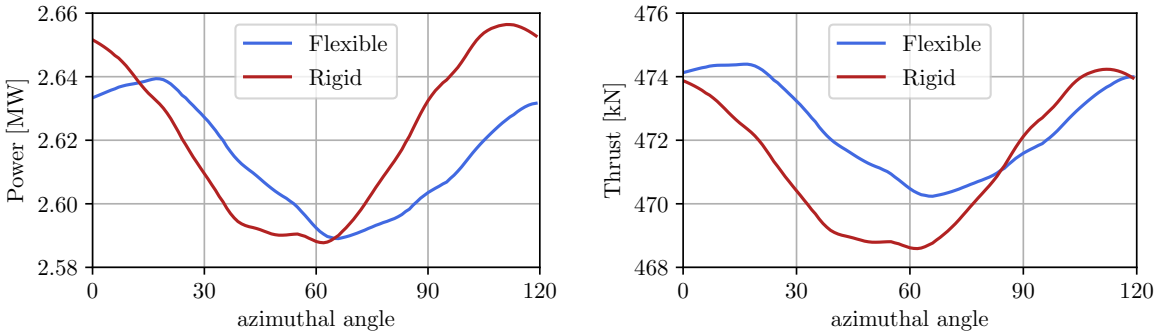


Figure 3: Power and thrust over one third of a rotation, as time-averaged over $\sim$ 50 rotation cycles. The azimuthal angle refers to the angle of one of the three blades

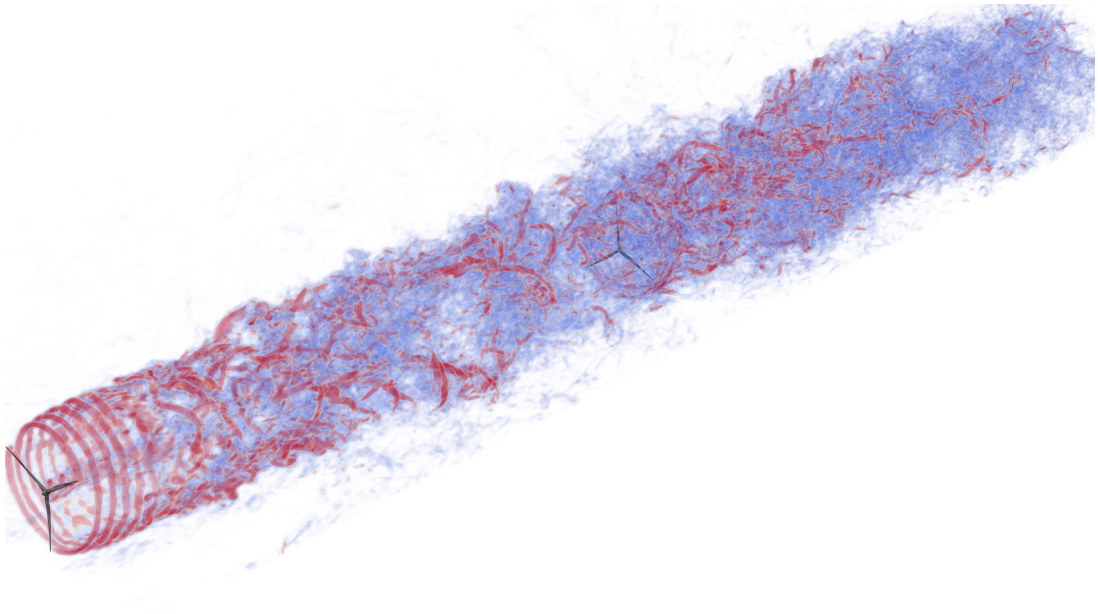


Figure 4: Volume rendering of the vorticity magnitude in the wake of the two rotors.

fore, the variations of the tip displacement, especially in the edgewise direction are significantly more important. Nevertheless, the phase lag of the power remains on the second wind turbine.

4 Conclusion

A flexible actuator curve method was presented. It allows to accurately represent a wind turbine including the structural deformations of the blade in a LES code. The method was applied to simulate a NREL-5MW reference wind turbine in a realistic atmospheric boundary layer and to compare the results with a rigid rotor, in order to better understand the implications of the deformations on the wind turbine. It appears that the blade mostly deforms according to its first bending mode and that its rotation in the sheared atmospheric flow is responsible for large amplitude deformations. However, the unsteady turbulent fluctuations also play a role in causing deformations at higher frequencies with a smaller amplitude. This is especially visible in the edgewise direction, that has a lower aerodynamic damping. The power evolution along one rotation is also modified when the flexibility is taken into account.

Whereas this study focused on the well-known NREL-5MW reference wind turbine, we expect the aeroelastic effects to be much more important for new generation turbine such as the IEA-15MW. Future work will therefore include the simulation of those rotors to assess if the current conclusions still hold.

Acknowledgements

This research was conducted in the frame of the PhairywinD project funded by the Belgian Federal government through the Energy Transition Fund. This research also benefited from computational resources made available on the Tier-1 supercomputer of the Fédération Wallonie-Bruxelles, infrastructure funded by the Walloon Region under the grant agreement No. 1117545. Computational resources were also provided by the *Consortium des Equipements de Calcul Intensif (CECI)*, funded by the *Fonds de la Recherche Scientifique de Belgique* under Grant No. 2.5020.11 and by the Walloon Region.

References

[1] M. Duponcheel, L. Bricteux, M. Manconi, G. Winckelmans, and Y. Bartosiewicz. Assessment of rans and improved near-wall modeling for forced convection at low prandtl numbers based on les up to re$_\tau$=2000. *International Journal of Heat and Mass Transfer*, 75:470 – 482, 2014.

[2] Maud Moens, Matthieu Duponcheel, Grégoire Winckelmans, and Philippe Chatelain. An actuator disk method with tip-loss correction based on local effective upstream velocities. *Wind Energy*, 21(9):766–782, 2018.

[3] P. K. Jha and S. Schmitz. Actuator curve embedding–an advanced actuator line model. *Journal of Fluid Mechanics*, 2018.

[4] Denis-Gabriel Caprace, Philippe Chatelain, and Grégoire Winckelmans. Lifting line with various mollifications: theory and application to an elliptical wing. *AIAA Journal*, 57(1):17–28, 2019.

[5] Kaya Onur Dağ and Jens Nørkær Sørensen. A new tip correction for actuator line computations. *Wind Energy*, 23(2):148–160, 2020.

[6] Luis A. Martínez-Tossas and Charles Meneveau. Filtered lifting line theory and application to the actuator line model. *Journal of Fluid Mechanics*, 863:269–292, Jan 2019.

[7] Joris Degroote. Partitioned simulation of fluid-structure interaction. *Archives of computational methods in engineering*, 20(3):185–238, 2013.

18th EAWE PhD Seminar on Wind Energy
2-4 November 2022
Bruges, Belgium

An open-source operational dynamic wake modeling framework

Maxime Lejeune[a], **Maud Moens**[a], and **Philippe Chatelain**[a]

[a]Thermodynamics and Fluid Mechanics, Institute of Mechanics, Materials and Civil Engineering, Université catholique de Louvain, Louvain, Belgium

E-mail: maxime.lejeune@uclouvain.be

Keywords: wake model; wake meandering ; flow sensing ; Lagrangian flow model ; particle

1 Introduction

Nowadays, wind turbines are typically operated in an uncoordinated fashion. This approach, though comparatively simple, often leads to a suboptimal operating point of the wind farm taken as a whole as it fails to account for wake effects. The development of new collective wind farm control strategies has therefore been identified as one of the major challenges to accelerate the wind energy deployment [11]. Recent studies (*eg*: [8, 6]) have demonstrated the great potential of both wake redirection and induction control strategies toward the improvement of wind farm performances. However, for most, these studies have been focusing on the design of model-based control schemes as model-free approaches tend to suffer from poor convergence rates due to the significant delay observed between a control input change and its impact on downstream wind turbines.

The performances of these model-based approaches will nonetheless always be bound by that of the underlying wake model. This therefore calls for a closed-loop solution where a computationally-tractable yet faithful wake model is continuously updated by the the wind farm measurements. Such a model should provide the control scheme with expert knowledge about the flow thereby allowing it to select the optimal control input.

This work pursues a very recent trend toward the design of such a control-oriented dynamic wake models (*eg*: [10, 2, 5].) We introduce an unified open-source framework based on previous investigations [9, 10] which merges together flow sensing and Lagrangian flow modeling. The resulting framework allows to track the main heterogenities of the ambient flow field as well as the main dynamic features of the wake, including its meandering, at a low computational cost. This work features an extensive refactoring of the previous code implementation in an attempt to improve its modularity and performances toward its open-source release. The overall framework is first presented and its performances are then validated against high-fidelity Large Eddy Simulations.

2 Methodology

Estimated snapshots of the wind farm flow field are reconstructed by propagating the information gathered at the wind turbine location through flow sensing. The proposed framework thus consists of two coupled modules: namely the *wind turbine state estimator* and the *Lagrangian flow model*.

2.1 Wind turbine state estimator

The *wind turbine state estimator* proposes to map the wind turbine measurements, $\mathbf{m}_{WT}$, to the estimated wind turbine state, $\hat{\mathbf{s}}_{WT}$. The latter is in turn fed to the Lagrangian flow model as an input and contains the operating settings and inferred flow features (*i.e.* freestream velocity, ambient turbulence intensity) of the wind turbine.

This *wind turbine state estimator* modules features various flow-sensing tools the user can pick from. Consistent with the turbine as a sensor approach [3], one may, for example, choose to consider each blade as moving sensor whose bending loads are directly connected to the inflow velocity through a Neural Net regressor [10] and/or Kalman filter [4]. The module also allows the user to easily implement its own estimator and to differentiate between the treatment of waked and freestream turbines.

2.2 Lagrangian flow model

The flow model is a physics-based two-dimensional wake model that propagates information in a fashion akin to the Lagrangian persistence methods used for nowcasting precipitations [12].

The farm flow field, $\mathbf{u}(\mathbf{x},t)$, is decomposed into two main coupled fields: the freestream velocity field, $\mathbf{u}_f(\mathbf{x},t)$, and the wake one, $\Delta\mathbf{u}(\mathbf{x},t)$:

$$\mathbf{u}(\mathbf{x},t) = \mathbf{u}_f(\mathbf{x},t) - \Delta\mathbf{u}(\mathbf{x},t) \tag{1}$$

As illustrated on Figure 1, each field is modeled as a series of information-carrying wake (W_i) and freestream (F_i) particles shed at successive time steps, t_i. The states of these two sets of particles are in turn concatenated into the global estimated flow state vector $\hat{\mathbf{s}}_{flow}$ while a source condition is provided at the wind turbine location by its estimated state, $\hat{\mathbf{s}}_{WT}$.

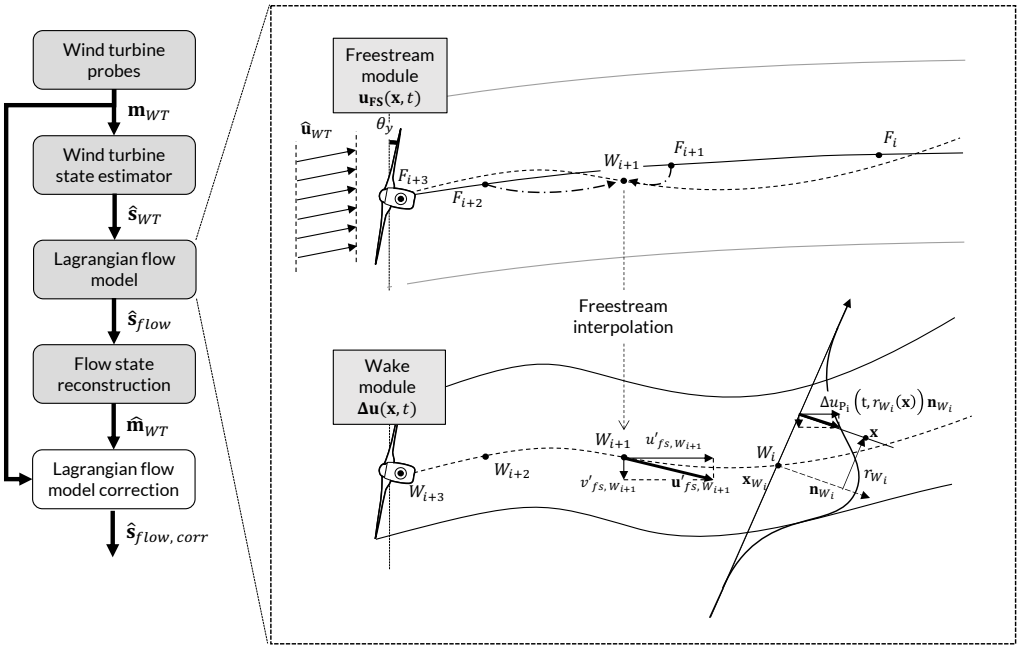


Figure 1: Description of the operational wake modeling framework proposed

The freestream flow field, $\mathbf{u}(\mathbf{x},t)$, is thus decomposed into a series of freestream particles, F_i, advected downstream at their own characteristic velocity, $\mathbf{u}_{fs,W_i}$. The wake field, $\Delta\mathbf{u}(\mathbf{x},t)$, on the other hand, is parametrized in a similar fashion as FAST-Farm [7]. A wake particle is essentially described by a position, $\mathbf{x}_{W_i}(t)$, an orientation, $\mathbf{n}_{W_i}(t)$, and a speed deficit field $\Delta u_{W_i}(t, r_{W_i}(x))$ where $r_{W_i}(x)$ and t denote the radial position of $\mathbf{x}$ relative to the wake particle and the current time respectively. The particle speed deficit is in turn obtained by projecting a simple analytic speed deficit model [1] along the particle orientation vector, $\mathbf{n}_{W_i}$. The wake is then reconstructed by advecting these particles downstream using the freestream flow field, $\mathbf{u}'_{fs,W_i}$ superimposed with this self-induced speed deficit, $\Delta u_{W_i}\ \mathbf{n}_{W_i}$.

2.3 Implementation

The initial version of this code underwent a complete refactoring toward its open-source release which features improved modularity and performances scalability. The ctypes Python foreign function library provides a direct coupling between the Python interface and the flow module written in C. This allows to maintain good computational performances while improving modularity thereby facilitating the interfacing with user-defined data sources, wind turbine state estimators or speed deficits. Future modules shall notably include state-correction methods allowing to correct the model states and/or parameters based on the measurements of impinged rotors.

3 Results

The framework presented was validated against high-fidelity Large Eddy Simulation of both isolated and waked wind turbine. Previous investigations demonstrated the good potential of the approach [9, 10]. It distinctly provides additional insight into the wake physics when compared to classical steady state wake model. The Lagrangian flow model manages to capture well the main dynamic features of the wake, including its meandering, and can handle large scale inflow heterogenities. Even so, it remains computationally tractable and runs in fast time (8×10^{-4} wall-clock second per simulation second for a 12 WTs wind farm). This study shall extend this validation to new cases where we will investigate the performances of the proposed framework to dynamically controlled wind farms.

4 Conclusion

In this abstract, we built on past investigations toward a new online dynamic wake modeling framework and introduced the first open-source release of the tools developed. These tools most notably include a Lagrangian wake model coupled to a wind turbine state estimator that allow to reconstruct estimated snapshots of the flow field across the wind farm based on the information gathered by the wind turbine. The updated framework features improved modularity and computational scalability while providing additional insight into the wake dynamics when compared to more classical, steady, approaches. Future investigations shall include the implementation of state-parameter correction strategies that should allow to better account for modeling errors.

Acknowledgements

This project has received funding from the European Research Council (ERC) under the European Union's Horizon 2020 research and innovation program (grant agreement no. 725627). Simulations were performed using computational resources provided by the Consortium des Équipements de Calcul intensif (CÉCI), funded by the Fonds de la Recherche Scientifique de Belgique (F.R.S.- FNRS) under Grant No. 2.5020.11, and computational resources made available on the Tier-1 supercomputer of the Fédération Wallonie-Bruxelles, infrastructure funded by the Walloon Region under the Grant Agreement No. 1117545.

References

[1] M. Bastankhah and F. Porté-Agel. Experimental and theoretical study of wind turbine wakes in yawed conditions. *Journal of Fluid Mechanics*, pages 506–541, 2016.

[2] M. Becker, B. Ritter, B. Doekemeijer, D. van der Hoek, U. Konigorski, D. Allaerts, and J.-W. van Wingerden. The revised floridyn model: Implementation of heterogeneous flow and the gaussian wake. *Wind Energy Science Discussions*, 2022:1–25, 2022.

[3] M. Bertelè and C. Bottasso. Non-deterministic wind observation from wind turbine loads. *Journal of Physics: Conference Series*, 1618:062022, sep 2020.

[4] C. Bottasso and C. Riboldi. Validation of a wind misalignment observer using field test data. *Renewable Energy*, 74:298–306, 2015.

[5] R. Braunbehrens, J. Schreiber, and C. L. Bottasso. Application of an open-loop dynamic wake model with high-frequency SCADA data. *Journal of Physics: Conference Series*, 2265(2):022031, may 2022.

[6] P. M. O. Gebraad, F. W. Teeuwisse, J. W. van Wingerden, P. A. Fleming, S. D. Ruben, J. R. Marden, and L. Y. Pao. Wind plant power optimization through yaw control using a parametric model for wake effects—a cfd simulation study. *Wind Energy*, 19(1):95–114, 2016.

[7] J. M. Jonkman, J. Annoni, G. Hayman, B. Jonkman, and A. Purkayastha. Development of fast.farm: A new multi-physics engineering tool for wind-farm design and analysis. *AIAA SciTech Forum: 35th Wind Energy Symposium*, 1 2017.

[8] G. Larsen, S. Ott, J. Liew, M. van der Laan, E. Simon, G. Thorsen, and P. Jacobs. Yaw induced wake deflection-a full-scale validation study. *Journal of Physics: Conference Series*, 1618:062047, sep 2020.

[9] M. Lejeune, M. Moens, and P. Chatelain. Extension and validation of an operational dynamic wake model to yawed configurations. *Journal of Physics: Conference Series*, page in press, 2022.

[10] M. Lejeune, M. Moens, and P. Chatelain. A meandering-capturing wake model coupled to rotor-based flow-sensing for operational wind farm flow prediction. *Frontiers in Energy Research (in press)*, 2022.

[11] J. Meyers, C. Bottasso, K. Dykes, P. Fleming, P. Gebraad, G. Giebel, T. Göçmen, and J.-W. van Wingerden. Wind farm flow control: prospects and challenges. *Wind Energy Science Discussions*, 2022:1–56, 2022.

[12] R. Prudden, S. Adams, D. Kangin, N. Robinson, S. Ravuri, S. Mohamed, and A. Arribas. A review of radar-based nowcasting of precipitation and applicable machine learning techniques, 2020.

18th EAWE PhD Seminar on Wind Energy
2-4 November 2022
Bruges, Belgium

Application of the wake identification via adaptive thresholding to wake characterization and lidar retrieval

Maria Krutova[a], **Mostafa Bakhoday-Paskyabi**[a], **Joachim Reuder**[a], and **Finn Gunnar Nielsen**[a]

[a]Geophysical Institute and Bergen Offshore Wind Center, University of Bergen

August 15, 2022
E-mail: Maria.Krutova@uib.no

Keywords: wind turbine wakes, lidar retrieval, wake identification, thresholding

1 Motivation

Wake identification, i.e., separating wake from the free-flow, is a necessary step in wake studies. Several approaches exist [1], with the Gaussian fit method being the most simple to use. The Gaussian method finds wake width and center by fitting a normal distribution to the wake deficit profile. The result can be further used to analyze wake meandering, yaw deflection and wake-wake or wake-turbine interaction [2, 3].

However, the Gaussian method does not explicitly separate wake from the free flow. Wake boundaries obtained via the Gaussian method can be projected into the coordinate grid of the flow field to split data points into the wake and free-flow points. The uncertainties in the wake width caused by noisy data or low resolution would then be carried over, and a Gaussian-identified wake may cover a larger area than the actual wake occupies.

Unlike fitting methods, thresholding methods operate directly on the data points. In wake identification, a thresholding method uses a specific criterion to split all available data points into two groups: wake or free-flow points. The most straightforward implementation of the method would be setting a threshold as a wake deficit value above which a point is considered to belong to the wake [4, 5]. While a fixed threshold may perform well on well-resolved flow fields (e.g., particle image velocimetry or large-eddy simulation), it requires adjustment for lidar scans to conform with varying data quality.

We developed Adaptive Thresholding Segmentation method (ATS) which explicitly separates wake points from the free-flow points in the data set, be it lidar scan, LES cross-section, image etc. [6] This work explores two possible applications of the method: wake centerline detection and wake masking for lidar retrieval.

2 Data and methodology

2.1 Lidar and mast data from FINO1

The regarded data set was obtained during Offshore Boundary-Layer Experiment at FINO1 (OBLEX-F1) campaign. The data set covers September 24 – October 3, 2016, and consists of lidar scans coupled with 10-minute averaged point measurements of wind speed and direction. The point measurements were recorded by vane and cup anemometer installed at FINO1 meteorological mast at 90 m and 100 m above sea level, respectively.

The scanning Doppler wind lidar Leosphere WindCube 100S installed at FINO1 platform was oriented towards the *alpha ventus* wind farm and scanned a sector in the azimuth range of $131.5° - 179.5°$ at the elevation angle of $4.62°$. The lidar finishes one scan in 50 s, approximately. The *alpha ventus* wind farm consists of 12 wind turbines organized in a rectangular pattern. The lidar captured only two turbines, but wakes from other *alpha ventus* turbines could be seen depending on the wind direction.

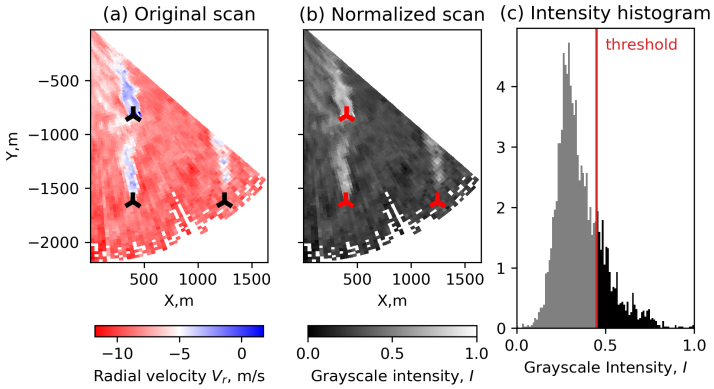


Figure 1: Preparatory steps for the ATS method: from the radial velocity to the intensity histogram

2.2 Methodology

The lidar measures radial velocity V_r (Fig. 1a) – the projection of the actual velocity to the lidar's line of sight as:

$$V_r = u \sin\phi \cos\theta + v \cos\phi \cos\theta + w \sin\theta \tag{1}$$

where u, v, and w are wind speed components, ϕ – azimuth and θ – elevation angle. Since the elevation angle of $\theta = 4.62^\circ$ is small enough to assume $\sin\theta \sim 0$ and $\cos\theta \sim 1$, Eq. (1) is simplified to

$$V_r = u \sin\phi + v \cos\phi \tag{2}$$

The ATS method can operate on either radial or actual velocity since it relies not on the exact values but on their distribution. Wake identification on the actual velocity field requires lidar retrieval to reconstruct the flow field first. Since the lidar retrieval can also benefit from the wake identification via thresholding, we demonstrate the method on the radial velocity, i.e., the original scan.

Before applying the ATS method, a lidar scan is cleaned from the spiked values and large clusters of non-physical velocities above 50 m/s. The radial velocity data is then normalized to the range of $[0,1]$ (Fig. 1b). The normalized field $\mathbf{I}$ can now be represented as an intensity histogram with a peak corresponding to the free-flow points and a tail containing wake points (Fig. 1c). The threshold T is calculated for each scan as described in [6]. The thresholded image is then constructed from a lidar scan as a binary matrix $\mathbf{WP}$:

$$\mathbf{WP}_{i,j} = \begin{cases} 0: & \mathbf{I}_{i,j} \leq T \text{ – free-flow point,} \\ 1: & \mathbf{I}_{i,j} > T \text{ – wake point.} \end{cases} \tag{3}$$

Points labeled as 1 in $\mathbf{WP}$ correspond to low radial velocities and can be used to mask the wakes and occasional noise from the scan (Fig. 2).

3 Results

3.1 Wake centerline detection

The identified wake points are split into groups based on their connectivity (Fig 2c). Large continuous shapes near wind turbine positions are considered wakes. Depending on the scan quality, the shapes capture either near and far wakes (homogeneous flow) or just a near wake (much background noise). Only the low-speed core of the far wake is identified in the best case, as the wake recovers and the wake deficit distribution becomes flatter.

When the wind blows along the wind turbines, the far wake from the upstream turbine may merge with the near wake of the downstream turbine (Fig. 2d). Defining the wake centerline as a series of shape's midpoints would produce an incorrect result. Instead, we select only midpoints along the wake direction. The wake direction is approximated from the wind direction measured at the meteorological mast. This allows estimating the wake centerline in the irregular wake shape.

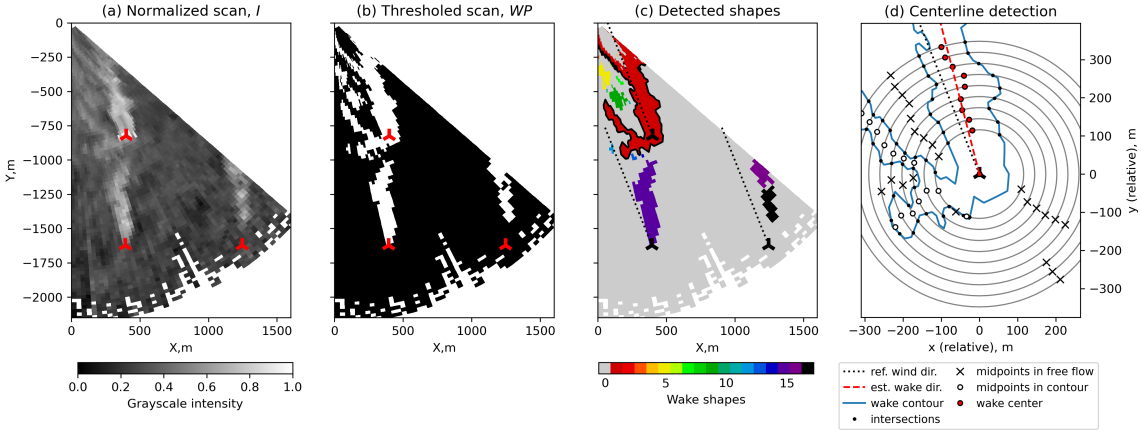


Figure 2: Centerline detection from a thresholded image of merging wakes

3.2 Lidar retrieval of the non-homogeneous flow

Lidar retrieval methods are widely used to reconstruct the actual wind field from the velocity data measured by a lidar. Conventional methods, such as Velocity Azimuth Display (VAR) or Volume Velocity Processing (VVP), are primarily developed for uniform flows and do not correctly interpret strong disturbances, like wakes. The 2D-VAR method was suggested in [7] as a way to process non-homogeneous lidar scans faster than conventional 4D-VAR-based methods while keeping the accuracy of the retrieval.

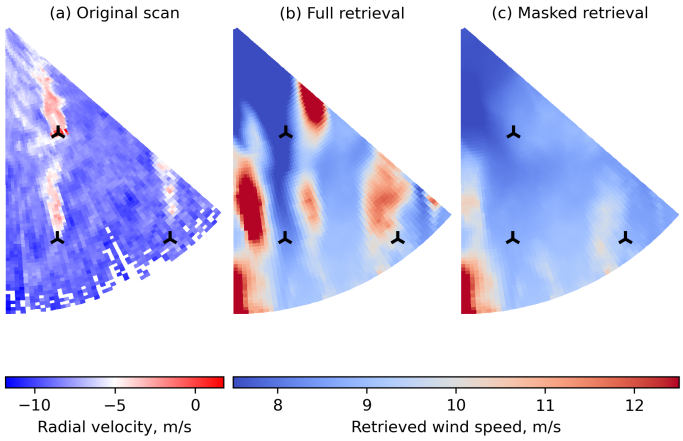


Figure 3: VVP retrieval method applied to the full lidar scan (b) and the same scan with the masked wakes (c)

The 2D-VAR method consists of two steps. First, VVP method is applied to retrieve the homogeneous field. The result is used for the second step to define the wake as the deviation from the free flow. The solution of VVP equations often produces areas of increased wind speed along the wakes (Fig. 3b). The influence of the wakes can be mitigated by excluding the wakes from the VVP processing. Masking the wake points from the thresholded image leaves the free flow to be passed to the VVP method. The homogeneity of the VVP result output (Fig. 3c) benefits the accuracy of the second step. If the retrieved field is converted back to the radial velocity using Eq. (2), the deviations from the original radial velocity are distributed more symmetrically in the VVP masked retrieval than when the VVP method is applied for full data (Fig. 4).

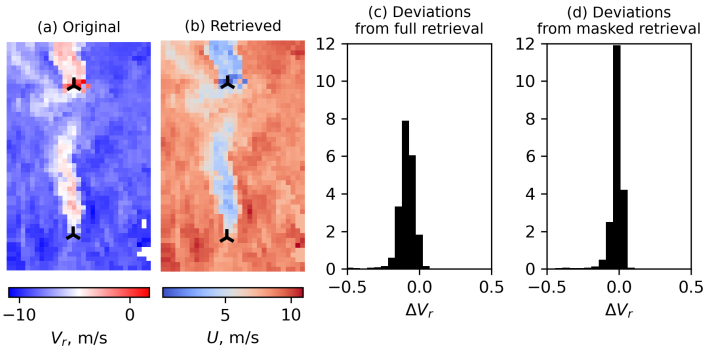


Figure 4: (a-b) Original and 2D-VAR retrieved data, (c-d) deviations between original radial velocity and radial velocity calculated from the retrieved data

4 Conclusion

We showed how lidar scan analysis could benefit from introducing the ATS method into the processing. A thresholded wake allowed mitigating insufficient data resolution and resolving challenging cases of merged wakes when performing wake characterization. The same thresholded wake also effectively acts as a mask and allows processing of the homogeneous free flow. Essentially, masking a wake acts as setting a zero weight to wake points in the VVP retrieval, except that the points were already identified automatically. Due to versatile application, wake identification via thresholding can reduce number of intermediate techniques used in the wake analysis.

Acknowledgements

The OBLEX-F1 field campaign was performed under the Norwegian Centre for Offshore Wind Energy (NORCOWE), funded by the Research Council of Norway (RCN) under project number 193821. The scanning Doppler wind lidar system (Leosphere WindCube 100S) has been made available via the National Norwegian infrastructure project OBLO (Offshore Boundary Layer Observatory) also funded by RCN under project number 227777.

References

[1] E. W. Quon, P. Doubrawa, and M. Debnath. Comparison of Rotor Wake Identification and Characterization Methods for the Analysis of Wake Dynamics and Evolution. In *J. Phys. Conf. Ser.*, volume 1452, page 012070. Institute of Physics Publishing, jan 2020.

[2] L. Vollmer, G. Steinfeld, D. Heinemann, and M. Kühn. Estimating the wake deflection downstream of a wind turbine in different atmospheric stabilities: An LES study. *Wind Energy Sci. Discuss.*, pages 1–23, mar 2016.

[3] R. Krishnamurthy, J. Reuder, B. Svardal, H.J.S. J.S. Fernando, and J.B. B. Jakobsen. Offshore Wind Turbine Wake characteristics using Scanning Doppler Lidar. *Energy Procedia*, 137:428–442, oct 2017.

[4] G. España, S. Aubrun, S. Loyer, and P. Devinant. Spatial study of the wake meandering using modelled wind turbines in a wind tunnel. *Wind Energy*, 14(7):923–937, oct 2011.

[5] D. Bastine, B. Witha, M. Wächter, and J. Peinke. Towards a Simplified DynamicWake Model Using POD Analysis. *Energies*, 8(2):895–920, jan 2015.

[6] M. Krutova, M. Bakhoday-Paskyabi, J. Reuder, and F. G. Nielsen. Development of an automatic thresholding method for wake meandering studies and its application to the data set from scanning wind lidar. *Wind Energy Sci.*, 7(2):849–873, apr 2022.

[7] N. W. Cherukuru, R. Calhoun, R. Krishnamurthy, S. Benny, J. Reuder, and M. Flügge. 2D VAR single Doppler lidar vector retrieval and its application in offshore wind energy. *Energy Procedia*, 137:497–504, 2017.

18th EAWE PhD Seminar on Wind Energy
2-4 November 2022
Bruges, Belgium

Calibrating the actuator line model in the large eddy simulation solver YALES2

Anand Parinam[a,b], **Pierre Benard**[b], **Dominic Von Terzi**[a], and **Axelle Viré**[a]

[a]TU Delft, Netherlands
[b]CORIA-CNRS, Rouen, France

E-mail: A.parinam@tudelft.nl

Keywords: Actuator Line Model, NREL 5MW, Wake flow study, CFD, LES

Introduction

Large Eddy Simulation (LES) is an accepted high-fidelity research tool to study unsteady phenomena in turbulent flows. One example is the understanding of the unsteady dynamics of large coherent structures in wind turbine wakes under different atmospheric conditions. There are many different techniques for analysing the flow over wind turbines: BEM, free-wake vortex models, actuator disk, line & surface methods, blade-resolved CFD techniques. Apart from a fully blade resolved rotor, the actuator line method of [5] is currently the most advanced rotor model. The trade-off between accuracy and computational cost makes ALM a very valuable model for fundamental studies of the flow.

In this research, the YALES2 platform is used [4]. YALES2 is a 4th order LES code with unstructured grid support. The presented research focuses on the calibration of the Actuator Line Model [1] in YALES2 and its cross-validation with state-of-the-art solvers in the literature.

Methodology

The reference wind turbine used in this case is the NREL 5MW which is a very well validated turbine with extensive existing literature. Validation of the code is performed by comparing the results with other LES codes namely SOWFA by NREL, SP-WIND by KU Leuven, EllipSYS3D by DTU and LESGO by JHU, using physical conditions as used by M.Tossaz et al. [2]. The LES-Smagorinsky model with a sub-grid scale filtering constant coefficient, $C_s = 0.16$ has been used. The rotor blade modeled by actuator line are discretized in the spanwise direction into 64 points. The sensitivity analysis of the factor that controls the smearing of forces computed at actuator points in actuator line over the fluid flow mesh called 'the Mollification Factors (MF)'[3] has been performed using three different values: $MF = \frac{\varepsilon}{\Delta x} = 2$, 3.5, and 5.08, where ε is mollification kernel width and Δx the mesh width.

The schematic of standard test case for NREL 5MW wind turbine with a $126m$ rotor diameter, simulated in the LES code is presented in figure 1. The boundary conditions for all the walls except the inlet and outlet are periodic. The domain is discretized using a structured grid resolution $\Delta/D = 0.015625$ in all three x, y and z directions. Uniform inflow conditions without turbulence has been used.The simulations were run for two flow-through times to give the wake time to develop, and then statistics were accumulated for 3 flow-through times.

Results

The results for streamwise variation of the mean velocities contours are presented in the figure 2, mean velocity and the Reynolds stress profiles at different downstream locations in the wakes are presented in the figure 3 and 4 respectively. It can be seen that the inflow is completely laminar and inviscid until turbulence is set off. There is a slight difference in the split streams for all codes which may be due to the numerical schemes. In the near wake region, all codes show similar variation in mean velocity due to lack of turbulence. In the far wake region,

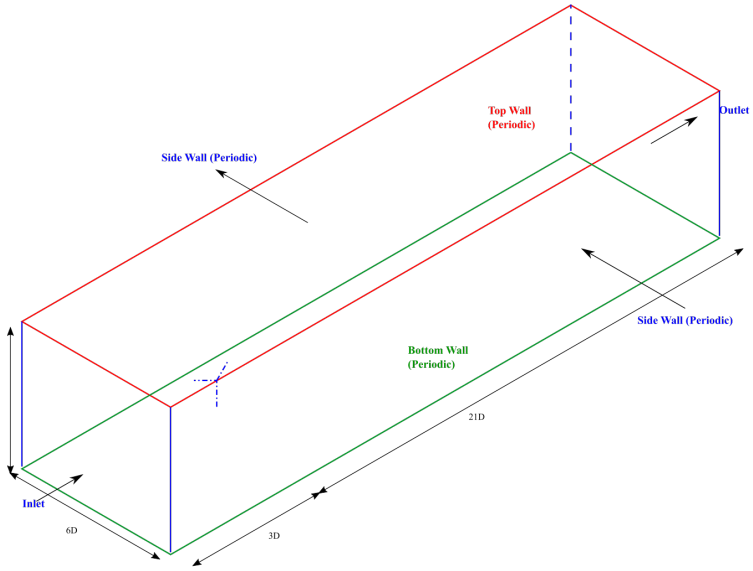


Figure 1: Flow Domain

all the codes show a transition to turbulence between 9D to 15D. The delay in transition to turbulence depends on the precision of the numerical discretization scheme. The spreading of the wake in the very far wake region is different which depends on the numerical turbulent dispersion. Despite very slight numerical dispersions, the results predicted by YALES2 are very well in line with the four other LES codes. This gave a confidence in the YALES2 solver and benchmarked it numerically to be able to use for further analysis of NREL 5MW and other wind turbine simulations.

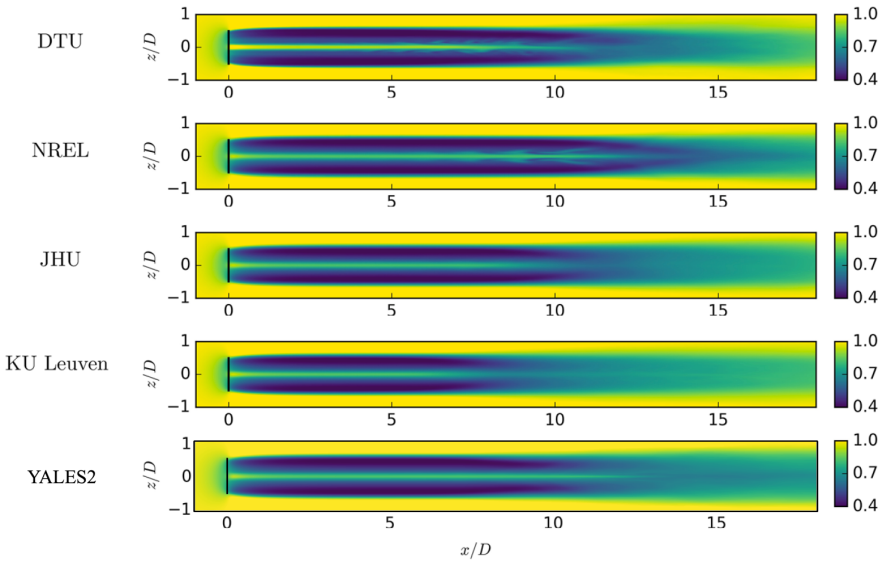


Figure 2: Mean velocity contours on X-plane for different LES codes

Figure 5 and 6 show the sensitivity of wake resolution to the parameter $\frac{\epsilon}{\Delta x}$ using the isocontour of Q-Criterion and Vorticity plane respectively. The results show that by decreasing the MF, the resolution of the numerical simulation can be significantly improved. In the case of higher MF, the breakdown of vortices is delayed hence the transition to turbulence too.

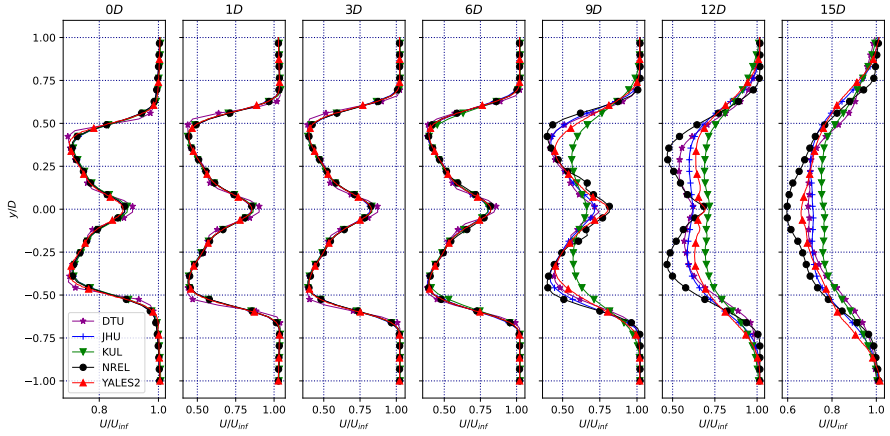


Figure 3: Evolution of the mean velocity as a function of height, for different distances downstream of the rotor (from 0D to 15D downstream). Results obtained with YALES2 (triangle symbol) are compared to those of 4 state-of-the-art LES codes.

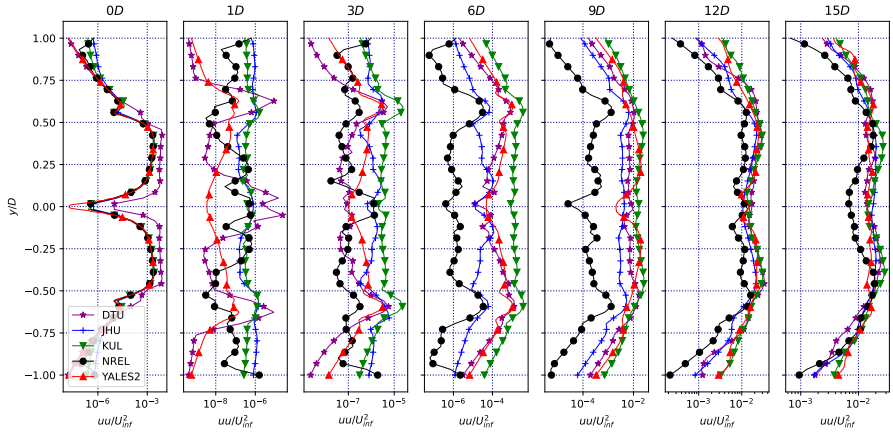


Figure 4: Evolution of the Reynolds stress tensor as a function of height, for different distances downstream of the rotor (from 0D to 15D downstream). Results obtained with YALES2 (triangle symbol) are compared to those of 4 state-of-the-art LES codes.

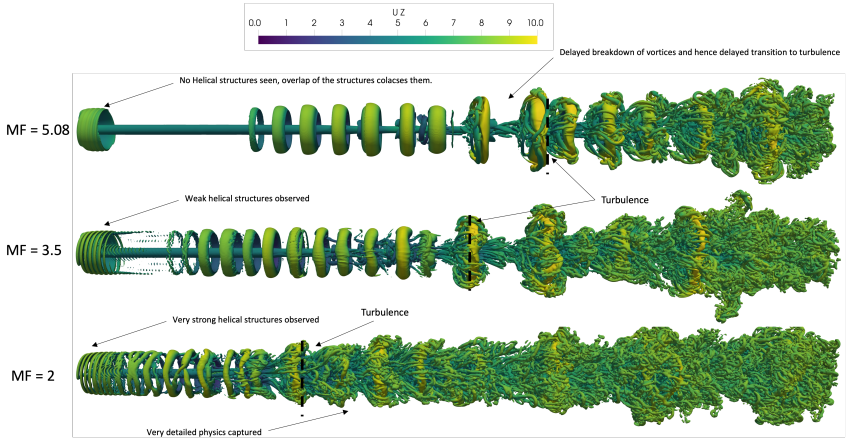


Figure 5: Q-Criterion contours on X-plane to for different mollification factors on wind turbine wakes

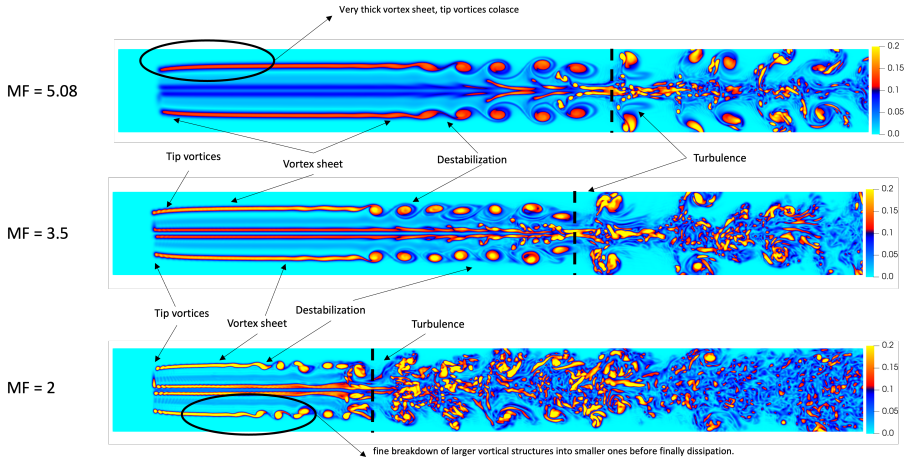


Figure 6: Vorticity contours on X-plane to for different mollification factors on wind turbine wakes

Conclusions and future work

This research numerically validated the Actuator Line Model in the YALES2 solver and benchmarked it against other LES codes. The study involving the effect of the turbulence model and mollification factor gave an insight into understanding the sensitivity of flow around wind turbines to these parameters. It also provided guidelines on which values of mollification factor are more suitable to capture very detailed physics. This will enable to extend the present research to extend the current capabilities of YALES2 to include Fluid-Structure interaction by coupling with a servo-elastic solver to examine the effect of rigidity of blades. This study can also be extended to larger turbines like the IEA 15 MW turbine.

Acknowledgements

Simulations have been performed using computational resources at TU Delft. This research has been supported jointly by TU Delft, Netherlands and Région Normandy, France.

References

[1] P. Benard, A. Viré, V. Moureau, G. Lartigue, L. Beaudet, P. Deglaire, and L. Bricteux. Large-eddy simulation of wind turbines wakes including geometrical effects. *Computers Fluids*, 173:133–139, 2018.

[2] L. A. Martinez-Tossas, M. J. Churchfield, A. E. Yilmaz, H. Sarlak, P. L. Johnson, J. N. Sorensen, J. Meyers, and C. Meneveau. Comparison of four large-eddy simulation research codes and effects of model coefficient and inflow turbulence in actuator-line-based wind turbine modeling. *Journal of Renewable and Sustainable Energy*, 10(3), 5 2018.

[3] L. A. Martínez-Tossas, M. J. Churchfield, and C. Meneveau. Optimal smoothing length scale for actuator line models of wind turbine blades based on gaussian body force distribution. *Wind Energy*, 20(6):1083–1096, 2017.

[4] V. Moureau, P. Domingo, and L. Vervisch. Design of a massively parallel cfd code for complex geometries. *Comptes Rendus Mécanique*, 339(2):141–148, 2011. High Performance Computing.

[5] J. N. Sorensen and W. Z. Shen. Numerical Modeling of Wind Turbine Wakes . *Journal of Fluids Engineering*, 124(2):393–399, 05 2002.

18th EAWE PhD Seminar on Wind Energy
2-4 November 2022
Bruges, Belgium

Comparison of generalized actuator disk and actuator line wind turbine models for varying atmospheric conditions

Baris Kale[a,b], **Sophia Buckingham**[a], **Jeroen van Beeck**[b], and **Alvaro Cuerva-Tejero**[b]

[a]von Karman Institute for Fluid Dynamics, Chaussée de Waterloo, 72, 1640, Rhode-St-Genèse, Belgium
[b]DAVE/UPM, E.T.S.I. Aeronáutica y del Espacio, Universidad Politécnica de Madrid, E-28040 Madrid, Spain

E-mail: baris.kale@vki.ac.be

Keywords: ABL, WRF, LES, wind turbine aerodynamics, generalized actuator disk, generalized actuator line

Introductory Summary

In this study, the aerodynamic performance and the wake characteristics of a wind turbine have been evaluated using generalized actuator disk (GAD) and actuator line (GAL) models. These two wind turbine models are implemented into a Numerical Weather Prediction (NWP) model (e.g., the Weather Prediction and Forecasting (WRF) model [1]) to perform high-fidelity large-eddy simulations (LESs) of wind energy applications. Results have been compared with the experimental and other available LES data obtained at the Scaled Wind Farm Technology (SWiFT) campaign, reported in a recent work by Doubrawa *et al.* [2]

1 Introduction

In the last decades, numerical simulations of atmospheric boundary layer (ABL) flows have gained popularity in the wind energy field thanks to today's computational resources and the existence of reliable wind turbine parameterizations. Although these numerical algorithms do not fully resolve the wind turbine rotor blade motion, they implicitly parameterize, in simplified way, the air flow-wind turbine interaction, based on momentum exchange. This is a complex dynamic phenomenon and requires a highly-resolved flow field around the blade in order to properly represent the aerodynamic forces exerted by rotor blades in the ABL flow. Therefore, wind turbine actuator schemes are often used for wind turbine wake modeling in LES. [3, 4]

Table 1: Simulated inflow conditions of each benchmark determined at the SWiFT facility [2].

Case study	U_{hub} [m s^{-1}]	$TI_{hub} = \sigma_u/U_{hub}$ [%]	$\zeta = z/L$ [-]	u_* [m s^{-1}]	$Q_s = (\overline{w'\theta'_v})_s$ [K m s^{-1}]
Neutral	8.7	10.7	0.004	0.45	−0.002
Unstable	6.7	12.6	−0.089	0.33	0.023
Stable	4.8	3.4	1.151	0.08	−0.005

Note. Mean horizontal wind speed and turbulence intensity were obtained at hub height, that is 32.1 m, while stability parameter and friction velocity were obtained at 10 m. Near-surface kinematic heat flux was measured at 2 m. U_{hub} is the mean horizontal wind speed at hub height at free-stream, that is 65 m upstream of the wind turbine, $TI_{hub} = \sigma_u/U_{hub}$ is the turbulence intensity at hub height, $\zeta = z/L$ is the stability parameter measured at height z, $L = -u_*^3\theta/\kappa g(\overline{w'\theta'_v})_s$ is the Obukhov length, $u_* = [\overline{u'w'}^2 + \overline{v'w'}^2]^{1/4}$ is the friction velocity, $\kappa = 0.4$ is the von Kármán constant, $g = 9.81$ m s^{-1} is the gravitational acceleration, $Q_s = (\overline{w'\theta'_v})_s$ is the near-surface kinematic heat flux, u', v', and w' are the fluctuating velocity components in the x, y, and z directions, respectively. θ'_v is the perturbation virtual potential temperature. The $\overline{(\cdot)}$ refers to the temporal average of the quantity of interest.

The ABL flows are driven by atmospheric events such as large-scale weather phenomena or weather-producing disturbances, which are non-stationary and turbulent in many cases. In this context, canonical Computational Fluid Dynamics (CFD) codes can hardly satisfy the need for realistic turbulent inflows required by wind turbine models. NWP models are usually preferable due to the capability of solving prognostic flow equations of atmosphere physics in the Reynolds-Averaged Navier-Stokes (RANS) form. A coupling algorithm between RANS and LES is necessary to model wind turbines in a multi-scale environment, the large range of scales involved the the problem, from the larger scales of the atmospheric flows to the smaller scales of the flow in the proximity of the blade airfoils. Though the WRF-LES model is able to simulate inter-scale ABL flow by downscaling turbulence from larger scales to wind turbine scales, an implicit algorithm is still necessary to represent wind turbine aerodynamics. For that reason, the GAD and GAL models have been implemented into the WRF-LES framework and validated against field measurements and results from other available LES codes, in the framework of the Scaled Wind Farm Technology (SWiFT) campaign, where a V27 Vestas wind turbine was tested under different atmospheric stability conditions.

2 Methodology

The most common approach for the modeling of wind turbine wakes is the generalized actuator disk model, in which the aerodynamic forces are computed on several radial lines that are representative of the wind turbine rotor disk [5]. In the GAD model, flow rotation is taken into account by adding a torque-creating force component and the flow velocity component relative to the actuator points originated by the blade rotation. Conversely, the generalized actuator line model can reproduce the wind turbine's blade rotation, giving more reliable results than the GAD, as the blade position is tracked at each time step.

In the present analysis, the vorticity field is computed to visualize differences between the GAD and GAL models, as well as nacelle and tower effects (hereinafter referred to as structure effects). There are no field measurements available for vorticity, thus WRF-LES, with both actuator models, are compared to each other. Figure 1

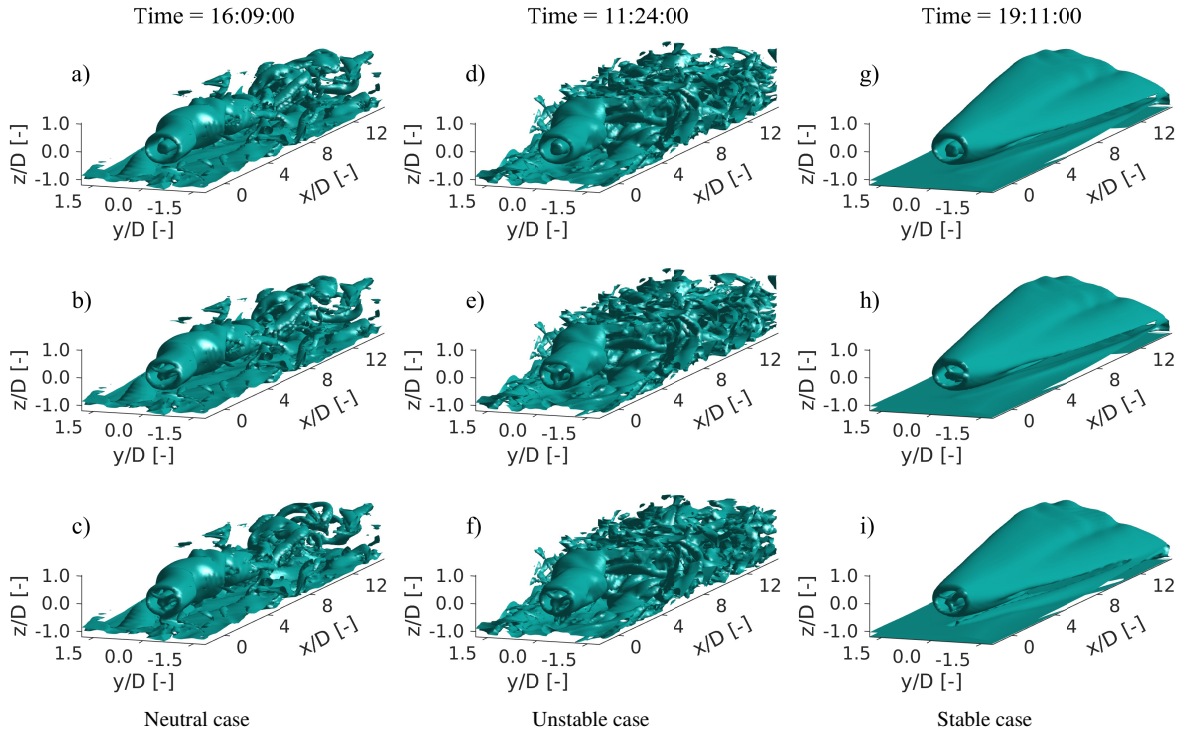


Figure 1: Instantaneous three-dimensional isosurface of the magnitude of total vorticity (ω) for the neutral GAD (a), GAL (b) and GAL with structure (c), unstable GAD (d), GAL (e), and GAL with structure (f), and stable GAD (g), GAL (h), and GAL with structure (i) simulations. The neutral, unstable and stable isosurfaces are plotted by using the isovalues of 0.6, 0.4, and 0.3, respectively.

shows the instantaneous three-dimensional isosurfaces of the magnitude of vorticity, given as

$$||\omega|| = \sqrt{\left(\frac{\partial \widetilde{w}}{\partial y} - \frac{\partial \widetilde{v}}{\partial z}\right)^2 + \left(\frac{\partial \widetilde{u}}{\partial z} - \frac{\partial \widetilde{w}}{\partial x}\right)^2 + \left(\frac{\partial \widetilde{v}}{\partial x} - \frac{\partial \widetilde{u}}{\partial y}\right)^2}. \quad (1)$$

In Equation 1, $\widetilde{u}, \widetilde{v}, \widetilde{w}$ denote filtered velocity components in the x, y, z directions, respectively.

Numerical simulations presented in this work consider a total simulation time of 1 h and 10 min with a time step of 0.0208 s. Output was collected every 1 min and the first ten minutes of the WRF-LES-GAD/GAL simulations was discarded in data processing. The WRF model applies an online nesting strategy, which enables downscaling turbulence from larger scales to the smaller scales. The coarser domain is run for several hours to ensure that turbulence in the finer domain is well developed and the numerical solution comes into balance with the applied geostrophic wind vector (i.e., spin-up or online pre-cursor simulation). Spin-up time for the neutral, unstable, and stable conditions are as follows: 15 h, 10 h, and 19 h for the neutral, unstable, and stable cases, respectively. Regardless of spin-up runs, WRF-LES simulations of neutral and unstable cases, including the GAD and GAL wind turbine models, took approximately 18 hours of wall-clock time, whereas the stable case took about 15 hours using 64 processors on a high-performance computing cluster. Simulated inflow conditions for neutral, unstable,

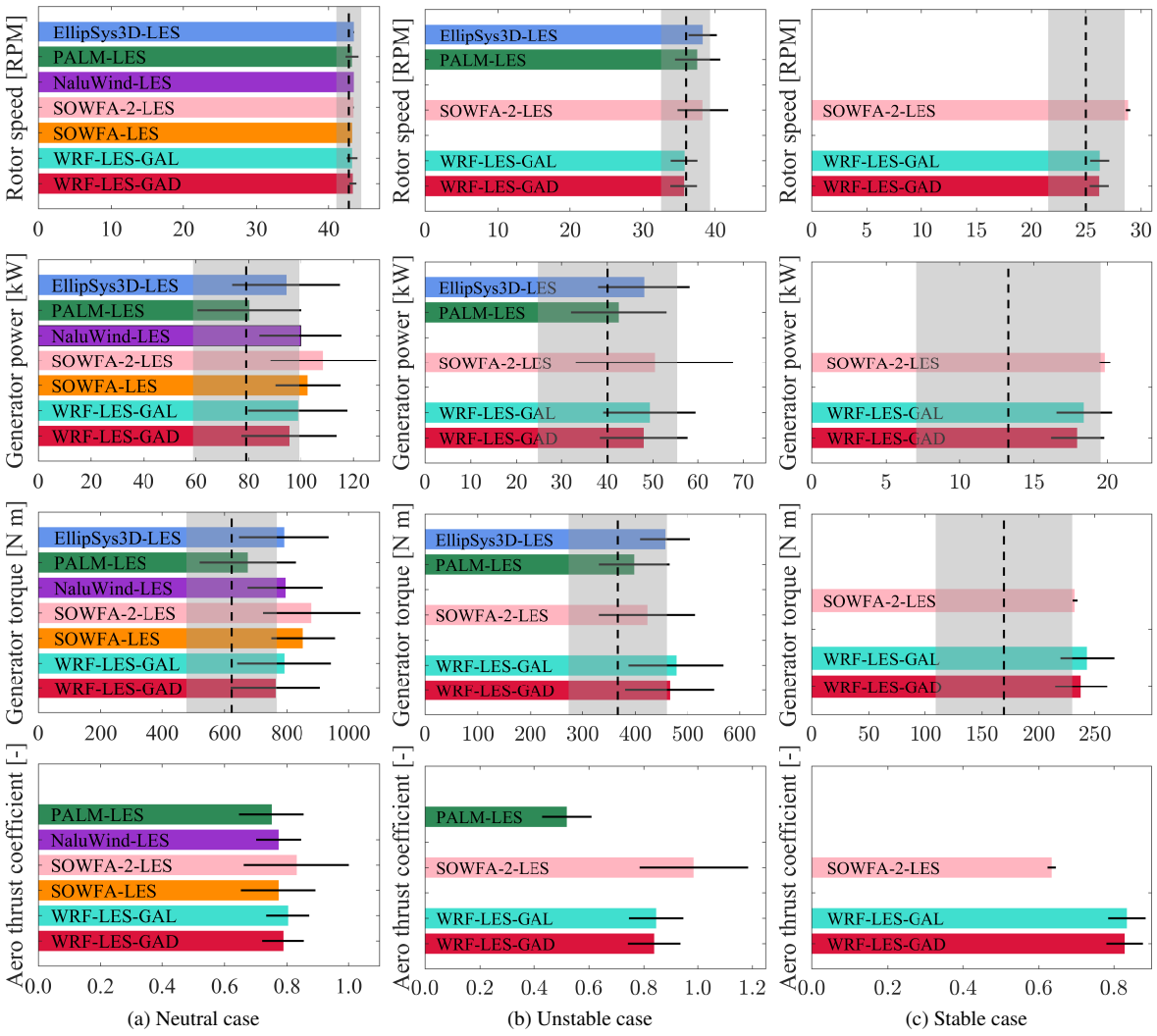


Figure 2: Comparison of mean and standard deviations of rotor speed, generator power, generator torque, and aerodynamic thrust coefficient, for different atmospheric conditions. Vertical black dashed lines show the mean of measurements whereas gray shaded regions represent the mean $\pm$ standard deviation interval. Colored horizontal bars show simulation results and black horizontal lines depict the mean $\pm$ standard deviation.

and stable conditions are summarized in Table 1. For details, see the study by Kale *et al.* [4]

3 Results and discussions

In this work, the performance of Vestas V27 has been evaluated using the GAD and GAL models under neutral, unstable and stable ABL conditions. In order to compare actuator models along with structure effects, a three-dimensional vorticity field is presented in Figure 1 for varying atmospheric conditions. In stable conditions, wake is stretched in the lateral direction because of wind veer and is longer due to lower turbulence levels. Although the difference between the GAD and GAL models is discernible in the rotor plane (the GAL model is able to capture the vorticity structure around the three blades), no significant impact was observed either in the near-field or far-field in all cases. Moreover, root and tip vortices, as well as nacelle effects, are not clearly visible, yet a wake signature behind the tower is barely distinguishable in the GAL model simulations. This might be due to the grid resolution that is the same for all cases ($\Delta x = \Delta y = 2$ m, and $\Delta z \approx 2$ m), and supports the necessity of a finer spatial resolution required by the GAL scheme.
The WRF-LES-GAD/GAL results for rotor speed, generator power, generator torque and aerodynamic thrust coefficient are presented in Figure 2. The effect of the structure has not been considered in the simulations. The results have been compared with experimental data and results from other available LES codes that use different implementations of the actuator line model. [2] For all cases, the WRF-LES-GAD/GAL models, without structure effects, perform as good as other LES codes and lay in the interval defined by the mean $\pm$ standard deviations of the experimental results. The difference between WRF-LES-GAD and WRF-LES-GAL models is small. Maximum deviation is observed under neutral conditions probably due to higher mean hub height wind speed and turbulence levels.

Acknowledgements

This research has been performed using computational resources of the von Karman Institute for Fluid Dynamics and has received funding from the European Union's Horizon 2020 research and innovation programme under the Marie Skłodowska-Curie project *zEPHYR: Towards a more efficient exploitation of on-shore and urban wind energy resources*, with grant agreement No 860101.

References

[1] William C Skamarock and Joseph B Klemp. A time-split nonhydrostatic atmospheric model for weather research and forecasting applications. *Journal of computational physics*, 227(7):3465–3485, 2008.

[2] Paula Doubrawa, Eliot W Quon, Luis A Martinez-Tossas, Kelsey Shaler, Mithu Debnath, Nicholas Hamilton, Thomas G Herges, Dave Maniaci, Christopher L Kelley, Alan S Hsieh, et al. Multimodel validation of single wakes in neutral and stratified atmospheric conditions. *Wind Energy*, 23(11):2027–2055, 2020.

[3] Richard JAM Stevens, Luis A Martínez-Tossas, and Charles Meneveau. Comparison of wind farm large eddy simulations using actuator disk and actuator line models with wind tunnel experiments. *Renewable energy*, 116:470–478, 2018.

[4] Baris Kale, Sophia Buckingham, Jeroen van Beeck, and Alvaro Cuerva-Tejero. Implementation of a generalized actuator disk model into wrf v4.3: A validation study for a real-scale wind turbine. *Renewable Energy*, 197:810–827, 2022.

[5] Jens Norkær Sorensen and Wen Zhong Shen. Numerical modeling of wind turbine wakes. *J. Fluids Eng.*, 124(2):393–399, 2002.

18th EAWE PhD Seminar on Wind Energy
2-4 November 2022
Bruges, Belgium

Coupling an atmospheric perturbation model to a wake-merging method to include meso-scale perturbations

Koen Devesse[a] and **Johan Meyers**[a]

[a]Department of Mechanical Engineering, KU Leuven, Leuven, Belgium

E-mail: koen.devesse@kuleuven.be

Keywords: Meso-micro Coupling, Gravity Waves, Atmospheric Boundary Layer, Engineering Wake Model

Recent research suggests that wind farms can trigger atmospheric gravity waves, which reduce the upstream flow velocity and the power output of a wind farm. Based on earlier work by Smith (2010), Allaerts and Meyers (2019) proposed a simplified Atmospheric Perturbation Model (APM) focused on the interaction between wind turbines and gravity waves [5, 1]. While the model is not as accurate and flexible in use as eg. Large-Eddy Simulations (LES) or Reynolds-Averaged Navier-Stokes (RANS) methods, it is far less computationally demanding.

As a meso-scale model, the APM does not have the resolution required to simulate turbine wakes within the farm. To predict wind farm performance, it is coupled to engineering wake models. In previous work, the model was coupled to a basic Gaussian wake model that assumes a constant background velocity throughout the farm [2, 4]. In this work, we couple the APM to a new wake merging approach that allows for velocity gradients [3]. Several approaches to this coupling are proposed, and a numerical analysis is performed. Figure shows the APM velocity for a reference flow case, and the background velocity perturbation that is the corresponding input to the wake merging method. Importantly, we identify parametrization issues that arise, and propose validation approaches using LES data.

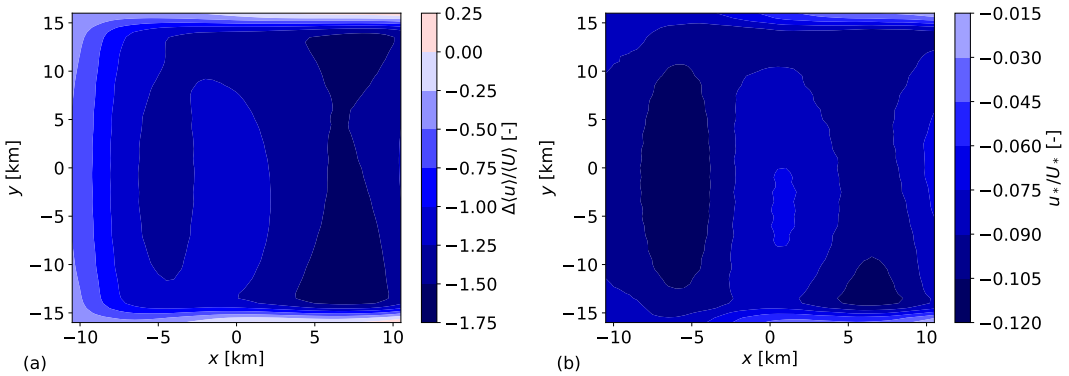


Figure 1: (a) APM velocity field throughout a wind farm. (b) Corresponding background friction velocity perturbation throughout a wind farm.

References

[1] D. Allaerts and J. Meyers. Sensitivity and feedback of wind-farm-induced gravity waves. *Journal of Fluid Mechanics*, 862:990–1028, 2019.

[2] M. Bastankhah and F. Porté-Agel. A new analytical model for wind-turbine wakes. *Renewable Energy*, 70:116–123, 2014.

[3] L. Lanzilao and J. Meyers. A new wake-merging method for wind-farm power prediction in the presence of heterogeneous background velocity fields. *Wind Energy*, 2021.

[4] A. Niayifar and F. Porté-Agel. Analytical Modeling of Wind Farms: A New Approach for Power Prediction. *Energies*, 9(9):741, sep 2016.

[5] R. B. Smith. Gravity wave effects on wind farm efficiency. *Wind Energy*, 13(5):449–458, 2010.

18th EAWE PhD Seminar on Wind Energy
2 – 4 November 2022
Bruges, Belgium

Coupling of a dynamic wake model with WRF: a case study of the Belgian wind farms

B Foloppe[a], W Munters[a], S Buckingham[a], L Vandevelde[b], J van Beeck[a]

[a] Environmental and Applied fluid dynamics Department, von Karman Institute for Fluid Dynamics, Belgium
[b] Electromechanical, Systems and Metal Engineering Department, Ghent University, Belgium

E-mail: benoit.foloppe@vki.ac.be

Keywords: FLORIS, dynamic wake model, WRF, wind farm, power forecast

Over the last decade, the size and the number of offshore wind turbines and wind farms are constantly increasing and ongoing projects show that this will continue. With tip height often above 200 meters, currently installed wind turbines are interacting and impacting massively the atmospheric boundary layer. Therefore, a new dynamic wake model that considers weather transient inputs has been developed [1] and coupled with a mesoscale weather prediction model in order to account for wake advection delays and mesoscale wind transients at the turbine level. In this context, the wind farm model is taking into account the unsteadiness of the background flow field. The Flow Redirection and Induction in Steady State (FLORIS) framework has been proven to be an easy to use, easy to tune, computationally inexpensive and powerful wake modelling tool even though lacking dynamical effects. Therefore, the extension of the FLORIS framework, named UFLORIS is including wake advection delays between wind turbines, time-varying and spatially heterogeneous wind conditions. The so-called Observation Points (OPs) are generated at the rotor centre location and, following a Lagrangian approach, the OPs are convected downstream, along the wake of the wind turbine, defining the wake centreline. It is during this process that the dynamics of wind turbine wake and background flow field unsteadiness are included.

To apply this new model, a wind farm power forecast is done over the Belgian cluster. As shown in Figure 1, the methodology is made of two steps. The first step is a numerical simulation with a large domain (D1) centred on the Belgian wind farms. It is performed with the Weather Research and Forecasting [2] (WRF) model using the Fitch parametrization [3] to represent the wind farm. The second step is a UFLORIS simulation using weather inputs at boundaries of the smallest domain (D4) of the WRF-Fitch simulation. A wind farm power comparison is made between the Fitch parametrization, FLORIS in quasi-steady mode and UFLORIS. The added value of FLORIS and UFLORIS strongly depend on the resolution of the WRF-Fitch run, i.e. whether it has one or multiple turbines within a single grid cell. However, UFLORIS is globally giving a more detailed view into turbine-specific power. The comparison with the data from the Belgian Transmission System Operator ELIA is also discussed.

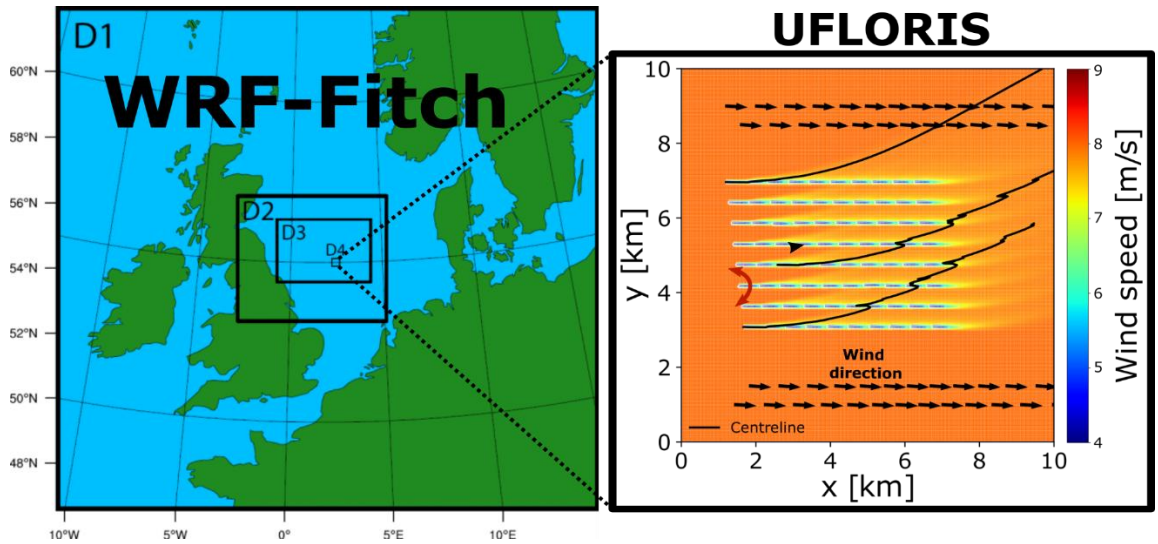


Figure 1: Illustration of the methodology: the WRF-Fitch simulation results at the boundaries of D4 are given as inputs to the UFLORIS simulation.

Acknowledgements

The authors acknowledge support from the PhairywinD project, funded by the Energy Transition Fund of the Belgian Federal Public Service for Economy, SMEs, Self-employed and Energy (FPS Economy).

References

[1] B. Foloppe, W Munters, S Buckingham, L Vandevelde and J van Beeck. Development of a dynamic wake model accounting for wake advection delays and mesoscale wind transients. *Journal of Physics: Conference Series,* 2265 022055, 2022

[2] W. C. Skamarock, J. B. Klemp, J. Dudhia, D. O. Gill, D. M. Barker, M. G. Duda, X. -Y. Huang, W. Wang and J. G. Powers. A Description of the Advanced Research WRF Version 3. *NCAR Technical Note* 2008

[3] A. C. Fitch, J. B. Olson, J. K. Lundquist, J. Dudhia, A. K. Gupta, J. Michalakes and I. Barstad. Local and Mesoscale Impacts of Wind Farms as Parameterized in a Mesoscale NWP Model. *Monthly Weather Review*, 140, 3017–3038, 2012

18th EAWE PhD Seminar on Wind Energy
2-4 November 2022
Bruges, Belgium

Development of a load surrogate model based on rotor-equivalent inflow quantities

Adrien Guilloré, **Filippo Campagnolo**, and **Carlo L. Bottasso**

Wind Energy Institute, Technical University of Munich, Garching, Germany

August 18, 2022

E-mail: adrien.guillore@tum.de

Keywords: Wind turbine loads, load surrogate model; inflow quantities; load-aware wind farm control

Introduction

In the last recent years, wind farm control has demonstrated its important potential to increase power capture [12, 5]. But large uncertainties remain on its effect on the loads, which was listed as a further research need [12]. Predicting turbine fatigue, using Damage Equivalent Loads (DELs), require computationally expensive aero-servo-elastic simulations, making it impractical to include in real-time control or in offline set-point optimizations [11]. The development of load surrogate models is thus of current interest as it could allow to tackle these challenges. Various approaches have been proposed, varying by the necessary inputs to be know for the surrogate models. Most often, a farm-level approach is taken [4, 8, 11, 3, 10]. This current work proposes to develop a load surrogate model based solely on local rotor-equivalent inflow quantities (REIQs) of each individual turbines. If it can be shown to be accurate enough, it is believed that this could lead to larger applicability (turbine model-specific but location-agnostic), as the trained surrogate model could be applied to any turbine regardless of its position in the farm or others unknown quantities on the local turbine-level (ambiant atmospheric conditions, wake interactions, local terrain specificity, etc.). The research objective of this work is to determine whether the knowledge of local REIQs is sufficient to accurately predict various DELs, and whether such a trained surrogate model can capture trends of DELs variation that were not included in its own training.

Methodology

1358 turbulent aero-servo-elastic simulations (each case averaging 6 10-min turbulent seeds generated using the Kaimal model on TurbSim [6]) have been run using three IEA 3.35MW reference wind turbines [2] on the FAST.Farm code [7], in order to create a training and validation dataset linking the REIQs to the DELs (4074 independent cases in total). The cases that were run vary the ambiant wind speed, turbulence intensity, wind direction, vertical shear, turbine spacing and yaw misalignments. The REIQs that are considered, from [9, 1], are:

- Rotor-equivalent wind speed (REWS): average wind speed over the rotor and simulation time.
- Rotor-equivalent turbulence intensity (RETI): standard deviation of the REWS time-series divided by its mean value.
- Rotor-equivalent vertical shear (REVS): vertical shear exponent (modeled as a power law).
- Rotor-equivalent horizontal shear (REHS): horizontal shear coefficient (modeled as a linear function).
- γ: yaw misalignement angle.

Figure 1 illustrates the methodology adopted to extract the REIQs in the FAST.Farm simulations. For application, one can think of using steady flow models or real-time flow estimators [9, 1]. A subset of the built dataset is used to train an artificial neural network, relating the REIQs to the DELs, as illustrated on figures 2 and 3.

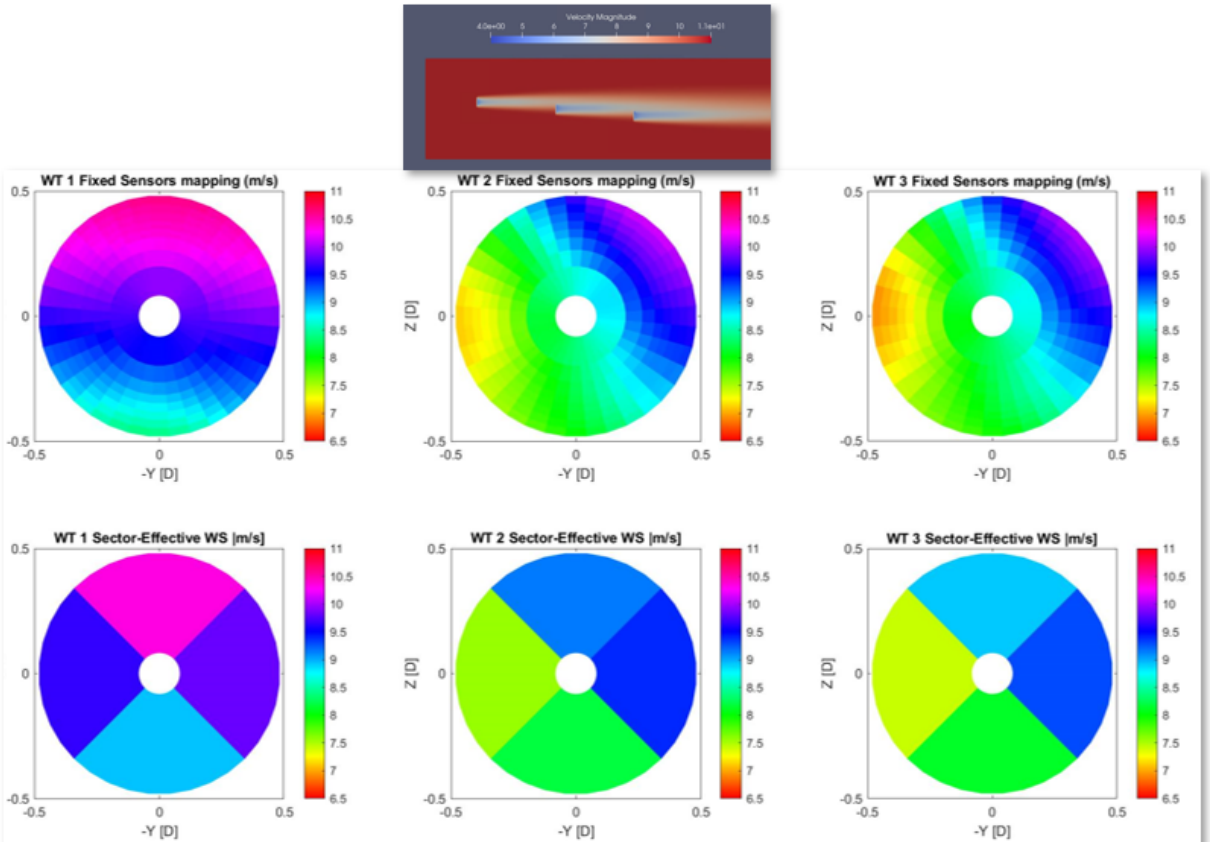


Figure 1: Illustration of the simulation set-up and the procedure to obtain the desired rotor-equivalent inflow quantities from virtual sensors using the sector-effective methodology [9]. The illustrated case has average ambiant wind speed of $9.8 m/s$, TI 6%, spacing 6D and wind direction $+5°$.

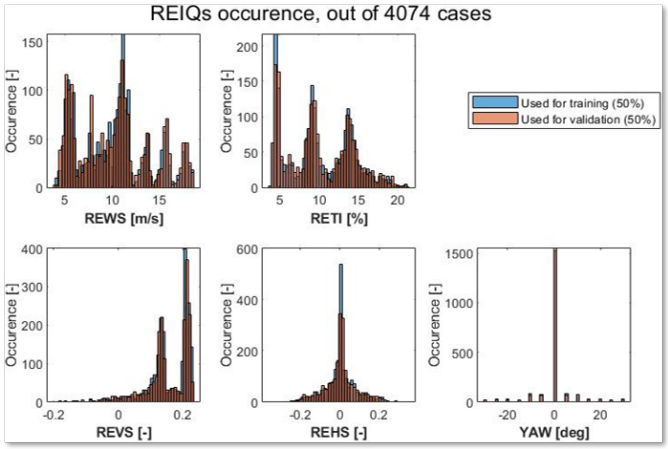


Figure 2: Obtained distribution of the REIQs.

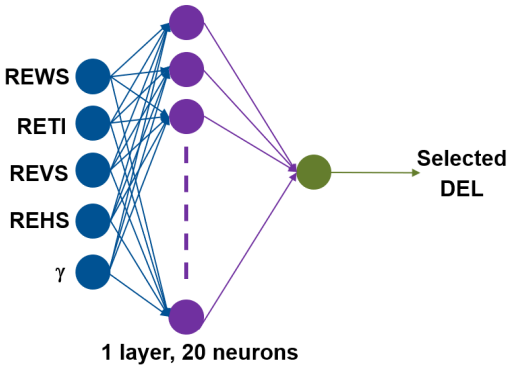


Figure 3: Illustration of the trained neural network.

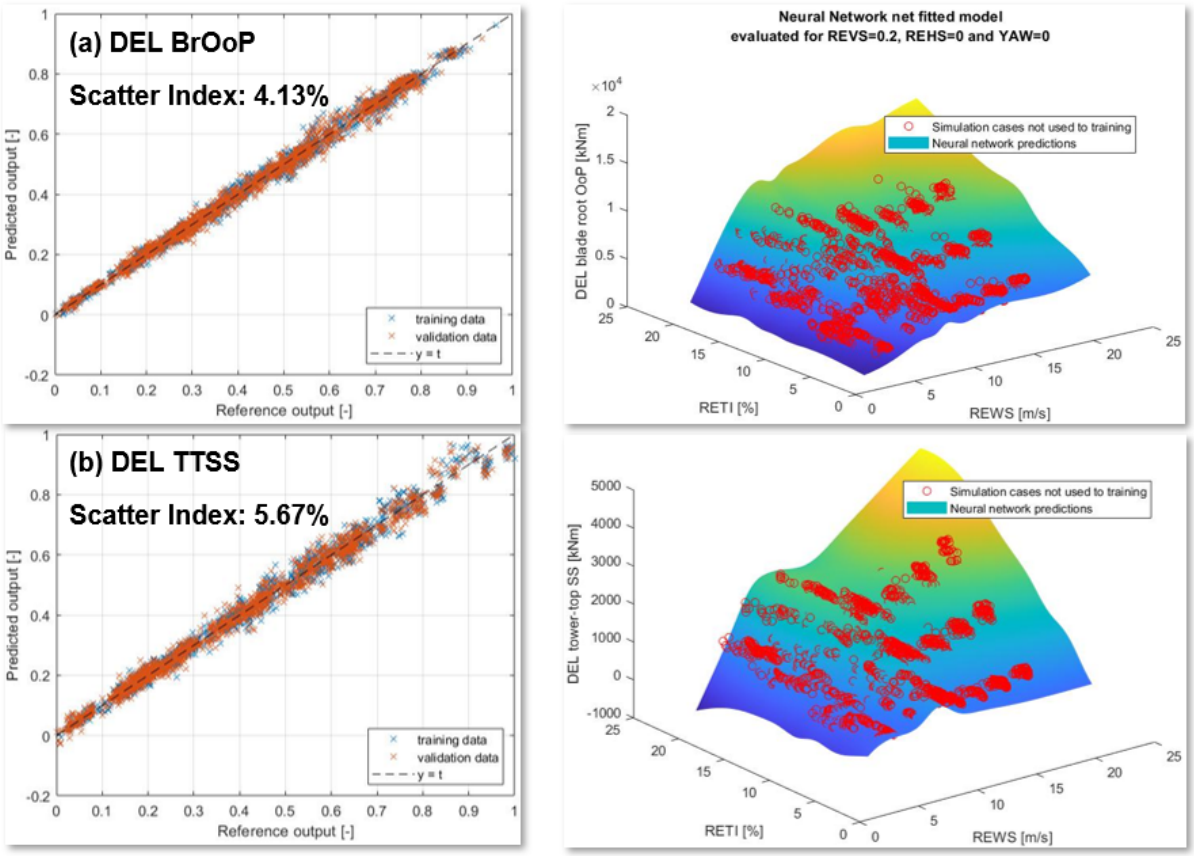


Figure 4: Left: predictions of the load surrogate model compared to reference values for the blade root out-of-plane DEL (BrOoP, top) and the tower top side-side DEL (TTSS, bottom). Right: 2D-visualization of the neural network prediction surface by REWS and RETI (for fixed vertical shear, horizontal shear and yaw for visualization purpose) compared to data points not included in its training.

Initial results

Figure 4 presents some initial results of the performance of the trained neural networks. Overall the predictions are considered to be rather good (low scatter index for the validation dataset, as reported on the graph) and this is promising to confirm the validity of the proposed approach using local REIQs as only inputs to the surrogate model. The scatter index does not increase significantly from the (randomly selected) training dataset to the validation dataset, which indicates that the neural network is not over-fitted and it is well applicable to unknown new data points. The fitted 2D surfaces show clearly that some non-linear DEL variations (as particularly the expected DEL peak around the rated wind speed of $9.8\,m/s$) are well captured by the surrogate model.

Finally, figure 5 further validates the approach. It can indeed be seen that the surrogate model is fairly well able to capture the variation of DELs by an effect not included as part of its input (here, the wind farm ambiant wind direction) but rather using only the information of local REIQs. The complete version of this work will further explain its methodology, more various results and observed limitations.

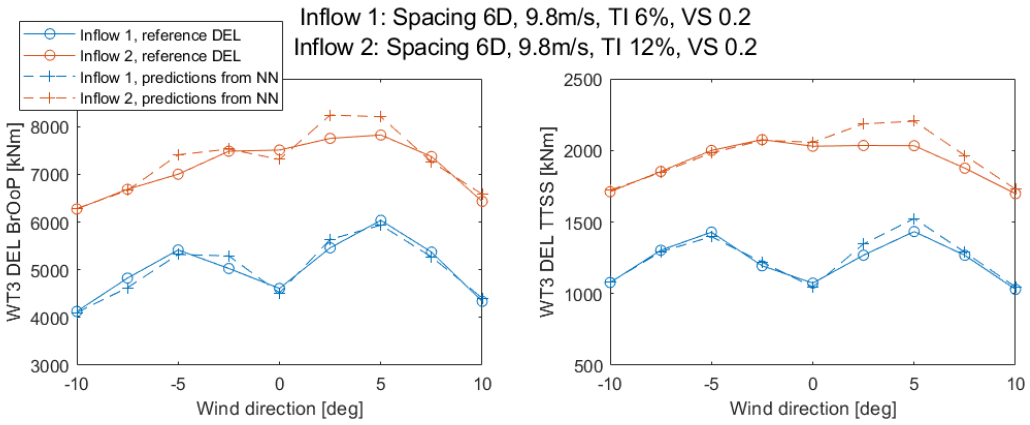


Figure 5: Predictions of two different DELs of the downstream (third) turbine by the trained neural network (dashed lines) compared to reference values (solid lines) for varying ambiant wind directions.

References

[1] M. Bertelè, C. L. Bottasso, S. Cacciola, F. Daher Adegas, and S. Delport. Wind inflow observation from load harmonics. *Wind Energy Science*, 2(2):615–640, 2017.

[2] P. Bortolotti, H. C. Tarres, K. L. Dykes, K. Merz, L. Sethuraman, D. Verelst, and F. Zahle. Iea wind tcp task 37: Systems engineering in wind energy - wp2.1 reference wind turbines.

[3] E. Bossanyi. Surrogate model for fast simulation of turbine loads in wind farms. *Journal of Physics: Conference Series*, 2265(4):042038, may 2022.

[4] N. Dimitrov, M. C. Kelly, A. Vignaroli, and J. Berg. From wind to loads: wind turbine site-specific load estimation with surrogate models trained on high-fidelity load databases. *Wind Energy Science*, 3(2):767–790, 2018.

[5] M. Howland, J. Quesada, J. Martnez, F. Larraaga, J. Chawla, V. Sivaram, and J. Dabiri. Collective wind farm operation based on a predictive model increases utility-scale energy production. *Nature Energy*, 08 2022.

[6] B. Jonkman and B. Jr. Turbsim user's guide. 01 2007.

[7] J. Jonkman, P. Doubrawa, N. Hamilton, J. Annoni, and P. Fleming. Validation of FAST.farm against large-eddy simulations. *Journal of Physics: Conference Series*, 1037:062005, jun 2018.

[8] H. Mendez Reyes, S. Kanev, B. Doekemeijer, and J.-W. van Wingerden. Validation of a lookup-table approach to modeling turbine fatigue loads in wind farms under active wake control. *Wind Energy Science*, 4(4):549–561, 2019.

[9] J. Schreiber, C. L. Bottasso, and M. Bertelè. Field testing of a local wind inflow estimator and wake detector. *Wind Energy Science*, 5(3):867–884, 2020.

[10] K. Shaler, J. Jasa, and G. E. Barter. Efficient loads surrogates for waked turbines in an array. *Journal of Physics: Conference Series*, 2265(3):032095, may 2022.

[11] A. P. J. Stanley, J. King, C. Bay, and A. Ning. A model to calculate fatigue damage caused by partial waking during wind farm optimization. *Wind Energy Science*, 7(1):433–454, 2022.

[12] P. Veers, K. Dykes, E. Lantz, S. Barth, C. L. Bottasso, O. Carlson, A. Clifton, J. Green, P. Green, H. Holttinen, D. Laird, V. Lehtomki, J. K. Lundquist, J. Manwell, M. Marquis, C. Meneveau, P. Moriarty, X. Munduate, M. Muskulus, J. Naughton, L. Pao, J. Paquette, J. Peinke, A. Robertson, J. S. Rodrigo, A. M. Sempreviva, J. C. Smith, A. Tuohy, and R. Wiser. Grand challenges in the science of wind energy. *Science*, 366(6464):eaau2027, 2019.

18th EAWE PhD Seminar on Wind Energy
2-4 November 2022
Bruges, Belgium

Development of filtering method for LiDAR measurements that retain the turbine wake information

Sebastian Pinilla[a]

[a]Carl von Ossietzky Universität Oldenburg, Ammerländer Heerstraße 114-118, 26129 Oldenburg, Germany

E-mail: sebastian.pinilla@uol.de

Keywords: LiDAR measurements, data filtering, wake effect

1 Introduction

Modern Lidar devices are able to collect a high amount of data that requires filtering before its desired use in the industry or research, due to affectation of the data quality by hard targets, atmospheric conditions and turbine characteristics. Some filtering approaches were already proposed like the Carrier to Noise *CNR* threshold based on the assumption that under certain *CNR* value the measurements uncertainty in the wind speed are really large to be contemplated as useful [3] or the Dynamic Data Filter by [2] which assumes self-similarity considering the proximity of each individual measurement of *CNR* and line of sight velocity u_{los} to their mean values, being the outliers defined by their longer distance. Nevertheless, a physical background behind the resulting labeling of the data (valid or invalid) needs to be provided more cleverly aiming to justify and improve the developing of some filtering approach, considering that the current filtering methods might filter out the wake due to its characteristics being substantially different from the undisturbed flow. The objective of this project is the developing of a filtering method that uses the approach proposed by [2] considering the wake effect. For this, it is necessary to get a first guess of the wake in space before the normalization required by the approach, which is presented in this abstract.

2 Methodology

The Lidar data used in this paper was obtained at the measurement campaign described by [4], with a Leosphere Windclube 200S pulsed Lidar device taking PPI scans downstream mounted above the nacelle of a 3.5MW on-shore wind turbine of 117m height and 126m diameter. The data was collected on April 13, 2021. The data was filtered with the Dynamic Data Filtering approach being represented with scatter plots of the *CNR* against u_{los} with a previous filter taking out the positive values of the *CNR* and u_{los} lower than zero. This can be seen in Figure 2a,b, where *b* shows that after the application of the approach one case presented invalid data even for a region of a high density data, as well as a lot of noise. By contrasting this with the behaviour of the *CNR* and u_{los} along the ranges (Figure 3), it is observed that the majority of the measurements for each elevation angle presented similar (and stable) behaviours, whereas at 0.14° the tendency is more unstable and not aligned with the other lines.
Next steps contemplate the analysis of the filtered data for each elevation angle at different times looking for similar behaviours and afterwards the analysis of the measurements along the wake by following [5] and [1] that described it compounded by regions with transversal shapes that can be fitted by Gaussian distributions.

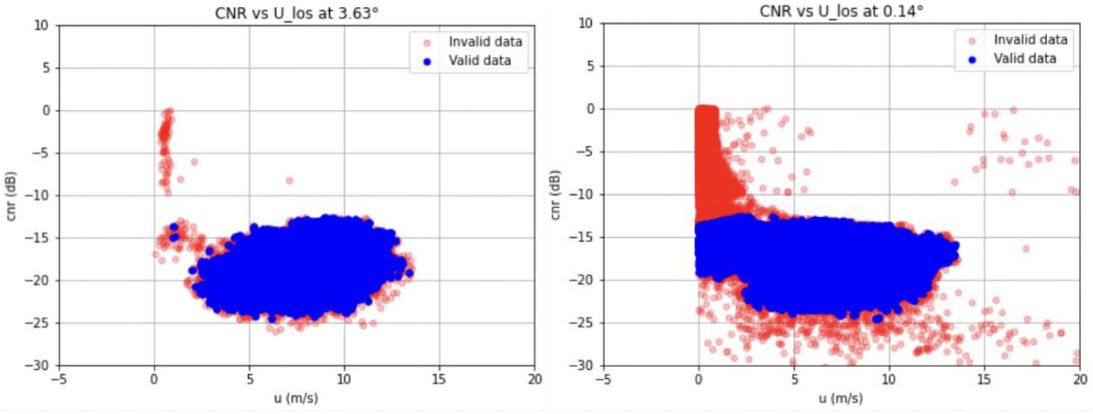


Figure 1: (a) Dynamic Data Filtering at 3.63°. (b) Dynamic Data Filtering at 0.14°. At this plot a high density data region is filtered as invalid data.

3 Preliminary results

The figures presented in this abstract suggest empirically that the wake effect could influence the resulting labeling of the used filtering approach, however more future tasks like the analysis of each PPI scan at different times and the modelling of the wake are contemplated to analyze these behaviours.

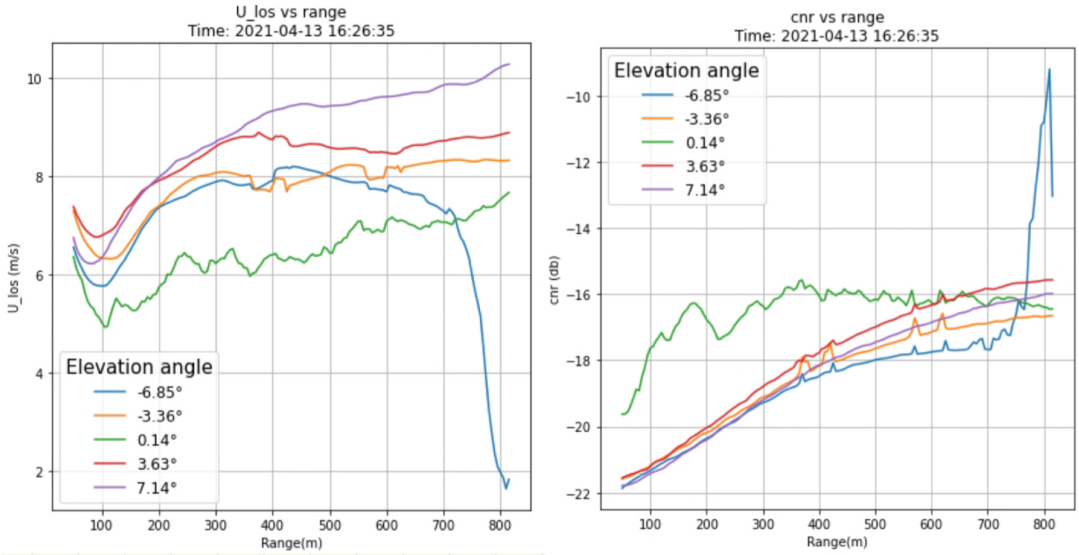


Figure 2: (a) u_{los} vs measurement ranges. (b) *CNR* vs measurement ranges. Due to the increasing *CNR* along the range observed in this plot [2] proposes the normalization of the data to get a frame of reference reducing absolute time and space differences. The tendencies observed at -6.85° from 700 meters for both variables are assumed due to the proximity of the signal to the ground.

Acknowledgements

The measurement campaign has been carried out within the national research project “CompactWind II” (FKZ 0325492H), funded by the Federal Ministry for Economic Affairs and Energy (BMWi) on the basis of a decision by the German Bundestag.

References

[1] M. L. Aitken and J. K. Lundquist. Utility-scale wind turbine wake characterization using nacelle-based long-range scanning lidar. *Journal of Atmospheric and Oceanic Technology*, 31:1529–1539, 2014.

[2] H. Beck and M. Kühn. Dynamic data filtering of long-range doppler lidar wind speed measurements. *Remote Sensing MDPI*, 9(6):516, 2017.

[3] R. Frehlich. Simulation of coherent doppler lidar performance in the weak signal regime. *Journal of Atmospheric and Oceanic Technology*, 13:646 – 658, 1996.

[4] P. Hulsman, C. Sucameli, V. Petrović, A. Rott, A. Gerds, and M. Kühn. Turbine power lossduring yaw-misaligned free field tests at different atmospheric conditions. *Journal of Physics: Conference Series*, 2265:032074, 2022.

[5] F. Porté-Agel, M. Bastankhah, and Shamsoddin. Wind-turbine and wind-farm flows: A review. *Boundary-Layer Meteorology*, 174:1–59, 2020.

18th EAWE PhD Seminar on Wind Energy
2-4 November 2022
Bruges, Belgium

Dynamic wake mitigation control: towards better understanding of wake physics using high-resolution large-eddy simulations

Marion Coquelet[a,b], **Laurent Bricteux**[b], **Matthieu Duponcheel**[a], **Maud Moens**[a], and **Philippe Chatelain**[a]

[a]Institute of Mechanics, Materials and Civil Engineering, Université catholique de Louvain, 1348 Louvain-la-Neuve, Belgium.
[b]Fluids-Machines Department, Université de Mons, 7000 Mons, Belgium.

E-mail: marion.coquelet@uclouvain.be

Keywords: Wind Farm Control, Pulse, Helix, Large Eddy Simulations, Vortex Particle-Mesh Method

1 Introduction

As wind turbines generate a wake behind their rotor, clustering them into wind farms creates an important challenge in terms of wake interaction. Many investigations have therefore emerged in the field of wind energy to mitigate wake interaction effects and seek to maximize wind farm power production.
Dynamic wake mitigation strategies have recently raised interest. Their principle is the reduction of the length of the wake recovery process, contrary to yaw redirection [4] which aims at deviating the wake from a downstream rotor. Past studies have shown promising results for strategies generating either a pulse [7] or an helix [5] in the wake. Nevertheless, the physics behind dynamic wake mixing still constitutes an open question.
This work aims at providing some answers in terms of wake dynamics using high resolution simulations, as they have seldom been proposed in the literature so far. High resolution indeed allows the proper computation of the vortex system behind the rotor by sharply capturing the helical tip vortices of the wake. In particular, we wish to determine the impact of the numerical resolution on the flow patterns and hence on the power gains that can be expected. Simulations are performed using a Vortex Particle-Mesh code, which is particularly well suited for wake problems, and blades are modelled using Immersed Lifting Lines.

2 Methodology

2.1 Numerical solver

The simulations are performed with an inhouse Vortex Particle-Mesh Method (VPM) [2] in which the Navier-Stokes equations are solved in their vorticity-velocity formulation. This Lagrangian approach is very well adapted for the computation of complex wakes as it avoids the numerical dissipation of Eulerian approaches thus allowing to properly capture the wake vorticity over long distances. Blades are modelled by Immersed Lifting Lines (ILL) [1] and the turbine dynamics are computed by the multi-body-system solver ROBOTRAN [3].

2.2 Controllers

We compare three types of control strategies: the standard one, the one generating pulses in the wake and the one leading to the formation of an helix. The way these controllers are implemented is described below.

Reference A standard Maximum Power Point Tracking (MPPT) controller is used for all turbines, whatever their operating conditions. It relies on a generator-torque controller and a collective blade pitch controller [6].

Pulse Periodical variations of the thrust force intensity result in pulsations in the wake which help the wake recovery process. It is implemented as a superimposition of low-frequency harmonic oscillations onto the collective pitch angle β_{MPPT} computed by the background MPPT controller. The optimal parameters of the harmonic oscillations are found in [5, 7]: $St = fD/U_{ref} = 0.25$ and $A = 2.5^{o}$ where St is the Strouhal number, D is the rotor diameter, U_{ref} is the mean wind speed and f and A are respectively the frequency and amplitude of the pitch oscillations. Eventually, the pitch angle evolution is dictated by

$$\beta_{CPC} = \beta_{MPPT} + A \sin\left(2\pi St \frac{U_{ref}\, t}{D}\right). \tag{1}$$

Helix Periodical variations of the thrust force orientation result in an helical shape of the wake which forces wake meandering and enhances the wake recovery process. Individual pitch control and the Coleman transform are used to produce that effect. We refer to Frederik [5] for further details and simply provide the expression of the individual pitch angle evolution of blade b given the rotation frequency f_{rot} of the rotor:

$$\beta_b = \beta_{MPPT} + A \sin\left(\frac{2\pi}{3} b + 2\pi \left(f_{rot} + St \frac{U_{ref}}{D}\right) t\right). \tag{2}$$

The parameters of the harmonic oscillations are similar to the pulse case: $St = fD/U_{ref} = 0.25$ and $A = 2.5^{o}$ [5].

2.3 Numerical set-ups

Simulations of the NREL 5MW [6] are performed at $U_{ref} = 9$ m/s, i.e. the turbine operates at an under-rated wind speed thus making the optimization related to wake interaction much needed. The aim is to understand what types of instabilities are generated and/or amplified by the control strategies. Still, we do not opt for an absolutely laminar flow to limit numerical effects regarding the triggering of the vortices destabilization. The inflow thus has a turbulence intensity of 1%.

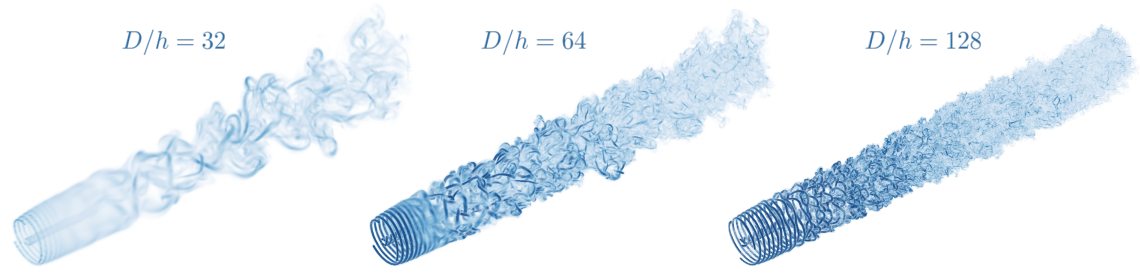
The numerical domain has dimensions of $12D \times 4D \times 4D$. The boundary conditions are inflow-outflow in the streamwise direction (x) and unbounded in the transverse directions (y and z). Three spatial resolutions (homogeneous throughout the domain) are investigated: $D/h = 32$, $D/h = 64$ and $D/h = 128$, leading to respectively 6×10^6 points, 50×10^6 points and 400×10^6 points. The simulations are run on massively parallel supercomputers using IvyBridge CPUs and the cost of each simulations are respectively 0.7×10^3 CPU$\times$hours, 8×10^3 CPU$\times$hours and 75×10^3 CPU$\times$hours.

3 Results

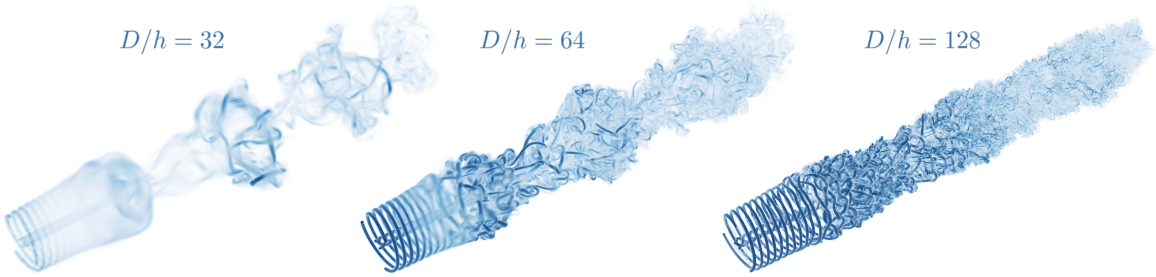
The volume rendering of the instantaneous vorticity field is provided for the three control cases and the three resolutions in Fig. 1. As expected, it is observable that, the higher the resolution, the sharper the structures that are shed. Low resolutions tend to produce a vortex tube behind the rotor, while higher resolutions really help discriminate between the helical tip vortices shed at the rotor. As the shed structures are different, the vortex dynamics destabilizing them are also different. There is thus a strong impact of the resolution on the wake development, especially when wake mitigation is performed. Indeed, the pulsations are less observable at higher resolution and the helical shape of the wake is also diminished with higher resolution. Additional diagnostics will be performed by the time of the conference to quantitatively characterize these observations. They will help the discussion regarding the implications on expected power gains in the wake.

4 Conclusions

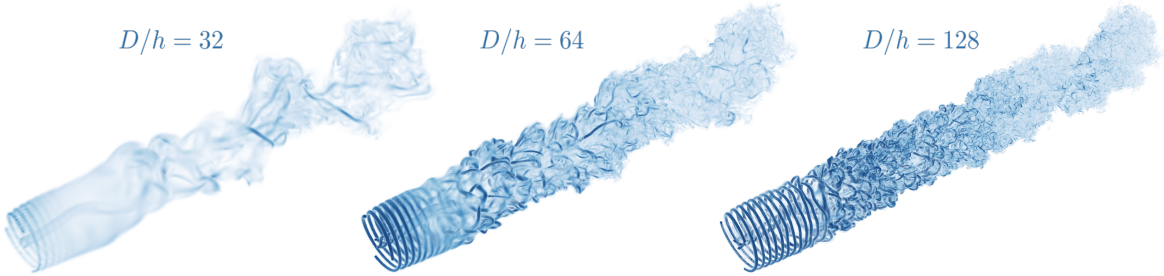
We propose high-resolution LES of the flow past wind turbines operated with wake mitigation strategies. We show that the resolution has a strong impact on the flow structures. Additional flow diagnostics will help quantify the results regarding the gain of available wind power in the wake and the impact on the loads. It would also be interesting to characterize the impact of turbulence, as it naturally generates instabilities and helps destabilizing the tip vortices and thus the wake.



(a) Reference



(b) Pulse



(c) Helix

Figure 1: Instantaneous volume rendering of the vorticity field for the three control cases at the three resolutions.

Acknowledgements

This project has received funding from the European Research Council under the European Union's Horizon 2020 research and innovation program (grant agreement No. 725627) and from the Université de Mons under the 50/50 PhD funding program. This research benefited from computational resources made available on the Tier-1 supercomputer of the Fédération Wallonie-Bruxelles funded by the Walloon Region under the grant agreement No. 1117545 and on resources provided by the Consortium des Equipements de Calcul Intensif, funded by the Fonds de la Recherche Scientifique de Belgique under Grant No. 2.5020.11 and by the Walloon Region.

References

[1] D.-G. Caprace, P. Chatelain, and G. Winckelmans. Lifting line with various mollifications: theory and application to an elliptical wing. *AIAA Journal*, 57(1):17–28, 2019.

[2] P. Chatelain, M. Duponcheel, D.-G. Caprace, Y. Marichal, and G. Winckelmans. Vortex particle-mesh simulations of vertical axis wind turbine flows: from the airfoil performance to the very far wake. *Wind Energy Science*, 2(1):317–328, 2017.

[3] N. Docquier, A. Poncelet, and P. Fisette. Robotran: A powerful symbolic gnerator of multibody models. *Mechanical Sciences*, 4:199–219, 05 2013.

[4] P. Fleming, P. Gebraad, S. Lee, J.-W. van Wingerden, K. Johnson, M. Churchfield, J. Michalakes, P. Spalart, and P. Moriarty. Evaluating techniques for redirecting turbine wakes using sowfa. *Renewable Energy*, 70:211–218, 2014.

[5] J. Frederik, B. Doekemeijer, S. Mulders, and J.-W. van Wingerden. The helix approach: Using dynamic individual pitch control to enhance wake mixing in wind farms. *Wind Energy*, 23(8):1739–1751, 2020.

[6] J. Jonkman, S. Butterfield, W. Musial, and G. Scott. Definition of a 5-mw reference wind turbine for offshore system development. Technical report, National Renewable Energy Lab.(NREL), 2009.

[7] W. Munters and J. Meyers. Towards practical dynamic induction control of wind farms: analysis of optimally controlled wind-farm boundary layers and sinusoidal induction control of first-row turbines. *Wind Energy Science*, 3(1):409–425, 2018.

[8] J. Wagenaar, L. Machielse, and J. Schepers. Controlling wind in ecn's scaled wind farm. *Proc. Europe Premier Wind Energy Event*, 1(01), 2012.

[9] A. Yilmaz and J. Meyers. Optimal dynamic induction control of a pair of inline wind turbines. *Physics of Fluids*, 30(8):085106, 2018.

18th EAWE PhD Seminar on Wind Energy
2-4 November 2022
Bruges, Belgium

Effect of data assimilation of local observations in WRF on the predictability of atmospheric variables for offshore wind energy applications

Tsvetelina Ivanova[a,b], **Wim Munters**[a], **Sara Porchetta**[a], **Sophia Buckingham**[a], **Jan Helsen**[b], and **Jeroen van Beeck**[a]

[a]Environmental and Applied Fluid Dynamics, von Karman Institute, Belgium
[b]Vrije Universiteit Brussel, Belgium

E-mail: tsvetelina.ivanova@vki.ac.be

Keywords: offshore wind energy, numerical weather prediction, WRF, 3D-Var data assimilation of local observations, wind farm parameterization.

1 Introduction

The renewable energy sector provides a significant part of the energy consumed in the European Union (more than one-fifth), and it has been expanding for decades. It is a sector of climatological and economical importance. Wind energy is one of the means to achieve the goals of the Paris Climate Change agreement, and offshore wind energy currently exceeds 10% of Europe's total wind energy capacity [1]. To help pursue a more sustainable future, the wind farms must be operated with informed decisions. Reliable weather predictions can aid the decision-making at the wind farms for more efficient wind turbine maintenance and power extraction, as well as contribute to the mitigation of leading edge erosion (LEE) of wind turbine blades.

This work involves numerical weather prediction (NWP) with the Weather Research and Forecasting (WRF) model [2] and data assimilation (DA) techniques [3] of local observations. The atmosphere is a complex nonlinear system and therefore NWP is highly sensitive to initial and boundary conditions. Imposing the initial conditions more accurately is essential for reliable numerical results, and a way to do so is by data assimilation. The main concept of DA is to find the optimal initial state of the atmosphere by combining numerical solutions with observations.

This PhD topic is part of the ICON project RAINBOW on optimized prediction and decision support for rain erosion of wind turbine blades. One of the objectives of this PhD is to optimally set up WRF for predicting weather conditions using data assimilation of local observations at the wind farms in the Belgian North Sea. As a consequence, decision support in the offshore wind farms can be improved. Another objective that relies strongly on NWP is to reach a further understanding of the drivers for LEE of the wind turbine blades, and to possibly better predict and mitigate it.

The current research focuses on defining an optimal WRF setup for wind energy applications including wake effects, and on the three-dimensional variational data assimilation technique (3D-Var DA) from WRF. With it, we are interested in the spatial and temporal effects that variational DA can have in the computational domain. Another question is what is the effect of assimilating these local observations on other relevant atmospheric variables such as precipitation. The latter is very relevant for wind energy and is crucial for LEE mitigation strategies. A next step will be to investigate other DA techniques and compare different approaches in their prediction capabilities in light of the specifics of the offshore wind farm sites in the Belgian North Sea.

This work is structured as follows. Section 2 contains the main tools that are necessary for the quest to achieving the goals of this PhD, and it describes the selected study case along with the numerical setup. Highlights from obtained results so far are discussed in Section 3, followed by conclusions and perspectives in Section 4.

2 Methodology

The techniques for DA in the WRF-v4.3 mesoscale model are four-dimensional data assimilation (FDDA, or nudging), and variational data assimilation, which can be three-dimensional variational DA (3D-Var WRFDA) or four-dimensional variational DA (4D-Var WRFDA) [4]. FDDA's working principle is to nudge the model state towards the observations by introducing terms in the equations, while the variational DA produces an optimal estimate of the true atmospheric state by iteratively solving a prescribed cost-function [2]. The capabilities of the nudging technique for short-term wind forecasts are emphasized in [5], and improvements of wind speed forecasts with variational data assimilation are presented in the very recent work [6].

This study is performed using ERA5 reanalysis data [7]. The selected analysis period is around Storm Eunice (February 2022), which was a remarkable storm that passed through Europe coming from South-West with wind gusts reaching up to 150 km/h, causing many power outbreaks [8]. The period for the WRF simulations in this work is from 15 February 12:00 to 16 February 00:00, before Storm Eunice occurred.

The available observations to be assimilated with 3D-Var DA are collected at the Belgian offshore wind farms and are measurements of wind speed and wind direction (from SCADA and LiDAR). In this numerical study, we use two setups that are optimized for wind energy applications as follows.

2.1 Setup 1

This numerical setup is adapted from the configuration for the New European Wind Atlas (NEWA) [9]. It has 61 vertical levels, 6 of which are below a typical hub height of an offshore wind turbine. The horizontal resolutions of the nested domains are 18 km, 6 km, and 2 km, as indicated also in Figure 1. The sizes in kilometers of the domains are as follows. For D01 – 1980 km by 1980 km, for D02 – 1320 km by 1194 km, and for D03 – 680 km by 596 km.

2.2 Setup 2

This setup has the same nested domains from Figure 1 in Setup 1, but is modified to take into account wind farm parameterization on domain D03 (with 2 km resolution) with the Fitch scheme [10]. Sufficient vertical resolution is a good practice, therefore the levels are now 81 with 10 of them being below typical offshore hub height (as compared to 6 levels in Setup 1).

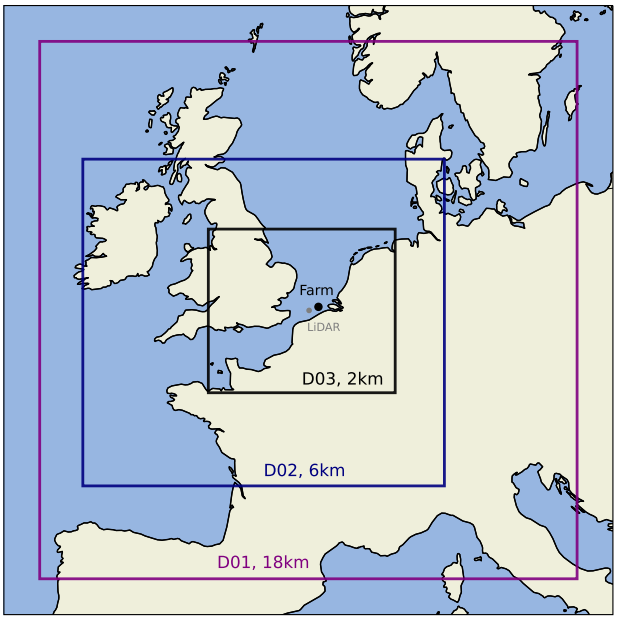


Figure 1: Nested domains with horizontal resolutions of 18 km (D01), 6 km (D02), 2 km (D03).

3 Results and discussion

This section shows results from the WRF model with settings tailored to the specifics of the offshore wind farm sites in the Belgian North Sea, as described in Section 2. As will be shown below, local predictions in the order of a few hours ahead of atmospheric variables can be improved using 3D-Var DA and wind farm parameterization. We observed that the temporal effect of local DA on the solutions was approximately equal to the time needed for the assimilated observations to be advected by the dynamics of the system, which in this case is up to 4-5 hours depending on atmospheric conditions. Additionally, WRFDA showed strong sensitivity to horizontal resolution when comparing results on D01 (18 km) and D02 (6 km) – its effects are much more pronounced on D02 than on D01. Performing variational DA on D02 (6 km) is in agreement with literature's recommendations for horizontal resolution for this (in [6], it is 5 km).

Below we highlight results for local predictions of wind speed from 15 February 12:00 to 16 February 00:00. We compare predictions with and without DA, as well as with and without wind farm parameterization.

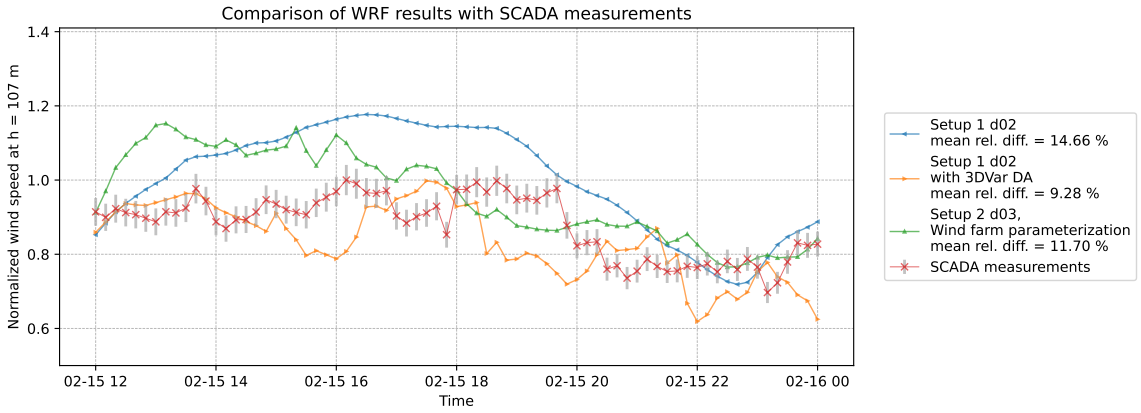


Figure 2: Local wind speed predictions in time at a Belgian offshore wind turbine. The improvement in wind speed prediction (with respect to SCADA observations at this wind turbine) is by 5.38% with 3D-Var data assimilation, and by 2.96% with wind farm parameterization. The mean relative differences in the legend are with respect to the observations. The wind speed is normalized by the maximum value of the SCADA measurements.

3.1 Influence on wind speed

Wind speed predictions for one offshore wind turbine location are shown in Figure 2. The wind speed fields are interpolated to 107 m hub height and the values are extracted at the turbine's specific location. The blue curve is a solution obtained with WRF Setup 1 (often referred to as initial guess), and the orange one is obtained with 3D-Var WRFDA Setup 1 (see Section 2.1). The 3D-Var data assimilation is performed every 3 hours (i.e., at four different times on 15 February 2022, which are 12:00, 15:00, 18:00, and 21:00). The green curve in Figure 2 has taken into account the wind farm parameterization from Setup 2 (see Section 2.2) and does not involve DA. These three solutions are compared to SCADA measurements collected at the specific location. Both DA and wind farm parameterization show a significant improvement in the predictability of wind speed for the simulated period (see Figure 2 for details). Accurate wind speed predictions are necessary for the wind energy sector, since the power extracted depends on the wind speed cubed, which means that any imprecision is amplified significantly in the uncertainty of the power predictions. In addition, often WRF solutions (without DA or wind farm parameterization) may over-predict wind speed since no wake effects and energy extraction from the flow are taken into account, which may result in premature shut down of the wind turbines.

3.2 Influence on precipitable water

Performing the numerical experiments in this PhD so far lead us to the conclusion that variational data assimilation of solely wind speed and wind direction has effect on other atmospheric variables besides these two, such as precipitable water fields. This is in line with conclusions from [11]. Although wind speed and precipitation are closely related, this effect is very relevant in the context of LEE of the wind turbine blades. It is encouraging to further investigate how data assimilation can alter local rainfall predictions with comparison to measurements in future works.

4 Conclusions and perspectives

The analysis so far shows that (frequent enough) 3D-Var DA of local observations affects the evolution of the atmospheric state to a large extent in space and time, and that this procedure is highly sensitive to horizontal resolution as its influence is more pronounced on a higher-resolution domain (of 6 km) in contrast to an 18 km domain. It is also encouraging to confirm that such local observations can influence other relevant atmospheric variables like precipitation and rainfall rates and thus provide better estimations for these in future works, which is useful for understanding blade erosion drivers.

Next steps of this research involve setting up WRF in forecasting mode with Global Forecast System (GFS) data, exploring the other available data assimilation techniques such as FDDA, and ultimately combining them with the optimal numerical setup that includes wind farm parameterization.

Acknowledgements

The current PhD topic is funded within the framework of the ICON project RAINBOW, which is supported by the Flemish Government via the Agency for Innovation and Entrepreneurship (VLAIO).
This work is performed using free and open-source software: we would like to express gratitude to the communities for building powerful tools from which everyone can benefit.

References

[1] Charlotte B. Hasager, Andrea N. Hahmann, Tobias Ahsbahs, Ioanna Karagali, Tija Sile, Merete Badger, and Jakob Mann. Europe's offshore winds assessed with synthetic aperture radar, ASCAT and WRF. *Wind Energy Science*, 5(1):375–390, Mar 2020.

[2] William C. Skamarock et al. A Description of the Advanced Research WRF Model Version 4. Technical report, UCAR/NCAR, 2019.

[3] Dale Barker et al. The Weather Research and Forecasting Model's Community Variational/Ensemble Data Assimilation System: WRFDA. *Bulletin of the American Meteorological Society*, 93(6):831–843, Jun 2012.

[4] Caroline Draxl. *On the Predictability of Hub Height Winds*. PhD thesis, DTU Wind Energy. Risø-PhD No. 84(EN), 2012.

[5] William Y.Y. Cheng, Yubao Liu, Alfred J. Bourgeois, Yonghui Wu, and Sue Ellen Haupt. Short-term wind forecast of a data assimilation/weather forecasting system with wind turbine anemometer measurement assimilation. *Renewable Energy*, 107:340–351, Jul 2017.

[6] Wei Sun, Zhiquan Liu, Guiting Song, Yangyang Zhao, Shan Guo, Feifei Shen, and Xiangming Sun. Improving Wind Speed Forecasts at Wind Turbine Locations over Northern China through Assimilating Nacelle Winds with WRFDA. *Weather and Forecasting*, 37(5):545–562, May 2022.

[7] Hans Hersbach et al. The ERA5 global reanalysis. *Quarterly Journal of the Royal Meteorological Society*, 146(730):1999–2049, Jun 2020.

[8] Severe Weather Forecast for Europe - February 18th, 2022. https://www.severe-weather.eu/weather-forecast/severe-weather-forecast-outlook-for-europe-february-18th-2022-mk. Accessed: 2022-07-27.

[9] Andrea N. Hahmann, Tija Sīle, Björn Witha, Neil N. Davis, Martin Dörenkämper, Yasemin Ezber, Elena García-Bustamante, J. Fidel González-Rouco, Jorge Navarro, Bjarke T. Olsen, and Stefan Söderberg. The making of the New European Wind Atlas – Part 1: Model sensitivity. *Geoscientific Model Development*, 13(10):5053–5078, Oct 2020.

[10] Anna C. Fitch et al. Local and mesoscale impacts of wind farms as parameterized in a mesoscale NWP model. *Monthly Weather Review*, 140(9):3017–3038, Sep 2012.

[11] Feng Gao et al. Assimilation of wind speed and direction observations: results from real observation experiments. *Dynamic Meteorology and Oceanography*, 67:27132, 2015.

18th EAWE PhD Seminar on Wind Energy
2-4 November 2022
Bruges, Belgium

Finite wind-farm operations in conventionally neutral boundary layers using a large-eddy simulation framework

Luca Lanzilao and **Johan Meyers**

Department of Mechanical Engineering, KU Leuven, Celestijnenlaan 300A–Bus 2421, B3001
E-mail: luca.lanzilao@kuleuven.be

Keywords: Flow blockage, Wind-farm induced gravity waves, Large-eddy simulation

1 Introduction

The flow slow-down upwind of large wind farms has been observed in both large-eddy simulation (LES) studies and measurements campaigns [1, 2, 4]. This velocity reduction is proportional to the momentum sink generated by the farm and is enhanced when turbines operate at high thrust coefficients under stable atmospheric conditions [8]. In the literature, this phenomenon is referred to as flow blockage and is often attributed to cumulative turbines induction effects [6]. However, we speculate that self-induced atmospheric gravity waves contribute to flow blockage in some specific atmospheric conditions. To support this idea, in the current work we perform 28 LES of a finite wind farm operating in conventionally neutral boundary layers (CNBLs) and neutral boundary layers (NBLs). In the first case, gravity waves are triggered by the upward displacement of the boundary layer. Conversely, an NBL is characterized by a constant with height potential temperature profile, so that buoyant forces do not play a role in the atmosphere dynamics. By comparing the results of these simulations, we will assess how the flow-blockage effect depends upon the atmosphere stratification. Moreover, we aim to advance the understanding of how gravity-wave induced pressure gradients affect the flow in and around the farm.

Case	H [m]	$\Delta\theta$ [K]	Γ [K/km]	U_{hub} [m/s]	TI_{hub} [%]	α [°]	Fr [–]	P_N [–]
H150-C8-Γ1,4,8	197	7.6	1,4,8	9.46	3.2	-19.3	1.27	7.08, 3.57, 2.55
H150-NBL	–	–	–	9.46	3.2	-19.3	–	–
H300-C5-Γ1,4,8	331	5.2	1,4,8	9.41	3.6	-12.6	1.25	4.74, 2.38, 1.66
H300-NBL	–	–	–	9.41	3.6	-12.6	–	–
H500-C2-Γ1,4,8	527	2.2	1,4,8	9.22	3.9	-8.9	1.50	3.03, 1.50, 1.06
H500-C5-Γ1,4,8	512	5.2	1,4,8	9.24	3.9	-9.1	1.00	3.11, 1.55, 1.10
H500-C8-Γ1,4,8	504	8.3	1,4,8	9.25	3.9	-9.1	0.80	3.11, 1.55, 1.10
H500-NBL	–	–	–	9.24	3.9	-9.1	–	–
H1000-C2-Γ1,4,8	1003	2.3	1,4,8	9.12	4.2	-7.9	1.10	1.63, 0.81, 0.58
H1000-C5-Γ1,4,8	1001	5.3	1,4,8	9.13	4.2	-7.9	0.72	1.63, 0.81, 0.58
H1000-C8-Γ1,4,8	1000	8.3	1,4,8	9.13	4.2	-8.0	0.57	1.63, 0.81, 0.58
H1000-NBL	–	–	–	9.13	4.2	-7.9	–	–

Table 1: Precursor simulations data averaged over the last 4 h of simulation. The height of the capping inversion H, its strength $\Delta\theta$ and the lapse rate in the free atmosphere Γ are evaluated using the Rampanelli and Zardi model [7]. U_{hub} and TI_{hub} refer to the velocity magnitude and turbulence intensity at hub height, respectively, while α denotes the geostrophic wind angle measured with respect to the x-axis. Finally, $Fr = \widetilde{U}/\sqrt{g'H}$ and $P_N = \widetilde{U}^2/NGH$, with $\widetilde{U}$ the boundary-layer bulk velocity and N the Brunt–Väisälä frequency.

2 Methods

The boundary-layer dynamics are modelled using Navier-Stokes equations for the three-dimensional velocity field $\mathbf{u} = (u, v, w)$ and a transport equation for the potential temperature field θ, together with the continuity equation which ensures incompressibility. The equation system is solved using SP-Wind, an LES code developed at KU Leuven [1]. Moreover, the effects of the turbines on the flow are modelled using the non-rotating actuator disk method [1].

First, the initial vertical velocity and temperature profiles need to be specified. We use the Zilitinkevich model [9] to specify the initial vertical velocity profile in the mixed layer, where we fix the friction velocity to $u_* = 0.26$ m/s and we adopt a constant surface roughness of $z_0 = 1 \times 10^{-4}$ m. Moreover, we assume a constant geostrophic wind of $G = 10$ m/s in the free atmosphere. The vertical potential temperature profile is specified using the Rampanelli and Zardi model [7], therefore assuming the presence of a CNBL. In this study, we select 24 vertical potential temperature profiles where we vary the capping inversion height H and strength $\Delta\theta$ together with the lapse rate Γ in the free atmosphere. Next, we add random divergence-free perturbation in the first 100 m to the vertical velocity profile and we advance the precursor simulation for 20 h. At this time, a statistically steady state has been reached and Table 1 reports several quantities of interest averaged over the last 4 h of simulation. Thereafter, we switch on the turbines in the main domain and we run main and precursor simulations in parallel. This second spin-up phase lasts for 1 h. Finally, we advance the simulations for 2 additional hours during which we collect statistics. Note that we define 4 additional cases in which we remove the capping inversion and free atmosphere stratification (only in the main domain - see [4]), so that the wind farm operates under an equal inflow velocity profile but with an NBL stratification. The fully developed turbulent inflow profiles are introduced in the main domain through a new fringe-region technique which imposes the desired inflow without triggering spurious gravity waves in the domain of interest [5]. Moreover, an efficient Rayleigh damping layer is used to avoid wave reflection from the top of the domain [5].

For the wind-farm setup, we consider a large farm with 160 turbines disposed in 16 rows and 10 columns in a staggered layout with respect to the main wind direction. The turbine-rotor diameter and hub height are $D = 198$ m and $z_h = 119$ m, which correspond to the dimensions of the IEA 10 MW offshore wind turbine [3]. Next, the streamwise and spanwise spacings are set to $s_x D = s_y D = 5D$. Moreover, the turbine set-point is fixed to $C_T = 0.88$, which corresponds to the value given by the thrust curve when the turbine operates at wind speeds considered in this study. This choice leads to a disk-based thrust coefficient of $C'_T = 1.94$. Finally, a simple yaw controller is implemented to keep the turbine-rotor disk perpendicular to the incident wind flow. The dimensions of the main domain are $40 \times 20 \times 25$ km^3. The precursor domain does not contain wind turbines nor a fringe region, therefore we select a streamwise length of 10 km. The lateral and vertical dimensions coincide with the ones of the main domain. The combination of precursor and main simulations leads to a total of 721.3×10^6 grid cells, resulting in 2.88×10^9 degrees of freedom.

3 Results and Conclusions

To explain the wind-farm induced gravity-wave mechanism, we first analyze two cases out of the 28 available, i.e H500-C5-G4 and H500-NBL. Only at the end of the section, we will show a preliminary comparison among all cases in terms of wind speed. A more in-depth analysis will be performed in a follow-up article.

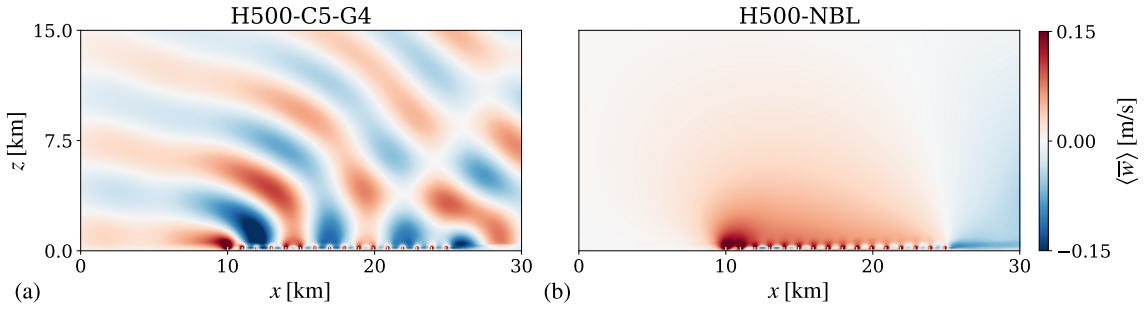


Figure 1: Contours of vertical velocity for cases (a) H500-C5-G4 and (b) H500-NBL, averaged over time and along x–z planes within the turbine columns footprint. The wind-turbine rotors are denoted with vertical white lines.

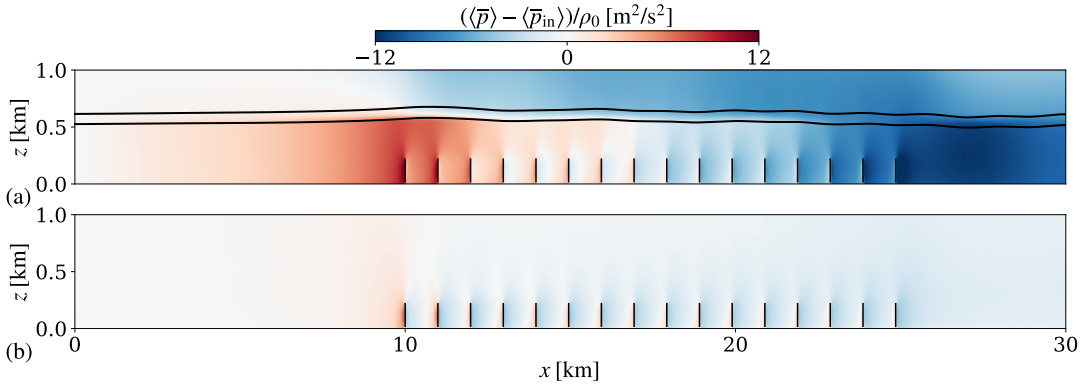


Figure 2: Contours of pressure perturbation with respect to the pressure measured at the inflow for cases (a) H500-C5-G4 and (b) H500-NBL, averaged over time and along x–z planes within the turbine columns footprint. The black solid lines show the time-averaged evolution of the inversion-layer base and top evaluated with the Rampanelli and Zardi model [7] while the wind-turbine rotors are denoted with vertical black lines.

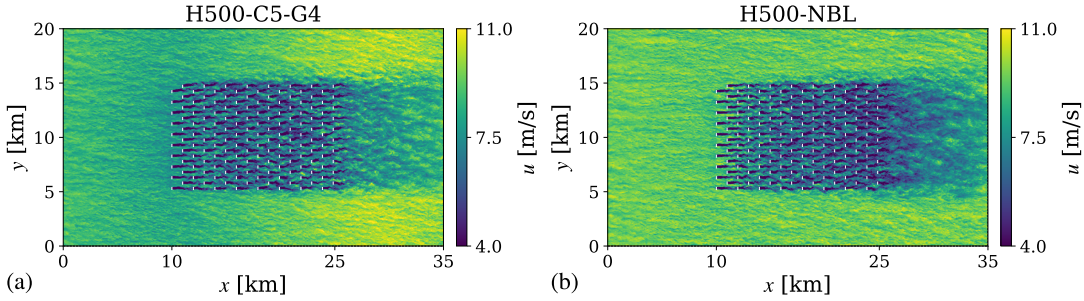


Figure 3: Instantaneous contours of streamwise velocity along a x–y plane at hub height obtained at the end of the wind-farm simulation for cases (a) H500-C5-G4 and (b) H500-NBL. The wind-turbine rotors are denoted with vertical white lines.

The vertical displacement of the capping inversion caused by the wind-farm induced momentum sink triggers gravity waves in the inversion layer and the free atmosphere. Contours of space and time-averaged vertical velocity along a x–z plane are shown in Fig. 1(a,b) for cases H500-C5-G4 and H500-NBL, respectively. Internal gravity waves transport energy upward in case of a stably stratified free atmosphere. Conversely, no gravity waves are observed in Fig. 1(b) since the vertical displacement of air parcels does not trigger oscillations in a neutral atmosphere. Gravity waves induce an unfavourable pressure gradient in the farm induction region which slows down the flow, and a favourable pressure gradient which redistributes energy through the farm, enhancing wake recovery. These two opposing effects are visible in Fig. 2(a), which illustrates time- and space-averaged pressure perturbation within the first 1 km for case H500-C5-G4. Conversely, case H500-NBL (i.e. Fig. 2(b)) shows only a minor pressure build-up in front of the farm, which we attribute to hydrodynamic effects. The pressure-gradient effects on the streamwise velocity are shown in Fig. 3. The unfavourable pressure gradient in case H500-C5-G4 causes lower wind speed in the farm induction region if compared against case H500-NBL. Moreover, the presence of the inversion layer forces the flow around the farm, as visible in Fig. 3(b).

Finally, Fig. 4 illustrates the velocity magnitude, normalized with the inflow value, obtained upstream of the farm for all atmospheric states reported in Table 1 (besides for the cases H300 which are currently running). Here, we can observe that the flow slow-down upstream of the farm is inversely proportional to the capping inversion height. Moreover, depending on the capping inversion strength, the flow blockage either increases or decreases while increasing the free atmosphere stability. A more in-depth analysis is necessary to fully comprehend how wind-farm operations are affected by self-induced gravity waves when varying the atmospheric state. We are planning to carry out such analysis in a follow-up article, together with a sensitivity study on the length and width of the computational domain.

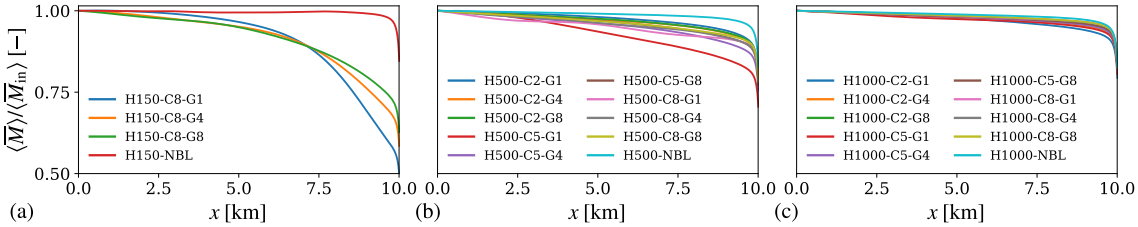


Figure 4: Velocity magnitude, normalized with the value at the inflow, averaged over time and over circular areas with diameter D centered at hub height and around each column of turbines obtained for cases (a) H150, (b) H500 and (c) H1000 with various capping inversion strengths and free lapse rates.

Acknowledgements

The authors acknowledge support from the Research Foundation Flanders (FWO, grant no. G0B1518N), and from the project FREEWIND, funded by the Energy Transition Fund of the Belgian Federal Public Service for Economy, SMEs, and Energy (FOD Economie, K.M.O., Middenstand en Energie). The computational resources and services in this work were provided by the VSC (Flemish Supercomputer Center), funded by the Research Foundation Flanders (FWO) and the Flemish Government department EWI.

References

[1] D. Allaerts and J. Meyers. Boundary-layer development and gravity waves in conventionally neutral wind farms. *J. Fluid Mech.*, 814:95–130, 2017.

[2] J. Bleeg, M. Purcell, R. Ruisi, and E. Traiger. Wind farm blockage and the consequences of neglecting its impact on energy production. *Energies*, 11:1609, 2018.

[3] P. Bortolotti, H. C. Tarrés, K. Dykes, K. Merz, L. Sethuraman, D. Verelst, and F. Zahle. Iea wind task 37 on systems engineering in wind energy wp2.1 reference wind turbines. *Technical report*, 2019.

[4] L. Lanzilao and J. Meyers. Effects of self-induced gravity waves on finite wind-farm operations using a large-eddy simulation framework. *Journal of Physics: Conference Series*, 2265(2):022043, may 2022.

[5] L. Lanzilao and J. Meyers. An improved fringe-region technique for the representation of gravity waves in large-eddy simulation with application to wind farms. *Manuscript in revision*, 2022.

[6] N. G. Nygaard, S. T. Steen, L. Poulsen, and J. G. Pedersen. Modelling cluster wakes and wind farm blockage. *J. Phys.: Conf. Ser*, 1618:062072, 2020.

[7] G. Rampanelli and D. Zardi. A method to determine the capping inversion of the convective boundary layer. *J. Appl. Meteor.*, 43:925–933, 2004.

[8] J. Schneemann, F. Theuer, A. Rott, M. Dörenkämper, and M. Kühn. Offshore wind farm global blockage measured with scanning lidar. *Wind Energy Science*, 6:521–538, 2021.

[9] S. S. Zilitinkevich. Velocity profiles, the resistance law and the dissipation rate of mean flow kinetic energy in a neutrally and stably stratified planetary boundary layer. *Boundary-Layer Meteorol.*, 46:367–387, 1989.

18th EAWE PhD Seminar on Wind Energy
2-4 November 2022
Bruges, Belgium

Identifying Turbulent Inflow Time Scales Beneficial for Wake Recovery

Emily L Hodgson[a], **Mads H A Madsen**[b], and **Søren J Andersen**[a]

[a]Technical University of Denmark, Department of Wind Energy, Anker Engelunds Vej 1, 2800 Kgs Lyngby, Denmark.
[b]Technical University of Denmark, Department of Wind Energy, Frederiksborgvej 399, 4000 Roskilde, Denmark
E-mail: emlh@dtu.dk

Keywords: Wind turbine, Wake recovery, Large Eddy Simulation, Turbulent scales, Optimisation

1 Introduction

For wind turbines operating in wind farms, the wakes of upstream turbines play a significant role in determining both the power production and component fatigue; therefore, the ability to control and enhance wake recovery could significantly improve the planning and operation of large wind farms. Improving wake recovery and inducing earlier breakdown of the tip vortices using various dynamic control strategies is widely studied in literature. The dynamic individual pitch control of Frederik *et al.* [1] aims to manipulate the wake; Brown *et al.* [2] studies how dynamic wake control could be used to excite the mutual inductance instability of the tip vortices; and the works of Munters and Meyers [3] use the adjoint method and Large Eddy Simulations to identify beneficial routines of dynamic induction and yaw control. These studies all focus on manipulating the operation of turbines, either individually or working collectively in a wind farm, to improve the wake recovery and overall power production.

Despite recognizing the importance of the turbulent inflow on wake recovery, few studies investigate the influence of the time and length scales of the turbulence beyond integrated quantities such as turbulence intensity. This work will examine how the scales of the inflow interact with those of the turbine(s), and use transient gradient-based optimisation within Large Eddy Simulations to identify turbulent time scales which are beneficial to wake recovery. This work builds on the findings of Hodgson *et al.* [4], which used a sinusoidal streamwise inflow variation to isolate the impact of different inflow time scales on wake behaviour. Using inflow time periods between 80s and 140s, it was found that the shorter time scales induced a faster roll up of the wake into periodic vortex ring shedding, and hence a faster wake recovery and improved power output downstream. However, several issues related to the simulation setup were noted: the difficulty in achieving time periods lower than 80s due to the dissipation of the sinusoid; the lack of a realistic wake breakdown; and the large computational expense due to the required domain size. The objective of the current work is firstly to identify a simulation setup which solves these issues and then to conduct optimisations with a robust methodology over a full range of inflow timescales.

2 Methodology

Flow modelling is achieved using EllipSys3D, the DTU three-dimensional multiblock Navier-Stokes solver [5, 6], using Large Eddy Simulations. To introduce specific turbulent time scales into the flow, turbulence boxes generated using the Mann spectral model [7, 8] are applied on a plane inside the domain. The desired time scale is introduced by changing the length of the turbulence box after it is generated - *i.e.* the same turbulent structures are either stretched or compressed to change the time scale without altering the overall energy content or turbulence intensity. Only the streamwise component of the turbulence box is used, and coarse resolution of the turbulence box filters out smaller scales such that only the enforced time scale and its harmonics are present in the resulting spectra. For these preliminary results to demonstrate the new setup, two simulations were conducted for $T_p = 60s$ and $T_p = 80s$, without any turbine present in the flow, to provide a verification that the desired turbulent time scales can be achieved while maintaining comparable flow scenarios.

3 Results

The background flow produced is assessed by using the mean and standard deviation of the momentum flow rate, calculated over planes with an area of $2R \times 2R$, placed every $1R$ starting at $5R$ downstream of the domain inlet. The momentum flow rate is calculated through the integral [9]:

$$\dot{M} = \int_{Y1}^{Y2} \int_{X1}^{X2} \rho U^2 dX dY \tag{1}$$

where $X1$, $X2$, $Y1$ and $Y2$ are the integration limits, ρ is the density, and U is the streamwise velocity. A centreline plane showing the streamwise velocity magnitude and graphs showing momentum flow rate spectra at different locations are shown in Figure 1, for $T_p = 60s$ and $T_p = 80s$. The comparisons of mean and standard deviation of momentum flow rate for the two simulations are shown below in Figure 2.

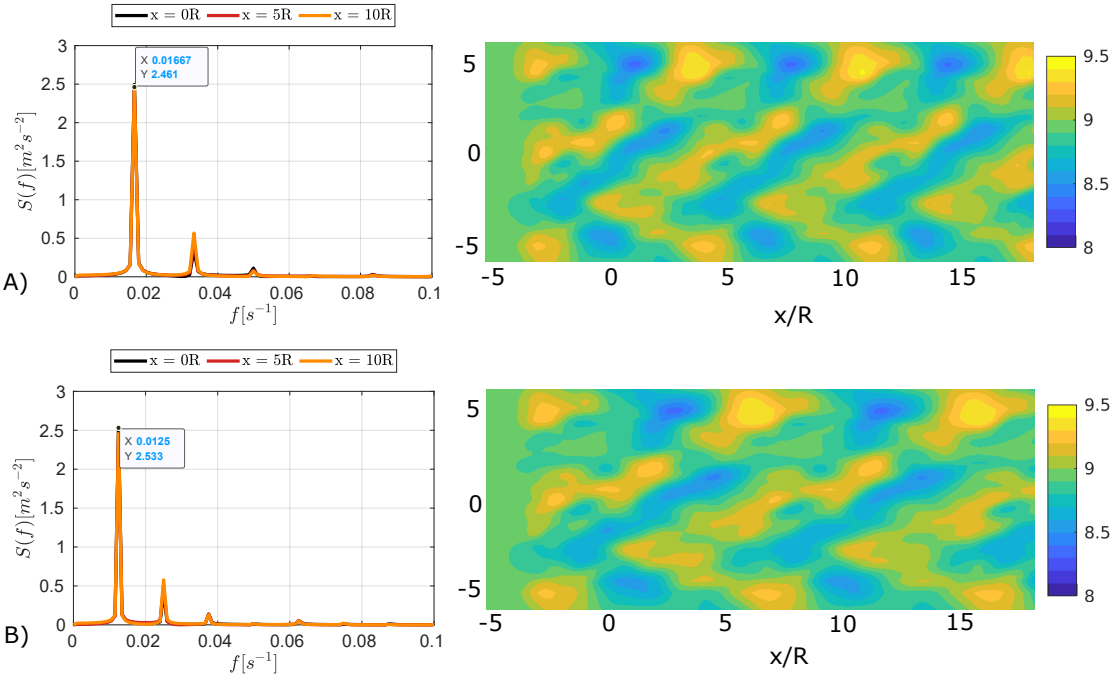


Figure 1: Spectra of momentum flux and streamwise velocity contours: A) $T_p = 60s$; B) $T_p = 80s$

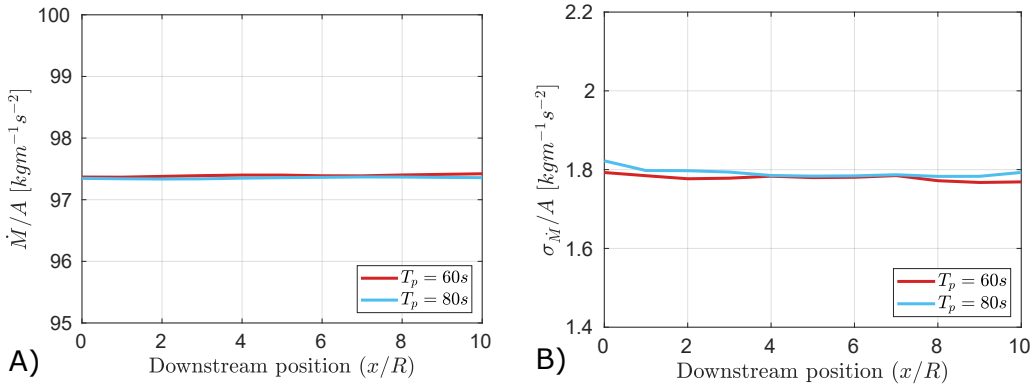


Figure 2: A) Mean momentum flow rate; B) Standard deviation of momentum flow rate

In Figure 1, the velocity contour plots show a clear periodic variation, and the momentum spectra verify that the desired predominant time scales are obtained; the spectral peaks occur at $(1/60)s^{-1}$ and $(1/80)s^{-1}$ respectively. Unlike the previous setup, some higher order harmonics are introduced as well as just the enforced signal, however these have significantly lower strength than the main frequency. This makes the background flow less idealised than that studied in [4], however is likely to provide a more realistic wake flow when a turbine is introduced into the domain. The comparison of the momentum flow rates in both mean and standard deviation shown in Figure 2 demonstrate that the new setup is capable of producing comparable flows even at lower time scales than was originally possible; the mean values agree to within 0.1%, and standard deviations to within 1%. This is due to using Mann turbulence rather than a purely sinusoidal forcing, as the spatial variation introduced means that the flow is more initially compliant with the Navier-Stokes equations and does not quickly degrade downstream. Additionally, the spatial variation and the fact that the Mann turbulence is applied over the entire domain area means that there is no shear layer produced by the forcing plane which could affect the downstream mixing.

4 Conclusions

The results presented here demonstrate the viability and robustness of the new computational setup, and that the three issues found previously - not reaching low time scales, unrealistic wake flow, and computational expense - are mitigated. A simulation setup which provides consistent background flow even at $T_p = 60s$ (and lower) is a significant improvement which will allow future work to identify optimum time scales for wake recovery over a much larger and more relevant range. This is achieved through the Mann model generated turbulence dissipating less, removing the blockage of the forcing plane which allows a much smaller domain area, and having spatial variation in the applied inflow turbulence. Additionally, assessing the flow using the streamwise momentum flow rate over the rotor area allows for a more rigorous comparison between different applied time scales than just centreline velocity measurements. Conducting optimisations to identify beneficial time scales for wake recovery behind a single turbine using the described setup is ongoing work.

Acknowledgements

The PhD of main author Emily Louise Hodgson is funded by the European Union Horizon 2020 research and innovation program under grant agreement no. 861291 as part of the Train2Wind Marie Skłodowska-Curie Innovation Training Network (https://www.train2wind.eu/).

References

[1] J. A. Frederik, B. M. Doekemeijer, S. P. Mulders, and J. W. van Wingerden, "The helix approach: Using dynamic individual pitch control to enhance wake mixing in wind farms," *Wind Energy*, vol. 23, 8 2020.

[2] K. Brown, D. Houck, D. Maniaci, and C. Westergaard, "Rapidly recovering wind turbine wakes with dynamic pitch and rotor speed control," *AIAA Scitech 2021 Forum*, 2021.

[3] W. Munters and J. Meyers, "An optimal control framework for dynamic induction control of wind farms and their interaction with the atmospheric boundary layer," *Philos. Trans. Royal Soc. A*, vol. 375, 4 2017.

[4] E. L. Hodgson, M. H. A. Madsen, N. Troldborg, and S. J. Andersen, "Impact of turbulent time scales on wake recovery and operation," *Journal of Physics: Conference Series*, vol. 2265, p. 022022, may 2022.

[5] J. A. Michelsen, "Basis3D – a Platform for Development of Multiblock PDE Solvers," tech. rep., DTU, 1992.

[6] N. N. Sørensen, *General Purpose Flow Solver Applied to Flow over Hills*. PhD thesis, DTU, 1995.

[7] J. Mann, "The spatial structure of neutral atmospheric surface-layer turbulence," *Journal of Fluid Mechanics*, vol. 273, pp. 141–168, 8 1994.

[8] J. Mann, "Wind field simulation," *Probabilistic Engineering Mechanics*, vol. 13, pp. 269–282, 10 1998.

[9] S. J. Andersen, N. N. Sørensen, and M. Kelly, "Les modelling of highly transient wind speed ramps in wind farms," *Journal of Physics: Conference Series*, vol. 1934, 2021.

18th EAWE PhD Seminar on Wind Energy
2 – 4 November 2022
Bruges, Belgium

Investigation of the Impact of Hub Height Optimization for Two Interacting Onshore Wind Farms

Gökay Kütükcü [a, b], **Oğuz Uzol** [c, d]

[a]Graduate Student, Dept. of Aerospace Eng., Center for Wind Energy Research (RÜZGEM), Middle East Technical University (METU), Ankara, Turkey
[b]Energy Expert, Energy Market Regulatory Authority (EMRA), Ankara, Turkey
[c]Professor, Dept. of Aerospace Engineering, METU, Ankara, Turkey
[d]Head, METU Center for Wind Energy Research (RÜZGEM), Ankara, Turkey

E-mail: uzol@metu.edu.tr

Keywords: Hub Height Optimization, FLORIS, Wind Turbine Wake, Wind Farm Interaction

1 Introduction

As the number of wind farms and installed capacity is increasing every year [1], inter-farm cluster-wake interactions become significant. Studies conducted in offshore wind farms in recent years show that wakes originating from large offshore wind power plants can reach up to 50 km in length and therefore impacting other neighbouring wind farms [2], [3]. Recent studies based on field measurements show that cluster wakes are in fact longer than previously predicted [2], [3], [4], [5], [6]. For the analysis of these wake interactions, analytical wake models are generally preferred due to their low computational cost especially when Annual Energy Production (AEP) estimations, wind farm layout optimizations or wind farm controller developments are studied [7], [8], [9]. Hub height optimization is one of the strategies investigated in literature to reduce the cluster wake effects in wind farms and thereby improve the AEP [10], [11]. This study presents the results of an investigation that focuses on finding the optimum hub height distributions for two interacting real onshore wind farms in Turkey, that are located on relatively complex terrain with significant elevation differences between turbines. Four different optimization scenarios are studied based on two different definitions of objective functions, which takes into account both the power production capacity and the relevant cost variations due to changing hub heights. The study is based on simulations performed using the FLORIS framework. We first introduce a methodology to be implemented in FLORIS such that existing significant variations in hub height levels due to elevation differences, hence partial wake interactions that are occurring as a consequence, are more realistically represented. After comparing the improvement levels obtained using this new methodology with SCADA data regarding AEP levels, we perform an optimization study for hub height distributions. The optimization is based on a systematic procedure that includes introducing definitions of Overall Evaluation Criteria (OEC) parameters for objective setting, generation of Design of Experiments (DoE) tables and related data through FLORIS simulations to properly cover the design space, Pareto analysis of generated data to find the most influential parameters, generation of response surfaces to represent these variations and Monte-Carlo based simulations to determine optimum hub height distributions.

2 Methodology

Two onshore wind farms located in the northern region of Turkey are selected (Figure 1). These wind farms are in close proximity of each other, about 3 km, and Havza wind farm operates under the influence Kayadüzü wind farm about 79 % of the year according wind direction data for the year 2021 obtained from the SCADA system. The details of the wind farms are given in Table 1.

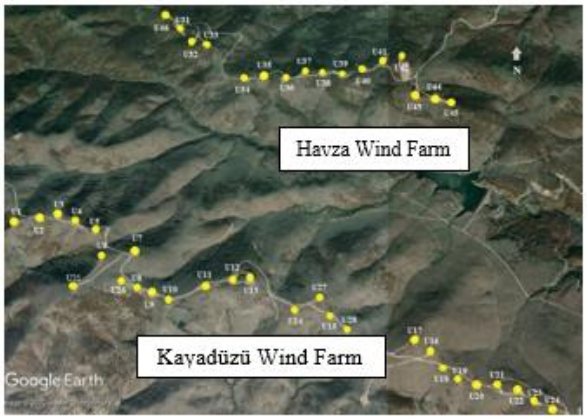


Figure 1: Turbine layouts of the selected wind farms.

Table 1: Details of Kayadüzü and Havza wind farms used in this study

	Capacity [MW]	Number of turbines	Rated power [MW]	Rotor diameter [m]	Hub height [m]
Kayadüzü	82	16	2.5	99.8	80
		14	3	116.8	91
Havza	56	16	3.5	138	111

Simulations of these wind farms are performed using the FLORIS framework. Because of the terrain, there are significant elevation differences between turbines and this is modelled through an easy to implement terrain elevation representation added to FLORIS as a part of this study that takes into account relative hub height and rotor overlap positions while using realistic estimates (i.e. consistent with SCADA data) for hub height velocity levels despite potentially large differences in hub heights of the wind turbines. Figure 2 shows sample FLORIS simulation results with and without terrain elevation model.

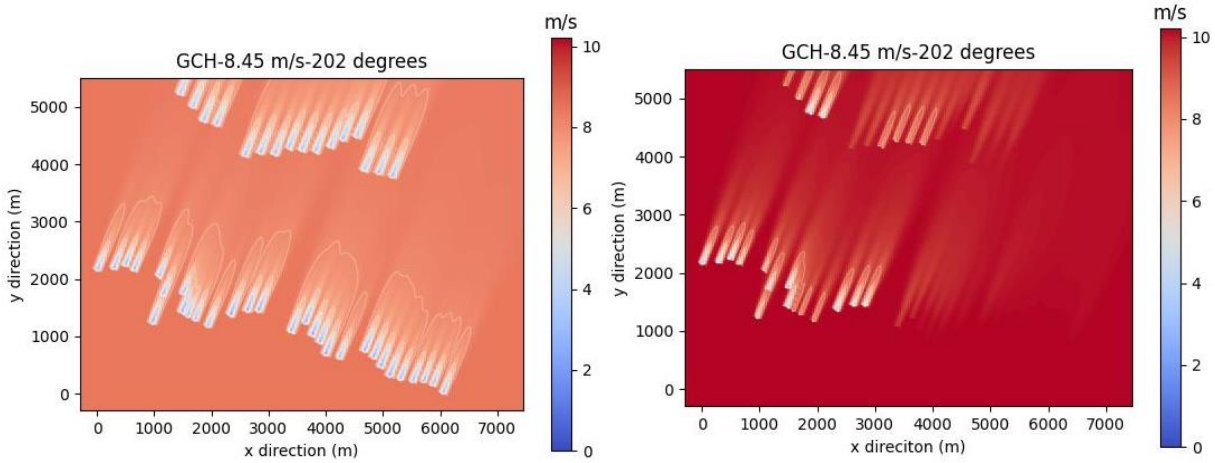


Figure 2: Sample FLORIS simulation results obtained using GCH wake model for 8.45 m/s and 202 degrees wind direction on the horizontal plane of the turbine U1 without terrain elevation representation (left) and with terrain elevation representation (right)

As optimization objectives, we introduce two Overall Evaluation Criteria (OEC) definitions: The first definition (OEC_1) only focuses on maximizing the total produced wind power, the second definition (OEC_2) introduces a

cost related parameter based on varying tower heights. Using these OEC definitions we studied four different cases to find optimum hub height distribution that maximizes the OECs:

Case-1: Finding optimum hub height distribution that maximizes OEC_1, including all turbines in both farms
Case-2: Finding optimum hub height distribution that maximizes OEC_2, including all turbines in both farms
Case-3: Finding optimum hub height distribution that maximizes OEC_1, including turbines in Havza wind farm
Case-4: Finding optimum hub height distribution that maximizes OEC_2, including turbines in Havza wind farm

We generate Design of Experiments (DoE) tables to cover the design space for each one of the four cases described above using fractional factorial scheme. Here, the hub height of each turbine is a design variable. For each design variable a variation range of ±15 m from the baseline hub heights is used, keeping in mind that increasing the hub height would generate an increase in tower costs and decreasing hub heights would reduce the ground clearance of the blades. This range would also influence how much would the downstream turbines be operating partially or fully immersed within the wakes of upstream turbines. Then, OEC data are generated through FLORIS simulations for each one of the investigated rows in the DoE tables. A Pareto analysis is performed for the generated data to determine which design variables are the most influential in affecting the OEC outputs. In other words, this analysis helps us to understand the sensitivity of the OEC values to the hub height variation of each individual turbine included in the design process. After the Pareto analysis is completed, second order Response Surface Equations (RSE) are obtained for the OEC variations of the determined most influential design parameters. The obtained response surfaces are then used for Monte-Carlo based simulations for obtaining the optimized hub height layout separately for each case, that is giving the maximum OEC value.

3 Results

According to the optimization results, the hub height distributions giving the maximum converged OEC values are obtained for each case separately and the optimization result of the case-2 is presented as a sample result in Table 2. The total farm power increased by 0.43 % and total tower height remained the same as the original. The hub height of the four turbines (i.e. U15, U16, U6 and U14) interacting with Havza wind farm decreased, hence reducing the effect of the cluster-wake on Havza wind turbines, while the hub height of the four turbines (i.e. U19, U18, U21 and U23) not interacting with Havza wind farm increased, hence benefiting from the higher wind speeds.

Table 2: Optimization results for Case 2 (Total wind farm optimization with OEC_2)

Turbine No.	**Turbine height_baseline [m]**	**Turbine height_optimized [m]**	**Change [m]**
U19	80	93	+13
U15	91	76	-15
U16	91	79	-12
U6	80	65	-15
U14	91	78	-13
U18	91	105	+14
U21	80	95	+15
U23	80	95	+15
		Total tower height change [m]	**0**
Farm Power	**Baseline [MW]**	**Optimized [MW]**	**Change (%)**
	70.871	71.170	0.42

4 Conclusions

Results show that partial wake interactions that occur at different elevations are captured with this terrain elevation method, which lead to more realistic representation of hub height velocities for the downstream wind farm that is operating within the cluster wake of the upstream wind farm. Hub height optimization results show that when both wind farms are included in the optimization process and if the cost related tower height parameter is not included in the objective function, the optimization process tends towards increasing the hub height of the turbines in the upstream wind farm to benefit from increased wind speeds at higher hub heights. However, when the cost related tower height is included, the optimization both tries to reduce wake interaction effects while increasing hub heights of the turbines that are not interacting with the downstream wind farm. When only the downstream wind farm is included in the optimization process but if the cost related tower height is not included in the objective function definition, the optimized results show that hub heights of all of the most influential turbines get increased. However when the cost related tower height is included, the optimized results show that the hub heights of the partially interacting turbines get decreased and those that are operating under stronger cluster-wake effects get increased.

Acknowledgements

We would like to thank the Havza wind farm and Kayadüzü wind farm operating companies for the information they have provided regarding the SCADA data.

References

[1] GWEC, “Global Wind Energy Report 2021,” Hamburg, Mar. 2021.
[2] B. Canadillo et al., “Offshore wind farm wake recovery: Airborne measurements and its representation in engineering models,” Wind Energy, vol. 23, pp. 1249–1265, Jun. 2020.
[3] T. Ahsbahs, N. G. Nygaard, A. Newcombe, and M. Badger, “Wind farm wakes from SAR and doppler radar,” Remote Sensing, vol. 12, no. 3, Feb. 2020, doi: 10.3390/rs12030462.
[4] V. Pettas, M. Kretschmer, A. Clifton, and P. W. Cheng, “On the effects of inter-farm interactions at the offshore wind farm Alpha Ventus,” Wind Energy Science, vol. 6, no. 6, pp. 1455–1472, Nov. 2021.
[5] N. G. Nygaard, S. T. Steen, L. Poulsen, and J. G. Pedersen, “Modelling cluster wakes and wind farm blockage,” in Journal of Physics: Conference Series, Sep. 2020, vol. 1618, no. 6. doi: 10.1088/1742-6596/1618/6/062072.
[6] M. P. van deer Loan et al., “An Improved k-ε model applied to a wind turbine wake in atmospheric turbulence,” Wind Energy, vol. 18, pp. 889–907, Apr. 2015.
[7] R. N. King, K. Dykes, P. Graf, and P. E. Hamlington, “Optimization of wind plant layouts using an adjoint approach,” Wind Energy Sci., vol. 2, no. 1, pp. 115–131, 2017, doi: 10.5194/wes-2-115-2017.
[8] E. G. A. Antonini, D. A. Romero, and C. H. Amon, “Optimal design of wind farms in complex terrains using computational fluid dynamics and adjoint methods,” Appl. Energy, vol. 261, Mar. 2020, doi: 10.1016/j.apenergy.2019.114426.
[9] J. Y. J. Kuo, D. A. Romero, J. C. Beck, and C. H. Amon, “Wind farm layout optimization on complex terrains – Integrating a CFD wake model with mixed-integer programming,” Appl. Energy, vol. 178, pp. 404–414, Sep. 2016, doi: 10.1016/j.apenergy.2016.06.085.
[10] A. Vasel-Be-Hagh and C. L. Archer, “Wind farm hub height optimization,” Applied Energy, vol. 195, pp. 905–921, 2017, doi: 10.1016/j.apenergy.2017.03.089.
[11] A. P. J. Stanley, A. Ning, and K. Dykes, “Optimization of the turbine design in wind farms with multiple hub heights, using analytic gradients and structural constraints,” Wind Energy, vol. 22, pp. 605–619, 2019, Accessed: May 09, 2022. [Online]. Available: https://onlinelibrary.wiley.com/doi/epdf/10.1002/we.2310

18th EAWE PhD Seminar on Wind Energy
2-4 November 2022
Bruges, Belgium

Mesoscale modelling of offshore wind farm wakes over the North Sea for different turbine densities

Ruben Borgers[a], **Marieke Dirksen**[b], **Andrew Stepek**[c], **Ine Wijnant**[c], **Ad Stoffelen**[c], **Naveed Akhtar**[d], **Jonas Van de Walle**[a], **Jérôme Neirynck**[a], **Johan Meyers**[e], and **Nicole P.M van Lipzig**[a]

[a]Department of Earth and Environmental Sciences, KU Leuven, Leuven, Belgium
[b]Faculty of Civil Engineering and Geosciences, TU Delft, Delft, Netherlands
[c]The Royal Netherlands Meteorological Institute (KNMI), De Bilt, Netherlands
[d]Helmholtz-Zentrum Hereon, Geesthacht, Germany
[e]Department of Mechanical Engineering, KU Leuven, Leuven, Belgium

E-mail: ruben.borgers@kuleuven.be

Keywords: COSMO-CLM, mesoscale modelling, Fitch, array- and cluster-scale wakes

1 Introduction

The rapid growth of the offshore wind energy sector emphasizes the need for realistic estimates of the energy yield and its variability for existing and planned offshore windfarms. As convection-permitting climate models can perform high-resolution, multi-year simulations over a domain that contains multiple wind farms and clusters, it is an excellent tool to make such quantifications. A wind farm parametrization scheme can be included in the mesoscale model to represent the interaction between wind farms and the atmosphere and in this way also the interactions between neighbouring wind farms. In our study, we employ the regional climate model COSMO5.0-CLM15 [1] extended with the wind farm parametrization of Fitch [2] to investigate the future impact of array- and cluster-scale wakes on the basin-wide wind energy potential over the North Sea by considering a future wind farm layout and future turbine specifications. This is further extended to different turbine spacings.

2 Model evaluation

The quality of the wind farm parametrization is essential in adequate simulation of these farm-scale wakes and has been evaluated in COSMO-CLM using large eddy simulations (LES) [3] and aircraft measurements of wakes [4]. However, the foundation of high-quality mesoscale wind farm wake simulations is the adequate simulation of the background conditions. Therefore a high-resolution, reanalysis-driven historical simulation was conducted for the period 2008-2020, a time period which ensures sampling of the natural variability [5] [6], in combination with an abundance of measurements: data from 19 in-situ stations and 6 wind lidars were collected, for which the locations can be identified on Fig. 1. The contour of the simulation domain is indicated in cyan. The mean bias [model - observations] for the different stations is indicated in Fig. 2. This shows that the model tends to be negatively biased closer to the surface, but above 90m, the bias is strongly reduced. A deeper inspection at turbine hub height shows that the overlap in the frequency distribution of wind speeds and wind directions between the model and the observations is generally above 95%. Moreover, the theoretically inferred capacity factors from these wind speed distributions of the model and the observations only differ 2% on average.

3 Wind farm modelling experiments

To explore the future impact of of array- and cluster-scale wakes, a series of experimental model runs were carried out using the evaluation setup of the previous section, extended with the wind farm parametrization. These ex-

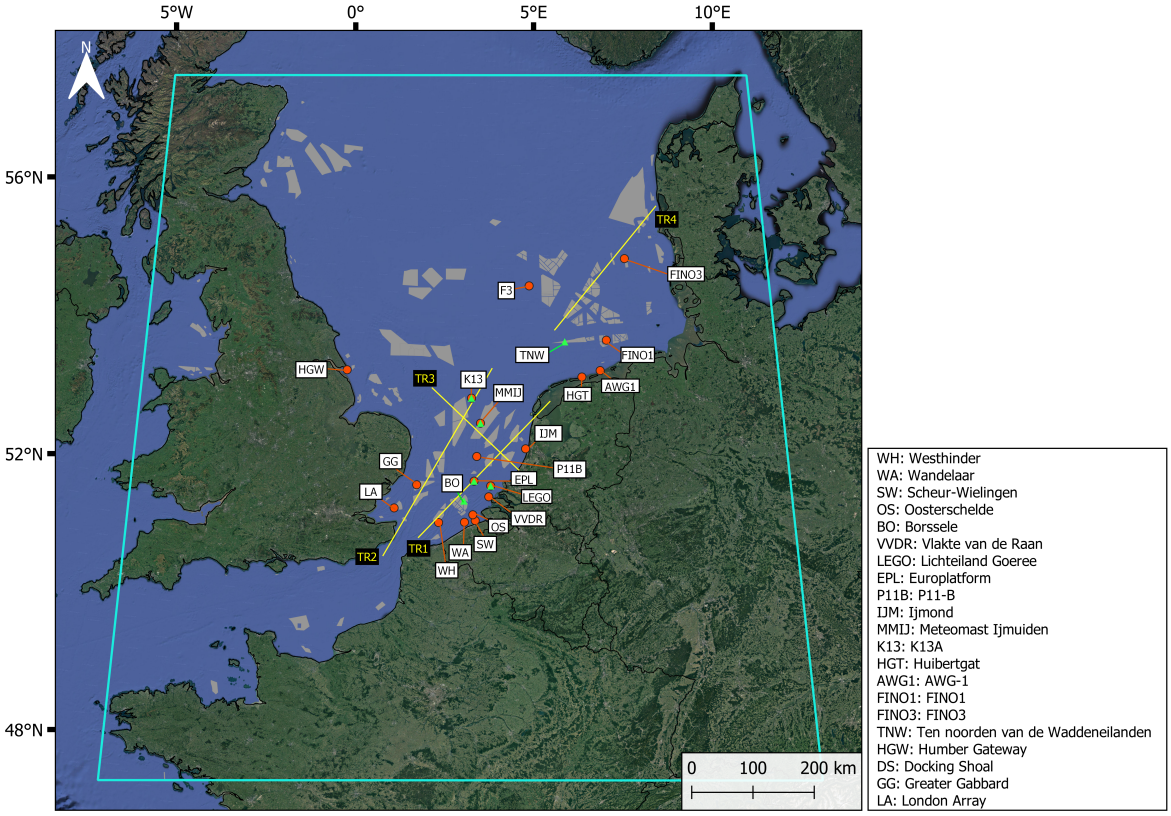


Figure 1: map of the study region (left). The simulation domain is indicated in cyan. In-situ stations are indicated with an orange dot and wind lidars with a green triangle. The future wind farm layout used in the experimental simulations is indicated in grey. The yellow transects are considered in the study of the wind farm wake climatology in the second part of the study. On the right, a table linking the names of the measurement stations and the abbreviations. Created with QGIS.

periments are summarized in Table 1. A projected wind farm layout was included in 4 of these simulations based on the EMODNET wind farm dataset [7] and GIS data from the Royal Belgian Institute for Natural Sciences [8] and is shown in Fig. 1. Considering the computational cost of these experiments, the timespan was limited to one representative year in terms of the North Sea wind field. The year 2016 was determined to be representative for the last 30 years based on the procedure outlined by Tammelin et al. [9]. The different simulations are compared along the transects indicated on Fig. 1. For this analysis, only the westerly winds in a sector of 30° around the transect orientation were selected based on the center grid cell on the transect.

Scenario	turbine type	capacity density (MW/km²)	Identifier
undisturbed	/	/	NOWF
present-day	NREL 5MW [SOURCE]	8.1	PD
future - low density	IEA 15MW	3.5	FUT_LD
future - medium density	IEA 15MW	8.1	FUT_MD
future - high density	IEA 15MW	10	FUT_HD

Table 1: Summary of the different modelling experiments conducted for the year 2016.

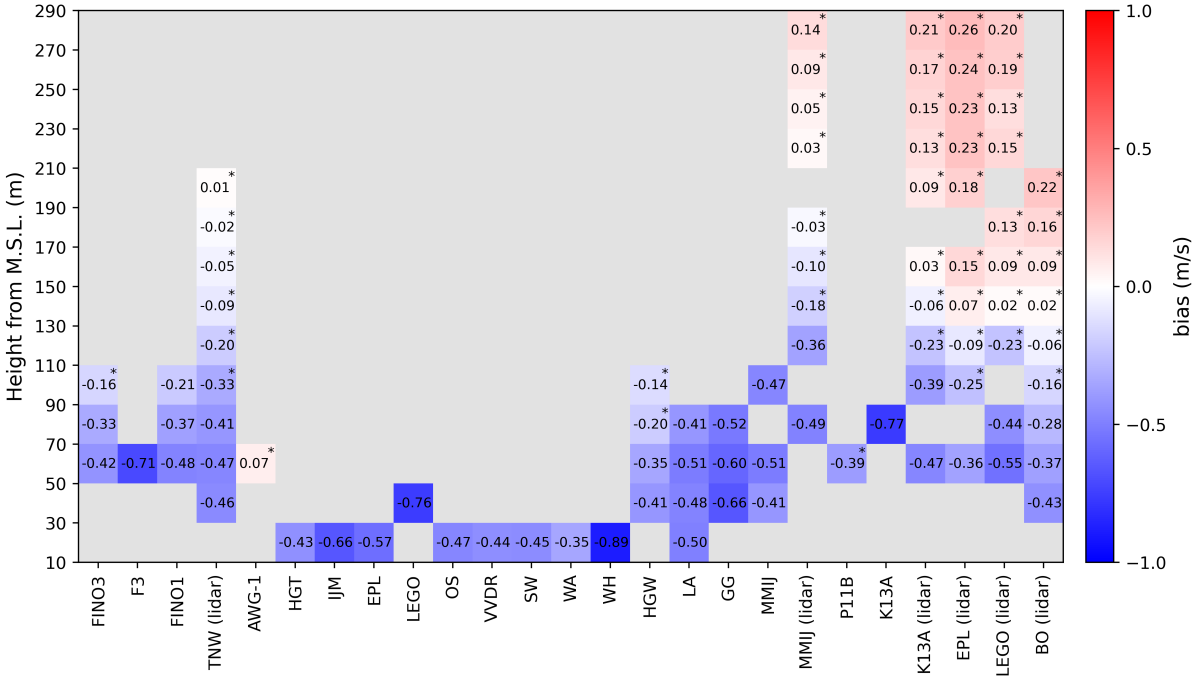


Figure 2: Wind speed bias (m/s) for the complete time period of the measurement data. This concerns measurements between 10 and 290 meters to MSL. The vertical range is subdivided into 20 meter intervals for readability. Stations are clustered per region.

These simulations show that the perturbation to the inflow climatology of neighbouring farms, and so, to the long-term capacity factor are much more severe under denser turbine spacings (up to 25%) than under a low-spacing scenario (up to 10%) (Fig. 3). Evidently, the impact depends strongly on the wind farm spacing. Another interesting finding is that the capacity factor reduction at 150m height is strongest in the simulation with 5MW turbines, which suggests that the strongest wind speed reductions do not take place at hub height. This has significant implications for the interaction between wind farms with strongly different turbine heights. This analysis is further expanded and extended to different dynamic stability classes.

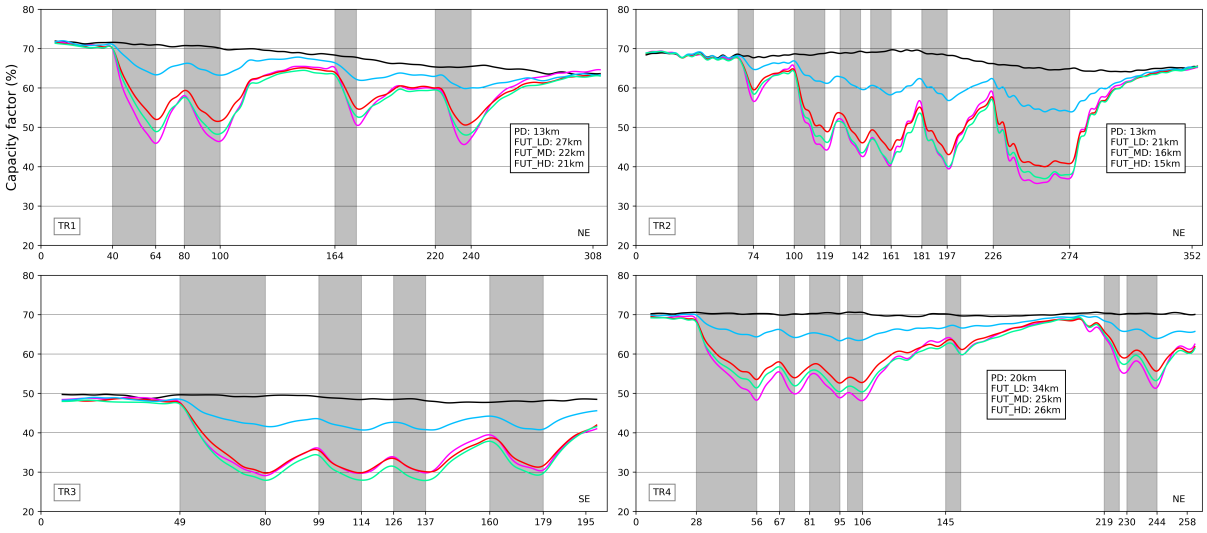


Figure 3: 2016 capacity factor transects for the four lines indicated on Fig. 1. for each of the 5 scenarios: NOWF (black), PD (magenta), FUT_LD (blue), FUT_MD (red), FUT_HD (green). The X-axis is in km. Wind data is only considered when the wind direction deviates within +-15° from the transect orientation (W to E) at the middle grid cell of each transect. Grey shadings represent wind farms. The text boxes summarize the e-folding distances for the capacity factor wake climatology downwind of the farm on the left of the respective text box.

References

[1] Rockel, B., Will, A., Hense, A. The regional climate model COSMO-CLM (CCLM). *Meteorologische Zeitschrift*, 17(4), 347-348. 2008.

[2] Fitch, A. C., Olson, J. B., Lundquist, J. K., Dudhia, J., Gupta, A. K., Michalakes, J., Barstad, I. Local and mesoscale impacts of wind farms as parameterized in a mesoscale NWP model. *Monthly Weather Review*, 140(9), 3017-3038. 2012.

[3] Chatterjee, F., Allaerts, D., Blahak, U., Meyers, J., van Lipzig, N. P. M. Evaluation of a wind-farm parametrization in a regional climate model using large eddy simulations. *Quarterly Journal of the Royal Meteorological Society*, 142(701), 3152-3161. 2016.

[4] Akhtar, N., Geyer, B., Rockel, B., Sommer, P. S., Schrum, C. Accelerating deployment of offshore wind energy alter wind climate and reduce future power generation potentials. *Scientific reports*, 11(1), 1-12. 2021.

[5] Geyer, B., Weisse, R., Bisling, P., Winterfeldt, J. Climatology of North Sea wind energy derived from a model hindcast for 1958–2012. *Journal of Wind Engineering and Industrial Aerodynamics*, 147, 18-29. 2015.

[6] Ronda, R. J., Wijnant, I. L., Stepek, A. Inter-annual wind speed variability on the North Sea. KNMI WindEurope. 2017

[7] Emodnet (2020). Wind Farms (Polygons) [Data set]. Emodnet. https://www.emodnet-humanactivities.eu/search-results.php?dataname=Wind+Farms+%28Polygons%29

[8] Laurence V. (2022). Shapefiles van de Belgische en Dunkirk offshore zones [Data set]. Royal Belgian Institute of Natural Sciences (RBINS).

[9] Tammelin, B., Vihma, T., Atlaskin, E., Badger, J., Fortelius, C., Gregow, H., ... Venäläinen, A. Production of the Finnish wind atlas. *Wind Energy*, 16(1), 19-35. 2013.

18th EAWE PhD Seminar on Wind Energy
2-4 November 2022
Bruges, Belgium

Modelling of ice throw from wind turbines: a case study

Kim Janovski[a] and **Edward Hart**[b]

[a]WAMESS CDT, University of Strathclyde, Glasgow
[b]Wind Energy and Control Centre, University of Strathclyde, Glasgow
E-mail: kim.janovski@strath.ac.uk

Keywords: ice, icing, trajectory

1 Background

This extended abstract aims to introduce the reader to an ice throw model which is currently being developed by Janovski et al., and is based on work of Biswas et al. [1]. In environments where low temperatures commonly occur, there is a chance blade icing occurs. This presents a risk of ice throw, and is likely to pose hazard to the site personnel, surrounding infrastructure and bypassers. It is important for this issue to be investigated, in order to enhance the safety conditions at wind farms and during wind farm planning. Code was written in Python to solve three 2^{nd} degree ODEs that describe the motion of the ice fragment in downwind (x), lateral (y) and vertical (z) directions, and determine its landing location. State-space model approach was used to define dynamics of the system, states being position and velocity, and state derivatives being velocity and acceleration. Two numerical ODE solvers have been assessed for their suitability: 4^{th} order Runge-Kutta and Euler. Euler method was about 4x faster, but further testing proved it was quite unreliable with small masses and large initial accelerations. Runge-Kutta (RK4) solver was coded from scratch, so the numerical integration can be applied to this specific problem, with wind speed, and position specific parameters being recomputed for each iteration of the solver. In-between each of the Runge-Kutta iterations, wind speed U and magnitude of the absolute velocity of the fragment relative to the wind $|V|$ were recalculated. The equations of motion used in the ODE solver stem from work by Biswas et al.[1], and were modified to be more accurate in the case of plate-like (sheet) fragment. Sensitivity study was run, to determine suitable timestep, and then the case study results are demonstrated.

2 Methodology

Initially, model was developed only for compact fragments, where lift force is not considered. Primary analysis of the model was be done on a bluff body with a drag coefficient of $C_D = 1$. Model assumes that the ice will always be released from the tip of the blade (worst case scenario), turbine is always facing into the wind (wind is always normal to the rotor plane), and yaw error is assumed to be zero. If [x,y,z] represent the along-wind, lateral and vertical dimensions, then the system of differential equations can be used to represent the motion of the fragment:

$$\dot{u} = \frac{\partial^2 x}{\partial t^2} = -\frac{1}{M}\frac{1}{2}\rho C_D A\,(u-U)\,|V| \tag{1}$$

$$\dot{v} = \frac{\partial^2 y}{\partial t^2} = -\frac{1}{M}\frac{1}{2}\rho C_D A\,(v)\,|V| \tag{2}$$

$$\dot{w} = \frac{\partial^2 z}{\partial t^2} = -g - \frac{1}{M}\frac{1}{2}\rho C_D A\,(w)\,|V| \tag{3}$$

where u, v and w are fragment velocity components in x, y and z directions, M is the mass of the ice fragment, and A is its frontal surface area. Standard acceleration due to gravity is given by g, whilst ρ and C_D are air density and drag coefficient, respectively. Overall velocity of the fragment (relative to the wind U), denoted as $|V|$, is calculated as:

$$|V| = \sqrt{\left[(u-U)^2 + v^2 + w^2\right]} \tag{4}$$

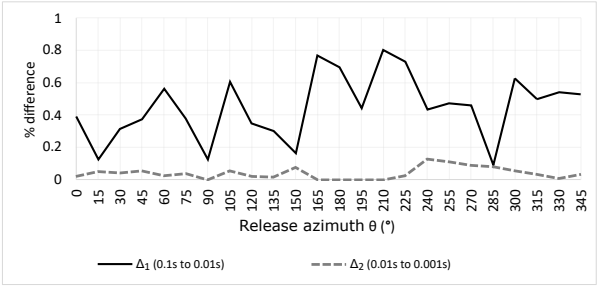
These equations are the same, simplified equations for compact fragments that Biswas et at. [1] used when developing their model. However, for sheet (or plate-like) fragments, effects of lift are not negligible. Using Rodrigues' rotation formula, vectorised equations were derived for the case with lift. Biswas et al. [1] had a similar idea, but used in-plane projections. By using the newly derived equations and plotting the trajectories and fragment landing locations, an issue was spotted in the original model by Biswas et al. [1], and lift plots they obtained were shown to be inaccurate. Final equations can be seen below, with all symbols having the same meaning as previously, and a newly defined lift coefficient C_L. Acceleration vector $[\dot{u}, \dot{v}, \dot{w}]$ is defined as:

$$\dot{u} = \frac{\partial^2 x}{\partial t^2} = \frac{1}{M}\left[-\frac{1}{2}\rho C_D A|V|(u-U) + \frac{1}{2}\rho C_L A\frac{|V|}{|V_H|}(-w)(u-U)\right] \tag{5}$$

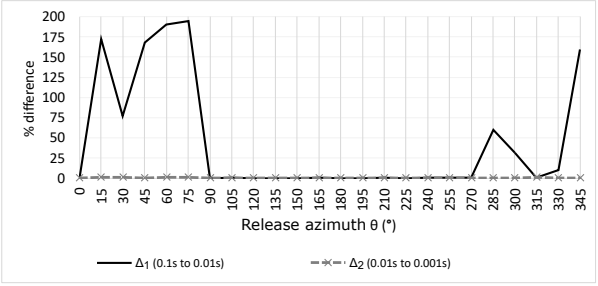
$$\dot{v} = \frac{\partial^2 y}{\partial t^2} = \frac{1}{M}\left[-\frac{1}{2}\rho C_D A|V|(v) + \frac{1}{2}\rho C_L A\frac{|V|}{|V_H|}(-wv)\right] \tag{6}$$

$$\dot{w} = \frac{\partial^2 z}{\partial t^2} = \frac{1}{M}\left[-g - \frac{1}{2}\rho C_D A|V|(w) + \frac{1}{2}\rho C_L A\frac{|V|}{|V_H|}\left(v^2 + (u-U)^2\right)\right] \tag{7}$$

Wind speeds were obtained from power law, and the shear coefficient (Hellman exponent) α = 1/7 was held constant during the study. Lift model does not account for tumbling, and plate is always oriented to maximise lift. Timesteps of 0.1s, 0.01s and 0.001s were considered. Absolute distance of the fragment throw was calculated using the final landing coordinates, x_{final} and y_{final} (at the instance when z = 0). Then, percentage difference was calculated for the absolute distance thrown between the timesteps, given in Figure 1. The analysis was run for two cases - drag only case (compact fragment), and the case with lift (plate-like fragment). Input parameters for sensitivity study were consistent with the Biswas study [1]: ρ = 1.225 kg/m^3, rotation speed of the rotor ω = 14.5 rpm, fragment area A = 0.08m^2, mass = 1 kg, wind speed at hub-height U_{hh} = 15 m/s, hub height z = 100m, blade radius r = 45m, drag coefficient C_D = 1, lift coefficient C_L = 1 (for case with lift only). Plate-like fragment



a)



b)

Figure 1: Time sensitivity percentage differences in distance thrown, between different timesteps. Results are given for a) compact fragment, and b) sheet fragment.

model showed a significantly greater sensitivity, especially for the release angles that imply the fragment is thrown upwards. Between the timesteps of 0.1s and 0.01s, the maximum difference was 194.2%. For the timesteps of 0.01s and 0.001s, the maximum difference was 1.55%, which corresponds to a difference of 7.75m if the throw distance was 500m. In the Biswas model, timestep of 0.02s was used, but the effects of lift were not explored in-depth. Speed of execution was not crucial in this study, so decision was made that a timestep of 0.001s would be used for better accuracy, due to the increased sensitivity of the lift inclusive model.

3 Case Study

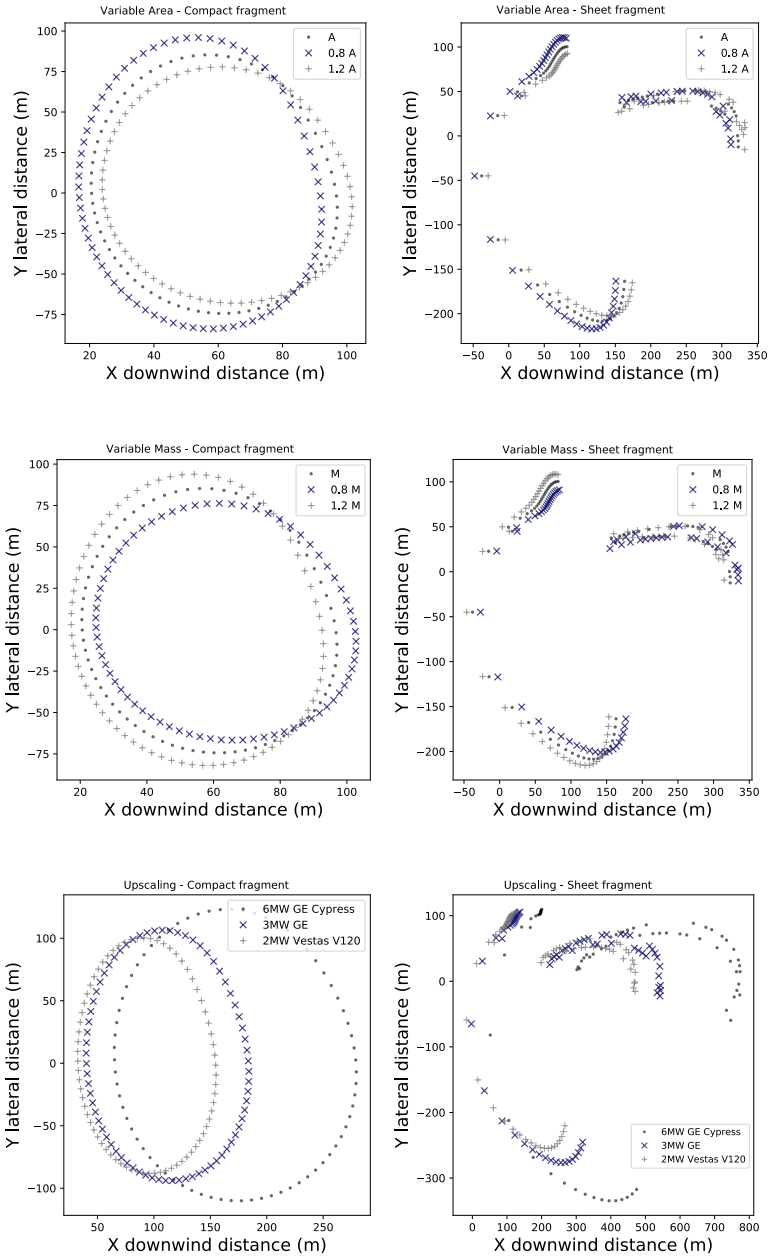


Figure 2: Case Study Plots - Final Fragment Landing Coordinates

A set of case studies was run for a fragment mass M = 0.5 kg and frontal surface area A = 0.03 m^2. Then, this mass and area were varied by 20%.

First two cases (rows 1 and 2) of Figure 2, use the same turbine and input parameters as in [1] (hub height 100m and blade radius 45m), but hub height wind speed U_{hh} was decreased to 8.5 m/s to reach the optimal tip speed ratio of 8. In the case of compact fragment, increase in mass led to an increase in the maximum throw distance. Because $C_D A/M$ component of drag force is decreased, they will decelerate more slowly and travel higher in the air - resulting in longer throw distance. For sheet fragments, the effect is mainly opposite, and increase in mass decreased the largest throw distance. This is counter-intuitive, but it was observed that all sheet fragments which travel the furthest experience lift effect as dominant (those are fragments with release angles where the blade is moving upwards). Therefore, when the mass is increased, dominant lift effect is decreased and they travel less

far. In the case of compact fragment, increase in area led to a decrease in the maximum throw distance. This is a directly opposite effect of increasing mass - $C_D A/M$ component of drag force is increased, resulting in higher drag and shorter throw distance. Initial release velocities are decelerated more quickly. For sheet fragments, the result is mainly opposite, and increase in area increases the largest throw distance. For those fragments that fly the furthest, lift effect is dominant. As the area is increased, lift effect is increased and they travel even further.

Row 3 (upscaling case) refers to more recent turbine models. Turbines have significantly evolved in size since 2012, when Biswas et al.[1] model was developed. For upscaled turbines, tip-speed ratio was kept at $\lambda = 8$ too, by slightly modifying the hub height wind speed U_{hh}. Speed of rotor rotation was kept constant in the simulation. Three models of a turbine were chosen, as a representative of modern turbines that are getting increasingly large in size. The first and the largest turbine considered is GE Cypress [4], a 6MW platform. This model is pushing the boundaries of what onshore turbines can achieve, and is a good representative of the future generations of turbines. Its hub height is 167m, and blade radius is 82m. In order to keep the optimal tip-speed ratio, while keeping angular speed constant, wind speed at hub height U_{hh} was set to 15.5m/s. The second turbine considered is a 3MW platform, [3], with hub height of 134m, and blade radius 65m. In order to keep the optimal tip-speed ratio while keeping angular speed of rotor constant, wind speed at hub height U_{hh} was set to 12.3m/s. The last turbine considered is Vestas V120, [5], a 2MW platform with hub height of 122m, and blade radius of 59m. In order to keep the optimal tip-speed ratio while keeping angular speed of rotor constant, wind speed at hub height U_{hh} was set to 11.2m/s. Area and mass of the fragment were the unchanged. Row 3 of Figure 2 shows that for the largest model of the turbine, fragment flies the furthest for both compact and sheet fragment, which was expected. These fragments also had the highest impact kinetic energies. The case for a sheet fragment, with GE Cypress, is the largest throw distance of 773.6m, and shows the upper limit of one of the largest platforms on the market. This is the theoretical ultimate worst case scenario, where a plate experiences no tumbling. Compact case scenarios (fragments are bluff bodies) are more realistic. The highest impact kinetic energy was 103.4J. For each of the scenarios plotted, the maximum impact energy surpassed the threshold of 40J, and should be considered fatal [2]. The results for the upscaling case are not directly comparable between the turbine models, as the wind parameters had to be altered slightly to account for the optimal tip speed ratio.

4 Future Work

Authors are working on the wake and turbulence additions to the model, which they are keen to publish soon. In the future, more case studies will be revisited, and more in-depth analysis of the model will be provided.

Acknowledgements

I would like to thank Dr Edward Hart, Dr Marco Vezza, Dr Adam Stock, Dr Fraser Tough, Marine Lannic and RES ltd., Dr Peter Jamieson, Dr Scott McLaren-Gow, Dr Sofia Koukoura, Dr Peter A. Taylor (co-author of [1]) - without your help, support and contributions, this work would not be possible.

References

[1] S. Biswas, P. Taylor, and J. Salmon. A model of ice throw trajectories from wind turbines. *Wind Energy*, 15(7):889–901, 2012.

[2] R. E. Bredesen, M. Drapalik, and B. Butt. Understanding and acknowledging the ice throw hazard - consequences for regulatory frameworks, risk perception and risk communication. *Journal of Physics: Conference Series*, 926:012001, nov 2017.

[3] GE Renewable Energy. 3 MW onshore wind turbine platform, https://www.ge.com/renewableenergy/wind-energy/onshore-wind/3mw-platform, 2017.

[4] GE Renewable Energy. Cypress onshore wind turbine platform, https://www.ge.com/renewableenergy/wind-energy/onshore-wind/cypress-platform, 2019.

[5] Vestas. V120-2.2MW onshore platform, https://www.vestas.com/en/system/links/external-links/2-mw-brochure, 2021.

18th EAWE PhD Seminar on Wind Energy
2-4 November 2022
Bruges, Belgium

Multi-rate integration techniques in wind farm LES using actuator line method

K Ntrelia[a] and **J Meyers**[a]

[a]Department of Mechanical Engineering, KU Leuven, Celestijnenlaan 300A, 3001 Leuven

E-mail: konstantina.ntrelia@kuleuven.be

Keywords: large-eddy simulation, wind turbine modeling, numerical time integration

1 Introduction

With the emergence of wind energy as one of the leading renewable sources of energy production, Large Eddy Simulation (LES) has proven as a crucial tool among the research society. LES enables the study of wind farm effects and the complex phenomena that take place within them. In these studies, wind turbines are usually represented through actuator models that replicate the forces acting on the flow. The actuator models that have been developed through a series of studies, may vary depending on their complexity and their accuracy of modeling wind turbines.

Starting from the Actuator Disk Model (ADM) [1], which is the most efficient but the least accurate model, as it neglects the geometry of the wind turbine, we end up to more accurate models. The Actuator Line Model (ALM)[2] is one such model. However, its time step limitations render ALM computationally inefficient, urging the necessity of developing new models. The Actuator Sector Model(ASM)[3] rises to the above needs, carrying however the disadvantages of the ADM inaccuracy. Thus, the present research explores novel ways of wind turbine modeling by employing multi rate-time stepping techniques. Multi-stepping methods enable the decoupling between the components of one's system. Applying a fine temporal time scale for the rotor dynamics, while coarser scales for the flow resolution, the requirements of ALM are respected. These methods, exhibit great computational benefits in LES, while maintaining a high order accuracy scheme.

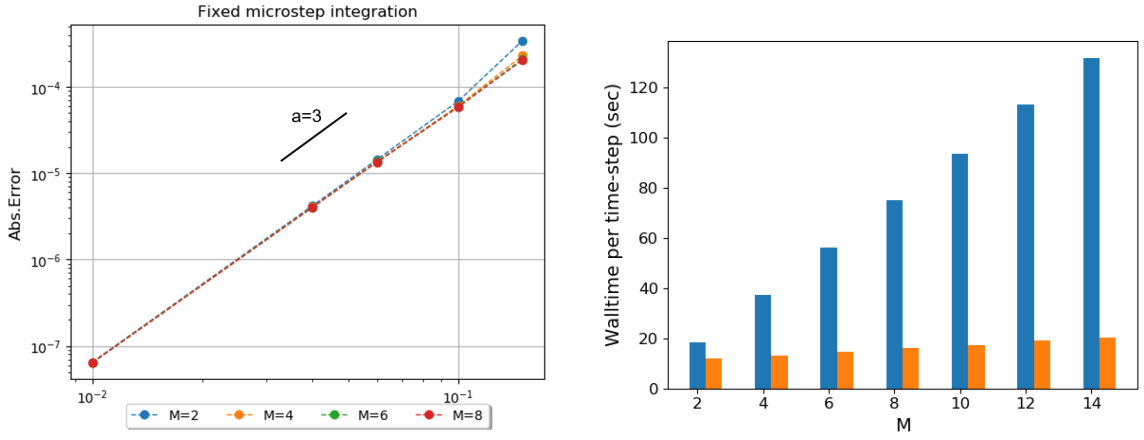
2 Methodology

Multirate Generalised Additive Runge-Kutta Methods(MRGARK)[4], fall into the category of generic Runge-Kutta methods. The fundamental theory of MRGARK methods, rely on the ability of a system's partitions to evolve at different time scales. Utilising the property above, the system's components can be decoupled, resulting in avoiding excess computational cost.

For the purpose of this study, MRGARK methods have been implemented into a pseudo-spectral LES framework, SP-Wind, developed in KU Leuven. The wind turbines are modeled using the actuator line model(ALM). Following the MRGARK concept, the system's governing equations are integrated using different time scales, depending on the respective components. The rotor dynamics are resolved using a finer time scale h, while the flow characteristics are resolved with a coarser scale H. The two time scales are related through the multi-rate ratio M, where $M = H/h$. Information between components is exchanged by a proper coupling, so that a homogeneous time marching is achieved.

3 Results and Discussion

In a first approach, MRGARK methods are implemented within the LES framework.Various high order schemes have been formulated by Sarshar, Roberts & Sandu [2] from which an explicit third order scheme (Ex3-Ex3 3[S]) has been selected. Following, the performance of the scheme in terms of accuracy and efficiency needs to be tested. For this reason, a simple study case is set up, using a NREL 15MW wind turbine inside a uniform inflow



(a) (b)

Figure 1: Absolute error in reference to time step. A fixed macro-step time integration is carried out with varying multi-rate step ratios M using Ex3-Ex3 3[S] scheme (a). Walltime per time step in reference to multi-rate ratios M, between fourth order Runge-Kutta (blue) and Ex3-Ex3 3[S](orange).

of 8 m/sec. For the integration, different time steps $H = 0.01sec, 0.04sec, 0.06sec, 0.1sec, 0.15sec$ and multi-rate factors $M = 2,4,6,8$ are employed. At this point, we need to clarify that due to the pseudo-spectral nature of the code, in order to avoid excess computational cost in the fast stages of the integration, that originates from the Fast Fourier transformations (FFT) of the fast velocity field, needed for the fast pressure-velocity coupling, the fast velocity field is preserved constant.

The performance of the scheme is first tested through an error analysis. The error is computed using the L_1 norm, where the same set up with a fourth order Runge-Kutta integration method with a very fine time step is used as the reference case. The obtained results of this analysis are depicted in Figure 1(a). The multi-rate scheme seems to predict with a high accuracy the solution, as well as the numerical order seems to match the theoretical order. Moreover, from Figure 1(b), it is evident that the MRGARK methods can offer great gains in terms of computational cost. The computational effort of LES indeed increases, when selecting higher multi-rate ratios, but not with the same rate as in the single rate case(orange). This can be attributed to the fact that on the multi-rate case the computational effort consumed in the flow resolution, which requires the most computational resources, remains constant

4 Future Work

Following the implementation and validation of MRGARK schemes within the LES framework, there are various suggestions and pathways towards future research. The next step within the scope of this study, would be to extend the framework and resolve the fast velocity and pressure, where the feedback of these fast fields would increase the complexity, but also the accuracy of the model itself. Moreover, in the context of wind turbine modeling, the final goal would be to integrate the structural dynamics of wind turbines in the multi-rate framework. In the cases of multibody dynamics, it is known that fine time-steps, even finer than those required in ALM techniques, are needed in order to capture the high frequency oscillations. In the end, the true benefits that MRGARK methods hold for LES will be revealed in the application of such complex cases.

References

[1] Froude, R. E. On the part played in propulsion by differences of fluid pressure, *Transactions of the Institution of Naval Architects*, 30:390-423 ,1889

[2] Sørensen, J. N. and Shen, W. Z. Numerical modeling of wind turbine wakes, *Journal of Fluids Engineering*,124:393–399,2002

[3] Storey, R. C., Norris, S. E., and Cater, J. E. An actuator sector method for efficient transient wind turbine simulation,*Wind Energy*,18:699 - 711,2015

[4] Sarshar A, Roberts S and Sandu A. Multirate Generalized Additive Runge-Kutta methods, *SIAM J. Sci. Comput.*41(2):816-847,2019

18th EAWE PhD Seminar on Wind Energy
2-4 November 2022
Bruges, Belgium

Simulating Large Wind Farms with the Lattice Boltzmann Method

Henry Korb[a], **Henrik Asmuth**[a], and **Stefan Ivanell**[a]

[a]Uppsala University

E-mail: henry.korb@geo.uu.se

Keywords: Large-eddy simulations, lattice Boltzmann method, wind farm simulations

A number of currently researched topics in wind energy science demand high-fidelity simulations of wind farms, such as wind farm control, wind farm blockage or the influence of stability [7]. However, simulations of the highest achievable fidelity, that is, large eddy simulations (LES) with the actuator line method, are extremely demanding in terms of computational resources and energy. Recent works have shown that the lattice Boltzmann method (LBM) is a viable alternative to Navier-Stokes based solvers for large-eddy / actuator line simulations [4, 3]. Due to excellent parallelizability, the implementation of LBM on massively parallel hardware, such as graphical processing units, is very efficient and scalable. This circumstance allowed the reduction of computational and energy demand by multiple orders of magnitude in simulations of a single turbine compared to a finite Volume Navier-Stokes code [5]. The reduction in time-to-solution not only increases the speed at which research cab be conducted, it allows the use of LES for new purposes, for example data generation for machine learning methods [2, 6] or uncertainty quantification. Furthermore, the low time-to-solution makes this method appealing for application in industry.

While the bulk scheme of the LBM is well developed, one of the major issues of the method has been the lack of well working boundary conditions in combination with wall models. Recently, Asmuth et al. introduced the inverse momentum exchange method, which the authors demonstrated to yield high quality results for simulations of the atmospheric boundary layer [1]. In combination with the previous proven potential for single turbine simulations, this opens the possibility to simulate full wind farms.

In our contribution, we will discuss the ramifications of simulating large offshore wind farms with LBM, such as hardware requirements and the development of that hardware, the models used and scalability of the method. Furthermore, we address current modelling gaps. We also aim at presenting initial results of full scale wind farm simulations, considering computational performance and scaling.

References

[1] H. Asmuth, C. F. Janßen, H. Olivares-Espinosa, and S. Ivanell. Wall-modeled lattice Boltzmann large-eddy simulation of neutral atmospheric boundary layers. *Physics of Fluids*, 33(10):105111, Oct. 2021.

[2] H. Asmuth and H. Korb. WakeNet 0.1 - A Simple Three-dimensional Wake Model Based on Convolutional Neural Networks. *Journal of Physics: Conference Series*, 2265(2):022066, May 2022.

[3] H. Asmuth, G. P. Navarro Diaz, H. A. Madsen, E. Branlard, A. R. Meyer Forsting, K. Nilsson, J. Jonkman, and S. Ivanell. Wind Turbine Response in Waked Inflow: A Modelling Benchmark Against Full-Scale Measurements. SSRN Scholarly Paper ID 3940154, Social Science Research Network, Rochester, NY, Oct. 2021.

[4] H. Asmuth, H. Olivares-Espinosa, and S. Ivanell. Actuator line simulations of wind turbine wakes using the lattice Boltzmann method. *Wind Energy Science*, 5(2):623–645, May 2020. Publisher: Copernicus GmbH.

[5] H. Asmuth, H. Olivares-Espinosa, K. Nilsson, and S. Ivanell. The Actuator Line Model in Lattice Boltzmann Frameworks: Numerical Sensitivity and Computational Performance. *Journal of Physics: Conference Series*, 1256:012022, July 2019.

[6] H. Korb, H. Asmuth, M. Stender, and S. Ivanell. Exploring the application of reinforcement learning to wind farm control. *Journal of Physics: Conference Series*, 1934(1):012022, May 2021.

[7] G. van Kuik and J. Peinke, editors. *Long-term Research Challenges in Wind Energy - A Research Agenda by the European Academy of Wind Energy*, volume 6 of *Research Topics in Wind Energy*. Springer International Publishing, Cham, 2016.

18th EAWE PhD Seminar on Wind Energy
2-4 November 2022
Bruges, Belgium

Study of wave effects on the wind turbine aerodynamics with large-eddy simulation in sigma coordinates

Xu Ning[a] and **Mostafa Bakhoday-Paskyabi**[a]

[a]Geophysical Institute, University of Bergen

E-mail: mostafa.bakhoday-paskyabi@uib.no

Keywords: Wave effects, LES, Sigma coordinates, wind turbine aerodynamics, wake

1 Introduction

The sea surface is always characterized by waves with a wide range of amplitudes, propagation speeds and directions. Previous observational and numerical studies[1, 2] have demonstrated that these waves can modify the exchange of heat and momentum between the air and the ocean, and thus change the wind shear, veer and turbulent flows. Though many numerical studies have focused on the mechanism of wind-wave interaction[3, 4, 5], not enough work has been done with regard to the influence of the ocean waves on the aerodynamics of wind turbines and their wakes under various wind-sea conditions. To this end, an wave-phase-resolved LES solver in Sigma coordinates is used in this study to perform high-fidelity simulations of the wind turbine wake flows under effects of waves with different parameters. The main objective of this work is to gain better knowledge on the following aspects:

1. The wave effects on the power production and the structural loads of wind turbine.
2. The effects of the wave-induced flow structures on the wind turbine wake development.
3. How these wave effects vary with different wind-wave conditions.

2 Numerical method and simulation setup

The open source LES code PALM (PArallelized Large-Eddy Model) is modified to solve the N-S equations in a wave-following coordinate system through a Sigma mesh transformation. Regular waves with prescribed parameters are imposed to the bottom of the domain and provide the boundary condition in terms of water surface elevation and velocity. Compared with parameterization methods for modelling wave effects, the wave-phase-resolved LES has the advantage of directly resolving the dynamic wave geometry and the wave-induced flow structures, reproducing not only the wave-modified mean wind but also the wave-coherent turbulent features, which is crucial in the analysis of wind turbine aerodynamics. In the present work, the wake flows of a NREL-5MW wind turbine represented by the Actuator Disk Model with rotation (AMD-R) in neutral boundary layer were simulated in various wind-wave conditions. We considered two hub height wind speeds, wind-driven young wave, and swell with wind-following and -opposing propagation directions in 8 cases. The setup information is summarized in Table 2. The OpenFAST[6], an engineering tool for modelling the dynamic response of wind turbines is also employed to analyse the wave-induced structural loads, using LES data as the inflow condition.

3 Results

We first study the change of mean wind speed and the energy spectra of turbulence caused by the various wave motions compared with flat surface condition, and then investigate the impacts of waves on the wind turbine aerodynamics including the power harvesting rate, the blade bending moments and the features of wake flow.

Table 1: Simulation setup

Case ID	hub height wind speed (m/s)	wave amplitude (m)	wave phase speed (m/s)	wave direction
1	12.0	-	-	-
2	12.0	1.0	7.1	following wind
3	12.0	2.0	14.1	following wind
4	12.0	2.0	14.1	opposing wind
5	5.0	-	-	-
6	5.0	1.0	7.1	following wind
7	5.0	2.0	14.1	following wind
8	5.0	2.0	14.1	opposing wind

Figure 3 shows the profiles of temporally (1 hour) and horizontally averaged wind statistics in two simulations without wave (black line) and with wind-following swell (blue line) respectively. Figure 3(a) illustrates that compared with the case without waves, the wind speed over wind-following swells is remarkably increased from the surface to the height of around 300m. This indicates that in the case of strong waves aligned with the wind, the ocean surface could provide a thrust force instead of friction and lead to an upward momentum flux from the wave to the wind. Figure 3(b) shows the wind direction is also turned toward north by about 10° in this height range due to the presence of waves. In Figure 3(c), the turbulence intensity near the ocean surface is also shown to be notably enhanced under the perturbations from the surface elevations. Considering that a modern offshore wind turbine usually works within a height of 300m, the waves can have strong impacts on the offshore wind farms by not only changing the total power production but also affecting the structural loads through the wave-induced turbulence.

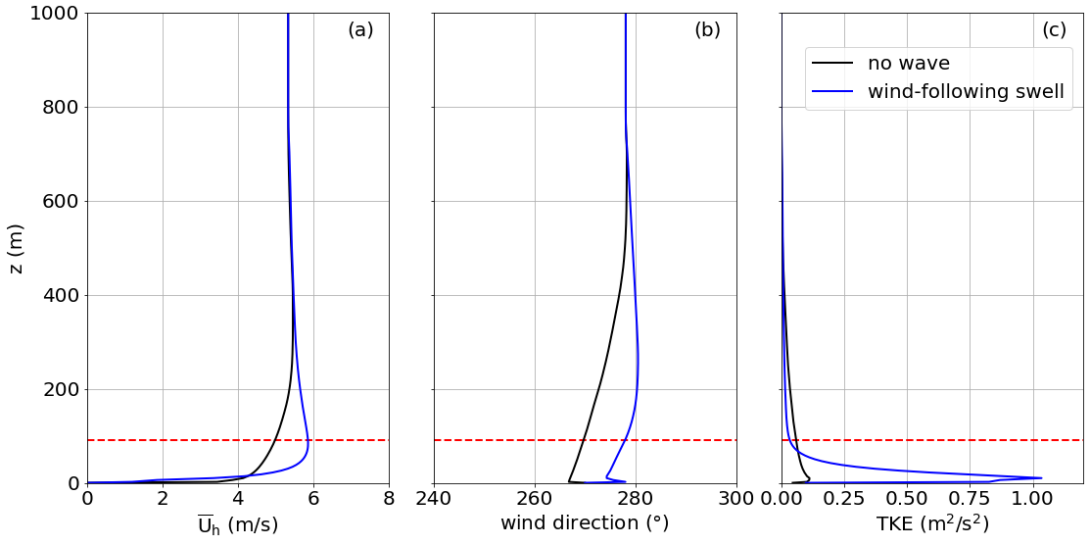


Figure 1: The profiles of 1-hour and horizontally averaged (a) wind speed (b) wind direction, and (c) turbulence kinetic energy in two cases with and without wave effects. The red dashed line represents the hub height of the wind turbine.

The analysis of the aerodynamics of the wind turbine and the results in other wind-wave regimes will be presented in details at the conference.

Acknowledgements

This work is part of the LES-WIND project and the authors would like to acknowledge the funding from the academic agreement between University of Bergen and Equinor. The simulations were performed on resources provided by UNINETT Sigma2 - the National Infrastructure for High Performance Computing and Data Storage in Norway.

References

[1] G. Deskos, J. C. Lee, C. Draxl, and M. A. Sprague. Review of wind–wave coupling models for large-eddy simulation of the marine atmospheric boundary layer. *Journal of the Atmospheric Sciences*, 78(10):3025–3045, 2021.

[2] P. P. Sullivan and J. C. McWilliams. Dynamics of winds and currents coupled to surface waves. *Annual Review of Fluid Mechanics*, 42:19–42, 2010.

[3] D. Yang, C. Meneveau, and L. Shen. Dynamic modelling of sea-surface roughness for large-eddy simulation of wind over ocean wavefield. *Journal of Fluid Mechanics*, 726:62–99, 2013.

[4] P. P. Sullivan, J. C. McWilliams, and E. G. Patton. Large-eddy simulation of marine atmospheric boundary layers above a spectrum of moving waves. *Journal of the Atmospheric Sciences*, 71(11):4001–4027, 2014.

[5] X. Hao and L. Shen. Wind–wave coupling study using les of wind and phase-resolved simulation of nonlinear waves. *Journal of Fluid Mechanics*, 874:391–425, 2019.

[6] M. A. Sprague, J. M. Jonkman, and B. Jonkman. Fast modular framework for wind turbine simulation: new algorithms and numerical examples. In *33rd Wind Energy Symposium*, page 1461, 2015.

18th EAWE PhD Seminar on Wind Energy
2-4 November 2022
Bruges, Belgium

Wind field reconstruction with LIDAR measurements

Rebeca Marini[a], **Konstantinos Vratsinis**[a], **Cédric Peeters**[a], and **Jan Helsen**[a]

[a]Vrije Universiteit Brussel, Pleinlaan 2, 1050 Brussels, Belgium

E-mail: rebeca.marini@vub.be

Keywords: wind field reconstruction, LIDAR, wind parameters

Abstract

The number of offshore wind farms has been rapidly growing worldwide. To further encourage the construction of offshore wind farms, it is important to maintain or decrease the levelized cost of energy at the same time that the annual energy production increases. The wind energy sector research has been focused in various topics in order to carry out this objective. An accurate wind field reconstruction (WFC) can be used for further improving the wind turbine's control, increasing the energy production efficiency and increasing its durability. The WFC can be created with the use of LIDAR measurements, either ground- or nacelle-mounted. This abstract presents a brief discussion on the implementation of two WFC methodologies with a nacelle-mounted LIDAR measurements.

1 Introduction

The European Union (EU) has set guidelines and targets to fulfil the United Nations' Agenda for 2030, to assure a better future for the next generations. One of these is to further decarbonize the current energy system, for example, by further investing in renewable energy research. Wind energy in the last two decades has been rapidly growing, representing more than 35% of the produced renewable energy in the EU during 2020 [1]. The European Wind Energy Association (EWEA) estimates this growth to reach almost 400 GW production by 2030, with 25% being produced in offshore wind farms [2].

The construction costs of an offshore wind farm are higher than an onshore one, due to cabling, mooring and maintenance. However, the increased wind potential and nature preservation leads to a growing number of offshore wind farms every year [3]. Moreover, wind turbines have also been growing in size, reaching more than 100m of blade length. With a higher Levelized Cost Of Energy (LCOE), in comparison with onshore wind farms, it is important to investigate ways of decreasing, or at least maintain, the current LCOE associated with offshore wind farms.

Light Detection And Ranging (LIDAR) devices have been in use in the wind energy sector as an alternative of the conventional meteorological mast, since it is a less expensive instrumentation [4]. The use of LIDARs in the wind energy sector is distinguished by the ground-based and the nacelle-mounted LIDARs. The former have been steadily progressing in reliability and performance, being demonstrated as a good alternative to mast. The next obvious step, is to turn focus on the possibility of having the LIDAR mounted at the nacelle of the wind turbine [5]. Presently, wind LIDARs have demonstrated its usability for:

- Wind speed, wind direction and turbulence profiling;
- Wind resource assessments;
- Wind turbine performance testing (power curves);
- Wind resource assessment via horizontal scanning over complex terrain and offshore.

The measurements from the LIDAR can be used to further improve wind field reconstruction models, which in turn can be used for improving the wind turbine's performance, through the use of the upstream approaching wind. This can be useful for a better yaw and pitch control, that can lead to prolonging the wind turbine longevity and consequently, lowering the LCOE [6]. The nacelle-mounted LIDAR has been previously tested, but there are further developments possible.

In the present abstract, an overview of the research done so far is shown. Firstly, the used nacelle-mounted LIDAR is presented and briefly explained. This is followed by the used methodology in use, namely the approach employed for the wind field reconstruction. Finally, some conclusions are drawn, as well as the future steps to be taken for this research.

2 Description of the LIDAR

The LIDAR is a remote sensor instrument capable of sampling the wind by means of infra-red laser beams. The light of the emitted laser will reflect when encountering aerosol particles in the wind, shifting its frequency due to Doppler effect. The variation is proportional to the relative movement between light and aerosol, thus it is possible to retrieve the projection of the aerosol velocity in the radial direction [7].

LIDARs can be separated into two categories that depend on the laser source, either it has a continuous-wave (cw) or a collimated laser. In the former configuration, the LIDAR will sample at a single distance from the wind turbine, with sampling frequencies ranging between 50 and 400 Hz. While the latter, allows for a simultaneous multiple-distance backscatter analysis, with a light frequency emission between 10kHz and 20kHz. The present research, has employed a 50 Hz continuous-wave nacelle-mounted LIDAR from ZX Lidars. This LIDAR was chosen due to its advantages, such as [8]:

- Up to 10 horizontal measurement ranges, with up to 12 vertical slices for each;
- Circular scan that allows the measurement of the wind field characteristics around the entire rotor;
- Rotor wind equivalent wind speed and wind direction calculations;
- Different data rates of the measured wind field: Raw in 50 Hz, Averaged in 1 Hz and Averaged-10 in 0.002 Hz.

3 Methodology

The LIDARs' wind field measurements have to be coupled with a wind field reconstruction model, since one laser beam cannot resolve the 3D wind vector due to the line-of-sight wind speed limitation. This limitation causes an ambiguity in the wind field reconstruction, usually called *"The Cyclops Dilemma"* [9]. However, it is possible to reconstruct the wind vector if one of the following assumptions is made:

1 no vertical and no horizontal wind component;

2 no vertical component and homogeneous flow.

The current research has, so far, been focusing on methodologies that take into account the second assumption, namely *Wagner et al.*[5] and *Borracino et al.*[10], also called as static methodologies. Therefore, the horizontal wind speed and wind direction are calculated by using two consecutive radial wind speeds, each from one line-of-sight (LOS). The methods are then compared with the wind measurements available of a near mast station.

In Figure 1, the wind speed measurements are compared with the results from both methods. Both reasonably agree with the measurements from the MET station. Although they may seem as promising methods, it is still necessary to evaluate the wind direction, as well as the wind veer and shear profiles, for to be possible to truly evaluating them.

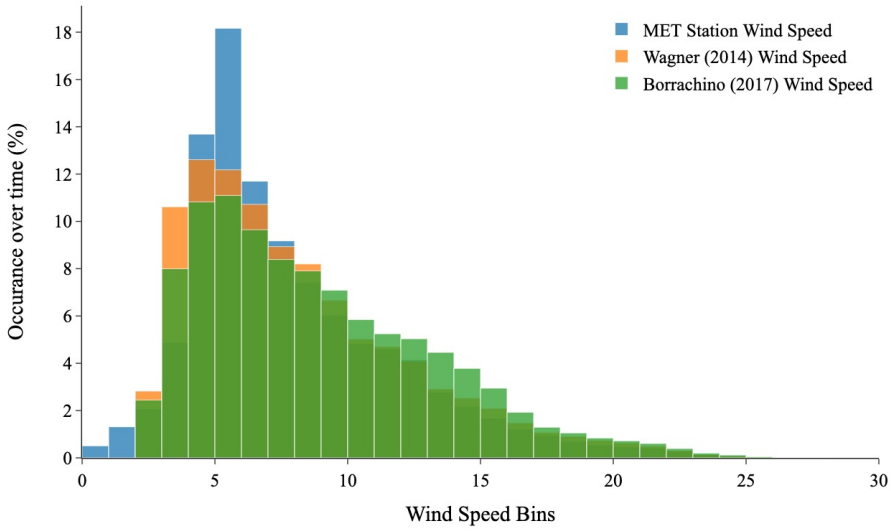


Figure 1: Histogram of the measured wind speed compared with two methodologies of static wind field reconstruction.

4 Conclusions

The wind field reconstruction development is considered a crucial step to further improve current wind turbine control, specifically to increase its life expectancy, consequently decreasing the levelised cost of energy. The goal of this step in the research is to analyse the current literature on wind field reconstruction and to develop existing techniques.

From the preliminary research, it is clear that the different existing methodologies can still evolve to be more accurate. Although both presented methods appear to be promising, it is still necessary to evaluate other wind field characteristics to conclude their ability on accurately reconstruct the incoming wind field.

The next step will be to finish the preliminary research, this is followed by studying and implementing dynamic wind field reconstruction models. Furthermore, this can be accompanied by a validation process with both computational results and field measurements.

References

[1] Hannah Ritchie and Max Roser. Energy. *Our World in Data*, 2020.

[2] EWEA. Aiming high rewarding ambition in wind energy. *The European Wind Energy Association*, 2015.

[3] Piotr Bórawski, Aneta Bełdycka-Bórawska, Krzysztof Józef Jankowski, Bogdan Dubis, and James W. Dunn. Development of wind energy market in the european union. *Renewable Energy*, 161:691–700, 2020.

[4] IEC 61400-12-1 2017. Wind energy generation systems – part 12-1: Power performance measurements of electricity producing wind turbines.

[5] R. Wagner, T.F. Pedersen, M. Courtney, I. Antoniou, S. Davoust, and R.L. Rivera. Power curve measurement with a nacelle mounted lidar. *Wind Energy*, 17(9):1441–1453, 2014.

[6] *Remote Sensing for Wind Energy*. DTU Wind Energy E. DTU Wind Energy, Denmark, 2013.

[7] Davide Trabucchi. *Lidar Measurements and Engineering Modelling of Wind Turbine Wakes*. PhD thesis, Oldenburg University, 2020.

[8] ZX Lidars. Zx tm lidars - product guide. 2019.

[9] David Schlipf. *Lidar-Assisted Control Concepts for Wind Turbines*. PhD thesis, University of Stuttgart, 2016.

[10] A. Borraccino, D. Schlipf, F. Haizmann, and R. Wagner. Wind field reconstruction from nacelle-mounted lidar short-range measurements. *Wind Energy Science*, 2(1):269–283, 2017.

18th EAWE PhD Seminar on Wind Energy
2-4 November 2022
Bruges, Belgium

Convective atmospheric boundary layer using LES

U. Vigny[a,b], **L. Voivenel**[b], **S. Zeoli**[a], and **P. Benard**[b]

[a]Université de Mons (UMONS), Polytechnic Faculty, Belgium.
[b]CORIA, CNRS UMR6614, Normandie Université, INSA and University of Rouen, 76801 Saint-Etienne-du-Rouvray, France.

E-mail: ulysse.vigny@umons.ac.be

Keywords: Convective boundary layer, Thermal stratification, Monin-Obukhov similarity theory, LES

1 Introduction

According to the current energetic and environmental challenges, maximizing the electric power generated in wind-farms and minimizing the wind turbine fatigue is a societal concern. To increase generated power, rotors size have significantly increased over time, leading to hundred of meters diameter wind turbine. Such wind turbines are no longer in micro-scale windflow but at the interface between micro-scale and meso-scale [1]. Therefore, a better understanding of the atmospheric flow physics around wind turbines at these scales is necessary. The aim is to accurately analyze the interaction between wind turbines wake and the atmospheric boundary layer. Various physical phenomena are implied in atmospheric flows, such as thermal stratification, Coriolis force, humidity effect, inflow turbulence, surface terrain, etc. This work focuses on one physical phenomenon: the thermal stratification. It has a significant impact on wind turbines [2], in terms of wake recovery, velocity deficit, induced turbulence, power production, loads and fatigue. Because of the large range of scale motions, direct numerical simulation (DNS) of turbulent flows is unrealistic on such applications. To allow an accurate numerical prediction of such flows, the large-eddy simulation (LES) technique appears promising. However, a LES resolving the whole atmospheric boundary layer is computationally unaffordable. Therefore, a model is needed to correctly predict the wall velocity and temperature profiles. For this purpose, the Monin-Obukhov Similarity Theory [3, 4] is used.

The goal of this work is to implement into the YALES2 solver [5] a wall model taking into account a non-neutral atmospheric boundary layer and thus to obtain accurate wind turbines and wind farm simulation in realistic atmospheric conditions. To do so, the Monin-Obukhov Similarity Theory, detailed in the Section 2, is implemented. The validation of this methodology is performed through a test case developed by Willis and Deardorff [6], detailed in Section 3. Results are compared with experimental data obtained later on by the same authors [6] and from Deardorff and Willis extensive results [7] as well as from Schmidt and Schumann numerical results [8].

2 Methodology

Taking thermal stratification effects into account in a wall-modeled LES approach is non-trivial due to the various possible atmospheric configurations: neutral, stable, unstable boundary layer. These three cases can be split as a function of the thermal flux, named Q_w. The neutral boundary layer is the configuration with no thermal effect, i.e. $Q_w = 0$. The stable boundary layer is the configuration with a negative flux, $Q_w < 0$, going from the top to the bottom of the domain. It means that cold air is at the bottom and hot air at the top. The unstable or convective boundary layer is the configuration with a positive flux, $Q_w > 0$, which goes from the bottom to the top, leading to cold air at the top and hot air at the bottom. The Monin-Obukhov similarity theory proposes velocity and temperature profiles adequate to each configuration where the approach is identical, but correction terms will differ [9]. Velocity profile can be expressed as a logarithmic law, with a correction term Ψ_m:

$$\bar{u}(z) = \frac{u_*}{k}\left[\ln\left(\frac{z}{z_0}\right) - \psi_m\left(\frac{z}{L}\right) + \psi_m\left(\frac{z_0}{L}\right)\right] \tag{1}$$

where $u_* = \sqrt{\tau_w/\rho}$ is the friction velocity. τ_w refers to the local shear stress at the wall. ρ is the fluid density. κ the von Karman constant. z_0 the roughness length. Ψ_m the correction function. L the Obukhov length which represents the height above the surface from where buoyancy first dominates shear computed as $L = -\frac{u_*^3 \theta_0}{\kappa g q_w}$. g is the Earth's gravity. q_w the kinematic surface heat flux. $\theta_0 = 299.8\,\mathrm{K}$ is the mean flow temperature.

For neutral cases, the correction term are zero, leading to a simple logarithmic velocity profile. For the stable configuration, the correction term becomes:

$$\Psi_m(\xi) = 1 - \phi_m(\xi) \tag{2}$$
$$\text{where} \quad \phi_m(\xi) = 1 + 5\xi \tag{3}$$

For the convective configuration, the same quantity writes:

$$\Psi_m(\xi) = 2\ln\left(\frac{1+\phi_m^{-1}(\xi)}{2}\right) + \ln\left(\frac{1+\phi_m^{-2}(\xi)}{2}\right) - 2\arctan\left(\phi_m^{-1}(\xi)\right) + \frac{\pi}{2} \tag{4}$$
$$\text{where} \quad \phi_m(\xi) = (1-16\xi)^{-1/4} \tag{5}$$

From Equation 1 it appears that the velocity is based on Monin-Obukhov length L, which depends on the friction velocity u_*, itself related to the velocity. Thus, an analytical solution cannot be found, and a numerical approach is needed. Therefore, a convergence algorithm based on u_* is implemented to find the correct velocity. This algorithm needs input data to start. These input data vary in the literature [10]. Apart from classical input data such as roughness, mean flow temperature, density, the use of sensible heat flux or temperature as a surface boundary condition is questionable. Even if it seems that for stable boundary layer it changes the result [10], it is not the case for convective boundary layer. That is why in this work, where we study a convective boundary layer, we used surface sensible heat flux.

3 Simulation framework

3.1 Flow solver

This methodology has been implemented in the massively-parallel finite-volume YALES2 flow solver [5], specifically tailored for Large-Eddy Simulation, which relies on a 4th-order central numerical scheme for spatial discretization associated to a 4th-order Runge-Kutta-like method for the time integration.

3.2 Numerical setup

In order to validate our methodology and the Monin-Obukhov similarity theory implementation, the test case developed by Willis and Deardorff [6] is reproduced. Our numerical results will be compared to Willis and Deardorff first experimental results [6], Deardorff and Willis extensive results [7] and Schmidt and Schumann numerical results [8].

The case investigated corresponds to a Convective Boundary Layer uniformly heated from below and topped by a layer of uniformly stratified fluid (*ie* the inversion layer). It corresponds to a periodic box of size $N_x \times N_y \times N_z = 256 \times 256 \times 128$ for a physical domain of size $L_x \times L_y \times L_z = 8000 \times 8000 \times 2400\,\mathrm{m}^3$. The spacial resolution is thus $\Delta_x = \Delta_y = 31.25$ and $\Delta_z = 18.75$m for all three directions . The initial height of the inversion layer is also used to specify the initial condition. The initial temperature profile corresponds to the one of a mixed layer initially at $\theta_0 = 299.8\,\mathrm{K}$ topped by an inversion layer of uniform stability $d\langle\theta\rangle/dz = 0.0027\,\mathrm{K.m}^{-1}$. Both temperature and velocity profiles are disturbed by a variable perturbation r randomly selected in $[-0.5;0.5]$. The initial temperature profiles thus reads:

$$\theta(z) = \begin{cases} \theta_0 + 0.1r\left(1 - \frac{z}{z_m}\right)\theta_C^0 & \text{if } 0 < z \leq z_{z_m}, \\ \theta_0 + (z - z_m)\frac{\mathrm{d}\langle\theta\rangle}{\mathrm{d}z} & \text{if } z > z_m\,. \end{cases} \tag{6}$$

Similarly, the initial velocity profile is given by:

$$w(z) = \begin{cases} 0.1r\left(1 - \frac{z}{z_m}\right)w_C^0 & \text{if } 0 < z \leq z_m, \\ 0, & \text{if } z > z_m, \end{cases} \tag{7}$$

where $z_m = 1400\,\mathrm{m}$ is the initial height of the mixed layer.

The fluid properties are typical of the ones encountered on a sunny day in southern Germany *ie* dry air of dynamic viscosity $\nu = 2.15 \times 10^{-5}\,\mathrm{m^2.s^{-1}}$ and thermal diffusivity $\alpha = 21.4 \times 10^{-6}\,\mathrm{m^2.s^{-1}}$.

As far as boundary conditions are concerned, the ground is heated by an uniform kinematic heat flux, $q_w = 0.06\,\mathrm{K.m.s^{-1}}$, while the roughness height is $z_0 = 0.16\,\mathrm{m}$. Schmidt & Schumann introduced a radiation boundary condition at the top of the domain to avoid spurious reflections of gravity waves. In our case, a sponge layer where source terms smoothly bring the velocity and scalar profiles up to their theoretical value is implemented for this purpose. This sponge layer has a height of 750 m and is discretized by 40 points. Our final domain dimension are then $L_x \times L_y \times L_z = 8000 \times 8000 \times 3150\,\mathrm{m^3}$ and the resolution remains the same as the one mentioned earlier. Finally, the lateral boundary conditions are considered periodic.

4 Results

Figures 1 and 2 represent the dimensionless horizontal and vertical velocity variance, respectively. The former is in overall lower than the latter, except at the edges of the mixed layer. Indeed, vertical velocity fluctuations are mostly due to buoyancy whereas horizontal velocity fluctuations mainly come from pressure fluctuations which are lower overall but predominant at the edges of the mixed layer. Both Figures 1 and 2 show that velocity profiles are matching those of Schmidt and Schumann. However, Deardorff and Willis's experimental data predicts higher horizontal velocity variances. Schmidt and Schumann [8] have suggested that horizontal variation of the surface heat flux, and thus the experimental setup itself, was the cause of those differences. Moreover, the Willis and Deardorff older measurements are much closer to all numerical results.

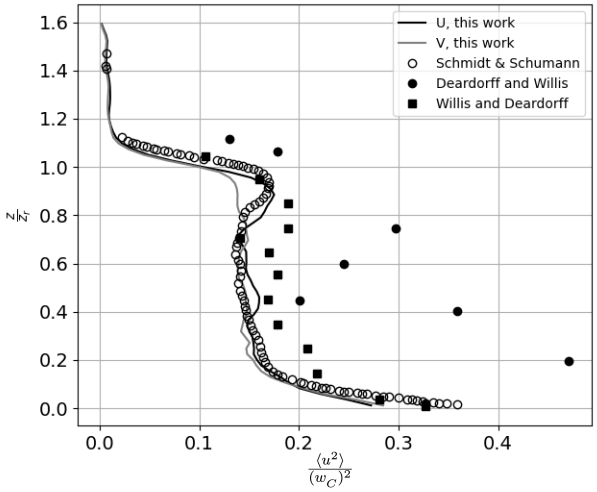


Figure 1: Dimensionless horizontal velocity variance function of dimensionless height.

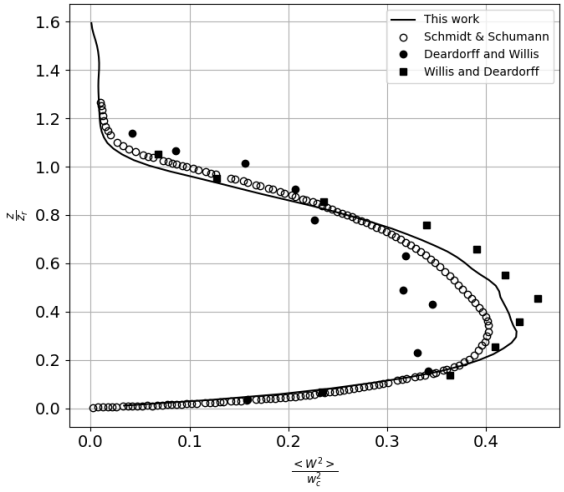


Figure 2: Dimensionless vertical velocity variance function of dimensionless height.

The dimensionless temperature and vertical heat flux variance are show on Figures 3 and 4, respectively. The temperature variance is low in overall, except at the edges of the mixed layer. Indeed, temperature variances are produced by the product of heat flux and temperature gradient, which is large near the surface and at the inversion height. On the other hand, vertical turbulent heat flux decrease linearly with height, up to the inversion layer. It implies a constant heating rate and thus the expected results. The obtained results match both Schmidt and Schumann's and the experimental data.

5 Conclusions

The implementation of the Monin-Obukhov similarity theory into YALES2 was performed and validated by reproducing a well known literature test case. Our results shown good agreement with experimental and numerical data. Therefore, convective boundary layer can now be used for real cases, such as wind turbine and wind farm

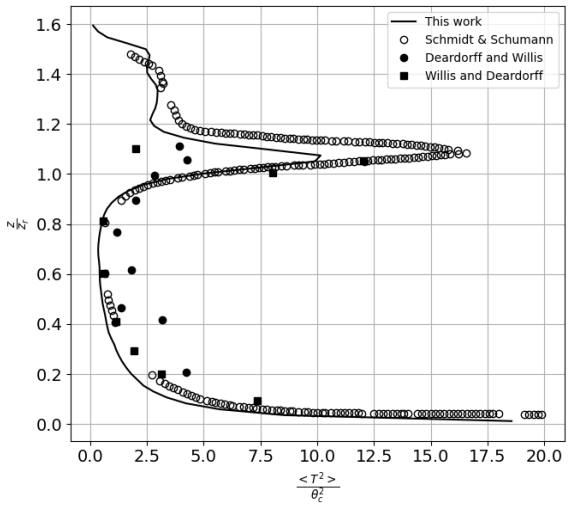


Figure 3: Dimensionless temperature variance function of dimensionless height.

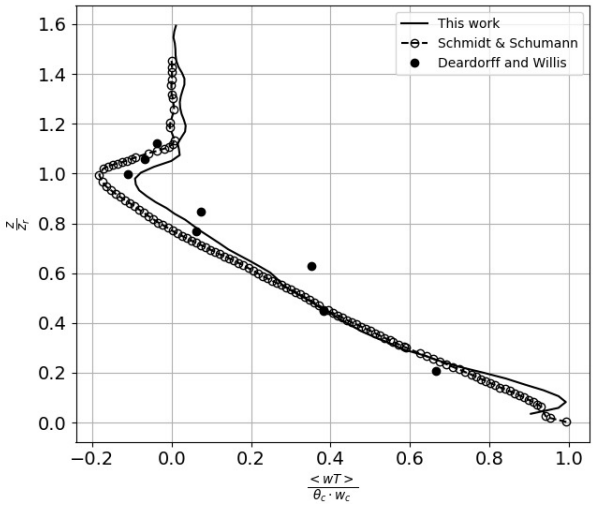


Figure 4: Dimensionless heat flux variance function of dimensionless height.

simulations. Yet, some investigation still needs to be done. Indeed it has been shown in [10] that this methodology, based on surface sensible heat flux, is suitable for convective boundary layer but not accurate for stable boundary layer. In this case, surface temperature based methodology leads to more reliable results. Therefore, it must be developed for this configuration.

References

[1] Paul Veers, Katherine Dykes, Eric Lantz, Stephan Barth, Carlo L Bottasso, Ola Carlson, Andrew Clifton, Johney Green, Peter Green, Hannele Holttinen, et al. Grand challenges in the science of wind energy. *Science*, 366(6464):eaau2027, 2019.

[2] Majid Bastankhah and Fernando Porté-Agel. A new analytical model for wind-turbine wakes. *Renewable energy*, 70:116–123, 2014.

[3] Andrei Sergeevich Monin and Aleksandr Mikhailovich Obukhov. Basic laws of turbulent mixing in the surface layer of the atmosphere. *Contrib. Geophys. Inst. Acad. Sci. USSR*, 151(163):e187, 1954.

[4] LD Landau and EM Lifshitz. Fluid mechanics. pergamon press, oxford. *Section 92, problem*, 2, 1959.

[5] Vincent Moureau, Pascale Domingo, and Luc Vervisch. Design of a massively parallel cfd code for complex geometries. *Comptes Rendus Mécanique*, 339(2-3):141–148, 2011.

[6] GE Willis and JW Deardorff. A laboratory model of the unstable planetary boundary layer. *Journal of Atmospheric Sciences*, 31(5):1297–1307, 1974.

[7] JW Deardorff and GE Willis. Further results from a laboratory model of the convective planetary boundary layer. *Boundary-Layer Meteorology*, 32(3):205–236, 1985.

[8] Helmut Schmidt and Ulrich Schumann. Coherent structure of the convective boundary layer derived from large-eddy simulations. *Journal of Fluid Mechanics*, 200:511–562, 1989.

[9] Jagadish Chandran Kaimal and John J Finnigan. *Atmospheric boundary layer flows: their structure and measurement*. Oxford university press, 1994.

[10] Sukanta Basu, Albert AM Holtslag, Bas JH Van De Wiel, Arnold F Moene, and Gert-Jan Steeneveld. An inconvenient "truth" about using sensible heat flux as a surface boundary condition in models under stably stratified regimes. *Acta Geophysica*, 56(1):88–99, 2008.

18th EAWE PhD Seminar on Wind Energy
2-4 November 2022
Bruges, Belgium

Wind turbine wake study considering the influence of atmospheric stability using lattice Boltzmann method

Ziwen Wang[a], **Jerome Jacob**[a], **Felix Marlow**[a], and **Pierre Sagaut**[a]

[a]Aix Marseille Univ, CNRS, Centrale Marseille, M2P2 UMR 7340, Marseille, France

E-mail:ziwen.wang@centrale-marseille.fr

Keywords: wind turbine, atmospheric boundary layer, thermal stability, lattice Boltzmann method

1 Abstract

Wind turbine wake under the influence of atmospheric thermal stability is investigated using the lattice Boltzmann method (LBM) combined with large eddy simulation (LES). The wind turbine is parameterized as an actuator line model (ALM) and ground momentum and thermal flux are modeled with the Monin-Obukhov similarity theory. The wake characteristics(including mean velocity and turbulence intensity) under stable and unstable atmosphere boundary layers (ABL) are analyzed and validated with Navier-Stokes-based large eddy simulation. The main differences come from the subgrid-scale model and the inflow turbulence generation method. Overall, our model gives quite good predictions, the ability of the current LBM-LES framework in wind engineering study is validated and would be beneficial for future study of more complex scenarios.

2 Introduction

Wind engineering has large computation demand because the complex flow of rotating wind turbines interacts with the atmosphere and the development of large-scale wind farms, which limited the application of the traditional Navier-Stokes-based simulation method in the wind industry. Lattice Boltzmann method[1], as an alternative powerful tool for the simulation of fluid flows, has got growing interest due to its advantages for massively parallel computing and suitability to handle very complex geometries. The LBM has been successfully applied in the aircraft and vehicle industries. However, there are few studies about the application of LBM in wind engineering. Asmuth et al.[2] investigated the wind turbine actuator line model incorporated with LBM. Deiterding and Wood[3] combined the LBM and LES to analyze the transient flow characteristics of a fully resolved MEXICO wind turbine and three V27 wind turbines. Li et al.[4] gives a further comprehensive study of the MEXICO wind turbine wake and investigates the impact of the sub-grid scale turbulence model.
This study combined the LBM with large eddy simulation (LES) to investigate the influence of atmosphere thermal stability on wind turbine wakes. According to thermal stratification, the atmospheric boundary layer can be classified into three types: stable, neutral, and unstable. In an unstable or convective atmospheric boundary layer (CBL), the surface temperature is higher than the air, so the transfer of heat between surface and air generates positive buoyancy, which enhanced the turbulence mixing. On the contrary, in a stable atmospheric boundary layer (SBL), the negative buoyancy force is generated, which destroys turbulence. For the neutral atmospheric boundary layer (NBL), no temperature gradient between the ground and air, so little influence on the turbulence development. The wind turbine is operated in the lowest part of ABL, so this thermal effect has a significant influence on the wind turbine wake evolution. The wind turbine induced forces are parameterized using actuator line model and the interaction between ground and atmosphere is described using the Monin-Obukhov similarity theory. Then, the external forces contributed by the wind turbine and thermal effect is incorporated with the lattice Boltzmann equation. Simulation results of wind turbine wake characteristics (averaged streamwise velocity, turbulence intensity) under stable and unstable ABL is shown below and compared with Navier-stokes simulation results.

3 Results

The Vestas V80-2MW wind turbine is with 80m rotor diameter (D), 70m hub height, and 16.1rpm rotation speed at a wind speed of 8m/s. The tabulated data, e.g. chord length, twist angle, lift and drag coefficient can be found in [5]. The computation domain is $2500m \times 500m \times 500m$ in the streamwise (x), lateral (y), vertical (z) direction, respectively. leading to a blockage ratio of 2%. The wind turbine is located in the center of the lateral direction and 10D from the inlet. 5m and 2.5m mesh sizes are chosen for the mesh resolution study with a refinement area from 1D in front of the wind turbine to 13D after the wind turbine. Key parameters for the two stratification cases are listed in table 1.

stability condition	friction velocity (m/s)	heat flux (K m/s)	eddy length (m)	mesh1 (m)	mesh2 (m)
Convective	0.46	0.048	120	5	2.5
Stable	0.31	-0.015	30	5	2.5

Table 1: atmosphere stability parameters.

The inflow mean velocity, temperature profiles, and Reynolds stress are described in [6]. The synthetic eddy method developed by Jarrin et al[7]. that considers turbulence as a superposition of coherent eddies, is adopted for generating inflow turbulence. The stable case has larger shear stress, which leads to smaller scale turbulence and lower boundary height. So to maintain the turbulence intensity along the domain, eddy length of 30m and 120m is adopted for stable and convective cases respectively. The simulations were run for 100 minutes and averaged in the last 60 minutes to achieve a steady enough state.
Figure 1 displays the contours of time-averaged streamwise velocity in the vertical x-z plane. It could be seen that our model well captured the typical behavior of wake velocity under different atmospheric stability. The wake recovers faster in the convective case and slower in the stable case, this is because the inlet turbulence intensity for the convective case is higher than in the stable case, which is consistent with the evidence that higher turbulence level leads to enhanced turbulence mixing and faster wake recovery. This phenomenon is also influenced by the temperature gradient. In the convective case, the temperature is higher on the ground compared to the air, which produces positive buoyancy flux that will increase the turbulence kinetic energy and speed up the turbulence mixing with the environment. On the contrary, the stable case has a lower turbulence level and negative buoyancy flux that damps the turbulence, which results in a long distance for the wake to recover. Detail comparisons concerning the time-averaged velocity deficit and turbulence intensity at different distance of the wake for different stability conditions are shown below. Velocity deficit is normalized as $\Delta U/U_{hub}$, where $\Delta U = U_{inflow} - U$. Turbulence intensity is computed as $TI = \sqrt{\frac{1}{3}\frac{1}{U_{hub}^2}(u'u' + v'v' + w'w')}$.

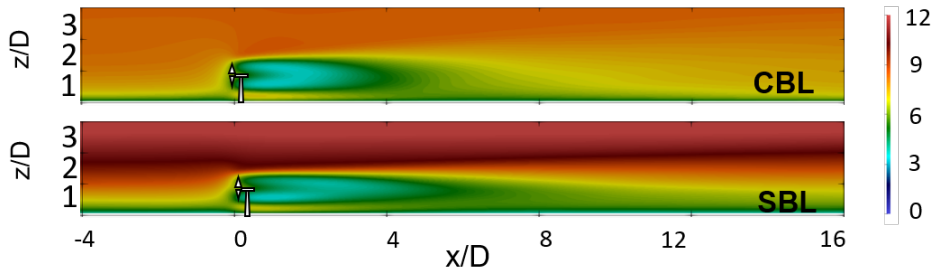


Figure 1: Contours of the time-averaged streamwise velocity in the middle x-z plane under different stability conditions

Figure 2 shows the velocity deficit profile under convective condition. It could be seen that at x=4D, the velocity deficit predicted by LBM is smaller than the reference, which is caused by a higher prediction of the wind turbine-induced turbulence, which could be seen in figure 3, as mentioned above, higher turbulence results in faster wake recovery. It could also be influenced by the wind turbine model parameters, like the mesh size and Gaussian smear width. From the x-y plane, it is evident that the wake center location deviated from the center line, which is denoted as wake meandering. Wake meandering is mainly dominated by large-scale eddies. In the present model, turbulent inflow is generated with uniform eddies, the inlet 120m eddy length for convective case, which is 1.5 times of wind turbine diameter. With development, these large-scale motions drive wake meandering. The wake

meandering also appeared in the z-y plane, but was smaller than in the x-y plane, because of the velocity vertical distribution of ABL inflow and the presence of ground. Concerning the inflow turbulence intensity, as shown in figure 3, the main difference comes from the area near the ground, which is dominated by the sub-grid scale turbulence parameterization. In the present model we are using the traditional Smagorinsky model with Cs=0.17, while in Abkar and Porte-Agel's work, a scale-dependent dynamic Smagorinsky model is hired. But this difference is reduced in the wake because it is compensated by the wind turbine generated turbulence. It could also be seen that the wind turbine produced turbulence is higher than predicted in the present model, which induced a smaller velocity deficit as mentioned before. In stable case, the smaller turbulence magnitude and inflow eddy size have a weaker influence on the wake. The velocity deficit profiles and turbulent intensity profiles match better compare to the convective case, as shown in figure 4 and 5. Grid resolution dependence is checked in all cases, it could be seen that the results are converged for 2.5m mesh size and 5m mesh size, which means the mesh size used is fine enough in this study. Overall, our model gives as good predictions as in the NS-LES framework. The differences mainly come from the turbulence generation method and subgrid-scale model, but not from the numerical scheme.

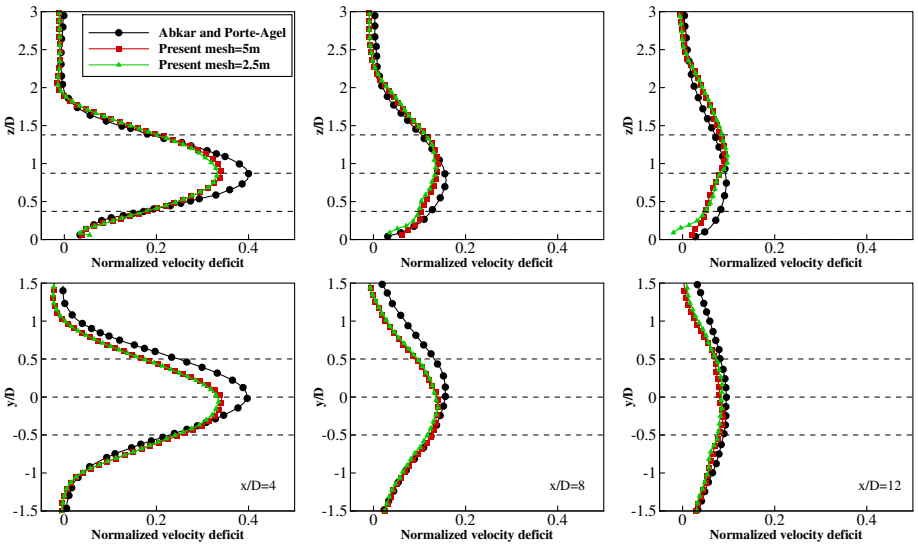


Figure 2: normalized velocity deficit profiles in vertical (up) and spanwise (down) through the hub level under CBL

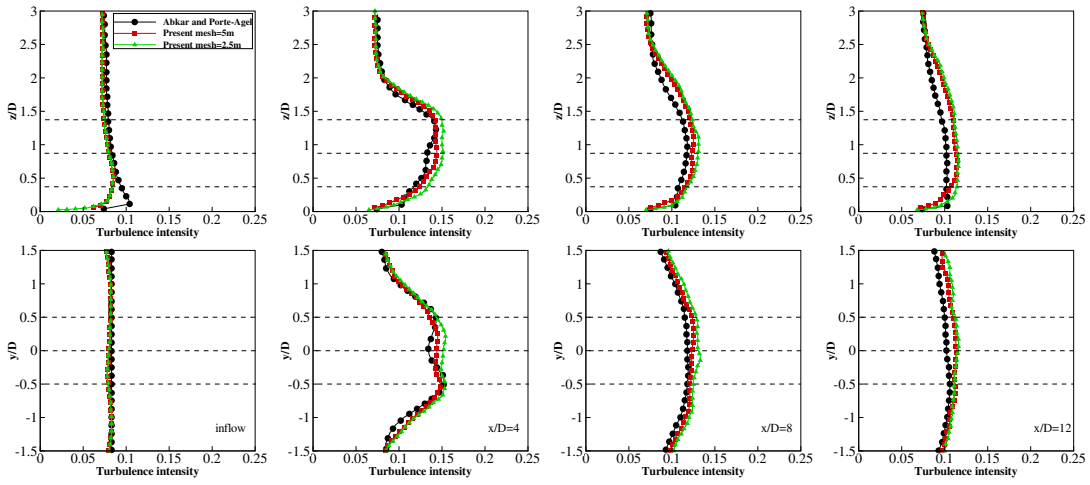


Figure 3: turbulence intensity profiles in vertical (up) and spanwise (down) through the hub level under CBL

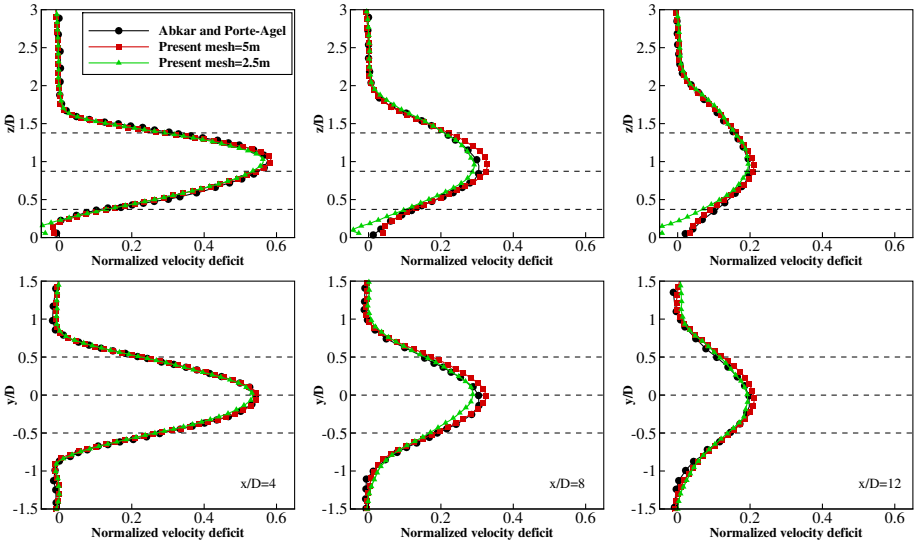


Figure 4: normalized velocity deficit profiles in vertical (up) and spanwise (down) through the hub level under SBL

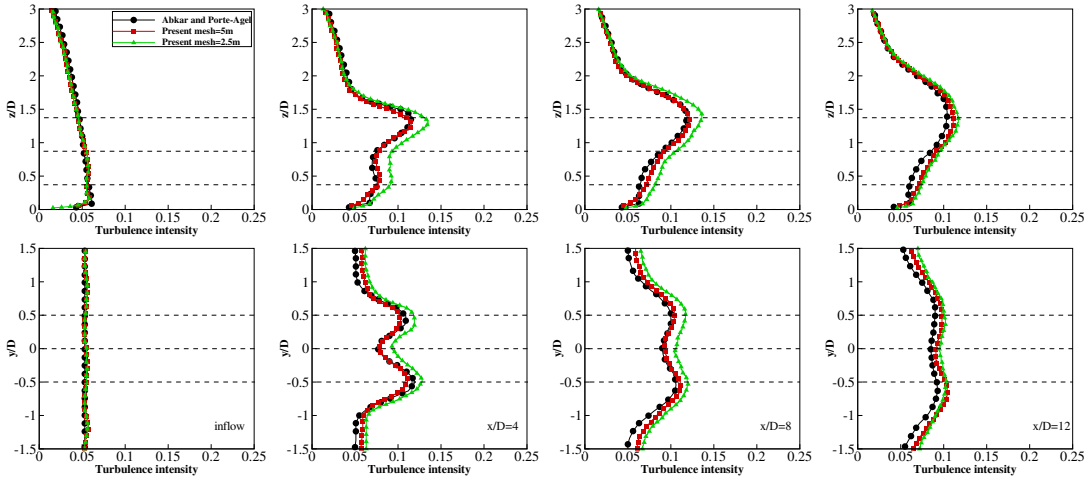


Figure 5: turbulence intensity profiles in vertical (up) and spanwise (down) through the hub level under SBL

4 Conclusions

The wind turbine wake velocity and turbulence intensity under stable and unstable atmospheric boundary layer is studied by using the lattice Boltzmann method combined with large eddy simulation and compared with Navier-stokes-based simulation results. The synthetic eddy method is applied to generate inflow turbulence and the traditional Smagorinsky model is employed for the simulation of sub-grid scale turbulence. Monin-Obukhov similarity theory is used for modeling the ground effect and wind turbines were parameterized as actuator line model. The simulation results show that our model well captured the influence of atmospheric stability on wind turbine wakes and give quite good predictions regarding the mean velocity deficit and wake turbulence intensity. The main differences come from the sub-grid scale model and inlet turbulence generation method but not from the numerical model. Overall, our model is suitable for simulating rotating wind turbines and complex boundary conditions, and could be further applied in wind farm study.

References

[1] Timm Krüger, Halim Kusumaatmaja, Alexandr Kuzmin, Orest Shardt, Goncalo Silva, and Erlend Magnus Viggen. The lattice boltzmann method. *Springer International Publishing*, 10(978-3):4–15, 2017.

[2] Henrik Asmuth, Hugo Olivares-Espinosa, Karl Nilsson, and Stefan Ivanell. The actuator line model in lattice boltzmann frameworks: Numerical sensitivity and computational performance. In *Journal of Physics: Conference Series*, volume 1256, page 012022. IOP Publishing, 2019.

[3] Ralf Deiterding and Stephen L Wood. Predictive wind turbine simulation with an adaptive lattice boltzmann method for moving boundaries. In *Journal of Physics: Conference Series*, volume 753, page 082005. IOP Publishing, 2016.

[4] Linmin Li, Chang Xu, Chen Shi, Xingxing Han, and Wenzhong Shen. Investigation of wake characteristics of the mexico wind turbine using lattice boltzmann method. *Wind Energy*, 24(2):116–132, 2021.

[5] Yu-Ting Wu and Fernando Porté-Agel. Modeling turbine wakes and power losses within a wind farm using les: An application to the horns rev offshore wind farm. *Renewable Energy*, 75:945–955, 2015.

[6] Mahdi Abkar and Fernando Porté-Agel. Influence of atmospheric stability on wind-turbine wakes: A large-eddy simulation study. *Physics of fluids*, 27(3):035104, 2015.

[7] Nicolas Jarrin, Sofiane Benhamadouche, Dominique Laurence, and Robert Prosser. A synthetic-eddy-method for generating inflow conditions for large-eddy simulations. *International Journal of Heat and Fluid Flow*, 27 (4):585–593, 2006.

Wind resources, turbulence and acoustics

18th EAWE PhD Seminar on Wind Energy
2 – 4 November 2022
Bruges, Belgium

A study on the performance of two ship-based profiling wind lidars under different motion scenarios in extreme cold climate

S. Malekmohammadi[a], H. Rubio[b], C. Duscha[a], J. Reuder[a], J. Gottschall[b],

[a] Geophysical Institute and Bergen Offshore Wind Centre, University of Bergen
[b] Fraunhofer Institute for Wind Energy System IWES, 27572 Bremerhaven, Germany
E-mail: shokoufeh.malekmohammadi@uib.no

hugo.rubio@fraunhofer.iwes.de

Keywords: Ship-based Lidar, Wind Speed Measurement, Offshore Wind, Motion-Compensation, Arctic

The use of lidars in wind energy covers a range of areas from wind resource assessment before establishing a wind farm to monitoring wind conditions during wind farm operation for control purposes. Compared to the traditionally used mast-mounted measuring devices, it has been proven that the wind lidars are flexible, robust and affordable instruments. For this reason, the interest in using these devices for the characterization of the wind has progressively grown in the last few years, with a particularly remarkable acceptance for offshore applications.

The employment of lidars in offshore areas can be achieved under different configurations, such as their installation in wind turbine nacelles or in floating platforms like buoys or ships. Ship-based lidars are an innovative technology that, compared with other measurement systems, provide benefits like an easier maintenance, flexibility to measure in deep water areas and their capabilities to provide highly reliable wind data within a wide spatial extent. It is, however, essential to overcome specific challenges in order to establish a reliable and reproducible method for deploying this technology within the wind energy sector. One of the main challenges is a detailed understanding of the motion induced errors on the lidar wind retrievals, and determining the optimal approach to mitigate them.

Previous publications has investigated different ways to take the motion effects out of the measurements, either by means of mechanical compensation systems [1]–[4], i.e active or passive stabilized instrument platforms, or through the implementation of post-processing motion compensation algorithms [5]–[9]. Applying complete motion correction or compensation methods has been shown to be a promising solution for removing the motion effect from the ship-based lidar wind measurements. There are a few lidars that provide off-the-shelf an integrated motion compensation algorithm, e.g., the WindCube v2 offshore. However, this motion compensation system corrects only for the error induced by angular motions (which might be sufficient for floating lidar deployed on buoys), but is not able to compensate for translatory motions that are relevant for ship based deployments. Therefore, the detailed understanding of the motion compensation algorithms and performance of the different available lidar devices under various motion scenarios and atmospheric conditions is of high relevance. In addition, being able to compare the performance of various lidars at different situations, provides the opportunity to optimize the setup for the execution of measurement campaigns using ship-based lidar systems in the future.

As an attempt to fill this knowledge gap, the study presented here investigates the performance of two state-of-the-art vertical profiling lidars deployed as ship-based lidar systems on an icebreaker research vessel. For this,

a sensitivity analysis is executed, with the aim of further understanding the reliability and accuracy of these instruments under different motion and weather conditions and considering some of the most relevant parameters such as the wind speed and direction, turbulence, pitch, roll, or ship speed over ground.

To carry out this study, we used the data retrieved during the cruise JC3 of the Nansen Legacy project [10]. During this campaign, a WindCube v2 offshore and a ZephIR ZX300 were installed together onboard the research vessel (R/V) Kronprins Haakon, retrieving wind data up to 300 m height for three weeks in the Barents Sea and the Artic Ocean as illustrated in Figure *1* (left) . Further sensors have been used in conjunction with these devices to obtain high-resolution motion information, such as tilting, ship position, and ship speed. The equipment was installed on the helicopter deck at a height of approximately 11 meters above sea level. The positioning and setup of the lidars can be seen in Figure *1* (right).

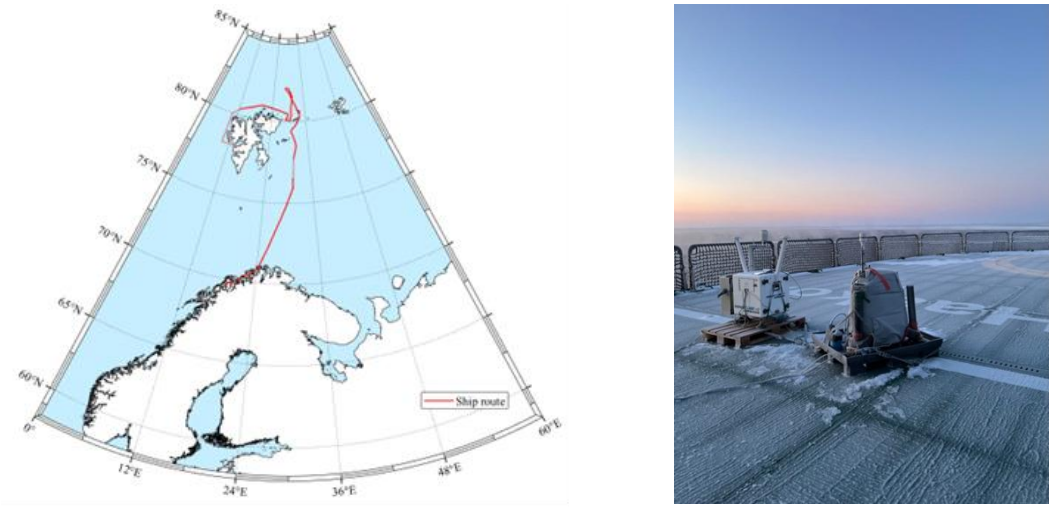


Figure 1- Path of cruise during the campaign (left), the dotted lines indicate the periods when systems were not operating. Lidars positioning and setup on board R/V Kronprins Haakon (right).

Further, Figure 2 and Figure 3 present a preliminary comparison of the uncorrected wind speeds measured by the lidars at three heights for one day with the ship cruising and one day with the ship at ice station, i.e. only slowly drifting with the floating ice.

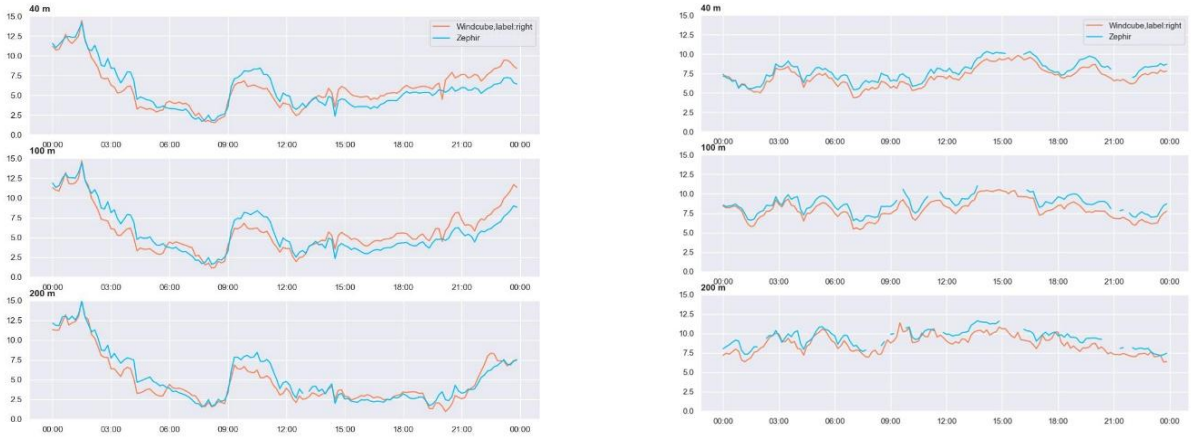


Figure 2- One-day comparison of horizontal wind speed measured by two lidars when ship is cruising (left) and during ice station (right).

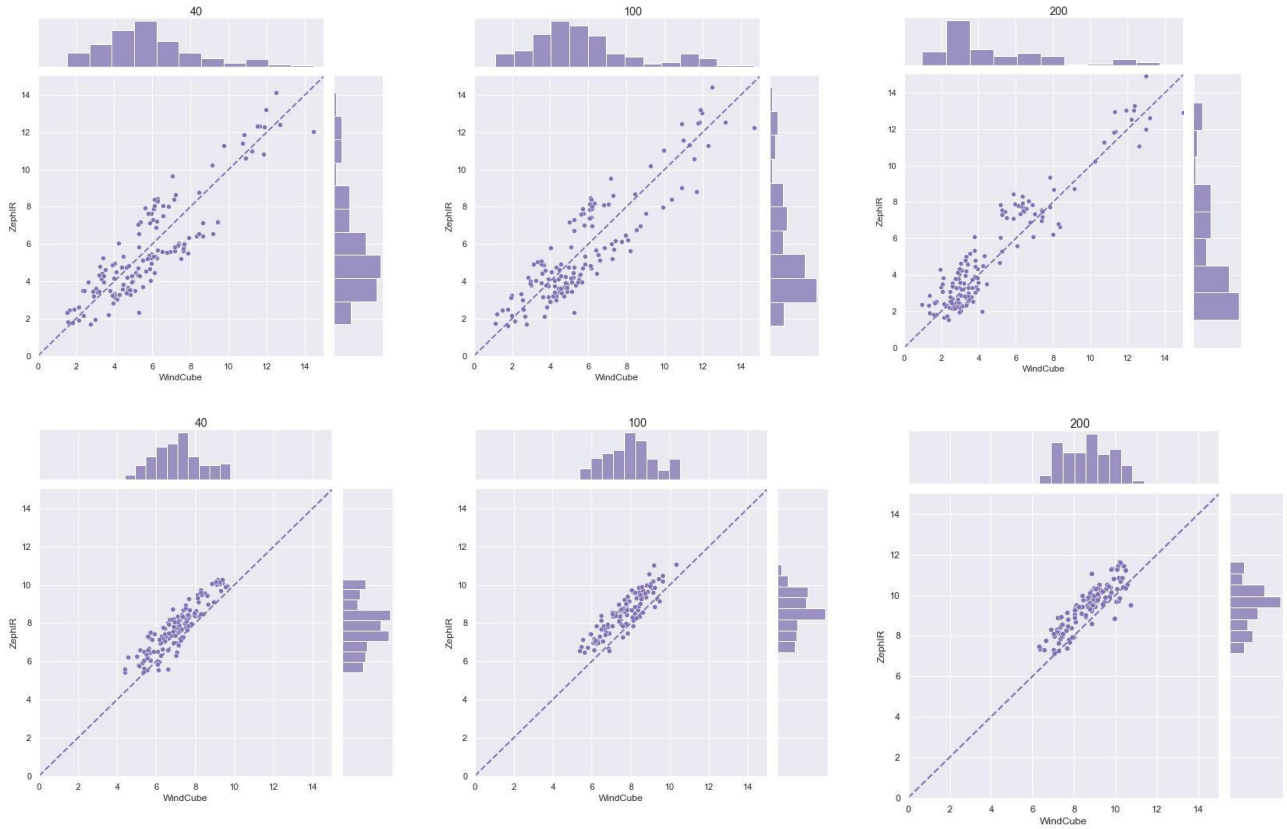


Figure 3- Distribution of measured wind speed by ZephIR vs WindCube V2 when ship is cruising (up) and during ice station (down).

Through the comparison of the performance of the two lidar devices, we aim to examine the capabilities and applicability of two of the most commonly used vertical profilers for ship deployments. By that, we will not only gain a better understanding of how lidar devices perform under a variety of meteorological and motion conditions, but also contribute to the improved design and operation of ship-based lidar systems in the future, ensuring highly accurate and reliable offshore wind observations.

Acknowledgements

The ESRs performing this study have been funded by the EU H2020-MSCA-ITN-2019 projects LIKE (grant number 858358) and TRAIN2WIND (grant number: 861291). Access to the research vessel K/V Kronprins Haakon and the associated travel costs for the cruise have been covered by the Nansen Legacy project funded by the Research Council of Norway RCN (project number: 276730). The two lidar systems deployed onboard the vessel have been provided by the National Norwegian infrastructure project OBLO (Offshore Boundary Layer Observatory) also funded by RCN (project number: 227777). The ship motion recordring unit was provided by Fraunhofer IWES.
We would like to extend our gratitude to cruise leaders Angelika Renner (IMR) and Rolf Gradinger (UiT) and all the scientific team as well as the crew members of the R/V Kronprins Haakon for all their support and for making this campaign a success.

References

[1] R. Zentek, S. H. E. Kohnemann, and G. Heinemann, "Analysis of the performance of a ship-borne scanning wind lidar in the Arctic and Antarctic," *Atmos. Meas. Tech.*, vol. 11, no. 10, pp. 5781–5795, 2018.

[2] S. C. Tucker *et al.*, "Doppler lidar estimation of mixing height using turbulence, shear, and aerosol profiles," *J. Atmos. Ocean. Technol.*, vol. 26, no. 4, pp. 673–688, 2009.

[3] Y. L. Pichugina, R. M. Banta, W. A. Brewer, S. P. Sandberg, and R. M. Hardesty, "Doppler lidar–based wind-profile measurement system for offshore wind-energy and other marine boundary layer applications," *J. Appl. Meteorol. Climatol.*, vol. 51, no. 2, pp. 327–349, 2012.

[4] P. Achtert *et al.*, "Measurement of wind profiles by motion-stabilised ship-borne Doppler lidar," *Atmos. Meas. Tech.*, vol. 8, no. 11, pp. 4993–5007, 2015, doi: 10.5194/amt-8-4993-2015.

[5] G. Wolken-Möhlmann, J. Gottschall, and B. Lange, "First verification test and wake measurement results using a Ship-LIDAR system," *Energy Procedia*, vol. 53, no. C, pp. 146–155, 2014, doi: 10.1016/j.egypro.2014.07.223.

[6] J. Gottschall, G. Wolken-Möhlmann, T. Viergutz, and B. Lange, "Results and conclusions of a floating-lidar offshore test," *Energy Procedia*, vol. 53, no. C, pp. 156–161, 2014, doi: 10.1016/j.egypro.2014.07.224.

[7] C. Duscha, M. B. Paskyabi, and J. Reuder, "Statistic and coherence response of ship-based Lidar observations to motion compensation," in *Journal of Physics: Conference Series*, 2020, vol. 1669, no. 1, p. 12020.

[8] F. Kelberlau, V. Neshaug, L. Lønseth, T. Bracchi, and J. Mann, "Taking the motion out of floating lidar: Turbulence intensity estimates with a continuous-wave wind lidar," *Remote Sens.*, vol. 12, no. 5, p. 898, 2020.

[9] J. Gottschall, G. Wolken-Möhlmann, T. Viergutz, and B. Lange, "Results and conclusions of a floating-lidar offshore test," *Energy Procedia*, vol. 53, pp. 156–161, 2014.

[10] The Nansen Legacy, "Nansen Legacy," *Nansen Leg. Rep. Ser.*, no. 31, May 2022, doi: 10.7557/nlrs.6547.

18th EAWE PhD Seminar on Wind Energy
2-4 November 2022
Bruges, Belgium

Advanced numerical modeling of the interaction between trees and the local wind climate

H A Pabst[a], **E Dellwik**[a], **N Angelou**[a], and **N Troldborg**[a]

[a]Technical University of Denmark, Department of Wind and Energy Systems,
Frederiksborgvej 399, 4000 Roskilde, Denmark
E-mail: healpa@dtu.dk

Keywords: Tree, immersed boundary method, wind resource assessment

1 Introduction

Globally installed onshore wind power capacity has nearly tripled over the past decade [14]. This development is accelerated by the significant reduction in electricity generation costs for onshore wind energy [13]. As a result, the market for profitable projects has expanded to sites with complex terrain, where predicting the wind conditions is more uncertain due to challenges in parameterizing the impact of the topography and vegetation in flow simulations. In recent years, much emphasis has been put on the influence of forest edges and canopies on wind resources ([8, 2, 5]). However, near-surface winds are also sensitive to small vegetation obstacles such as tree lines [12] and solitary trees [1]. Not taking into account their total effect over a landscape can lead to severe overestimation of the local wind climate [15]. Thus, developing accurate numerical models for smaller scale vegetation is of great importance for a correct wind resource assessment. Furthermore, simulating the nonlinear interaction of trees with the wind poses huge challenges on the tree's geometrical reconstruction as well as on capturing its aerodynamics. Characteristics, such as their flexible multi-scale structure and growth make trees differ from classical fluid-structure interaction problems [9]. Despite significant advances in the numerical modeling of wind-tree interaction, from porous, highly simplified geometric shapes [11] to models with spatially varying plant area density [4], these approaches still have significant drawbacks, as they rely on measurements for parameter calibration. One way to overcome this issue is to directly resolve the tree in a high-detail numerical simulation. Creating a surface-conforming grid for such complex objects is, however, exceptionally difficult. The immersed boundary method (IBM) [17] overcomes this by allowing arbitrary geometries to be represented on Cartesian grids. It's capability to capture forces and wake field for the main structural part of a tree was recently demonstrated by Troldborg et al. [20] by comparing experimental observations (Figure 1c) to numerical predictions (Figure 1d). Nevertheless, explicit tree modeling remains challenging so that only simulations of the stem and major branches have been carried out so far. Other advanced approaches, like the work of Endalew et al. [6, 7], rely on artificially generated tree structures rather than real trees. For fractal tree-like geometries Chester et al. [3] as well as Graham and Meneveau [10] showed that while the IBM was employed to represent the large tree scales, a model could account for smaller scales. However, it remains unknown to which extent this is applicable to real tree geometries.

2 Objectives

The PhD project aims to improve current capabilities in simulating the effect of trees on local wind conditions. The focus is on solitary trees and clusters of multiple trees. The first part of the project concentrates on fundamental aspects. It aims to conduct the first structure-resolving simulations of real trees in nature under wind load. It will explore the current capabilities of resolving tree geometries in numerical flow simulations and will further develop and validate currently available numerical methods. This involves a detailed, yet suitable for use in numerical simulations, reconstruction of a tree's geometry from point cloud data. The influence of the cut-off between resolved and modeled tree scales, as well as proper parameterization of small scales, will be investigated. This knowledge will be essential for a highly accurate and consistent treatment of trees in numerical simulations. In the project's second part, insights gained for individual trees will be used for developing methods to accurately account for the effect of trees in parameterizations suitable for larger scale models.

3 Methodology

The finite-volume code EllipSys3D [16, 18] will be used for the simulations. The IBM, which was recently implemented in the flow solver by Troldborg et al. [20, 19], will be applied and further developed. The starting point of the investigations will be an open-grown, mature, European oak tree (Figure 1a). It is located at the Risø campus of the Technical University of Denmark (DTU) on the east coast of the Roskilde Fjord. Based on point cloud data from terrestrial lidar scans an exceptionally detailed surface model of the tree's geometry has been developed by Villesen [21] (Figure 1b). This high-resolution tree model will be used to investigate how its level of detail affects the simulated flow field. The results will be compared to other approaches with varying degrees of fidelity. Additionally, the possibilities of adaptive grid refinement for modelling wind-tree interaction will be explored. To validate the numerical analysis, comprehensive measurement data obtained from ten sonic anemometers and three scanning Doppler wind lidar instruments will be used. The highly detailed, spatially resolved wind observations were obtained as part of the unique full-scale single tree experiment of Angelou [1].

4 Expected outcomes

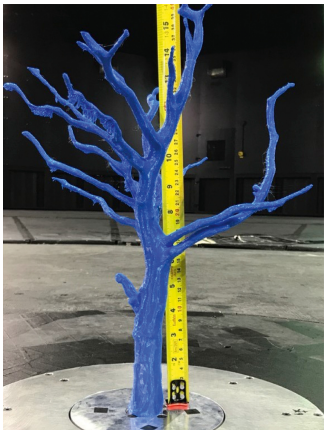
The integration of highly resolution tree models into numerical simulations, together with a better understanding of the influence of unresolved scales, is expected to significantly improve accuracy and reliability of numerical simulations of the local wind conditions. Combined with the available extensive measurement data, the numerical analysis will facilitate the development of new approaches and future methods to predict the wind climate of landscapes containing trees and other complex multi-scale objects. Thus, the findings of this project will reduce the uncertainty in wind resource assessments for complex terrain, allowing for more reliable feasibility and profitability prognoses for onshore wind energy projects. This will further pave the way for extending the growing wind energy sector to new sites.



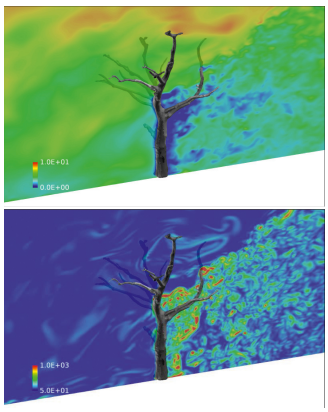
(a) Photograph of the oak tree at Risø campus with a leafless crown [21].



(b) Detailed model of the leafless tree obtained from point cloud data [21].



(c) 3D printed model tree skeleton in the WindEEE Dome at Western University, Canada [20].



(d) IBM simulation for major model tree structures; instantaneous velocity (top) and vorticity (bottom) [20].

Figure 1: Oak tree to be investigated in the first phase of the project.

References

[1] N. Angelou. *Wind-tree interaction: An experimental study on a solitary tree*. PhD thesis, Denmark, 2020.

[2] L.-É. Boudreault, S. Dupont, A. Bechmann, and E. Dellwik. How forest inhomogeneities affect the edge flow. *Boundary-Layer Meteorology*, 126:375–400, 2016.

[3] S. Chester, C. Meneveau, and M. B. Parlange. Modeling turbulent flow over fractal trees with renormalized numerical simulation. *Journal of Computational Physics*, 225:427–448, 2007.

[4] E. Dellwik, M. van der Laan, N. Angelou, J. Mann, and A. Sogachev. Observed and modeled near-wake flow behind a solitary tree. *Agricultural and Forest Meteorology*, 265:78–87, 2019.

[5] C. Desmond, S. Watson, and P. Hancock. Modelling the wind energy resources in complex terrain and atmospheres. numerical simulation and wind tunnel investigation of non-neutral forest canopy flows. *Journal of Wind Engineering and Industrial Aerodynamics*, 166:48–60, 07 2017.

[6] A. M. Endalew, M. Hertog, M. Delele, K. Baetens, T. Persoons, M. Baelmans, H. Ramon, B. Nicolaï, and P. Verboven. Cfd modelling and wind tunnel validation of airflow through plant canopies using 3d canopy architecture. *International Journal of Heat and Fluid Flow*, 30(2):356–368, 2009.

[7] A. M. Endalew, M. Hertog, M. G. Gebrehiwot, M. Baelmans, H. Ramon, B. Nicolaï, and P. Verboven. Modelling airflow within model plant canopies using an integrated approach. *Computers and Electronics in Agriculture*, 66(1):9–24, 2009.

[8] R. Floors, P. Enevoldsen, N. Davis, J. Arnqvist, and E. Dellwik. From lidar scans to roughness maps for wind resource modelling in forested areas. *Wind Energy Science*, 3(1):353–370, 2018.

[9] F. P. Gosselin. Mechanics of a plant in fluid flow. *Journal of Experimental Botany*, 70:3533–3548, 06 2019.

[10] J. Graham and C. Meneveau. Modeling turbulent flow over fractal trees with renormalized numerical simulation: Alternate formulations and numerical experiments. *Physics of Fluids*, 24:125105, 2012.

[11] G. Gross. A numerical study of the air flow within and around a single tree. *Boundary-Layer Meteorology*, 40(4):311–327, 09 1987.

[12] W. Hopwood. Observations and parametrization of momentum transfer in heterogeneous terrain consisting of regularly spaced obstacles. *Boundary-Layer Meteorology*, 81:217–243, 07 1996.

[13] IRENA. Renewable power generation costs in 2020. Technical report, International Renewable Energy Agency, 2021. https://www.irena.org/publications/2021/Jun/Renewable-Power-Costs-in-2020.

[14] IRENA. Renewable capacity statistics 2022. Technical report, International Renewable Energy Agency, 2022. https://irena.org/publications/2022/Apr/Renewable-Capacity-Statistics-2022.

[15] J. Jong, A. Vries, and W. Klaassen. Influence of obstacles on the aerodynamic roughness of the Netherlands. *Boundary-Layer Meteorology*, 91:51–64, 04 1999.

[16] J. A. Michelsen. Block structured multigrid solution of 2d and 3d elliptic pde's. Technical report, Technical University of Denmark, 1994.

[17] C. S. Peskin. Flow patterns around heart valves: A numerical method. *Journal of Computational Physics*, 10:252–271, 1972.

[18] N. N. Sørensen. *General purpose flow solver applied to flow over hills*. PhD thesis, 1995. Risø National Laboratory.

[19] N. Troldborg, N. N. Sørensen, and F. Zahle. Immersed boundary method for the incompressible reynolds averaged navier–stokes equations. *Computers & Fluids*, 237:105340, 2022.

[20] N. Troldborg, N. N. Sørensen, E. Dellwik, and H. Hangan. Immersed boundary method applied to flow past a tree skeleton. *Agricultural and Forest Meteorology*, 308–309:108603, 2021.

[21] I. B. Villesen. Reconstruction of botanical trees from optically acquired point clouds, 2020. Bachelor's thesis, DTU Compute, Department of Applied Mathematics and Computer Science.

18th EAWE PhD Seminar on Wind Energy
2-4 November 2022
Bruges, Belgium

Characterization of the effect of inflow turbulence on vortex shedding engineering models parameters using Large Eddy Simulations

Ricardo Fernandez-Aldama[a], **Oscar Lopez-Garcia**[a], **Sergio Avila-Sanchez**[a], **Alvaro Cuerva-Tejero**[a], and **Cristobal Gallego-Castillo**[a]

[a]Aircraft and Space Vehicles Department, Universidad Politécnica de Madrid, Plaza Cardenal Cisneros 3, 28040 Madrid, Spain

E-mail: ricardo.fdealdama@upm.es

Keywords: Vortex Shedding, Turbulence, LES, Cylinder, High-Order Discontinuous Galerkin

1 Introduction

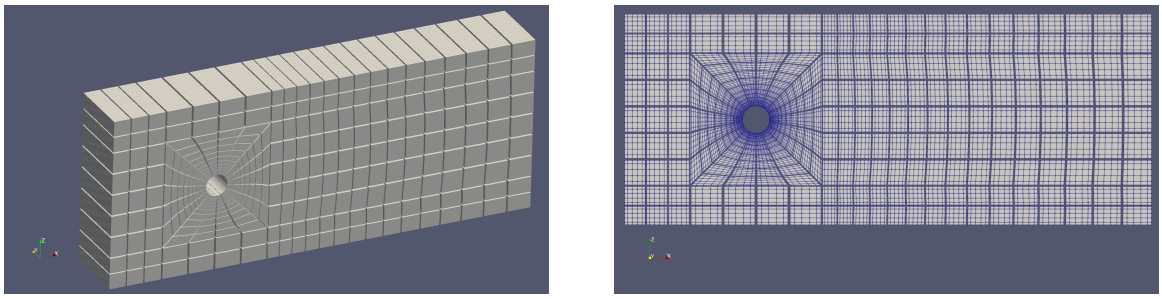
Vortex shedding behind structures is a source of vibrations and fatigue damage, and thus a lot of effort has been put by the engineering community in predicting vortex-induced vibrations (VIV); nonetheless, the complexity of the phenomenon makes VIV engineering models to be semi-empirical in nature, and prone to large errors, as evident in [9]. One source of uncertainty of these models comes from the dependency of their parameters with inflow turbulence characteristics [1]. Limited experimental data is available regarding these dependencies, and models typically rely on semi-empiric relationships proposed at the end of the 20th century or do not include these dependencies at all, see [6], [4].

In particular, the wind energy industry is becoming increasingly concerned with the VIV problem as wind turbines become larger and more flexible [14]. For wind turbine towers, VIV are more critical during transport and installation [8]. In [13] the influence of VIV on fatigue has been studied regarding wind turbine assembly strategies, and there is an interest to extend this analysis to include rotor azimuthal and yaw positions (this is one of the objectives of the Project which funds the present research, see acknowledgments). VIV calculations may be embedded into the aeroelastic simulations used in loads calculation processes for design and certification of wind turbines, as per the design requirements standard [7], as done in [11].

One way of determining the vortex shedding turbulence related dependencies, alternative to experimental work, is by means of CFD simulations including synthetically generated turbulent flow time series as inflow boundary conditions. In this work, a high-order nodal Discontinuous Galerkin Spectral Element Method Large Eddy Simulation solver is used to obtain the flow past a circular cylinder at Re=3900. Multiple synthetic turbulent wind time series with a range of turbulence intensities and turbulent length scales are generated using the Sandia method [15], and used as inflow boundary conditions to the CFD simulations. As validation, firstly, a simulation has been performed which is representative of some of the experimental results found in [12] for the very low turbulence case, and results show good agreement. A further case from this reference is to be simulated, this time for a higher turbulence intensity, in order to validate the proposed setup. Finally, another simulation of the fluid domain without the cylinder will be performed, in order to assess the inflow synthetic turbulence behaviour. Then, the parameters used in two different well-known vortex shedding engineering models will be obtained from the parametric simulations, in order to propose semi-empirical relationships with the turbulence characteristics. These relationships may be used to reduce the uncertainty in wind turbine towers fatigue assessments.

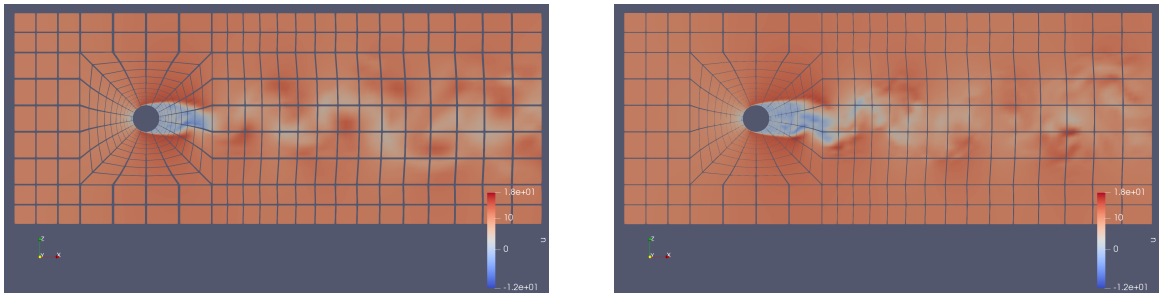
2 CFD simulations

CFD Large Eddy Simulations have been performed using the HORSES3D numerical framework, see [5], which is a high-order Discontinuous Galerkin Spectral Element Method (DGSEM) solver. The pressure distribution around a cylinder of diameter $D = 6$mm, and length $3D$ is analysed. The fluid domain height is $8D$, and the length is $5D$



(a) (b)

Figure 1: Mesh views. (a) 3D view and (b) 2D view with high order nodes for $P = 5$.



(a) (b)

Figure 2: Instantaneous longitudinal velocity u. For (a) $P = 5$ and (b) $P = 7$. Note that the time instant is not the same in both cases.

before the cylinder axis and $15D$ after the axis. The mesh is structured, with refinement close the cylinder walls. The polynomial order has been set to $P = 5$, and additionally $P = 7$ will be used to verify the independence of the results to refinement. The mesh has 5640 hexahedral elements, which results in a number of degrees of freedom equal to $n_{\text{DOF}} = n_{\text{mesh}} (P+1)^3 = 1.22 \times 10^6$ for $P = 5$ and $n_{\text{DOF}} = 2.89 \times 10^6$ for $P = 7$. The flow simulated is air with an inflow mean wind speed of $U = 10$m/s, leading to a Reynolds number of $\text{Re} = 3900$. Note that due to both experimental and computational limitations, most vortex shedding studies are performed at low Reynolds number values, compared to the typically supercritical or transcritical regime of wind turbine towers [3], including canonical results such as [16] and [10], being high Reynolds CFD simulations limited to less realistic 2D URANS cases [17], [3].

The boundary conditions are the following. Cylinder: no slip wall. Inlet: inflow; wind velocity is imposed, being either constant or synthetically generated. Front and back (i.e. where the cylinder axis meets the domain limits): periodicity. Top and bottom: free slip. Outlet: outflow.

A three dimensional view of the domain mesh can be seen in Figure 1(a). A view of the mesh with the high order discretization is shown in Figure 1(b). Figure 2 shows a 2D view of the longitudinal wind speed $\tilde{u}$ for illustration purposes.

Note that the mesh is relatively dense in all the domain. This is because the whole domain before the cylinder has to be dense in order to retain turbulence with little dissipation, and the domain in the cylinder wake also has to be dense to capture vortex shedding.

A preliminary validation of the results obtained can be seen in Figure 4, where the instantaneous pressure coefficient distribution over one side of a circular section for $\text{Re} = 3900$ is compared to available experimental data at $\text{Re} = 3010$ from [12].

It is worth noting that state of the art CFD is not yet fully validated for complex problems like the one presented here, but some efforts to overcome this are currently underway, for example see [2].

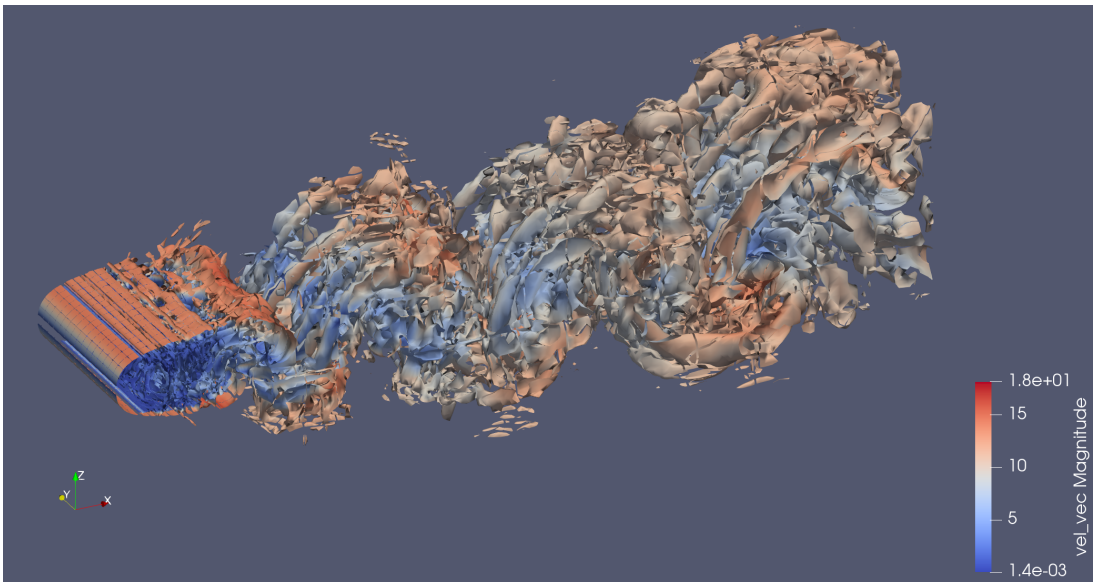


Figure 3: Instantaneous Q-criterion iso-surface for a value of $Q = 0.5$, coloured by velocity magnitude. Obtained with $P = 7$.

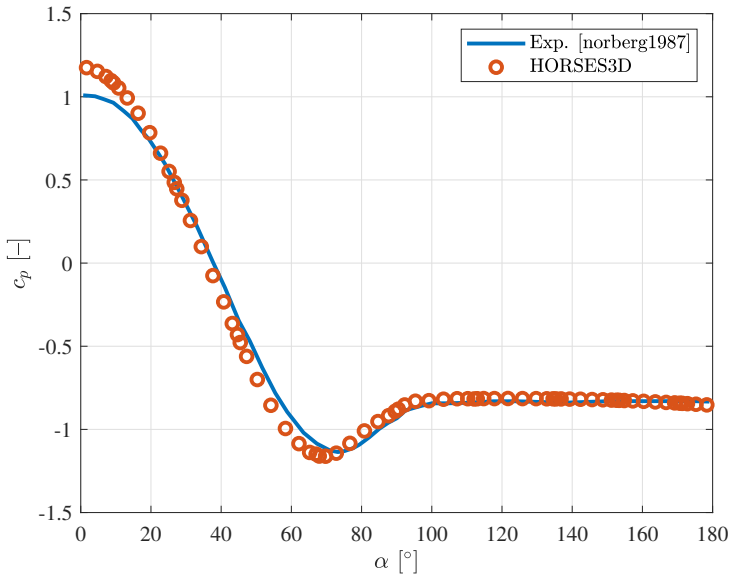


Figure 4: Pressure coefficient distribution around one half of a cylinder section. Comparison between experimental results from [12] at Re = 3010 and calculated CFD results for $P = 5$ at Re = 3900.

Acknowledgements

The present work has been funded by MCIN/AEI/10.13039/501100011033 under Project RTI2018-095592-B-I00 "Stochastic Models of the aeroelasticity of stopped wind turbines". First author's grant PRE2019-089821 has been financed by MCIN/AEI/10.13039/501100011033 and the European Social Fund "ESF Investing in your future". Additionally, the authors gratefully acknowledge Universidad Politécnica de Madrid for providing computing resources of the CeSViMa Supercomputer Magerit.

References

[1] R. Basu. Aerodynamic forces on structures of circular cross-section. Part 2. The influence of turbulence and three-dimensional effects. *Journal of Wind Engineering and Industrial Aerodynamics*, 24(1):33–59, 1986.

[2] S. Breitkopf and A. Sander. Bluff Body Benchmark. `https://bluffbodybenchmark.science/`, visited on 2022/08/06.

[3] A. Derksen. *Numerical simulation of a forced and freely-vibrating cylinder at supercritical Reynolds numbers*. PhD thesis, MS thesis, TU Delft and Siemens, Delft, the Netherlands, 2019.

[4] Eurocode 1: Actions on structures – Part 1–4: General actions–Wind actions. European standard, 2010.

[5] E. Ferrer, G. Rubio, G. Ntoukas, W. Laskowski, O. Mariño, S. Colombo, A. Mateo-Gabín, F. M. de Lara, D. Huergo, J. Manzanero, et al. HORSES3D: a high-order discontinuous Galerkin solver for flow simulations and multi-physics applications. *arXiv preprint arXiv:2206.09733*, 2022.

[6] J. K. Galsworthy. *Aspects of across-wind loads and effects on large reinforced concrete chimneys*. National Library of Canada= Bibliotheèque nationale du Canada, Ottawa, 2001.

[7] IEC. IEC 61400-1: Wind turbines part 1: Design requirements. *International Electrotechnical Commission*, 2005.

[8] D. Livanos. *Investigation of vortex induced vibrations on wind turbine towers*. PhD thesis, MS thesis, TU Delft and Siemens, Delft, the Netherlands, 2018.

[9] F. Lupi, H.-J. Niemann, and R. Höffer. A novel spectral method for cross-wind vibrations: application to 27 full-scale chimneys. *Journal of Wind Engineering and Industrial Aerodynamics*, 171:353–365, 2017.

[10] F. Lupi, H.-J. Niemann, and R. Höffer. Aerodynamic damping model in vortex-induced vibrations for wind engineering applications. *Journal of Wind Engineering and Industrial Aerodynamics*, 174:281–295, 2018.

[11] D. I. Manolas, P. K. Chaviaropoulos, and V. A. Riziotis. Assessment of Vortex Induced Vibrations on wind turbines. In *Journal of Physics: Conference Series*, volume 2257, page 012011. IOP Publishing, 2022.

[12] C. Norberg. Effects of Reynolds number and a low-intensity freestream turbulence on the flow around a circular cylinder. *Chalmers University, Goteborg, Sweden, Technological Publications*, 87(2):1–55, 1987.

[13] C. Nunez-Casado, O. Lopez-Garcia, E. G. de las Heras, A. Cuerva-Tejero, and C. Gallego-Castillo. Assembly strategies of wind turbine towers for minimum fatigue damage. *Wind & structures*, 25(6):569–588, 2017.

[14] P. Veers, C. Bottasso, L. Manuel, J. Naughton, L. Pao, J. Paquette, A. Robertson, M. Robinson, S. Ananthan, A. Barlas, et al. Grand Challenges in the Design, Manufacture, and Operation of Future Wind Turbine Systems. *Wind Energy Science Discussions*, pages 1–102, 2022.

[15] P. S. Veers. Three-dimensional wind simulation. Technical report, Sandia National Labs., Albuquerque, NM (USA), 1988.

[16] B. J. Vickery and A. W. Clark. Lift or across-wind response of tapered stacks. *Journal of the Structural Division*, 98(1):1–20, 1972.

[17] A. Viré, A. Derksen, M. Folkersma, and K. Sarwar. Two-dimensional numerical simulations of vortex-induced vibrations for a cylinder in conditions representative of wind turbine towers. *Wind Energy Science*, 5(2):793–806, 2020.

18th EAWE PhD Seminar on Wind Energy
2 – 4 November 2022
Bruges, Belgium

Climate Change Impact on the Offshore Wind Energy over the North Sea and the Irish Sea

Stefano Susini[1], Melisa Menéndez[1], Pablo Eguia[2], Jesus Maria Blanco[3]

[1] IHCantabria - Instituto de Hidráulica Ambiental de la Universidad de Cantabria, Santander, Spain.
[2] Department of Electrical Engineering, University of the Basque country UPV/EHU, Bilbao, Spain
[3] Department of Nuclear Engineering and Fluid Mechanics, University of the Basque Country UPV/EHU, Bilbao, Spain

stefano.susini@unican.es

Keywords: annual energy production, capacity factor, climate change, regional climate model, renewable energy, weather types, wind resource assessment

1 Context and Research questions

Electricity and heat generation sectors account for the largest share of global greenhouse gas (GHG) emissions, principal responsible for global warming. Hence, a firm effort is aimed at harvesting renewable energy sources. Offshore wind capacity has increased its importance, as it grew from 1% of the total installed wind power in 2008 to 19% in 2021. An accurate description of the environmental conditions is required to facilitate this progressive shift to offshore areas, characterized by more intense and uniform wind resources [1]. Climate change, in turn, may indeed influence the wind resources in terms of spatial distribution and temporal variability [2]. The effects of variations in large-scale circulation are expected to modify the frequency of climate extremes in North Europe [3]. Several authors [4], [5] found a small decrease in the offshore wind resource in the North Sea, though these studies rely on the outcomes from Atmospheric Ocean General Circulation Models (AO-GCMs) characterized by a coarse spatial resolution.

This abstract contains the main findings of the homonymous research article [6], which describes an evaluation of the impact of climate change in the offshore wind sector over the North Sea and the Irish Sea region (Figure 1) both at spatial and offshore wind farm (OWF) scale, by addressing the following research questions:

- Can the evaluation of the atmospheric circulation patterns provide added information about the suitability of the climate models to estimate changes in the wind patterns for the wind energy industry?
- What indicators can we use to assess the impact of climate change in OWFs?

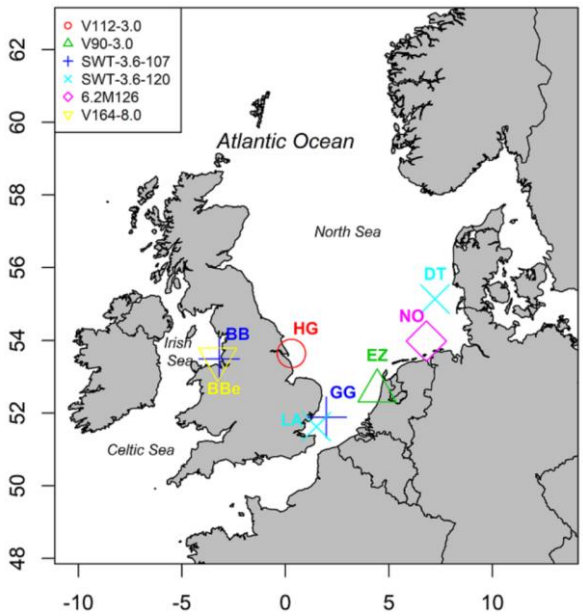


Figure 1. Study domain with the offshore wind parks analyzed and the turbines installed.

2 Data and Methods

In order to address the research questions previously defined, we propose a methodology that combines different sources of wind speed and sea level pressure data, namely: in situ measurements from seven operating wind farms, ERA5 reanalysis time series for the historical reference period (1985-2004), seven regional climate model (RCM) simulations for the historical and future (2081-2100) period in an rcp8.5 scenario.

The in situ measurements are employed to validate the ERA5 reanalysis. Hence, the ERA5 sea level pressure, horizontal and meridional wind speed fields are used to derive a weather type (WT) classification through the application of a combination of principal component analysis (PCA) and K-Mean Analysis (KMA), and the associated frequency of occurrence of each of the 100 WTs is evaluated (Figure 2).

The so-obtained clusters are then applied to both historical and rcp8.5 RCMs simulations and the correspondent frequencies of occurrence are evaluated: we compare the frequencies provided by each of the seven RCM historical simulations with the ERA5 benchmark, and evaluate their performance through the calculation of statistical indexes (Scatter Index, Relative Entropy) [7]. Variations in the frequency of occurrence of WTs between historical and future period for the ensemble of the RCM simulations are also analyzed and successively related to modifications in mean and extreme climatology.

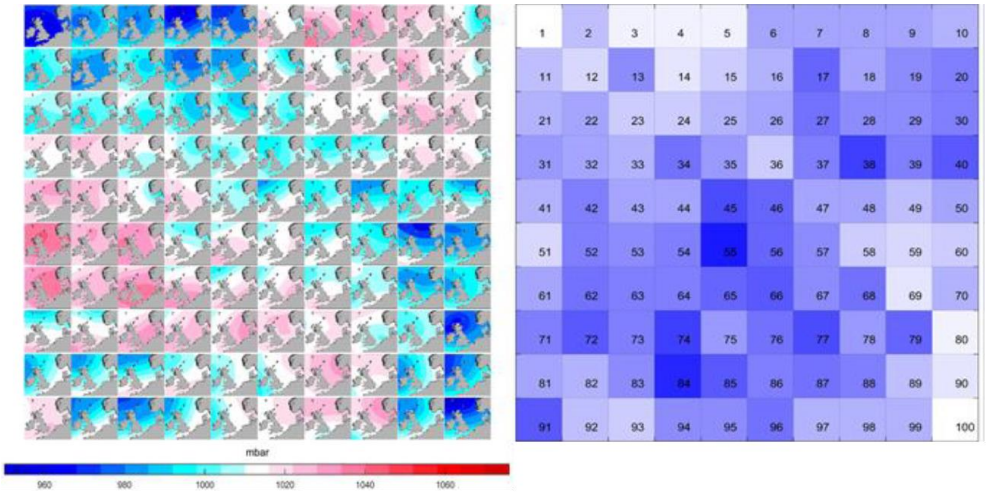


Figure 2. The sea level atmospheric pressure fields associated with the weather types derived from ERA5 and their correspondent frequency of occurrence.

Finally, we apply the empirical quantile mapping bias correction to both historical and future simulations provided by the RCMs in order to evaluate the selected impact parameters (mean and 99th percentile wind speed, mean Wind Power Density, Operation Time, Annual Energy Production, and Capacity Factor) at offshore wind farm scale.

3 Results

The WT analysis is used to evaluate the historical RCM simulations through the calculation of statistical indexes. Overall, a homogenously good performance of the RCMs in reproducing the interannual variability is found, though some differences appear in the Scatter and Relative Entropy indexes. Then, the ensemble mean of the RCMs simulations is calculated, and frequencies discrepancies with respect to ERA5 analyzed. The description of the past climate provided by the RCMs is found satisfactory.

Variations in the frequency of occurrence of a specific WT between historical and future simulations are evaluated for each simulation and then ensembled. We find an increase in the occurrence of WTs characterized by low-pressure systems in the NW part of the domain and a correspondent overall reduction of stable conditions. The changes at synoptic scales are related to mean and 99th percentile wind speed variations. Projected changes at offshore wind farm scale confirm the generalized decrease of the wind resource, and the increase of the extreme conditions for the wind farms located along the continental coast of the domain (Figure 3).

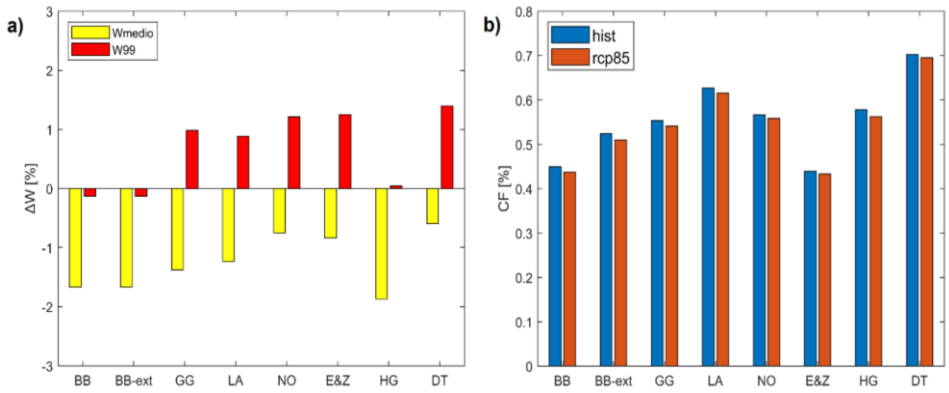


Figure 3. Projected variations in mean and 99th percentile wind speed (a) and capacity factor (b) for the period 2081-2100 under RCP8.5 scenario.

List of References

[1] M. Esteban, J. Diez, J. López, and V. Negro, "Why offshore wind energy ?," vol. 36, no. 2, pp. 444–450, 2011.

[2] S. Pryor, R. Barthelmie, and E. Kjellström, "Potential climate change impact on wind energy resources in northern Europe : analyses using output from a regional climate model," *Geophys. Res. Abstr.*, vol. 7, no. 12, pp. 815–835, 2005.

[3] A. Scaife, C. Folland, L. Alexander, A. Moberg, and J. Knight, "European Climate Extremes and the North Atlantic Oscillation," *J. Clim.*, vol. 21, no. 1, pp. 72–83, 2008.

[4] D. Carvalho, A. Rocha, M. Gómez-Gesteira, and C. Silva Santos, "Potential impacts of climate change on European wind energy resource under the CMIP5 future climate projections," *Renew. Energy*, vol. 101, no. 2017, pp. 29–40, 2017.

[5] J. Moemken, M. Reyers, H. Feldmann, and J. G. Pinto, "Wind speed and wind energy potentials in EURO-CORDEX ensemble simulations: evaluation, bias-correction and future changes," *Geophys. Res. Abstr. EGU Gen. Assem.*, vol. 19, no. May, pp. 2017–13305, 2017.

[6] S. Susini, M. Menendez, P. Eguia, and J. M. Blanco, "Climate Change Impact on the Offshore Wind Energy Over the North Sea and the Irish Sea," *Front. Energy Res.*, vol. 10, no. May, pp. 1–17, 2022.

[7] J. Perez, M. Menendez, F. J. Mendez, and I. J. Losada, "Evaluating the performance of CMIP3 and CMIP5 global climate models over the north-east Atlantic region," *Clim. Dyn.*, vol. 43, no. 9–10, pp. 2663–2680, 2014.

18th EAWE PhD Seminar on Wind Energy
2-4 November 2022
Bruges, Belgium

Effect of free-stream turbulence on the performance of a simplified wind turbine: a wind-tunnel study

M. Dumanoir[a,b], **A. Leroy**[a], and **S. Loyer**[b]

[a]Ecole de l'Air et de l'Espace, CREA, Salon, France
[b]Université d'Orléans, INSA-CVL, PRISME, EA 4229, F-45072, Orléans, France

E-mail: mylene.dumanoir@ecole-air.fr

Keywords: wind turbine blade aerodynamics, turbulence effects, wind tunnel experiment

1 Introduction

1.1 Context and motivation of the thesis

In wind farms, wake flows developing downstream of wind turbines have an impact on the aeroelastic loads of the wind turbines that are subjected to them. It leads to a decrease in energy production and an increase in mechanical loads due to the related specificities to shear and turbulence of these flows. To bring new insights on such wake effects, the French MOMENTA research project has for main objective to improve the estimation of the aeroelastic loads in the specific case of a wind turbine subject to the wake turbulence characteristics of another wind turbine. These specific configurations induce small turbulent structures [3], which are a source of additional load fluctuations on the blade [2], and therefore an increase in fatigue of the wind turbine. Due to the improvement of the wake-induced turbulence description, this project aims at providing a first step toward optimized wind farm layouts in dense configurations, in terms of both energy yield and load reduction. It involved 6 partners with different skills (in-field measurements, CFD, experimental studies).

As part of the MOMENTA project, this PhD thesis relies on an experimental approach to study turbulence effects on local and global aerodynamics of a simplified wind turbine model. Results will be later compared with CFD simulations and analyzed in order to improve the modeling of wake-induced turbulence for aeroelastic load prediction. Experiments are performed in the low Reynolds wind tunnel of the PRISME laboratory. This paper presents preliminary results obtained from the first test campaign which was focused on the analysis of free-stream turbulence effects on aerodynamic loads, modeled in the wind tunnel by turbulence grids.

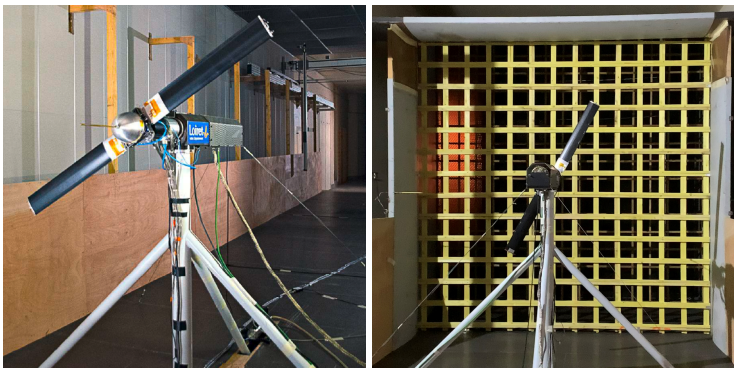
1.2 State-of-art

Studies of the turbulence effects have continued to expand over the years. The wind tunnel measurements carried out by Chamorro and Porté-Agel have shed light on the effect of the atmospheric boundary layer on a wind turbine model [4] and a wind field model [5]. Thus, the far wake is subject to a velocity deficit, a dissipation of turbulence with distance, and an added turbulence intensity that persists even in the very far wake. In addition, the non-axisymmetric distribution of the turbulent intensity seems to have an important role in the fatigue of wind turbines in the wake. In the wind farm model, the turbulent flow from the turbine's top tip height would directly affect its performance. Churchfield *et al.* conducted a large-eddy simulation to study the effects of atmospheric turbulence and the wake on the dynamics of the wind turbine [6]. The root-mean-square of the blade root out-of-plane bending moment and shaft torque at low speeds are higher when the atmospheric boundary layer is unstable than when it is neutral. Similarly, the power ratio produced by the downstream turbine compared to the upstream one is 15-20% higher when the conditions are unstable compared to neutral.

Aerodynamic studies at the blade scale remain less common in the literature. Mishra *et al.* raised the question of the relevance of turbulence on the blade aerodynamics to overcome the low Reynolds effects, characteristic of work in a wind tunnel [7]. It has been shown that increasing the turbulent intensity makes it possible to delay the stall angle, which is very useful in wind tunnel experiments to replicate high Reynolds conditions.

2 Experimental setup

The experimental data are measured in the return test-section of the "Lucien Malavard" wind tunnel of PRISME laboratory in Orléans (France). The wind turbine bench is positioned at the exit of a convergent which has a section of 3x3 meters (see Figure 1(a)). The incoming velocity is equal to 10 m/s. Three different passive grids are used to increase wind tunnel free stream turbulence up to 13.3% (see Figure 1(b)).



(a) (b)

Figure 1: Experimental setup: (a) wind turbine bench in the wind tunnel, (b) free-stream turbulence grid

The wind turbine bench is a two-bladed rotor with a rotor diameter of $D = 1.4$m. The airfoil section is a NACA 65_4-421-CC modified and the blades are straight. The wind turbine bench is made up of a reversible motor Phase Ultract 509 that enables the monitoring of the turbine rotational velocity up to 1000 rpm in order to have similarity in tip speed ratio. The servomotor provides energy when the working point of the turbine is propulsive and dissipates energy when the working point is extractive (present case). This wind turbine bench was already used for a previously study described in Baleriola *et al.* [1]. It allows the measurement of different quantities of interest thanks to the following sensors:

- **Pitot probes** One is installed at the hub and gives the pressure 0.4m upstream from the rotor. A second is installed on the wall of the wind tunnel, about 1m from the rotor. The static $P_{\infty,hub}$ and total $P_{t,hub}$ pressures are connected to the pressure scanner that allows the measurement of blade surface pressures. The second Pitot gives $P_{dyn,wall}$ that provides the incoming flow velocity speed U_∞.
- **Blade surface pressure** 20 pressure taps are placed on one of the two blades, at three different possible radial positions r. It allows to measure the pressure coefficient C_p defined as $C_p = \frac{P_{local} - P_\infty + P_{cent}}{\frac{1}{2}\rho(U_\infty^2 + (\Omega r)^2)}$ where P_{local} is the local pressure measured at the blade surface, P_∞ a reference static pressure, P_{cent} the centrifugal force correction term, ρ the air density and Ω is the rotational velocity of the turbine.
- **Strain gages** It gives the flapwise bending moment M_{fbm}. Gages are placed at the roots of the blades. Each blade has its set of four 120ohm gages. This is also a local measurement.
- **Tachymeter** The rotation frequency of the turbine is measured.
- **Torque Q and drag F** These global rotor variables are captured by a sensor placed at the rear of the turbine hub. It allows to calculate the power C_{power} and thrust C_{thrust} coefficients using the following formulas: $C_{power} = \frac{Q\Omega}{\frac{1}{2}\rho U_\infty^3 S_{rotor}}$ and $C_{thrust} = \frac{F}{\frac{1}{2}\rho U_\infty^2 S_{rotor}}$ where S_{rotor} is the rotor swept area.

This campaign of tests started with the characterization of turbulence grid. For this purpose, a three-component Dantec hot-wire probe was used. Table 1 summarizes the characteristics of the three passive grids used.

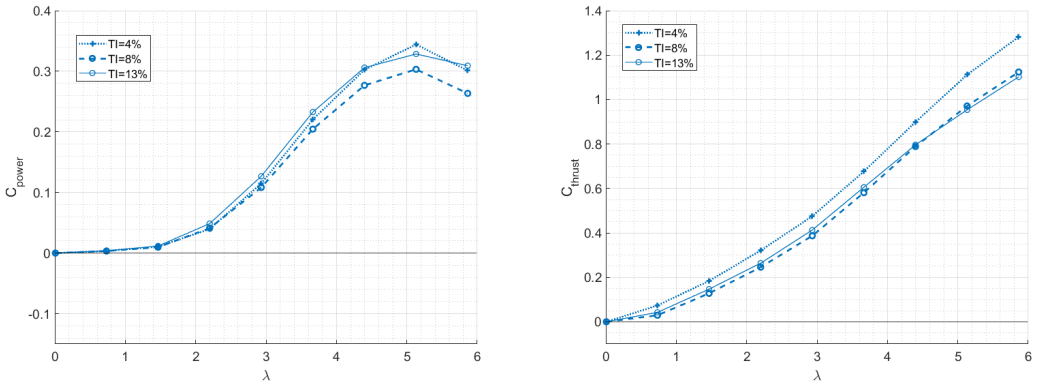
Turbulence intensity (%)	Bar width b (mm)	Mesh size M (mm)	Distance grid-rotor d	Macro-scale length Λ_x (mm)
3.8	25	225	5.4D	59
8	25	225	2.3D	39
13.3	50	225	2.3D	49

Table 1: Summary of homogeneous turbulence grid features

3 Some results and discussions

3.1 Global rotor variables: turbine power and thrust

Figure 2 shows the power coefficient C_{power} (a) and the thrust coefficient C_{thrust} (b) as a function of the tip-speed ratio λ for three different turbulent intensities TI. Dotted, dashed and solid curves correspond to the measurements for a turbulent intensity TI of 3.8%, 8%, and 13.3% respectively.



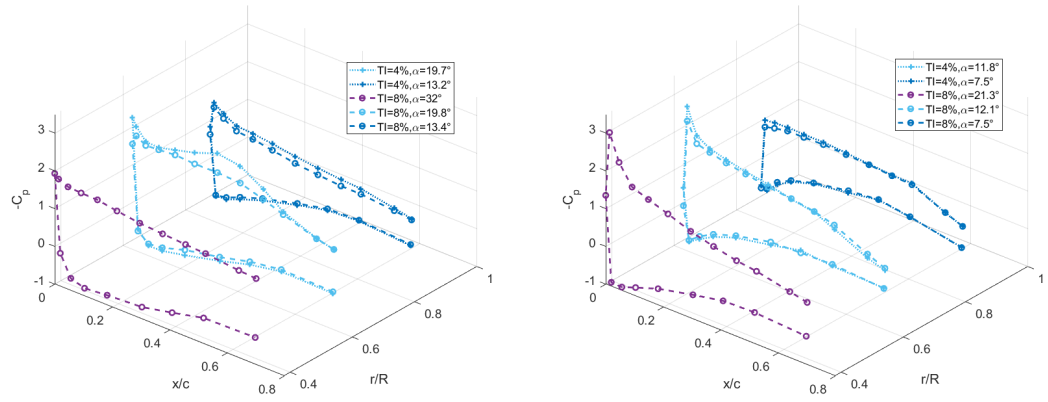
(a) (b)

Figure 2: (a) Power and (b) thrust coefficients as a function of the tip-speed ratio λ and for three turbulent intensities TI - In the legend of the plots, the case $TI = 4\%$ stand for the case $TI = 3.8\%$

The highest C_{power} is reached for a turbulent intensity TI=3.8% with an optimum tip-speed ratio λ at 5.1. As for the power coefficient, the thrust coefficient decreases with a higher turbulent intensity TI. This effect is more significant for high tip-speed ratios.

3.2 Local rotor variables: surface pressure and flapwise bending moment

Figure 3 shows the pressure coefficient C_p distribution as a function of the radial position r/R for two different turbulent intensities TI and two tip-speed ratio λ. Dotted and dashed line curves correspond to the measurements for a turbulent intensity TI of 3.8% and 8% respectively. The case with a turbulent intensity TI of 3.8% and with the pressure taps at $r/R = 0.38$ was not carried out. In the legend of the plots is specified the geometrical angle of attack α without considering the axial and radial induction factors of the turbine.



(a) λ=2.2 (b) λ=5.1

Figure 3: Pressure coefficient C_p distribution as a function of r/R and two different intensity turbulence TI

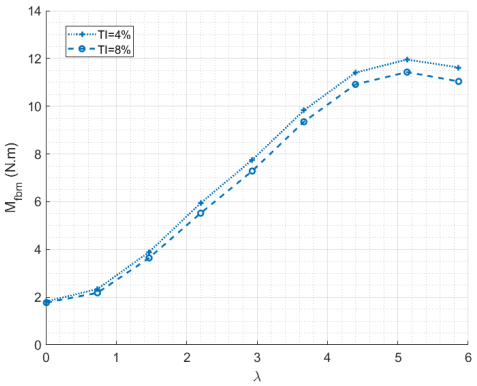


Figure 4: Flapwise bending moment M_{fbm} as a function of the tip-speed ratio λ

For the two tip-speed ratios, C_p decreases along the suction side of the blade for both tip-speed ratio values, except at the $r/R = 0.88$. Thus, it seems that the flow is globally attached along the surface, meaning these cases of λ lead to a case where the lift coefficient varies linearly with the angle of attack. A turbulence effect can be observed on the upper surface, contrary to the lower surface where it is not significant. The deficit of the pressure coefficient increases slightly when the turbulent intensity TI increases. As the lift gradient generally decreases as the turbulence increases, it could be expected that the lift is here slightly reduced.

This is actually coherent with bending moment measurements plotted on Figure 4 which represents the flapwise bending moment Mfbm as a function of the tip-speed ratio λ for two different turbulent intensities TI. Dotted and dashed lines correspond to the two different turbulent intensities TI: 3.8% and 8% respectively.

4 Conclusion

In this communication, some examples of processed data are presented to illustrate typical aerodynamic values obtained from this wind turbine bench. For the case presented here related to the attached flow condition, we observed that when the turbulent intensity TI increases from 4% to 8%, the aerodynamic coefficients decrease, as well as the bending moment and the pressure coefficient distribution.

The data set of this first campaign is still being processed and analyzed. The behavior of the case at $TI = 13.3\%$ requires more in-depth study and possibly validates our experimental results using U-RANS type numerical simulation.

Acknowledgements

This study is funded by the French national project ANR MOMENTA (ANR-19-CE05-0034).

References

[1] S. Baleriola, A. Leroy, S. Loyer, P. Devinant, and S. Aubrun. Experimental lift control using fluidic jets on a model wind turbine. *Journal of Physics: Conference Series*, 1037:022014, 2018.

[2] J. Bartl and L. Sætran. Blind test comparison of the performance and wake flow between two in-line wind turbines exposed to different turbulent inflow conditions. *Wind Energy Science*, 2(1):55–76, 2017.

[3] L. P. Chamorro, M. Guala, R. Arndt, and F. Sotiropoulos. On the evolution of turbulent scales in the wake of a wind turbine model. *Journal of Turbulence*, 13:N27, 2012.

[4] L. P. Chamorro and F. Porté-Agel. A Wind-Tunnel Investigation of Wind-Turbine Wakes: Boundary-Layer Turbulence Effects. *Boundary-Layer Meteorology*, 132(1):129–149, 2009.

[5] L. P. Chamorro and F. Porté-Agel. Turbulent flow inside and above a wind farm: A wind-tunnel study. *Energies*, 4(11):1916–1936, 2011.

[6] M. J. Churchfield, S. Lee, J. Michalakes, and P. J. Moriarty. A numerical study of the effects of atmospheric and wake turbulence on wind turbine dynamics. *Journal of Turbulence*, 13:N14, 2012.

[7] R. Mishra, I. Neunaber, E. Guilmineau, and C. Braud. Wind tunnel study: is turbulent intensity a good candidate to help in bypassing low reynolds number effects on 2d blade sections? *Journal of Physics: Conference Series*, 2265(2):022095, 2022.

18th EAWE PhD Seminar on Wind Energy
2-4 November 2022
Bruges, Belgium

Further characteristics of the atmospheric turbulent wind: Periods of constant wind speed and waiting times between gusts

D. Moreno[a], **J. Friedrich**[a], **M. Wächter**[a], and **J. Peinke**[a]

[a]ForWind, University of Oldenburg, Küpkersweg 70, D-26129 Oldenburg, Germany

August 15, 2022

E-mail: aura.daniela.moreno.mora@uni-oldenburg.de

Keywords: wind turbulence, statistics, velocity increments, gusts, waiting times

1 Introduction

The loads affecting an operating wind turbine are estimated using numerical simulations that aim to reproduce the real interactions between the turbine and the incoming wind. Then, accurate descriptions of both, the physical turbine and the atmospheric wind, to be included in the numerical estimations are essential in the design, manufacturing and operation processes of a wind turbine. Particularly, the characterization of the atmospheric turbulent wind is currently performed based on the standard guideline proposed by the International Electrotechnical Commission (IEC 61400-1)[3]. Although this guideline accounts for essential descriptions of the atmospheric wind, some further statistical characteristics have been poorly addressed. As a result, operating wind turbines might react unpredictably to such structures that have not been properly identified and parametrized from atmospheric data and later included within the numerical models. In this work, we introduce and parametrize two additional features from the atmospheric turbulent wind that have not been considered by the current IEC guideline: the periods of constant wind speed (T_c) and waiting times between wind gusts (T_g). We hypothesize that certain conditions of these events on the wind might induce unexpected dynamic responses in the turbine. Therefore, we focus on the statistical description of those features on the wind in terms of their magnitude, probability of occurrence and possible extreme events.

2 Definition of the extended characteristics

2.1 Periods of constant wind speed T_c

A period of constant wind speed T_c is shown in Fig. 1 for an exemplary time series of the wind speed $u(t)$. Over T_c, the wind speed remains within an interval $u_i \pm \varepsilon$ where ε limits the range or the width of the interval and u_i corresponds to a reference wind speed value. The horizontal red bars in Fig. 1 depict the defined interval $u_i \pm \varepsilon$. For a given point u_i in the time series, the length of the period T_c is measured by considering both directions, forward and backward from u_i. The length of T_c is calculated for each of the data points in the time series. In the case of overlapping periods, only the magnitude of the longest T_c is registered.

2.2 Waiting times between gusts T_g

Given a time series of the wind speed $u(t)$, the velocity increments are defined as $u_\tau = u(t+\tau) - u(t)$ where τ corresponds to a time lag. In the context of atmospheric turbulent wind, extreme events of u_τ are called wind gusts. When considering short time scales of τ, extreme events of u_τ translate into abrupt changes in the wind speed that might affect the dynamics and loads on the wind turbine.

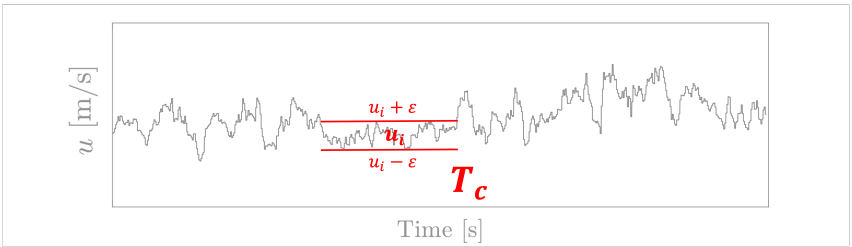


Figure 1: Time series of the wind speed $u(t)$ with an observable period of constant speed T_c.

Fig. 2 shows an exemplary time series of the velocity increments $u_\tau(t)$ for a given time increment τ. The period T_g displayed in Fig. 2 corresponds to a waiting time between two successive gusts. An increment u_τ is considered a gust when its magnitude exceeds a defined threshold S. Therefore, the time intervals between two consecutive points of $u_\tau(t)$ whose magnitude is over S correspond to the called waiting times T_g. In order to avoid counting the same event several times, the minimum value of T_g is conditioned to be the fixed time lag τ for calculating the increments $u_\tau(t)$. The statistical description of such waiting times between large increments was previously addressed in [2].

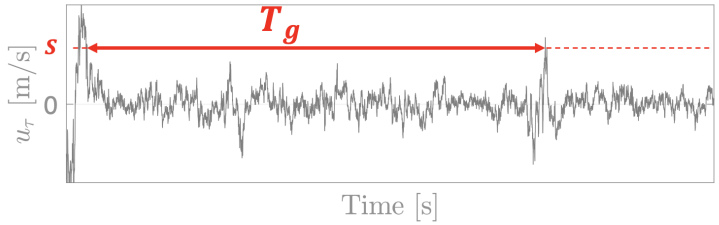


Figure 2: Time series of the increments of the wind speed $u_\tau(t)$ with a period T_g between two successive gusts.

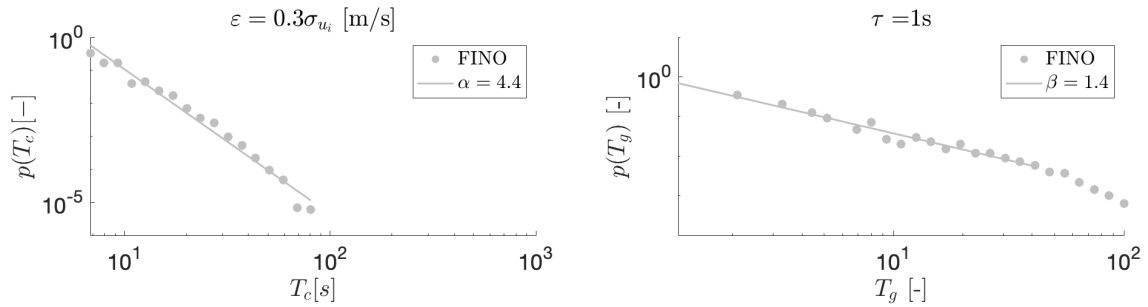
3 Results on the characterization

For illustration purposes, we characterize wind speed data from the research platform FINO 1 [1] located in the North Sea. The data correspond to measurements recorded at 100m height, with a sampling frequency of 1Hz and a length of 1 month.

Fig. 3(a) shows in log-log scale the probability distributions of the length of the periods of constant wind speed $p(T_c)$. For the definition of the interval $u_i \pm \varepsilon$ we consider ε=0.3σ_{u_i}, where σ_{u_i} is the standard deviation of the wind speed time series $u(t)$. Then, in this case, $u(t)$ is considered constant as long as the magnitude of the fluctuations forward and backwards at a reference point u_i, remains lower than 0.3 times the standard deviation calculated over the whole time series. Interestingly, the results of $p(T_c)$ show a power-law decay with an exponent α so that $p(T_c|\varepsilon) \approx T_c^{-\alpha}$. That means, very long (T_c) are expected to happen. For the considered case, α=4.4. As expected from our definition of the interval ε=0.3σ_{u_i} for considering $u(t)$ as constant, the threshold ε affects the critical exponent α; the higher the value of ε, the lower the value of α. Comparisons to pure turbulence suggest that this feature is characteristic of the atmospheric wind, given that such long events are not found in the laboratory data. Moreover, the results of $p(T_c)$ for synthetic wind data generated by standard models [3] reveal those very long periods T_c in the atmospheric turbulent wind are underestimated by the standard assumptions. Of special attention is the value of the exponent α; for certain values of α, $p(T_c|\varepsilon)$ may have divergent moments [4].

Fig. 3(b) presents in log-log scale the probability distributions of the waiting times between successive gusts T_g. The incremental time series $u_\tau(t)$ are calculated with a time lag τ of 1s. The threshold S for identifying the gusts along the time series $u_\tau(t)$ is defined as S=2σ_{u_τ} where σ_{u_τ} is the standard deviation of the incremental time series $u_\tau(t)$. That means that the waiting times T_g are measured between the increments whose magnitude is higher than twice the standard deviation of $u_\tau(t)$. In agreement with the results reported in [2], the waiting time distribution $p(Tg)$ follows a power-law $p(T_g|\tau, S) \approx T_g^{-\beta}$ with a characteristic exponent β for the power-law approximation. For the given values of τ and S, β=1.4. Additionally, the authors in [2] stated that such power-law decay was not

observed on stationary laboratory wind, but particularly identified in the atmospheric data.



(a) (b)

Figure 3: Time series of the increments of the wind speed $u_\tau(t)$ with a period T_g between two successive gusts.

4 Conclusions and outlook

The statistical characterization of atmospheric wind data in terms of periods of constant wind speed T_c and waiting times between successive gusts T_g have been performed. These features have not been addressed by the standard guidelines for the parametrization and modelling of atmospheric wind. The probability distributions $p(T_c)$ and $p(T_g)$ exhibit a power-law decay parametrized by the exponents α and β respectively. From an engineering perspective, very long periods of constant wind speed T_c might be undesirable for an operating wind turbine. As an example, if a such long event is located on a specific area of the rotor plane, it may lead to unexpected periodic loads resulting from the blade passing through the constant speed structure at the given location on the plane. On the other hand, the time between two consecutive large increments might be of high relevance for the dynamic response of the wind turbine. Specific times T_g that coincide with the characteristic frequencies of the turbine, might either intensify or diminish oscillations of the structure.

Consequently, in combination with the characterization of features such as T_c and T_g, it is essential to investigate the impact of those structures carried by the wind on the response of the wind turbine. Fig. 4 shows the results of a preliminary study on the effect of the magnitude of T_g on numerically simulated loads. The two rows in Fig. 4 correspond to different values of T_g. The plots on the left show the time series of the wind speed with different temporal separations between the two imposed 'top-hat' gusts. Respectively, the plots on the right present the time series of a resulting bending moment measured at the base of the tower. As can be observed, the variation in the

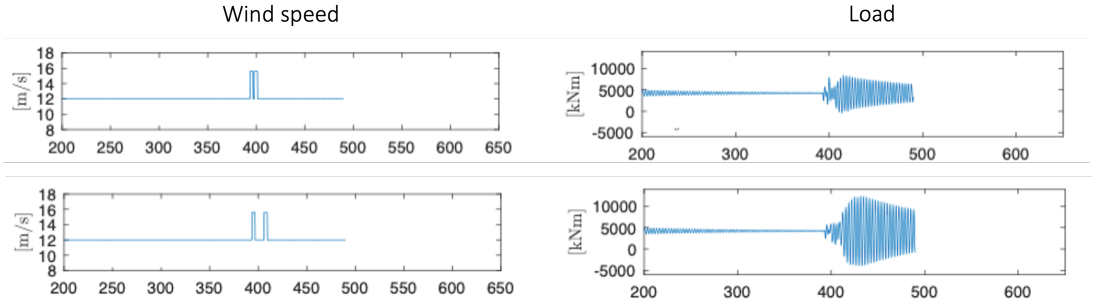


Figure 4: Example of preliminary results on the analysis of the effect of T_g on the response of a simulated wind turbine.

waiting time for the second gust to reach the turbine induces a different load on the tower of the turbine. For the longer T_g, shown in the bottom row, the magnitude of the cyclic load is amplified with respect to the case for a shorter T_g presented in the row above.

Therefore, future work has to be devoted to a deeper understanding of the characteristics of events such as T_c and T_g on the atmospheric wind, their dependence on the parameters for their definitions and their relation to a purely turbulent flow. Additionally, evaluating the response of a wind turbine under different scenarios involving these structures might be beneficial, firstly as an insight into the source of unpredicted measured loads on an operating wind turbine or secondly, as improvements to current control practices.

Acknowledgements

This project has received funding from the German Federal Ministry for Economic Affairs and Climate Action under code 03EE2024/PASTA. In general, we gratefully appreciate the support from the partners involved in the PASTA project.

References

[1] FINO1-Research Platform. https://www.fino1.de/en/.

[2] F. Boettcher, C. Renner, H.-P. Waldl, and J. Peinke. On the statistics of wind gusts. *Bound.-Layer Meteorol.*, 108(1):163–173, 2003.

[3] International Electrotechnical Comission. IEC 61400-1 Wind energy generation systems - Part 1: Design requirements. Standard, Feb 2019.

[4] M. Newman. Power laws, pareto distributions and zipf's law. *Contemporary Physics*, 46(5):323–351, Sep 2005.

18th EAWE PhD Seminar on Wind Energy
2 – 4 November 2022
Bruges, Belgium

GIS-based inverse Sound Propagation Modelling

Henning Arends[a,b], Jan-Hendrik Piel[a], Clemens Hübler[b], Tobias Bohne[b], Raimund Rolfes[b]

[a] Nefino GmbH, Andreaestr. 2a, D-30159 Hannover, Germany
[b] Leibniz University Hannover, Institute of Structural Analysis, Appelstr. 9a, D-30167 Hannover, Germany

E-mail: henning.arends@nefino.de

Keywords: Geographic Information System, Acoustics, Sound Propagation, Spatial Analysis

1 Introduction

The work presented in this abstract is part of the research project WindGISKI. The goal of WindGISKI is the development of an AI that is capable of assessing potential areas for wind energy development in Germany based on a Geographic Information System (GIS). Next to spatial restrictions like nature reserves or protected forests the AI shall take sociological, avifaunistic and wind related influencing factors into account in order to objectively rate potential areas. Planning authorities in Germany do not consider sound propagation effectively when determining priority areas for wind energy use. These priority areas are those areas in Germany on which new wind farms shall be built.

The approval of wind turbines in Germany is regulated in the approval procedure in accordance with the Federal Immission Control Act [3]. §48 of the Federal Immission Control Act states that legal ordinances are issued for immission limitations. In case of sound immissions, the Technical Instructions for protection against noise (TA Lärm) [6] has been issued for this purpose. Together with the ISO 9613-2 [4] the Interim procedure for the prognosis of noise immissions from wind turbines [8] and the Notes on noise immission control for wind turbines [2] the legal framework for sound prognosis is set. In order to obtain a permit, wind energy project developers must comply with the sound immission limits as described in the TA-Lärm. However, when it comes to the designation of priority areas for wind energy use by planning authorities the outlined legal framework is not applied. Noise emissions are taken into account indirectly via blanket distance regulations according to § 249 federal building code [1].

By using blanket distances planning authorities circumvent precise sound calculations. Blanket distances are not only used by german planning authorities to avoid sound calculations but also by Siyal et al. [7] in their analysis in Sweden as well as by Latinopoulos [5] in an analysis in Greece. This approach does not take into account sound attenuating factors like wind direction, land coverage, topography or operating modes of wind turbines and excludes large potential areas for wind energy use. Regardless of whether a house, forest or mountain stands between a residential building or a wind turbine, the same distance is always assumed.

To be independent of blanket distances the WindGISKI-AI needs to be capable to take into account realistic sound propagation. Based on a sound propagation model developed by the Institute of Structural Analysis, Nefino will develop a sound propagation metamodel that is capable of fulfilling the AI´s requirements.

This work will present a backwards sound propagation approach that allows for a fast and precise determination of potential areas for wind energy use based on sound level restrictions and a reference wind turbine.

2 Planned Methodology

For the calculation of sound propagation, the complex propagation effects of a wind turbine are reduced to a point source at hub height [8]. From this source the sound is distributed on a sphere. Respectively the energy decreases with increasing distance from the source. Various effects further reduce the sound level at the immission location or increase it due to reflections. The sound propagation starts at the location of the wind turbine. When looking for potential wind energy areas it is not expedient to place an infinite number of wind turbines and observe the sound propagation emanating from them.

Blanket distances from certain areas and buildings like residential areas, residential buildings, hospitals and recreational areas are used in the designation of priority areas for wind energy use by planning authorities (see Figure 1). This circumvents the realistic and complex simulation of sound propagation, but ensures compliance with TA-Lärm restrictions, since the blanket distances are chosen quite conservatively. This way an exclusion zone for wind energy use around e.g. a residential building is created with a radius r that is determined by the respective planning authority according to § 249 building code and can, as in Bavaria, be 10 times the total height of a wind turbine. A simplified example of blanket distance regulation is visualized in Figure 1.

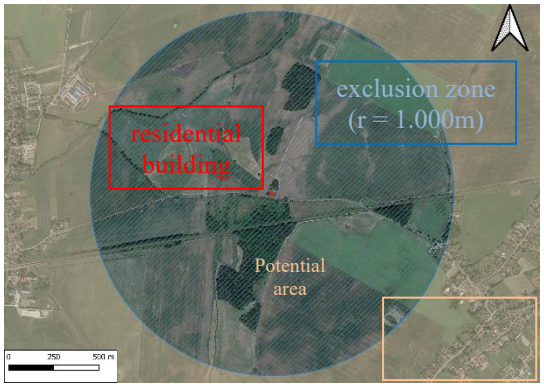


Figure 1: Example of blanket distancing, exclusion zone (r = 1.000 m) around a residential building

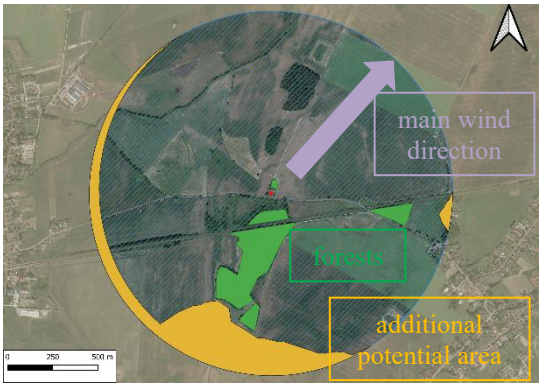


Figure 2: Expected shift of exclusion zone in consideration of wind direction and forests

It is planned to develop a new approach that allows the determination of a more realistically shaped exclusion zone around industrial areas, settlements, residential buildings as well as around spa- and clinic areas by reversing the sound propagation model taking into account attenuating factors like land coverage, building density, topography and wind direction.
First, the sound level limits according to TA-Lärm at the edge of a building are considered. Based on these limits, sound attenuating factors are considered in a 360° radius and a backward sound simulation is performed. This way, the minimum distance of a reference wind turbine, whose hub height and sound level are known, to the edge of a building can be determined. This results in distances that vary depending on the influencing variables around the building. Figure 2 visualizes a simplified example of how the main wind direction and forests might influence the exclusion zone and allow for additional potential areas for wind energy use.
In a following step the WindGISKI-AI can apply this model nationwide in order to make a more precise assessment of potential areas in Germany.

Acknowledgements

This work was funded by the Bundesministerium für Umwelt, Naturschutz, nukleare Sicherheit und Verbraucherschutz (BMUV, Federal Ministry for the Environment, Nature Conservation, Nuclear Safety and Consumer Protection) – FKZ: 67KI21003A.

References

[1] Baugesetzbuch (Federal Building Code), 2022.
[2] Bund/Länder-Arbeitsgemeinschaft Immissionsschutz (LAI), *Hinweise zum Schallimissionsschutz bei Windkraftanlagen (WKA)* (Notes on noise immission control for wind turbines), 2016.
[3] Gesetz zum Schutz vor schädlichen Umwelteinwirkungen durch Luftverunreinigungen, Geräusche, Erschütterungen und ähnliche Vorgänge (Federal Immission Control Act), 2013.
[4] ISO 9613-2: Acoustics – Attenuation of sound during propagation outdoors – Part 2 General method of calculation, 1996.
[5] D. Latinopoulos, K. Kechagia. A GIS-based multi-criteria evaluation for wind farm site selection. A regional scale application in Greece. *Renewable Energy*, 78: 550 – 560, 2015.
[6] Sechste Allgemeine Verwaltungsvorschrift zum Bundes-Immissionsschutzgesetz (Technical Instructions for Protection against Noise), 1998.
[7] S.H. Siyal, U. Mörtberg, D. Mentis, M.Welsch, I.Babelon and M. Howells. Wind energy assessment considering geographic and environmental restrictions in Sweden: A GIS-based approach. *Energy*, 83:447 – 461, 2015.
[8] Unterausschuss NA 001-02-03-19 UA "Schallausbreitung im Freien", *Dokumentation zur Schallausbreitung: Interimsverfahren zur Prognose der Geräuschimmissionen von Windkraftanlagen* (Interim procedure for the prognosis of noise immissions from wind turbines), 2015.

18th EAWE PhD Seminar on Wind Energy
2-4 November 2022
Bruges, Belgium

Mesoscale structure of typhoons for wind energy applications

Sara Müller[a] and **Xiaoli G. Larsén**[a]

[a]Wind and Energy Systems Department, Risø Campus of the Danish Technical University, Frederiksborgvej 399, 4000 Roskilde, Denmark

E-mail: samul@dtu.dk

Keywords: tropical cyclones, WRF mesoscale modelling

1 Introduction

Wind farms are increasingly planned and installed in regions where tropical storms are frequent. During tropical cyclones passages wind turbines are exposed to high wind speeds, veer, strong turbulence and rapid wind direction changes [9, 7]. However, the impact of these extreme conditions on loads acting on wind turbines are poorly understood. Current international design standards IEC [5] remain loosely formulated for tropical cyclone conditions. To more adequately define design standards a better characterization of the tropical cyclone wind field is needed.

In the first part of this PhD project the goal is to characterize the wind field in a large number of tropical cyclones. To reach this goal the Weather Research and Forecasting model WRF [14] is used. WRF allows to use different parametrization schemes to account for non-resolved processes [14]. Model results clearly depend on model configuration and chosen parametrizations schemes. In particular boundary layer parametrization schemes have been shown to affect the structure and development of tropical cyclones [8, 12] and are likely to directly affect the boundary layer wind field. A first study assesses the sensitivity of the mesoscale model on the boundary layer parametrization based on one selected typhoon. Two boundary layer schemes are compared: the Mellor-Yamada Nakanishi and Niino level 2.5 scheme [10] and the Yonsei University scheme (YSU) [4] scheme. The two schemes differ in how they treat turbulent fluxes through the boundary layer. MYNN is a local scheme with prognostic TKE, while YSU is a non-local scheme. The following points are assessed in the study:

1. Can model runs with the boundary layer schemes simulate the observed typhoon and its track?
2. To which extend do the simulations reproduce variability in the horizontal wind field?
3. How does the vertical wind-profile of the simulations compare to observations?

2 Data and Methods

The category 5 typhoon MEGI hit Taiwan in September 2016. Typhoon MEGI is selected for this case study due to the availability of satellite data. To evaluate the influence of the boundary layer parametrization schemes, a 48 hour WRF simulation is run on three stationary domains with the horizontal resolution of 27, 9, and 3 km on 60 vertical levels. Two simulations varying only in their boundary layer and surface layer parametrizations are compared: 1.) the YSU simulation, using the YSU boundary layer scheme with the MM5 surface layer layer scheme [11] and 2.) the MYNN simulation using the MYNN2.5 boundary layer scheme and the MYNN surface-layer scheme [2].
To evaluate the simulations, the simulated typhoon tracks are compared to best track data from the Japan Meteorological Agency (JMA) [6]. The horizontal wind field is analysed and compared to wind maps retrieved from satellite Synthetic Aperture Radar (SAR) available on [1]. To assess simulated horizontal wind field variability the 2D wind speed power spectra in the wave number domain is calculated from the simulations. It is evaluated against the 2D power spectrum of wind speed from SAR wind maps. Wind profiles from the simulations are compared to those from dropsondes and empirical models from different publications [13, 15, 7].

3 Results

Figure 1 shows typhoon MEGI's track in the two simulations, based on the location of the minimal mean sea level pressure. The two simulations capture MEGI's north eastward propagation towards Taiwan between 25 to 27 September. The simulated tracks agree reasonably well with the JMA best track data.

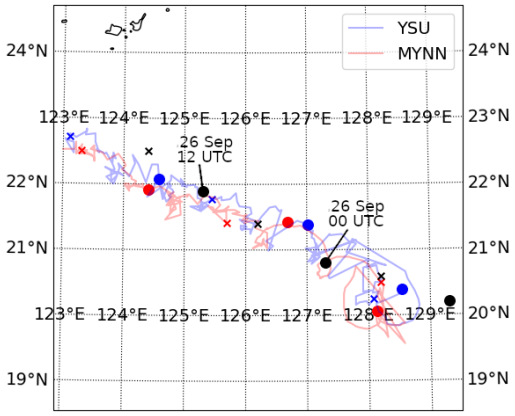


Figure 1: Comparison of the simulated typhoon track to the best track archive from the Japan Meteorological Agency (JMA) [6]. Lines show the central position between 12 UTC on September 25 and 12 UTC on September 26 for the YSU (blue) and MYNN (red) simulation. Points (at 00 and 12 UTC) and crosses (at 6 and 18 UTC) show the JMA central position (black) at the available time steps. The same time steps are shown for the YSU (blue) and MYNN (red) simulation.

Figure 2 shows the instantaneous wind field at 6 UTC on 26 September for the two simulations. Both simulations show low wind speeds in the eye and cyclonic winds with up to 40 m/s in the eye wall. However, differences are evident in wind speed variability at scales of 10 to 100 km. The YSU simulation exhibits distinct wind speed maxima on scales of a few kilometers, while the MYNN simulation generates a smoother wind field. This observation is confirmed for the simulated period by spectral analysis of the wind speed (Figure 3a). A spectral slop equal or bigger than $-5/3$ is obtained from spectral analysis of SAR images. This slope can be reproduced by the YSU simulation for waves lager than 10 km. The MYNN spectra shows a smaller slope, indicating missed variability in the MYNN simulation.

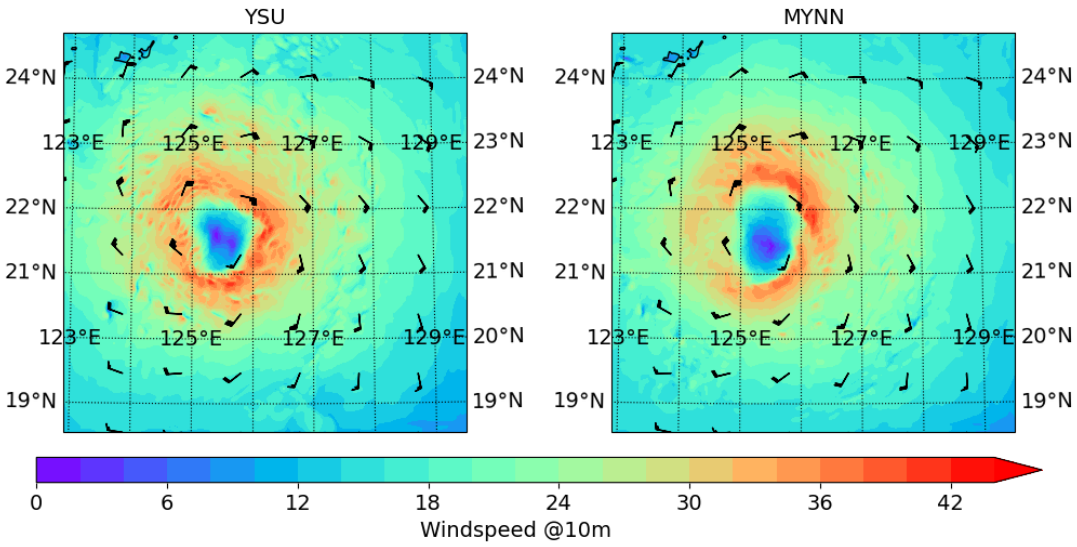


Figure 2: 10 m wind field for the YSU (left) and the MYNN (right) simulations at 6 UTC on 26 September.

Because the vertical wind shear is particularly important for wind turbines, vertical eye-wall wind profiles of the two simulations are compared in Figure 3b. The profiles are averaged over a 29 h simulation period and over all grid points within a 80-150 km distance from the cyclone center. In agreement with observations [13, 15, 7] wind speed increases approximately logarithmically with height up to around 300 m for both simulations. Over the whole profile the YSU simulation shows slightly higher wind speeds than MYNN. The difference increases above 300 m. Here, the YSU deviates from the logarithmic profile and the wind speed increases stronger with height than in the MYNN simulation. Further away from the cyclone center the wind speeds decreases, but the simulated profiles have similar structures as in the eye-wall region (not shown). Over the whole profile the wind speed decreases faster with distance for YSU than for MYNN. Differences in magnitude are small outside of the eye-wall, at distances between 200-400 km from the cyclone center.

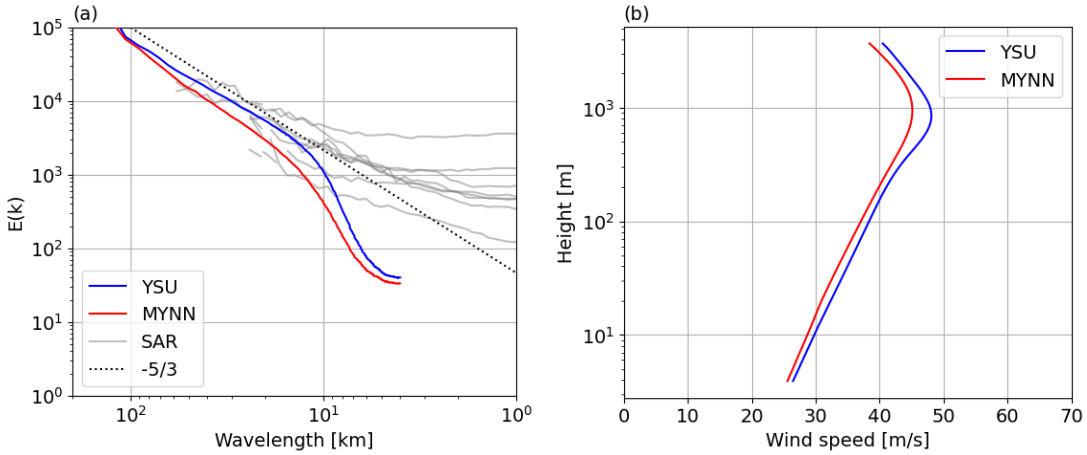


Figure 3: (a) 2D wind speed power spectra in the wave number domain for the YSU (blue) and the MYNN (red) simulation, averaged over 29 simulation hours. Grey lines show the spectra calculated from 8 SAR images covering different parts of MEGI on 26 September. The black dotted line indicates a slope of $-5/3$. (b) Eye wall wind profile form the YSU simulation (blue) and the MYNN simulation (red). The profiles are averaged over 29 simulation hours and over all grid points within a 80-150 km distance from the cyclone center.

4 Discussion and Outlook

Simulations with the MYNN and the YSU boundary layer schemes could reproduce the track of the selected typhoon. Small differences may come from errors in the initial conditions provided by ERA5 [3] data, missing air-see interactions and further model assumptions.

The 10 m horizontal wind field suggests, that MYNN stronger under-predicts spacial variability than YSU on scales up to 100 km. The underestimation might result from too strong local mixing in the MYNN parametrization scheme.

The magnitude of the wind speed is hard to evaluate without direct measurements. The pronounced increase in the YSU wind profile above 300 m is not observed in drop sound measurements as documented in [13, 15]. However, it remains unclear weather this particular typhoon produced such a feature in its profile.

The case study emphasises the importance of the choice of the boundary layer scheme when simulating tropical storms. The results might vary for different typhoon sizes and categories. Further studies including a large number of different tropical storms are planned. Further interactions with other parametrization schemes will be calculated and analysed. When a satisfactory understanding of the model limitations is reached, WRF will be used to get a climatology of wind-fields in typhoons for wind energy applications. In later phases of the PhD project, high resolution observations will be used to characterize turbulence in typhoons. In the final phase, turbulent loads acting on wind turbines during typhoon passage will be analysed.

References

[1] M. Badger, I. Karagali, and D. Cavar. Offshore wind fields in near-real-time. `https://doi.org/10.11583/DTU.19704883.v1`, 2022. Accessed: 2022-07-03.

[2] A. Dyer and B. Hicks. Flux-gradient relationships in the constant flux layer. *Quarterly Journal of the Royal Meteorological Society*, 96(410):715–721, 1970.

[3] H. Hersbach, B. Bell, P. Berrisford, S. Hirahara, A. Horányi, J. Muñoz-Sabater, J. Nicolas, C. Peubey, R. Radu, D. Schepers, et al. The ERA5 global reanalysis. *Quarterly Journal of the Royal Meteorological Society*, 146(730):1999–2049, 2020.

[4] S. Y. Hong, Y. Noh, and J. Dudhia. A new vertical diffusion package with an explicit treatment of entrainment processes. *Monthly Weather Review*, 134(9):2318–2341, 9 2006.

[5] IEC. IEC 61400-1 Ed4: Wind turbines - Part 1: Design requirements. standard, International Electrotechnical Commission, Geneva, Switzerland, 2019.

[6] JMA. Japan Meteorological Agency. `https://www.jma.go.jp/jma/jma-eng/jma-center/rsmc-hp-pub-eg/besttrack.html`, 2022. Accessed: 2022-06-010.

[7] A. Kapoor, S. Ouakka, S. R. Arwade, J. K. Lundquist, M. A. Lackner, A. T. Myers, R. P. Worsnop, and G. H. Bryan. Hurricane eyewall winds and structural response of wind turbines. *Wind Energy Science*, 5(1):89–104, 1 2020.

[8] J. D. Kepert. Choosing a boundary layer parameterization for tropical cyclone modeling. *Monthly Weather Review*, 140(5):1427–1445, 5 2012.

[9] S. E. Larsen, Ejsing Jørgensen, M. C. Hans; Kelly, X. G. Larsén, S. Ott, and E. Jørgensen. Elements of extreme wind modeling for hurricanes. *DTU Wind Energy*, 2016.

[10] M. Nakanishi and H. Niino. An improved mellor-yamada level-3 model: its numerical stability and application to a regional prediction of advection fog. *Boundary-Layer Meteorology*, 119:397–407, 2006.

[11] P. A. J. Nez, J. Dudhia, J. F. Gonza´lez, G. Gonza´lez-Rouco, J. Navarro, J. P. Monta´vez, M. Monta´vez, E. Garci´a, and G. Garci´a-Bustamante. A revised scheme for the WRF surface layer formulation. *American Meteorological Society*, 2012.

[12] D. S. Nolan, J. A. Zhang, and D. P. Stern. Evaluation of planetary boundary layer parameterizations in tropical cyclones by comparison of in situ observations and high-resolution simulations of hurricane Isabel (2003). part I: initialization, maximum winds, and the outer-core boundary layer. *Monthly Weather Review*, 137(11):3651–3674, 11 2009.

[13] M. D. Powell, P. J. Vickery, and T. A. Reinhold. Reduced drag coefficient for high wind speeds in tropical cyclones. *Nature*, 422(6929):279–283, 2003.

[14] W. C. Skamarock, J. B. Klemp, J. Dudhia, D. O. Gill, Z. Liu, J. Berner, W. Wang, J. G. Powers, M. G. Duda, D. M. Barker, and X.-Y. Huang. A description of the advanced research WRF model version 4. *National Center for Atmospheric Research: Boulder, CO, USA*, page 145, 2019.

[15] P. J. Vickery, D. Wadhera, M. D. Powell, and Y. Chen. A hurricane boundary layer and wind field model for use in engineering applications. *Journal of Applied Meteorology and Climatology*, 48(2):381–405, 2 2009.

18th EAWE PhD Seminar on Wind Energy
2-4 November 2022
Bruges, Belgium

Mesoscale variability in wind speed, a study for the Kattegat (Denmark)

J. Neirynck[a], **J. Van de Walle**[a], **R. Borgers**[a], **S. Jamaer**[a], **J. Meyers**[b], and **N.P.M. van Lipzig**[a]

[a]Department of Earth and Environmental Sciences, KU Leuven, Leuven, Belgium
[b]Department of Mechanical Engineering, KU Leuven, Leuven, Belgium

E-mail: jerome.neirynck@kuleuven.be

Keywords: wind, mesoscale, convection permitting climate models, resource assessment

Over the past few years technological advancements allow for ever larger wind turbines to be constructed. Due to their elevated wind speeds offshore environments are best suited for these wind turbines. In order to lower construction & maintenance costs these turbines are often built near each other in a wind farm, in the vicinity of coastlines. Modern offshore wind farms reach dimensions comparable to those of mesoscale weather systems that might occur in an offshore environment, such as seabreeze systems. In order to study these effects we have set up a convection permitting climate simulation in the COSMO model [3]. The study area for this simulation is the Kattegat strait between Denmark and Sweden (figure 1). The reason for chosing this area is twofold. First it's a very coastal rich environment, and should provide plenty of opportunity to study coastal effects. Secondly it also features the Anholt wind farm centrally located in the Kattegat, and SCADA data from this wind farm is available. The simulation has a horizontal resolution of 1.5×1.5 km^2, which allows for deep convection to be fully resolved in the model. The dynamical core of the COSMO model is expanded with a parametrization for, amongst others, shallow convection [6], subgrid-scale turbulence [1], [5], [4], and micro-physical cloud processes & radiative transfer [2]. The model is driven directly with ERA5 reanalysis data, which has a horizontal resolution of $\approx 30 \times 30$ km^2. On either side of the simulation domain 20 grid points are used for relaxation and spin up for the forcing data. These points are excluded from the analysis domain.

To study the mesoscale wind speed variability we have come up with a metric for the mesoscale wind speed component. This component is extracted from the 100 m wind field by sliding two square windows of different sizes over the study area. Within both of these windows the mean wind speed is constantly calculated. The smallest window contains 10×10 pixels, which is comparable to the effective resolution of the COSMO model. The large window size is chosen in such a way that it should follow the synoptic background of the wind speed. The ratio between the two mean wind speeds gives a dimensionless number quantifying the mesoscale wind speed component. High values in this mesoscale wind speed component help us to detect when a mesoscale system travels over the Kattegat, but this also gives us the opportunity to do some statistics. We can group the values for this mesoscale wind speed component per hour and compare winter and summer with each other (figure 2). Here we see that there is a larger mesoscale wind speed component in summer compared to winter, and that the diurnal amplitude of the mesoscale wind speed component is also larger in summer. In summer the Sun heats the land surrounding the Kattegat more efficaciously. This results in higher temperature over land and can, in combination with the lower temperatures over the seawater, be a reason for the higher mesoscale component in summer.

In order to study the temporal variability in wind speed the frequency spectrum of the wind speed time series for every offshore pixel in the study area was estimated using the Welch method [7]. Integrating all these spectra over different time intervals makes it possible to compare them visually. Integrating the 100 m wind speed over timescales from 8h to 12h (figure 3) shows a difference in winter and summer. In summer there is namely a larger variability in wind speeds on these time scales compared to winter. Integrating the 100 m wind speed over shorter timescales (figure 4) result in a different picture. Here a larger intensity is found in winter. Shorter timescale variability in wind speed is often linked to convective systems. These systems often occur in winter, when the relatively warm seawater creates unstable conditions.

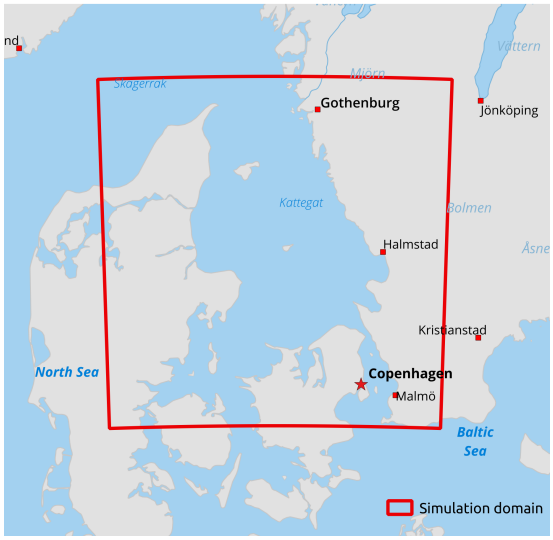


Figure 1: Map of the simulation domain.

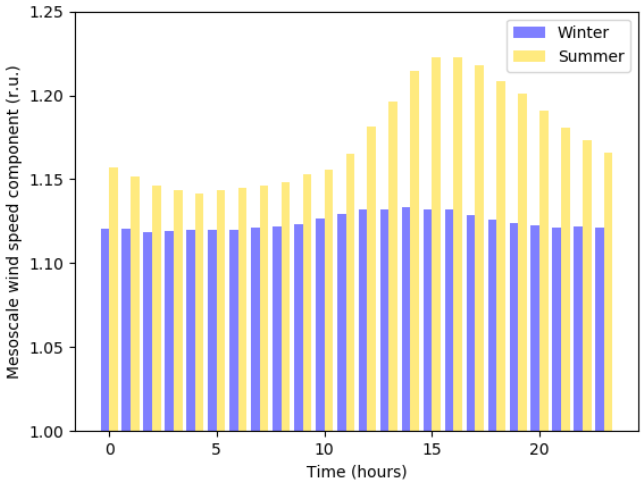
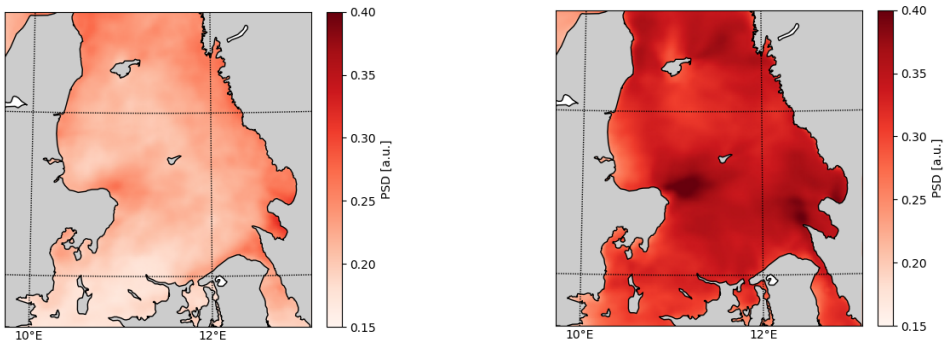


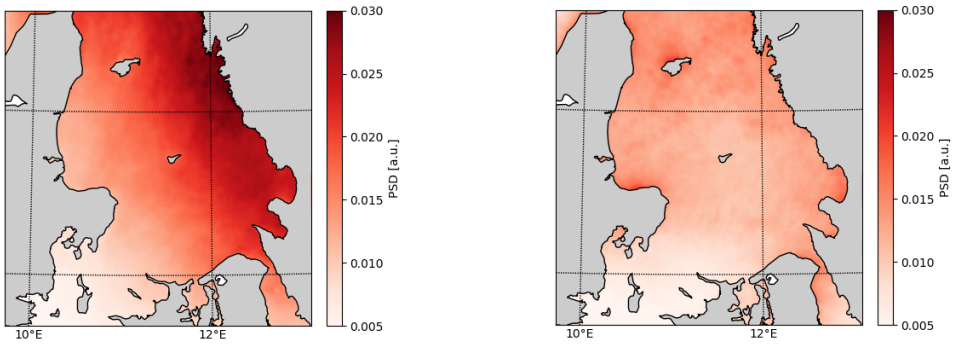
Figure 2: Diurnal distribution of the mesoscale wind speed component, for both the winter regime and the summer regime.



(a) Winter, 8h to 12h

(b) Summer, 8h to 12h

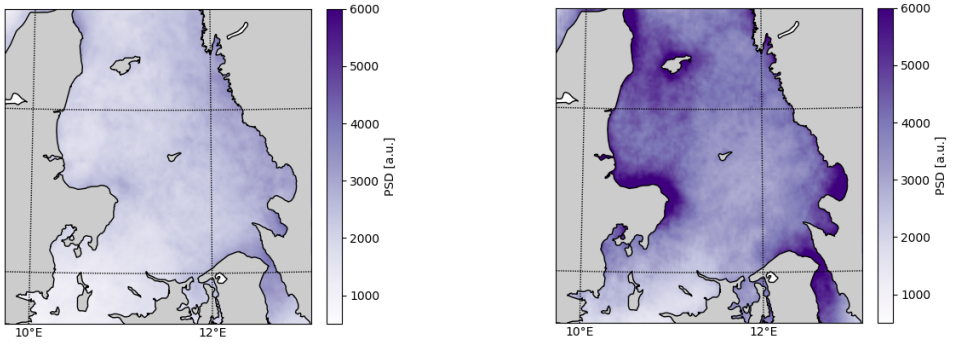
Figure 3: Periodogram of the wind speed integrated over a time period of 8h to 12h for both the winter (**a**) as for the summer (**b**).



(a) Winter, 20 min to 1h

(b) Summer, 20 min to 1h

Figure 4: Periodogram of the wind speed integrated over a time period of 20 minutes to 1h for both the winter (**a**) as for the summer (**b**).



(a) Winter, 20 min to 1h

(b) Summer, 20 min to 1h

Figure 5: Periodogram of the wind power integrated over a time period of 20 minutes to 1h for both the winter (**a**) as for the summer (**b**). Contrary to figure 4 the larger variations in potential wind power are found here in summer, while the larger fluctuations in wind speed are found in winter. This is related to the wind speed being lower in summer, where the derivative of the wind power with respect to the wind speed is larger compared to the wind speed in winter.

The periodograms discussed above can also be estimated for wind power spectra. Using the power curve of a wind turbine the time series of the wind speed is first converted to wind power. Then using the Welch method again the frequency spectrum of the time series of the wind power is estimated. Integrating these spectra over the short timescales (figure 5) gives us some different result compared to the integrated spectra for just the wind speed. Here we have a lower variability of wind power in winter compared to summer, while in figure 4 we have the opposite result for the wind speed variability. This discrepancy is related to the mean wind speed which is higher in winter compared to the summer. In winter the wind speed is often found near the rated wind speed. Between the rated wind speed and the cut-out wind speed the power output is constant, resulting in no variability in the spectrum. In summer the mean wind speed is lower, and can be situated more in the region where the power output is related to the cube of the wind speed, resulting in larger variability. A lot of variations in wind speed thus don't directly translate to a lot of variations in power output.

References

[1] M. Raschendorfer. The new turbulence parameterization of lm. *COSMO newsletter*, 1:89–97, 2001.

[2] B. Ritter and J.-F. Geleyn. A comprehensive radiation scheme for numerical weather prediction models with potential applications in climate simulations. *Monthly weather review*, 120(2):303–325, 1992.

[3] B. Rockel, A. Will, and A. Hense. The regional climate model cosmo-clm (cclm). *Meteorologische Zeitschrift*, 17(4):347–348, 2008.

[4] J.-P. Schulz. Introducing sub-grid scale orographic effects in the cosmo model. *COSMO Newsl*, 9:29–36, 2008.

[5] J.-P. Schulz. Revision of the turbulent gust diagnostics in the cosmo model. *COSMO Newsletter*, 8:17–22, 2008.

[6] M. Tiedtke. A comprehensive mass flux scheme for cumulus parameterization in large-scale models. *Monthly weather review*, 117(8):1779–1800, 1989.

[7] P. Welch. The use of fast fourier transform for the estimation of power spectra: a method based on time averaging over short, modified periodograms. *IEEE Transactions on audio and electroacoustics*, 15(2):70–73, 1967.

18th EAWE PhD Seminar on Wind Energy
2-4 November 2022
Bruges, Belgium

Noise Source Identification on a Diffuser-Augmented Wind Turbine Using Ffowcs Williams–Hawkings Analogy

J. Manoel Freire-Guimaraes[a], **Francesco Avallone**[a], and **Daniele Ragni**[a]

[a]Delft University of Technology, Delft, The Netherlands

E-mail: J.M.FreireGuimaraes@tudelft.nl

Keywords: Ducted Wind Turbines, Aeroacoustics, Noise Source Identification

1 Introduction

Wind energy has become an essential contributor to producing cleaner and renewable energy. By 2030, the contribution of wind resources is expected to cover 29% of Europe's electricity demand [4]. The application of DAWT can be further extended by placing smaller wind turbines both close to residential or rural locations [5]. However, due to small wind turbines being generally placed close to the ground or within the complex urban canopy, the DAWT is subject to lower wind speeds and high turbulent fluctuations. To overcome these limitations, several types of so-called wind concentrators have been proposed [7, 9, 8, 10]. The most widely used is diffuser-augmented wind turbine (DAWT), also called: ducted, shrouded, or augmented wind turbine.

In DAWTs, a diffuser is used to surround the rotor and increase the overall power extraction per unit of frontal area by inducing a circulation around the diffuser and thus increasing the mass flow swallowed by the rotor [2]. As a result, the DAWT increases the power for a given rotor area. Moreover, the diffuser also reduces the tip losses [11] and makes the rotor performance less sensitive to slight yaw variations when compared to its bare counterpart [3]. These characteristics corroborate its application in urban areas.

Although the DAWT can be subjected to stricter regulations regarding acoustic pollution than larger wind turbines placed in unpopulated areas, few studies have been done on the DAWT noise emissions. They are mostly focused on the influence of diffuser geometry on noise generation [6], the impact of the tip gap [1], and the effect of yaw angle [3]. Yet, a description of the contributions from individual parts of the DAWT to the far-field noise emissions is still missing in the literature. Such description is useful to determine correct noise control methodologies based on each noise generation mechanism.

The goal of the paper is two address two main points: characterise the noise contribution from the rotor and the diffuser and to analyse the shielding effect due to the diffuser's presence. To achieve this, this work uses Lattice Boltzmann simulation combined with Ffowcs Williams-Hawkings analogy, considering both solid and permeable formulations.

2 Modelling

This study is based on the DonQi® DAWT, displayed in Figure 1, which has a three-blade rotor and a diffuser with an airfoil cross-section. The diffuser has a chord equal to $c_{diff} = 1m$ and a diameter of $2m$ at the exit. The rotor has radius $R_0 = 0.75m$ and tip gap ratio, defined as the ratio between the tip clearance and the rotor radius, $t_g = 2.5\%$. The rotor blade consists of NACA 2207 airfoil profiles of chord and twist distribution shown in Figure 1 left side. The blades are connected to a hub (upstream) and a nacelle (downstream). The hub is composed of a cylinder, with a diameter and length equal to 125 mm and 100 mm. The latter is obtained through the rotation of a quarter of an ellipsis. The nacelle has a cylinder length equal to 75 mm.

The free-stream velocity is $U_\infty = 5m/s$, which is a characteristic value for urban wind turbines, corresponding to free-stream Mach number and Reynolds number based on the diffuser chord equal to 0.015 and 3.31×10^5 respectively. The rotational speed is $\omega = 39.84rad/s$, corresponding to a tip-speed ratio $\lambda = \omega R/U_\infty = 6$, which has been demonstrated as the optimum value [13].

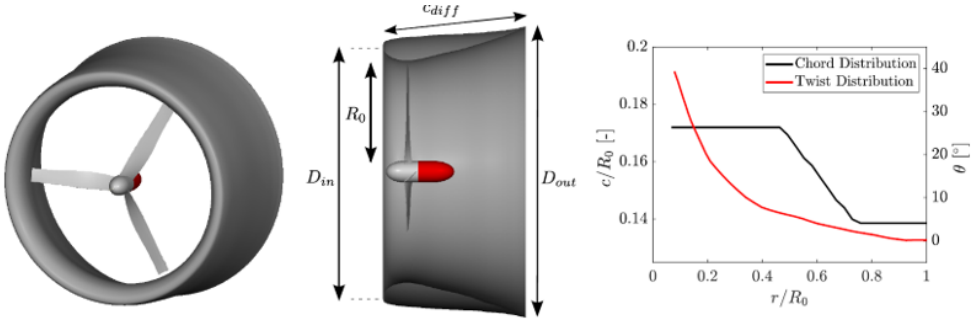


Figure 1: DonQi Wind turbine ad its geometrical description.

The high fidelity simulation was conducted using the Lattice-Boltzmann solver PowerFlow. The simulation domain is a box of length equal to c in the streamwise direction and $26c$ in the y-z plane, with the rotor being placed $9c$ downstream the inlet. Free-stream inlet boundary conditions are applied at $x = -9c$ while pressure boundary conditions are used at the other wall. The region with the highest resolution is the offset corresponding to 2400 voxel per diffuser chord. A convergence study, detailed description of the model and validation against experimental data can be found in [1].

The noise radiated by the DAWT is calculated using the Ffwocs-Williams-Hawkings (FWH) analogy [14], which uses transient pressure information recorded at a surface mesh that can be either defined as the surface of a solid body (known as solid formulation) or as a permeable surface surrounding the system under investigation (known as permeable formulation). While the latter includes all the terms on the FWH equation, including quadrupole sources associated with noise generated by turbulence, the solid formulation only models monopoles (associated with volume displacement) and dipoles (associated with surface forces).

Furthermore, the solid formulation can provide an insight into the generation of sound from different parts of a complex system by isolating the surfaces from where the pressure fluctuations are recorded but fails to address acoustic interactions such as the shielding due to the presence of a body between the emitter and the receiver [12].

Similar to the study of [1], the far-field noise is obtained on a circular array of equally spaced microphones placed at $2R_0$ from the center of the rotor. Two circular arrays, one in the $x-y$ plane and one in the $x-z$ plane, with 36 microphones per arc are used. Thus the angular spacing between the microphones is of 10°. The results are averaged over the four microphones at the same directivity angle for each azimuthal position.

In this work, the acoustic pressure is calculated considering three different scenarios. (i) FWH Permeable: a box with dimensions $3R_0$ in the y direction, $2c$ in the x direction, and $3R_0$ in the z direction is centered at the hub location and the unsteady pressure fluctuation is then sampled on this permeable surface; (ii) FWH Solid (Rotor Only): the pressure fluctuation is only sampled at the surfaces related to the rotor e.g. blades, hub, nacelle, and tripping surfaces. (iii) FWH Solid (All Parts): in this scenario, the pressure fluctuations are sampled at the rotor surfaces and the surfaces related to the diffuser.

3 Far-field Noise Results

Figure 2 shows the Power Spectrum Density (PSD) at 30°, 90° and 120°, (0° being upstream the rotor). The tonal noise component of the noise spectra is dominant over the broadband noise, being up to 40 dB higher at 90° and 120°, as observed in [1]. Additionally, a clear separation between low and high-frequency noise is noticeable around 60 Hz. The two dominant noise generation mechanisms can explain this differentiation: rotor loading and thickness noise and rotor/diffuser broadband trailing edge noise.

The matching between permeable and solid formulations with all the parts at high frequencies confirms the negligible presence of quadrupoles sources related to turbulence-generated noise. Moreover, the difference between Rotor Only and All Parts configurations shows that the dominant broadband noise source is the diffuser, having levels up to 20 dB higher than the broadband noise generated by the rotor. On the other hand, there is a difference between both scenarios at the low-frequency range. The increase of the noise at the first Blade Passing Frequency when the diffuser is considered in the solid formulation may be explained by the high-pressure zone on the diffuser wall generated by the blade's tip, thus causing an unsteady force that rotates at the same speed as the rotor.

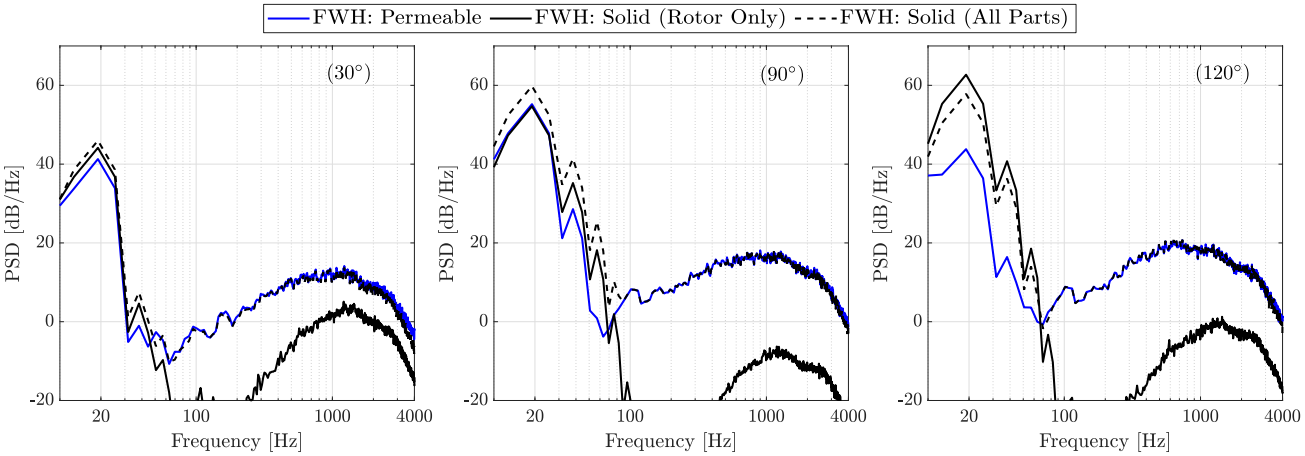


Figure 2: Power Spectrum Density at different positions using high and low fidelity approaches.

When the solid and permeable formulations are compared, the shielding effect due to the presence of the diffuser is observed. This is more noticeable the higher the harmonic numbers, since the shielding becomes more intense the higher Helmholtz number $He = 2\pi L/\lambda$, where L is the characteristic length of the shielding body and λ is the acoustic wavelength emitted by the source. For a better understanding of the shielding effect and its influence on low-frequency noise attenuation, Figure 3 shows the directivity of the SPL integrated from 0.5×BPF to 1.5× BPF.

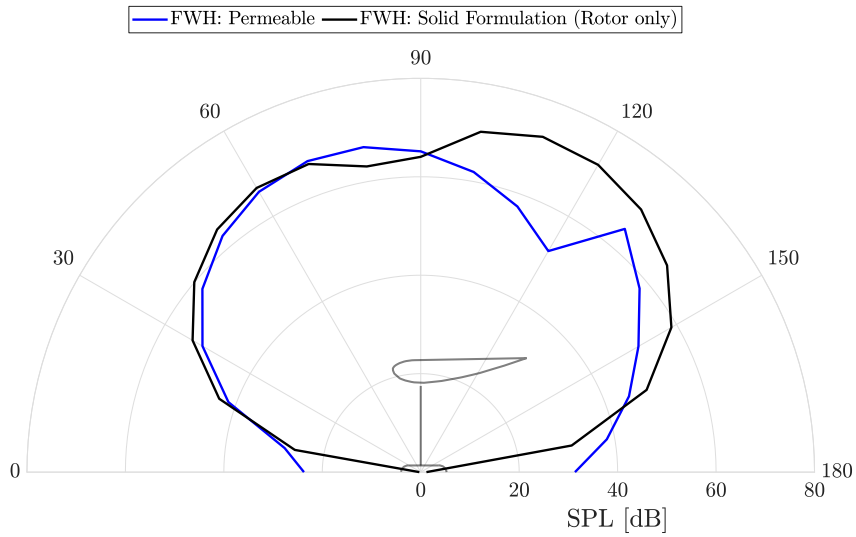


Figure 3: Directivity pattern of the 1st BPF.

The agreement between solid and permeable formulations from 0° to 70° shows no relevant influence of the diffuser in shielding the noise emitted by the rotor or modal contribution. However, from 70° to 120° an attenuation of up to 20 dB is observed. This is explained by the apparent characteristic length of the diffuser between the rotor and the observer since the rotor is not positioned at the middle span of the duct.

4 Conclusions

This presents the analysis of the noise sources of a DAWT. Results show the dominance of the diffuser's trailing edge noise at mid and high frequencies. The shielding due to the presence of the diffuser is observed from directivity angles from 90° to 120° and has a significant impact ah higher harmonics of the BPF due to the non-

compactness of the shielding body at high frequencies.

Acknowledgements

The project as received funding from the European Union's Horizon 2020 research and innovation programme under the Marie Sklodowska-Curie grant agreement No 860101

References

[1] F. Avallone, D. Ragni, and D. Casalino. On the effect of the tip-clearance ratio on the aeroacoustics of a diffuser-augmented wind turbine. *Renewable Energy*, 152:1317–1327, 2020.

[2] R. Bontempo and M. Manna. On the potential of the ideal diffuser augmented wind turbine: an investigation by means of a momentum theory approach and of a free-wake ring-vortex actuator disk model. *Energy Conversion and Management*, 213:112794, 2020.

[3] V. V. Dighe, F. Avallone, and G. van Bussel. Effects of yawed inflow on the aerodynamic and aeroacoustic performance of ducted wind turbines. *Journal of Wind Engineering and Industrial Aerodynamics*, 201:104174, 2020.

[4] W. Europe. Wind energy in europe: Scenarios for 2030. *Wind Europe: Brussels, Belgium*, 2017.

[5] S. Evans, J. Kesby, J. Bradley, and P. Clausen. Commercialization of a diffuser augmented wind turbine for distributed generation. In *Journal of Physics: Conference Series*, volume 1452, page 012014. IOP Publishing, 2020.

[6] I. Hashem, M. H. Mohamed, and A. A. Hafiz. Aero-acoustics noise assessment for wind-lens turbine. *Energy*, 118:345–368, 2017.

[7] T. A. Khamlaj and M. P. Rumpfkeil. Analysis and optimization of ducted wind turbines. *Energy*, 162:1234–1252, 2018.

[8] F. Nardecchia, D. Groppi, D. A. Garcia, F. Bisegna, and L. de Santoli. A new concept for a mini ducted wind turbine system. *Renewable Energy*, 175:610–624, 2021.

[9] Y. Ohya and T. Karasudani. A shrouded wind turbine generating high output power with wind-lens technology. *Energies*, 3(4):634–649, 2010.

[10] L. Ramayee and K. Supradeepan. Performance evaluation of cowl-augmented wind turbine. *Journal of the Brazilian Society of Mechanical Sciences and Engineering*, 43(1):1–13, 2021.

[11] A. Saleem and M.-H. Kim. Performance of buoyant shell horizontal axis wind turbine under fluctuating yaw angles. *Energy*, 169:79–91, 2019.

[12] P. R. Spalart, K. V. Belyaev, M. L. Shur, M. Kh Strelets, and A. K. Travin. On the differences in noise predictions based on solid and permeable surface ffowcs williams–hawkings integral solutions. *International Journal of Aeroacoustics*, 18(6-7):621–646, 2019.

[13] F. van Dorst. An improved rotor design for a diffuser augmented wind turbine: Improvement of the donqi urban windmill. 2011.

[14] J. F. Williams and D. L. Hawkings. Sound generation by turbulence and surfaces in arbitrary motion. *Philosophical Transactions for the Royal Society of London. Series A, Mathematical and Physical Sciences*, pages 321–342, 1969.

18th EAWE PhD Seminar on Wind Energy
2-4 November 2022
Bruges, Belgium

Simulating spatio-temporal varying waves using a WRF-LES-IBM system

Hamzeloo, S.[a], **Peña, A.**[a], and **Hahmann, A. N.**[a]

[a]DTU Wind and Energy Systems, Frederiksborgvej 399, 4000 Roskilde, Denmark

E-mail: siham@dtu.dk

Keywords: offshore wind energy, WRF-IBM, WRF-LES, marine boundary layer, wind-wave interaction

Offshore wind turbines highly interact with the flow in the marine boundary layer. Moreover, surface waves have the potential to interact and modify the local atmospheric flow (e.g., through modification of the surface roughness, flow separation, and sheltering) [2]. Thus, wave fields can influence the marine boundary layer structure as well as offshore wind turbine performance. Few efforts have been dedicated to studying wave effects on the marine atmospheric boundary layer and wind turbines' performance. Most of those focused on sea roughness parameterizations and wind-wave coupled models [4]. Both approaches are mostly appropriate for mesoscale simulations.

The Weather and Research Forecast (WRF) model is a well-known tool for mesoscale simulations. The WRF model follows a terrain-following vertical structure. For high spatial resolutions, when computational mesh sizes reach the order of meters, the terrain-following approach becomes limited because of the poor mesh quality. When increasing the resolution some issues might arise. Sharp changes in geometrical features of the terrain can skew the grid cells, which leads to numerical errors [3]. Therefore, approaches such as the immersed boundary method (IBM) can be used to overcome this in the WRF model [1]. At high resolution, we can run WRF in large-eddy simulation (LES) mode (WRF-LES). This PhD study aims at using a WRF-LES-IBM system for the implementation of varying wave fields as a moving terrain. To achieve this, time-varying wave fields will be applied as the surface boundary condition in the simulation. In this fashion, we can investigate how wave fields modify the marine boundary layer, and atmospheric flow characteristics, and eventually wind turbine and wind farm performance.

Acknowledgements

This PhD project is part of the Multi-scale Atmospheric Modeling Above the Seas (MAMAS) project funded by the Independent Research Fund Denmark (Danmarks Frie Forskningsfond DFF), which is lead and conducted by DTU Wind and Energey Systems.

References

[1] J. Bao, F. K. Chow, and K. A. Lundquist. Large-eddy simulation over complex terrain using an improved immersed boundary method in the Weather Research and Forecasting model. *American Meteorological Society*, 146:2781–2797, 2018.

[2] A. P. Cifuentes-Lorenzen. The wave boundary layer over the open ocean and the implications to air-sea interaction. *University of Connecticut, Doctoral Dissertations 175.*, 2013.

[3] M. H. Daniels, K. A. Lundquist, J. D. Mirocha, D. J. Wiersema, and F. K. Chow. A new vertical grid nesting capability in the Weather Research and Forecasting (WRF) model. *American Meteorological Society*, 144:3725–3747, 2016.

[4] A. A. Sam, R. Szasz, and J. Revstedt. The influence of sea waves on offshore wind turbine aerodynamics. *Energy Resources Technology*, 137:051209–051219, 2015.

18th EAWE PhD Seminar on Wind Energy
2-4 November 2022
Bruges, Belgium

Statistical characteristics of turbulent wind inflow obtained from WRF-LES simulations for the SWiFT test site

Mohanad Elagamy[a], Baris Kale[a,b], Cristobal Gallego-Castillo[a], Alvaro Cuerva-Tejero[a], Sophia Buckingham[b], Jeroen van Beeck[b], Oscar Lopez-Garcia[a], and Sergio Avila-Sanchez[a]

[a]Aircraft and Space Vehicles Department, Universidad Politécnica de Madrid, Plaza Cardenal Cisneros 3, 28040 , Madrid, Spain.
[b]Environmental and Applied Fluid Dynamics Department, von Karman Institute for Fluid Dynamics, Rhode-Saint-Genèse, Belgium

E-mail: mohanad.elagamy@upm.es

Keywords: weather research and forecasting model, large-eddy simulation, atmospheric boundary layer, atmospheric stability, SWiFT, statistical analysis, power spectral density

Abstract

This work provides a preliminary study of the wind field statistics of high resolution WRF-LES simulation of SWiFT test site. The aim is to analyze the capabilities of the WRF-LES approach to reproduce the wind field characteristics that are relevant for the aeroelastic simulation of wind turbines. In addition, information, about the wind loads experienced by the wind turbine, is also provided. The statistical characteristics of the turbulent wind inflow are presented for the unstable, neutral and stable atmospheric boundary layer. Typical mean speed and variances profiles, for flat terrain, are obtained. Furthermore, the longitudinal integral length scale is sensitive to the approach used to evaluate it.

1 Introduction

Sandia National Laboratories' Scaled Wind Farm Technology (SWiFT) facility, located in Lubbock, Texas, USA [2], provides researchers a unique opportunity to validate their numerical simulations in realistic turbulent flows, such as wind turbine wakes, under varying atmospheric stability conditions. The test field is located on flat terrain and is, therefore, exempt from complex terrain effects. The inflow conditions were measured at a 60 m meteorological mast located 65 m upstream of the first-row wind turbines, when winds come from the south. In order to properly reproduce inflow conditions for all atmospheric stability cases, namely neutral, unstable, and stable conditions, the simulated turbulent inflow is calibrated against measurements taken from the met mast. For clarity, this calibration analysis is not provided in the present study, although the simulated inflow conditions match the measurements at the met mast position fairly well [5]. The stability parameters z/L, where $z$is the measurement height 56 m and L is the Obukhov length, for the unstable, neutral and stable is equal to -0.089, 0.004 and 1.151, respectively.

The statistical characteristics of the turbulent wind inflow, for different atmospheric stability conditions, affecting the Vestas V27 wind turbine (WT) installed at the SWiFT test site, is analyzed in this work. The objective is to provide information about the wind loads applied on the WT in realistic atmospheric conditions. This is crucial because the loads applied to the WT have a significant impact on the lifetime of the wind turbine components and om its the power production [1], [8]. The capability of WRF-LES (Weather Research and Forecasting - Large Eddy Simulation), to reproduce the statistical characteristics of real wind fields, for different stability conditions, is analyzed. The present work is organised as follows. Sections 2 and 3 describe the WRF-LES simulation setup and the statistical analysis performed, respectively. In Section 4, the statistical characteristics obtained for the turbulent wind inflow are shown. Concluding remarks concerning to the entire study are provided in Section 5.

2 WRF-LES Simulation setup

The WRF model [9] is a non-hydrostatic, fully compressible numerical weather prediction (NWP) solver that solves the Euler and energy equations for high Reynolds number flows using the finite difference method. It uses a staggered Arakawa C-grid and a terrain-following hydrostatic-pressure coordinate system in the vertical direction, given by $\eta = (p - p_t)/(p_s - p_t)$, for solving the discretized governing equations. Here, p_t and p_s are the pressure values at the model top and surface, respectively. Temporal discretization is achieved by the third-order Runge-Kutta scheme, whereas the horizontal and vertical advection schemes are based on fifth- and third-order finite difference approximations.

Two nested LES domains in flat terrain were utilized to provide homogeneous inflow conditions to the inner domain, using vertical sounding profiles at the domain inlet. The parent domain uses periodic lateral boundaries in both directions, and information is transferred via one-way nesting, meaning that the coarse LES solution updates turbulent boundary conditions for the finer domain, yet receives no information from its child domain. Coarse domains use horizontal resolutions of $\Delta x = \Delta y = 6$ m, whereas fine domains use $\Delta x = \Delta y = 2$ m. All cases use vertical resolution, Δz, approximately equal to the Δx value of the nested domain in both domains. For each case, the values of Δz were kept constant up to a height of 60 m and stretched up to the domain top, using a hyperbolic tangential vertical grid stretching algorithm. A Rayleigh damping layer with a coefficient of 0.003 s^{-1} was utilized in the upper part of the inversion layer. Zero vertical velocity and zero stress boundary conditions were imposed at the domain top. A single-layer capping inversion was applied at 1000 m above the ground for neutral and unstable cases, while it was placed at the height of 200 m for the stable case, to prevent turbulence from reaching the model top. Aerodynamic roughness length was set to $z_0 = 0.014$ m for neutral, $z_0 = 0.01$ m for unstable and stable cases, with a Coriolis forcing of $f = 0.805 \times 10^{-4}$ s^{-1}.

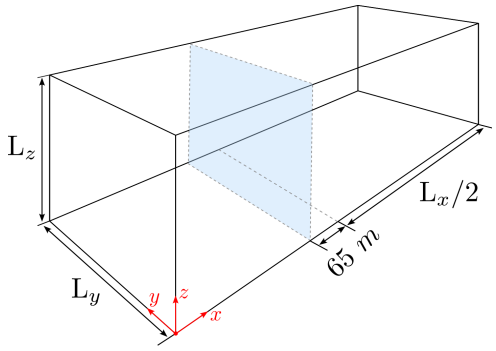


Figure 1: Schematic of the fine-resolution (nested) WRF-LES domain ($L_x = 670$ m, $L_y = 300$ m and $L_z = 64.2$ m). The $YZ-$plane (blue) is the data sampling plane, located at 65 m upstream of the domain center.

A spin-up LES is run for 10 h for the unstable case and 15 h for the neutral and stable cases. Thereafter, the nested domain is introduced, and data sampled along a vertical line centered in the y-direction, $L_y/2$, and in a vertical plane are saved every 1 second (see Figure 1). Both the vertical line and the plane, where the simulated data are collected, are located 65 m upstream of the domain center. For the stable case, a uniform surface cooling boundary condition is applied at the surface at the beginning of hour 15, prescribing the surface temperature as the horizontal average of temperature at the first grid point in the vertical direction. A cooling rate of $\frac{2}{3}$ K h^{-1} was applied, and the simulation was run for 12 h more. Numerical results were then analyzed to check if the model could reach the ensemble-averaged observed value of kinematic heat flux at the surface. Due to the sensitivity to small changes in the geostrophic forcing during stable conditions, the wind direction was no longer aligned with the domain after 20 h (e.g., wind veer). The nested domain was turned on at the beginning of hour 19 h and run for 1 h and 10 [min]. It is also important to note that, after spin-up runs for each case, both domains were run simultaneously for 1 h and 10 min, and the first ten minutes data set of the nested domain simulations was discarded to ensure that turbulence structures are well developed in the inner domain. For details see the study by Kale *et al.* [5]

3 Statistical analysis

The wind velocity components expressed in the WRF-LES coordinates system, identified by subindex "s", are transformed to the streamwise coordinates system as follows [4]:

$$\begin{bmatrix} \tilde{u} \\ \tilde{v} \\ \tilde{w} \end{bmatrix} = \begin{bmatrix} \cos(\gamma_s) & 0 & \sin(\gamma_s) \\ 0 & 1 & 0 \\ -\sin(\gamma_s) & 0 & \cos(\gamma_s) \end{bmatrix} \begin{bmatrix} \cos(\varphi_s) & \sin(\varphi_s) & 0 \\ -\sin(\varphi_s) & \cos(\varphi_s) & 0 \\ 0 & 0 & 1 \end{bmatrix} \begin{bmatrix} \tilde{u}_s \\ \tilde{v}_s \\ \tilde{w}_s \end{bmatrix}, \tag{1}$$

where the velocity components, $\tilde{u}, \tilde{v}$ and $\tilde{w}$, with no subscript indicate that the velocity time series are expressed in the streamwise coordinates system. φ_s $(= (180/\pi)\tan^{-1}_{\pi,-\pi}(V_s, U_s))$ is the mean wind direction during the evaluated period, γ_s $(= (180/\pi)\tan^{-1}_{\frac{\pi}{2},-\frac{\pi}{2}}(W_s, U_h))$ is the mean inclination angle during the analyzed period, U_h is the horizontal wind velocity ($U_h = \sqrt{U_s^2 + V_s^2}$), U_s is the mean value of the longitudinal velocity component $\tilde{u}_s$, V_s is the mean value of the lateral velocity component $\tilde{v}_s$ and W_s is the mean value of the vertical velocity $\tilde{w}_s$. The wind velocity components, $\tilde{u}, \tilde{v}$ and $\tilde{w}$ are decomposed as follows (Reynolds's decomposition):

$$\tilde{u} = U + u, \quad \tilde{V} = V + v \quad \text{and} \quad \tilde{w} = W + w, \tag{2}$$

where U, V and W are, respectively, the mean value of the velocity components $\tilde{u}$, $\tilde{v}$ and $\tilde{w}$, and u, v and w are their fluctuations. The longitudinal integral length scales in the streamwise longitudinal direction L_u^x [m] are calculated from the corresponding integral time scales and the application of the Taylor's Frozen Turbulence Hypothesis,

$$L_u^x = \frac{U}{\overline{u^2}} \int_0^{\tau^*} \gamma_u(\tau) d\tau, \tag{3}$$

where $\tau (= t_2 - t_1)$ [s] is the time lag, $\overline{u^2}$ is the variance of the longitudinal velocity component (where $\overline{(\cdot)}$ indicates time average), τ^* is upper limit of the integration and γ_u [m^2/s^2] is the Autocovariance Function (ACF) of the longitudinal wind velocity fluctuation. Note that, numerical integration (Trapezoidal method) was used to calculate Equation (3). Two approaches were considered in order to define the upper limit of the integration τ^*, to check the sensitivity of integral length scale to different calculation approaches. The first method (first zero-crossing approach) considers the upper limit τ^* equal to the time lag, τ_c, at which the ACF reaches its first zero value [3]. Whereas, the second approach ($1/e$ approach) approximates the integral time constant as the value of τ^*, τ_e limit, τ^*, for which the normalized ACF, $\gamma_u(\tau_e)/\gamma_u(0)$, is equal to $1/e$ [4]. The Power Spectral Density (PSD) was calculated by using Welch's method [6]. The number of discrete Fourier transform (DFT) points was selected to be 2^{18}, with $f_{min} \approx 0.0022$ [Hz] and the Hamming window was used. Homogeneity was assumed in the y-direction at the hub height.. In order to provide information on the two points-two times statistics of the longitudinal components of the wind velocity, the coherence function is used. The coherence $Coh_u(f, r)$, as a function of frequency f and a separation distance r, is defined by [8]

$$Coh_u(f, r) = \frac{|S_{u_1 u_2}(f, r)|^2}{S_{u_1}(f) S_{u_2}(f)}. \tag{4}$$

The coherence function, Coh_u, is evaluated between two points located at the root and the tip of a 13.5 [m] long Vestas wind turbine blade [2], for cases of horizontal and vertical blade orientation.

Some relevant statistical characteristics obtained for the wind field are represented, in the following Section 4, as quantile distributions, Qt $10\%, 25\%, 50\%, 75\%, 90\%$ along height, which provides more information about the changes in the probability distribution function (PDF) of the corresponding parameter with elevation. Note that, these distributions are obtained based on the homogeneity hypothesis in the $y-$direction (considering the time series in $y-$direction at the same height).

4 Results

The quantiles distributions of the mean wind speed, U, are shown in Figure $2(a)$. As expected, the mean of the longitudinal velocity component, U, for the unstable ABL, exhibits a steep gradient near the surface. Although, with increasing height, this steep variation in U decreases, and the variation with height is almost smoothed out due to the strong convective mixing, which occurs under unstable ABL conditions. Whereas, for the neutral and

the stable conditions, this is not the case, and the U increases gradually with height. Due to the transformation from the WRF-LES coordinates system to the streamwise coordinates system, the values of V and W are zero. The quantiles distributions of the variances of the longitudinal and vertical wind velocity components, $\overline{u^2}$ and $\overline{w^2}$, are shown in figures $2(b)$ and $2(c)$, for different stability conditions. Note that, the variance of the lateral velocity component, $\overline{v^2}$, exhibits an analogous behavior to the variance of the longitudinal velocity component, $\overline{u^2}$, therefore, it is not shown. As anticipated, both the variances $\overline{u^2}$ and $\overline{v^2}$, for the unstable ABL, show their maximum value near the surface, then their values slightly decrease with increasing height. Whilst, the lowest value of the variance of the vertical velocity component, $\overline{w^2}$ is obtained at the ground level and it increases with height until it reaches its maximum value, then it decreases with further increase of the height z. For the neutral and stable case, the maximum value of the variances, $\overline{u^2}, \overline{v^2}$ and $\overline{w^2}$ is obtained $z/h_{ABL} < 0.25$ and their values monotonically decrease to 0 with increasing z/h_{ABL}. The distributions of the normalized variances $\overline{u^2}$ and $\overline{w^2}$, over the $YZ-$plane (Figure 1), for different atmospheric stability, are shown in Figure 3. For the neutral and stable cases, the $\overline{u^2}$ and $\overline{w^2}$ show a clear homogeneity in the y direction. Note that, in Figure 3, the normalized $\overline{w^2}/\overline{w^2}_{max}$, for the stable case, exhibits high values at certain location, however, the $\overline{w^2}_{max}$ is nearly equal to zero. Whereas, for the unstable case, the $\overline{u^2}$ and $\overline{w^2}$ show some variations along the y-direction, where the homogeneity assumption is more valid for $z/h_{ABL} > 0.6$. For all the ABL stability cases, the obtained covariance $\overline{uw}$ has a negative value, as expected and its values go to zero with height.

In Figure 4, the quantiles distributions of the longitudinal integral length scale for the longitudinal velocity component, L_x^u, calculated by using the two mentioned approaches (see Section 3), is shown. The L_x^u, evaluated by using the first zero-cross approach, showed a strong variation, within the range $0 < z/h_{ABL} < 0.25$, for the unstable and the neutral ABL cases. Whilst, the L_x^u, evaluated by using the $1/e$ approach, increase monotonically until it reaches $z/h_{ABL} \sim 0.3$ (for the neutral case $h_{ABL} = 1000$ m, then $z \sim 300$ m) and then it starts to gradually decreasing at higher elevations, for neutral ABL case. This result is coherent with the proposal of most of standards (ASCE 7-16, AIJ 2004, Eurocode 2005), which suggest that L_x^u increases monotonically up to a height $z \approx 200 - 300$ m [7]. For the unstable ABL, the L_x^u, obtained by utilizing the $1/e$ approach, is almost constant within the range $0 < z/h_{ABL} < 0.3$, then, it increases until it reaches it maximum at $z/h_{ABL} \sim 0.65$, and it starts to decrease. The L_x^u obtained from both approaches, for the stable case, exhibited the same behaviour, a large increase in its value is obtained at $z/h_{ABL} \sim 0.3$. This shows that the longitudinal integral length scale is sensitive to the method used to determine its value. The distributions of the normalized longitudinal integral length scale for the longitudinal velocity component, L_x^u/L_{xmax}^u, over the $YZ-$plane (Figure 1), for different atmospheric stability, is shown in Figure 5. Similarly as observed in the variances distributions in Figure 3, the L_x^u/L_{xmax}^u, for the neutral and the stable ABL, shows homogeneity along the $y-$direction, however, for the unstable case, L_x^u/L_{xmax}^u exhibits some variations along the $y-$direction.

The normalized PSDs for the three velocity components, $fS_i/\overline{i^2}$, for $i = u, v, w$, in terms of the non-dimensional frequency fz/U, are shown in Figure 6 with inclined line indicating $-2/3$ slope. The $-2/3$ line has been included to ease the identification of the inertial subrange. Further analysis, considering the effect of the LES filtering, the sampling rate and PSD calculation setup, is required but a more process identification of the different regions of the normalized spectra such as the peak region, the inertial subrange or the LES-filtered interval. The normalized vertical spectrum, $fS_w/\overline{w^2}$, showed that most of the energy is contained at high frequencies. The coherence function, $Coh_u(f,r)$, evaluated between two points located at the center of the WT hub and the tip of the WT blade, for horizontal and vertical blade orientations, is shown in Figure 7. Note that, the obtained coherence functions, $Coh_u(f,r)$, are fitted by using a polynomial. For the horizontal blade orientation, the $Coh_u(f,r)$ shows a decay, for all the stability cases, until it reaches $fr/U_{av} \sim 0.15$. For $fr/U_{av} > 0.15$, the $Coh_u(f,r)$ remains more or less constant except for the stable ABL, a high jump is obtained and high values for the $Coh_u(f,r)$ is obtained for high frequencies. Whereas, for the vertical blade orientation, a rapid decay is obtained for $Coh_u(f,r)$, compared to the $Coh_u(f,r)$ for the horizontal blade orientation. The $Coh_u(f,r)$ decreases until it reaches $fr/U_{av} \sim 0.1$, for the three stability conditions, then it remains almost constant for higher frequencies.

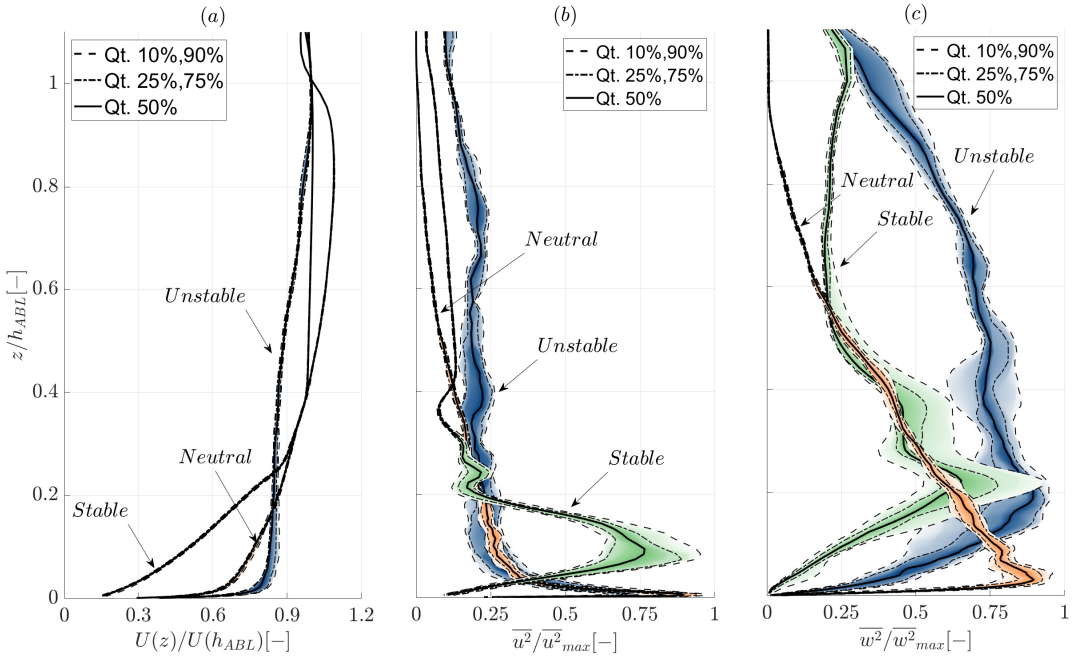


Figure 2: The quantiles distributions, against the non-dimensional height z/h_{ABL}, for: (a) the normalized mean wind speed, $U/U(h_{ABL})$, (b) the normalized longitudinal variance, $\overline{u^2}/\overline{u^2}_{max}$ and (c) the normalized vertical variance, $\overline{w^2}/\overline{w^2}_{max}$, evaluated for unstable ($h_{ABL} = 1000$ m, $U(h_{ABL}) = 8.2$ m / s, $\overline{u^2}_{max} = 1.16$ m^2/s^2, $\overline{w^2}_{max} = 0.53$ m^2/s^2), neutral ($h_{ABL} = 1000$ m, $U(h_{ABL}) = 13$ m / s, $\overline{u^2}_{max} = 1.91$ m^2/s^2, $\overline{w^2}_{max} = 0.33$ m^2/s^2) , and stable ($h_{ABL} = 200$ m, $U(h_{ABL}) = 7.5$ m / s, $\overline{u^2}_{max} = 0.1$ m^2/s^2, $\overline{w^2}_{max} = 0.0006$ m^2/s^2) ABL.

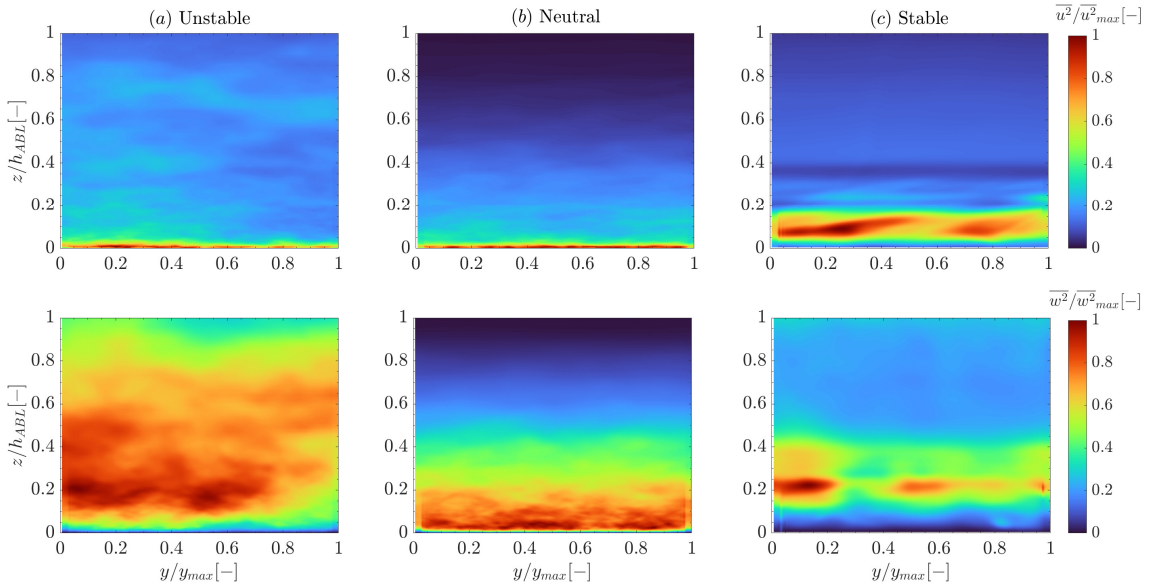


Figure 3: Variances distributions, $\overline{u^2}$ (top row) and $\overline{w^2}$ (bottom row), over the $YZ-$plane (Figure 1), for atmospheric stability conditions: (a) Unstable ($h_{ABL} = 1000$ m, $\overline{u^2}_{max} = 1.16$ m^2/s^2, $\overline{w^2}_{max} = 0.53$ m^2/s^2), (b) Neutral ($h_{ABL} = 1000$ m, $\overline{u^2}_{max} = 1.91$ m^2/s^2, $\overline{w^2}_{max} = 0.33$ m^2/s^2) and (c) Stable ($h_{ABL} = 200$ m, $\overline{u^2}_{max} = 0.1$ m^2/s^2, $\overline{w^2}_{max} = 0.0006$ m^2/s^2) ABL.

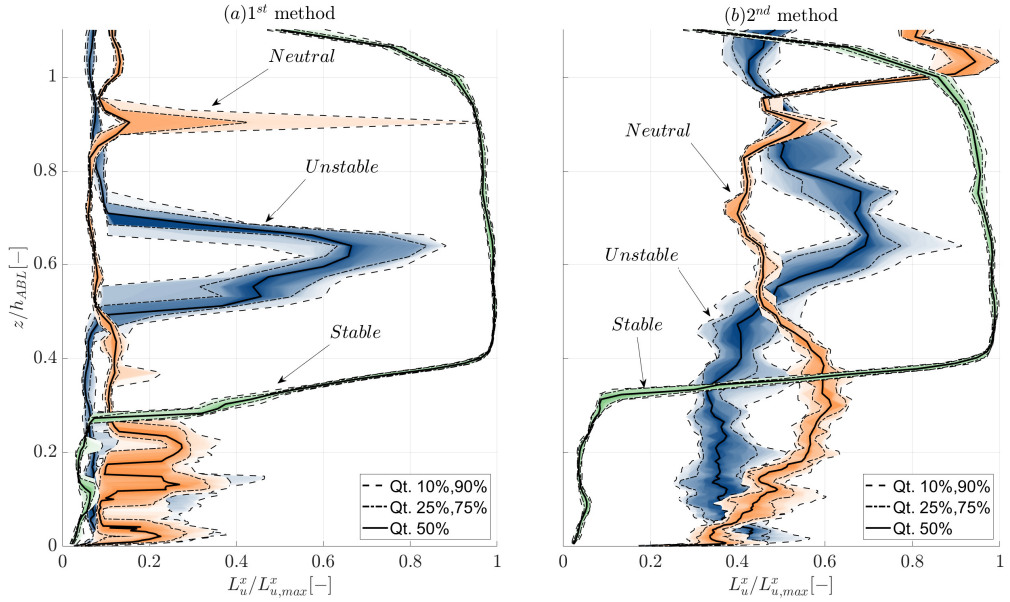


Figure 4: The quantiles distributions of the normalized longitudinal integral length scale for the longitudinal velocity component, $L_x^u/L_{x\,max}^u$, against the non-dimensional height z/h_{ABL}, for unstable ($h_{ABL} = 1000$ m, $L_{x.max}^{u,1st} = 1634$ m, $L_{x,max}^{u,2nd} = 187.4$ m), neutral ($h_{ABL} = 1000$ m, $L_{x.max}^{u,1st} = 1292$ m, $L_{x,max}^{u,2nd} = 167$ m) and stable ($h_{ABL} = 200$ m, , $L_{x.max}^{u,1st} = 4551$ m, $L_{x,max}^{u,2nd} = 3864$ m) ABL. The integral length scale is evaluated by using (a) first zero-crossing approach (1^{st} method) and (b) $1/e$ approach (2^{nd} method) (See Section 3).

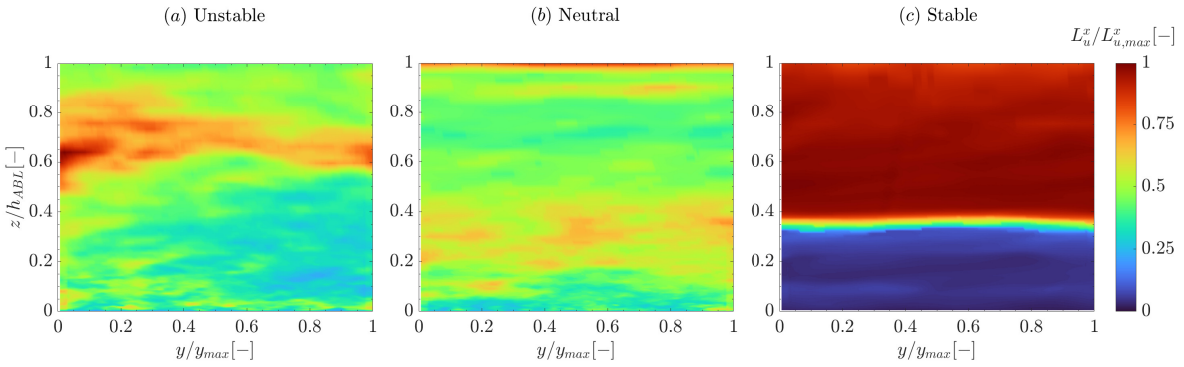


Figure 5: Normalized longitudinal integral length scale distributions for the longitudinal velocity component, $L_x^u/L_{x\,max}^u$, over the $YZ-$plane (Figure 1), for atmospheric stability conditions: (a) Unstable ($h_{ABL} = 1000$ m, $L_{x,max}^{u,2nd} = 187.4$ m), neutral ($h_{ABL} = 1000$ m, $L_{x,max}^{u,2nd} = 167$ m) and stable ($h_{ABL} = 200$ m, $L_{x,max}^{u,2nd} = 3864$ m) ABL. The integral length scale is evaluated by utilizing $1/e$ approach (See Section 3).

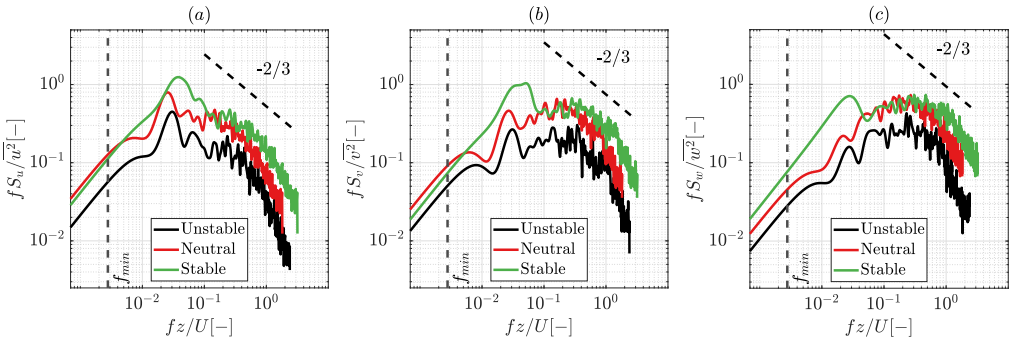


Figure 6: Normalized PSD, $fS_i/\overline{i^2}$, for $i = u,v,w$, in terms of the non-dimensional frequency fz/U, at the hub height ($z = 32.1$ m), for different stability ABL condition: (a) Unstable, (b) Neutral and (c) Stable (where $f_{min} \approx 0.002$ Hz).

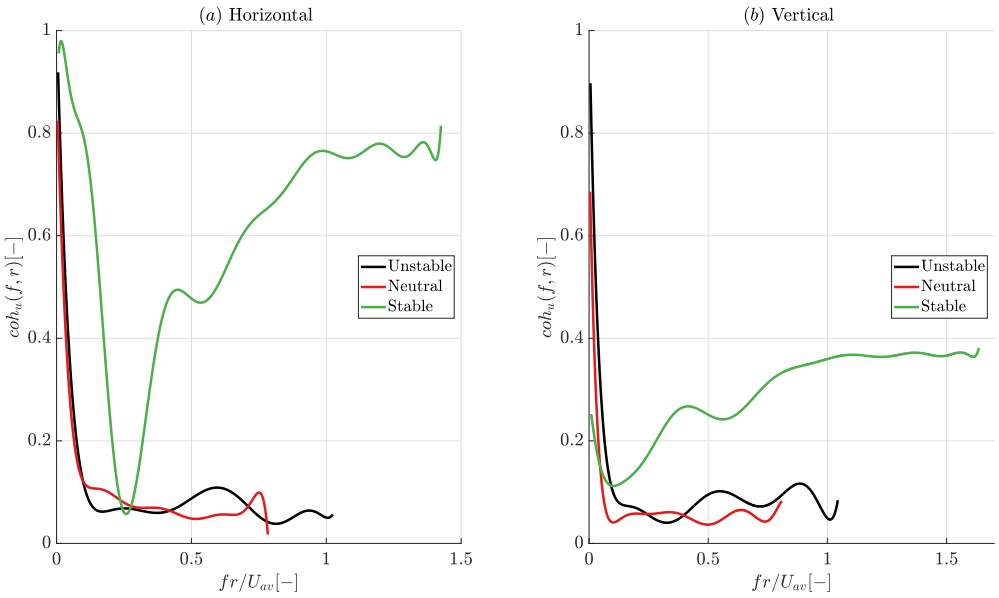


Figure 7: Coherence function, $Coh_u(f,r)$, as a function of the frequency, f, calculated between two points at the root and the tip of the WT blade, with separation distance $r = 13.5$ m, for blade orientations: (a) Horizontal and (b) Vertical. Note that U_{av} is the average mean speed of the mean wind speed at the center of the WT hub and the tip of the WT blade.

5 Conclusion

This work presents a preliminary study of the statistical characteristics of the turbulent wind inflow for the wind turbine at SWiFT test site. The turbulent wind field is provided, at a plane located 65 m upstream of the domain center, by WRF-LES simulation. The simulation was obtained for the turbulent wind field for the three ABL stability conditions: unstable, neutral and stable. The obtained mean speed profiles, for the different stability conditions, match the typical wind speed profiles seen over a flat terrain. The longitudinal integral length scale is sensitive to the approach used to determine its value. The longitudinal integral length scale, evaluated by using $1/e$ approach, for the neutral case, has the same profile as described in the standards. Homogeneity along the

$y-$direction is observed for neutral and stable ABL. Whereas, for the unstable case some variations along the y-direction were observed. The stability condition of the ABL has an influence on the spectrum obtained for the wind velocity components. A further analysis of the spectra is required to better identify the inertial subrange and the location of the peak of the normalized spectra in terms of the stability condition. The coherence function between the points at the center of the WT hub and the WT blade is affected by the orientation of the WT blade as a faster decay with frequency in the coherence function was observed for the vertical blade orientation than the horizontal blade orientation. A further analysis of the influence of, both, the ABL stability condition and the approach used to calculate the PSD, on the coherence function is required.

Acknowledgements

This research has been undertaken as a part of the zEPHYR project. This project has received funding from the European Union's Horizon 2020 research and innovation programme under Grant Agreement No EC grant 860101. The high-performance computing resources and services used in this study were provided by the von Karman Institute for Fluid Dynamics in Belgium.

References

[1] N. Dimitrov, A. Natarajan, and J. Mann. Effects of normal and extreme turbulence spectral parameters on wind turbine loads. *Renewable Energy*, 101:1180–1193, 2017.

[2] P. Doubrawa, P. Moriarty, M. Debnath, E. Branlard, T. Herges, B. Naughton, D. Maniaci, and C. Kelley. The SWiFT Benchmarks, Part of IEA Wind Task 31 Phase 3, Kick-off Webinar. Technical report, 2018.

[3] M. Emes, M. Arjomandi, R. Kelso, and F. Ghanadi. Integral length scales in a low-roughness atmospheric boundary layer. *Australasian Wind Engineering Society*, 2016.

[4] J. C. Kaimal and J. J. Finnigan. *Atmospheric boundary layer flows: their structure and measurement*. 2019.

[5] B. Kale, S. Buckingham, J. van Beeck, and A. Cuerva-Tejero. Implementation of a generalized actuator disk model into WRF v4.3: A validation study for a real-scale wind turbine. *Renewable Energy*, 2022.

[6] S. L. Marple Jr and W. M. Carey. Digital spectral analysis with applications, 2019.

[7] T. N. Nandi and D. Yeo. Estimation of integral length scales across the neutral atmospheric boundary layer depth: a large eddy simulation study. *Journal of Wind Engineering and Industrial Aerodynamics*, 218:104715, 2021.

[8] D. Sharpe and D. Sharpe. *Wind energy handbook*. John Wiley & Sons, Ltd, 2001.

[9] W. C. Skamarock and J. B. Klemp. A time-split nonhydrostatic atmospheric model for weather research and forecasting applications. *Journal of computational physics*, 227(7):3465–3485, 2008.

18th EAWE PhD Seminar on Wind Energy
2 – 4 November 2022
Bruges, Belgium

Uncertainties of long-term wind speed predictions for site assessment tasks

Johanna Borowski[a], Sandra Schwegmann[a], Martin Dörenkämper[a]

[a] Fraunhofer IWES, Fraunhofer Institute for Wind Energy Systems IWES

E-mail: johanna.borowski@iwes.fraunhofer.de

Keywords: wind energy site assessment, interannual variability, wind climate, uncertainties, Measure-Correlate-Predict (MCP)

Precise knowledge of the wind climate at a site is crucial for estimating the wind potential not only in the planning phase of wind turbines, but also during their lifetime of around 25 years. For this purpose, in the planning phase of wind energy projects, measurement campaigns are typically carried out covering a full yearly cycle. However, due to interannual to decadal scales, the data of one year are not sufficient to capture the full wind climatology of a site. Therefore, on-site measurements are extended with a by systematic errors corrected numerical wind time series, which usually covers at least 10 years, but often up to 30 years. Reanalysis data like ERA5 [1] and MERRA2 [2] are frequently used for this purpose due to their high resolution, their global coverage and their public availability. The link between the short-term and long-term data is typically established by statistical methods based on the overlapping time period of both data sets, commonly known as Measure-Correlate-Predict (MCP) methods [3]. Using this method, predictions of the wind climate are done based on the long-term reference data and the relationship between them and the short-term data found for their overlap period. A schematic illustration of the MCP approach is given in Figure 1.

However, as the wind climate underlies an interannual variability, but the relationship is only based on one specific year and furthermore, the reanalysis data cover wider areas than the measurements do, the predictions suffer from uncertainties.

In this study, the uncertainties connected to the availability of only one specific year for the short-term measurement are analysed. For this purpose, long-term wind measurements of met masts at three different sites with terrain of various complexity (Cabauw (NL) [4], Lindenberg (GER) [5], Karlsruhe (GER) [6]) are considered. All of these sites provide at least nine overlapping years of hub-height wind speed and direction measurements. In order to analyse the influence of interannual variability, varying individual years of the measurements are used to predict the wind conditions using MCP and different reanalysis data sets as long-term reference. The spread between these individual wind speed predictions serves as uncertainty information (Figure 2).

Results of the study reveal that the uncertainty varies depending on the site, the reanalysis data set used, and the year chosen from the short-term measurement for the MCP approach. On average, an uncertainty of about 2.5 % to 4.5 % was found using ERA5 and NOAA20CR [7], while the uncertainty using MERRA2 reanalysis as long-term reference increases to around 6 %. This is likely related to the fact that the wind speed output of MERRA2 is provided at 50 m height, while it is available at 100 m height for the other two reanalysis data sets as well as the measurements. However, a larger impact can be seen on sites with more complex terrain. While the uncertainties at the site Cabauw, which is located in flat terrain, hardly differ, the uncertainties at the more complex, in particular forested, sites Lindenberg and Karlsruhe increase by about 0.5 - 1 % and about 1 - 2 %, respectively. This demonstrates the relevance of high-quality reference data close to the measurement height for the MCP approach, in particular in more complex areas.

In a further step, we show whether the uncertainties can be significantly reduced by extending the on-site measurements from one to two years. And we present the impact of applying more complex machine learning (ML) approaches instead of the de facto industry-standard of a linear regression in the MCP process.

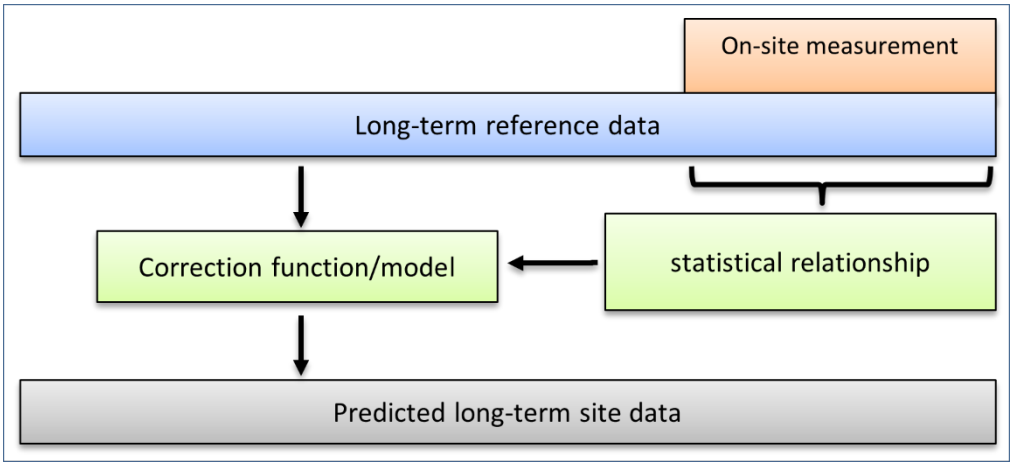


Figure 1: Schematic illustration of the Measure-Correlate-Predict (MCP) approach.

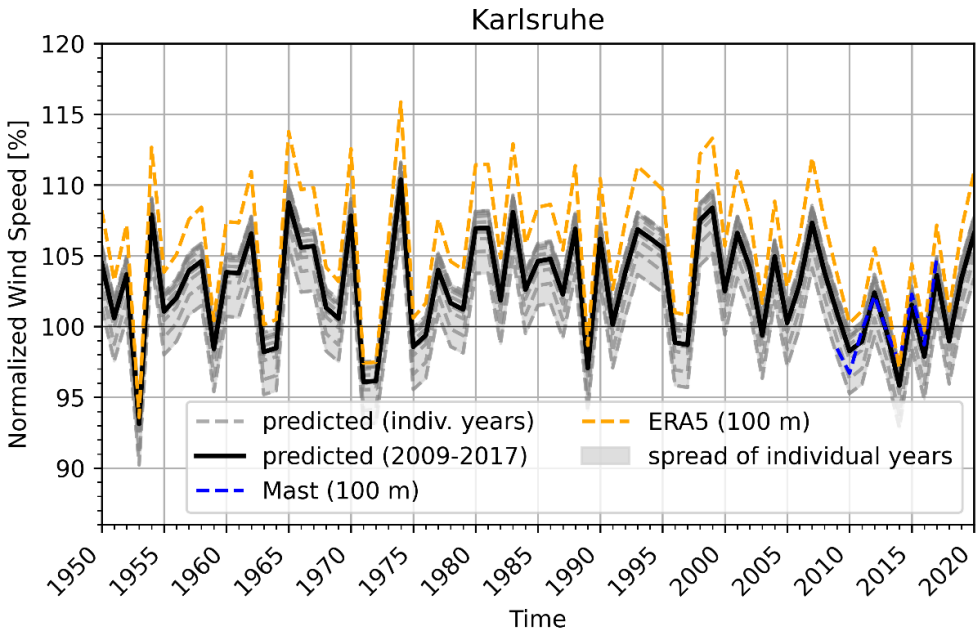


Figure 2: Normalized wind speed of the reanalysis ERA5 (orange) and measured wind speed in Karlsruhe at a height of 98 m (blue), predicted wind speed with MCP for individual years (grey) and for the entire measurement years (black). In shaded grey the spread of the predicted wind speed is shown.

Acknowledgements

The study is carried out in the framework of the KliWiSt project "The influence of climate change on wind energy site assessment" (grant no. 03EE3041A) funded by the Federal Ministry of Economic Affairs and Climate Action. We acknowledge the Royal Netherlands Meteorological Institute, the Deutscher Wetterdienst (German Weather Service) and the Karlsruhe Institute of Technology to grant access to the met mast data used in the analysis. We also thank the ECMWF, NASA and NOAA for providing the ERA5, MERRA2 and NOAA20CR reanalyses, respectively.

References

[1] H. Hersbach *et al.*, „The ERA5 global reanalysis", *Q.J.R. Meteorol. Soc.*, Bd. 146, Nr. 730, S. 1999–2049, Juli 2020, doi: 10.1002/qj.3803.
[2] R. Gelaro *et al.*, „The Modern-Era Retrospective Analysis for Research and Applications, Version 2 (MERRA-2)", *JOURNAL OF CLIMATE*, Bd. 30, S. 36, 2017.
[3] J. A. Carta, S. Velázquez, und P. Cabrera, „A review of measure-correlate-predict (MCP) methods used to estimate long-term wind characteristics at a target site", *Renewable and Sustainable Energy Reviews*, Bd. 27, S. 362–400, Nov. 2013, doi: 10.1016/j.rser.2013.07.004.
[4] F. C. Bosveld, „The Cabauw In-situ Observational Program 2000 – Present: Instruments, Calibrations and Set-up", Ministry of Infrastructure and Water Management, Royal Netherlands Meteorological Institute (KNMI), De Bilt: KNMI, Technical report, 2020.
[5] J. Neisser, W. Adam, F. Beyrich, U. Leiterer, und H. Steinhagen, „Atmospheric boundary layer monitoring at the Meteorological Observatory Lindenberg as a part of the ‚Lindenberg Column': Facilities and selected results", *metz*, Bd. 11, Nr. 4, S. 241–253, Okt. 2002, doi: 10.1127/0941-2948/2002/0011-0241.
[6] M. Kohler, J. Metzger, und N. Kalthoff, „Trends in temperature and wind speed from 40 years of observations at a 200-m high meteorological tower in Southwest Germany", *Int. J. Climatol*, Bd. 38, Nr. 1, S. 23–34, Jan. 2018, doi: 10.1002/joc.5157.
[7] G. P. Compo *et al.*, „The Twentieth Century Reanalysis Project: The Twentieth Century Reanalysis Project", *Q.J.R. Meteorol. Soc.*, Bd. 137, Nr. 654, S. 1–28, Jan. 2011, doi: 10.1002/qj.776.

Turbine technology and control

18th EAWE PhD Seminar on Wind Energy
2-4 November 2022
Bruges, Belgium

A Force Partitioned Approach for Numerical Analysis of Vortex-Induced Vibrations on Wind Turbine Towers

S. VimalKumar[a,b], **A. Viré**[a], **D. de Tavernier**[a], **D. von Terzi**[a], and **M. Belloli**[b]

[a]TU Delft
[b]Politecnico Di Milano

E-mail: s.vimalkumar@tudelft.nl

Keywords: Wind Turbine Tower, VIV, and Vortex Shedding

1 Introduction

To meet the greater demand for maximum energy production per wind turbine, large-scale designs of wind turbines are being developed, which are characterised by taller turbine towers. The wind turbine towers, particularly when they are taller, exhibit unsteady physical phenomena that should be considered during the design phase. The present research focuses on analysing the aerodynamic phenomenon called vortex-induced vibrations (VIV).

It is of great importance to analyse the contribution of different force-generating mechanisms leading to VIV. The work by Quartapelle and Napolitano [1] proved to be a fundamental base for the force partitioning method. A generic formula was derived for the force and moment of a rigid body immersed in incompressible flow. It was achieved by solving the Navier-Stokes equations where the momentum equation was projected on a gradient of harmonic function, which satisfies appropriate boundary conditions. Chang et al. [2] further showed the force contribution due to potential flow, vorticity within the flow, and surface vorticity on the finite body, subsequently providing further understanding of different force components.

The influence of different forces on the oscillation of a rigid body provides more insight into the nature of the force mechanism. Morse and Williamson [3] showed that the energy extracted in forced oscillations is closely related to amplitude response in free oscillations. This is found to be useful in complicated nonlinear responses and has been shown for oscillating cylinders by Williamson and Govardhan [4]. This was combined along with the force partitioned approach to analyse the force mechanisms in the sustenance of VIV by Menon and Mittal [5]. The vortex shedding behind the cylinder contributes only during the initiation of the VIV and the vorticity in the shear layer leads to the sustenance of the VIV. Hence, the vortex-induced force was found to be the most crucial for oscillations during VIV, compared to the vortices in the wake behind the cylinder.

Due to the large structure of wind turbines and the wind speed, the flow around wind turbines is characterised by high Reynolds number ($Re > 3.5 \cdot 10^6$). The VIV of circular cylinders have been extensively studied in the past. However, study of VIV of cylinders under the influence of high Reynolds number flows and large mass ratio are still limited. Hence, the objective of the current work is to determine the nature of the force mechanism during the super-critical Reynolds number regime. Additionally, it is intended to derive a correlation between the oscillations of the wind turbine tower and different force mechanisms using the above-mentioned approaches.

2 Methodology

The numerical simulations are initially carried out for a 2D cylinder section in the open-source software OpenFOAM-v2012 [6]. The flowchart of the implementation is shown in Figure 1.

The total force acting on the body, B, is obtained by projecting Navier-Stokes equation onto the gradient of harmonic function, $\phi^{(i)}$. The harmonic function satisfies the following equation at any time instance t:

$$\nabla^2\phi^{(i)} = 0, \qquad \text{with} \qquad \vec{n}.\vec{\nabla}\phi^{(i)} = \begin{cases} n_i, & \text{on } B(t) \\ 0, & \text{on } \Sigma \end{cases} \tag{1}$$

where Σ represents the outer boundary of the computational domain and $i = 1,2,3$ depending on the direction of the force. Equation 1 corresponds to potential associated with the flow around the body for a shape and position for time t. The harmonic function is solved for every time step in the modified pimple solver in OpenFOAM, which will be explained later in the section. The total force acting on the body is then formulated as:

$$\begin{aligned} F = & \underbrace{-\rho \int_B \vec{n} \cdot \frac{d\vec{U}}{dt}\phi^{(i)} dS - \rho \int_B \frac{1}{2} U^2 \vec{n} \cdot \nabla\phi^{(i)} dS}_{\text{kinematic force}} \\ & \underbrace{+\rho \int_V \nabla \cdot (\vec{\omega} \times \vec{u})\phi^{(i)} dV + \rho \int_V \nabla^2 \left(\frac{1}{2}u_v^2 + \vec{u_\phi} \cdot \vec{u_v}\right)\phi^{(i)} dV}_{\text{vortex-induced force}} \\ & \underbrace{+\mu \int_B (\vec{\omega} \times \vec{n}) \cdot \vec{\nabla}(\phi - \hat{e}_i) dS}_{\text{viscous force}} \\ & \underbrace{+\rho \int_V \nabla^2 \left(\frac{1}{2}u_\phi^2\right)\phi^{(i)} dV}_{\text{potential flow force}} \\ & \underbrace{-\rho \int_\Sigma \frac{d\vec{U}}{dt} \cdot \vec{n}\phi^{(i)} dS + \mu \int_\Sigma (\vec{\omega} \times \vec{n}) \cdot \nabla\phi^{(i)} dS}_{\text{force due to flow and vortices at outer boundary}} \end{aligned} \tag{2}$$

The coefficients of various force components are calculated by $C_i = F_i / \frac{1}{2}\rho U_\infty^2 D$. For a multi-dimensional force analysis, the variable i can be fixed for the directions of interest to calculate the force magnitude and the components in each direction.

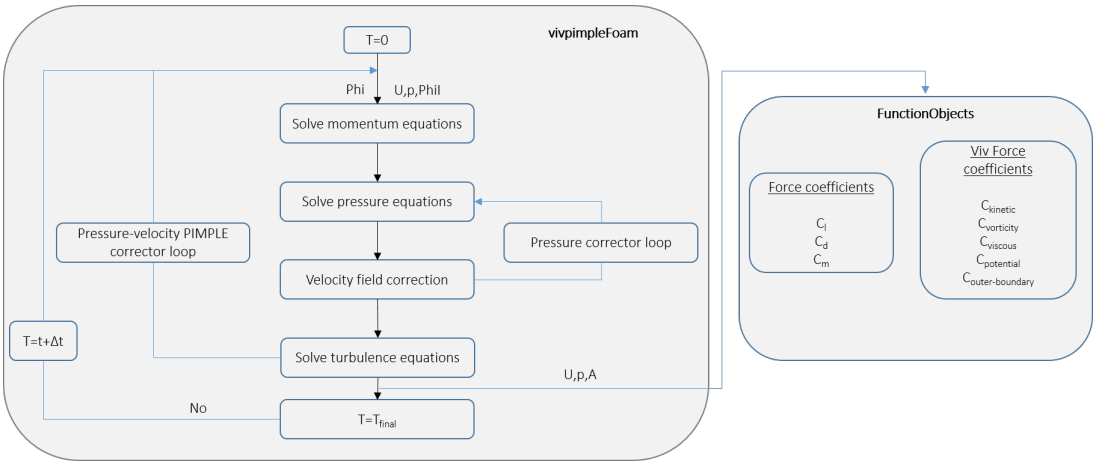


Figure 1: Flowchart of implementation in OpenFOAM.

The above equations are implemented in OpenFOAM in three different parts. The existing pimpleFoam is modified to calculate the harmonic function $\phi^{(i)}$. The constraint mentioned in Equation 1 has been implemented as a modification to the fixedGradient boundary condition. Finally, the force coefficients, shown in Equation 2, are calculated as a custom function object, which stores all the information for every time step calculated.

3 Results

Figure 2 shows the result of the lift force coefficient partitioned to various force components as mentioned above. The simulation was initially carried out for a cylinder of $D = 1\,m$ at Reynolds number, $Re = 1000$. It is noticeable that the major force driving the oscillation is the force due to vorticity. The kinematic force is sinusoidally opposite to the total force, which reinforces the fact that the acceleration of the cylinder reduces towards the end of its oscillation. The contribution of force due to added mass, viscous force, and vortex-induced force predominates the total force contribution. This conclusion aligns with the conclusion drawn from [7] and [5].

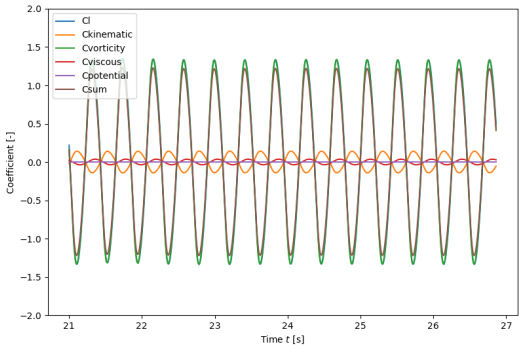


Figure 2: Force partitioned coefficients of lift on a cylinder of $D = 1\,m$ for a Reynolds number, $Re = 1000$.

The model is currently implemented in the OpenFOAM and preliminary analysis has been carried out for subcritical Reynolds number regime. It is planned to carry out extensive analysis of VIV at supercritical Reynolds numbers and perform fluid-structural coupled simulations.

4 Acknowledgement

The authors would like to thank the support of Simon van Hulle for his contribution to the development of the numerical model.

References

[1] L. Quartapelle and M. Napolitano. Force and moment in incompressible flows. *AIAA Journal*, 21(6):911–913, 1983.

[2] C.-C. Chang. Potential flow and forces for incompressible viscous flow. *Proceedings of the Royal Society of London. Series A: Mathematical and Physical Sciences*, 437(1901):517–525, 1992.

[3] T. L. Morse and C. H. K. Williamson. Prediction of vortex-induced vibration response by employing controlled motion. *Journal of Fluid Mechanics*, 634:5–39, 2009.

[4] C. Williamson and R. Govardhan. Vortex-induced vibrations. *Annual Review of Fluid Mechanics*, 36(1):413–455, 2004.

[5] K. Menon and R. Mittal. On the initiation and sustenance of flow-induced vibration of cylinders: insights from force partitioning. *Journal of Fluid Mechanics*, 907:A37, 2021.

[6] Openfoam-v2012. https://www.openfoam.com/news/main-news/openfoam-v20-12. Accessed: 2022-08-15.

[7] C. Zhang, T. L. Hedrick, and R. Mittal. Centripetal acceleration reaction: An effective and robust mechanism for flapping flight in insects. *PLoS ONE 10(8): e0132093*, 2015.

18th EAWE PhD Seminar on Wind Energy
2-4 November 2022
Bruges, Belgium

A Self-Similarity scaling for Integral Boundary Layer analysis of Vortex Generators

Abhratej Sahoo[a,b]

[a]TNO Energy Transition, Wind Energy
[b]TU Delft, Aerospace Engineering

E-mail: abhratej.sahoo@tno.nl

Keywords: vortex generators, boundary layer, integral boundary layer methods, mixing layer, self-similarity, XFOIL, RFOIL

Abstract

As the demand for renewable energy increases, wind turbine rotors will become larger with slender blades. Vortex Generators (VGs) are one of the most common methods of passive flow control to avoid flow separation and loading on the root section of slender blades due to their simplicity, inexpensiveness, and the ability to retrofit them to blades. Aerodynamic load calculations for VGs involve long experimental campaigns or resource-intensive CFD calculations. Most time intensive aeroelastic optimisation and design tools prefer to use lower fidelity methods made accurate with empirical models and corrections for aerodynamic load calculations of clean airfoils. One such class of tools are viscous-inviscid interaction solvers that use Integral Boundary Layer (IBL) methods for viscous calculations in the boundary layer coupled with an inviscid solver for the rest of the domain. This research applies an IBL framework to vortex generators modelling the effect of VGs on integrated boundary layer quantities. Further, the paper also explores a self-similarity scaling inspired from free-shear plane mixing layer theory for the boundary layer profile downstream of VGs.

1 Introduction

Studies on the projected capacity of future wind turbine rotors indicate an increasing trend for bigger rotors with low induction and slender blades [11, 20]. Thick airfoils (with thicknesses up to 60% of the chord) [20] and thick trailing edges [10] balance the structural loads on inboard sections. However, they have a higher sensitivity to flow separation and leading edge roughness, directly affecting the turbine's annual energy production and increasing levelised cost of energy [16]. Passive flow control technologies are still preferred over active control and redesign due to their simplicity and ability to retrofit standard blades with static add-ons. Of these options, Vortex Generators (VGs) are one of the oldest and most studied ways to delay flow separation [22, 14]. Optimising passive VG arrays involves extensive parametric studies through experiments or computations. Typically, flow around VGs is computed using CFD analysis with a body-fitted mesh, or with partly modelled and partly resolved approaches like the BAY model [4] or its variations [12] (an overview of these methods is presented in [1]). These methods still require a large computation time, despite recent advances in computational capacity. The motivation for this research thus comes from the need to perform fast and accurate analysis of airfoils equipped with VGs.

For clean airfoils, lower fidelity airfoil analysis tools like RFOIL [19] (based on XFOIL [8]) provide a fast and reliable way of estimating lift, drag, and moments. RFOIL couples an inviscid panel method and a viscous solver based on Integral Boundary Layer (IBL) methods [7] with appropriate viscous-inviscid interaction schemes. This research aims to extend IBL methods to VGs for fast and accurate analysis.

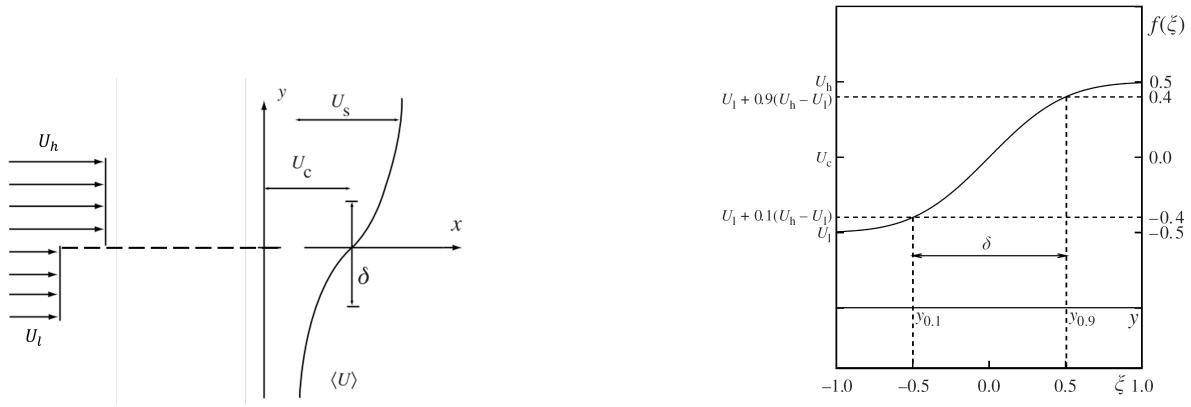
IBL methods use self-similar velocity profiles for laminar and turbulent boundary layers to provide closures to the integral boundary layer equations [17]. The inherent three-dimensionality of the vortices shed by VGs [24] makes it difficult to estimate a two-dimensional profile that can be fitted into an IBL framework. Velte [25] and Fernandez-Gamiz et al. [9] show helical symmetry and self-similarity of the vortex structure up to 13 VG heights downstream. Thus, for a counter-rotating VG array with common upflow or downflow, self-similarity can be imagined in those spanwise planes where the flow has negligible spanwise components. This study proposes a scaling framework inspired by the self-similar two-dimensional plane mixing layer [5, 3] to show self-similarity in

characteristic spanwise planes for boundary layers developing downstream of triangular and rectangular vane type VG arrays. Additionally, it is seen that the scaled profiles also match the analytical solution for a plane mixing layer in the region influenced by the vortex in the boundary layer. This self-similarity scaling can be used to propose a new velocity profile for VG boundary layers.

2 Proposed Self Similar Scaling

2.1 Plane Mixing Layer

A plane mixing layer is a turbulent flow that forms between two uniform parallel streams of flow with different velocities. An illustration of a plane mixing layer allowed to grow in free shear flows is presented in Figure 1. The flow develops in the streamwise and cross-stream directions, and the flow statistics are considered to be independent of the spanwise coordinate.



(a) (b)

Figure 1: (a) Unscaled and (b) scaled velocity profiles of a plane mixing layer. (a) shows convection and slip velocities U_c and U_l while (b) shows the scaling quantities $y_{0.1}$, $y_{0.9}$, and δ. The scaled velocity profile $f(\xi)$ is represented by the error function of the scaled wall normal coordinate ξ. *(Reproduced from Pope, 2000 [18])*

2.2 Modified Plane Mixing Layer Scaling

A plane mixing layer has two imposed velocities - the upper velocity U_h and the lower velocity U_l with $U_h > U_l \geq 0$. The case of $U_l = 0$ corresponds to a plane jet flow. The flow is scaled using the convection velocity U_c, the velocity difference U_s (Equation (2)), the width of the mixing layer $\delta(x)$, and the midpoint of the mixing layer $\bar{y}(x)$. Every normal location $y_\alpha(x)$ is defined as the location where mean velocity $\langle U(x, y_\alpha(x), 0) \rangle$ (Equation (3)) is attained. The width of the mixing layer $\delta(x)$ (Equation (4)) is the distance between $y_{0.9}(x)$ and $y_{0.1}(x)$. Subsequently, the midpoint $\bar{y}(x)$ (Equation (5)) is the midpoint between $y_{0.9}(x)$ and $y_{0.1}(x)$. Each of these reference quantities and their meaning in terms of actual flow velocities is presented in Figure 1b.

To apply the plane mixing layer to the flow downstream of a vortex generator, the VG is imagined as a flow stagnation drag producing element that slows down the flow in front of it while speeding up the rest of the flow. Thus, the flow up to the VG height in the boundary layer is considered the low velocity stream, while the flow in the rest of the boundary layer is considered the high velocity stream. The constant characteristic velocities U_h and U_l from the free shear plane mixing layer theory are represented as integral quantities (Equation (1)) analogous to the ratio of integral momentum flux to integral mass flux (Note: δ in Equation (1) is the edge of the boundary layer). Ravishankara et al. [13] recommend computing the characteristic velocities downstream of the VG after the vortex-induced mixing process has fully developed. In this paper, they are computed at a streamwise location $\frac{\Delta x}{h} = \frac{x - x_{VG}}{h_{VG}} = 5$ for rectangular VGs and $\frac{\Delta x}{h} = 3$ for triangular VGs.

$$U_l = \frac{\int_0^{h_{VG}} (\rho u)\, u dy}{\int_0^{h_{VG}} (\rho u)\, dy}, \quad U_h = \frac{\int_{h_{VG}}^{\delta} (\rho u)\, u dy}{\int_{h_{VG}}^{\delta} (\rho u)\, dy} \tag{1}$$

$$U_c \equiv \frac{1}{2}(U_h + U_l), \quad U_s \equiv U_h - U_l \tag{2}$$

$$\langle U\left(x, y_\alpha\left(x\right), 0\right)\rangle = U_l + \alpha\left(U_\mathrm{h} - U_l\right), \quad 0 < \alpha < 1 \tag{3}$$

$$\delta\left(x\right) = y_{0.9}\left(x\right) - y_{0.1}\left(x\right) \tag{4}$$

$$\bar{y}\left(x\right) = \frac{1}{2}\left[y_{0.9}\left(x\right) + y_{0.1}\left(x\right)\right] \tag{5}$$

These quantities are then used to define the scaled cross-stream coordinate ξ (Equation (6)) and the scaled velocity $f(\xi)$ (Equation (7)). Since the separation line between the velocity streams lies at the tip of the VG ($y = h_{VG}$) and not $y = 0$, this is reflected in Equation (6) by subtracting the h_{VG} term in the numerator. These are then used to define the boundary layer equation for the self-similar mixing layer (Equation (8)) with $g(\xi)$ as the scaled shear stress.

$$\xi = \frac{y - \bar{y}\left(x\right) - h_{VG}}{\delta\left(x\right)} \tag{6}$$

$$f\left(\xi\right) = \frac{\left(\langle U\rangle - U_\mathrm{c}\right)}{U_\mathrm{s}} \tag{7}$$

$$\left(\frac{U_\mathrm{c}}{U_\mathrm{s}}\frac{\mathrm{d}\delta}{\mathrm{dx}}\right)\left(\xi + \frac{U_\mathrm{s}}{U_\mathrm{c}}\int_0^\xi f\left(\hat{\xi}\right)\mathrm{d}\hat{\xi}\right) f' = g', \quad \text{where} \quad g(\xi) \equiv \langle uv\rangle / {U_s}^2 \tag{8}$$

The analytical solution (Equation (9)) for the self-similar scaled velocity profile $f(\xi)$ is an error function of the scaled flow normal coordinate ξ [18]. σ is a scaled turbulent viscosity and is expressed in terms of the turbulent viscosity ν_T and the scaled spreading rate S.

$$f(\xi) = \frac{1}{2}\mathrm{erf}\left(\frac{\xi}{\sigma\sqrt{2}}\right), \quad \sigma = \sqrt{\frac{\nu_T}{S}} \approx 0.3902, \quad S = \frac{U_\mathrm{c}}{U_\mathrm{s}}\frac{\mathrm{d}\delta}{\mathrm{dx}} \tag{9}$$

3 Methodology

To verify the applicability of this modified mixing layer scaling to the flow developed downstream of a VG, stereoscopic PIV measurements of a flat plate equipped with counter-rotating VG array with common downflow, acquired during the AVATAR project [2], were used. Two kinds of VGs were used —a rectangular vane type, and a triangular vane type. Table 1 presents a summary of the test cases and Table 2 presents the VG array geometry. Of these, cases 1 and 3 with zero pressure gradient and zero yaw were chosen for this paper. Details of the wind tunnel conditions, data acquisition process and quality can be found in the publication by Baldacchino et al. [2].

Table 1: Summary of test cases. *(Table taken from Baldacchino et al., 2015 [2])*

Case	Pressure Gradient	Yaw	Shape	Planes ($\Delta x/h$)
1	ZPG	0°	Rect	$5-10, 15, 25, 50$
2	ZPG	10°	Rect	$5-10, 15, 25, 50$
3	ZPG	0°	Tri	$2-10, 15, 25, 50$
4	APG 1	0°	Rect	$5-10, 15, 25, 50$
5	APG 1	0°	Tri	$2-10, 15, 25, 50$
4	APG 2	0°	Tri	$2-10, 15, 25, 50$

As a first step of analysis, the boundary layer profiles from the flat plate measurements are presented in an integral boundary layer framework in Section 4.1 to verify the effect of VGs on integral boundary layer quantities according to existing literature. Then, in Section 4.2 the mixing layer scaling presented in Section 2.2 is applied to the boundary layer profiles to investigate the accuracy with which a plane mixing layer framework can approximate the flow downstream of a VG.

Table 2: VG array geometry. *(Table taken from Baldacchino et al., 2015 [2])*

VG property	Symbol	Value	Size as a multiple of VG height h
Device height	h	$5mm$	1
Trailing edge separation	d	$12.5mm$	2.5
Vane length	l	$12.5mm$	2.5
Pair separation	D	$30.0mm$	6
Inclination angle	β	18°	—
VG trailing edge location w.r.t to plate leading edge	x_{VG}	$985mm$	197

4 Results and Discussion

4.1 Integral Boundary Layer Analysis

For a VG array applied to a flat plate, the boundary layer is expected to become more energetic due to the added momentum of the shed vortices from the VGs which move energetic fluid towards the boundary layer [22, 6, 15]. The momentum thickness θ and the kinetic energy thickness δ_k increase while the displacement thickness δ^* decreases. In addition, the shed vortex diffuses as it grows in size in streamwise direction, with a marked decay in peak vorticity. This causes the vortex to flatten out in an elliptical shape with a helical path line due to wall-vortex interactions [26].

Figure 2 presents the spanwise variation of the shape factors H and H_k for a zero pressure gradient, zero yaw, triangular vane VG case. A clear redistribution of momentum and energy between the vanes is seen in these spanwise plots. Section 4.1 presents the comparison of both the shape factors with a clean boundary layer without VGs 50 VG heights downstream. The shape factor shows a drop while the kinetic energy shape factor shows a peak compared to the rest of the flow span. The vortex spread is also visible as the peak gets wider and wider as the vortex moves from 10 VG heights downstream to 25 VG heights downstream aft of the VG pair. The vortex peak location stays at the $z = 0$ spanwise location i.e. between the two VG vanes in the pair. The vortex strength also reduces slightly as it moves downstream, as demonstrated by the reduction in the peak value of H_k as one moves further downstream from 15 to 50 VG heights. These observations are consistent with the descriptions of the shed vortex structure, strength, and path from literature, as well as the expected effects of the vortices on integral boundary layer quantities.

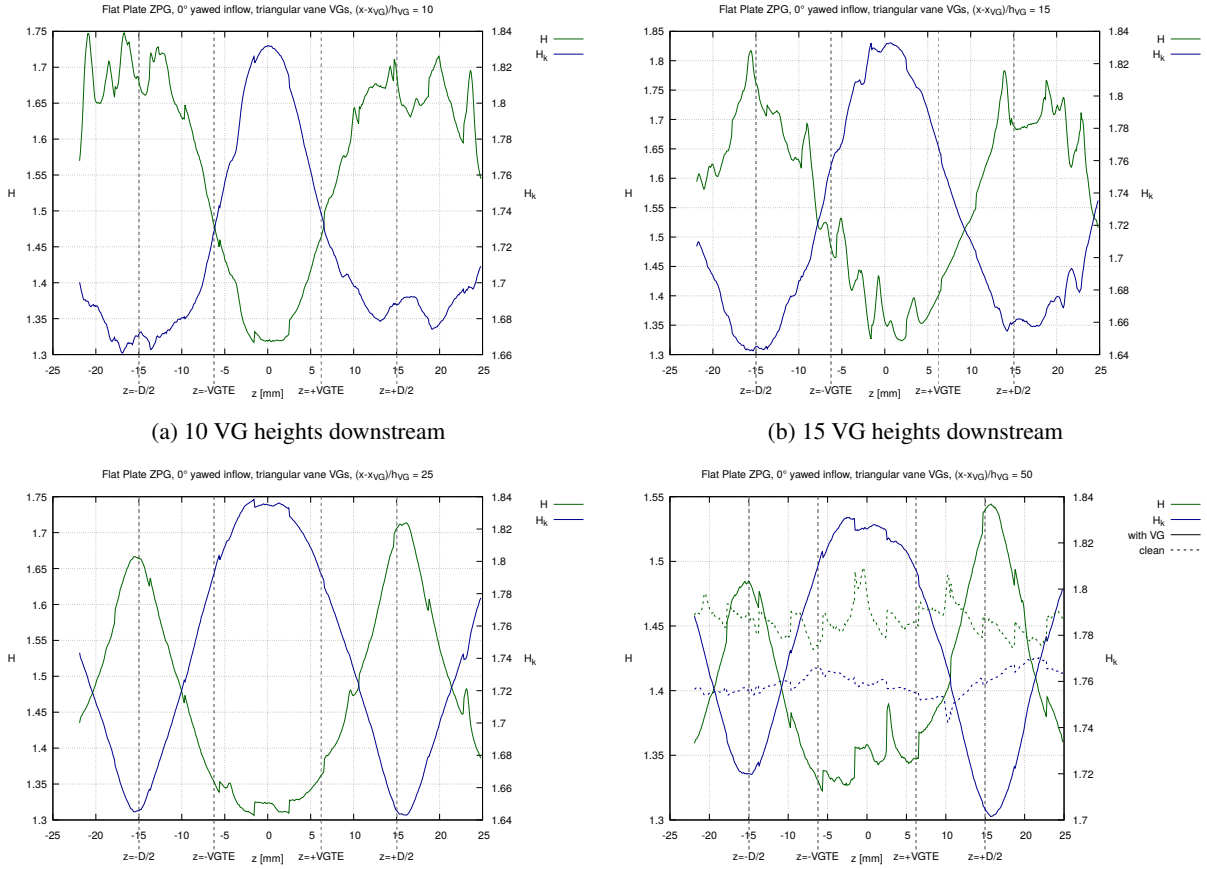
4.2 Plane Mixing Layer Scaling

Figures 4 to 6 present the plane mixing layer scaled profiles for different spanwise slices —the plane between the VG vanes $z = 0$, and the planes between the VG pairs $z = D/2$ and $z = -D/2$. For all the spanwise planes, the velocity profiles are self-similar within the mixing region with this modified plane mixing layer scaling. The mixing region is only a small part of the boundary layer and the self-similarity breaks down outside the mixing region. The mixing region is visualised in the planar flow field for the streamwise position $\Delta x/h = 10$ in Figure 3. The flowfield shows streamwise vorticity ω_x and the planar velocity vectors $V = \sqrt{{V_y}^2 + {V_z}^2}$. The shed vortex core is located closer to the wall at $y/h = 2$ for rectangular VGs while it is near the edge of the boundary layer at $y/h = 4.5$ for triangular VGs. The vortex location corresponds to a shed vortex path line directed by the vane. The triangular vane directs the vortex upward while the rectangular vane directs the vortex parallel to the flat plate surface. Hence, the mixing regions of each vane are at different locations in the boundary layer. Secondly, the large deviation near the wall is because the no-slip wall prevents the mixing region from growing freely by damping the influence of the vortex.

The self-similar velocity profiles also match the analytical plane mixing layer profile within the mixing region. This region is different for the $z = \pm D/2$ planes, and the $z = 0$ plane. While the flow fields show qualitatively that the velocity and vorticity in these planes is different, a quantitive relationship between the self-similar region and vortex dynamics can be investigated further in future work.

4.3 Application to IBL methods

Most IBL methods use the turbulent boundary layer velocity profile to form a closure set for the integral boundary layer equations. RFOIL uses the two-parameter self-similar turbulent velocity profile proposed by Swafford for



(a) 10 VG heights downstream

(b) 15 VG heights downstream

(c) 25 VG heights downstream

(d) 50 VG heights downstream

Figure 2: Spanwise variation of the shape factor H and kinetic energy shape factor H_k downstream of a triangular vane VG array on a flat plate with zero external pressure gradient. The case of $\Delta x/h = 50$ is also compared with a clean flat plate measurement.

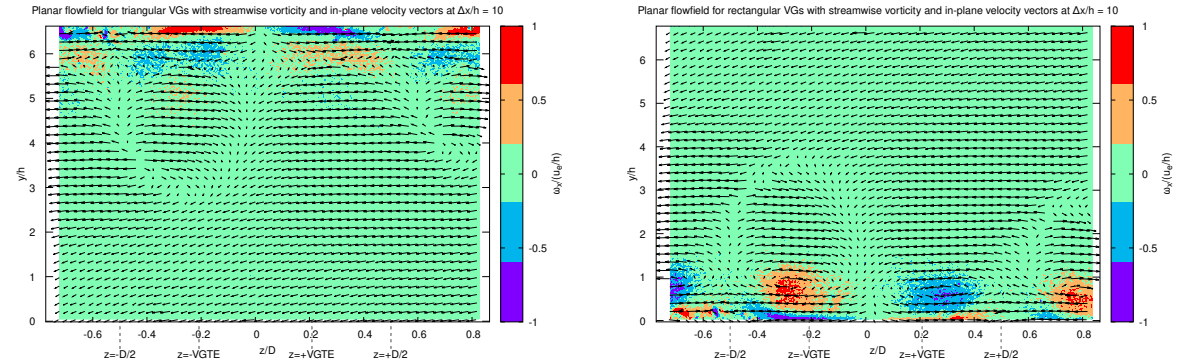
turbulent flows [23]. Turbulent boundary layers are divided into several regions —the viscous sub-layer where viscous shear stresses dominate over turbulent shear stresses, the buffer layer where both stresses are comparable, and the outer layer where turbulent stresses dominate. The Swafford profile (Equation (10)) reformulates the turbulent 'law of the wall' [21] and superposes two matched asymptotic solutions —an inner solution for the viscous and buffer region, and an outer solution for the log and wake region.

$$\frac{u}{u_e} = \frac{u_\tau}{u_e}\frac{s}{0.09}\arctan\left(0.09y^+\right) + \left(1 - \frac{u_\tau}{u_e}\frac{s\pi}{0.18}\right)\tanh^{\frac{1}{2}}\left(a(y/\theta)^b\right) \tag{10}$$

$$\text{where } \frac{u_\tau}{u_e} = \left|\frac{C_f}{2}\right|^{\frac{1}{2}} \quad s = \frac{C_f}{|C_f|} \quad y^+ = \frac{\rho u_\tau}{\mu}y \tag{11}$$

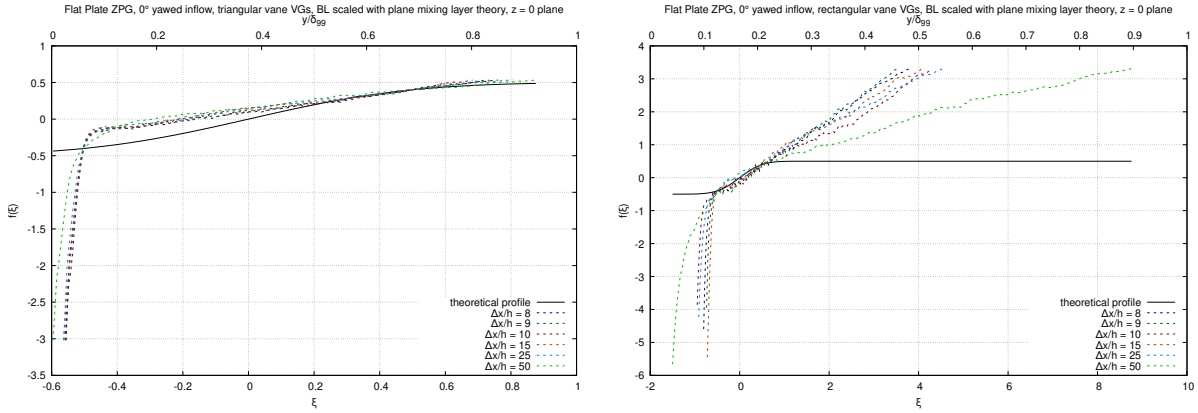
where u is the streamwise velocity in the boundary layer, u_e is the streamwise velocity at the edge of the boundary layer, u_τ is the friction velocity, C_f is the skin friction coefficient, θ is the momentum thickness, y is the wall normal coordinate, and a and b are the two fitting parameters [23]. A typical closure set presents the IBL parameters like skin friction C_f, kinetic energy shape factor H_k, dissipation coefficient C_D, and turbulent shear stress coefficient C_τ in terms of the shape factor H and momentum thickness Reynolds number Re_θ.

The similarity scaling described in this paper produces self-similar scaled velocity profiles in the mixing region influenced by the shed vortices from VGs. Thus, in the mixing region, the Swafford profile can be replaced with this new scaled velocity profile. Characterising the bounds of the exact mixing region in terms of the vortex structure and consequently the VG geometry can produce a modified IBL method for VGs in boundary layers.



(a) Triangular VGs (b) Rectangular VGs

Figure 3: Boundary layer flow fields at $\Delta x/h = 10$ with streamwise vorticity and in-plane velocity.



(a) Triangular VGs (b) Rectangular VGs

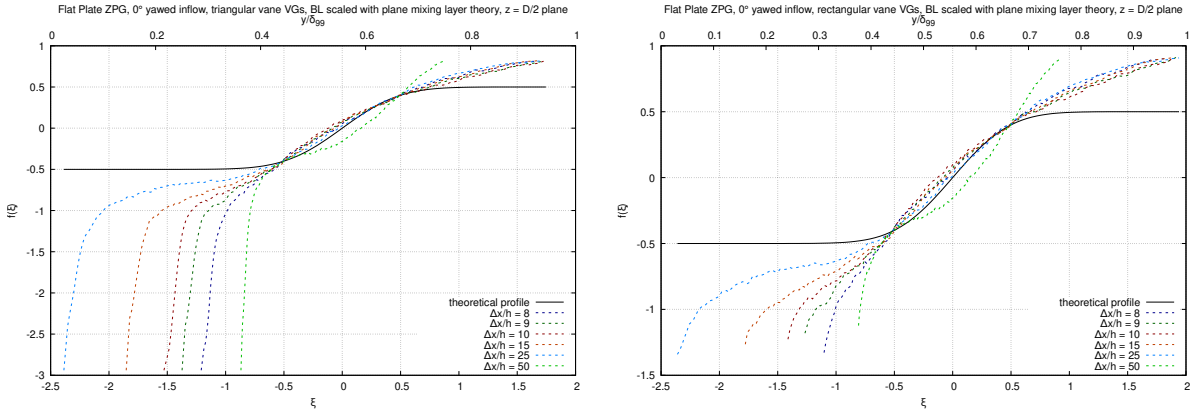
Figure 4: Farfield velocity profiles ($\Delta x/h = 8-50$) scaled with the modified plane mixing layer scaling in the $z = 0$ plane between the VG vanes in a pair.

5 Conclusions and Outlook

A similarity scaling approach inspired from a free-shear plane mixing layer is presented to obtain self-similar velocity profiles for VG boundary layers of two different types of VG vanes. In addition, an integral boundary layer analysis of VG boundary layers is presented to characterise the shed vortex in terms of IBL quantities. The proposed similarity scaling also shows that the mixing mechanism induced by VGs in different characteristic spanwise planes can be approximated with an analytical plane mixing layer profile within the mixing region. Further investigation is necessary to establish a quantitative approach to identify the bounds of the mixing region from the shed vortex structure and VG geometry. Further the scaled velocity profile can be used instead of the two-parameter Swafford profile within the mixing region with appropriately matching boundary conditions and closure sets. These boundary conditions and closure sets to superpose the proposed similarity scaling with the Swafford profile will be the focus of future investigations.

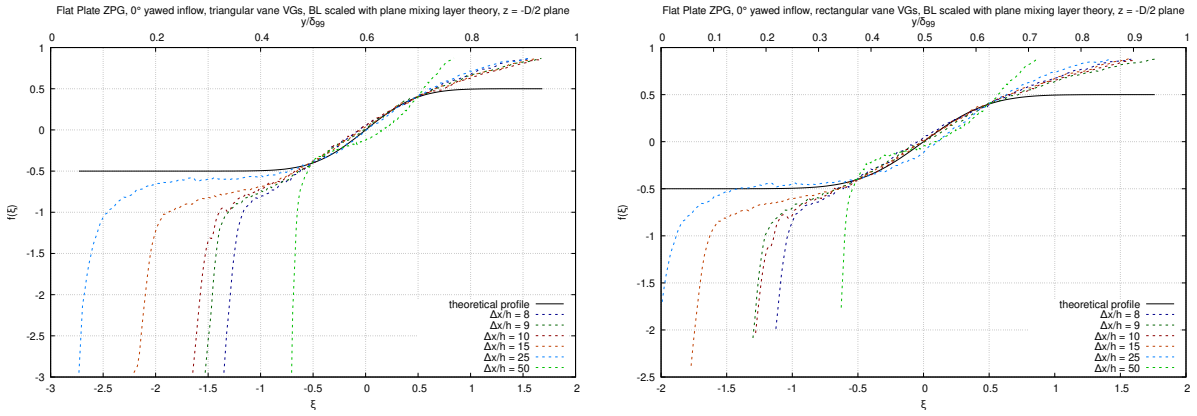
Acknowledgements

This work is part of the VoGUe project between TNO Energy Transition, Vestas Wind Systems A/S, and TU Delft. The project is funded through TKI PPS-toeslag from the Netherlands Enterprise Agency (RVO).



(a) Triangular VGs (b) Rectangular VGs

Figure 5: Farfield velocity profiles ($\Delta x/h = 8-50$) scaled with the modified plane mixing layer scaling in the $z = D/2$ plane between the VG vanes in a pair.



(a) Triangular VGs (b) Rectangular VGs

Figure 6: Farfield velocity profiles ($\Delta x/h = 8-50$) scaled with the modified plane mixing layer scaling in the $z = -D/2$ plane between the VG vanes in a pair.

References

[1] D. Baldacchino, M. Manolesos, C. Ferreira, A. G. Salcedo, M. Aparicio, T. Chaviaropoulos, K. Diakakis, L. Florentie, N. R. García, and G. Papadakis. Experimental benchmark and code validation for airfoils equipped with passive vortex generators. In *Journal of Physics: Conference Series*, volume 753, page 22002. IOP Publishing, 2016.

[2] D. Baldacchino, D. Ragni, C. Simao Ferreira, and G. van Bussel. Towards integral boundary layer modelling of vane-type vortex generators. In *45th AIAA Fluid Dynamics Conference*, page 3345, 2015.

[3] J. H. Bell and R. D. Mehta. Development of a two-stream mixing layer from tripped and untripped boundary layers. *AIAA Journal*, 28(12):2034–2042, dec 1990.

[4] E. E. Bender, B. H. Anderson, and P. J. Yagle. Vortex generator modeling for Navier-Stokes codes. In *3rd ASME/JSME Joint Fluids Engineering Conference*, page 1, 1999.

[5] F. H. Champagne, Y. H. Pao, and I. J. Wygnanski. On the two-dimensional mixing region. *Journal of Fluid Mechanics*, 74(2):209–250, mar 1976.

[6] A. Cutler and P. Bradshaw. The interaction between a strong longitudinal vortex and a turbulentboundary layer. In *4th Joint Fluid Mechanics, Plasma Dynamics and Lasers Conference*, page 1071, 1986.

[7] M. Drela. TWO-DIMENSIONAL TRANSONIC AERODYNAMIC DESIGN AND ANALYSIS USING THE EULER EQUATIONS. Technical report, 1986.

[8] M. Drela. XFOIL: An Analysis and Design System for Low Reynolds Number Airfoils. In T. J. Mueller, editor, *Low Reynolds Number Aerodynamics*, number 54, pages 1–12, Berlin, Heidelberg, 1989. Springer Berlin Heidelberg.

[9] U. Fernández-Gámiz, C. Marika Velte, P. E. Réthoré, N. N. Sørensen, and E. Egusquiza. Testing of self-similarity and helical symmetry in vortex generator flow simulations. *Wind Energy*, 19(6):1043–1052, jun 2016.

[10] F. Grasso and O. Ceyhan. Non-conventional flat back thick airfoils for very large offshore wind turbines. *33rd Wind Energy Symposium*, 2015.

[11] P. H. Jensen, T. Chaviaropolos, and A. Natarajan. LCOE reduction for the next generation offshore wind turbines: Outcomes from the INNWIND.EU project. *Innwind.eu*, 325(October), 2017.

[12] A. Jirásek. Vortex-generator model and its application to flow control. *Journal of Aircraft*, 42(6):1486–1491, 2005.

[13] A. Koodly Ravishankara, H. Ozdemir, and A. Franco. Towards a Vortex Generator Model for Integral Boundary Layer Methods. In *AIAA Scitech 2019 Forum*, page 803, 2019.

[14] J. C. Lin. Review of research on low-profile vortex generators to control boundary-layer separation. *Progress in Aerospace Sciences*, 38(4-5):389–420, may 2002.

[15] O. Lögdberg, K. Angele, and P. H. Alfredsson. On the robustness of separation control by streamwise vortices. *European Journal of Mechanics - B/Fluids*, 29(1):9–17, jan 2010.

[16] R. McKenna, P. Ostman, and W. Fichtner. Key challenges and prospects for large wind turbines. *Renewable and Sustainable Energy Reviews*, 53:1212–1221, jan 2016.

[17] H. Özdemir. Interacting Boundary Layer Methods and Applications. *Handbook of Wind Energy Aerodynamics*, pages 1–53, 2020.

[18] S. B. Pope. *Turbulent flows*. IOP Publishing, aug 2000.

[19] V. Rooij and R.P.J.O.M. Modification of the boundary layer calculation in RFOIL for improved airfoil stall prediction, 1996.

[20] J. G. Schepers, O. Ceyhan, F. J. Savenije, M. Stettner, H. J. Kooijman, P. Chaviarapoulos, G. Sieros, C. S. Simao Ferreira, N. Sørensen, M. Wächter, B. Stoevesandt, T. Lutz, A. Gonzalez, G. Barakos, A. Voutsinas, A. Croce, and J. Madsen. AVATAR: Advanced aerodynamic tools for large rotors. In *33rd Wind Energy Symposium*, pages 291–310. American Institute of Aeronautics and Astronautics Inc.(AIAA), 2015.

[21] H. Schlichting and K. Gersten. *Boundary-layer theory*. Springer, 2016.

[22] G. B. Schubauer and W. G. Spangenberg. Forced mixing in boundary layers. *Journal of Fluid Mechanics*, 8(1):10–32, 1960.

[23] T. W. Swafford. Analytical approximation of two-dimensional separated turbulent boundary-layer velocity profiles. *AIAA journal*, 21(6):923–926, 1983.

[24] C. M. Velte. *Characterization of vortex generator induced flow*. PhD thesis, 2009.

[25] C. M. Velte. Vortex generator flow model based on self-similarity. *AIAA Journal*, 51(2):526–529, feb 2013.

[26] C. M. Velte and M. O. Hansen. Investigation of flow behind vortex generators by stereo particle image velocimetry on a thick airfoil near stall. *Wind Energy*, 16(5):775–785, jul 2013.

18th EAWE PhD Seminar on Wind Energy
2-4 November 2022
Bruges, Belgium

Active Trailing Edge Flap on a 4.3 MW wind turbine: characterization and aeroelastic modeling of a pneumatic flap actuator

A Gamberini[a,b]

[a]Siemens Gamesa Renewable Energy A/S, Brande, Denmark
[b]DTU, Dept. of Wind and Energy Systems, Roskilde, Denmark
E-mail: andgam@dtu.dk

Keywords: Trailing Edge Flap, Aeroelastic model, Validation

1 Introduction

Several studies have shown that actively controlled flaps located at the Wind Turbines (WT) blade trailing edge, so-called Active Trailing Edge Flap Systems (ATEFS), are a promising technology for reducing fatigue and ultimate loads and increasing Annual Energy Production, see e.g. [1].
The validation of ATEFS aeroelastic engineering models and their load reduction applications at a full scale is limited and difficult to perform. In [10], state-of-the-art BEM models of WT equipped with ATEFS have been compared with models of higher fidelity, including free-wake lifting line and fully resolved CFD models for an extensive code-to-code comparison. Subsystem validations have been performed with wind tunnel tests, and on an outdoor rotating rig [7]. As for field tests on a full-scale WT, only three are known: [2], [3], and the most recent one [6] where a 4.3 MW rated power and 120m diameter wind turbine prototype (PT) has been equipped with an ATEFS on a single blade, as part of a project between Siemens Gamesa Renewable Energy (SGRE) and DTU called Validation of Industrial Aerodynamic Active Add-ons (VIAs). Based on the data acquired in the VIAs project, [5] validated the aeroelastic models of ATEFS currently developed for BHawC [4] and HAWC2 [8] aeroelastic codes under stationary flap condition. Model validation for dynamic flap states, like activation and deactivation phases, has not been investigated yet.
This abstract presents the first results of the characterization of the pneumatic actuator of the ATEFS installed on the PT. These results will allow for tuning the aeroelastic model of the flap actuator, an initial fundamental step in validating the ATEFS aeroelastic models under dynamic flap states.

2 Methodology

The pneumatic actuator system of the ATEF installed on the PT is detailed described in [6]. It can be briefly described as an air tank connected via pipes to a flexible hose placed inside the flap. The hose inflation moves the flap from the neutral to the activated position, and the hose deflation brings the flap back to the neutral position. A remotely controlled pressure valve controls the airflow and air pressure inside the pneumatic actuator system.
The pneumatic actuator system is modeled as a chain of three different blocks, as shown in figure 1:

1. Pressure block: modeling the pressure transient in the hose as a function of the control command.
2. Flap motion block: modeling the flap deflection as a function of the hose pressure.
3. Aerodynamic block: modeling the variation of the aerodynamic properties as a function of the flap deflection.

[9] performed a field campaign where a pressure belt measured the pressure distribution at the flap location on the PT. For several flap activation and deactivation cycles, time series of the actuator pressure and the lift coefficient were obtained. In addition, a video camera recorded the flap deflection. Time series and videos are used to define the shape and constants of the transfer functions defining the three blocks of the ATEFS pneumatic actuator.

3 Results

From the controller and pressure SCADA data, the time responses of the control signal and the actuator pressure are obtained for both activation and deactivation of the flap. Via a video tracking tool, the time responses of the flap deflection are extracted from the flap activation and deactivation videos. The lift coefficient time responses are computed from the pressure belt data. Figure 1 shows the computed time responses.

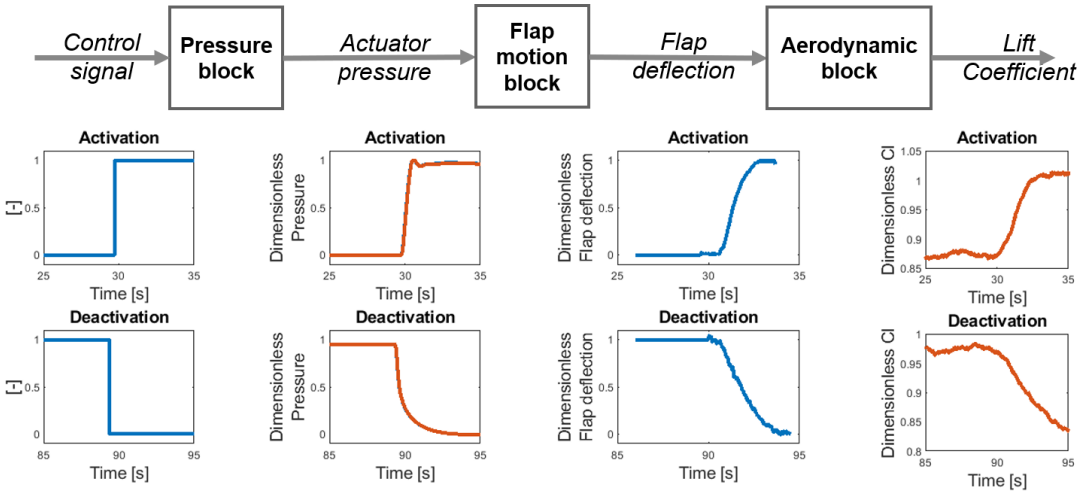


Figure 1: (Up) Flap pneumatic actuator system model. (Down) Dimensionless time responses for both flap activation and deactivation of Flap control signal, Actuator pressure, Flap deflection and Lift coefficient.

4 Conclusions

Time responses for flap activation and deactivation of the Flap control signal, Actuator pressure, Flap deflection, and Lift coefficient have been computed. They will be crucial for tuning the global flap actuator model that will be implemented in the ATEFS aeroelastic models. This tuning will enable the missing dynamic validation of the flap aeroelastic model based on the field data obtained from the VIAs project.

Acknowledgements

This industrial PhD is funded by Danmarks Innovationsfond, Case no. 9065-00243B, PhD Title: ”Advanced model development and validation of Wind Turbine Active Flap system”.

References

[1] T. Barlas, V. Pettas, D. Gertz, and H. A. Madsen. Extreme load alleviation using industrial implementation of active trailing edge flaps in a full design load basis. In *Journal of Physics: Conference Series*, volume 753. Institute of Physics Publishing, oct 2016.

[2] J. C. Berg, M. F. Barone, and B. R. Resor. Field test results from the sandia smart rotor. *51st Aiaa Aerospace Sciences Meeting Including the New Horizons Forum and Aerospace Exposition 2013*, 2013.

[3] D. Castaignet, T. K. Barlas, T. Buhl, N. K. Poulsen, J. Wedel-Heinen, Jens, N. A. Olesen, C. Bak, and T. Kim. Full-scale test of trailing edge flaps on a vestas v27 wind turbine: active load reduction and system identification. *Wind Energy*, 17(4):549–564, 2014.

[4] P. Fisker Skjoldan. *Aeroelastic modal dynamics of wind turbines including anisotropic effects*. Risø National Laboratory, 2011.

[5] A. Gamberini, A. Gomez Gonzalez, and T. Barlas. Aeroelastic model validation of an active trailing edge flap system tested on a 4.3 mw wind turbine. *Journal of Physics. Conference Series*, 2265(3):032014, 2022.

[6] A. Gomez Gonzalez, P. B. Enevoldsen, H. A. Madsen, and A. Barlas. Test of an active flap system on a 4.3 MW wind turbine. *TORQUE 2022*, 2022.

[7] A. G. Gonzalez, P. Enevoldsen, T. K. Barlas, H. A. Madsen, and A. S. Olsen. Consolidated results of the laboratory and full scale field validation of an active flap system. 1618(5):52024, 2020.

[8] T. Larsen and A. Hansen. *How 2 HAWC2, the user's manual*. Number 1597(ver. 3-1)(EN) in Denmark. Forskningscenter Risoe. Risoe-R. Risø National Laboratory, 2007.

[9] H. A. Madsen, T. Barlas, A. Fischer, A. Olsen, and A. Gomez Gonzalez. Inflow and pressure measurements on a full scale turbine with a pressure belt and a five hole pitot tube. *Journal of Physics: Conference Series*, 2265(2):022096, 2022.

[10] J. M. Prospathopoulos et al. Simulation of oscillating trailing edge flaps on wind turbine blades using ranging fidelity tools. *Wind Energy*, 24(4):357–378, 2021.

18th EAWE PhD Seminar on Wind Energy
2-4 November 2022
Bruges, Belgium

Comparison of different wind farm control strategies in a quasi-static closed-loop control framework

Ishaan Sood[a] and **Johan Meyers**[a]

[a]Department of Mechanical Engineering, KU Leuven, Celestijnenlaan 300A, 3001, Leuven, Belgium.

E-mail: ishaan.sood@kuleuven.be

Keywords: Wind farm control, Closed loop, Large Eddy Simulations

1 Introduction

Modern mega-watt sized wind turbines are often placed in clusters called wind farms to reduce installation and operational costs. However due to their close arrangement, the wakes of upstream turbines tend to superimpose on downstream turbines leading to performance losses and fatigue degradation across the farm. To counteract this effect, recent literature has proposed wind-farm control strategies such as wake steering and induction control which can be employed together or individually, in either an open-loop or closed-loop control framework [8]. Compared to open-loop control, the closed-loop methodology has the added benefit of online calibration of the wind-farm state model used for optimization, through state estimation and parameter tuning of the included wake models [4, 13]. While previous closed-loop control studies have been predominantly focused on boosting farm wide power production, recent studies have shown that focusing solely on power optimization could lead to significant increase in turbine fatigue across the wind farm [15]. Furthermore, the effect of the control strategy chosen, i.e. yaw control, induction control or a combination of both, on the overall farm performance while considering fatigue loading is still an open question. Therefore, in this work we aim to investigate different control strategies in a closed loop control framework, and compare the performance against a previously developed reference database for greedy operation under the same operating conditions.

2 Methodology

An overview of the closed-loop methodology is shown in Figure 1. The wind farm state model comprises of a recursive gaussian wake model, combined with a fatigue LUT developed offline for the DTU 10MW turbine

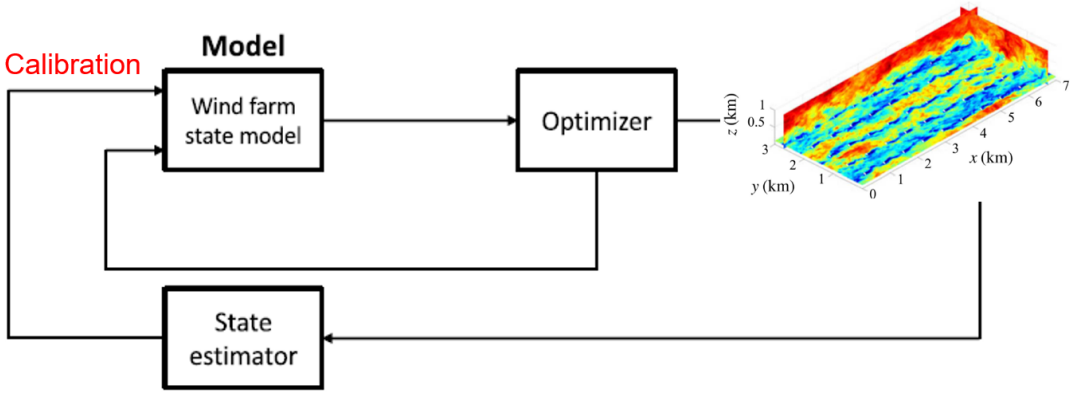


Figure 1: Closed-loop wind-farm control methodology.

Table 1: Specifications of the reference database

Case No.	Inflow	Wind direction	Hub height wind speed	Hub height TI
1	*PDk*	0°	9.4 m s^{-1}	5.15%
2	*CNk2*	300°	11.0 m s^{-1}	3.66%
3	*CNk2*	330°	11.0 m s^{-1}	3.66%
4	*CNk4*	300°	11.3 m s^{-1}	3.65%
5	*CNk4*	0°	11.3 m s^{-1}	3.65%

using OpenFast [3, 6]. To cover different operational states, the LUT was developed across a range of values for different turbine yaw and pitch angles, while operating under different inflow conditions governed by wind speed and turbulence intensity. Turbine set-point optimization is carried out by minimizing the following cost function

$$\min_{\gamma, C_T} \quad -1 * w_P * \sum_{k=1}^{N_t} \frac{1}{2} \rho C_P(\gamma_k, C_{Tk}) A_k U_k^3(\gamma, C_T) + w_L * \sum_{k=1}^{N_t} DEL_k(\gamma_k, C_{Tk}). \tag{1}$$

The first term in the cost function is the power maximization term, while the second term deals with the minimization of fatigue loads in the form of blade root Damage Equivalent Loads (DEL). Weights w_P and w_L are added in the cost function to control the relative importance of the two terms. C_P is the coefficient of power of each turbine, evaluated for a yaw angle γ_k according to the cosine power law [4]. The effect of induction control by using a sub-optimal thrust coefficient C_T was determined by using a look-up table which was previously developed using OpenFast. The variables γ and C_T are vectors containing the yaw and thrust set-points for all the turbines across the farm. Turbine yaw angles are limited between $\pm 30°$ to prevent excessive fatigue and the thrust coefficient is limited between 0 and 1 to avoid turbine shutdown or over-induction. Furthermore, A_k is the area of each turbine, and U_k is the inflow velocity of each turbine determined using the wake model. Based on the control strategy chosen, the cost function is modified to either keep C_T constant (wake steering), γ constant (induction control), or optimize both the parameters on a per turbine basis. The optimisation problem is solved to obtain the turbine set-points using the SLSQP solver from the SciPy Python package, while utilizing the multi-start approach of basin-hopping to avoid local minima [16].

Reference wind farm cases operating under normal operation and open-loop control are required to demonstrate the benefits of closed-loop control. To this end, we make use of the publicly available TotalControl reference wind farm database which comprises of numerical measurements obtained from Large Eddy Simulations (LES) spanning different two different types of boundary layers, Pressure Driven Boundary Layers (PDBL) and Conventionally Neutral Boundary Layers (CNBL), and different wind directions for the TotalControl reference wind farm [2]. All the selected cases for optimization have been summarized in Table 1. *PDk* refers the Pressure Driven Boundary Layer (PDBL) simulations and *CNk2* and *CNk4* refer to Conventionally Neutral Boundary Layer (CNBL) simulations, with the suffix 2 and 4 denoting the strength of the capping inversion. Further details regarding the inflow database is available at the publicly available TotalControl inflow database [11, 12, 9, 10].

The closed-loop controller is tested in the same LES environment which was used to develop the reference database using the aeroelastic SP-Wind framework. SP-Wind has been extensively used in the past years for wind farm simulations and optimizations [5, 1, 7]. Turbines in SP-Wind are represented using an aeroelastic actuator sector model to allow for time series analysis of turbine power and structural loading [17]. Turbine power, thrust and velocity measurements are either measured or estimated online during the simulation runs to calibrate the wake model parameters through a ridge regression based tuning framework [14].

Acknowledgements

The computational resources and services used in this work were provided by the VSC (Flemish Supercomputer Center), funded by the Research Foundation Flanders (FWO) and the Flemish Government department EWI.

References

[1] D. Allaerts and J. Meyers. Gravity Waves and Wind-Farm Efficiency in Neutral and Stable Conditions. *Boundary-Layer Meteorology*, 166(2):269–299, 2018.

[2] S. J. Anderson, J. Meyers, I. Sood, and N. Troldborg. TotalControl D 1.04 Flow Database for reference wind farms, 2020.

[3] C. del Fosse et d'Espierres. Design of a load lookup table for wind farm optimization, 2021.

[4] B. M. Doekemeijer, D. van der Hoek, and J. W. van Wingerden. Closed-loop model-based wind farm control using FLORIS under time-varying inflow conditions. *Renewable Energy*, 156:719–730, 2020.

[5] J. P. Goit and J. Meyers. Optimal control of energy extraction in wind-farm boundary layers. *Journal of Fluid Mechanics*, 768:5–50, 2015.

[6] L. Lanzilao and J. Meyers. A new wake-merging method for wind-farm power prediction in the presence of heterogeneous background velocity fields. *Wind Energy*, 07 2021.

[7] W. Munters, C. Meneveau, and J. Meyers. Turbulent Inflow Precursor Method with Time-Varying Direction for Large-Eddy Simulations and Applications to Wind Farms. *Boundary-Layer Meteorology*, 159(2):305–328, 2016.

[8] W. Munters and J. Meyers. Dynamic strategies for yaw and induction control of wind farms based on large-eddy simulation and optimization. *Energies*, 11(1), 2018.

[9] W. Munters, I. Sood, and J. Meyers. Precursor dataset cnk2, Apr. 2019.

[10] W. Munters, I. Sood, and J. Meyers. Precursor dataset cnk4, Apr. 2019.

[11] W. Munters, I. Sood, and J. Meyers. Precursor dataset pdk, Apr. 2019.

[12] W. Munters, I. Sood, and J. Meyers. Precursor dataset pdkhi, Apr. 2019.

[13] I. Sood and J. Meyers. Tuning of an engineering wind farm model using measurements from large eddy simulations. *Journal of Physics: Conference Series*, 2265(2):022045, may 2022.

[14] I. Sood and J. Meyers. Tuning of an engineering wind farm model using measurements from Large Eddy Simulations. *Journal of Physics: Conference Series*, ((accepted)), 2022.

[15] I. Sood and J. Meyers. Validation of an analytical optimization framework for wind farm wake steering applications. AIAA SCITECH 2022 Forum, 2022.

[16] P. Virtanen, R. Gommers, T. E. Oliphant, M. Haberland, T. Reddy, D. Cournapeau, E. Burovski, P. Peterson, W. Weckesser, J. Bright, S. J. van der Walt, M. Brett, J. Wilson, K. J. Millman, N. Mayorov, A. R. J. Nelson, E. Jones, R. Kern, E. Larson, C. J. Carey, İ. Polat, Y. Feng, E. W. Moore, J. VanderPlas, D. Laxalde, J. Perktold, R. Cimrman, I. Henriksen, E. A. Quintero, C. R. Harris, A. M. Archibald, A. H. Ribeiro, F. Pedregosa, P. van Mulbregt, and SciPy 1.0 Contributors. SciPy 1.0: Fundamental Algorithms for Scientific Computing in Python. *Nature Methods*, 17:261–272, 2020.

[17] A. Vitsas and J. Meyers. Multiscale aeroelastic simulations of large wind farms in the atmospheric boundary layer. *Journal of Physics: Conference Series*, 753(8):082020, sep 2016.

18th EAWE PhD Seminar on Wind Energy
2-4 November 2022
Bruges, Belgium

Decentralized Q-learning for Wind Farm Control under Dynamic Conditions

Claire Bizon Monroc[a,b], **Eva Bouba**[b], **Ana Bušić**[a], **Donatien Dubuc**[b], and **Jiamin Zhu**[b]

[a]Inria and DI ENS, École Normale Supérieure, CNRS, PSL Research University
[b]IFP Energies nouvelles

E-mail: claire.bizon-monroc@inria.fr

Keywords: wind farms, reinforcement learning, control, multi-agent

1 Introduction

Wind farms are subject to the so-called "wake effect", where upstream turbines facing the wind create sub- optimal wind conditions for turbines located downstream. One strategy to address this issue is to use yaw actuators to misalign the wind turbines with regard to the incoming wind direction, thus deflecting wakes away from downstream turbines. Yet finding the optimal yaws for any given farm layout and wind conditions is a challenging problem. Traditional control approaches build a model of the wind farm and optimize control inputs with respect to this approximation, but tractable models for yaw optimization are subject to inaccuracies, ignore wake dynamics and lack adaptability. This incentivizes the use of model-free method.

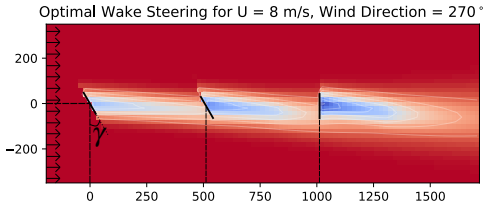
Reinforcement learning (RL) algorithm could provide a solution: following a data-driven approach, they directly infer the best actions solely by observing the system's responses to input changes. This online learning approach is particularly interesting because of the need to recover in the field from sub-optimal behaviors due to differences between simulation and reality. Different centralized RL methods have been used to control yaw angles on wind farms [8] [2]. These methods see the dimension of their problem grow exponentially in the number of turbines, raising issues of scalibility. In this context, decentralized learning schemes are a promising way towards more scalable farm control algorithms. They have been shown to lead to significant increase in total power production on wind farms, but only with steady-state wake models. The validation of a decentralized approach in simulations with realistic dynamics of wake propagations is therefore still an open problem. This is especially critical because decentralized algorithms limit the observability of the problem for each turbine, rendering their environment non-stationary. Meanwhile, realistic wake dynamics prevent the observation of a controller's impact until the wake has propagated downstream, and make the assignment of variation to any controller harder because of wake merging.

The remainder of this abstract is organized as follows. Section 2.1 provides background information on reinforcement learning. In section 3, we show that decentralized Q-learning successfully increases the total power output for two farm layouts under dynamical wind conditions, and can be combined with steady-state models in a two-step warm start approach. Finally, Section 4 discusses possible paths forward.

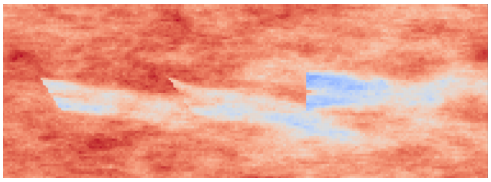
2 Reinforcement Learning for Wind Farm Control

2.1 Background: Reinforcement Learning

We define a Markov Decision Process (MDP) $\{S,A,r,P\}$, with S the state space, A a discrete action space, P the matrix of transition probabilities of the environment and $r : S \times A \to \mathbb{R}$ a reward function. We write $A(s)$ the subset of actions $a \in A$ available in state s. An agent interacts with the environment by following a stochastic policy $a \sim \pi(s), s \in S, a \in A(s)$, where $\pi(a|s)$ is the probability of choosing action a when in state s. If the policy is deterministic, there exists an a' for which $\pi(a'|s) = 1$ and we directly write $a' = \pi(s)$. The agent's goal is then to find a policy π^* that maximizes the expectation of its infinite-horizon discounted reward, or discounted return:



(a) Total farm power output



(b) Individual turbine power production

Figure 1: Simulation of our 3-turbines layout (a) on low-fidelity simulator FLORIS and (b) on on mid-fidelity simulator FAST.Farm. Compared to FLORIS, FAST.Farm simulates turbulence and wake dynamics, including wake meandering and merging.

$G = \sum_{k=0}^{\infty} \beta^k r(s_k, a_k)$ with $0 < \beta < 1$ the discount factor, s_0 the initial state, and $\{s_k, a_k\}_{k=0...\infty}$ the trajectory of the agent in the environment under policy π. For a policy π, we define the state-action value function, or q function Q, as: $Q_\pi(s,a) := \mathbb{E}\left[\sum_{k=0}^{\infty} \beta^k r(s_k, a_k) | s_0 = s, a_0 = a\right]$ with $a_k \sim \pi(s_k)$. For any state-action pair (s,a), $Q_\pi(s,a)$ is therefore the expected value of choosing action a in state s, and then following policy π. We define an optimal q function Q^* such that: $\forall (s,a), Q^*(s,a) = \max_\pi Q_\pi(s,a)$. To search for the best policy in a given environment, one can directly attempt to learn Q^*. One of the most popular RL algorithm, Watkins' Q-learning [9] directly learns an estimate $\hat{Q}$ of the optimal q function $Q^*(s,a)$ for each state-action (s,a) pair.

When several agents seek to learn optimal policies to maximize a shared team reward, the task is one of cooperative multi-agent RL (MARL). The agents can equally be thought of as solving a distributed optimization problem [6]. This is a challenging task: because all agents concurrently interact with the environment, the stationarity assumptions supporting convergence guarantees no longer hold. A naive approach however, can be to simply apply the single-agent Q-learning algorithm to the multi-agent case: much simpler, this decentralized approach has also been empirically shown to converge to a good equilibrium in certain settings [1], and a good proof-of-concept with steady-state modeling has been provided by [7] for the wind farm optimization case in a simple environment.

2.2 Application to Wind Farm Control: a multi-agent optimization problem

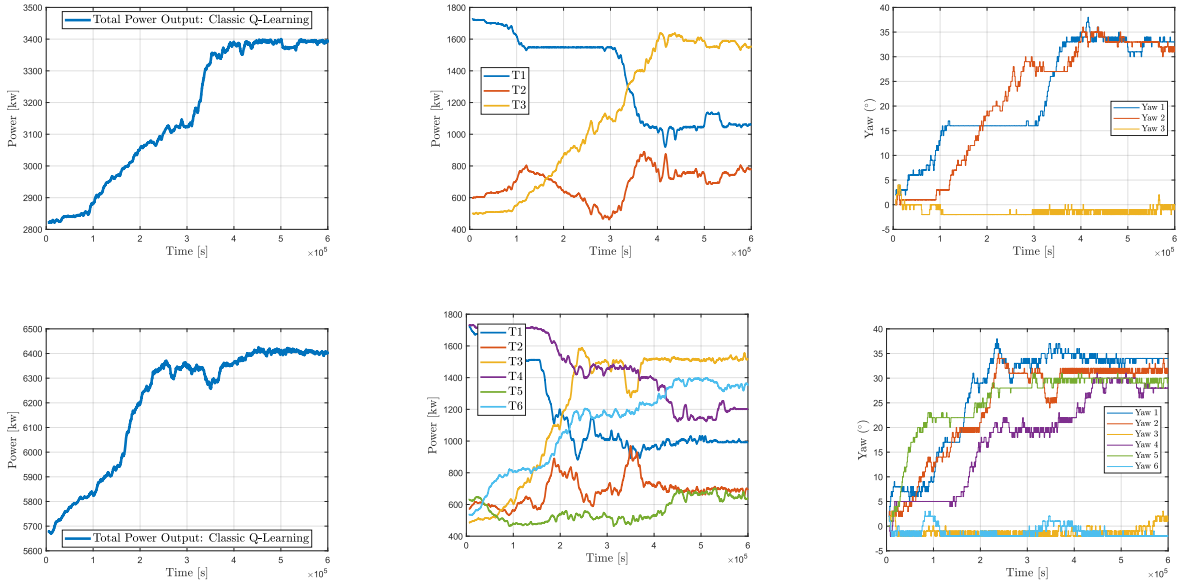
We consider a wind farm with M turbines. For a space of admissible angles $\mathscr{Y}$, each turbine i has a current yaw $\gamma_{i,k} \in \mathscr{Y}$ and generates a power $P_{i,k}$. For any given k we want to maximize the total power output of the wind farm $P_k = \sum_{i=1}^{M} P_{i,k}$. This problem can be seen as a distributed optimization task, where every turbine is an agent interacting with the environment and all maximize a common objective. Under the cooperative multi-agent RL framework mentioned in 2.1, this can be done in a decentralized fashion with M RL agents independently learning local optimal policies to maximize a shared team reward. Under stationary wind conditions, each agent observes his local state at each timestep $s_{i,k} = [\gamma_{i,k}]$, $\gamma_{i,k} \in \mathscr{Y}$. The local action spaces are defined as $\forall i, A_i = A = \{-1, 0, 1\}$. Each chosen action $a_i \in A$ leads to an update in the corresponding yaw defined by $a \times (\Delta\gamma)$, with $\Delta\gamma$ a predefined step size matching the real constraints and limitations on turbine yaw actuation. As mentioned in 2.1, we can then learn M single-agent Q-learning algorithms simultaneously.

3 Simulation Results

We first seek to validate our approach: is a decentralized Q-learning robust to dynamic wake propagation with turbulent wind? To answer that question, we first test a decentralized Q-learning algorithm without any prior knowledge of optimal yaws in an environment with simulated wake dynamics. Then, we evaluate a two-step warm start approach with yaw and Q-table initialization to accelerate convergence.

3.1 Simulation Setup

All our experiments are done on FAST.Farm, a midfidelity simulation environment [5] which accounts for wake deficits, advection, deflection, meandering, and merging, and with results validated against high-fidelity large-eddy simulations. [4]. On Figure 1, an example of these realistic wind fields can be compared to a similar simulation done with FLORIS. We consider two farms of NREL offshore 5-MW turbines: in the first farm (Layout 1), 3 turbines are spread in a row in the center of the farm, while the second farm (Layout 2) has 6 turbines spread in



(a) Total farm power output

(b) Individual turbine power production

(c) Turbine yaws

Figure 2: Results of decentralized Q-learning without two-step warm start on 2 wind farms simulated on FAST.Farm: 3 turbines (first row) and 6 turbines in 2×3 layout (second row). Evolution of total power output [kW], individual turbine power [kW], and turbine yaws [°]. Power measures are averaged over 1 hour.

2×3 layout. In order to replicate realistic wind conditions, a time series of 3D wind velocity vectors is generated in the flow field based on data from the turbulent-wind simulator TurbSim [3]. The average freestream velocity is $u_k^\infty = 8m/s$ and the turbulence is of 8%.

3.2 Results

We first train the algorithm in FAST.Farm for 600ks, corresponding to 2.3×10^5 iterations. The results are depicted on Figure 2. Compared to the greedy strategy baseline, the total power output of the farm is increased by 20% for Layout 1 and by 14% for Layout 2. In both cases, the algorithm reaches convergence around $450ks$, corresponding to 150k iterations. Despite doubling the size of the farm, we are therefore able to sensibly keep the same time of convergence, which points towards a key advantage over both centralized or locking approaches. On Layout 2, as expected pairs of turbines with the same y-axis coordinates converge towards similar yaw angles. These preliminary results validate a decentralized Q-learning approach even with realistic turbulent wind and accurate wake dynamics.

3.3 Two-Step Warm Start Approach

The time needed for decentralized Q-learning to converge creates a significant loss of production. We could increase the total power output over the period by exploiting known information about the region of optimal yaws in the search space. A valuable clue can be given by industry practices, who use low-fidelity steady-state models to tune the yaws in a simplified environment. As reported in Table 1, that simple heuristic performs relatively well, but modeling uncertainties prevent it from finding the optimal yaws. In a two-step warm start approach, we can train a simple decentralized Q-learning algorithm in the steady-state simulation environment before pursuing the learning on the dynamic environment. A comparison of total power output evolution with and without warm-start is displayed on Figure 3. To account for rapidity of convergence, stability, and final performance, the average power produced during the time of the simulation is reported in Table 1.

Figure 3: Evolution of total farm power output averaged over 1 hour with and without warm start, compared to the greedy approach ($\gamma_i = 0°$). Simulation on FAST.Farm.

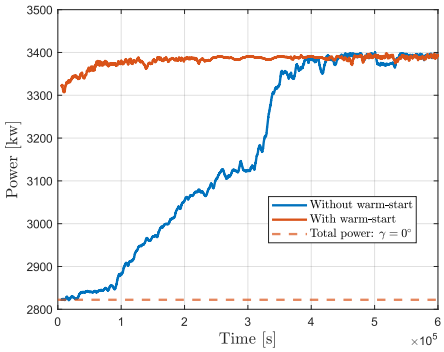


Table 1: Decentralized Q-learning with and without initialization in the 3 turbines layout. Results after 600ks. Mean power output measured during the learning period, and final percentage increase compared to the 0° yaw initialization.

Method	**Avg Measure [kW]**	**Final Performance (%)**
FLORIS Routine	3312.22	17.3
Dec Q learning	3164.30	**20.29**
+ Two Step Warm Start	**3381.25**	20.18

4 Conclusions and Future Works

Our results show that decentralized single agent Q-learning algorithms can be robust to realistic wake dynamics, and motivate further research investigating:

- **Extension to non-stationary wind conditions** Evaluating the behavior of this approach under non-stationary wind conditions is an important step towards designing deployable solutions.
- **Scalibility** The similar convergence times observed for 3 and 6 turbines are a promising indication towards subexponential complexity in the number of turbines, and further experiments on larger farms should be pursued to validate that intuition.
- **Convergence guarantees** Why does this work ? Tools from the literature on both cooperative MARL and distributed optimization can help us work towards theoretical guarantees.

References

[1] L. Busoniu, R. Babuska, and B. De Schutter. *Multi-agent Reinforcement Learning: An Overview*, volume 310, pages 183–221. 07 2010.

[2] H. Dong, J. Zhang, and X. Zhao. Intelligent wind farm control via deep reinforcement learning and high-fidelity simulations. *Applied Energy*, 292(C), 2021.

[3] B. Jonkman and B. Jr. Turbsim user's guide. 01 2007.

[4] J. Jonkman, P. Doubrawa, N. Hamilton, J. Annoni, and P. Fleming. Validation of FAST.farm against large-eddy simulations. *Journal of Physics: Conference Series*, 1037:062005, jun 2018.

[5] J. M. Jonkman, J. Annoni, G. Hayman, B. Jonkman, and A. Purkayastha. *Development of FAST.Farm: A New Multi-Physics Engineering Tool for Wind-Farm Design and Analysis*.

[6] D. Lee, N. He, P. Kamalaruban, and V. Cevher. Optimization for reinforcement learning: From single agent to cooperative agents. *CoRR*, abs/1912.00498, 2019.

[7] P. Stanfel, K. Johnson, C. J. Bay, and J. King. Proof-of-concept of a reinforcement learning framework for wind farm energy capture maximization in time-varying wind. *Journal of Renewable and Sustainable Energy*, 13(4), 8 2021.

[8] S. Vijayshankar, P. Stanfel, J. King, E. Spyrou, and K. Johnson. Deep reinforcement learning for automatic generation control of wind farms. In *2021 American Control Conference (ACC)*, pages 1796–1802, 2021.

[9] C. Watkins and P. Dayan. Technical note: Q-learning. *Machine Learning*, 8:279–292, 05 1992.

18th EAWE PhD Seminar on Wind Energy
2-4 November 2022
Bruges, Belgium

Dynamic modelling of wind farms for closed-loop control applications

Jaime Liew[a]

[a]Department of Wind Energy, Technical University of Denmark (DTU), Frederiksborgvej 399, 4000 Roskilde, Denmark.

E-mail: jyli@dtu.dk

Keywords: Wind farm control, Reinforcement learning, System identification, Aeroelastic wind farm simulations

1 Introduction

Wind energy researchers continue to draw their attention to wind farm control methods such as wake steering [2], static induction control [13] and dynamic induction control [18]. Using these methods, power output in a wind farm can be increased by several percent as shown in various simulations, wind tunnel experiments and field tests [5]. Despite promising results, the majority of these wind farm control strategies are presented in steady-state and open-loop forms, failing to account for realistic dynamic considerations such as the limited observability of a wind farm system, and the time-varying wind and operational conditions in both short and long term time scales. For this reason, it is uncertain how a wind farm controller can seek an optimal configuration to maximize an objective in a causal, non-linear, time-varying, and stochastic environment. It is crucial to address these considerations to make these theoretical wind farm control strategies a reality. This motivates the development of the two focuses of this project: 1) a realistic dynamic wind farm simulation methodology, and 2) a real-time robust implementation of a closed-loop wind farm controller.

Accurate wind farm simulation methods are required to test and verify these control methods. Aeroelastic wind farm simulations are particularly relevant as they are able to capture short-term dynamic effects in a wind farm, unlike steady wind farm simulations which are typically used. Furthermore, dynamic simulation frameworks such as HAWC2Farm [9] and FAST.Farm [3] can simulate closed-loop implementations of wind farm controllers as well as evaluate the structural loading on the turbines [19]. In this project, we present the development, verification and validation of HAWC2Farm as a viable software for aeroelastic wind farm simulations for closed-loop wind farm control.

The second part of this study addresses the wind farm controller, and how it decides the best control action in a given scenario. The majority of wind farm control papers identify that there are optimal yaw steering arrangement in steady state simulations, and, assuming the wind turbines can reach the optimal set points, the wind farms can achieve an annual energy output increase of several percent [1]. In a realistic wind farm setting, the wind farm controller needs to not only identify the correctly control actions given limited information, but also guide the wind turbines to these orientations. The controller should be robust enough to operate using only available information, which is typically noisy and miscalibrated, yet adaptable enough to accommodate changing and unpredictable conditions. Using a model-based approach is a typical approach in literature - predetermine the best set-points based on a wind farm model and apply them at the right time. Model uncertainties can be addressed using uncertainty quantification, however, the wide range of time and length scales that exist in a wind farm system make the model extremely complex and prone to errors. The control method presented in this study is a model-free approach, using only typical real-time data streams available to a wind farm operator. Reinforcement learning methodologies such as gradient policy methods in particular [4, 20], are used to decide on an optimal policy for the wind farm controller to follow. Real-time system identification is performed using streaming dynamic mode decomposition (both exact and model-reduced) to forecast and train the agent to perform power maximisation [22].

In summary, the research outcomes of this project are as follows:

- Develop an aeroelastic wind farm simulation software for the purpose of load evaluation and closed-loop control applications [9, 11, 12].
- Identify time-varying dynamics of a wind farm over short and long time scales using data-driven methods [10].
- Develop a closed-loop control strategy using realistic inputs available in a wind farm.

2 Method

2.1 Simulation method

The aeroelastic wind farm simulation framework, HAWC2Farm, was developed for the purpose of this project. HAWC2Farm models each turbine using the aeroelastic code, HAWC2 [8, 15], while also modelling the turbine wake interactions using the dynamic wake meandering model (DWM)[7, 14] and the turbulent wind field, either using the Mann model [16] or a pre-generated large-eddy simulation (LES) flow field. The DWM implementation is modified to allow for wake deflection using a verified method described in [6]. Hence, we couple a mid-fidelity multi-body finite element solver and a flow solver, providing a computationally efficient wind farm simulation platform with applications in wind farm flow control. HAWC2Farm has been numerically verified against LES performed using Ellipsys3D [17, 21] as a high fidelity reference [9]. The verification shows that HAWC2Farm can capture wind farm operational conditions, wind field flow, and turbine structural influences using a fraction of the computational resources of LES. An additional validation study is currently being performed comparing HAWC2Farm against real-world measurements from the Lillgrund wind farm.

2.2 Model-free closed-loop control method

With a wind farm simulation platform at our disposal, it is possible to test various real-time model-free algorithms in a realistic wind farm setting. In reality, wind farms are only partially observable, with information being delivered from the available sensors. Typical sensors include cup anemometers and wind vanes on the turbine nacelle, as well as power output measurements, rotor speed, yaw orientation, and blade pitch angles. More advanced sensors such as LIDARs or load strain gauges exist, however, the availability of these is non-standard. To complicate matters, there are variations in the wind farm system over both long and short time scales. Long time scale effects, which occur over the span of hours to years, include evolving weather conditions (wind speed, direction, stability, precipitation) and changes in the wind turbine systems, such as leading edge erosion, component degradation, sensor miscalibration, sensor drift, and turbine shutdowns. Short term variations are largely driven by turbulence, making the system stochastic and chaotic. Despite these complications, it is shown in this project that there exist observable high-rank dynamics which can be identified. Using a streaming modification of the dynamic mode decomposition (DMD) algorithm, we show that the power output of the turbines in a wind farm can be forecast 20 minutes into the future using only sensors available in a typical wind farm. The streaming DMD algorithm, is robust and adaptive, adjusting to new measurements as they are made available. It is able to identify the deterministic components of the system while ignoring the purely stochastic components. As a result, the algorithm can outperform persistent forecasting by over 23% [10].

Streaming DMD provided promising results for model-free real-time forecasting in a wind farm using only a small subset of sensors. In an additional study, we investigate the use of streaming DMD to perform model-free closed-loop wind farm control using wake steering. Using reinforcement learning methodologies, an adaptive control algorithm is developed which is able to explore and learn the wind farm system behaviour while simultaneously approaching the optimal control settings. This is achieved by using a policy gradient method, in which the control set-points are continuously modified to maximise an objective function by following the gradient of the reward function. The gradient is estimated using a modified streaming DMD algorithm combined with a random yaw input signal which is dispatched to the turbine yaw controllers. The random yaw signal, although potentially detrimental to the performance of the wind turbines, allows the algorithm to identify the direction of the reward gradient. It is hypothesised that by approaching the optimal reward in real-time, the negative effects of the random yaw signal will be counteracted.

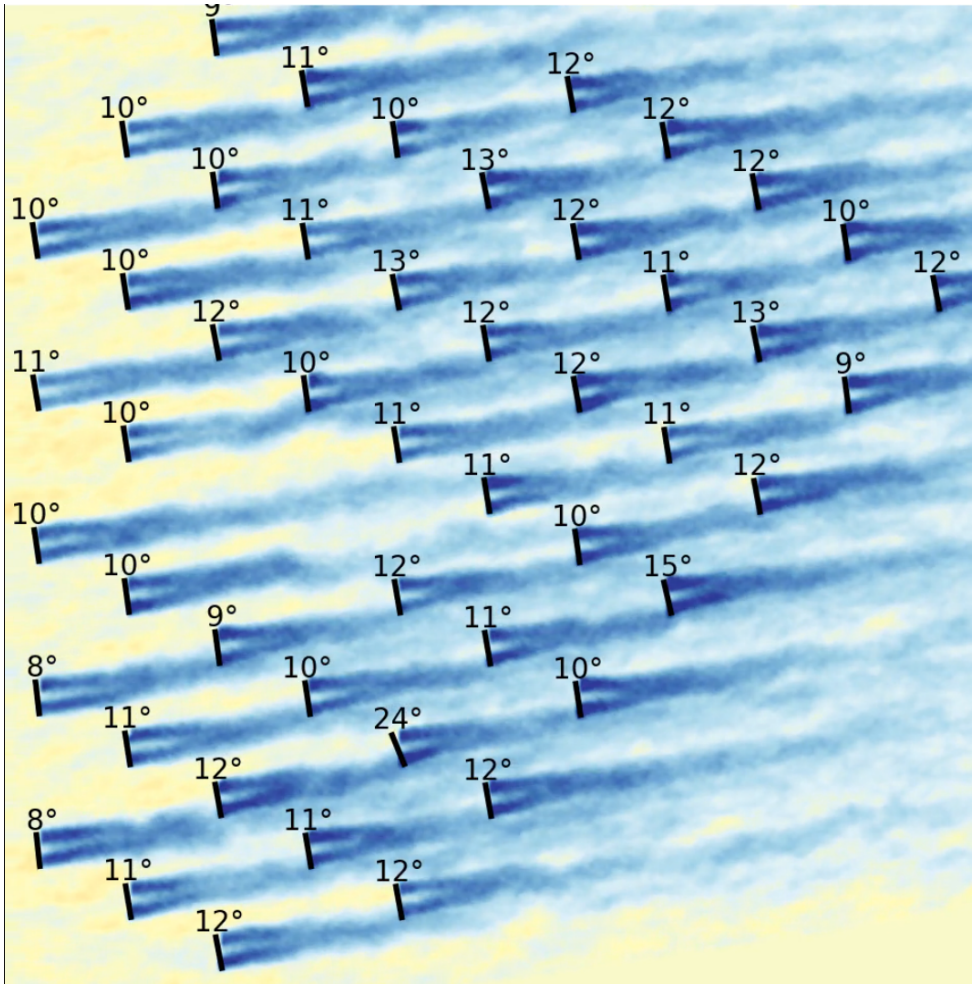


Figure 1: Snapshot of the Lillgrund wind farm dynamically simulated in HAWC2Farm with yaw misalignment of a single turbine.

3 Outcomes

- A dynamic wind farm simulation method (HAWC2Farm) was developed to capture dynamic wind farm behaviour in both short and long time scales, including aeroelastic turbine response, turbulence, dynamic wake effects, and with the ability to perform closed-loop control.
- The dynamic wind farm simulation method was verified against large-eddy simulations and is currently being validated against real-world measurements from the Lillgrund wind farm.
- A streaming algorithm was developed which is able to forecast wind farm power up to 20 minutes into the future while outperforming persistent forecasting.
- A model-free closed-loop wind farm control methodology using wake steering is currently being developed and tested using the HAWC2Farm framework.

References

[1] P. Gebraad, J. J. Thomas, A. Ning, P. Fleming, and K. Dykes. Maximization of the annual energy production of wind power plants by optimization of layout and yaw-based wake control. *Wind Energy*, 20(1):97–107, 2017.

[2] P. M. Gebraad, F. Teeuwisse, J. Van Wingerden, P. A. Fleming, S. Ruben, J. Marden, and L. Pao. Wind plant power optimization through yaw control using a parametric model for wake effects—a cfd simulation study. *Wind Energy*, 19(1):95–114, 2016.

[3] J. Jonkman, P. Doubrawa, N. Hamilton, J. Annoni, and P. Fleming. Validation of FAST.farm against large-eddy simulations. *Journal of Physics: Conference Series*, 1037:062005, jun 2018.

[4] S. M. Kakade. A natural policy gradient. *Advances in neural information processing systems*, 14, 2001.

[5] A. C. Kheirabadi and R. Nagamune. A quantitative review of wind farm control with the objective of wind farm power maximization. *Journal of Wind Engineering and Industrial Aerodynamics*, 192:45–73, 2019.

[6] G. Larsen, S. Ott, J. Liew, M. van der Laan, E. Simon, G. Thorsen, and P. Jacobs. Yaw induced wake deflection-a full-scale validation study. In *Journal of Physics: Conference Series*, volume 1618, page 062047. IOP Publishing, 2020.

[7] G. C. Larsen, H. A. Madsen, K. Thomsen, and T. J. Larsen. Wake meandering: a pragmatic approach. *Wind Energy*, 11(4):377–395, 2008.

[8] T. J. Larsen and A. M. Hansen. How 2 hawc2, the user's manual. *target*, 2(2), 2007.

[9] J. Liew, S. J. Andersen, N. Troldborg, and T. Göçmen. Les verification of hawc2farm aeroelastic wind farm simulations with wake steering and load analysis. In *Journal of Physics: Conference Series*, volume 2265, page 022069. IOP Publishing, 2022.

[10] J. Liew, T. Göçmen, W. H. Lio, and G. C. Larsen. Streaming dynamic mode decomposition for short-term forecasting in wind farms. *Wind Energy*, 25(4):719–734, 2022.

[11] J. Liew and G. C. Larsen. How does the quantity, resolution, and scaling of turbulence boxes affect aeroelastic simulation convergence? In *Journal of Physics: Conference Series*, volume 2265, page 032049. IOP Publishing, 2022.

[12] J. Liew, G. R. Pirrung, and A. M. Urbán. Effect of varying fidelity turbine models on wake loss prediction. In *Journal of Physics: Conference Series*, volume 1618, page 062002. IOP Publishing, 2020.

[13] W. H. Lio, M. Mirzaei, and G. C. Larsen. On wind turbine down-regulation control strategies and rotor speed set-point. In *Journal of Physics: Conference Series*, volume 1037, page 032040. IOP Publishing, 2018.

[14] H. A. Madsen, G. C. Larsen, T. J. Larsen, N. Troldborg, and R. Mikkelsen. Calibration and validation of the dynamic wake meandering model for implementation in an aeroelastic code. *Journal of Solar Energy Engineering*, 132(4), 2010.

[15] H. A. Madsen, T. J. Larsen, G. R. Pirrung, A. Li, and F. Zahle. Implementation of the blade element momentum model on a polar grid and its aeroelastic load impact. *Wind Energy Science*, 5(1):1–27, 2020.

[16] J. Mann. Wind field simulation. *Probabilistic engineering mechanics*, 13(4):269–282, 1998.

[17] J. A. Michelsen. Basis3D-a platform for development of multiblock PDE solvers. *Report AFM, Risø*, 1992.

[18] W. Munters and J. Meyers. Towards practical dynamic induction control of wind farms: analysis of optimally controlled wind-farm boundary layers and sinusoidal induction control of first-row turbines. *Wind Energy Science*, 3(1):409–425, 2018.

[19] K. Shaler, J. Jonkman, G. E. Barter, J. J. Kreeft, and J. P. Muller. Loads assessment of a fixed-bottom offshore wind farm with wake steering. *Wind Energy*, n/a(n/a).

[20] D. Silver, G. Lever, N. Heess, T. Degris, D. Wierstra, and M. Riedmiller. Deterministic policy gradient algorithms. In *International conference on machine learning*, pages 387–395. PMLR, 2014.

[21] N. N. Sørensen. *General Purpose Flow Solver Applied to Flow over Hills*. PhD thesis, Technical University of Denmark, 1995.

[22] H. Zhang, C. W. Rowley, E. A. Deem, and L. N. Cattafesta. Online dynamic mode decomposition for time-varying systems. *SIAM Journal on Applied Dynamical Systems*, 18(3):1586–1609, 2019.

18th EAWE PhD Seminar on Wind Energy
2 – 4 November 2022
Bruges, Belgium

FE Model Validation and Progressive Damage Analysis of a 5-m Composite Wind Turbine Blade under Monotonic Loading

C Muyan [a,b], OA Batmaz [a,b], D Coker [a,b]

[a] Dep. of Aerospace Engineering, Middle East Technical University, 06800, Cankaya, Ankara, Turkey
[b] RUZGEM (METUWIND), METU Center for Wind Energy Research 06800, Cankaya, Ankara,Turkey

E-mail: coker@metu.edu.tr

Keywords: progressive damage analysis, wind turbine blade, finite element model

Abstract

Main failure mechanisms of the 5-meter glass-fiber-reinforced-polymer (GFRP) RUZGEM wind turbine blade are investigated by implementing Puck's physically based phenomenological damage model. Initially the blade fe model is validated based on modal tests for the free-free boundary condition. Good agreement of the first five eigenfrequencies and eigenmodes between test and FE simulation is observed. After validating the model, the progressive damage analysis is conducted. Load is applied as a single point load in order to simulate full-scale testing conditions of blade subjected to flapwise (max) loading. As a result of progressive damage analysis utilizing Puck's model, the failure initiation region of the blade is predicted in the root transition region, at the spar-suction side intersection. Furthermore, with only Puck's model decrease in the load-displacement curve is observed after %99 loading.

1. Introduction

Wind turbine blades are among the most important components of a wind turbine with respect to turbine efficiency and cost. Severe blade failures, where repair is necessary may lead to a long wind turbine downtime. In order to prevent long wind turbine downtimes due to blade failures, reliable rotor blade designs are essential. This can be achieved with a broad understanding of the blade failure mechanisms. The scope of this work is limited to the understanding the main failure mechanisms of 5-m glass-fiber-reinforced-polymer (GFRP) RUZGEM wind turbine blade by using a global finite element modeling approach and progressive damage analysis under flapwise (max) loading.

2. Method

In order to validate the 5-m RUZGEM blade FE model, utilizing a modal shaker, experimental modal analyses are conducted. Blade testing condition is simulated by single the displacement-controlled load application at station 3.25 m, which resembles the bending moment over the blade segment 0-3.25 m range. For the progressive failure analysis of the blade, Puck's physically based phenomenological model is used [1]. ANSYS Parametric Design Language (APDL) is utilized to implement Puck's 2-D damage progressive model into the RUZGEM FE model. According to the Puck's progressive damage model, the degradation rules are applied to the plane stress elements as explained in [2].

3. Results and Discussions

5-m RUZGEM Blade is validated based on modal analysis results. The deviation of the eigenfrequencies for the first four eigenfrequencies between experiments and ANSYS simulations is less than 7%. For the fifth eigenmode which is torsion, the deviation between experiment and fe simulation is less than 11%. The reason for the higher deviation of the torsion eigenmode is attributed to the fact that shell elements used for building 5-m RUZGEM blade FE Model cannot predict torsion mode accurately. As seen Figure 1, Puck's physically based phenomenological model shows that laminate cracks initiate and propoagte at the root transition region. Decrease in the load-displacement curve is observed after %99 loading under flapwise (max) loading.

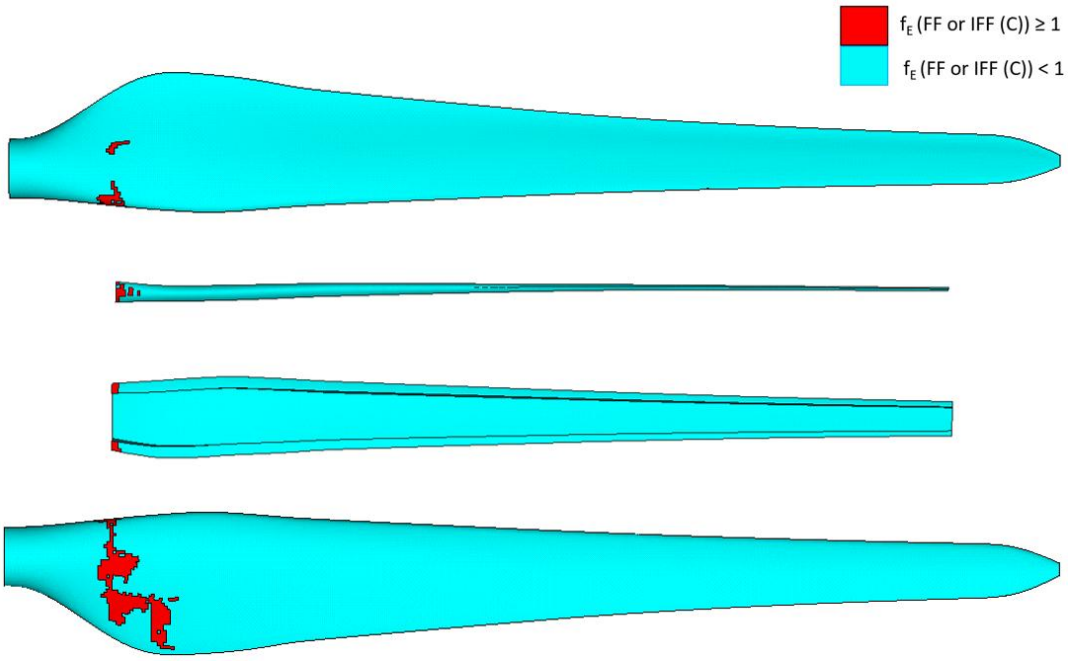


Figure 1: Element failure pattern in the pressure side, internal flange, spar and suction side of the blade (from top to bottom in a panel) before blade collapse under flapwise (max) loading.

Acknowledgements

This work was partly supported by RUZGEM (METUWIND), METU Center for Wind Energy Research at Middle East Technical University.

References

[1] A Puck, H Schürmann H. Failure Analysis of FRP laminates by means of physically based pheonomenological models. *Composites Science and Technology* 58:1045–1067, 1998.

[2] C Muyan, D Coker. (2020) Strength analysis of a 5-m composite wind turbine blade under static and fatigue loading conditions. *IOP Conference Series: Materials Science and Engineering. IOP Publishing,* p 012045, 2020.

18th EAWE PhD Seminar on Wind Energy
2-4 November 2022
Bruges, Belgium

Mitigating leading edge erosion in wind farms through optimal erosion-safe mode control

Jens Visbech[a]

[a]Department of Wind and Energy Systems, Technical University of Denmark (DTU), 4000 Roskilde, Denmark

E-mail: jvima@dtu.dk

Keywords: leading edge erosion, wind farm control, wakes, optimization

1 Introduction

Leading edge erosion (LEE) on wind turbine blades is a common problem that is heavily affected by the local wind and rain climate. Without preventive initiatives, LEE can occur after just a few years of operation and may require expensive unplanned repairs [4]. In addition, LEE negatively affects the aerodynamic properties of the blade as it degrades over time [2].
This study investigates the effects of implementing a simple LEE control strategy in a wind farm optimization framework. The LEE control strategy will utilize an operational mode called erosion safe mode (ESM) in which the rotor speed is reduced during heavy rainfall to limit the impact velocity of the droplets. This operational mode causes a negative impact on energy production but can potentially reduce repair costs during the operational phase [1].
The implementation of the ESM will be simulated on different sites using mesoscale weather data provided by the Danish Meteorological Institute (DMI) to characterize the joint wind and rain climate. The optimal control settings of the ESM will be determined using numerical optimization and the sensitivity to different input parameters will be tested. To capture the effects on both energy production and operational costs, the optimization problem is formulated such that it seeks to minimize the levelized cost of energy (LCoE).

2 Methodology

The optimization problem can be classified as a non-linear, continuous optimization where variables and models are continuous. In addition, the optimization is constrained by a single, deterministic objective. Finally, the optimization involves multiple different disciplines such as wind turbine control, meteorology, and cost modeling. The mathematical formulation of the optimization problem can be written as:

$$\min_{\omega_{ESM}, I_{thres} \in \mathbb{R}} \quad LCoE(\omega_{ESM}, I_{thres})$$

subject to

$$AEP_{loss} \leq AEP_{loss,upper}$$
$$0 \leq \omega_{ESM} \leq \omega_{rated}$$
$$0 \leq I_{thres}$$

where $LCoE(\omega_{ESM}, I_{thres})$ is the objective function which in this case is the levelized cost of energy. Two design variables are considered, namely the maximum allowed rotor speed during ESM operation ω_{ESM} and the rain rate threshold which activates the ESM operation I_{thres}. The optimization problem is subjected to a single inequality constraint which limits the AEP loss when running in ESM operation. In addition, there are bounds on the two design variables.

The optimization and design problem will be implemented through TOPFARM, a wind farm optimization tool under development by DTU Wind Energy, based on FUSED-Wind and OpenMDAO [5]. The overall flow of the ESM implementation is visualized in Figure 1.

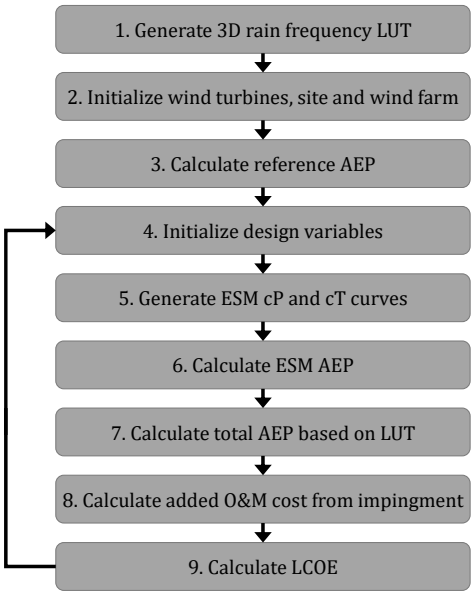


Figure 1: Flow diagram of the optimization steps.

Initially, the mesoscale weather data will be used to generate a 3D look-up table (LUT) which will have dimensions (wind speed bins, wind direction bins, and rain rate threshold). The value of each element will correspond to the normalized number of rain events above the threshold in each wind speed and wind direction bin, e.g. for a slice with a rain rate threshold of 0 mm/hr, we would simply consider all events and thereby get the original joint distribution of wind speed and direction. This look-up table will be used during optimization to calculate the fraction where ESM operation is activated.

Next, we will need to instantiate the wind farm by specifying turbine type, site conditions, and layout. Given the wind farm layout, we can compute the reference AEP which represents the energy production we would obtain without any ESM operation.

We then get to the actual optimization loop, which starts with initializing the design variables, i.e. the maximum tip speed during ESM operation and the rain threshold at which the ESM operation is activated. Using the maximum tip speed during ESM operation, we can compute a new rotor speed curve assuming that the ratio between power or thrust and rotor speed does not change when switching between normal and ESM operation. These new curves should be re-calculated every time the maximum tip speed is updated.

Based on the new ESM power and thrust curves, we then calculate the AEP we would get from operating entirely in ESM. Next, we extract the slice from our 3D look-up table corresponding to the chosen rain threshold. This slice allows us to estimate the ratio between normal and ESM operation. This value indicates how big of a fraction we should take from the reference AEP and ESM AEP. We use this to calculate the actual AEP (and AEP loss compared to the reference AEP). This AEP value is fed directly into our objective function.

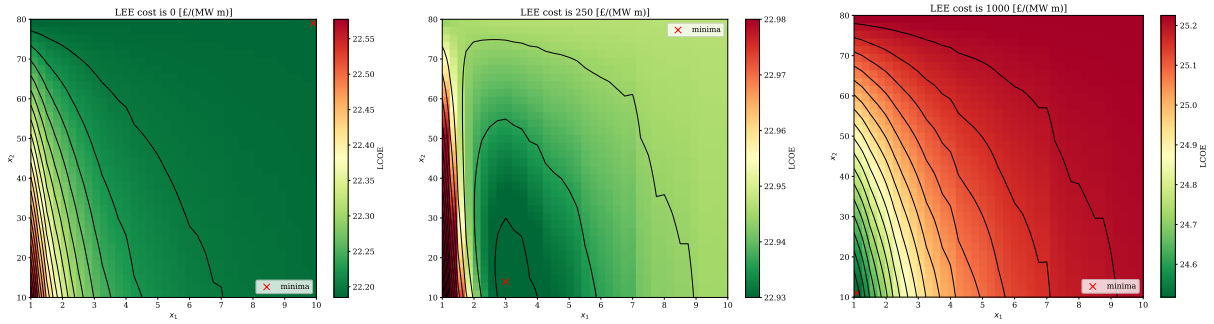
Finally, we will need to define the cost components that go into calculating the LCoE. For simplicity, we assume a fixed cost for the initial investment. We will use an erosion prediction model to determine the damage state of the blade, which can directly be linked to repair costs [6].

3 Preliminary results and future works

As a motivating example, we run an optimization for the offshore wind farm Princess Amalia located on the Dutch Continental Shelf in the Netherlands. The wind farm consists of 60 Vestas V80-2MW wind turbines. For simplicity, we will assume that the liquid impingement can be used as a proxy for erosion. The liquid impingement is defined as the amount of rain that hits the tip of the blade and can therefore be calculated based on the wind speed, rain rate, and rotor speed curve of the turbine [3]. We can then simply account for the added erosion costs by assuming a fixed price for every meter of impingement. This way we penalize the objective function when operating at high rotor speeds during rain. The added erosion cost was assumed to be fixed at 250 EUR/(MW·m).

The optimization was performed using random search which is a heuristic method that is already implemented in TOPFARM. The optimization was found to be feasible with a global minimum corresponding to a unique set of design variables. We find the optimal design variables as $\omega_{ESM} = 14.1$ m/s and $I_{thres} = 3.0$ mm/hr. It was found that these settings activated ESM operation 0.46 % of the time which resulted in an AEP loss of 0.30 %. The improvement in LCoE when using ESM with the optimal settings was found to be 0.13 %. Though this improvement appears to be very small, the actual cost savings from using optimal ESM operation will amount to several thousand euros.

In addition, we have performed a small parametric study to evaluate the sensitivity of the erosion cost parameter. We evaluate the surface response of the objective function for three different erosion costs, i.e. 0, 250, and 1000 EUR/(MW·m). The results can be found in Figure 2 which shows that the optimal ESM settings are very sensitive to the added erosion cost parameter.



(a) (b) (c)

Figure 2: Surface response of the objective function with added erosion costs of a) 0, b) 250 and c) 1000 EUR/(MW·m)

This preliminary study was used as a proof of concept to show the potential of implementing a leading edge erosion control strategy in a wind farm optimization framework. Numerical optimization was used to determine the optimal ESM control settings for a simplified case study of the offshore wind farm Princess Amalia. The optimization was feasible with an optimal LCOE of 22.92 EUR/MWh corresponding to a reduction of 0.13 % from the reference design. The optimization problem was found to be very sensitive to erosion cost parameters representing the added expense from operating during rainfall.
The simplistic implementation will be further improved by:

- Implement the erosion prediction model to get more realistic erosion cost estimates
- Extend the ESM control settings from a global wind farm level to individual turbines.
- Implement the effects of aerodynamic degradation on energy production.
- Perform a sensitivity analysis of the wind and rain climate to assess how the optimal control settings would vary for other sites

References

[1] J. I. Bech, C. B. Hasager, and C. Bak. Extending the life of wind turbine blade leading edges by reducing the tip speed during extreme precipitation events. *Wind Energy Science*, 3(2):729–748, 2018.

[2] N. Gaudern. A practical study of the aerodynamic impact of wind turbine blade leading edge erosion. In *Journal of Physics: Conference Series*, volume 524, page 012031. IOP Publishing, 2014.

[3] F. Heymann. Erosion by liquids. *Mach. Des*, 10:118–124, 1970.

[4] L. Mishnaevsky Jr and K. Thomsen. Costs of repair of wind turbine blades: Influence of technology aspects. *Wind Energy*, 23(12):2247–2255, 2020.

[5] P.-E. Réthoré, P. Fuglsang, G. C. Larsen, T. Buhl, T. J. Larsen, and H. A. Madsen. Topfarm: Multi-fidelity optimization of wind farms. *Wind Energy*, 17(12):1797–1816, 2014.

[6] J. Visbech, T. Göçmen, C. B. Hasager, H. Shkalov, M. Handberg, and K. P. Nielsen. Introducing a data-driven approach to predict site-specific leading edge erosion. *Wind Energy Science Discussions*, pages 1–30, 2022.

18th EAWE PhD Seminar on Wind Energy
2-4 November 2022
Bruges, Belgium

Modeling of wind energy systems under non-axial inflow conditions and the effect of low Reynolds number

Nadiia Afanasieva[a]

[a]RWTH Aachen University, Germany

E-mail: nadezda.a.afanasyeva@gmail.com

Keywords: reduced-order modeling, small variable-speed wind turbine, non-axial inflow, yaw angle.

1 Introduction

Present requirements for the high wind direction instability (so called Extreme Direction Change), which are typical at low hub heights and low wind speed, do not ensure an efficient operation of small wind turbines [4]. The basic consequence of low wind speed for a small wind turbine is low Reynolds number at the rotor blades [5], while wind direction variability leads to non-axial inflow (typically in the three dimensions) and associated imbalanced force distribution across the disk. When it comes to simulating the conditions highlighted the low accuracy of the reduced-order models of wind turbine aerodynamics used within the multiphysics simulation and bench tests of small horizontal axis wind turbines (SHAWT) is the typical issue, since low computational cost of the model is required in this case. This study addresses both the non-axial inflow conditions as well as the issue of low Reynolds number and the commonly used assumption of static Reynolds number, i.e., independent of wind speed and kinematic viscosity.

2 Methods

To solve the problem stated the traditional BEM-based (Blade Element Momentum Theory) aerodynamic model of the wind turbine rotor was extended with a correction model based on vortex theory to improve the accuracy of induced velocity calculation [1]. Based on the Biot-Savart law and the vortex cylinder model of the turbulent wake behind the rotor [2, 3] a correction model for induced velocity calculation was developed. The model allows to take into account the inflow angle three-dimensionally, as well as predicting the induced velocity profile on the rotor disk by introducing spatial parameters of the turbulent wake at a specific point of time into the model.

The volumetric vortex system of the turbulent wake is reduced to the distribution of vorticity on a cylindrical surface, to the so-called vortex cylinder (VC). Within the model, a radially discrete circulation distribution was proposed assuming that the circulation at each blade element is locally constant, and each blade element forms a vortex cylinder that is isolated and does not affect the neighboring ones. Thus, the vortex wake model takes the form of a system of nested elementary vortex cylinders. The model also takes into account the induced velocity due to the tower shadow effect.

The validation of the developed model was performed using the published experimental and calculated data of the projects “MEXICO” (Model Rotor Experiments in Controlled Conditions) and MexNext [6].

To simulate the conversion of kinetic energy in the wind into electrical energy a functional modelling of the system was performed, , based on a division of the computational process into functional blocks.

Using the methodology and MATLAB Simulink programming environment, a simulation model of a wind turbine based on a permanent magnet synchronous generator (PMSG) [7] was developed (fig. 1). The computational costs of the electrical energy conversion sub-model was reduced by simplifying the buck-boost DC-DC converter part, so that the proposed model of wind turbine aerodynamics allows to take into account the effect of non-axial inflow, tower shadow, and wind share.

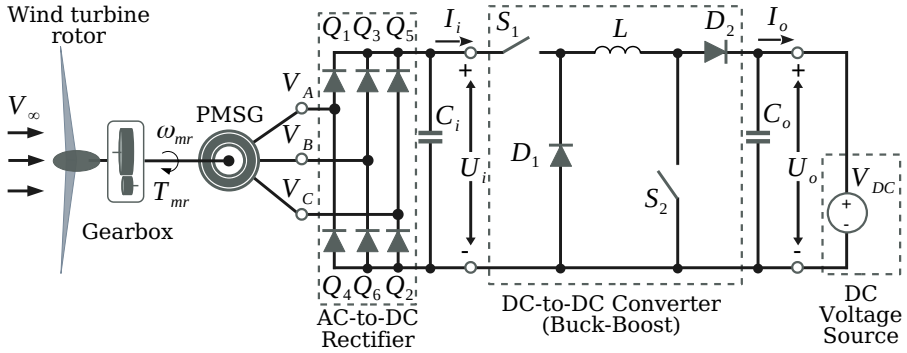


Figure 1: The coupled aerodynamic-mechanical-electrical model of PMSG-based wind energy system with speed control by ZDC-method and block determining the parameters controlling the DC-to-DC converter

3 Results and Discussions

The model was tested for a small two-blade HAWT with a radius of 1 m and a nominal wind speed of 12 m/s.

Figure 2 illustrates the imbalanced distribution of aerodynamic parameters across the disk under non-axial inflow conditions, as well as how this parameters influence each other.

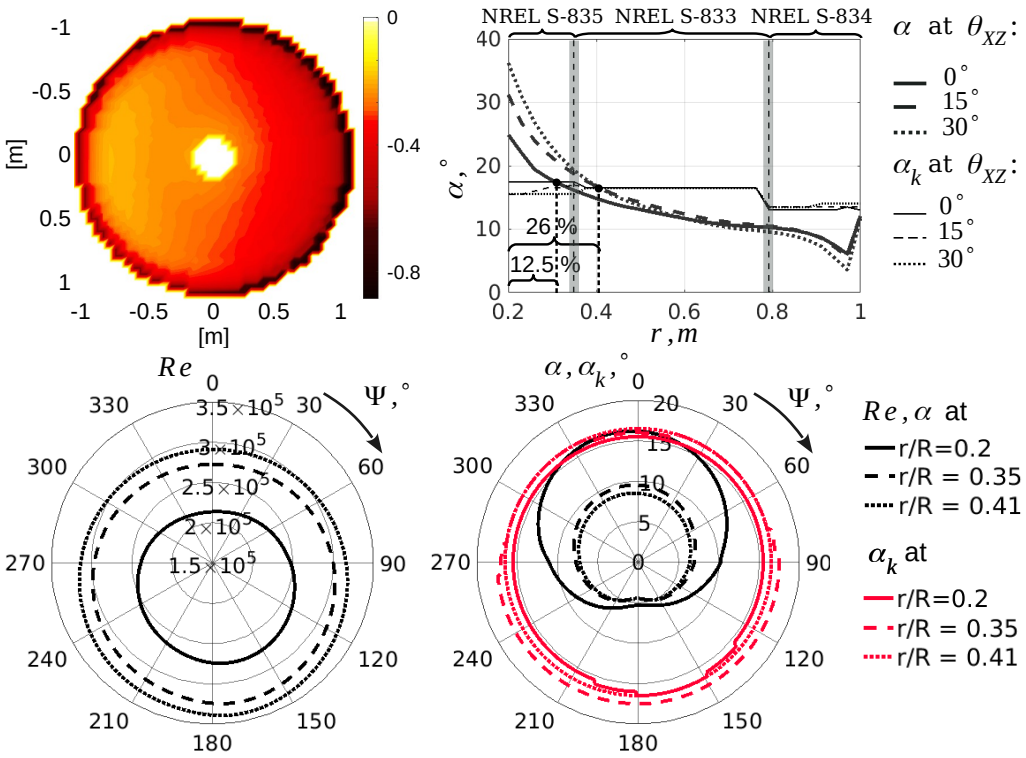


Figure 2: Profile of axial induced velocity coefficient on the rotor disk at $\theta_{XZ} = 30°$ (upper left), radial distribution of angles α_k (thin lines) and α (upper left) at $V_\infty = 17$ m/s (upper blade position, azimuth, $\Psi = 352°$), as well as azimuthal distribution of angles α_k, α (lower right) and Re (lower left) at $V_\infty = 12$ m/s and $\theta_{XZ} = 15°$

It can be seen (fig. 2, lower left) that the order of Re at nominal WT operating mode does not exceed 10^5. It follows that the lift and drag coefficients as a function of angle of attack, $C_L(\alpha)$ and $C_D(\alpha)$, respectively, and hence the forces and critical angle of attack, α_k, vary significantly withing one order of magnitude of Re. This fact emphasizes the value of the observed imbalance of aerodynamic parameters

across the disk at non-axial inflow.

Another interesting observation obtained relates to the condition $\alpha > \alpha_k$, which corresponds to the situation where stall at the blade is very likely. Under the nominal operating mode of the WT the condition $\alpha > \alpha_k$ is satisfied only at large values of θ_{XZ}. At $V_\infty = 17$ m/s (fig. 2, upper right) the radial distribution of Re changes and therefore changes the radial distribution of α and α_k. Even at $\theta_{XZ} = 0°$ the length of the section where $\alpha > \alpha_k$ amounts 12.5% of the blade length, while at $\theta_{XZ} = 30°$ this section reaches a value of 26%.

Thus, since the distribution of Re across the disk strongly affects the forces acting on the turbine blades, this could effect both the calculated operating loads and the estimated power curve of the WECS.

The variable Re allows performing more accurate simulations also at low wind speeds. At the same time, as the profile of aerodynamic parameters is predicted within the developed model, the oscillation of mechanical torque at the rotor shaft under various inflow angles can be modeled more precisely, allowing also the spectral decomposition of the oscillations. In multiphysics modeling, this expands the scope of application of the model, since the mechanical oscillations occurring under non-axial inflow conditions propagate further in the system causing also the oscillations of the electrical parameters (fig. 3).

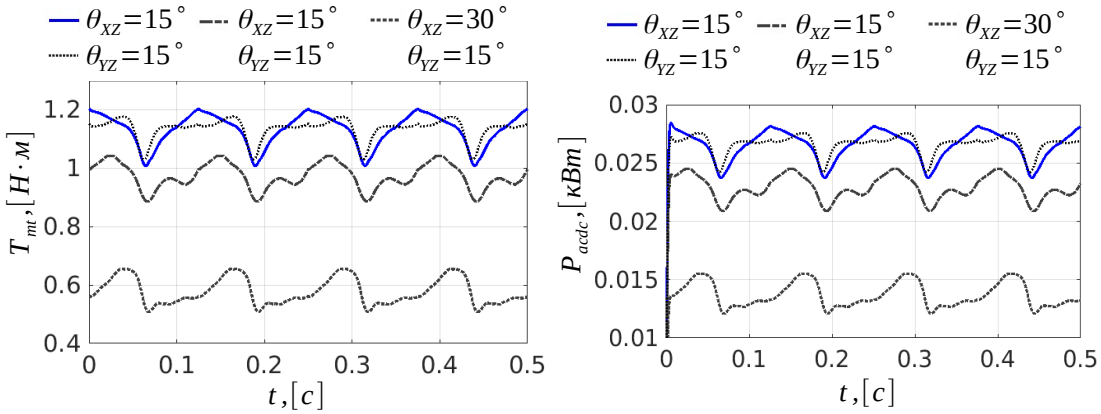


Figure 3: Time plots of the mechanical torque at the rotor shaft, T_{mt}, (left) and electrical power at the output of electrical system P_{acdc} (right) at $V_\infty = 4$ m/s and different angles of attack in the horizontal plane, θ_{XZ}, and vertical, θ_{XY}, planes

Finally, figure 4 shows the calculated theoretical power coefficient at the WECS output, $C_{P.acdc}$, at various values of θ_{XZ} as a function of V_∞. The calculation cases with static Re (i.e., independent of V_∞ and kinematic viscosity, constant within the blade segment with constant airfoil type) and variable Re (determined for each design element of the blade) are compared. It can be seen that the effect of Re is most pronounced at low wind speeds and at high θ_{XZ} angles.

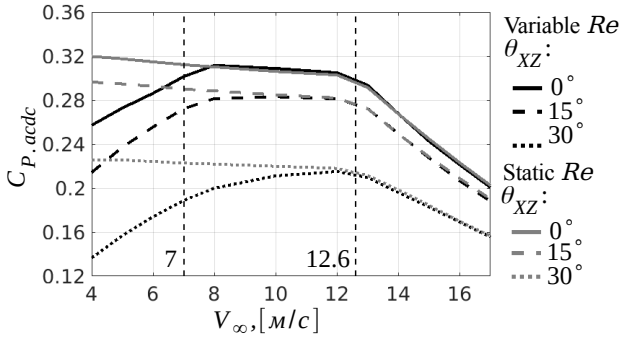


Figure 4: The average values of aerodynamic power coefficient, $C_{P.acdc}$, vs. wind speed, V_∞, as the yaw error, θ_{XZ}, increases from 0° to 30° for the cases of static and variable Re

The study shows that the peculiarities of the aerodynamic operating conditions of small HAWTs have a sufficient influence not only on their aerodynamic performance, but also on the system as a whole.

Two factors, the three-dimensional non-axial inflow and the low Reynolds number, are analyzed in detail, showing the superposition of both factors and their effects on the predicted parameters of the HAWT. The proposed model allows the highlighted factors to be taken into account, thus increasing the accuracy of multiphysics models while keeping the computational cost relatively low.

Acknowledgements

The author gratefully acknowledges the financial support of the German Academic Exchange Service – DAAD ("Michail Lomonosov" programme, ID 57391663) and the Ministry of Education and Science of the Russian Federation (applied scientific research task, ID 9.12731.2018/12.2).

References

[1] N. A. Afanasyeva. Wind turbines under yaw conditions. cylindrical vortex wake model for induced velocity calculation. In Materialien zum wissenschaftlichen Seminar der Stipendiaten der Programme «Michail Lomonosov» und «Immanuel Kant» 2018/2019, volume 15, pages 53–60, Moscow, 2019. DAAD, DAAD.

[2] E. Branlard. Wind turbine aerodynamics and vorticity-based methods, volume 10. Springer, 2017.

[3] R. P. Coleman, A. M. Feingold, and C. W. Stempin. Evaluation of the induced-velocity field of an idealized helicoptor rotor. Technical report, National Aeronautics and Space Administration Langley Research Center, 1945.

[4] T. Forsyth and R. Baranowski. IEA Wind TCP Task 27 Small Wind Turbine Technical Report. 9 2018.

[5] H. Lee and D.-J. Lee. Low reynolds number effects on aerodynamic loads of a small scale wind turbine. Renewable Energy, 154:1283–1293, 2020.

[6] W. Z. Shen, W. J. Zhu, and J. N. Sørensen. Actuator line/navier–stokes computations for the mexico rotor: comparison with detailed measurements. Wind Energy, 15(5):811–825, 2012.

[7] B. Wu, Y. Lang, N. Zargari, and S. Kouro. Power conversion and control of wind energy systems, volume 76. John Wiley & Sons, 2011.

18th EAWE PhD Seminar on Wind Energy
2-4 November 2022
Bruges, Belgium

Numerical simulations for active power control of wind farms

Simone Tamaro[a] and Carlo L. Bottasso[a]

[a]Technical University of Munich, Wind Energy Institute, Boltzmannstrasse 15, 85748, Garching, Germany

E-mail: simone.tamaro@tum.de

Keywords: wind farm control, CFD, power tracking

1 Introduction

The uncertainty of the power output of wind farms is a relevant issue for manufacturers, transmission system operators (TSO) and wind farm operators, since it can introduce additional and relevant costs for the stakeholders in order to balance the electrical grid [1]. With the growing penetration of wind energy in the electricity market, active power control (APC) methods are gaining strong interest in the industry as valid tools to balance power production and power consumption. Although APC is nowadays a basic requirement in the industry, the current practice is to derate the individual turbines to build an active power reserve, necessary to respond to potential fluctuations in the grid [2]. The aim of this research project is to advance the current status of power tracking control for wind farms, by developing affordable and reliable APC methods to optimize the distribution of set points in a waked wind farm with the goals of extending its lifetime, reducing risks of failures and optimizing the energy extraction.

2 Methodology

Feedback loop controllers for APC have been investigated extensively by [1, 3]. These controlling strategies take as input a reference signal from the TSO and compute the optimal set points distribution to achieve a wind farm output that matches the reference power signal. The non-unique solution of the problem makes it possible to combine power tracking with additional goals, such as structural fatigue mitigation. Figure 1 provides a sketch of a feedback loop for APC that operates according to real-time data from the wind turbines.
This research methodology aims at improving the current strategies for APC with high fidelity LES simulations. In particular, the non-uniqueness of the solution of APC is exploited to maximize the margin of each wind turbine within the wind farm, with the ultimate goal of improving the integration of wind energy into the electricity market. Computational fluid dynamics (CFD) is used as main tool to research and to test new control strategies. A version of the open-source software SOWFA developed at TUM will be used due to its reliability and suitability to deal with the complex dynamics typical of wind turbine wakes and wake interactions [4, 5]. The filtered-actuator line method (ALM) [6, 7] is used to model the blades, by projecting body forces computed with BEM onto the LES mesh grid.

The results carried out with this study will allow to improve the current integration of wind plants into the electricity grid, by providing the industrial stakeholders with methods at reduced costs and limited complexity.

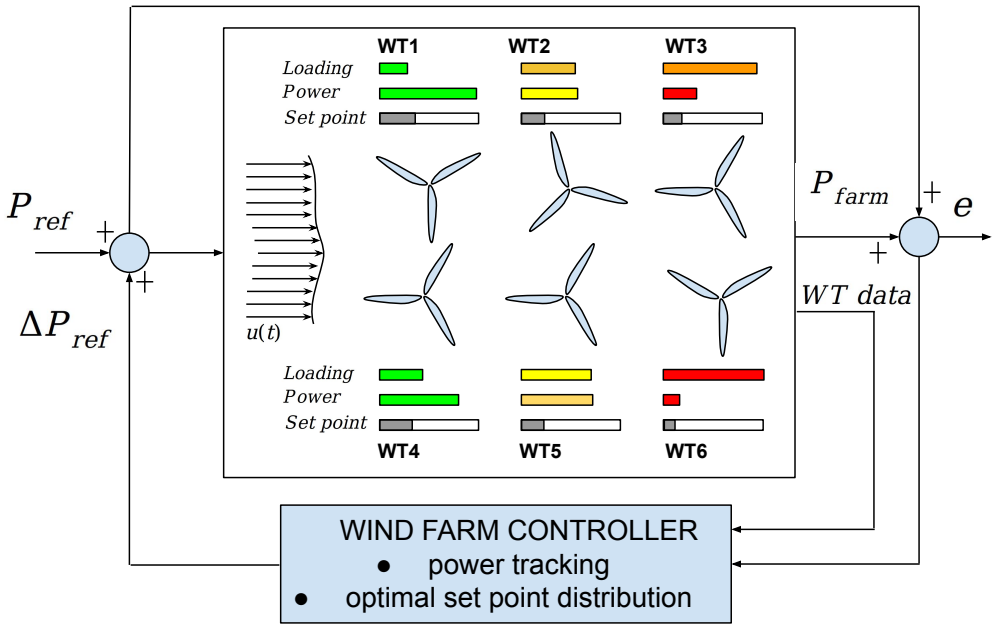


Figure 1: Schematic representation of a wind farm feedback control architecture for power tracking. The availability of real-time data from the wind turbines in the farm allows to achieve APC with additional objectives, such as loads minimization.

Acknowledgements

The authors acknowledge the support of the German Federal Ministry for Economic Affairs and Energy (BMWi) within the PowerTracker project to the present research project. The authors express their appreciation to the Leibniz Supercomputing Centre (LRZ) for providing access and computing time on the SuperMUC Petascale System under Projekt-ID pr84be Large-eddy Simulation for Wind Farm Control.

References

[1] van Wingerden J W, Pao L, Aho J and Fleming P 2017 *IFAC-PapersOnLine* **50** 4484–4491 ISSN 2405-8963 20th IFAC World Congress URL https://www.sciencedirect.com/science/article/pii/S240589631730722X

[2] Aho J, Buckspan A, Laks J, Fleming P, Jeong Y, Dunne F, Churchfield M, Pao L and Johnson K 2012 *2012 American Control Conference (ACC)* pp 3120–3131

[3] Vali M, Petrović V, Steinfeld G, Y Pao L and Kühn M 2019 *Wind Energy Science* **4** 139–161 URL https://wes.copernicus.org/articles/4/139/2019/

[4] Wang J, Wang C, Campagnolo F and Bottasso C L 2019 *Wind Energy Science* **4** 71–88 URL https://wes.copernicus.org/articles/4/71/2019/

[5] Wang C, Wang J, Campagnolo F, Carraón D B and Bottasso C L 2018 *Journal of Physics: Conference Series* **1037** 062007 URL https://doi.org/10.1088/1742-6596/1037/6/062007

[6] Troldborg N, Sørensen J N and Mikkelsen R 2007 *Journal of Physics: Conference Series* **75** 012063 URL https://doi.org/10.1088/1742-6596/75/1/012063

[7] Martnez-Tossas L A and Meneveau C 2019 *Journal of Fluid Mechanics* **863** 269292

18th EAWE PhD Seminar on Wind Energy
2 – 4 November 2022
Bruges, Belgium

On a nonlinear, objective coupling element in a director-based finite element formulation for structural modelling of wind energy turbines

David Märtins[a], Daniel Schuster[a], Christian Hente[a], Raimund Rolfes[a], Cristian Guillermo Gebhardt[b]

[a] Leibniz Universität Hannover, Institute of Structural Analysis, ForWind
[b] University of Bergen, Geophysical Institute (GFI) and Bergen Offshore Wind Centre (BOW)
E-mail: d.maertins@isd.uni-hannover.de

Keywords: multibody system, director-based finite element method, nonlinear coupling element, structural modelling, wind turbine

In recent decades, the demand for clean energy has increased significantly. As a result, larger wind turbines are needed to satisfy this demand efficiently today and in the future. With larger turbines, the dimensions of the whole structure increase and thus its sensitivity to large structural deformations becomes more relevant. The demand for a simulation tool analysing and designing those wind turbines requires a robust nonlinear structural model which allows to consider large deformations and large rotations in long-time simulations without suffering from numerical errors due to an inaccurate representation of physical quantities like objectivity and path independence as well as conservation of invariants.

There exist several well-established software tools to investigate the aeroelastic behaviour of wind energy turbines, e.g., FAST [1]. Bladed [2] or HAWC2 [3]. The structural model of those tools include multi-body approaches consisting of finite elements and rigid bodies based on geometrically linear or slightly nonlinear theories and kinematical descriptions in an updated Lagrangian formulation, which does not satisfy objectivity and path independence. These theories are well suited for analysing wind turbine structures where small to moderate deformations and rotations occur but cannot represent higher-order geometrically nonlinear effects with adequate accuracy.

However, maintaining objectivity, path independence and preserving invariants is crucial to avoid cumulative errors in nonlinear dynamic calculations, especially simulating long-term periods, as it is necessary for wind turbine design. In the structural model of our aeroelastic framework, we concentrate especially on this point to develop a nonlinear structural model. It consists of a robust nonlinear multibody system finite element scheme in the total Lagrangian description, considering director-based kinematics [4] to present geometrically exact kinematics. In order to ensure the conservation of energy and to preserve linear and angular momentum, we apply a conservative and dissipative time integration scheme developed by Gebhardt et al. [5]. In modelling a wind turbine, geometrically exact beam elements are used to model the tower and the slender blades. Rigid components, like hub and nacelle, are idealized by rigid bodies. Connections between the components, e.g., the driveshaft, the blade root-hub connection of a wind turbine have so far been assumed to be rigid and massless. In this work, we concentrate on developing a new generic nonlinear coupling element considering mass, stiffness and damping for modelling connections in our wind turbine model, see figure 1. Considering nodes A and B, a relative displacement generates elastic forces. Accordingly, a relative velocity causes damping forces and relative accelerations cause inertial forces. The main innovation is maintaining objectivity, following the philosophy of our structural model.

At the time being, the stiffness of the coupling element has already been developed and verified. It is based on a non-linear, objective deformation quantity to evaluate relative deformations between two finite element nodes. Nonlinear transformation matrices are derived to calculate an objective elastic stiffness matrix according to our director-based formulation. For verification of the coupling element comparative calculations were carried out with the commercial FE-software Abaqus FAE on the example of a flexible support of a beam loaded with a constant force on the tip. A relative deviation of 0.39% resulted for the static tip deflection. The first natural frequency of this system deviates by 0.29%.
In future work, mass and damping terms will be included. For the latter, it is necessary to determine a damping function that similarly does not violate objectivity. It is expected that a stress-dependent and velocity-dependent damping function will have to be developed, as it was worked out in likewise manner by Armero et al. [6].

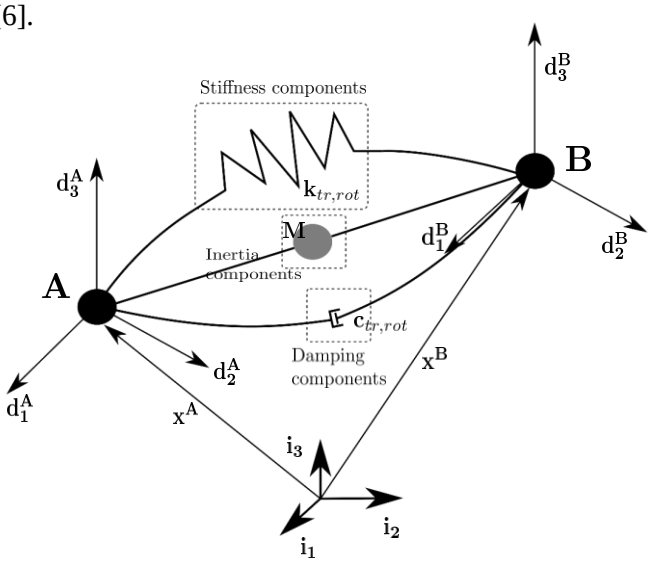


Figure 1: schematic illustration of the coupling element between two finite element nodes A and B

Acknowledgements

This work was funded by the Deutsche Forschungsgemeinschaft (DFG, German Research Foundation) Project-ID 434502799 – SFB 1463.

References

[1] Jonkman, J.M., Buhl Jr, M.L., 2005. FAST User's Guide National Renewable Energy Laboratory

[2] Bossanyi, E.A., Witcher, D., Quarton, D.C., 2003 GH Bladed User Manual

[3] Larsen, T.J., Hansen, A.M., 2019. How 2 HAWC2, the user's manual. Risø National Laboratory

[4] Gebhardt, C., Hofmeister, B., Hente, C. & Rolfes, R., 2019. Nonlinear dynamics of slender structures: a new object-oriented framework. *Computational Mechanics*, 63:219-252

[5] Gebhardt, C., Romero, I., Rolfes, R., 2019. A new conservative/dissipative time integration scheme for nonlinear mechanical systems. *Computational Mechanics* 65:405-427

[6] Armero, F., Romero, I., 2003. Energy-dissipative momentum-conserving time-stepping algorithms for the dynamics of nonlinear cosserat rods. *Computational Mechanics* 31, 3-26

Electrical conversion, energy system and wind power-to-X

18th EAWE PhD Seminar on Wind Energy
2 – 4 November 2022
Bruges, Belgium

Advance Generative Model for Scenario Generation of Wind Power Distributions With Hight Granularity

Seyyed Ahmad Hosseini[a], Jean-François Toubeau[a], Francois Vallee[a]

[a] Electrical Power Engineering Unit, University of Mons, Mons, Belgium

E-mail: seyyedahmad.hosseiniqarehtapeh@umons.ac.be

Keywords: *Wind power distribution, Scenario Generation, Generative model*

1 Abstract

The current wind farm control schemes qualify wind power producers (WPPs) to provide balancing services in modern electricity markets. Accordingly, WPPs are responsible for real-time deviations in the reserve market, settled every few seconds within a market period [1]. Therefore, WPP require to integrate intra-period wind variability in energy trading framework. As a main ingredient of such frameworks, in this work, we devise a novel scenario generation technique, i.e., Auxiliary Classifier Wasserstein Generative Adversarial Networks (ACWGAN), to produce intra-period wind power distribution with high-temporal-resolution. Notably, the generator of the neural network is appropriately constrained to return temporal distributions as the output.

2 Introduction

The recent advancements in generative adversarial networks (GANs) draw wide attention to their application regarding model-free scenario generation for renewable energy sources [2]. In [3], CWGAN is used to model load forecast uncertainty based on historical load measurements. However, the performance of CWGAN can be further improved by exploiting an auxiliary classifier (ACWGAN) in the network design to predict the class labels instead of feeding them as an input to the network. It is shown in [2] that such a design can return high-quality outputs for wind trajectories. This advanced architecture will be used and optimized in this paper to generate representative forecast scenarios of wind distribution, which requires advanced adaptation based on wind power expertise.

3 Methodology

A GAN consists of an interconnected network comprising a generator $G_\alpha(\cdot)$ and discriminator $D_\beta(\cdot)$ which compete in a zero-sum game. The neural networks' parameters are shown by subscripts. The generator $G_\alpha(\cdot)$ samples a latent noise vector z from the latent space with the probability distribution $\mathcal{P}_Z$, as input and attempts to map it to realistic-looking data s_g in the output $G_\alpha(z)$. Conventional CWGAN learns a representation of z that depends on class labels as it receives them as input to the network. In other words, CWGAN requires D_β to return an estimate of the distance between generated and real joint distributions of class labels c and samples, by merging c to either z or s_r (real samples), since it receives them as input. The complicated task of D_β, measuring the discrepancy between the real and generated joint distributions, and G_α, mapping the latent space to real data distribution, can be alleviated by incorporating a new agent into the adversarial training process. The additional agent, which is a classifier $\mathcal{C}_\varsigma(\cdot)$ and cooperates with $D_\beta(\cdot)$ and $G_\alpha(\cdot)$, estimates the conditional probability of the class labels given the received samples.

The input-output diagram of ACWGAN is shown in Fig. 1. It is seen that the critic of ACWGAN, has two outputs, shown by green arrows. The first output, $D_\beta\big(H_h(\cdot)\big)$, obtains the WD between real and

generated distributions while the second output, $\mathcal{C}_\varsigma(H_h(\cdot))$, predicts the class label of the provided sample (H_h is the hidden layers of the critic). Finally, ACWGAN is trained by sequentially updating the parameters of the new critic and generator through loss feedbacks $\mathcal{L}_{AW}^{D}$ and $\mathcal{L}_{AW}^{G}$. The loss function of critic and generator are respectively represented by (1) and (2):

$$\begin{aligned}\mathcal{L}_{AW}^{D} = &\max_{\{h,\beta,\varsigma\}} \mathbb{E}_{s_r\sim\mathcal{P}_r}\left[D_\beta\left(H_h(s_r)\right)\right] \\ &- \mathbb{E}_{s_g\sim\mathcal{P}_g}\left[D_\beta\left(H_h(s_g|c)\right)\right] - \eta_{GP}\mathbb{E}_{\hat{s}\sim\hat{\mathcal{P}}}\left[\left(\nabla_{\hat{s}}\left\|D_\beta\left(H_h(\hat{s}|c)\right)\right\|_2 - 1\right)^2\right] \\ &+ \eta_c\mathbb{E}_{s_r\sim\mathcal{P}_r}\left[\log\mathbb{P}\left(\mathcal{C}_\varsigma\left(H_h(s_r)\right) = c\right)\right] \\ &+ \eta_c\mathbb{E}_{s_g\sim\mathcal{P}_g}\left[\log\mathbb{P}\left(\mathcal{C}_\varsigma\left(H_h(s_g)\right) = c\right)\right]\end{aligned} \quad (1)$$

$$\begin{aligned}\mathcal{L}_{AW}^{G} = &\max_{\alpha}\mathbb{E}_{s_g\sim\mathcal{P}_g}\left[D_\beta\left(H_h(s_g|c)\right)\right] \\ &+ \eta_c\mathbb{E}_{s_g\sim\mathcal{P}_g}\left[\log\mathbb{P}\left(\mathcal{C}_\varsigma\left(H_h(s_g)\right) = c\right)\right]\end{aligned} \quad (2)$$

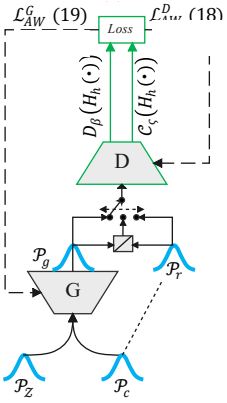


Fig.1. The training of the proposed ACWGAN

where η_{GP} is the gradient penalty coefficient concerning the 1-Lipschitz regularity condition and $\hat{s}$ symbolizes the linearly interpolated data points belonging to $\mathcal{P}_r$ and $\mathcal{P}_g$. $\nabla\|\,.\,\|_2$ is the gradient norm and η_c is the classifiers scale coefficient. $\log\mathbb{P}(\,)$ is the log-likelihood loss.

The generator's output layer should satisfy the conditions imposed by general distributions' shape. To do so, we use a SoftMax layer at the output of G_α to guaranty that the generated mass on each interval sums up to 1 and is non-negative. The standard (unit) softmax function $\sigma(z)\colon \mathbb{R}^K \to (0,1)^K$ is defined when K is greater than one by $\sigma(z)_i = \frac{e^{z_i}}{\sum_{j=\{1,\dots,K\}} e^{z_j}}$.

The output of generator after training for a given condition is given in Fig.2. In this figure scenarios corresponding to the predicted trajectory (in black) is given by coloured curves. In future, the proposed method will be used to generate wind distribution scenario using real data.

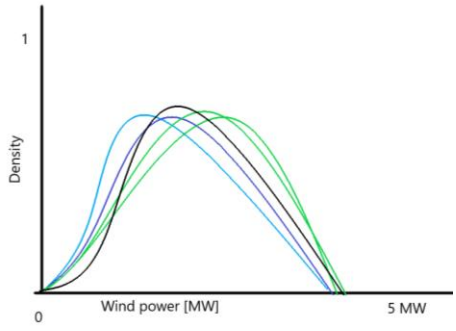


Fig. 2. The candidate scenarios generated with respect to black wind distribution.

References

[1] S. A. Hosseini, J.-F. Toubeau, Z. De Grève and F. Vallée, "An advanced day-ahead bidding strategy for wind power producers considering confidence level on the real-time reserve provision", *Appl. Energy*, vol. 280, p. 115973, 2020.

[2] S. A. Hosseini, J. F. Toubeau, Z. de Greve, Y. Wang, N. Amjady, and F. Vallee, "Data-Driven Multi-Resolution Probabilistic Energy and Reserve Bidding of Wind Power," *IEEE Transactions on Power Systems*, 2022.

[3] Y. Wang, G. Hug, Z. Liu and N. Zhang, "Modeling load forecast uncertainty using generative adversarial networks", *Electr. Power Syst. Res.*, vol. 189, p. 106732, 2020.

18th EAWE PhD Seminar on Wind Energy
2 – 4 November 2022
Bruges, Belgium

Comparison of Hybrid Wind Power Plant Sizing Optimization Methods

Charbel Assaad[a], Juan Pablo Murcia Leon[a]

[a] DTU Wind Energy

E-mail: chass@dtu.dk

Keywords: Hybrid Power Plants, Sizing, Optimization

1. Introduction

Fuelled by environmental concerns, incentive policies and technological advancement, renewables and storage devices have become cost competitive. To further enhance sustainable energy production, researchers combined various production (mainly renewables) and storage technologies in one power plant known as a Hybrid Power Plant (HPP).
HPP present many advantages, compared to a single-technology power plant, such as [1], [2]:

- Reduction of variability thanks to synergies between technologies, like wind and solar.
- Economies of scope: reduced land usage, shared electrical infrastructure and soft costs.
- Improved grid stability: HPPs can provide more grid support due to their increased availability.
- Participation to various electrical markets (bulk, balancing, ancillary…) thanks to HPP's flexibility.

However, for such advantages to materialize, the planning process of a HPP needs to be optimized. Within that process, optimal sizing of each component and the operational strategy, is among the first crucial step and will be the focus of this paper.
In the past decades, the research has mainly focused on off-grid HPP [3], [4]. However, to increase the environmental impact of sustainable production, utility-scale grid connected HPP should be developed.
This work provides a preliminary review on sizing optimization methodologies for HPP. The relevance of utility-scale HPP and the importance of considering uncertainty in the sizing is also reviewed.
This preliminary review is a first step towards a more extensive review on the identification of utility-scale HPP sizing needs and research gaps.

2. Sizing optimization methodologies

Within the scope of this review, a HPP comprises at least two production units of which one must be renewable based, the presence of a storage is optional. Grid-connected and off-grid systems will be considered.
Sizing optimization of HPP seeks to identify the best configuration and capacity of each component to maximize or minimize for a given metric.
From a power plants developer's point of view, the initial sizing of a HPP serves as a screening for the viability of a project. Hence, the developed sizing methodology should be relatively fast.

Figure 1 presents optimization technics used for HPP sizing.

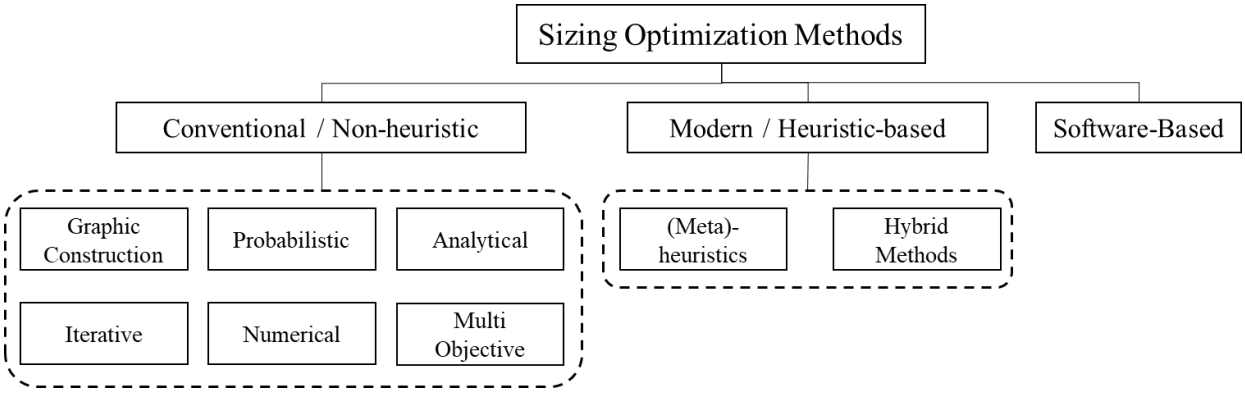


Figure 1 Optimization Technics for Sizing of HPP

L. K. Anoune et al. [5] presented each of the above-mentioned technics while S. Sinha. et al. [6] highlighted the strength and weakness of the most used heuristic-based technics and A. Chauhan et al. [7] underlined the differences within the commercial software tools used for sizing of HPP.

For a given category and method, differences can still be observed. Sizing optimization doesn't only involve the selection of the sizing method but also, the selection of the objective function (which metric is maximized/minimized), the design variables (what is allowed to vary to reach the optimal objective function), and the constraints (including the modeling of each component).
Objective functions can be classified in one of the following categories: economical, reliability, environmental, or social. M. Al-falahi et al. [8] presented an extensive list of objective functions used in the research field for PV and Wind-based power plants. W. Theo et al. [3] reviewed several models for wind and solar power generation that could be used for sizing.

3. Trends in HPP sizing optimization

3.1. Heuristics and Classical methods

During the past two decades, trends within the field have emerged.
The conventional technics (also known as classical or traditional technics in the literature) were initially predominant. However, with the development of Artificial Intelligence (AI), heuristic-based technics became the dominant category for sizing optimization. In fact, this category is often called trending or new generation. S. Sinha et al. [6] illustrated this trend for PV-Wind based power plants within published papers between 1996 and 2015.
Heuristics-based method are seen as more flexible with good convergence speed. They are generally easy to implement and can be manipulated with ease. They also provide a fast and more efficient global search solution. However, they do not guarantee optimality, and it is not possible to identify the gap to the global optimal solution.
Hybrid metaheuristic algorithm combine at least two different metaheuristics. They are typically complementary, combining the strength of an algorithm to cover for the drawback of another, or additive, the strength of an algorithm is further reinforced by another one.
While this tends to result in a more efficient solution that converges faster, it comes with higher coding complexity and is harder to manipulate as more parameters are used.
Nonetheless, M. Al-falahi et al. [8] showed a (slightly) increasing trend in hybrid algorithm being used in the research field for sizing optimization of HPP.

The advantages and drawbacks for the three most used metaheuristics technics are given below:

Metaheuristic	Advantage	Drawback	Source
GA: Genetic Algorithm	Easy to understand and transferable/adaptable to different problems. Suitable for the multi-objective optimizations. High performance in the search process.	Could converge towards local optima or arbitrary points. No constant optimization response times. It requires many iterations, which increase response time.	[9], [10], [11]
PSO: Particle Swarm Optimization	Converges fast. Calculation is very simple as compared to other methods. Needed iterations to reach optimum is less affected by objective function.	Problem needs to be formulated in the coordinate system. Easily reaches partial optimism/premature convergence.	[6], [12], [13]
SA: Simulated Annealing	Avoids local minima trapping. Can deal with highly nonlinear models, chaotic and noisy data, and many constraints.	Poor outcome quality as compared to other metaheuristics.	[6]

Table 1 Advantages and Drawbacks of Metaheuristic-based technics

3.2. Mono-objective and multi-objective optimization

A shift from mono-objective to multi-objective optimization has been observed by A. Mahesh et al. [10].
This is in partly driven by the need to consider more than just the economic aspect of the power plant. Reliability and environmental aspects are playing an increasingly important role in the sizing decisions.
There are two general approaches to solve multi-objective optimization problems.
The problem can be reduced to a mono-objective problem by:

- Combining all objective functions into one with a weighted sum. The weights can also be subject to an optimization process.
- Introduce each objective function as a constraint, except for one (which becomes the main objective function that is being optimized for).

The second approach is to find the Pareto optimal set. Which is the set of solutions where none of the objective functions can be further improved without degrading the value of another objective function.
T. Tezer et al. [15] Reviewed multi-objective approaches used to optimized off-grid HPP. Conventional and Heuristic-based methods were also presented.

3.3. Objective functions

There are four main categories of objective functions: Economic, Reliability, Environment, and Social. For a given site, the final sizing obtained from the optimization process can be greatly influenced by the objective function. J. Lian et al. [15] showed that the most used metrics fall in the category of “Economic” for (single-objective problems) and “Reliability and Economic” (for multi-objective problems).
Economic criteria are dominating since financial investments can hardly be justified without an economically viable project. As for reliability, it is of great concern for off-grid systems (which are predominant) since a stable energy production is often desirable.

3.4. Grid connected and Off-grid

Another staggering trend is the proportion of HPP not connected to the grid. Through all the reviewed papers, J. Lian et al. [15] showed that 80% of HPP studied were off-grid. When considering the main driver for the initial development of HPP, this trend isn’t surprising. Historically, they have been developed to provide energy (electrical or thermal) for rural areas where extending the grid isn’t economically viable. However, since the first HPP has been installed, renewables have developed considerably, the electricity market is evolving, and new opportunities for large-scale grid connected HPP have emerged.
This will be the focus of section 5.

4. Comparison of optimization methods

In this section, a case study will be used to compare the results of sizing optimization formulated with a Mixed-Integer Linear Programming (MILP) formulation and a heuristic-based formulation.
The sizing methodology will be based on the study from R. Rigo-Mariani et al. [21]. It will be briefly presented in the following subsection.
The results of the comparison will be presented during the Seminar, as they are not available yet.

4.1. Methodology

The method developed in [21] is a 2-level optimization process. The objective is to minimize the Total Cost of Ownership of a grid connected HPP. The produced energy can be sold to the gird or provided to a load.
An Efficient Global Optimization (EGO) algorithm is used to optimize the size of the HPP. The EGO investigates a surrogate of the cost function (created with Kriging Interpolation) to identify the best design variables to be used in the next optimization iteration.
For a given iteration, once the sizing is fixed, the CapEx can be determined. The OpEx can be then determined by optimizing Energy Management System (EMS) over 365 days (the simulation period). The EMS is optimized with a MILP.

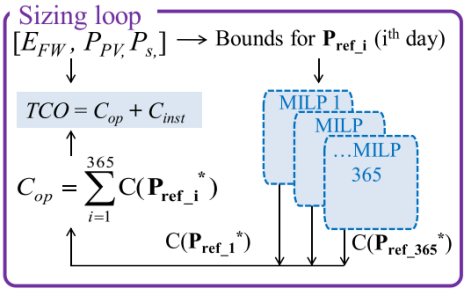


Figure 2 Design approach of the microgrid with a bi-level optimization [21]

5. Utility-scale HPP (UHPP)

Unlike off-grid HPP, grid-connected utility-scale HPP (UHPP) range between several MW to hundreds of MW with an objective to maximize profit from the market.
Hence, UHPP could be seen as one solution that can massively contribute to the green transition by replacing existing conventional power generation units.

5.1. Relevance of Utility-scale HPP (UHPP)

Combining wind and solar on a large scale can significantly decrease the power output fluctuation and ramp rates, as shown in [1].
Capital Expenditure (CapEx) and Operational Expenditure (OpEx) reduction can also be expected as electrical infrastructure can be shared. Additionally, over-planting per substation without any added curtailment is possible as mentioned by the report [16].
The presence of storage can provide access to various electrical markets, conferring a high level of flexibility to the power plant. Depending on the type of storage, a UHPP can participate in the day-ahead and intraday markets, balancing markets, and ancillary services markets.
Storage systems can also further reduce the power fluctuation from the stochastic solar radiation and wind speed [17]. This is relevant to fulfil grid code requirements.
Furthermore, existing onshore wind power plants under-use the available land to produce electricity. PV panels could be added to exploit the available space and produce energy. A. R. Silva et al. [22] have demonstrated the added value of converting wind power plants into UHPP by adding solar PV.

5.2. Important consideration: uncertainty

The inherent stochastic nature of wind and solar radiation is the source one major difficulties in analysing power system performances. The resulting high uncertainty has thawed the development of UHPP. This intermittency in power production is also found in hydroelectric power plants due to the seasonal variability in rainfall intensities.
Hence, to further develop UHPP, it is recommended to consider uncertainties in the sizing process.
Traditionally, off-grid HPP for application that require to abide by rigorous norms of power supply reliability as hospitals and telecommunication towers, used diesel generators as a back-up source. This led to oversizing and considerable added costs. To avoid oversizing, few authors included uncertainty considerations in their sizing optimization. [18] have sized an off-grid HPP using Monte-Carlo simulations to account for uncertainties in resources (wind speed, solar radiation). [19] added another dimension by considering uncertainties related to load demand.
Grid-connected UHPP differ from off-grid HPP in terms of uncertainty considerations. As UHPP provide energy to the grid, the load demand uncertainties are of no concern. However, uncertainties due to market forecasts is another dimension that should be considered. In his M.Sc. thesis, S. Satheesh [20] has developed an algorithm for multiple market participation while considering forecast uncertainties of wind and solar energy. However, only the battery energy system was sized, wind and solar capacities were given as input. Market price uncertainties were also not considered.

6. Conclusion

Sizing optimization techniques can be roughly divided in two categories, the traditionally used technics also known as classical and the heuristic-bases techniques. While each have their specific uses, the research community has leaned towards heuristic-based techniques for sizing optimization. Out of these methods, GA, PSO and SA are mostly used. They are easy to implement and provide good convergence speed with efficient global search results. To further improve these search algorithms, hybrid metaheuristic algorithm, combining more than one heuristic technique were developed and are gaining in popularity. The need to consider more than just the economic aspect in the design of HPP has led to the use of multi-objective optimization. Nonetheless, economics-based objective-functions are still the dominant metric.
Historically, HPP were developed to provide electricity for rural areas that aren't connected to the grid. However, with the increase in renewable technology's maturity and decreasing prices, grid-connected utility-scale HPP is becoming a viable alternative to conventional power plants. Increasing the viability of UHPP requires, among other things, considering uncertainties in the initial design. The main sources of uncertainties are wind and solar power forecasting, and market price forecasts. As this is one of the major obstacles to the development of UHPP and there is little research on it, I will contribute to it in my PhD.

Acknowledgements

This research is conducted in the scope of a Ph.D. hosted by DTU Wind.
Warm thanks to Juan Pablo Murcia Leon, Kaushik Das, and Katherine Dykes, who supervised my work.

References

[1] K. Das et al. Enhanced Features of Wind-Based Hybrid Power Plants. *4th International Hybrid Power Systems Workshop,* 2019.
[2] K. Dykes. Opportunities for Research and Development of Hybrid Power Plants. *NREL/TP-5000-75026,* 2020.
[3] W. Theo et al. Review of distributed generation (DG) system planning and optimisation techniques: Comparison of numerical and mathematical modelling methods. *Renewable and Sustainable Energy Reviews* 67:531-573, 2017.
[4] Faccio, M., et al. *State-of-art review of the optimization methods to design the configuration of hybrid renewable energy systems (HRESs)*. Frontiers in Energy 12, 591–622, 2018.
[5] K. Anoune, M. Bouya, A. Astito, A. B. Abdellah, *Sizing methods and optimization techniques for PV-wind based hybrid renewable energy system: A review*. Renewable and Sustainable Energy Reviews.

93: 652–673, 2018.

[6] S. Sinha, S. S. Chandel, *Review of recent trends in optimization techniques for solar photovoltaic-wind based hybrid energy systems*. Renewable and Sustainable Energy Reviews. 50: 755–769, 2015.

[7] A. Chauhan, R. P. Saini, *A review on Integrated Renewable Energy System based power generation for stand-alone applications: Configurations, storage options, sizing methodologies and control*. Renewable and Sustainable Energy Reviews. 38: 99–120, 2014.

[8] M. D. A. Al-falahi, S. D. G. Jayasinghe, H. Enshaei, *A review on recent size optimization methodologies for standalone solar and wind hybrid renewable energy system*. Energy Conversion and Management. 143: 252–274, 2017.

[9] Eftichios Koutroulis, Dionissia Kolokotsa, Antonis Potirakis, Kostas Kalaitzakis. *Methodology for optimal sizing of stand-alone photovoltaic/wind-generator systems using genetic algorithms*, Solar Energy, 80: 1072-1088, 2006.

[10] A. Mahesh, K. S. Sandhu. *Hybrid wind/photovoltaic energy system developments: Critical review and findings. Renewable and Sustainable Energy Reviews*. 52:1135–1147, 2015.

[11] R. Siddaiah, R. P. Saini. *A review on planning, configurations, modeling and optimization techniques of hybrid renewable energy systems for off grid applications.* Renewable and Sustainable Energy Reviews. 58: 376–396, 2016.

[12] M. Sharafi, T. Y. ELMekkawy. *Multi-objective optimal design of hybrid renewable energy systems using PSO-simulation based approach*. Renewable Energy, 68:67-79, 2014.

[13] M. Amer, A. Namaane, N.K. M'Sirdi. *Optimization of Hybrid Renewable Energy Systems (HRES) Using PSO for Cost Reduction.* Energy Procedia, 42:318-327, 2013.

[14] T. Tezer, R. Yaman, G. Yaman. *Evaluation of approaches used for optimization of stand-alone hybrid renewable energy systems*. Renewable and Sustainable Energy Reviews. 73:840–853, 2017.

[15] J. Lian, Y. Zhang, C. Ma, Y. Yang, E. Chaima, *A review on recent sizing methodologies of hybrid renewable energy systems.* Energy Conversion and Management. 199, 2019

[16] K. Knorr, B- Zimmermann, S Bofinger, A-K. Gerlach, T. Bischof-Niemz, C. Mushwana, *Wind and Solar PV Resource Aggregation Study for South Africa*," reprot by Fraunhofer IWES, November, 2016

[17] G. Wang, M. Ciobotaru and V. G. Agelidis, *Power Smoothing of Large Solar PV Plant Using Hybrid Energy Storage*. IEEE Transactions on Sustainable Energy, 5:834-842, July 2014.

[18] M. Bashir and J. Sadeh. *Optimal sizing of hybrid wind/photovoltaic/battery considering the uncertainty of wind and photovoltaic power using Monte Carlo.* 11th International Conference on Environment and Electrical Engineering pp. 1081-1086, 2012.

[19] A. Maleki, M. G. Khajeh, M. Ameri. *Optimal sizing of a grid independent hybrid renewable energy system incorporating resource uncertainty, and load uncertainty*.International Journal of Electrical Power & Energy Systems,. 83:514-524, 2016.

[20] S. Satheesh. *Market participation of large-scale Hybrid power plant.* Aalborg University Energy Technology, EPSH4-1039, 2020-05.

[21] *R. Rigo-Mariani, B. Sareni, X. Roboam, Integrated optimal design of a smart microgrid with storage. IEEE Transactions on Smart Grid. 8, 1762–1770 (2017).*

[22] A. R. Silva, A. Estanqueiro, *From Wind to Hybrid : A Contribution to the Optimal Design of Utility-Scale Hybrid Power Plants*. Energies 15, no. 7: 2560, 2022.

18th EAWE PhD Seminar on Wind Energy
2-4 November 2022
Bruges, Belgium

Increasing the Magnetic Permeability of Wind Turbine Generator Air-gaps

Fergus Hall[a] and **Alasdair MacDonald**[a]

[a]Institute for Energy Systems, School of Engineering, University of Edinburgh, Edinburgh, EH9 3FB, U.K

E-mail: fergus.hall@ed.ac.uk

Keywords: Generators, Permanent Magnets, Ferrofluid, Direct Drive, Air-gap

1 Introduction

Permanent magnet (PM) direct drive (DD) wind turbine generators (WTGs) are a favourable drive train configuration for offshore installations due to their high efficiency and reliability [1, 11, 8]. The substantial torques that result from their low-speed and high-power operation lead to electrical machine designs with a large rotor radius and air-gap magnetic flux density. A significant amount of rare earth PM material is required in their construction which is both expensive and environmentally damaging to procure - for example, the NREL 15 MW reference WTG design includes 24.2 tonnes of N40 grade NdFeB PM material [3].

The requirement for PM material can be reduced by decreasing the air-gap clearance at the expense of an increased structural stiffness requirement that quickly leads to an unacceptable generator mass [6]. A practical lower limit is also imposed due to the radial tolerance stack up of the generator components.

In this work, an alternative method is considered in which the magnetic permeablity of the air-gap region is increased by replacing the air with ferrofluid. Ferrofluid is a colloidal suspension of iron oxide nanoparticles within a carrier fluid such as water or oil. It exhibits strong magnetic properties when exposed to a magnetic field while maintaining a liquid state with relatively low viscosity [10]. Previous work has shown promising results for this application of ferrofluid when applied to motors [9, 5, 12], yet there is a lack of research for this application of ferrofluid in the context of PM DD WTGs where the potential benefits appear to be substantial and the downsides relatively insignificant.

2 Magnetic Circuit Analysis

In order to obtain an indication of ferrofluid's potential for reducing PM material requirements a magnetic circuit analysis of the NREL 15 MW generator is conducted where a conventional air-gap is compared against a ferrofluid-filled *ferrofluid-gap*.

The permeability of the rotor and stator iron is assumed infinite, magnetic leakage effects are neglected, the air-gap clearance l_g is a constant 10.16 mm, the remanent flux density B_r and relative permeability μ_{PM} of the PM is 1.28 T and 1.06 respectively, and a no load condition is assumed. The magnetic properties of *PBG900* ferrofluid are used for the ferrofluid-gap - the magnetic circuit is solved through iteration to account for the low saturation magnetisation of 99 mT [2].

The air-gap flux density B_g is calculated for a range of magnet heights h_m and compared for both cases. The increased permeability of the air gap region μ_g due to the ferrofluid causes the air-gap reluctance R_g to decrease. The subsequent reduction in the required magnetomotive force F_{PM}, and therefore h_m, further lowers the total reluctance of the magnetic circuit R_T since the magnet reluctance R_{PM} is also reduced. The combined decrease in both R_g and R_{PM} permits a significant reduction in the amount of PM material required in the generator despite the relatively low saturation magnetisation of the ferrofluid.

The magnetic circuit diagram is presented in Figure 1 along with a plot of B_g vs h_m for both the conventional air- and ferrofluid-filled gap. A a 9.1 % reduction in required h_m is found for the range of B_g investigated - including

the NREL specification of 1.06 T - this would translate to a 2.2 tonne reduction in the amount of PM material required. Equation 1 provides the relationship between the magnetic circuit parameters.

$$B_g = \frac{\Phi_g}{A_M} = \frac{F_{PM}}{R_T A_M} = \frac{F_{PM}}{(R_g + R_{PM}) A_M} = \frac{B_r h_m}{\frac{\mu_{PM} l_g}{\mu_g} + h_m} \tag{1}$$

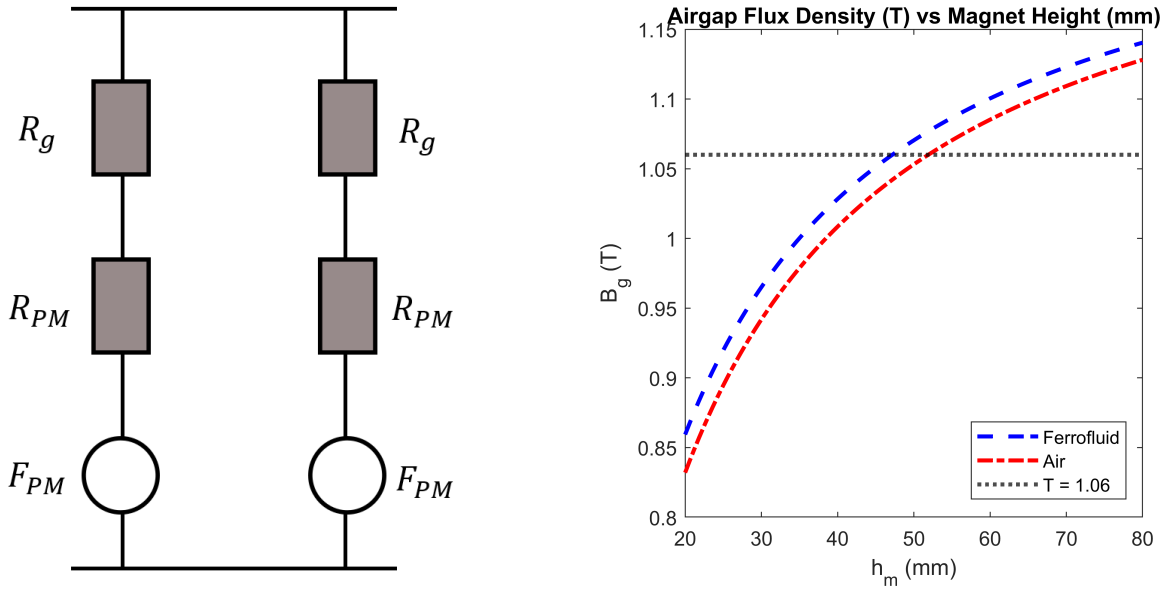


Figure 1: *Left*: Magnetic circuit diagram for a pole pair of the NREL 15 MW reference WTG. *Right*: Air-gap flux density B_g vs magnet height h_m for a conventional air- and ferrofluid-filled gap.

3 Viscous Rotor Drag Analysis

The introduction of fluid into the air-gap region will result in an increased drag upon the rotor which will reduce the efficiency of the generator; a simplified analysis of the expected efficiency loss for both DD and geared WTGs follows.

The rated shaft power developed from a wind turbine rotor P_{Shaft} can be calculated from the density of air ρ_{Air}, the rated wind speed U_{Wind}, the swept radius of the rotor R_{Swept}, and the aerodynamic efficiency of the rotor η_{Aero}:

$$P_{Shaft} = \frac{1}{2} \pi \rho_{Air} U_{Wind}^3 R_{Swept}^2 \eta_{Aero} \tag{2}$$

The angular velocity of the shaft ω_{Rated} can be determined from the tip speed ratio λ:

$$\omega_{Shaft} = \frac{\lambda U_{Wind}}{R_{Swept}} \tag{3}$$

The torque carried by the shaft τ_{shaft} can then be calculated:

$$\tau_{shaft} = \frac{P_{Shaft}}{\omega_{Shaft}} \tag{4}$$

For a geared drive train the input angular velocity $\omega_{Gen} = \omega_{Shaft}\, GR$ and torque into the generator $\tau_{Gen} = \tau_{shaft} \,/\, GR$ can be determined based on the gearbox ratio GR (assuming no losses). Whereas, for a DD drive train ω_{Gen} and τ_{Gen} are assumed equal to ω_{Rated} and τ_{shaft} respectively. The required generator rotor radius R_r can then be determined if the aspect ratio k and the electromagnetic shear stress σ at rated power are known:

$$R_r = \sqrt[3]{\frac{\tau_{shaft}}{4\,\pi\,k\,\sigma}} \tag{5}$$

It is assumed that the air-gap clearance l_g is equal to $1/500$ of the rotor radius and that the inner radius of the stator bore $R_s = R_r + l_g$. The fluid flow within the air-gap can be conveniently characterised as *Taylor-Couette* flow [4]. For laminar flow and neglecting end-effects the viscous power loss P_L can be calculated analytically [7]:

$$P_L = 4\,\pi\,\mu\,\omega_{Gen}^2\, L\, \frac{R_r\, R_s}{R_s^2 - R_r^2} \tag{6}$$

Where, μ is the fluid dynamic viscosity and L is the length of the generator core. The reduction in efficiency can then be estimated (neglecting conventional generator losses):

$$1 - \eta_{Gen} = \frac{P_L}{P_{Shaft}} \tag{7}$$

Typical values for the various parameters are used: $\rho_{Air} = 1.225\,kg/m^3$, $U_{Wind} = 10.6\,m/s$, $\eta_{Aero} = 0.5$, $\lambda = 9$, $AR = 0.2$, $\sigma = 40\,kPa$, $\mu = 0.1\,Pa.s$. A range of P_{Shaft} and corresponding ω_{Shaft} is obtained from a series of R_{Swept} values. The expected loss in efficiency is then compared for DD and geared drive trains for a multi-megawatt range of P_{Shaft} relevant to modern offshore WTGs.

Figure 2 presents a dramatic difference in efficiency loss: the DD configuration has a loss of less than $0.25\,\%$ for $P_{Shaft} > 10\,MW$ whereas a severe efficiency loss is apparent for the geared generators.

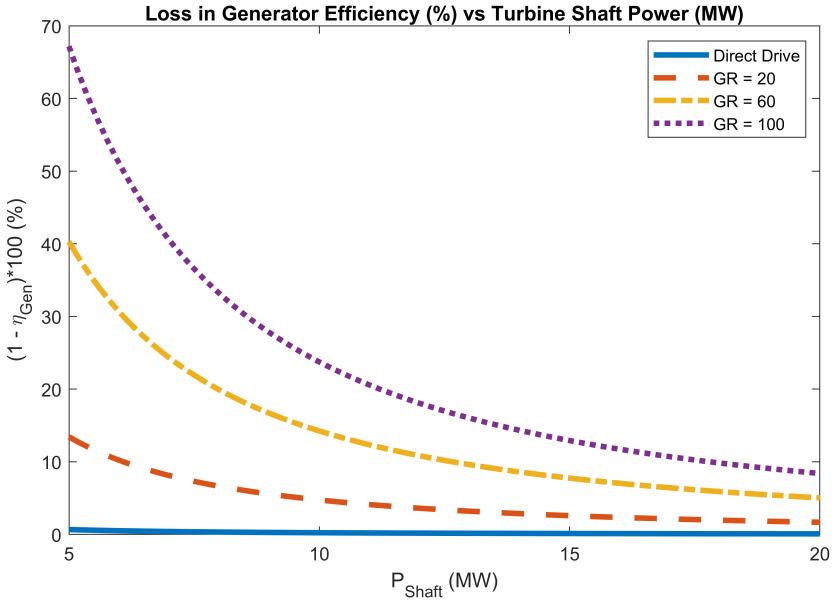


Figure 2: Reduction in generator efficiency $(1 - \eta_{Gen}) * 100$ vs rotor shaft power P_{Shaft} for DD and geared drive trains with ratios of 20, 60, and 100.

4 Conclusions and Future Work

A preliminary analysis of the ferrofluid-gap concept applied to DD WTGs indicates that they may be compatible. The massive quantity of PM material required in their construction provides an opportunity for substantial cost saving, while their unique geometry and low-speed operation results in a significantly smaller loss in efficiency compared to geared alternatives. This investigation is being taken much deeper in the PhD project that is now under way. A combination of mathematical modelling, multi-physics simulation, and scaled physical testing will contribute towards the theoretical framework that is necessary for conducting a detailed feasibility study of the concept.

References

[1] J. Carroll, A. McDonald, D. McMillan, T. Stehly, C. Mone, and B. Maples. Cost of energy for offshore wind turbines with different drive train types. *EWEA 2015 Annual Event*, 2015.

[2] FerroTec. Pbg series ferrofluids - pbg900. https://ferrofluid.ferrotec.com/products/ferrofluid-pbg/pbg900/. accessed: 16.08.2022.

[3] E. Gaertner, J. Rinker, L. Sethuraman, F. Zahle, B. Anderson, G. E. Barter, N. J. Abbas, F. Meng, P. Bortolotti, W. Skrzypinski, G. N. Scott, R. Feil, H. Bredmose, K. Dykes, M. Shields, C. Allen, and A. Viselli. Iea wind tcp task 37: Definition of the iea 15-megawatt offshore reference wind turbine.

[4] S. Grossmann, D. Lohse, and C. Sun. High–reynolds number taylor-couette turbulence. *Annual Review of Fluid Mechanics*, 48(1):53–80, 2016.

[5] L. Günther, R. Steinmeier, F. Becker, V. Lysenko, V. Minchenya, I. Zeidis, and K. Zimmermann. Approaches to the application of magnetic fluids in electromechanical drive systems. 09 2017.

[6] P. Jaen-Sola and A. S. McDonald. Structural analysis and characterization of radial flux pm generators for direct-drive wind turbines. In *3rd Renewable Power Generation Conference (RPG 2014)*, pages 1–6, 2014.

[7] Y. Li, Z. Jiao, T. Yu, and Y. Shang. Viscous loss analysis of the flooded electro-hydrostatic actuator motor under laminar and turbulent flow states. *Processes*, 8(8), 2020.

[8] A. R. Nejad, J. Keller, Y. Guo, S. Sheng, H. Polinder, S. Watson, J. Dong, Z. Qin, A. Ebrahimi, R. Schelenz, F. Gutiérrez Guzmán, D. Cornel, R. Golafshan, G. Jacobs, B. Blockmans, J. Bosmans, B. Pluymers, J. Carroll, S. Koukoura, E. Hart, A. McDonald, A. Natarajan, J. Torsvik, F. K. Moghadam, P.-J. Daems, T. Verstraeten, C. Peeters, and J. Helsen. Wind turbine drivetrains: state-of-the-art technologies and future development trends. *Wind Energy Science*, 7(1):387–411, 2022.

[9] A. Nethe, T. Scholz, and H.-D. Stahlmann. Improving the efficiency of electric machines using ferrofluids. *Journal of Physics: Condensed Matter*, 18(38):S2985–S2998, sep 2006.

[10] C. Scherer and A. Figueiredo Neto. Ferrofluids: Properties and applications. *Brazilian Journal of Physics*, 35:718–727, 09 2005.

[11] D. Sumner and A. Yardley. System performance, availability and reliability trend analysis, portfolio review, 2020/21. Technical report, Offshore Renewable Energy Catapult Ltd., 2022.

[12] G. Zeng, Y. Xiang-yu, H. Yin, Y. Pei, S. Zhao, J. Cao, and L. Qiu. Asynchronous machine with ferrofluid in gap: Modeling, simulation, and analysis. *IEEE Transactions on Magnetics*, 56(1):1–4, 2020.

18th EAWE PhD Seminar on Wind Energy
2-4 November 2022
Bruges, Belgium

Machine Learning-based Methodologies for Grid Compliance Assessment of Wind Turbines and Farms

Gabriel Miguel Gomes Guerreiro[a,b], **Guangya Yang**[a], and **Frank Martin**[b]

[a]Department of Wind and Energy Systems, DTU - Technical University of Denmark
[b]Siemens Gamesa Renewable Energy A/S

E-mail: gabriel.gomes@siemensgamesa.com

Keywords: Grid Compliance, Wind Turbines, Subsystem Testing, HiL, SiL, Machine Learning

1 Introduction

Wind Turbines have been integrated to the power system for more than 30 years now. In the beginning, their impact in the grid was considerably small once the share of this source was reduced when compared to more conventional energy sources. During the last decades, the rapid growth of wind power has forced transmission system operators (TSOs) to increase their efforts in defining the frameworks and rules for the connection of such wind power plants (WPPs), making the grid codes more complex and testing/validation more demanding for Wind Turbine (WT) manufacturers and WPPs developers [1, 2].

Nowadays, in order for the turbine to be accepted as compliant with grid connection requirements, thousands of full-scale type tests and simulations are performed before the product is delivered to the market. Traditionally, wind turbine manufacturers carry out these testing campaigns on prototypes of full-scale turbines installed on test sites, which can nowadays last for several months or even years, depending on product, site, and weather conditions. Despite testing on a prototype turbine on site offering the highest fidelity level possible, there are many drawbacks to using only this method, when it comes to equipment limitation, wind availability, system frequency (two separate prototypes for 50 and 60 Hz tests), complex testing scope, weak-grid conditions, etc. Thus, as the power ratings of wind turbines are becoming higher for improving the economy of scale, type test of wind turbines is increasingly challenging and costly, with more complex requirements and larger test equipment needed.

On the other hand, to ensure that the Wind Farms are compliant with the grid codes, farm developers and other stakeholders obtain validated models from equipment manufacturers and carry out extensive validation at the plant level. Usually such studies must be carried out long before any physical equipment is installed and commissioned on site in order to ensure that no compliance problems will be found due to equipment's hardware or software characteristics. The increasingly diversity of requirements due to new markets combined with the increasingly complex requirements poses challenges to the performance verification of wind farms since such simulation studies take longer and longer and is forcing farm developers to start studies even earlier, putting pressure on manufacturers to deliver highly accurate models faster.

These increasingly challenges pose threats to the industry regarding being able to reliably and sustainably meet the society's net zero targets for the next decades. It becomes clear that there is a concrete need for developing new efficient testing, validation, modelling and digitized methodologies, that together are able to efficiently and optimally obtain performance verification of wind turbines and farms in a more agile manner.

2 Future outlook with Machine Learning-based methodologies

As a way to address the challenges on both the development of new wind turbines/farms and the overall system operation and studies performed by different actors in the industry, two new methodologies, among others, are gaining attention in the last few years and promise to be two of the main drivers forward regarding grid compliance assessment in the wind sector.

On the turbine level, upcoming standards such as "61400-21-4 : Wind turbine components and subsystems" [3] propose that instead of solely using full-scale type tests, wind turbines can be divided into several subsystems

based of on the conversion process, nacelle, generator, converter, including their control and protection systems. Therefore, wind turbine grid compliance tests can be faithfully replaced by a series of coordinated tests of subsystems, shorter and more accurate product development cycle can be achieved with less investment in testing facility upgrade. Furthermore, based on results of such extensive testing of subsystems and experience on full-scale turbines, new characteristics and techniques for grid compliance assessment can be developed more easily as large amounts of highly accurate data become available.

At the farm level, proposed standards such as the IEC standard "IEC 61400-21-5 : Configuration, functional specification, and validation of hardware-in-the-loop test bench for wind power plants" [4] propose that Hardware/Software-in-the-loop (HiL/SiL) are used for faster grid compliance verification during development phases and for continuous monitoring during operational phases. Such testing environments nowadays are commonly called Replicas or Digital Twins and will be more and more present in the future energy system.

In light of the increasing challenges and upcoming solutions presented above, the possibilities of obtaining highly accurate responses on controllable subsystem testing environments and HiL/SiL test benches create new pathways for integrating the large amounts of data with novel methodologies for grid compliance assessment of turbines and farms. This projects aims to propose disruptive data-driven methodologies that together with the upcoming methodologies can drive the technology development and operation of WT and WFs towards new horizons, as it can be seen in Figure (1).

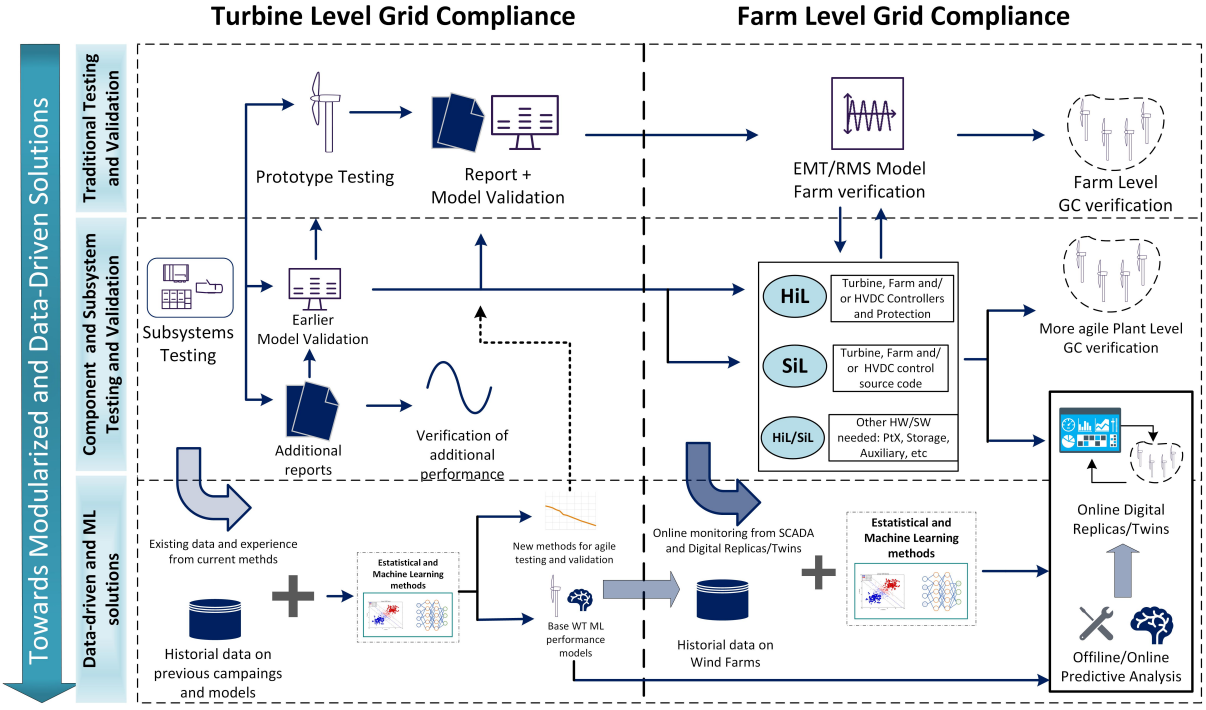


Figure 1: New pathways for Grid Compliance Assessment of Wind Turbines and Wind Farms.

During the project, dynamic performances of the turbines will be analyzed by leveraging historical data, subsystem and HiL test-rigs testing and simulation models. The signatures of such faults including signals of frequency, voltage, current, among others, can provide a wide range of insights of the conditions a certain specific fault happened at. The testing and modelling aim to increase the understanding about the behavior of turbines and power plants concerning grid compliance aspects following grid codes, standards, and future trends [2, 5].

Machine learning algorithms will be used to extract various information from the signatures (e.g. Boosting/Bagging statistical models as well as Deep Learning with Artificial Neural Networks through Physics-Informed approaches and etc). All the data available from model and test-rigs with historical data will be utilized aiming to design pattern recognition models that can be used for future turbine development and for operational grid compliance observation. The feasibility of each tool will be thoroughly assessed depending on the desired task (classification and regression) and the nature of the data and target (linear or non-linear behaviors). Finally, the feasibility studies will lead to the deployment of such digital representations on the existing industrial framework,

achieving real Digital Twin(s) representation of certain dynamic behaviors of the turbine.

Acknowledgements

The work realised is developed under the umbrella of the project InnoCyPES (Innovative tools for cyber-physical energy systems). This project has received funding from the European Union's Horizon 2020 research and innovation programme under the Marie Sklodowska Curie grant agreement No 956433.

References

[1] S. W. Ali, M. Sadiq, Y. Terriche, S. A. R. Naqvi, L. Q. N. Hoang, M. U. Mutarraf, M. A. Hassan, G. Yang, C.-L. Su, and J. M. Guerrero, "Offshore Wind Farm-Grid Integration: A Review on Infrastructure, Challenges, and Grid Solutions," *IEEE Access*, vol. 9, pp. 102811–102827, 2021.

[2] P. Ghimire, F. Martin, and S. Azarian, "Demystifying Grid Compliance – from grid code towards wind turbine capability and their testing," *20th Wind Integration Workshop,Berlin, Germany.*, 29-30 September 2021.

[3] "IEC TS 61400-21 wind energy generation systems - Part 21-4: Wind turbine components and subsystems," 2022.

[4] "IEC TS 61400-21 wind energy generation systems - Part 21-5: Configuration, functional specification and validation of hardware-in-the-loop test bench for wind power plants," 2022.

[5] P. Ghimire, I. Szczesny, R. Sharma, F. Martin, and P. Mahat, "Use of Full-order Electro-magnetic transient models for grid compliance assessment of wind turbines: Part I"," *17th Wind Integration Workshop, Stockholm, Sweden*, 2018.

18th EAWE PhD Seminar on Wind Energy
2 – 4 November 2022
Bruges, Belgium

Model-based Control and Operation of Large-Scale Water Electrolyser Plants for Optimal Integration into Modern Power Systems

Jonathan Riofrio[a], Shi You[a], Tilman Weckesser[a]

[a] Technical University of Denmark (DTU)

E-mail: aurio@dtu.dk

Keywords: Electrolyser, Hydrogen, Modelling, Power-to-X, Renewable energy plants

1. Introduction

Current global decarbonization strategies are driven to look for new technologies and primary energies to satisfy the growing energy needs with a low carbon footprint [1]. Therefore, more and more renewable energy plants (REPs) and other disruptive technologies are being connected to power systems, becoming key actors of the modern power systems [2], [3]. Particularly, wind energy has shown a steady increase in the installed capacity for onshore and offshore wind turbines across Europe. To illustrate, an installed capacity over 320 GW (central scenario) is expected to be reached by 2030, from where 254 GW corresponds to onshore installations and 66 GW to offshore wind [4].

This extra installed generation capacity emerges as an idoneal scenario to apply the Power-to-X (PtX) concept in Europe. PtX can be defined as a process in which electricity from REPs is used for generating green hydrogen [5], [6] which appears as a clean and versatile energy carrier [1], [7]. In the same way, after being produced by electrolysis, green hydrogen is featured by lightness, storability, energy density, and no production of greenhouse gases [8].

In various PtX applications, electrolysers are crucial equipment, and they have already started to interact with power systems [5], [6], [9], [10]. Additionally, and within the European context, an installed capacity around 40 GW is expected from electrolysers until 2030. A particular case is Denmark, where a capacity of almost 4.5 GW electrolyser plants using MW-scale solutions will be deployed and primarily powered by wind energy [1]. This expected capacity corresponds to approximately 70% of today´s peak load of the country [11].

2. Hypothesis and Goals

The mentioned European goals regarding the inclusion of numerous electrolyser plants with large-rated capacities in the close future have created the need for going deep into the dynamic operation of power systems and electrolyser, assuming the next hypothesis:

- Existing models and control solutions have been conducted for electrolysers that are rated below MW, often connected to distribution grids or low voltage levels.
- Future electrolysers will be large-scale, i.e. at least multi-MW, connected to medium or high voltage levels, or even directly to renewable power plants.
- The design principles of future electrolysers will revolutionize the energy sector due to emerging needs, such as using renewable power, support power system operation and revenue stacking (e.g. delivering hydrogen, heat and grid services simultaneously), etc.

In this regard, this research is intended to develop and built comprehensive mathematical /computational models of controllers, power converters, and electrolysers for large-scale systems in specialized power system analysis software. The developed models should be able to become good tools for supporting the correct design and operation of the next generation of large-scale electrolysers, enabling improved characterization and stressing their flexibility. Additionally, they should provide reliable results to ensure a secure integration of large-scale electrolysers and smooth operation of modern power systems. To conclude, these digital models are intended to be tested in different study cases, mainly addressed to the dynamic operation of power systems under the scope of PtX as well as the high participation of renewable energies and the spread of electrolysers plants.

Likewise, the project wants to develop advanced model-based control and operation methods for large-scale water electrolyser plants in order to achieve an optimal integration into power systems. The research focus of the project is threefold:

- Evaluating the impacts of water electrolysers on power system operation and dynamics.
- Assessing the potential capability of using the electrolyser plant to support power system operation by offering a variety of grid services, e.g., load tracking and frequency support, etc.
- Developing advanced grid-supporting control and operation methods for the electrolyser plants.

Finally, the resulting computational models will be enriched with real-world data from the GreenHyScale project [12], which will enable this research to characterize the individual components of the electrolyser plant with a good level of accuracy.

3. Methodology

Considering that the research is carried out altogether with several industrial stakeholders and academic partners, an initial methodology based on some tasks has been defined during the first months of this project, and it is depicted in Fig. 1. In addition, it should be highlighted that the research is being performed from June 2022 until May 2025, so there are not tangible results to show yet.

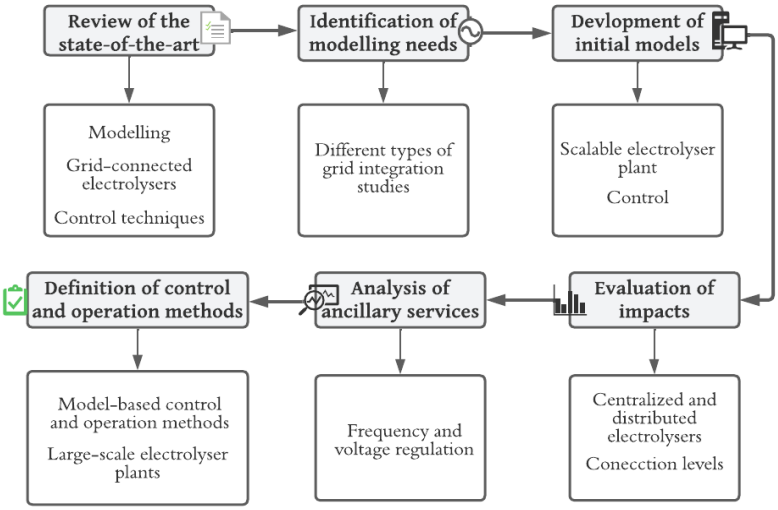


Figure 1: Main tasks of the designed methodology.

References

[1] M. Ciechanowska, “Hydrogen strategy for a climate-Neutral Europe,” *Naft. - Gaz*, vol. 2020, no. 12, pp. 951–954, 2020, doi: 10.18668/NG.2020.12.09.

[2] N. R. Nair and M. Ebenezer, “Operation and control of grid connected wind — PV hybrid system,” in *2014 International Conference on Advances in Green Energy (ICAGE)*, 2014, pp. 197–203. doi: 10.1109/ICAGE.2014.7050165.

[3] A. Younesi, H. Shayeghi, Z. Wang, P. Siano, A. Mehrizi-Sani, and A. Safari, "Trends in modern power systems resilience: State-of-the-art review," *Renew. Sustain. Energy Rev.*, vol. 162, p. 112397, 2022, doi: https://doi.org/10.1016/j.rser.2022.112397.

[4] European Wind Energy Association, "Wind energy scenarios for 2030," *Ewea*, no. August, pp. 1–16, 2015, [Online]. Available: http://www.ewea.org/fileadmin/files/library/publications/reports/EWEA-Wind-energy-scenarios-2030.pdf

[5] Z. Chehade, C. Mansilla, P. Lucchese, S. Hilliard, and J. Proost, "Review and analysis of demonstration projects on power-to-X pathways in the world," *Int. J. Hydrogen Energy*, vol. 44, no. 51, pp. 27637–27655, 2019.

[6] Y. Zheng, S. You, H. W. Bindner, and M. Münster, "Incorporating Optimal Operation Strategies into Investment Planning for Wind/Electrolyser System," *CSEE J. Power Energy Syst.*, vol. 8, no. 2, pp. 347–359, 2022, doi: 10.17775/CSEEJPES.2021.04240.

[7] M. Balat, "Potential importance of hydrogen as a future solution to environmental and transportation problems," *Int. J. Hydrogen Energy*, vol. 33, no. 15, pp. 4013–4029, 2008, doi: https://doi.org/10.1016/j.ijhydene.2008.05.047.

[8] P. A. Pilavachi, A. I. Chatzipanagi, and A. I. Spyropoulou, "Evaluation of hydrogen production methods using the Analytic Hierarchy Process," *Int. J. Hydrogen Energy*, vol. 34, no. 13, pp. 5294–5303, 2009, doi: https://doi.org/10.1016/j.ijhydene.2009.04.026.

[9] C. Huang, Y. Zong, S. You, C. Træholt, Z. Zheng, and Q. Xie, "Cooperative Control of Wind-Hydrogen-SMES Hybrid Systems for Fault-Ride-Through Improvement and Power Smoothing," *IEEE Trans. Appl. Supercond.*, vol. 31, no. 8, pp. 1–7, 2021, doi: 10.1109/TASC.2021.3103729.

[10] G. Matute, J. M. Yusta, and L. C. Correas, "Techno-economic modelling of water electrolysers in the range of several MW to provide grid services while generating hydrogen for different applications: A case study in Spain applied to mobility with FCEVs," *Int. J. Hydrogen Energy*, vol. 44, no. 33, pp. 17431–17442, 2019.

[11] J. Ladenburg, P. Hevia-Koch, S. Petrović, and L. Knapp, "The offshore-onshore conundrum: Preferences for wind energy considering spatial data in Denmark," *Renew. Sustain. Energy Rev.*, vol. 121, p. 109711, 2020, doi: https://doi.org/10.1016/j.rser.2020.109711.

[12] CORDIS, "100 MW Green hydrogen production in a replicable and scalable industrial hosting environment." https://cordis.europa.eu/project/id/101036935

18th EAWE PhD Seminar on Wind Energy
2-4 November 2022
Bruges, Belgium

Offshore Wind Farm Power Prediction For Security of Supply Assessment Using a Unique Machine Learning Proxy

Thuy-hai Nguyen[a], **Nicolas Thils**[a], **Jean-François Toubeau**[a], **Emmanuel De Jaeger**[b], and **François Vallée**[a]

[a]Power Systems & Market Research Group, University of Mons (Belgium)
[b]Mechatronic, Electrical Energy and Dynamic Systems, Université Catholique de Louvain (Belgium)

thuy-hai.nguyen@umons.ac.be

Keywords: Machine Learning, Offshore Wind, Power Prediction, Power Systems, Wake effects

1 Introduction

Large-scale offshore wind will be an important part of the future carbon-neutral electricity system. Offshore wind has the potential to deliver large amounts of clean, renewable energy to fulfill the electrical needs, and it has become cost-competitive with fossil-powered alternatives. 2021 was a big year for the fast-growing offshore wind sector, with a total of 21.1 GW of offshore wind installed around the world. This brings the global cumulative offshore wind power capacity to 56 GW [1]. The proportion of offshore wind generation is likely to sharply increase in future power systems. It becomes thus essential to be able to accurately predict the power output of offshore wind farms when assessing the security of electricity supply. In power systems adequacy computations, when the offshore generation has to be evaluated for thousands and even millions of states, aerodynamic effects occurring in offshore wind farms are ignored or overly simplified, due to computational matters [2, 3]. This results in inaccurate power predictions, as factors such as wake effects and turbulence clearly impact the produced power. The challenge is thus to have accurate wind farm models while avoiding high computational costs.

Hence, the objective of this paper is to develop a unique data-driven Machine Learning (ML) proxy that provides a fast and reliable prediction of offshore wind farms output power. As wind farm data are rarely available, the output of wind farm simulations are used to train the Machine Learning model. The latter then learns the complex relationship between free flow wind information and wind farm power. Geometric features based on the wind farm layout are also added as inputs to the model. This allows the Machine Learning proxy to generalize to any wind farm layout. Therefore, once the model is trained, it can be used in power system computations, e.g., adequacy studies, to predict the power output of any considered offshore wind farm, in a fast and accurate way.

2 Methodology

The proposed methodology is summarized in fig. 1.

2.1 Wind farm simulations

Wind farm simulations cannot be directly integrated in power system computations such as Monte-Carlo simulations (used to assess the adequacy of power systems), wherein millions of power system states are simulated. Therefore, a database is generated from wind farm simulations, which can then be used to train the Machine Learning model. This database is created through multiple simulations run with Floris (FLOw Redirection and Induction in Steady state), developed by the National Renewable Lab [4]. The inputs needed by Floris simulations are the wind farm layout, the wind turbines characteristics (diameter and hub height), and a list of wind speeds and directions. The output of the Floris simulations are the total farm power as well as the wind turbine individual powers associated with a given incoming wind speed and wind direction. Furthermore, it is assumed that the wind

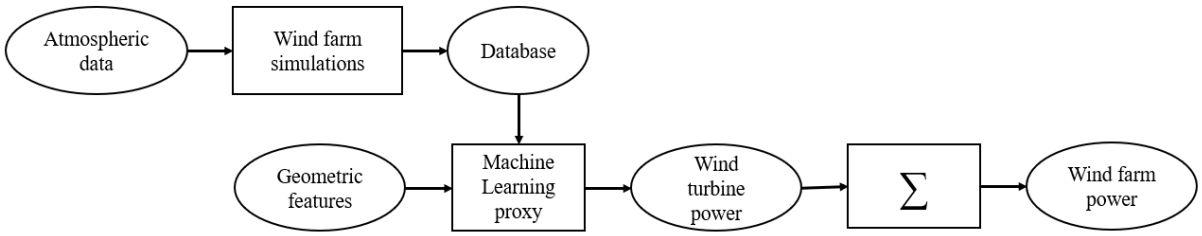


Figure 1: Methodology scheme

turbine is actively controlled in order to optimize the extracted power without exceeding the maximum allowed power and maximum rotor speed. The nacelle is also controlled so that the rotor is always perfectly facing the incoming main wind direction. Indeed, in this work, we are interested in the hourly output of offshore wind farms for power system reliability computations or annual energy assessment, therefore active yaw control and dynamic effects are not taken into account.

The Lillgrund offshore wind farm, located near the coast of Sweden, is chosen for building the database [5]. The layout of the wind farm is presented in fig. 2a. It consists of 48 pitch-controlled, variable speed wind turbines (Siemens 2.3MW with diameter D = 93m and hub height of 63.4 m), with a total rated capacity of 110MW. The layout is quite tight, so it is representative of wind farms with closed-spaced wind turbines (which is common, for economic reasons and when the sea space is limited). Moreover, the ”hole” in the middle of Lillgrund also creates situations with distant wind turbines. Therefore, the layout allows to account for many configurations of waked wind turbines.

For the list of wind speeds and directions, we use the ERA5 dataset provided by the European Centre for Medium-Range Weather Forecasts (ECMWF) [6]. Three years of hourly wind (2019 to 2021) as well as extreme scenarios (very high wind speeds) were used as atmospheric input. Hence, a total of 26,311 simulations simulations were run with Floris.

2.2 Geometric features

In addition to free-flow wind speed and wind direction, five geometric features are appended to the database. These features computations are based on the farm layout and the incoming wind direction. Therefore, they will allow the Machine Learning model to learn the spatial configurations of the wind turbines and how it impacts the wake effects and thus the power produced.
For each wind turbine and each wind direction, the geometric features are:

- Number of upstream blocking wind turbines: the sum of any upwind turbine whose swept area coincides with the rotor area of the considered wind turbine. The amount of blocking is not considered here.
- Mean distance of blocking wind turbines: the averaged distance between the considered wind turbine and the upwind blocking turbines. The distances are averaged without weight.
- Distance to the first blocking wind turbine: distance between the considered wind turbine and the closest upwind blocking turbine
- Blocking ratio: the fraction of the swept area of turbine i that is blocked by the swept area of any wind turbine upstream [7]
- Blocking distance: the weighted average distance to the upstream blocking turbines [7].

2.3 Machine Learning

The database built from wind farm simulations is divided so that each sample is associated with a single turbine within the wind farm. Each sample therefore consists of the wind speed, the wind direction, the geometric features computed for the considered wind turbine, and the power output of the turbine in the wind conditions.

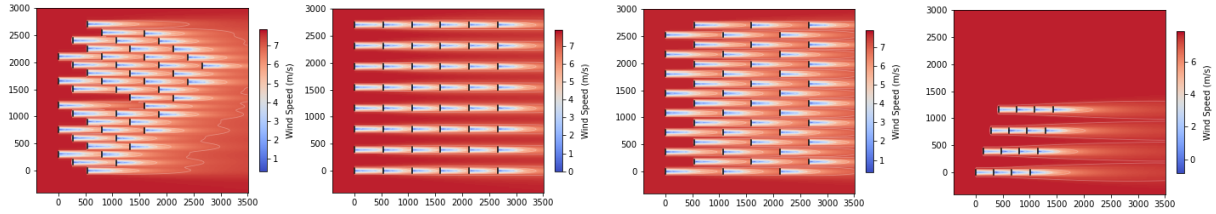
To avoid having one ML model per wind turbine, cross-series learning is used. Cross-learning approach allow models to learn from multiple series and then to accurately predict individual ones. It allows for various common

patterns observed along related series to be effectively learned. Learning from related series not only allows to obtain cross-series information, but it also multiply the number of data. Moreover, only one model is built for multiple series, allowing to save time and computational costs for model selection and hyperparameters tuning. The sub-samples are correlated, as the power produced by a wind turbine depends on the wake (and thus the power) generated by the neighbouring turbines. The ML model should be able to learn from these correlations in order to understand the interactions between wind turbines. For a given set of wind conditions, the powers are predicted one by one, and regrouped afterward to form the total wind farm generation.

The relationship between the wind power output and raw wind information is highly non-linear, which motivates the use of the four following supervised Machine Learning algorithms: Decision tree, Random Forest (RF), Gradient Boosting Regression Tree (GBRT), Neural network (NN, more specifically: multi-layer perceptron). The hyperparameters of each algorithm are chosen after a dedicated study. They should provide a compromise between model complexity, prediction accuracy and computational time.

3 Preliminary Results

To assess the ability of the ML model to generalize to unseen data, hourly power outputs for a year were computed for three test wind farms. The configuration of these test farms are quite different than the original Lillgrund layout: the first has a regular rectangular layout (fig. 2b), the second has a staggered layout (fig. 2c) and the third one is rhomboid (fig. 2d). The first two test farms have the same number of wind turbines than Lillgrund (48) while the last one only has 16 turbines (to apply the model on a smaller wind farm). The three farms are set up for testing purpose, so they do not exist in real-life. However, the presented layouts are consistent with already built wind farms in Europe. The annual powers are first computed with Floris simulations, using data from the year 2021 of the ERA5 wind database. The power is then predicted with the unique general ML model (for each algorithm, the same model is used for the three different layouts), and compared with the Floris results in Table 1. The metrics for comparison are the root mean squared error (RMSE) and mean absolute error (MAE) in MW, but also in percentage of the wind farm total capacity. The computation time is indicated as well.



(a) Original layout, 48 turbines

(b) Regular rectangular layout, 48 turbines

(c) Staggered layout, 48 turbines

(d) Small wind farm, 16 turbines

Figure 2: Layouts of (a) the original Lillgrund wind farm and (b), (c), (d) test wind farms

	Rectangular layout				Staggered layout				Small layout			
	Tree	RF	GBRT	NN	Tree	RF	GBRT	NN	Tree	RF	GBRT	NN
RMSE [MW]	2.06	1.83	0.86	0.90	2.02	1.80	0.84	0.94	0.57	0.49	0.24	0.26
RMSE [%]	1.86	1.66	0.78	0.82	1.83	1.63	0.76	0.85	1.55	1.33	0.65	0.71
MAE [MW]	1.26	1.13	0.53	0.62	1.23	1.10	0.52	0.64	0.33	0.28	0.15	0.17
MAE [%]	1.14	1.02	0.48	0.57	1.12	0.99	0.47	0.58	0.9	0.75	0.41	0.47
Comp. time [s]	72	155	235	70	71	157	243	70	29	113	100	34

Table 1: Comparison of hourly powers for a year between Floris simulations and Machine Learning predictions for the three test wind farms

Every ML algorithm shows strong performance in terms of prediction accuracy and computation time (time needed to predict the yearly output, i.e. 8760 samples). The decision tree is the fastest algorithm but the accuracy is the lowest. Random forests slightly improve the error metrics, but at the cost of a higher prediction time. GBRT exhibits the highest accuracy but the longest inference time. The neural network takes less time to give predictions and is slightly less accurate than GBRT. Therefore, the neural network seems to be the best compromise between

accuracy, speed and complexity. For this algorithm, the RMSE and MAE represent less than 1% of the total wind farm installed capacity.
For comparison, the time necessary to produce such an output (8760 samples) using Floris simulations is 3757 seconds for the rectangular layout, 3779 seconds for the staggered layout and 898 seconds for the small layout. The huge difference in computation time between Floris and the ML models clearly proves the relevance of using such models as surrogates of wind farm simulations in power system computations.

The model has been tested and can thus be integrated in a power system reliability assessment, using e.g. adequacy studies. With that model, it would be possible to account for uncertainty of future wind farm layouts by considering multiple designs (one ML model for all wind turbine configurations). Another possible application for this general model includes offshore wind farm layout/design optimization. Indeed, for these computations, the hourly power output is needed for thousands or even millions of system states. The neural network model would allow to give an accurate power prediction while maintaining a very low computation time.

4 Conclusion

In this work, a unique general Machine Learning model applicable to any wind farm layout has been developed. It allows to produce accurate and fast predictions of offshore wind farms steady-state power output. The model was trained on the real-life Lillgrund wind farm, then tested on three wind farms with different layouts, using four Machine Learning algorithms. The performance are compared and results show that every algorithm exhibits low RMSE, MAE and computation time.

Perspectives to this work include using a better tool for wind farm simulations than Floris (an engineering model with limitations on accuracy). If the training database is built with a more accurate model, the methodology still works (and the accuracy would increase). Moreover, future work involves generalizing the model to any wind turbine model as well (different rotor diameter, hub height, cut-in and cut-out wind speeds)

Acknowledgements

This research is supported by the Energy Transition Funds project ”PhairywinD”, organized by the Belgian FPS economy.

References

[1] Global offshore wind report 2022. Technical report, Global Wind Energy Council, 2022.

[2] R. Billinton, R. Karki, Y. Gao, D. Huang, P. Hu, and W. Wangdee. Adequacy assessment considerations in wind integrated power systems. *IEEE Transactions on Power Systems*, 27(4):2297–2305, 2012.

[3] N. B. Negra, O. Holmstrom, B. Bak-Jensen, and P. Sorensen. Aspects of relevance in offshore wind farm reliability assessment. *IEEE Transactions on energy conversion*, 22(1):159–166, 2007.

[4] NREL. FLORIS. Version 2.2.3, 2020.

[5] J.-A. Dahlberg. Assessment of the Lillgrund Windfarm, Power Performance and Wake Effects. Lillgrund Pilot Project, June 2009.

[6] H. Hersbach, B. Bell, P. Berrisford, G. Biavati, A. Horányi, J. Muñoz Sabater, J. Nicolas, C. Peubey, R. Radu, I. Rozum, D. Schepers, A. Simmons, S. C., D. Dee, and J.-N. Thépaut. ERA5 hourly data on single levels from 1959 to present. Copernicus Climate Change Service (C3S) Climate Data Store (CDS), 2018. Last access on 18th of July, 2022.

[7] N. S. Ghaisas and C. L. Archer. Geometry-based models for studying the effects of wind farm layout. *Journal of Atmospheric and Oceanic Technology*, 33(3):481–501, 2016.

18th EAWE PhD Seminar on Wind Energy
2-4 November 2022
Bruges, Belgium

Stability enhancement of weakly-connected offshore wind power plants by wind turbines with grid-forming converter control

Sulav Ghimire[a,b], **Guangya Yang**[a], **Kim H Jensen**[b], **Tonny W Rassmussen**[a], and **Emerson D Guest**[b]

[a]Department of Wind and Energy Systems, Technical University of Denmark
[b]Siemens Gamesa Renewable Energy A/S

E-mail: sulav.ghimire@siemensgamesa.com

Keywords: Grid forming converters, grid following converters, stability, small-signal stability, frequency domain model, transients, frequency response, inertia.

Grid forming converters are becoming increasingly necessary in power grids at the current stage due to the reduction in physical inertia with the increase in power-electronics based generation [5, 4]. To sustain a power electronics dominant grid, the power-electronic converters need to be able to exhibit synchronous machine-like behavior, namely, voltage regulation, contribution to frequency response, inertial response, droop-based active power contribution and reactive-power support, fault-handling capabilities, damping, and synchronization. Grid-forming converters can, as opposed to the grid-following converters, achieve some of these behavior [4]. However, each grid-forming control (GFC) method has its own drawbacks and is sometimes limited by its control algorithms to achieve all or part of the aforementioned behaviors.

One of the most widely used GFC algorithms is virtual synchronous machine based method which tries to emulate the inertial behavior of synchronous machines. It synchronizes with the grid using a power control loop, is capable of droop-response, and can help in frequency response of a power system. Another type of control method under study is virtual oscillator control (and an improved version of it: dispatchable virtual oscillator) which synchronizes based on the principles of oscillators taking transmission line dynamics into consideration. One of its states include the PCC voltage and hence it has the characteristics of a conventional phase-locked loop (PLL). Cascaded voltage and current control loops with droop-based or PI-based power control is another well known control method. It is comparatively fast in its response which could be adjusted by changing the PI-control variables in the current and voltage controllers.

The objective of this project is to investigate, develop and verify grid-forming converter control that enhances the stability of weakly-connected offshore wind power plants (WPPs) i.e. WPPs connected to weak external grids through long high-voltage AC (HVAC) export cables. The project will also study in detail the methods to enhance the stability of such plants and verify these methods using different tools/methods. Most standard stability studies like small-signal stability and transient stability [3] will be performed. We also plan to use the electromagnetic transients (EMT) studies which are crucial for fast-operating power-electronic devices used in the converters. Further validation and testings will be done via hardware in the loop (HiL) tests using RSCAD/RTDS simulator. Last but not the least, the GFC used in offshore WPPs need to be compliant with the grid codes [1, 2]; thus a study of grid codes and developing/adapting the selected GFC algorithm to specific grid codes is also necessary by the end of this project.

The study of different GFCs, their characteristics, and selection of a candidate GFC methods will be based on extensive literature review, stability studies, transient responses, and their ability to comply with standard grid-codes. A full-scale model of the GFC under study will be developed: this model will include all the control loops, protection system and limiting blocks so as to consider all the dynamics of the converter under study. It will be used for different analysis and testing: frequency domain stability analysis, time domain simulations for transient responses and EMT studies.

An illustration of the project plans is presented in figure 1. Firstly, individual study of different grid-forming control algorithms will be performed on a system with a single turbine connected to the power grid. Then during the testing phase, studies will be done on multi-turbine to grid, or single/multiple wind farms to grid systems for

further understanding and validation. In all of these studies and tests, the stability studies will be based on tools like eigenvalues and participation factor analyses, bode, polar, and Nyquists plots, study of inter-mode coupling and oscillations, response to time-domain changes, and so forth.

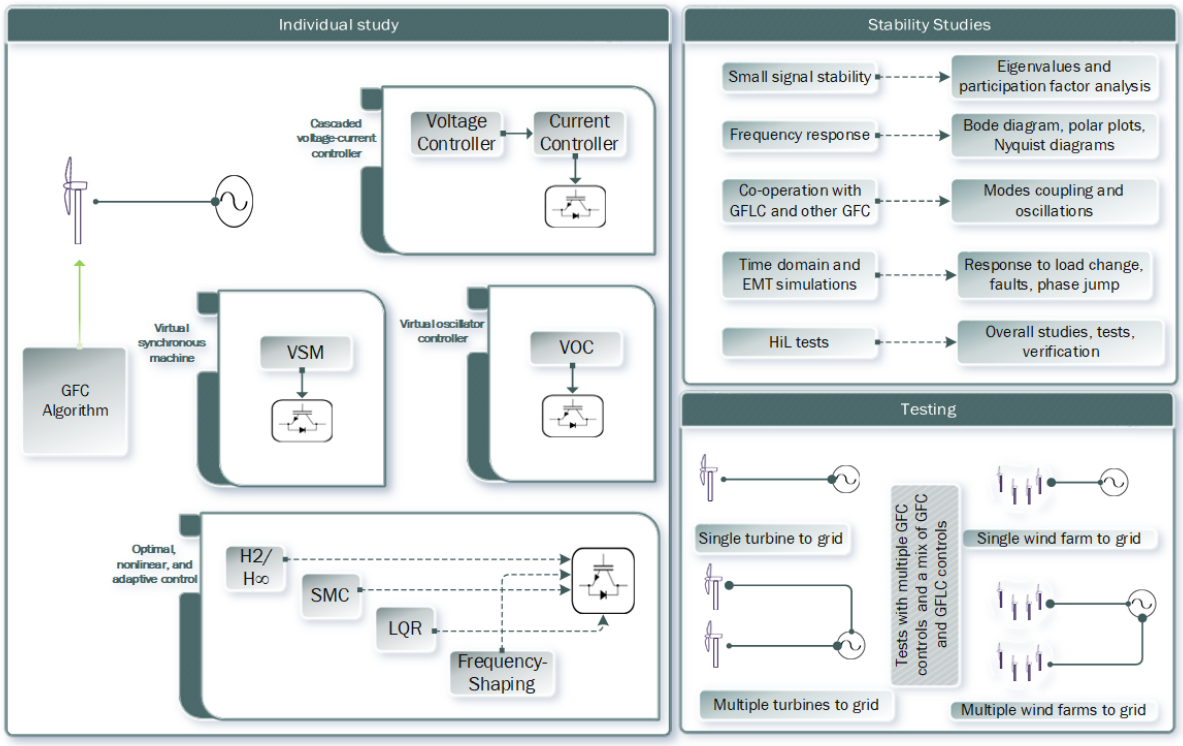


Figure 1: Work plan to determine the suitable GFC for offshore WPP application and its stability study

The research outcome and results of this project will be applicable to different offshore WPP operators, grid-operators, and also useful to academic researchers.

References

[1] Energinet. Classification: Offentlig/public technical regulation 3.2.5 for wind power plants above 11 kw. 2016.

[2] W. C. GC0137. Gc0137: Minimum specification required for provision of gb grid forming (gbgf) capability (formerly virtual synchronous machine/vsm capability). 2021.

[3] P. Kundur, J. Paserba, V. Ajjarapu, G. Andersson, A. Bose, C. Canizares, N. Hatziargyriou, D. Hill, A. Stankovic, C. Taylor, et al. Definition and classification of power system stability ieee/cigre joint task force on stability terms and definitions. *IEEE transactions on Power Systems*, 19(3):1387–1401, 2004.

[4] Y. Lin, J. H. Eto, B. B. Johnson, J. D. Flicker, R. H. Lasseter, H. N. Villegas Pico, G.-S. Seo, B. J. Pierre, and A. Ellis. Research roadmap on grid-forming inverters. Technical report, National Renewable Energy Lab.(NREL), Golden, CO (United States), 2020.

[5] F. Milano, F. Dorfler, G. Hug, D. J. Hill, and G. Verbic. Foundations and challenges of low-inertia systems (invited paper). In *2018 Power Systems Computation Conference (PSCC)*, pages 1–25, 2018.

18th EAWE PhD Seminar on Wind Energy
2 – 4 November 2022
Bruges, Belgium

Wind Farm and Hydrogen Storage Co-location System for Frequency Response Provision in the UK

Shanay Skellern[a], Fulin Fan[a], David Campos-Gaona[a]

[a] Dept. Electronic and Electrical Engineering, University of Strathclyde, Glasgow, G1 1XW, United Kingdom

E-mail: shanay.skellern@strath.ac.uk

Keywords: Frequency Response, Hydrogen Storage Optimisation, Wind Farm, UK Perspective

1. Introduction

Hydrogen-based storage systems (HSS) are becoming increasingly important in the transition to low-carbon energy systems with the aim of a net-zero carbon future [1, 2]. In particular, they are increasingly explored for the provision of ancillary services by co-location with renewable energy generators, such as wind farms. An HSS for the frequency response provision can work as follows: an electrolyser splits the water into hydrogen (H_2) and oxygen using an electric current passed through a chemical solution, which delivers high-frequency (HF) responses. The H_2 produced at a low-pressure is then pressurised using a compressor and stored in a H_2 storage tank at a high-pressure for later use. To transform the H_2 back to electricity, a fuel cell stack is used, where the H_2 taken from the storage tank reacts with a catalyst, often platinum, stripping it of its electrons that are forced to move along an external circuit, creating electricity for low-frequency (LF) responses [3]. Considering the great investment and the existence of multiple components in an HSS, it is necessary to optimise the capacity and coordination of different HSS components so as to evaluate the techno-economic feasibility of the HSS project.

Previous work by the University of Strathclyde and the Offshore Renewable Energy Catapult has optimised the use of battery energy storage systems (BESS) in delivering frequency response services to the AC grid [4, 5]. From an economic optimisation perspective, the optimal BESS size and operating strategies were determined to maximise the profitability of a wind farm co-located with a BESS for frequency response provision. The aim here is to adapt the optimisation algorithm to explore the feasibility of a HSS in providing Dynamic Regulation (DR) that is one of the end-state frequency response products introduced by the National Grid Electricity System Operator (NGESO) in the GB. Based on the DR market mechanisms and the technical characteristics of HSS components, an operating strategy is developed to dispatch power and hydrogen flows within an onshore HSS that delivers DR responses to the AC grid through the existing connection point of a particular wind farm. The resulting DR payments and other cash flows are translated into the net profit of the HSS co-location project, which is then maximised by a particle swarm optimisation (PSO) algorithm, suggesting the best sizes of the HSS components and the optimal strategy variables for their coordination.

2. Operating Strategy of HSS for DR Service Provision

2.1. Dynamic Regulation Service

The end-state frequency response products introduced by the NGESO, including the DR, allow a provider to tender for either or both HF and LF services with unequal capacities. This will benefit energy storage technologies which have a low round-trip efficiency (e.g., an HSS) by combining a higher HF capacity with

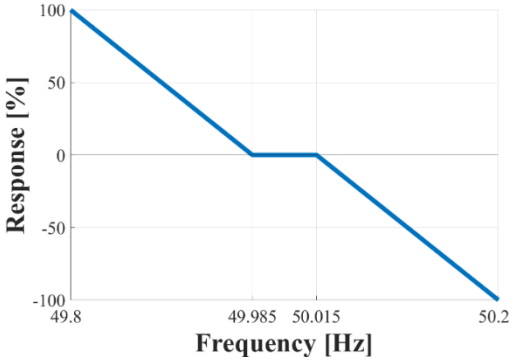


Figure 1: Dynamic Regulation (DR) response requirements curve.

a lower LF capacity. Furthermore, the DR aiming to slowly correct continuous frequency deviations requires a provider to start providing a response within 2 seconds and reach the full response within 10 seconds [6], which can be met by the electrolyser and fuel cell technologies [7]. In addition, a provider must be able to sustain the full response for at least 60 minutes [6], which specifies the minimum size requirement of H_2 storage tank. The DR response curve required by the NGESO can be visualised by Figure 1 [6].

2.2. HSS Simulation

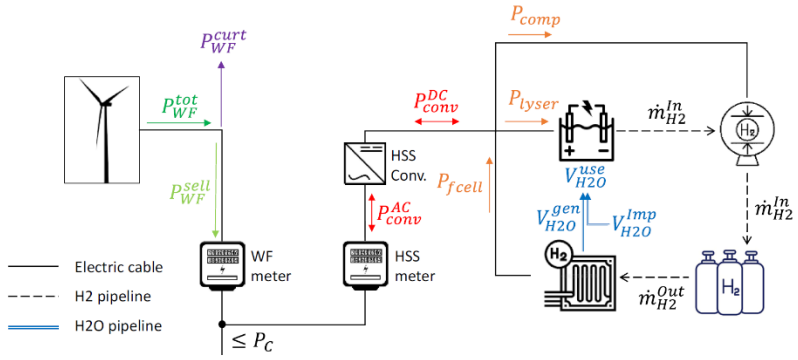


Figure 2: Configuration of wind farm and HSS with a common point of connection. Power, hydrogen and water flows are denoted by P , ṁ and V, respectively.

Figure 2 shows the configuration of a particular wind farm and HSS co-location system. The HSS consists of a converter, electrolyser (used during HF provision), compressor, storage tank and fuel cell (used during LF provision). The power, H_2 and water flows within the system must remain balanced. The power flow balance, as illustrated in Figure 2, is formulated using Equation (1) for the AC side, and Equation (2) for the DC side, where P_{WF}^{tot} is the available power output from the wind farm, P_{WF}^{curt} is the curtailed wind power, P_{conv}^{AC} and P_{conv}^{DC} are the converter power on AC and DC sides, P_{WF}^{sell} is the wind power sold, P_C is the ampacity of the connection point, P_{comp} is the power consumed for the compression of the H_2, and P_{lyser} and P_{fcell} denote the electrolyser import and the fuel cell export, which will be driven by HF and LF signals respectively.

$$P_{WF}^{tot} - P_{WF}^{curt} \pm P_{conv}^{AC} = P_{WF}^{sell} \pm P_{conv}^{AC} \leq P_C \quad (1)$$

$$P_{fcell} - P_{lyser} - P_{comp} = \pm P_{conv}^{DC} \quad (2)$$

The H_2 and water flow balance is described by Equations (3) and (4), respectively, where $\dot{m}_{H_2}^{in,i,t}$ and $\dot{m}_{H_2}^{out,i,t}$ are the H_2 flows (kg/h) in and out of the storage tank, and $M_{store}^{i,t}$ is the hydrogen (kg) stored in the asset at time step t in a half-hour settlement period (SP) i. Similarly, $V_{H_2O}^{imp,i,t}$ is the water externally imported, $V_{H_2O}^{use,i,t}$ is the water consumed for the creation of H_2, and $V_{H_2O}^{gen,i,t}$ is the water generated when the H_2 is converted to electricity.

$$M_{store}^{i,t} = M_{store}^{i,t-1} + (\dot{m}_{H_2}^{in,i,t} - \dot{m}_{H_2}^{out,i,t}) \cdot \Delta t \quad (3)$$

$$V_{H_2O}^{imp,i,t} = \sum V_{H_2O}^{imp,i,t-1} + \sum V_{H_2O}^{use,i,t} + \sum V_{H_2O}^{gen,i,t} \quad (4)$$

2.3. Operational Baseline Calculation

In the end-state frequency response service markets, a provider needs to inform the NGESO of its operational baseline over a future SP. This allows an energy-limited provider to manage its state of energy (SOE) during the provision of frequency response [8]. The delivery contracts of DR services are allocated in 4-hourly electricity forward agreement (EFA) blocks, each consisting of 8 SPs. According to the SOE rules specified by the NGESO for energy-limited providers [8], the HSS is designed here to submit its operational baselines for future SPs with the objective of restoring its hydrogen storage back to the target storage region before the start of the subsequent contracted EFA block.

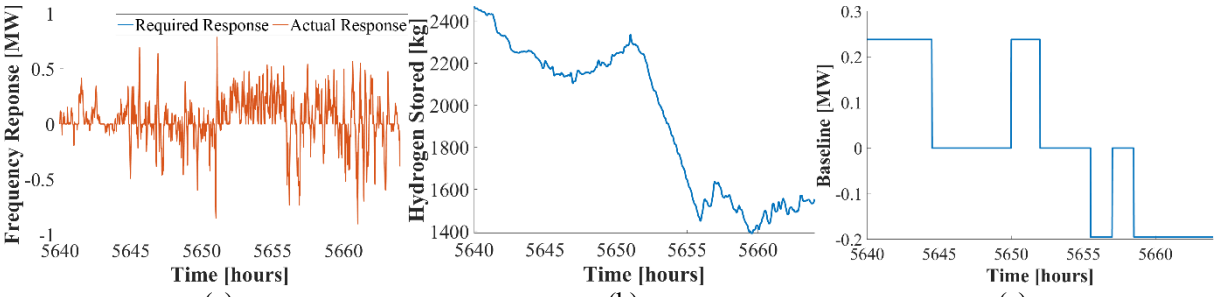
3. Optimisation Results and Discussion

The HSS optimisation algorithm is tested here based on a particular 76 MW wind farm in the GB. The HSS component sizes, LF and HF DR tender capacities and the target region for hydrogen storage restoration are co-optimised to maximise the equivalent annual benefit (EAB) of the wind farm and HSS co-location project, based on a DR unit price of £17/MW/h and the electrolyser/fuel cell unit prices predicted for 2030 [9]. Table 1 lists the optimised technical variables and the resulting EAB and internal rate of return (IRR) respectively, which suggest a profitable HSS co-location project with a notable IRR of 12%. Furthermore, it is noted that the ratio of the LF tender capacity (16 MW) to HF tender capacity (50 MW) is close to the ratio of the electrolyser efficiency (18 kg/MWh) to fuel cell efficiency (60 kg/MWh). This demonstrates that the best tender capacities of LF and HF services are very reliant on the efficiencies of electrolyser and fuel cell.

Table 1: Results of PSO-algorithm Simulation.

Variable	Value
Net Present Value (NPV) [£]	11,440,465
Equivalent Annual Benefit (EAB) [£]	1,332,662
Internal Rate of Return (IRR) [%]	12
Electrolyser [MW]	46.72
Fuel Cell [MW]	17.09
Low Frequency Power [MW]	16
High Frequency Power [MW]	50

The optimisation-based simulation of DR responses, baselines and H_2 storage levels over a particular day is shown in Figure 3, respectively. Figure 3(a) shows that the required DR responses are completely delivered by the HSS. The resulting H_2 storage variation is shown in Figure 3(b) where the stored H_2 firstly declines slightly, followed by a slight increase as the HF responses are delivered, and the electrolyser creates the H_2. The stored H_2 then decreases quite a bit due to the continuous LF events over 5651 h to 5655 h, where the fuel cell converts the H_2 back to electricity. Figure 3(c) illustrates the corresponding changes in baselines from more electricity export (for H_2 release) at the start of the day, where the H_2 storage is higher, to electricity import (for H_2 recovery) towards the end of the day, where the H_2 storage is lower. These results illustrate the effectiveness of the model and operating strategy in managing the HSS for DR provision and operational baseline submission.



(a) (b) (c)

Figure 3: (a) The actual delivery and requirements of DR (MW), (b) hydrogen storage levels (kg) and (c) operational baselines of the HSS simulated over a particular day, shown from 5640 h to 5664 h.

Figure 4(a) compares the DR response curve against the actual delivery throughout the 15-year project lifespan, which covers a wide frequency range. The HSS is shown to give a better performance in HF delivery than LF delivery, as can be seen by the higher density of the dots falling below the DR curve on the LF side. Figure 4(b) shows the distribution of H_2 storage levels over the full 15 years, which tends to be Normal, slightly skewed to the left. Furthermore, the storage tank is almost empty for around 0.02% of the time, which explains the worse performance in LF DR delivery.

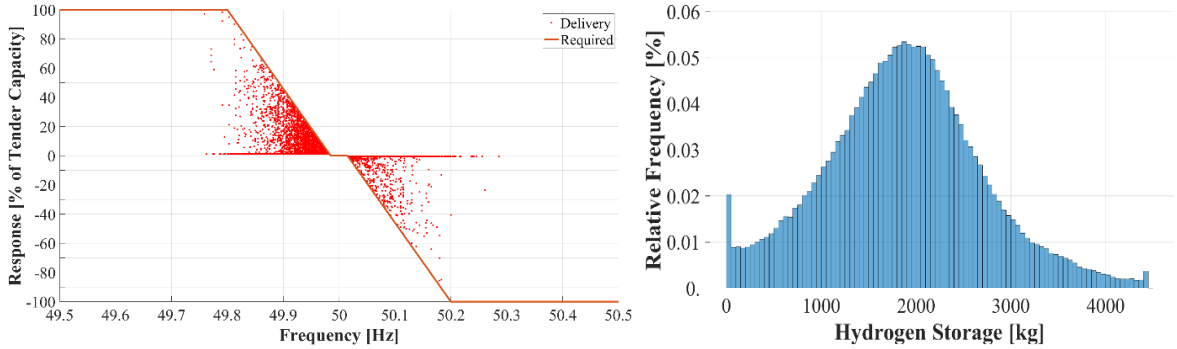


Figure 4: (a) The DR response curve against the actual delivery and (b) the relative frequency of hydrogen storage levels simulated for the full 15 years.

4. Conclusions

This paper has developed an economic optimisation algorithm to optimise the co-location of a wind farm with an onshore hydrogen-based storage system (HSS) for the provision of Dynamic Regulation (DR) frequency response in GB. A particular operating strategy has been designed to use an electrolyser and fuel cell to provide high- (HF) and low-frequency (LF) DR responses, respectively, as well as manage the hydrogen storage via operational baselines, while respecting the balance of power, hydrogen and water flows within the co-location system. The effectiveness of the HSS optimisation algorithm has been examined based on a particular 76 MW wind farm, combined with the unit prices of the electrolyser and fuel cell predicted for a 2030 scenario. The co-located HSS has been suggested to tender for 16 MW LF and 50 MW HF DR, indicating a strong correlation to the fuel cell and electrolyser efficiencies. Although the low round-trip efficiency and limited storage size of the HSS resulted in the occurrence of under-delivery events and penalties (especially for LF DR), the optimised HSS co-location project is predicted to be profitable for DR provision, showing a notable IRR of 12%.

Building on the present work, the operating strategy will be developed further to include the power consumed for keeping the electrolyser at the correct temperature and pressure in a hot-standby mode. Furthermore, active interaction between wind farm and HSS will be explored by use of an additional power converter to enable their energy interchange. In addition, the use of the hydrogen produced in HF events for local hydrogen supply will be investigated as an alternative to the hydrogen re-electrification for LF delivery.

References

[1] International Renewable Energy Agency, “Hydrogen from renewable power: Technology outlook for the energy transition,” Abu Dhabi, UAE, Sep. 2018.

[2] F. Lehner and D. Hart, “Chapter 1. The importance of water electrolysis for our future energy system.” Elsevier, Oct. 2021, pp. 1–36.

[3] T. Smolinka and J. Garche, *Electrochemical Power Sources: Fundamentals, Systems, and Applications: Hydrogen by Production by Water Electrolysis*. Elsevier, 2021.

[4] F. Fan, G. Zorzi, D. Campos-Gaona, et al., “Sizing and coordination strategies of battery energy storage system co-located with wind farm: the UK perspective,” *Energies*, vol. 14, no. 5, p. 1439, Mar. 2021.

[5] F. Fan, G. Zorzi, D. Campos-Gaona, and J. Nwobu, “Wind-plus-battery system optimisation for frequency response service: The UK perspective,” *Electric Power Systems Research*, vol. 211, p. 108400, Oct. 2022.

[6] NGESO, “Dynamic Regulation (DR),” https://www.nationalgrideso.com/industry-information/balancing-services/Frequency-Response-Services/Dynamic-Regulation, accessed on 2022-06-15.

[7] Fuel Cells and Hydrogen Joint Undertaking, “Study on early business cases for H2 in energy storage and more broadly power to H2 applications,” Brussels, Belgium, Jun. 2017.

[8] NGESO, “Dynamic Containment participation guidance document,” Warwick, UK, Oct. 2021, https://www.nationalgrideso.com/document/177121/download, accessed on 2022-06-15.

[9] International Energy Agency, “Technology roadmap: Hydrogen and fuel cell,” Paris, France, Jun. 2015.

Production, O&M, decommissioning and lifetime extension

18th EAWE PhD Seminar on Wind Energy
2 – 4 November 2022
Bruges, Belgium

Characterisation of fatigue life and short fatigue crack growth for welds used in offshore turbine monopile

Hasan Saeed[a], Somsubhro Chaudhuri[a], Wim De Waele[a]

[a] Department of EMSME, Laboratory Soete, Faculty of Engineering and Architecture, Ghent University, Technologiepark 46, BE-9052 Zwijnaarde, Belgium

E-mail: *hasan.saeed@ugent.be*

Keywords: Fatigue, Corrosion, Short crack, Pitting, Large-scale testing, S-N Curves

Offshore structures are subjected to fatigue resulting from cyclic loading of wind and waves, combined with corrosion damage due to the marine environment. It is well-known that a corrosive environment reduces the fatigue strength of steel [1]. Corrosion pits could act as nucleation sites for fatigue damage. The fatigue life comprises of three regimes; (a) crack initiation, (b) short crack growth, and (c) long crack propagation leading up to failure [2]. Offshore foundations such as monopiles are constructed by welding several cans. These welds potentially increase the risk of crack initiation due to geometrical stress concentrating features and heterogeneities in microstructure [3].

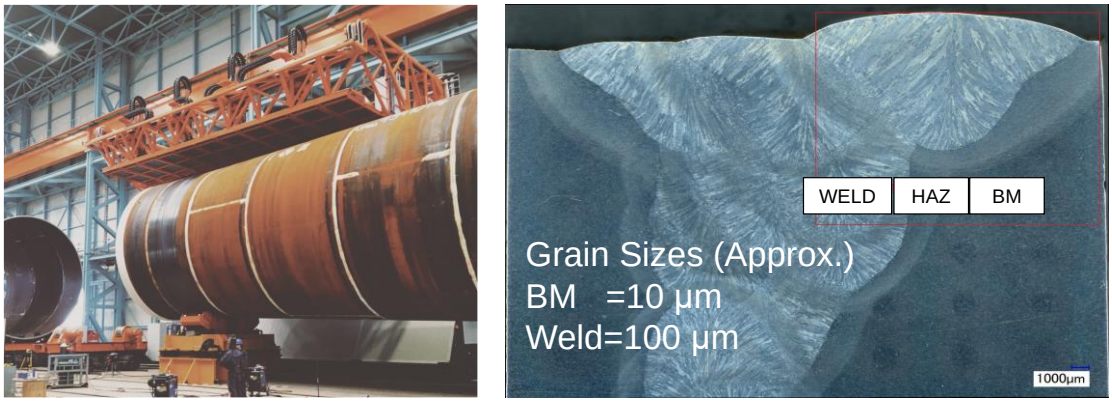


Figure 1: (Left) Weld segments in OWT monopile [4]. (Right) Microstructure of welded region.

The lifetime prediction of a component subjected to corrosion fatigue is challenging because of the need to address the phenomena of pit initiation and growth, the transition from a corrosion pit to a crack, and the subsequent fatigue crack growth in both short and long crack regimes [5]. Corrosion protection techniques are used to avoid or reduce degradation, but due to their offshore location, maintenance is challenging and expensive. For cases where the original corrosion protection system becomes defective [6], damage accumulation in periods of corrosive exposure should be investigated. The research project FATCOR investigates the physical mechanisms of corrosion fatigue for different environmental and load conditions with the aim to develop fundamental knowledge for estimating the residual life of welded steel monopiles of OWTs. This in conditions where the structure was originally protected against corrosion, but where the corrosion protection is no longer effective at a later time. The methods applied are a combination of numerical and experimental investigations:

1. A numerical analysis of (a) the stress concentration factor caused by weld geometry and corrosion pits, and (b) the stress intensity factor for small cracks that start at pits.
2. Experimental characterisation of (a) crack growth due to cyclic mechanical load combined with exposure to a corrosive environment, and (b) a representative S-N curve for butt welds used in monopile construction.

This abstract focuses on the experimental activities described under point 2.

1.1 (Short) fatigue crack growth

For steel components, the fatigue crack propagation and remaining lifetime can be predicted using linear elastic fracture mechanics based solutions available in standards [7], e.g. the well-known Paris law. However, the size of cracks initiating from pits are typically in the range of so-called short cracks [8] of which the growth cannot be quantified by classical fatigue crack growth solutions [9]. Therefore, fatigue experiments are performed on samples with notch depths (300, 500 and 700 micron) based on the grain size of the material to be representative of short cracks [10] and pit sizes investigated from industrial assets [11]. Single edge notched bending specimens (SENB-4P) for 4-point bending experiments have been extracted from welded plates of S355 steel and subjected to fatigue loading in air and immersed in synthetic seawater (ASTM D1141-98).

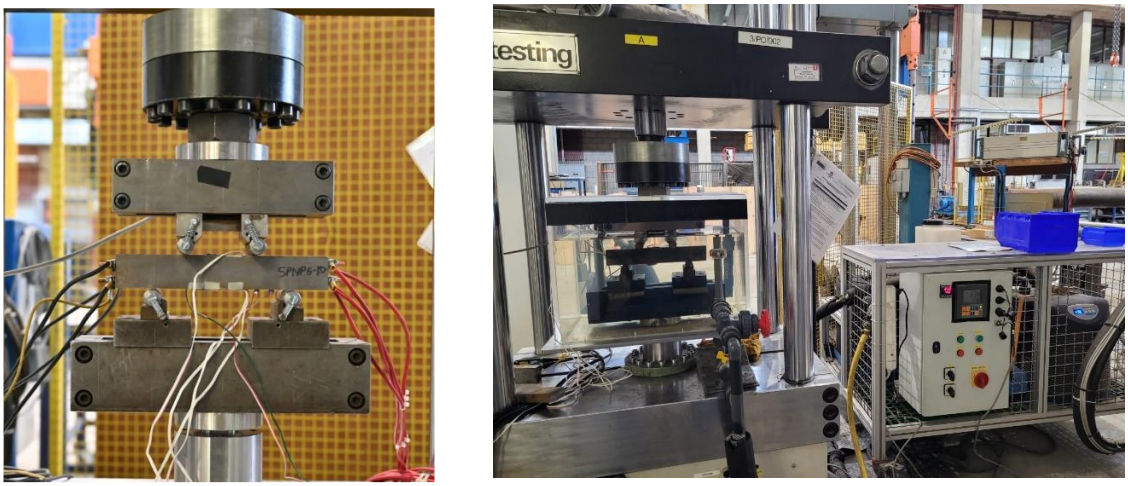


Figure 2: SENB-4P fatigue testing in air (left), and in synthetic seawater (right).

Advanced instrumentation methods have been developed to characterize the short crack growth regime using a combination of strain compliance [12], direct current potential drop (DCPD), and analysis of beach marks on the fracture face (see Figure. 3). Quantification of the crack growth rates will allow to bridge the scale of short crack to long crack propagation.

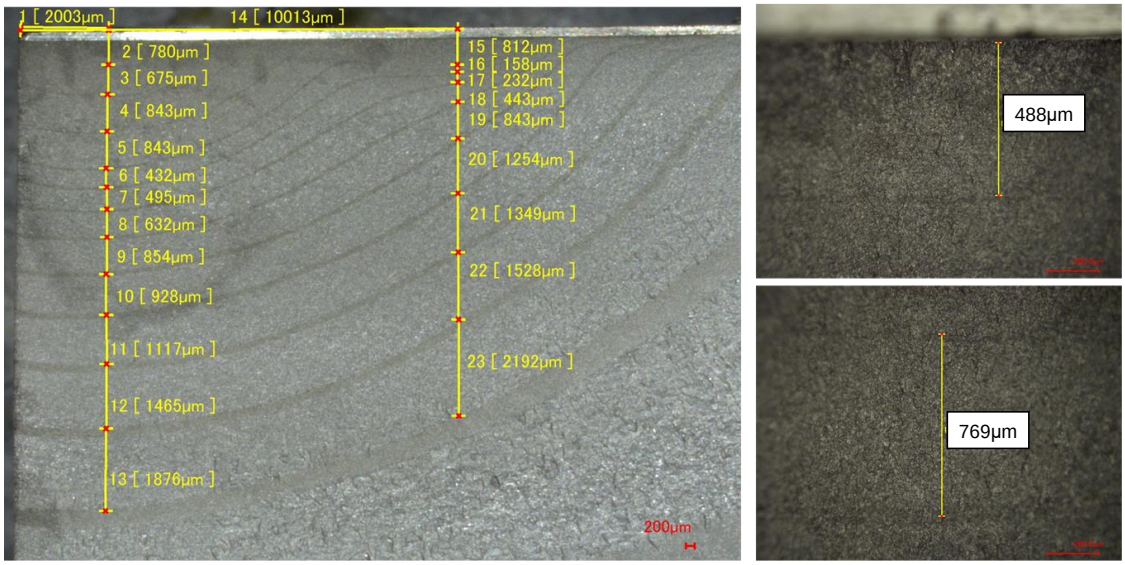


Figure 3: Detail of a fracture surface of an SENB-4P specimen tested in air with clear presence of beach marks that can be used for short crack growth rate quantification.

First analysis of the results of the SENB-4P tests performed in air shows that the majority of the fatigue life comprises of initiation and short crack growth. Similar fatigue tests with specimens immersed in synthetic seawater have been started to study the short crack growth rate in a corrosive environment and its influence on the total fatigue life.

1.2 Representative S-N curve for butt welds used in monopiles

Fatigue strength of welded joints depends on the local stresses at the weld toe and root and the corresponding stress concentration factor (SCF) [13]. To characterize the fatigue strength of welded joints it is common practice to use the endurance method based on an S-N curve [14], where S is the stress range and N represents number of load cycles to failure. S-N tests are commonly performed on small scale specimens to decrease the cost of testing, but this has the drawback of introducing a scale factor and it neglects residual stresses present due to welding [15]. In this study, however, large scale welded specimens of steel grade S355 are tested for determining an S-N curve representative for joints used offshore. The results obtained are benchmarked against S-N curves defined in BS7608-2014+A1-2015 [15] and will be compared with experimental results from small-scale experiments performed by project partners.

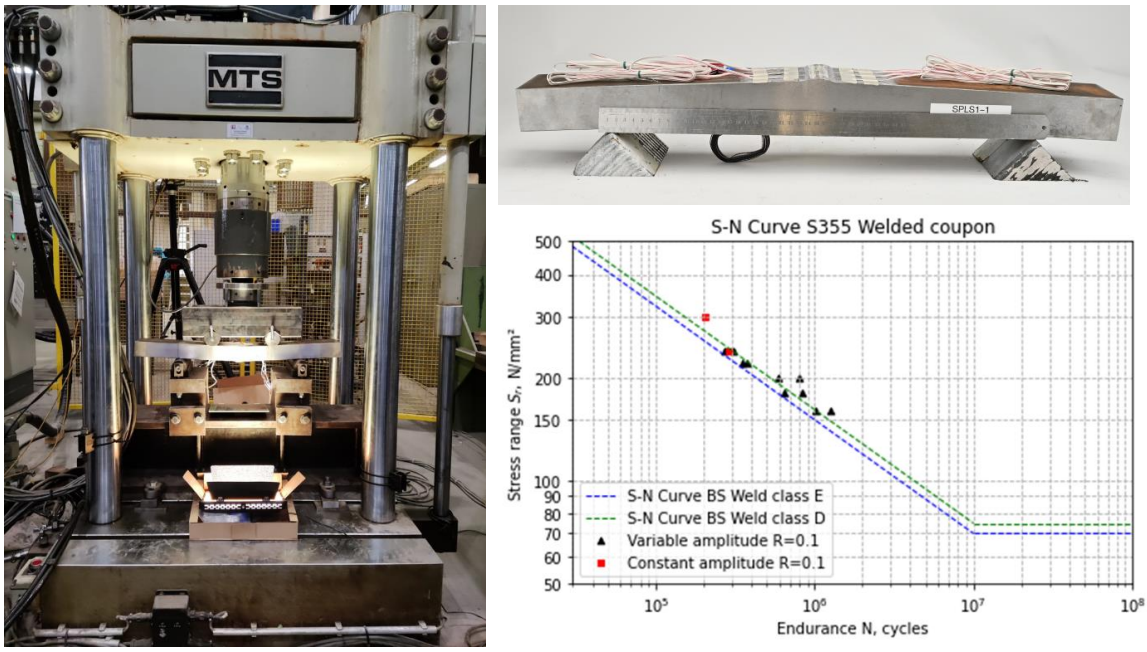


Figure 4: (Left) Fatigue testing of large-scale S355 welded coupons. (Right top) Bending specimen measuring 700mm in length, 100mm in width and 50mm in thickness. (Right bottom) Experimental results and S-N curves present in standard BS7608-2014+A1-2015 [15].

The large scale tests show that the obtained fatigue life results are in good agreement with representative S-N curves present in the BS7608-2014+A1-2015 standard [15]. Future experiments will further investigate the influence of loading and the influence of pits present in the weld region.

Acknowledgements

The authors would like to acknowledge the financial support of the Energy Transition Fund of the Federal Government of Belgium, and the contributions of project partners OCAS NV, Belgium Welding Institute (BIL), Otary, Parkwind and Smulders.

References

[1] P. M. Krol, “Productization and Instrumented Testing of a Corrosion Fatigue Test Device,” 2018.
[2] B. Main, M. Jones, and S. Barter, “The practical need for short fatigue crack growth rate models,” *Int. J.*

Fatigue, vol. 142, no. September 2020, p. 105980, 2021, doi: 10.1016/j.ijfatigue.2020.105980.

[3] N. Arzola and E. Hernández, "Experimental characterization of fatigue strength in butt welded joint considering the geometry and the effect of cooling rate of the weld," *J. Phys. Conf. Ser.*, vol. 843, no. 1, 2017, doi: 10.1088/1742-6596/843/1/012047.

[4] "Haane welding system." https://haane.de/en/fields-of-application/offshore-industry/. (accessed Aug. 08, 2022).

[5] J. A. Balbín, V. Chaves, and N. O. Larrosa, "Pit to crack transition and corrosion fatigue lifetime reduction estimations by means of a short crack microstructural model," *Corros. Sci.*, vol. 180, no. December 2020, p. 109171, 2021, doi: 10.1016/j.corsci.2020.109171.

[6] "State of the Art Study on Materials and Solutions against Corrosion in Offshore Structures," Nessie Project, 2018. [Online]. Available: www.nessieproject.com.

[7] BS 7910, "BSI Standards Publication Guide to methods for assessing the acceptability of flaws in metallic structures," *BSI Stand. Publ.*, no. UK, p. 490, 2015.

[8] S. Suresh and R. O. Ritchie, "Propagation of short fatigue cracks," *Int. Met. Rev.*, vol. 29, no. 1, pp. 445–473, 1984, doi: 10.1179/imtr.1984.29.1.445.

[9] R. Singh, A. Singh, P. K. Singh, and D. K. Mahajan, "Effect of microstructural features on short fatigue crack growth behaviour in SA508 Grade 3 Class I low alloy steel," *Int. J. Press. Vessel. Pip.*, vol. 185, no. May, p. 104136, 2020, doi: 10.1016/j.ijpvp.2020.104136.

[10] ASTM, "ASTM E647-00 Standard Test Method for Measurement of Fatigue Crack Growth Rates," 2001.

[11] C. Vanden Haute and P. Thibaux, "Quantification of pitting and stress concentration factors on steel coupons exposed to seawater in the north sea," in *Proceedings of the ASME 2022, 41st International Conference on Ocean, Offshore and Arctic Engineering OMAE2022*, 2022, pp. 1–7.

[12] H. Saeed, S. Chaudhuri, and W. De Waele, "Extended back-face strain compliance solution for physically short crack regime in SENB-4P specimen," in *Book of Abstracts, 23rd European Conference on Fracture*, 2022, p. 327, [Online]. Available: https://www.ecf23.eu/abstracts/ECF23_Book_of_Abstracts.pdf.

[13] S. J. Maddox, *Fatigue design rules for welded structures*. Woodhead Publishing Limited, 2011.

[14] N. Micone and W. De Waele, "Comparison of fatigue design codes with focus on offshore structures," in *International Conference on Offshore Mechanics and Arctic Engineering*, 2015, vol. 56475, p. V001T01A033.

[15] BS 7608-2014+A1-2015 -, "Guide to fatigue design and assessment of steel products," pp. 1–140, 2014.

18th EAWE PhD Seminar on Wind Energy
2 – 4 November 2022
Bruges, Belgium

Circular Supply Chain Management for the German Wind Energy Industry

Kathrin Julia Kramer

Institute of Product and Process Innovation (PPI), Leuphana University, 21335 Lüneburg, Germany

E-mail: kathrin.kramer@leuphana.de

Keywords: Circular Supply Chain Management, Sustainability, Circular Economy, Wind Energy, Demand Forecast, Capacity Planning, Stock Planning, Germany

1. Motivation and Problem Definition

Supply chains have to be designed, planned and managed in a way that they can handle complexity and uncertainties while simultaneously achieving a system change towards more sustainability [1,2]. In this context, circular economy (CE) is a concept that lately gains interest as it could empower a sustainable and resilient system [1,4,3,5]. CE is defined as "*economic system that is based on business models which replace the 'end-of-life' concept with reducing, alternatively reusing, recycling and recovering materials in production/distribution and consumption processes, thus operating at the micro level (products, companies, consumers), meso level (eco-industrial parks) and macro level (city, region, nation and beyond), with the aim to accomplish sustainable development, which implies creating environmental quality, economic prosperity and social equity, to the benefit of current and future generations*" [6]. Central is to change the system, products and processes by designing out waste and pollution. It can be achieved through circular business models and adequate infrastructure [3]. Hence, the circular thinking has also to be embedded into supply chain management (SCM), known as circular supply chain management (CSCM) [7]. CSCM focuses on the material, information and financial flows within a supply chain by considering circular thinking.

A key guiding principle of CSCM is to use regenerative and restorative materials instead of finite ones [3,8]. For example, the steel industry aims at using renewable energy for their production instead of fossil energy [9]. Therefore, governments such as Germany have announced high expansion targets for renewable energy sources, especially for wind turbines and photovoltaic plants [10]. However, the wind energy and photovoltaic industry are still linear systems that are built on finite materials. Especially, the waste volumes of wind turbines are expected to increase massively in absolute terms if the wind energy industry does not transform to a circular system with regenerative and restorative cycles [11]. Despite, research on CSCM for the wind energy industry is still rare. So far, no structured overview of the circular supply chains of the wind energy industry exists [12]. Therefore, the PhD thesis will focus on the wind energy industry as a suitable application for further research on CSCM. For transforming to a circular system, strategies that narrow, slow and close flows need to be investigated: On the one hand for the existing portfolio of wind turbines (e.g. design of a reverse supply chain) and on the other hand for newly to be installed turbines (e.g. product design for circularity like modularization) [13].

The scope of the thesis is limited to a country-wide market for having an object of investigation with similar market conditions. Germany is chosen as it has an established wind energy industry with several stakeholders and a comprehensive market register. The first turbine was installed in 1983, thus the German market has a track record of more than 30 years. As of end April 2022, more than 30,000 wind turbines are in operation, of which 27% operate with an age of 20 years or older [14,15]. With lifespans of roughly 20-30 years a high turnover of materials

is expected for the next years. That highlights the importance to focus on CSCM for the German wind energy industry as it could strengthen the availability of turbines, components and materials. For example, supply chain managers could reduce dependencies from scarce raw materials by using secondary materials [16]. This is important for Germany as the country is scarce of raw materials [17]. Moreover, the expansion of renewable energies is of central importance to become more self-sufficient from importing energy and achieving carbon neutrality [10].

In summary, the aim of the PhD thesis is to contribute to a CSCM for the German wind energy industry. First, the CSCM is conceptualized for the research subject in order to frame a theoretical understanding as a basis for the dissertation. Secondly, as empirical investigations (e.g. case studies) on CE or CSCM applications are still a research gap [18–20], requirements for implementing a CSCM are outlined. Essential is the establishment of a closed material flow across the supply chain, hence also enabling to return goods [7,21]. For its efficient development, reliable long-term forecasts of when and where which turbine or component will be returned are crucial [15,22]. This is of importance to empower long-term capacity and stock planning (e.g. acquisition of machines or vessels) for different stakeholders (e.g. (re)manufacturer, recycling company) of the supply chain. This would avoid capacity and stock surpluses and shortages, enabling viable business models for each player in the supply chain.

This leads to the three research questions (i) "h*ow does the CSCM for the German wind energy industry look like?*", (ii) "*what are key requirements for the implementation of a CSCM?*" and (iii) "*when and where will how many turbines be returned and what are the resulting capacity and stock requirements for supply chain actors?".*

2. Planned Research Methods

To answer the first research question, mixed methods are used to develop a conceptual overview of CSCM for the German wind energy industry. As no overview for the object of research exists, general concepts on CSCM form the basis. Through a literature review, existing research is identified and analysed. Further research at the intersection of CE and wind energy as well as on SCM and wind energy are identified to adapt a general CSCM framework with specifics from the wind energy industry. Finally, semi-structured interviews with experts from the German wind energy industry as well as analyses of market data (e.g. register by Bundesnetzagentur [14]) are conducted to refine the conceptual CSCM overview for the German wind energy industry.

For answering the second research question, existing theoretical and empirical literature on the implementation of CSCM and more broadly of CE are identified (e.g. Mendoza et al. [22], Poulsen et al. [23], Kirchherr et al. [19]). CE is reflected to increase the number of relevant publications and consequently not to overlook important requirements that could also be meaningful for the CSCM implementation. Kirchherr et al. [19], for example, performed a survey in the European Union on the barriers to CE adoption. They differ between technological, market, cultural and regulatory barriers that also form the basis for clustering the identified publications herein. As CE and CSCM are still emerging, it is likely that no empirical case studies will be found that address a multi-level, multi-objective CSCM. Kramer/Schmidt [12] conclude this for wind energy-specific CSCM. In this case, empirical studies covering some aspects are analysed. Finally, the identified articles should be summarized in an overview that could distinguish between (i) empirical and theoretical studies that investigate (ii) CE or CSCM, (iii) technological, market, cultural or regulatory requirements and (iv) general or industry-specific applications. The findings of the papers are analysed regarding their similarities and differences. To evaluate the findings and their relevance for the German wind energy industry semi-structured interviews with industry experts will be conducted. The clustered results of the literature review are the foundation for preparing the interview guide. The method is chosen as it enables the interviewer to comprehensively explain the CSCM concept and the interviewee can answer the questions in more depth than if alternatively, a survey would be conducted [24]. This is of importance as CE/CSCM is still a new concept and there is no standard definition [6,21]. Thus, the risk of different understandings of the CSCM concept can be reduced.

The third research question is answered by developing a capacity and stock overall model that can handle the uncertainty and complexity of the system. To begin with, potential factors that influence the date of decommissioning a wind turbine are analysed, using quantitative and qualitative methods. As a quantitative

analysis, available data of the 621 decommissioned plants in Germany is considered and statistical as well as machine learning methods are used to identify potential patterns. For instance, the current spot power prices or the current prices on secondary components could influence the decision. Secondly, semi-structured interviews with industry experts, that base on the quantitative findings, will supplement the list of influencing factors. These factors form the basis for the deductively development of a capacity and stock overall model for supply chain stakeholders. Different scenarios can be simulated and used to forecast reasonable CE developments paths in the German wind energy industry.

3. Expected Outcomes

The expected outcome of the first part of the PhD thesis is a multi-level, multi-objective CSCM conceptual overview for the German wind energy industry. It is likely that it could base on the work by Montag et al. [8] as identified as a suitable CSCM overview in preparatory work [15]. Kramer/Schmidt propose a preliminary concept with an organization, products and processes level. Additional findings from literature, market data and expert interviews are used to refine this work. For instance, the processes according to Vegter et al. [25] will be further described. Secondly, an overview of requirements for the implementation of a CSCM or CE, that were discussed in literature, is given. Moreover, the findings from the interviews will evaluate the identified requirements in regards to the relevance for the German wind energy industry and will also enable to add further requirements, if applicable. One requirement that is of relevance for the German wind energy industry is the knowledge of when and where how many turbines will be returned [15,22]. This is of importance for the determination of required capacities (e.g. number of workers, machines, warehouses) and stocks (e.g. number of spare parts, raw material). Thus, the aim is to provide a rough overall model for the capacity and stock planning that reflects influencing factors for the return of turbines. Through simulations, the model could reflect current events and could update predictions. Overall, the model could function as a foundation for decisions of politicians, industry associations and companies in regards to a reasonable development of a CSCM in the German wind energy industry.

In conclusion, the PhD thesis proposes a potential CSCM for the German wind energy industry and highlights its requirements for implementation. By providing a deductive model, different stakeholders receive a basis for decision making that could enable the development of viable business models. Consequently, the results could increase the sustainability and resilience of the German wind energy industry.

Acknowledgements

Funded by the Lower Saxony Ministry of Science and Culture under grant number ZN3489 within the Lower Saxony “Vorab” of the Volkswagen Foundation and supported by the Center for Digital Innovations (ZDIN).

References

[1] Bocconi University, Ellen MacArthur Foundation, Intesa Sanpaolo, 2021. *The circular economy as a de-risking strategy and driver of superior risk-adjusted returns.* http://www.ellenmacarthurfoundation.org/publications. Accessed 21 February 2022.

[2] Khan, S.A.R., Yu, Z., 2019. *Strategic Supply Chain Management*. Springer International Publishing, Cham.

[3] Ellen MacArthur Foundation, 2019. *Completing the Picture: How the Circular Economy Tackles Climate Change*. www.ellenmacarthurfoundation.org/publications. Accessed 21 February 2022.

[4] Chaouni Benabdellah, A., Zekhnini, K., Cherrafi, A., 2021. *Sustainable and Resilience Improvement Through the Design for Circular Digital Supply Chain*, in: Dolgui, A., Bernard, A., Lemoine, D., Cieminski, G. von, Romero, D. (Eds.), Advances in Production Management Systems. Artificial Intelligence for Sustainable and Resilient Production Systems, vol. 633. Springer International Publishing, Cham, pp. 550–559.

[5] Negri, M., Cagno, E., Colicchia, C., Sarkis, J., 2021. *Integrating sustainability and resilience in the supply chain: A systematic literature review and a research agenda*. Bus Strat Env 30 (7), 2858–2886.
[6] Kirchherr, J., Reike, D., Hekkert, M., 2017. *Conceptualizing the circular economy: An analysis of 114 definitions*. Resources, Conservation and Recycling 127, 221–232.
[7] Farooque, M., Zhang, A., Thürer, M., Qu, T., Huisingh, D., 2019. *Circular supply chain management: A definition and structured literature review*. Journal of Cleaner Production 228, 882–900.
[8] Montag, L., Klünder, T., Steven, M., 2021. *Paving the Way for Circular Supply Chains: Conceptualization of a Circular Supply Chain Maturity Framework*. Front. Sustain. 2.
[9] Bundesministerium für Wirtschaft und Energie, 2020. *Für eine starke Stahlindustrie in Deutschland und Europa!: Handlungskonzept Stahl*.
[10] Sozialdemokratische Partei Deutschland, Bündnis 90 / Die Grünen, Freie Demokratische Partei, 2021. *Mehr Fortschritt wagen - Bündnis für Freiheit, Gerechtigkeit und Nachhaltigkeit: Koalitionsvertrag zwischen SPD, Bündnis 90/ Die Grünen und FDP*, 178 pp.
[11] European Environment Agency, 2021. *Expected growth of waste materials generated by the clean-energy infrastructure*. https://www.eea.europa.eu/publications/emerging-waste-streams-opportunities-and. Accessed 10 May 2022.
[12] Kramer, K.J., Schmidt, M., in press. *Circular Supply Chain Management in the Wind Energy Industry - A Systematic Literature Review*.
[13] Velenturf, A.P.M., 2021. *A Framework and Baseline for the Integration of a Sustainable Circular Economy in Offshore Wind*. Energies 14 (17), 5540.
[14] Bundesnetzagentur für Elektrizität, Gas, Telekommunikation, Post und Eisenbahnen, 2022. *Marktstammdatenregister*. https://www.marktstammdatenregister.de/MaStR/. Accessed 3 June 2022.
[15] Kramer, K.J., Schmidt, M., in press. *Circular supply chain management for the wind energy industry: Conceptional ideas towards more circularity*.
[16] Wannenwetsch, H., 2014. *Integrierte Materialwirtschaft, Logistik und Beschaffung*, 5., neu bearb. Aufl. ed. Springer-Vieweg, Berlin, Heidelberg, 794 pp.
[17] Alves Dias, P., Bobba, S., Carrara, S., Plazzotta, B., 2020. *The role of rare earth elements in wind energy and electric mobility: An analysis of future supply/demand balances*. Publications Office of the European Union, Luxembourg, 1 online resource.
[18] Corvellec, H., Stowell, A.F., Johansson, N., 2021. *Critiques of the circular economy*. Journal of Industrial Ecology, 1–12.
[19] Kirchherr, J., Piscicelli, L., Bour, R., Kostense-Smit, E., Muller, J., Huibrechtse-Truijens, A., Hekkert, M., 2018. *Barriers to the Circular Economy: Evidence From the European Union (EU).* Ecological Economics 150, 264–272.
[20] Lopes de Sousa Jabbour, A.B., Jabbour, C.J.C., Godinho Filho, M., Roubaud, D., 2018. *Industry 4.0 and the circular economy: a proposed research agenda and original roadmap for sustainable operations*. Ann Oper Res 270 (1-2), 273–286.
[21] Lengyel, P., Bai, A., Gabnai, Z., Mustafa, O.M.A., Balogh, P., Péter, E., Tóth-Kaszás, N., Németh, K., 2021. *Development of the Concept of Circular Supply Chain Management—A Systematic Review*. Processes 9 (10), 1740.
[22] Mendoza, J.M.F., Gallego-Schmid, A., Velenturf, A.P., Jensen, P.D., Ibarra, D., 2022. *Circular economy business models and technology management strategies in the wind industry: Sustainability potential, industrial challenges and opportunities*. Renewable and Sustainable Energy Reviews 163, 112523.
[23] Poulsen, T., Lema, R., 2017. *Is the supply chain ready for the green transformation? The case of offshore wind logistics*. Renewable and Sustainable Energy Reviews 73, 758–771.
[24] Bryman, A., 2012. *Social research methods*, 4. ed. ed. Oxford Univ. Press, Oxford, 766 pp.
[25] Vegter, D., van Hillegersberg, J., Olthaar, M., 2020. *Supply chains in circular business models: processes and performance objectives*. Resources, Conservation and Recycling 162, 105046.

18th EAWE PhD Seminar on Wind Energy
2-4 November 2022
Bruges, Belgium

I spy with my little eye, or: estimating offshore wind farm installation times utilizing satellite data

Aljoscha Sander[a,c], **Albert Baars**[b], and **Eize Stamhuis**[a]

[a]Energy and Sustainability Research Institute Groningen, University of Groningen, Groningen, The Netherlands
[b]University of Applied Sciences Bremen, Bremen, Germany
[c]Institute for Integrated Product Development, University of Bremen, Bremen, Germany

16.08.2022

E-mail: aljoscha.sander@rug.nl

Keywords: Offshore Wind Farm Installation, GNSS, ERA5

Introduction

With 5,795 offshore wind turbines operational in Europe alone (June 2022), offshore wind has become a major source of electricity in several countries, and 22 years of installing offshore wind farms has led to a significant amount of learning in the industry. While a great deal of scientific literature is available on wind turbine design and operations, the body of literature dealing with offshore wind farm installations is comparatively small, even though installing wind turbines offshore imposes a complex and thus scientifically interesting problem.

The installation of an offshore wind farm is by no means an easy undertaking: metocean conditions must be within narrow limits to allow save operations. Specialized equipment, vessels, and crews are required. The continuously increasing size of turbines, as well as increasing water depths, and new locations where little experience is available, add to the risks associated with installations. Unforeseen downtimes are costly and put additional strain on already difficult operations.

In this study, we investigate how metocean conditions correlate with offshore wind farm installation times. We compile a statistical overview of offshore wind farm installations: from satellite data, we extract correlations between turbine size, wind farm locations, installation vessels and installation duration with metocean conditions during the installation process. Finally, we extract the observed metocean limits for turbine sizes, manufacturers, vessels, and locations.

Methods

To reliably extract installation times for as many offshore wind farms as possible, we acquired hourly *Automatic Identification System* (AIS) vessel data from a data broker. The AIS data includes 9 offshore wind installation vessels over a period of 11 years (see Table 1).

Each AIS vessel record includes latitude, longitude, speed, heading, course and a timestamp for a given vessel. To extract installation times per turbine per offshore wind farm, we preselected vessel records where the speed of the vessel was 0 and further removed records where the vessel was close to shore or in port. The vessel records were then automatically clustered using the DBSCAN algorithm as implemented in the scikit-learn python package. These clusters were then cross-referenced with the locations of offshore wind farms to select vessel records within a given radius of a known wind farm. To yield vessel records corresponding to single turbine installations, each wind farm cluster was clustered again with the DBSCAN algorithm, yielding vessel records corresponding to individual turbines. Only turbine locations where at least two vessel records were available were kept for further analysis. Installation times per turbine were then calculated by assuming, that the first available

Table 1: AIS vessel data used in this study.

MMSI	Name	Data time range
218389000	Thor	2010 - 2021
218657000	Vole au Vent	2013 - 2021
219019002	Sea Challenger	2013 - 2021
229044000	Brave Tern	2012 - 2021
229080000	Bold Tern	2013 - 2021
235090598	Blue Tern	2015 - 2021
245179000	Aeolus	2010 - 2021
245924000	MPI Adventure	2010 - 2021
246777000	MPI Resolution	2010 - 2021

AIS vessel record corresponds to the beginning of turbine installation activities and the last AIS record marks the end of installation activities. Based on the time stamps of the AIS records per turbine, ERA5 metocean data was requested for the wind farm location. ERA5 data includes wind speed and wind direction at several altitudes, wave direction, wave period and significant wave height. For each wind farm, metadata such as wind turbine model, rated power and foundation type were collected, and all data was combined into a SQLite database. The database will be made available to the public once analysis has been completed.

Results

Figure 1 shows several potential wind farms as extracted from the AIS vessel records of the installation vessel Sea Challenger. As an example, cluster 3 (Figure 2) corresponds to the offshore wind farm Gode Wind.

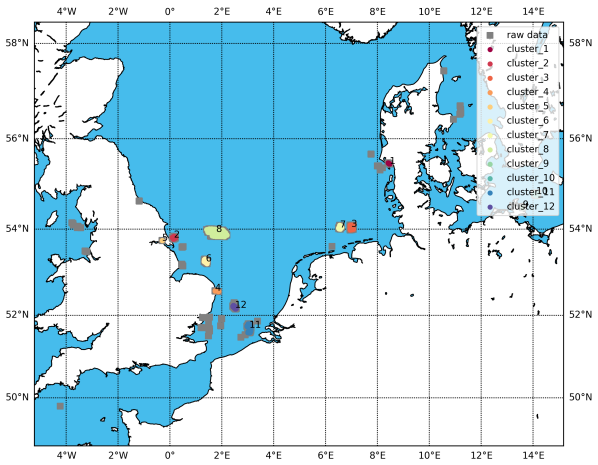


Figure 1: Potential wind farms automatically extracted from AIS vessel records of the vessel Sea Challenger. Cluster 3 corresponds to the offshore wind farm Gode Wind, located in the German Bight in the North Sea.

Applying the clustering algorithm to cluster 3 in Figure 1 yields vessel tracks corresponding to individual wind turbines.

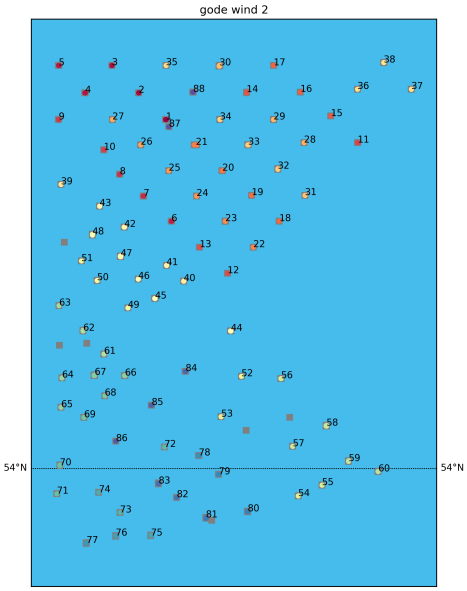


Figure 2: Individual turbines extracted from AIS vessel records for the offshore wind farm Gode Wind.

18th EAWE PhD Seminar on Wind Energy
2 – 4 November 2022
Bruges, Belgium

Leading edge erosion of wind turbine blades, lifetime and roughness modelling for coatings

Antonios Tempelis [a], Leon Mishnaevsky Jr [a]

[a] Department of Wind and Energy Systems, Technical University of Denmark, DTU Risø Campus, Denmark

E-mail: atem@dtu.dk

Keywords: leading edge erosion, finite element modeling, coatings, lifetime prediction, roughness, digital twin

1. Introduction

Surface erosion of wind turbine blades is one of the challenges compromising the development of the wind energy [1, 2]. As an example, the Danish energy company Ørsted had to repair a number of blades at the Anholt Offshore Wind Farm in 2016. Surface erosion affects mostly the leading edge of wind turbine blades. Leading edge erosion can lead to elevated repair and maintenance costs as well as the stopping of the turbine's operation for the repairs to take place. The energy production of the turbine is limited to zero during the repair time. Furthermore, an eroded leading edge can limit the energy production capacity during the operation of the turbine by increasing the blade's drag coefficient and decreasing the generated lift force. The figure below shows an example of an eroded leading edge on a wind turbine blade.



Figure 1: Errored leading edge (by Christian Bak) [1]

Leading edge erosion of wind turbine blades is a result of repeated multiple liquid impacts by raindrops, combined with hail, wind pressure variations, moisture, insects, sand, dust, ultraviolet and thermal environmental loading. A rain droplet hits surfaces, leading to contact pressure on the surface, and triggering wave propagation in protective layers. This leads to the damage initiation, materials degradation, fatigue, and then to coating cracking, debonding, cracks in composite, surface roughening. Figure 2 shows the schema of the erosion of coatings. Leading edge erosion of wind turbine blades is also a complex problem for computational modelling, including material fatigue, viscoelastic deformation of coatings, multiple dynamic impacts, damage mechanics, stochastic factors and stress wave propagation.

2. Scope of this work

The droplet impact phenomenon has been studied by Adler [3] and the mechanisms, negative effects of leading edge erosion and possible solutions have been studied in a review made by Keegan et al. Analytical Lifetime

prediction methods have been developed by Springer [4] and Slot [5]. Computational studies and lifetime prediction tools have been developed by Amirzadeh et al. [6].

This project aims at developing a computational predictive model for the evaluation and prediction of leading edge erosion based on understanding of the physical mechanisms of erosion, computational mechanics of materials and possibly artificial intelligence methods.

At a later stage, the feasibility of informing the computational model with real world data from a real wind turbine will be assessed, with the aim of creating a digital twin. This digital twin should be able to collect erosion data from the leading edge of a blade and then utilize this data to perform predictions for the remaining lifetime of the leading edge protection as well as estimations for the resulting roughness values.

3. Tools and methods

A model-based lifetime estimation solution will be examined first. Finite element models of a single droplet impact on a small representative volume of the leading edge protection material will be used to study the impact phenomenon and calculate the stresses generated during the impact. The results of the finite element models will be used to calculate a stress-based damage value for the leading edge protection. This damage value will be the basis for the lifetime estimation, as well as for the estimation of roughness by creating a damage field over a small area of the leading edge. The outcome of this model will be compared to data from rain erosion testing.

Then, a data driven approach will be examined, where lifetime and roughness data from rain erosion testing will be used to make predictions based on a number of parameters. These parameters are the tip speed of the blade, the raindrop diameters, the rain intensity and the duration of a rain event. An artificial intelligence-based approach will be used for this purpose.

For the digital twin part, data in the form of pictures of the eroded leading edge are to be used. Meteorological data such as rain duration and rain intensity will be used in conjunction with images to generate lifetime and roughness predictions for the leading edge protection.

4. Expected outcomes

The following outcomes are expected from this research projects:

1. A model able to adequately predict coating lifetimes based on meteorological data and material data for the coating of the blade.
2. A model that can generate roughness values estimations of the leading edge which can be used in Annual Energy Production (AEP) losses for wind turbines.
3. A feasibility study of using data in the forms of images to accurately assess the existing damage due to leading edge erosion and make predictions for the remaining lifetime.
4. A parameter study of how material properties of the coatings affect their performance against rain erosion.

References

[1] L. Mishnaevsky Jr., C. Hasager, C. Bak, A.M. Tilg, J. I. Bech, S. D. Rad, S. Fæster, Leading edge erosion of wind turbine blades: Understanding, prevention and protection, *Renewable Energy*, 169:953-969, 2021

[2] N.F.J. Johansen, L. Mishnaevsky Jr., A. Dashtkar, N. A. Williams, A. Silvello, I.G.Cano, H. Hadavinia, Nanoengineered graphene reinforced coating for leading edge protection of wind turbine blades, *Coatings,* 11(9):1104, 2021.

[3] W. F. Adler, The mechanics of liquid impact. *Academic Press, Treatise on Materials Science and Technology,* 16:127-183, 1979.

[4] G. S. Springer, Erosion by liquid Impact, 1976.

[5] H.M. Slot, E.R.M. Gelinck, C. Rentrop, E. van der Heide, Leading edge erosion of coated wind turbine blades: Review of coating life models, *Renewable Energy*, 80:837-848, 2015.

[6] B. Amirzadeh, A. Louhghalam, M. Raessi, M. Tootkaboni, A computational framework for the analysis

of rain-induced erosion in wind turbine blades, part I: Stochastic rain texture model and drop impact simulations, *Journal of Wind Engineering and Industrial Aerodynamics*, 163:33-43, 2017.

[7] S.D. Rad, L. Mishnaevsky Jr, Leading edge erosion of wind turbine blades: Computational modelling of multiaxial fatigue, *Wind Energy,* 23(8): 1752-1766, 2020.

[8] L. Mishnaevsky Jr., S. Fæster, L. P. Mikkelsen, Y. Kusano and J.I. Bech, Micromechanisms of leading-edge erosion of wind turbine blades: X-Ray tomography analysis and computational studies *Wind Energy*, 23(3):1–16, 2019.

18th EAWE PhD Seminar on Wind Energy
2-4 November 2022
Bruges, Belgium

Predicting the Mechanical Performance of Composite Materials and Sub-components for Wind Turbine Blades Through Manufacturing Modelling

J. K. Jørgensen[a], **L. P. Mikkelsen**[a], **T. L. Andersen**[a], and **P. U. Haselbach**[b]

[a]DTU Wind and Energy Systems - Section of Composites Manufacturing and Testing
[b]DTU Wind and Energy Systems - Section of Structural Design and Testing

E-mail: jkjjo@dtu.dk

Keywords: Numerical simulation, polymer curing, residual stresses, simulation couplings

1 Modelling the Cure-induced Process-strains in Composite Material

1.1 Affects of Residual Stresses on Composite Performance

Through years of study it is known that composites are susceptible to the presence of residual stresses. This is known to affect the physical appearance of the product negatively as well as reduce the mechanical performance, especially regarding fatigue [1] [2].

Predicting the development of these residual stresses is found by studying the curing of the polymer resin and the shrinkage it attains. The curing of the polymer is found to come from two main contributions.

One of these are the chemical shrinkage developing as the curing progresses. The resin changes from a liquid to a solid through polymerisation and cross-linking of the polymer. In this process the resin reaches a point where it can transfer load to the fibres embedded in the resin. This point of cure is known as the "*point of gelation*", where the resin enters a rubber-like phase. From this point and onward, the resin can be characterised as a material with its own modulus of elasticity. Which further develops until the material is fully cured. This in turn, results in a chemical strain due to the compaction and cross-linking of the polymer chains.

The second contribution is a thermal strain introduced from the exothermal nature of the chemical reaction, as well as the process temperature cool-down. Together, these strains are referred to as the cure-induced strains achieved from manufacturing of the composite.

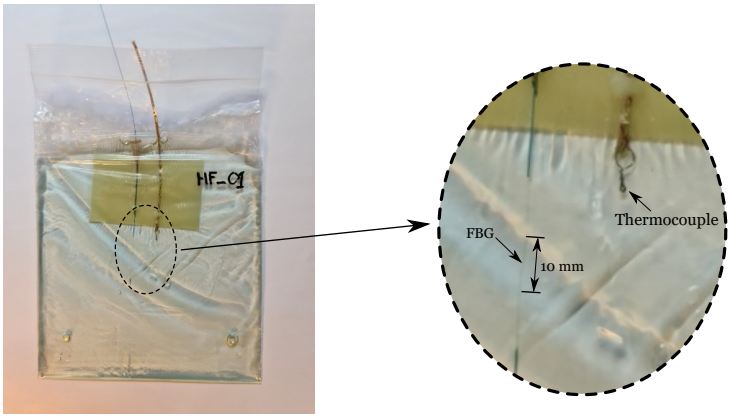


Figure 1: Experimental setup of the neat unconstrained resin with thermocouple and FBG sensor, with the 10 mm measurement path shown.

1.2 Measuring the Cure-induced Strains in Neat Unconstrained Resin

To quantify the amount of strain introduced into composites, the section of Composites Manufacturing and Testing (COM) at the Technical University of Denmark has developed a unique test setup, see Figure 1. This setup is based on measuring the cure-induced strains introduced by curing neat unconstrained polymers (e.g. epoxy) in an oven. The strains are measured with a Fibre-Bragg-Grating sensor, also known as FBG. This gives the opportunity to make in-situ measurements of the cure-induced strains. Including the measurements of the oven and material temperature through thermocouples [3].

1.3 Predicting the Cure-induced Strains Through Coupled Simulation

This PhD project aims to further understand the development of residual stresses through finite element models able to predict this material behaviour.

The experimental setup explained in subsection 1.2 will be modelled with the purpose of reproducing the measurements through the model. The purpose of which is to accurately capture the strains induced and then be able to further develop models capturing the residual stresses in manufactured composites. The model is made in

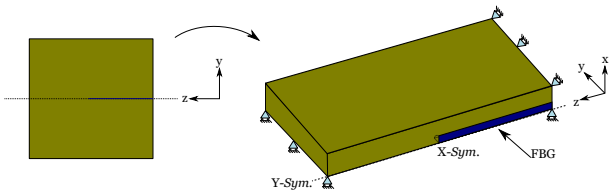


Figure 2: The concept of the FE model based on the neat resin experiment.

the commercial finite element software ABAQUS®. Where the complex curing will be handled by coupling with the multiscale material modelling tool Digimat®. The model is based on a quarter of the neat resin experiment modelled with symmetry conditions. The basic concept of which can be seen in Figure 2

The software Digimat® is a product supplied by the Hexagon Group with many material models implemented, including curing of polymers. The program can run in parallel with computations in ABAQUS. The Digimat® software is setup to handle the curing through the user-defined subroutines interface in ABAQUS®. The resin properties are updated in every integration point for every simulation increment. Results are given as State-Dependent-Variables (SDV) in the output file, giving information about Degree of Cure (DoC), thermal strains, chemical strains and the total strains for the cure cycle of the resin. This makes it possible to monitor the development of the strains induced as curing progresses over time. An example of which is shown in Figure 3. The goal of the model implementation is to accurately capture the behaviour of the experiment and then further expand with more complex models taking viscoelastic relaxation and presence of fibres into account over the duration of the PhD.

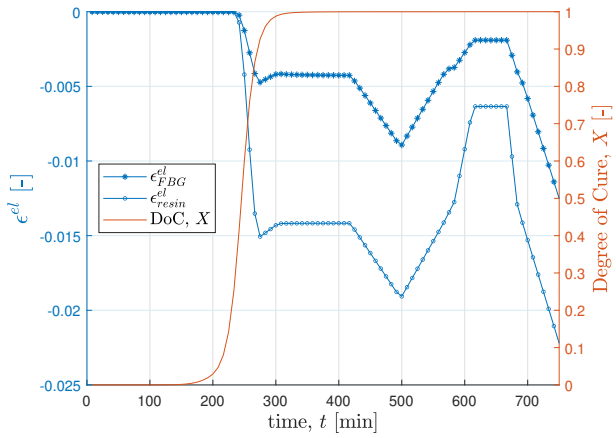


Figure 3: An example of simulation DoC and strains monitored in the FBG and the resin over time.

References

[1] Marco Aurelio Miranda Maduro. *Influence of Curing Cycle on the Build-up of Residual Stresses and the Effect on the Mechanical Performance of Fibre Composites*. PhD thesis, The Technical University of Denmark, Denmark, 2021.

[2] Ulrich Andreas Mortensen. *Process Parameters and Fatigue Properties of High Modulus Composites*. PhD thesis, Technical University of Denmark (DTU), Denmark, 2019.

[3] L. P. Mikkelsen. In-situ measurements of the load transferring shrinkage of thermosets used in composite materials for wind turbine blades. (62456), 2022. ECCM20 - Composites Meets Sustainability.

18th EAWE PhD Seminar on Wind Energy
2-4 November 2022
Bruges, Belgium

Rolling horizon based adjustable maintenance management: A case study of a 3-MW wind turbine

Mingxin Li[a], **Xiaoli Jiang**[a], **James Carroll**[b], and **Rudy R. Negenborn**[a]

[a]Department of Maritime and Transport Technology, Delft University of Technology, Delft, The Netherlands
[b]Department of Electronic and Electrical Engineering, University of Strathclyde, Glasgow, United Kingdom

E-mail: m.li-6@tudelft.nl

Keywords: Rolling Horizon; Wind Energy; Operation and Maintenance

1 Introduction

Operation and maintenance (O&M) cost accounts for about 30% of the life cycle costs for wind energy [8]. With offshore wind energy, this proportion is higher due to marine environment [5]. In order to ensure the business case for many sites, it is necessary to improve the current maintenance management plan and reduce the related O&M cost.

The existing models mostly use an open-loop approach to optimize the maintenance strategy [1, 2]. The main focus of past studies is developing the model illustrating the target maintenance strategy applied on the onshore/offshore wind projects, and then using an optimizer to optimize the developed model. The optimization process is only performed once to determine the optimal solution. This solution instructs the performance of maintenance activities during the entire lifetime of the project.

However, such an open-loop decision-making approach ignores the variable states of the wind project [6]. In the context, the research question emerges: How can an adjustable wind farm maintenance strategy that captures varying operational states be developed?

2 Method

2.1 Decision-making framework

Fig. 1 illustrates a maintenance decision-making framework. The decision-maker (wind farm owner and operator or maintenance service provider) uses a combination of a maintenance model and an optimizer to determine a set of maintenance decisions for the maintenance implementer. Given this strategy, the maintenance implementer decides whether to start a cycle of maintenance according to the observation of the wind turbine health states. The condition monitoring and remaining useful life (RUL) prediction technology is employed to judge the component states. Once a maintenance cycle begins, the specific maintenance vessels, spare parts, and technicians are mobilized to carry out the planned maintenance actions. In addition, the future maintenance plan is designed considering the current wind turbine state. Then, the decision-maker uses the model with the updated wind turbine state to determine a new maintenance strategy for the next period of time. In this way, an adjustable maintenance management plan is proposed following such a closed-loop approach.

2.2 Wind turbine system and maintenance model

A discrete manner is proposed to represent the wind turbine state, where the information is updated every time period of Δs, thereby existing U time periods where $U = S/\Delta s$. For the time period starting at point u, where $u \in \{0, \ldots, U-1\}$, the wind turbine state $\boldsymbol{R}^{\mathrm{a}}(u)$ has a set of variables representing the start state $\boldsymbol{\xi}^{\mathrm{a}}(u)$ defined

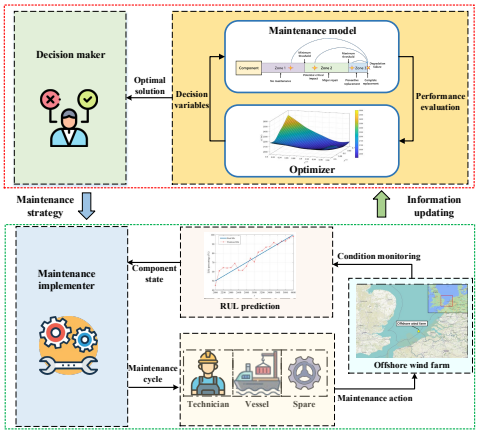


Figure 1: Schematic diagram of maintenance decision-making framework

on $\boldsymbol{\Xi}^{\mathrm{a}}(u)$ and a set of variables representing the end state $\boldsymbol{\omega}^{\mathrm{a}}(u)$ defined on $\boldsymbol{\Omega}^{\mathrm{a}}(u)$. The matrix represents the the interior state $\boldsymbol{\kappa}^{\mathrm{a}}(u)$ defined on $\boldsymbol{K}^{\mathrm{a}}(u)$, which is neither start state nor end state. The start state $\boldsymbol{\xi}^{\mathrm{a}}(u)$ and the end state $\boldsymbol{\omega}^{\mathrm{a}}(u)$ connect the current time period and the previous or subsequent time period, respectively, thereby

$$\boldsymbol{\xi}^{\mathrm{a}}(u+1) = \boldsymbol{\omega}^{\mathrm{a}}(u) \tag{1}$$

Then, the wind turbine state at uth period $\boldsymbol{R}^{\mathrm{a}}(u)$ consists of start, interior, and end state, as shown as

$$\boldsymbol{R}^{\mathrm{a}}(u) = \left[\boldsymbol{\xi}^{\mathrm{a}}(u), \boldsymbol{\kappa}^{\mathrm{a}}(u), \boldsymbol{\omega}^{\mathrm{a}}(u)\right] \tag{2}$$

The state $\boldsymbol{R}^{\mathrm{a}}(u)$ is used to illustrate the failures and maintenance which the wind turbine system suffers from during the uth period. It is necessary to model this process in order to demonstrate how the system state transforms successively with the time going.

Similarly, the decision-maker uses a maintenance model to simulate the life cycle of the wind turbine and the maintenance activities performed. Hereby, the simulated wind turbine state is represented as:

$$\boldsymbol{R}^{\mathrm{b}}(u) = \left[\boldsymbol{\xi}^{\mathrm{b}}(u), \boldsymbol{\kappa}^{\mathrm{b}}(u), \boldsymbol{\omega}^{\mathrm{b}}(u)\right] \tag{3}$$

In summary, the matrix $\boldsymbol{R}^{\mathrm{a}}(u)$ represents the real state of the wind turbine system, which keeps changing with the time going. The matrix $\boldsymbol{R}^{\mathrm{b}}(u)$ represents the simulated states in the maintenance model which the decision-maker uses. We assume the difference between $\boldsymbol{R}^{\mathrm{a}}(u)$ and $\boldsymbol{R}^{\mathrm{b}}(u)$ arises from the existence of the model parameter uncertainty. Due to the inaccuracy and incompleteness of the available database, the decision-maker may be confronted with the situation where the input parameters of the model is uncertain [3]. The decisions made in an uncertain decision-making environment is sub-optimal or even inappropriate for the real wind turbine system.

2.3 Rolling horizon method

We suppose that the decision-maker employs a decision-making step of time $\triangle T$, where $\triangle T = \rho \Delta s$. The objectives are finite sequences of optimization problems minimizing the annual loss of profit $\{P_0, ..., P_{\mathrm{Z}}\}$. Each optimization problem belongs to a step of decision-making z where $z \in \{0, ..., Z\}$, and is only dependent on the determined maintenance decisions. The maintenance strategy designed for future T_z steps is updated at zth step.

At the zth timestep, the maintenance strategy that controls the maintenance management is implemented, and the process starts over when the step is at $(z+1)$th. The strategy $c(z)$ defined on a domain C, is represented by the decision variables as

$$c(z) = [\psi_{\max}(z), \psi_{\min}(z), \vartheta(z)] \tag{4}$$

where $\psi_{\max}(z)$, and $\psi_{\min}(z)$ are the maintenance thresholds determining preventive replacement and major repair; $\vartheta(z)$ represents the proportion of ageing components in the wind farm.

Therefore, the problem, P_{z_0}, defined to start at step z_0 and applied to the period from z_0th to $(z_0 + T_{z_0})$th decision steps, can be formulated as follows:

$$\min \sum_{z=z_0}^{z=z_0+T_{z_0}} \ell(c(z_0)) \tag{5}$$

where $\ell(c(z_0))$ represents the revenue losses under the maintenance strategy $c(z_0)$.

A series of consequent strategies $\boldsymbol{c} = \text{col}(c(0), c(1), ..., c(Z))$ constitute the overall maintenance strategy during the wind turbine lifetime. A PSO (Particle Swarm Optimization) algorithm is applied to solve the optimization problem to obtain the most cost-effective solution.

3 Case study

The proposed approach is applied in a 3 MW wind turbine system composed of five components. The detailed parameter in the real wind turbine system is shown in Table 1 [4, 7]. The maintenance strategy is updated every 5 years. The estimation of the lifetime scale parameters in the maintenance model is 20% larger than the real values. The ideal RUL prediction accuracy is 93%, while the real accuracy in practice reduces to 87%. The uncertainty level of maintenance quality in the real system and the ideal maintenance model is 0.1 and 0.01 respectively. The standard deviation in the coefficient between maintenance quality and cost/time is assumed as 0.1 in the maintenance model, and the value increases to 0.3 in practice.

Table 1: Parameters of critical components

	Failure distribution and parameter		Repair cost (k€)		
Component	Weibull scale parameter (days)	Weibull shape parameter	Failure replacement	Preventive replacement	Basic repair
rotor and blade	3000	3	185	60	4
bearing	3750	2	45	15	1
gearbox	2400	3	230	75	5
generator	3300	2	60	20	1.5
pitch	1858	3	14	5	0.5

4 Results

Five cases are compared in this section, which are listed as:

- Case 1: The model parameters are known, optimize the strategy in an open-loop approach
- Case 2: The model parameters are known, optimize the strategy in a rolling-horizon approach
- Case 3: The model parameters are unknown, optimize the strategy in an open-loop approach
- Case 4: The model parameters are unknown, optimize the strategy in a rolling-horizon approach

The annual loss of profit of four cases are shown in Table 2. These results revealed that:

- The existence of uncertain model parameters increases the loss of profit.
- The rolling horizon approach capturing the wind system states reduces the loss of profit

Table 2: Comparison of four cases

Case	Case 1	Case 2	Case 3	Case 4
Annual cost (k€/year)	179.5	177.8	187.7	184.6

5 Conclusion

The maintenance management for wind sector is a complicated task where changeable wind turbine system states and potential model parameter uncertainty is involved. The existing studies widely use an open-loop decision-making process, which may not perform well in the perspective of cost-effectiveness. In this paper, a rolling-horizon based adjustable maintenance management framework is proposed. A case study of a 3MW wind turbine has shown that the existence of uncertainty leads to a higher loss of profit, and the rolling horizon approach achieves a reduction in the loss of profit.

References

[1] K. Atashgar and H. Abdollahzadeh. Reliability optimization of wind farms considering redundancy and opportunistic maintenance strategy. *Energy Conversion and Management*, 112:445–458, 2016.

[2] A. Erguido, A. C. Márquez, E. Castellano, and J. G. Fernández. A dynamic opportunistic maintenance model to maximize energy-based availability while reducing the life cycle cost of wind farms. *Renewable Energy*, 114:843–856, 2017.

[3] M. Li, X. Jiang, J. Carroll, and R. R. Negenborn. A multi-objective maintenance strategy optimization framework for offshore wind farms considering uncertainty. *Applied Energy*, 321:119284, 2022.

[4] M. Li, X. Jiang, and R. R. Negenborn. Opportunistic maintenance for offshore wind farms with multiple-component age-based preventive dispatch. *Ocean Engineering*, 231:109062, 2021.

[5] M. Li, J. Kang, L. Sun, and M. Wang. Development of optimal maintenance policies for offshore wind turbine gearboxes based on the non-homogeneous continuous-time markov process. *Journal of Marine Science and Application*, 18(1):93–98, 2019.

[6] M. Li, M. Wang, J. Kang, L. Sun, and P. Jin. An opportunistic maintenance strategy for offshore wind turbine system considering optimal maintenance intervals of subsystems. *Ocean Engineering*, 216:108067, 2020.

[7] B. R. Sarker and T. I. Faiz. Minimizing maintenance cost for offshore wind turbines following multi-level opportunistic preventive strategy. *Renewable Energy*, 85:104–113, 2016.

[8] M. Shafiee and J. D. Sørensen. Maintenance optimization and inspection planning of wind energy assets: Models, methods and strategies. *Reliability Engineering & System Safety*, 192:105993, 2019.

18th EAWE PhD Seminar on Wind Energy
2 – 4 November 2022
Bruges, Belgium

Runup under Waves and Current to Improve Offshore Wind Marine Operations

Ivandito Herdayanditya[a,b], Pieter Rauwoens[a], Evert Lataire[b]

[a] Department of Civil Engineering, KU Leuven, Bruges, Belgium
[b] Maritime Technology Division, Ghent University, Belgium

E-mail: ivandito.herdayanditya@kuleuven.be

Keywords: monopile, runup, wave, current, marine operation

Abstract: Monopile has been widely used as the Offshore Wind Turbine (OWT) support structure. Wave-field around a monopile is one of important factors to conduct safe marine operations that are performed near a monopile. Crew transfer operation is an example of marine operations that takes place close to an OWT. This extended abstract is a small part of PhairywinD project to offer a better OWT marine operation analysis by improving wave prediction around a monopile. The Belgian Part of the North Sea is taken as a study case in the project where there is also a significant ocean tidal current speed in the area. Therefore, it is important to include not only wave load but also current load in the simulation. This study provides initial study of the wave-current effects on the runup of a monopile.

1. Introduction

Wave field around a monopile is usually represented by the runup around a monopile. Runup on a monopile measures the free surface elevation on the perimeter of the monopile. Runup on a monopile was first analytically investigated by MacCamy and Fuchs [1] where linearised potential flow assumption is employed. Due to this linearisation, this solution is only applicable when the wave steepness is considerably low. The improper estimation of linear potential flow solutions to runup experiments has also been noticed by Kriebel [2] where for second order wave conditions (i.e. higher steepness waves), the linear potential flow fails to predict the runup experiment of a monopile. On the other hand, the second-order potential flow solution provides better estimation of the experiment campaigns, although it expectedly fails in higher steepness conditions. Furthermore, Fully Nonlinear Potential Flow, which accounts for actual free surface nonlinearity, rather than truncated free surface elevation, has been developed to see the effects of waves nonlinearity [3] and is found that nonlinearity of the free surface affects significantly the runup estimation.

The complexity of runup increases when current is superimposed in the environment load. The wave-current interaction itself would alter the wave height and wave length characteristics [4]. Moreover, the interaction of wave-current-monopile would also induce different dynamics of runup. Several potential flow solutions have been offered to assess the wave-current-monopile condition. An analytical solution to assess the monopile force and runup under this condition has been derived in Malenica et al. [5]. Employing Approximate Forward Speed (AFS) methodology summarised by Donatini et al. [6], the force on a monopile is replicated by Herdayanditya et al. [7] with verification case of Malenica et al. [5]. The potential flow case (e.g. [5], [7]) is with large cylinder case, $R = h$ (R is monopile radius and h is water depth), and small current speed ($Fr = \pm 0.05$). Therefore, viscosity effect can be neglected. Ferrant [8] also employed the large cylinder case to parametrically study the effect of current speed and wave steepness. However, large cylinder case cannot represent the existing wind turbines. It is not expected that in the intermediate water depth the monopile size will reach the same radius as the depth. Therefore, in smaller diameter the viscosity becomes more important as fluid separation becomes more pronounced.

This extended abstract shows initial verification of wave-current-monopile runup simulations solved in viscous fluid condition rather than potential flow assumptions. Large cylinder case is still taken as a matter of verification to the potential flow results which are available in the literature. The actual size of monopile for wind turbines will be delivered further in another publication but with the same methodology as provided in this extended abstract.

2. Methodology

The simulation case is with a large monopile case taken from Kim and Kim [9] where $R/h = 1$ with radius of 1m and water depth of 1m. One wave condition is selected in this simulation where the wave height, $H = 0.1$m so that $H/R = 0.1$. The wave period (T) is selected to be 2.30 sec so that the wave scattering parameter, kR=1.0 ($k = 2\pi/\lambda$; k is wave number and λ is wavelength). Three current speed conditions were simulated where the Froude Number, $Fr = U/\sqrt{gh}$, are -0.05, 0, and +0.05 respectively (U is current speed and g is gravity acceleration). Positive and negative Fr represents following current and opposing current case.

The simulations were performed in OpenFOAM where waves2Foam library was utilized to generate and absorb the waves with relaxation zone technique. In the relaxation technique, the total numerical domain consists of generation zone, simulation zone, and absorption zone [10]. Figure 1 illustrates the numerical domain of the wave-current-monopile simulation. waves2Foam library is at first modified by superposing current velocity in the generation and absorption zone. This is required to account for wave-current interaction. Both the generation and absorption length are 2.5λ which comes after checking the relaxation zone length sensitivity on the reflection coefficient. This length gives reflection coefficient of less than 2%. The simulation zone length is set to be 2λ for this condition. The numerical domain is discretised in three vertical layers so that the free surface layer has finer mesh. After sensitivity analysis to find the horizontal discretisation (longitudinal discretisation, dx, and transversal discretisation, dy; $dx = dy$) and vertical discretisation (dz), it is found that the free surface discretisation is with $\lambda/dx = 200$ and $H/dz = 8$. Moreover, $k - \omega\ SST$ is used to model the turbulence with control from Larsen and Fuhrman [11] to reduce numerical diffusion on the free surface.

Runup is computed by measuring the free surface elevation at the first cells on the monopile surface. The coordinate system to define runup position is shown in Figure 2. The runup is defined as mean value of the crest of the free surface elevation time series, averaged for a specific range of time. In this initial study, the time range is selected to be between $5T - 10T$ where the waves are already stable and reflection effect is not yet seen. Furthermore, the model pre-processing (e.g. defining the size of the domain and mesh) and post-processing are done with in-house code called *BNG* which its features are updated continuously during this project.

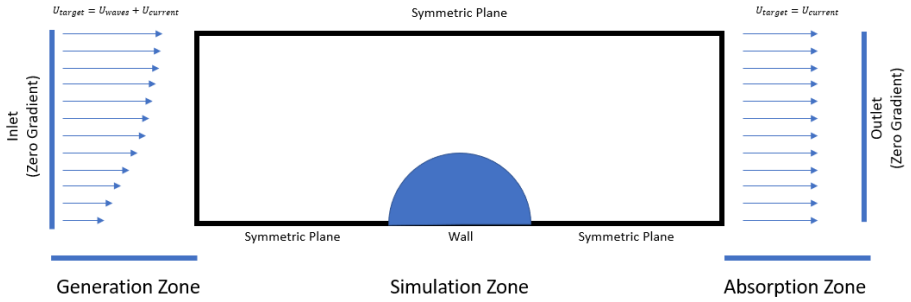


Figure 1: Schematic view of the numerical domain to simulate wave-current-monopile

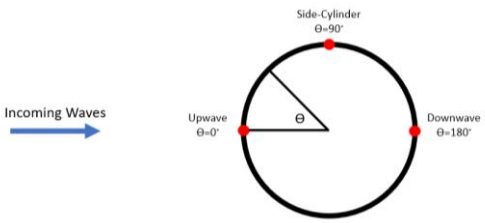


Figure 2: Probes location coordinate on the perimeters of the monopile relative to the incoming wave direction.

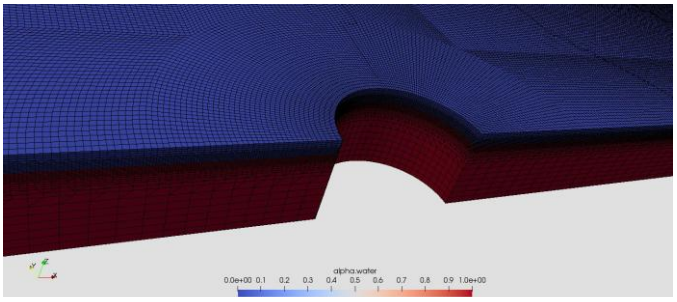


Figure 3: The numerical model of the monopile. The fluid domain is discretised in cells where the vertical discretization is with three layers so that the free surface has finer mesh but with decent numerical effort

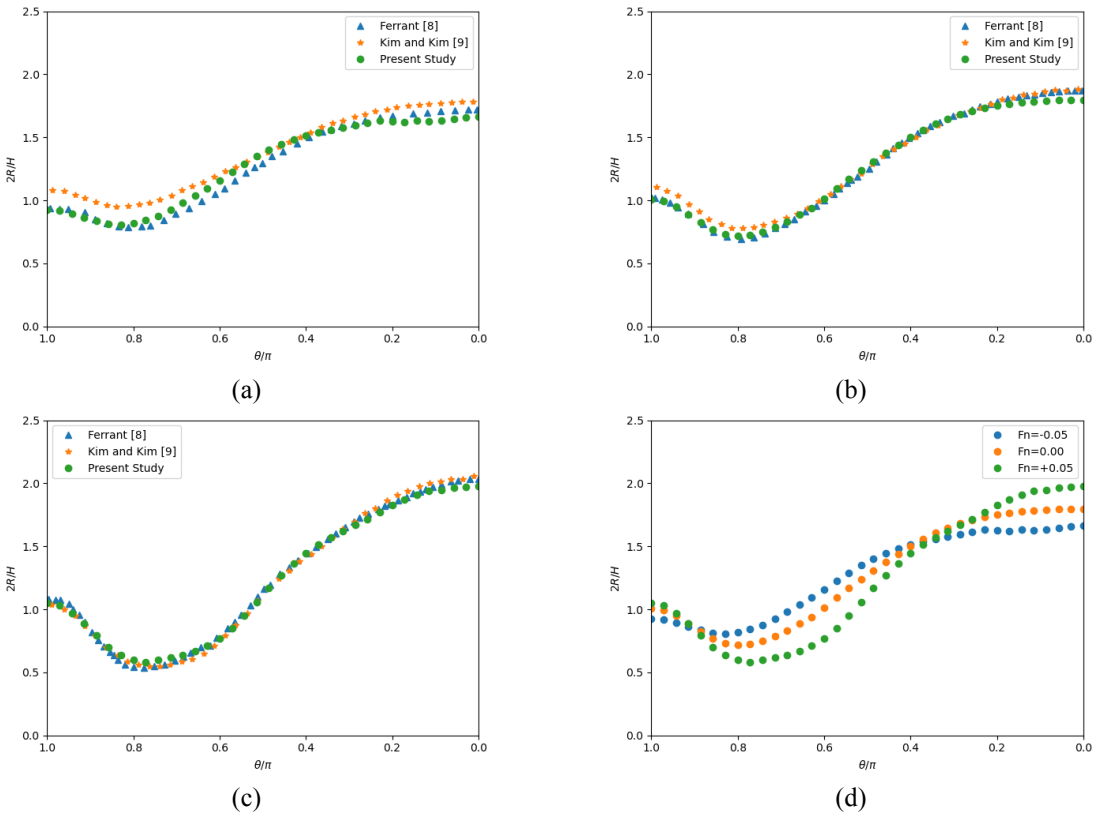


Figure 4: Runup envelope of several conditions from present study compared to literatures where: (a) with opposing current case, Fr=-0.05, (b) with zero current case (wave only case), Fr=0.00, and (c) with following current case, Fr=+0.05. All the different speed conditions from present study are compared in (d)

3. Results and Discussion

Figure 3 shows the monopile model in the numerical domain. The mesh is seen to have three vertical layers and radial mesh in position closed to the cylinder to provide good mesh discretisation. Two-phase fluid is monitored by employing VOF (Volume of Fluid) concept where fraction of 0 represents fully air cell, 1 for fully water cells, and in between is typical value on the air-water interface. This parameter is seen in the colour of *alpha.water*.

The free surface elevation envelopes for three speed conditions are shown in Figure 4. The runup (R) is normalised with wave height in the *y-axis*. The *x-axis* represents the position of point on the perimeter of the monopile as illustrated in Figure 2. From Figure 4a-c, it is seen that the present methodology obtains decent agreement with estimation from potential flow solution. It is expected because viscous effect in large cylinder

with small velocity condition in wave-current condition is small. Therefore, although the simulation is with viscous solver, the results collapse with potential flow solution. Furthermore, it is observed that current affects the runup envelope (Figure 4d). It is seen that the current effect is seen in upwave, side-cylinder, and downwave. However, the upwave appears to be more sensitive than the downwave side. It should be noted, nevertheless, that when the reflection waves start to arrive at the monopile position, the runup estimation differs from potential flow estimation especially on the upwave condition. This should be further investigated in further study, especially if long-run simulation is aimed, for instance for irregular wave cases.

4. Conclusion

The present methodology which uses velocity superposition shows a promising method to simulate waves-current condition on the OWT monopile. Wave field, which in this study, is represented by runup is seen to agree well with previous studies. It is seen that taking only waves would give improper wavefield estimation to do marine operation near the OWT. Future work should include the cases where monopile size is with the actual OWT, nevertheless, the study in this extended abstract should still be included as a verification step. Furthermore, this tool will be employed as numerical tool to investigate a 'wave transfer function' behind a monopile that is extracted from simulations with present methodology, that would be used with vessel transfer function for predicting the final motion of the vessel in the OWT marine operations.

Acknowledgements

This research is funded from the Energy Transition Fund (ETF) under the PhairywinD project.

References

[1] MacCamy and Fuchs, "Wave forces on piles: A diffraction theory," 1954.
[2] D. L. Kriebel, "Nonlinear Wave Interaction with A Vertical Circular Cylinder. Part II: Wave Run-Up," 1992.
[3] P. Ferrant, S. Malenica, and B. Molin, "Nonlinear wave loads and runup on a vertical cylinder," 1999.
[4] D. H. Peregrine, "Interaction of Water Waves and Currents," *Advances in applied mechanics,* vol. 16, pp. 9–117, 1976.
[5] S. Malenica, P. J. Clark, and B. Molin, "Wave and current forces on a vertical cylinder free to surge andsway," *Applied Ocean Research*, vol. 17, no. 2, pp. 79–90, 1995.
[6] L. Donatini, G. V. Fernandez, and G. Delefortrie, "Implementation of Forward Speed Effects On An Open Source Seakeeping Solver," in *In 6th MASHCON: International Conference on Ship Manoeuvring in Shallow and Confined Water*, 2022, pp. 20–33.
[7] I. Herdayanditya and G. V. Fernandez, "Waves-Current Effect Investigation on Monopile Excitation Force Employing Approximate Forward Speed Approach," in *In 6th MASHCON: International Conference on Ship Manoeuvring in Shallow and Confined Water*, 2022, pp. 73–80.
[8] P. Ferrant, "Runup on a Cylinder Due to Waves and Current: Potential Flow Solution with Fully Nonlinear Boundary Conditions," *International Journal of Offshore and Polar Engineering*, vol. 11, no. 1, 2001, [Online]. Available: http://onepetro.org/IJOPE/article-pdf/2180432/isope-01-11-1-033.pdf/1
[9] S. J. Kim and M. H. Kim, "The nonlinear wave and current effects on fixed and floating bodies by a three-dimensional fully-nonlinear numerical wave tank," *Ocean Engineering*, vol. 245, Feb. 2022, doi: 10.1016/j.oceaneng.2021.110458.
[10] N. G. Jacobsen, D. R. Fuhrman, and J. Fredsøe, "A wave generation toolbox for the open-source CFD library: OpenFoam®," *International Journal for Numerical Methods in Fluids*, vol. 70, no. 9, pp. 1073–1088, Nov. 2012, doi: 10.1002/fld.2726.
[11] B. E. Larsen and D. R. Fuhrman, "On the over-production of turbulence beneath surface waves in Reynolds-averaged Navier-Stokes models," *Journal of Fluid Mechanics*, vol. 853, pp. 419–460, Oct. 2018, doi: 10.1017/jfm.2018.577.

Reliability, monitoring and sensing technology

18th EAWE PhD Seminar on Wind Energy
2-4 November 2022
Bruges, Belgium

A Novel Approach for Constructing Health Indicators for Degrading Wind Turbine Components

Ali Eftekhari Milani[a], **Donatella Zappalá**[a], and **Simon J. Watson**[a]

[a]TU Delft, Kluyverweg 1, 2629 HS Delft, Netherlands

E-mail: a.eftekharimilani@tudelft.nl

Keywords: wind turbines, prognostics, RUL estimation, condition-based maintenance, health indicator, degradation, particle swarm optimization, convolutional autoencoder

1 Introduction

One of the main challenges in wind energy production is reducing the costs of Operation and Maintenance (O&M), which contributes to a significant portion of the Levelised Cost of Energy (LCOE) produced by wind farms, especially offshore, where O&M costs typically account for 23% of the LCOE, compared to 12% for onshore assets [1]. This factor becomes even more important as the capacity of the installed wind turbines increases. Also, more and more wind farms are being installed deeper in the sea, where wind conditions are harsher and access for maintenance is far more limited. Therefore, it is necessary to replace the existing corrective and preventive maintenance interventions with predictive Condition-Based Maintenance (CBM) schemes [2].

Successful implementation of CBM in wind industry necessitates developing methods to predict the remaining useful life (RUL) of wind turbine components once abnormal conditions are detected. These methods afford the wind farm operators the possibility of optimally planning the necessary maintenance. For example, maintenance interventions required for several wind turbine components can be grouped together, considerably reducing the transportation and labour costs, especially offshore.

Fault detection in wind turbine components and subsystems has been well studied in the last decade. Since around 2015, numerous papers have been published proposing novel solutions for this problem [3], showing a gradual shift from vibration and signal processing techniques towards AI and deep learning methods. However, very little research has been carried out in the field of wind turbine fault prognostics and most of the proposed methods mainly focus on early detection approaches rather than RUL estimation[4]. The number of publications are even fewer if we consider studies using only SCADA data for prognostics, which is preferred, since implementing such methods does not necessitate extra costs for setting up measurement equipment. Gearbox has received the most attention, since it is the most complex and expensive component of a wind turbine [4]. In [5], the authors develop a data-driven model for wind turbine gearbox prognostics using high-frequency SCADA data. An ANN is used to model the normal behaviour of the gearbox. Then, using a one-class support vector machine classifier, the normal behaviour model error is analysed to develop a robust threshold to distinguish anomalous wind turbine operation. In another work [6], the authors use physics-based models to augment [7] SCADA data. They mark the data from one month leading to the failure as faulty and investigate different supervised data-driven methods for identifying gearbox bearing failure in advance. However, these methods only detect a point in time at which a component starts functioning in an abnormal condition which will lead to a failure, and do not predict how much time is remaining at each given instant until failure. In other words, they are early detection methods rather than remaining useful life prediction methods. Besides the gearbox, a few papers have been published addressing the problem of fault prognosis in the generator, the main bearing, and the blades [8].

It is interesting to note that, according to several studies about the distribution of failures in wind turbines [9], bearings in different sub-assemblies, such as main bearing, high-speed shaft bearing, gearbox bearings, and generator bearings, are by far the most liable sub-assemblies that are subject to failure, leading to increased downtime and maintenance costs [8]. Furthermore, considering the main bearing in an offshore wind turbine, although it is not as expensive as the gearbox, its failure will necessitate the dismantling of the whole drivetrain, leading to large downtime and high maintenance costs. This component becomes even more important to study in terms of

failure prognostics in light of the increasing popularity of direct drive wind turbines. Hence, developing a failure prognostic method for wind turbine main bearings is as much justified as it is for the gearbox. In [10], the authors develop an innovative physics-informed machine learning method for calculating the cumulative fatigue damage in the main bearing which can be used to predict its RUL. However, the method is not tested on real SCADA data. In another work [11], an ANN-based normal behaviour model is coupled with a custom anomaly indicator to detect wind turbine main bearing failures several months in advance. However, the RUL is not predicted.

The methods proposed in the literature for the problem of RUL estimation have been divided into three classes: ”physics-based”; ”data-driven”; and ”hybrid” [12]. However, another useful classification can be dividing the methods into ”direct” and ”indirect” classes. The former refers to methods which aim at modelling the process and evolution of degradation in the component, while the latter methods first construct a health indicator (HI) which is correlated with the degradation process, and then aim at modelling its trend and predicting the time at which it crosses a failure threshold. Although they include an added step in the process of RUL prediction, indirect methods can be considered more explainable, especially compared to direct data-driven methods, because the evaluation of the constructed health indicators in terms of their congruence with the expected trend and regime of degradation can be considered an added sanity check step in the process of RUL prediction.

One of the most recent and successful approaches for constructing HIs, which has been mainly applied to prognostics of rotating machines such as bearings, focuses on the monotonicity of the obtained HIs (congruent with the irreversible nature of component degradation) as a major performance metric [13]. Sensor signals measured in a degrading industrial system are functions of various factors, such as the level of degradation, seasonality, operational condition, and process and measurement noise [14]. Therefore, the problem of extracting the degradation factor from the sensor signals can be reduced to the problem of finding a decomposition of the sensor signals which produces a highly monotonic factor. In [14], the authors propose a deep Sparse Autoencoder (AE) for this task and test it on a synthetic dataset of run-to-failure sensor signals of an industrial component. The synthetic dataset (Figure 1) contains 10 sensor signals which are obtained by non-linearly combining three factors representing the degradation, the environmental and operational behaviour, and the process noise. The hyperparameters and the architecture of the AE are searched by trial and error so that the obtained health indicator is as monotonic as possible, which is very time-consuming. It is important to note that, since monotonicity is related to the whole run-to-failure dataset and not individual samples, it is not possible to maximize it during the training of the AE if the training is done by backpropagation. In [15], the authors develop a multi-objective Coevolutionary optimization approach for the problem of setting the hyperparameters and the architecture of the deep sparse AE used for constructing health indicators from sensor signals. This solution automatizes the framework proposed in [14], however, it is very computation-intensive, since in each generation of the proposed algorithm, all candidate AEs need to be trained by backpropagation. In [16], the authors propose a Convolutional AE (CAE) for constructing a health indicator from sensor signals of a degrading bearing. Instead of directly maximizing the monotonicity of the obtained HI, they assume that the HI follows a monotonic cubic regime and label the outputs of the middle layer of the AE (i.e., the HI) according to a cubic function whose value is 1 for the first sample and 0 for the last sample of the run-to-failure dataset. The mean squared error between the true and predicted label values of the HI is added to the training loss function. This approach is innovative and performs well in terms of the constructed HIs and reasonably well in predicting the RUL. However, assuming a cubic regime for the HI is ad hoc and may not be suitable for all cases.

In this work, we propose a CAE for constructing HIs from run-to-failure sensor signals, whose weights are trained by Particle Swarm Optimization (PSO) algorithm. Unlike [16], this method requires no assumptions about the regime of the HI, other than its monotonicity. Further, since the training is done by PSO algorithm rather than backpropagation, it is possible to maximize the monotonicity of the constructed HI at the same time as minimizing the reconstruction error. Hence, the problem of high computation requirement in [15] is mitigated, where each chromosome in each generation of the Coevolutionary algorithm was mapped to an AE and was trained by backpropagation. Another important aspect of the proposed CAE compared to the AE with fully-connected layers used in [15] is that it has considerably fewer weight parameters, which renders the search space smaller, leading to a better search by PSO algorithm. In this work, the proposed method is applied to the synthetic dataset used in [14] and [15] and the results show its ability to construct a HI which is considerably more monotonic, with around two orders of magnitude less runtime compared to [15]. Further, the method is demonstrated via a case study to construct monotonic HIs for degrading wind turbine components by using a real SCADA dataset.

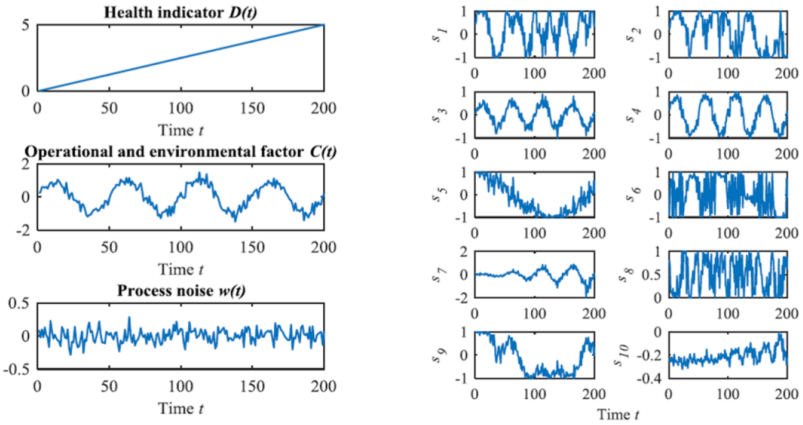


Figure 1: (Left) The three proposed factors. (Right) The 10 synthetic sensor signals. [14]

2 Proposed method

2.1 Autoencoder

An AE [17] is a neural network which consists two modules: the Encoder (E) and the Decoder (D). The Encoder maps the high-dimensional input signals $\vec{\mathbf{x}} \subset \mathbb{R}^F$ to a low-dimensional latent representation $\vec{\mathbf{z}} \subset \mathbb{R}^G$, and the Decoder reconstructs the original signals and outputs $\hat{\vec{\mathbf{x}}} \subset \mathbb{R}^F$ by mapping the latent low-dimensional representation output from the Encoder to the original high-dimensional space, where $F \gg G$ (Figure 2). Therefore:

$$\hat{\vec{\mathbf{x}}} = D\left(E\left(\vec{\mathbf{x}}\right)\right) \approx \vec{\mathbf{x}} \tag{1}$$

In other words, the AE is trained to deconstruct and reconstruct the input signals, passing them through a bottleneck in the inner layer. Hence, it learns to maintain in the inner layer only the information required for reconstructing the signals, yielding a condensed representation of the input signals.

2.2 Convolutional Autoencoder

A Convolutional Autoencoder (CAE) is an AE whose layers are convolutional layers instead of fully-connected layers as in a vanilla AE. Considering the problem of HI construction from sensor signals of a degrading equipment where the dataset is organized in a 2-dimensional matrix whose dimensions are equal to the number of signals (feature domain) and the number of samples (time domain), for each time instance t, a window of the previous w samples in the dataset $(t-w+1,...,t-1,t)$ can be selected for constructing the HI at time t, i.e., $\vec{\mathbf{z}}(t)$. In this manner, for a sensor signal dataset of shape $T \times F$, where T is the length of the time domain and F is length of the

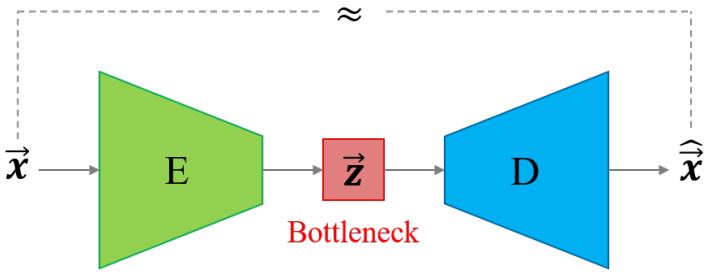


Figure 2: General architecture of an Autoencoder. E is the Encoder and D is the Decoder.

feature domain, a time series dataset of $T-w+1$ samples of shape $w \times F$ can be formed and each sample can be input into a CAE for deriving its HI value.

In this work, an Encoder with two convolutional layers has been used, since it performs adequately. The first layer performs convolution only in time domain and uses a filter of shape $w \times 1$, transforming the input matrix of shape $w \times F$ to a vector of length F. The second layer, on the other hand, performs convolution in the feature domain and uses a filter of shape $1 \times F$, transforming the output vector of the first layer to a scalar value which is the HI. The number of filters in the first and second layer is experimentally set to 8 and 1 respectively. The Decoder has a symmetric architecture and transforms the output of the Encoder to the original $w \times F$ shape by performing upsampling and deconvolution in the feature and time domain.

2.3 The proposed framework

The aim of this work is to train the CAE so that, firstly, it is able to reconstruct successfully the input signals by ensuring that important information is not removed by the Encoder, and secondly, the output of the Encoder is highly monotonic. This means that the CAE has learned to amplify the monotonic degradation factor of the input signals and dampen the other non-monotonic features. The first objective is attainable by training the CAE using backpropagation with a cost function such as mean squared error between the input and the output of the network. However, the monotonicity of the obtained HI calculated using the Mann-Kendall (MK) monotonicity test [18] cannot be maximized during backpropagation, because it is measured for the whole run-to-failure process and not for individual samples or batches of samples. As discussed in the Introduction, some methods have been proposed in the literature for maximizing the monotonicity of the constructed HIs [14], [15] which are highly computation-intensive and time-consuming. In this work, we train the CAE using Particle Swarm Optimization (PSO) algorithm [19]. PSO is able to effectively search the weight space of neural networks and is a good alternative to the back-propagation training algorithm [20]. This approach allows effectively searching the large space of the weights of the CAE and optimizing both objectives. The fitness function adopted in this study is:

$$f = |\tau_{\mathrm{MK}}(\vec{\mathbf{z}})| - \frac{1}{wF}\sum_{i=1}^{w}\sum_{j=1}^{F}(x_{i,j}-\hat{x}_{i,j})^2 \tag{2}$$

where the first term is the absolute value of the τ score of MK monotonicity test [18] and the second term is the mean squared error between the input and the output of the CAE. w is the time window of each time series sample (which is a 2-dimensional $w \times F$ matrix), F is the number of signals, $x_{i,j}$, $i = 1,\ldots,w$, $j = 1,\ldots,F$ is the input time series sample, and $\hat{x}_{i,j}$, $i = 1,\ldots,w$, $j = 1,\ldots,F$ is the reconstructed time series sample. In [18], two monotonicity scores, ρ_{MK} and τ_{MK}, are proposed, and for both parameters, values close to zero indicate lack of a monotonic regime, larger positive values indicate a monotonically increasing trend, and larger negative values indicate a monotonically decreasing trend. ρ_{MK}, which is used for evaluation in [14] and [15], is uncapped, while τ_{MK} is constrained between -1 and 1. They are computed according to the equations below:

$$\rho_{\mathrm{MK}} = \begin{cases} \frac{S-1}{\sigma} & \text{if} \quad S>0 \\ 0 & \text{if} \quad S=0 \\ \frac{S+1}{\sigma} & \text{if} \quad S>0 \end{cases} \tag{3}$$

$$\tau_{\mathrm{MK}} = \frac{S}{D} \tag{4}$$

$$S = \sum_{k=1}^{n-1}\sum_{j=k+1}^{n}\mathrm{sign}(X_j - X_k) \tag{5}$$

$$\sigma = \sqrt{\frac{n(n-1)(2n+5)}{18}} \tag{6}$$

$$D = \frac{1}{2}n(n-1) \tag{7}$$

where X_i, $i = 1,2,\ldots,n$ are the elements of the considered sequence.

3 Case study 1

3.1 Dataset

This case study includes the synthetic dataset developed in [14]. It is assumed that 10 sensor signals are available which are built out of 3 factors representing degradation, seasonal and operational behaviour, and process noise, by non-linearly combining them (Figure 1) according to 10 functions defined in [14]. The equations related to the degradation factor $D(t)$, the seasonal and operational factor $C(t)$, and the process noise $w(t)$ are reported below:

$$D(t) = \alpha t, \quad \alpha = 0.025, \quad t = 1,2,\ldots,T, \quad T = 200 \tag{8}$$

$$C(t) = \sin\left(\frac{1}{25}\pi t\right) + w_c, \quad t = 1,2,\ldots,T, \quad T = 200, \quad w_c \sim N(\mu = 0, \sigma = 0.2) \tag{9}$$

$$w(t) \sim N(\mu = 0, \sigma = 0.1), \quad t = 1,2,\ldots,T, \quad T = 200 \tag{10}$$

where α is the slope of the linear degradation factor, w_c represents the stochasticity inherent to environmental and operational conditions and follows a normal distribution (N) with mean of 0 and standard deviation of 0.2, and $w(t)$ represents the process noise and follows a normal distribution with mean of 0 and standard deviation of 0.1. The number of samples is assumed to be $T = 200$ and is in arbitrary time units. In this case study, $F = 10$ which is equal to the number of signals, and w is set to 10, which is the number of time instances for each time series sample.

3.2 Experiment 1

The proposed method has been applied to the synthetic dataset (normalized between 0 and 1). The PSO algorithm converged within 200 generations. The number of particles was experimentally set to 20 and the algorithm runtime was around 5 minutes (CPU: 11$^{\text{th}}$ Gen Intel(R) Core(TM) i7-1185G7 – RAM: 16.0 GB). The progression of the average fitness is plotted in Figure 3. The best solution corresponding to the particle in the final population with the highest fitness value is shown in Figure 4. It refers to a HI following the linear trend of the degradation factor, $D(t)$, of the input data and has MK monotonicity scores of $\rho_{\text{MK}} = 18.2586$ and $\tau_{\text{MK}} = 0.8889$. The methods proposed in [14] and [15] yielded less monotonic HIs with lower ρ_{MK} scores, 15.7612 and 15.5647 respectively, with considerably higher runtime and computation intensity. For example, the Coevolutionary optimization framework proposed in [15] had a runtime of more than 10 hours on a similar system.

3.3 Experiment 2

In this experiment, the proposed method has been applied to the three cases shown in Figure 5, referring to three different functions for the degradation factor, $D(t)$. These three cases were selected, firstly, to study the perfor-

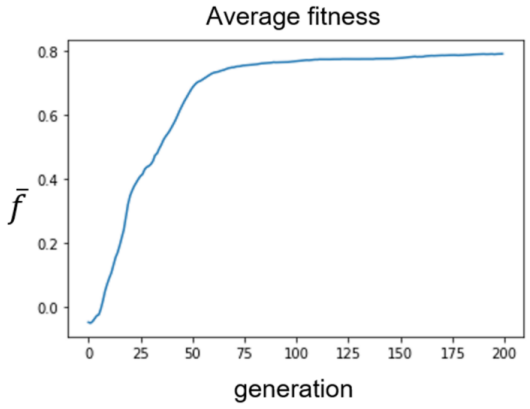


Figure 3: Case study 1, Experiment 1 – Average fitness vs. generation

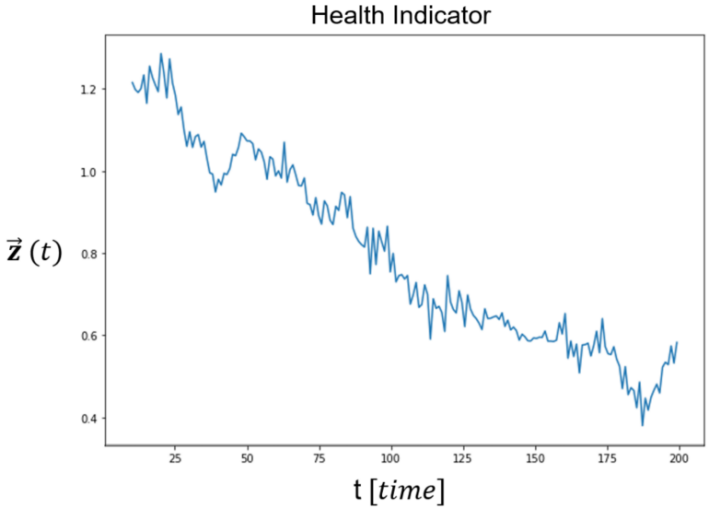


Figure 4: Case study 1, Experiment 1 – Best HI obtained

mance of the proposed method when there is no degradation present, and secondly, to see whether the constructed HIs follow the true degradation regime in the data.

1. No degradation present: $D(t) = 0$
2. Degradation follows a linear trend, but the onset of degradation is at $t = T/2$ instead of $t = 0$:

   $$D(t) = \begin{cases} 0, & \text{if } t \leq T/2 \\ \alpha t, & \text{otherwise} \end{cases}$$

   $$\alpha = 0.025, \quad t = 1, 2, \ldots, T, \quad T = 200$$

3. Degradation follows an exponential trend: $D(t) = \frac{1000^{\frac{t}{T}} - 1}{T}, \quad t = 1, 2, \ldots, T, \quad T = 200$

$C(t)$, $w(t)$, and the 10 functions producing the 10 signals have been assumed to be equal to the ones proposed in [14]. The HIs corresponding to these three degradation regimes are shown in Figure 6. The comparison of the results shows that, firstly, the method is only able to construct monotonic HIs if the dataset includes a monotonic degradation factor, i.e. if degradation is present, and secondly, the method is able to construct HIs which visually seem to follow the true degradation regime.

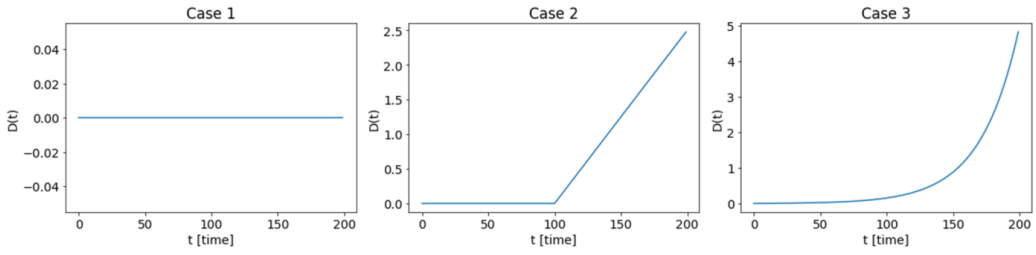


Figure 5: Case study 1, Experiment 2 – Assumed regimes for $D(t)$

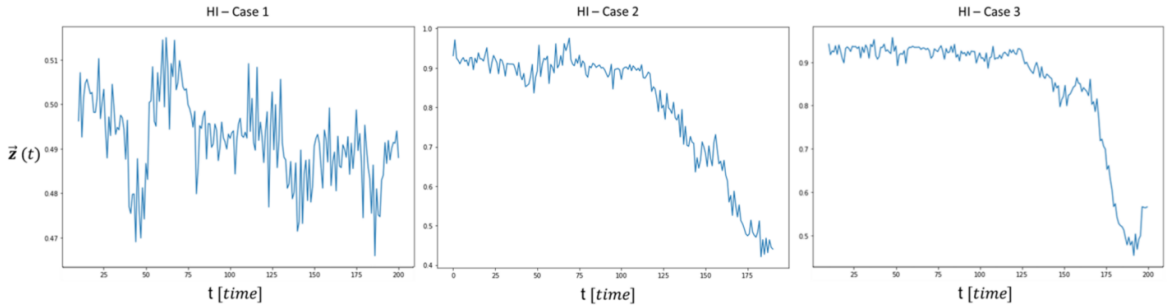


Figure 6: Case study 1, Experiment 2 – HIs obtained for the three degradation regimes

4 Case study 2

4.1 Dataset

The second case study refers to a real SCADA dataset of a wind turbine which has experienced a gearbox failure. The dataset is from the WinJi gearbox fault detection challenge posted on the "WeDoWind" platform[1]. The dataset features 22 SCADA signals, including environmental data, rotor and generator speed, blade angles, produced power, temperature sensor recordings, and pressure sensor recordings. The data is available in 10-minute time frame and it includes 763 days of recorded SCADA signals.

4.2 Data pre-processing

The dataset was first pre-processed to eliminate the data related to non-operational wind turbine states. Samples referring to wind speeds lower than the cut-in and higher than the cut-out wind speed, to zero or negative produced power, or to zero rotational speed have been all filtered out. Further, out of the 22 signals available, 11 signals characterised by the least cross-correlation were selected for the analysis ($F = 11$). Each signal was then normalized between 0 and 1 and the dataset was down-sampled to an hourly time frame. Finally, the portion of the data starting from the first sample recorded and ending with the last sample before failure, with around 9100 samples, was selected as the run-to-failure dataset.

4.3 Experiment

The last 30 days leading to gearbox failure, i.e., 720 samples of the run-to-failure dataset, were selected for analysis. A time window of $w = 120$, equivalent to 5 days, was selected for preparing the input time series dataset of the CAE, which was trained by PSO algorithm. The resulting health indicator $\vec{\mathbf{z}}(t)$ is plotted in Figure 7.

The obtained HI follows an almost exponential degradation regime, similar to the one assumed in the third case of experiment 2 in case study 1. This indicates that the development of the degradation is slower initially and accelerates considerably around 4 days before the failure of the gearbox. Also, it is important to consider that, in this case study, the number of trainable weight parameters of the CAE is 2114, while in the previous case study it was 338. Therefore, the PSO algorithm is searching (with a runtime of around 45 minutes) a large 2114-dimensional space of CAE weight parameters to maximize the fitness function. Considering such complexity, the obtained result is promising.

5 Conclusion and future work

This paper proposes a CAE trained by PSO algorithm for the task of constructing health indicators for degrading wind turbine components. Application of this method to a synthetic dataset of run-to-failure sensor signals shows that this method is able to construct HIs which follow the true degradation regime assumed in the dataset, is considerably less computation-intensive than other solutions proposed in the literature for the same synthetic dataset, and yields a better HI in terms of monotonicity. The second case study demonstrates the applicability of the proposed

[1] https://www.wedowind.ch/

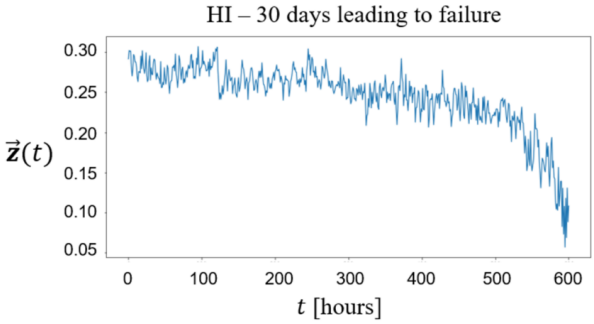


Figure 7: Case study 2 – Wind turbine HI

HI construction method to a run-to-failure SCADA dataset of a wind turbine with gearbox failure. Current work is on implementing a multi-objective PSO for optimizing in a more effective way the two training objectives, i.e., the MSE between the AE input and the output signals and the monotonicity of the constructed HI.

One of the challenges of constructing HIs and predicting RUL for wind turbine components is the variable nature of the operational and environmental conditions among different machines in a wind farm and at different points in time. This results in very different conditions leading to failure of a component in each run-to-failure dataset. Therefore, generalization can be one of the main challenges for applying the proposed method to a wind turbine SCADA dataset. Further work will focus on the application of the proposed method to a real bearing experimental dataset with multiple run-to-failure instances, and to a wind farm SCADA dataset with multiple failures of specific components, such as the gearbox or the main bearing. This will allow testing the generalization ability of the proposed method when multiple run-to-failure datasets are available. For addressing the case where adequate run-to-failure data is not available, data-driven and hybrid data augmentation methods will be investigated for producing synthetic run-to-failure data. Also, further work will be done on development of a method for predicting the RUL using the constructed HIs.

References

[1] J. Tautz-Weinert and S. J. Watson, "Using scada data for wind turbine condition monitoring - a review," *IET Renewable Power Generation*, vol. 11, pp. 382 – 394, 2017.

[2] A. K. Jardine, D. Lin, and D. Banjevic, "A review on machinery diagnostics and prognostics implementing condition-based maintenance," 2006.

[3] J. Chatterjee and N. Dethlefs, "Scientometric review of artificial intelligence for operations & maintenance of wind turbines: The past, present and future," *Renewable and Sustainable Energy Reviews*, vol. 144, p. 111051, 2021.

[4] G. de Novaes Pires Leite, A. M. Araújo, and P. A. C. Rosas, "Prognostic techniques applied to maintenance of wind turbines: a concise and specific review," *Renewable and Sustainable Energy Reviews*, vol. 81, pp. 1917 – 1925, 2018.

[5] A. Verma, D. Zappalá, S. Sheng, and S. J. Watson, "Wind turbine gearbox fault prognosis using high-frequency SCADA data," *Journal of Physics: Conference Series*, vol. 2265, no. 3, p. 032067, 2022.

[6] A. Desai, Y. Guo, S. Sheng, C. Phillips, and L. Williams, "Prognosis of wind turbine gearbox bearing failures using scada and modeled data," *Proceedings of the Annual Conference of the Prognostics and Health Management Society, PHM*, vol. 12, no. 1, 2020.

[7] C. Shorten and T. M. Khoshgoftaar, "A survey on image data augmentation for deep learning," *Journal of Big Data*, vol. 6, no. 1, 2019.

[8] M. Rezamand, M. Kordestani, R. Carriveau, D. S.-K. Ting, M. E. Orchard, and M. Saif, "Critical wind turbine components prognostics: A comprehensive review," *IEEE Transactions on Instrumentation and Measurement*, vol. 69, 2020.

[9] H. D. M. de Azevedo, A. M. Araújo, and N. Bouchonneau, "A review of wind turbine bearing condition monitoring: State of the art and challenges," *Renewable and Sustainable Energy Reviews*, vol. 56, pp. 368–379, 2016.

[10] Y. A. Yucesan and F. A. C. Viana, "A physics-informed neural network for wind turbine main bearing fatigue," *INTERNATIONAL JOURNAL OF PROGNOSTICS AND HEALTH MANAGEMENT*, vol. 11, no. 1, 2020.

[11] A. Encalada-Davila, B. Puruncajas, C. Tutiven, and Y. Vidal, "Wind turbine main bearing fault prognosis based solely on scada data," *Sensors*, vol. 21, no. 6, 2021.

[12] G. de Novaes Pires Leite, A. M. Araujo, and P. A. C. Rosas, "Prognostic techniques applied to maintenance of wind turbines: a concise and specific review," *Renewable and Sustainable Energy Reviews*, vol. 81, pp. 1917–1925, 2018.

[13] H. Zhou, X. Huang, G. Wen, Z. Lei, S. Dong, P. Zhang, and X. Chen, "Construction of health indicators for condition monitoring of rotating machinery: A review of the research," *Expert Systems with Applications*, vol. 203, p. 117297, 2022.

[14] Z. Yang, P. Baraldi, and E. Zio, "Automatic extraction of a health indicator from vibrational data by sparse autoencoders," *Proceedings - 2018 3rd International Conference on System Reliability and Safety, ICSRS 2018*, pp. 328–332, 2019.

[15] A. E. Milani, F. Antonello, P. Baraldi, and E. Zio, "A coevolutionary optimization approach with deep sparse autoencoder for the extraction of equipment degradation indicators," *Proceedings of the 30th European Safety and Reliability Conference and the 15th Probabilistic Safety Assessment and Management Conference*, 2020.

[16] D. Chen, Y. Qin, Y. Wang, and J. Zhou, "Health indicator construction by quadratic function-based deep convolutional auto-encoder and its application into bearing rul prediction," *ISA Transactions*, vol. 114, pp. 44–56, 2021.

[17] G. E. Hinton and R. R. Salakhutdinov, "Reducing the dimensionality of data with neural networks," *Science*, vol. 313, no. 5786, pp. 504–507, 2006.

[18] T. Pohlert, "Non-parametric trend tests and change-point detection," 2015.

[19] R. Poli, J. Kennedy, and T. Blackwell, "Particle swarm optimization," *Swarm Intelligence*, vol. 1, pp. 33–57, 2007.

[20] A. Suresh, K. Harish, and N. Radhika, "Particle swarm optimization over back propagation neural network for length of stay prediction," *Procedia Computer Science*, vol. 46, pp. 268–275, 2015. Proceedings of the International Conference on Information and Communication Technologies, ICICT 2014, 3-5 December 2014 at Bolgatty Palace and Island Resort, Kochi, India.

18th EAWE PhD Seminar on Wind Energy
2-4 November 2022
Bruges, Belgium

Budget constrained modelling for the reliability assessment of offshore wind substructures under accidental impact events

Jonathan Morán A.[a], **Pablo G. Morato**[a], and **Philippe Rigo**[a]

[a]ANAST, Department of ArGEnCo, University of Liege, 4000 Liege, Belgium

E-mail: jmoran@uliege.be

Keywords: surrogate modelling, structural reliability, nonlinear structural mechanics

Introduction

Offshore wind substructures are subject to environmental and operational conditions that influence optimal decisions engineers make in order to preserve a reliable functionality of the entire wind turbine during its lifetime. A system level analysis of such substructures typically involves the complex interaction of its components raising to a considerable number of possible failures scenarios. Moreover, a wide spectrum of engineering analyses require a large exploration of out-coming Quantities of Interest (QoIs) given the join probability distribution of input random variables, e.g., global optimization, sensitivity, and risk analyses. To this end, it is important to have certain degree of accuracy in the estimation of such QoIs from systems that, very often, follow a naturally nonlinear behaviour, e.g., fatigue-corrosion component deterioration, ultimate strength, and structural resistance under accidental loads. In this context, high-fidelity simulations have become the preferred tool to solve the above-mentioned problems although time-consuming. For instance, due to the innate difficulty in the analysis of accidental events derived from the combination of complex geometries, contact mechanics and complicated treatment of nonlinear constitutive loads, Finite Element Methods (FEM) have provided ground truth information for optimization analyses [1, 2]. High-fidelity models of single collision scenarios, however, are costly in terms of computational time and unaffordable in practice for probabilistic quantification of QoIs. To reduce the simulation cost in accidental events analyses, tailored closed-form solutions have been developed, e.g., to predict the dissipated energy experienced between the collision of a ship and an offshore substructure [3]. Nonetheless, approaching such nonlinear structural scenarios with closed-form solutions introduces inevitable simplifications that constrain the domain of application.

Based on a finite dataset retrieved from high-fidelity simulations or experimental observations, surrogate models (a.k.a. metamodels or response surfaces) are advanced regression methods able to efficiently learn mathematical relationships between random input variables to relevant output QoI. Their computational performance enables to map multi-physics engineering responses without imposing physical simplifications and have been also employed in wind turbine applications, e.g., to predict the short-term damage equivalent load, the electrical power [4] and to perform fatigue reliability assessment through a surrogate limit-state function [5, 6]. For such purposes, the computational budget needed to generate training samples is normally dedicated to reducing the global generalization error then relying on accurate predictions of unseen events. In the case of structural reliability analysis, the aim is to assess the effect of uncertainties by the estimation of the failure probability associated with a surrogate limit-state function. In this work, we conduct a surrogate-based reliability assessment of an impacted offshore substructure with a limited number of high-fidelity simulations. The computational resources are exploited to define a surrogate model with the minimum generalization error able to accurately map the output QoI, e.g., the limit-state function of a jacket subject to accidental impact. A semi-analytical solution that models the impact of a ship against an offshore wind turbine jacket foundation can be used to generate the maximum values of penetration and dissipated energy [3]. Different batches sizes are used to train and validate the prediction performance of the surrogate function. For all the response surfaces it is performed a structural reliability assessment of the substructure given an accidental event. The computational cost associated with the evaluation of the limit-state function to estimate the failure probability is compared between surrogate-based approach and other methodologies.

Offshore wind turbine impacts

The common approach to assess the structural damage of collision events is through explicit nonlinear finite elements simulations since experimental methods are costly and fully analytical expressions are particularly demanding. For ship collisions, the problem is investigated between the interaction of the internal mechanical deformation and the external dynamics loads. This dynamic interaction proposed by [7] and [8] , is usually adopted for the study of collision scenarios by finite element solvers. The methodology was initially proposed to evaluate the structural damage of a submarine-ship collision and later extended for a case of a ship-ship collision events [9]. The simulation of a collision scenario considers first, the internal mechanical deformation produced by buckling, yielding and rupture of the materials given the contact mechanics. Subsequently, the total forces are transmitted to the centre of gravity of the collied structures so that they behave as rigid bodies subject to hydrodynamic loads. To solve the discrete equation of motion, a direct integration scheme is addressed which is unconditionally stable for time steps usually in the order of 1E-6 sec, therefore, expensive in terms of computational time.

A semi-analytical approach, assisted by the afore-mentioned methodology, was derived to perform faster crashworthiness analyses of offshore wind turbines based on closed-form solutions [3]. Given the initial velocity and the direction of a striking ship, the total resistance curve of a jacket foundation is obtained from the contribution of different deformation modes until the ship stops, neglecting the hydrodynamic effects and some shear effects on certain local tubular members. In the present context, this development is adapted to generate dataset from the exploration of input random variables, inside the simulator domain of application. The maximum penetration, also provided as a QoI, will be restricted to a failure threshold to estimate the probability of failure associated with the performance of the substructure given accidental events.

Surrogate Models

Many engineering design problems require large number evaluations of a QoI with certain degree of fidelity over a random joint probability distribution, e.g., global optimization, sensitivity, and risk analyses. The basics of machine learning stands for the task of performing regression given a set of n observations, which is associated with the learning capacity of a surrogate model [10]. To predict a numerical value, a learning algorithm is required to output a function $f : \mathbb{R}^n \rightarrow \mathbb{R}$, different to classification task where the function has to specify the output class over a set of categories. Thus, based on small datasets directly retrieved from high-fidelity engineering simulations, and without imposing additional physical simplifications, surrogate (meta)models are able to efficiently learn mathematical relationships between input design variables to relevant output QoI. In this section is described one of the elementary surrogate models proposed to inexpensively map nonlinear responses derived from a physics-based solver.

Design of experiments

The global metamodeling process consists of building a model able that accurately map deterministic simulation-based problems with reasonable computational effort. This process is carried out following two main steps: the sampling stratification or Design of Experiments (DoE) and the fitting of a metamodel over the design space [11]. The DoE is the choice of how to gather informative samples, that intrinsically influences the prediction performance and the budget dedicated during the global metamodeling. The conventional approach to provide a global metamodel accuracy relies on the generation of one-shot uniform distributed samples, said to be *space-filling*. A commonly used stratification of samples follows a uniform projection of samples onto the axes of the design space, that is divided into equal sized hypercubes (bins). One sample is allocated in each bin so that we can exit the design space along any direction parallel to any of other axes without finding any other occupied bin. This strategy for stratification of samples is known as *Random Latin Hypercubes* [12] which is the one applied to the further presented case study. The metamodel fitting strategy adopted given a fixed set of samples is commonly defined as passive learning, while the procedure in which the model is able to explore and suggest new samples for local or global accuracy improvement is known as active learning.

Polynomial response surface

According to the sampling plan $\mathbf{X} = \{\mathbf{x_1}, \mathbf{x_2}, \mathbf{x_3}, \ldots, \mathbf{x_n}\}^T$ and corresponding observations $\mathbf{y} = \{y_1, y_2, y_3, \ldots, y_n\}^T$, an m-order polynomial approximation of a scalar-valued function f can be formulated as a linear combination of *basis functions*:

$$f \approx \widehat{f}(\mathbf{x}) = \sum_{i=1}^{n_b} \omega_i \psi^{(i)}, \tag{1}$$

where the basis ψ are selected from the set of all possible terms of order less or equal than m. For polynomials of degree 2, for instance, $\psi^{(i)} \in \left[x_1, x_2, x_1x_2, x_1^2, x_2^2\right]$ and ω are the set of weights that are adjusted through maximum likelihood parameter estimation [12]. The risk of poor generalization for such kind of models is associated with the Taylor series expansion of f truncated after $m+1$ terms. It is expected the learning capacity increase with greater values of m, however, the model becomes more flexible and biased to the training data set that is not able to make predictions over new input data, a hazard of surrogate models known as *overfitting*. To overcome this issue, the goodness criteria employed to evaluate the performance of the model should be done over a test data set, which is usually part of the initial data. A simple way to estimate the global generalization error is through the least square error, $LSE = \sum_{i=0}^{n} (y_i - \widehat{y}_i)^2$, which measures the unbiased performance of the predictions. The test data set, however, represents an additional burden in terms of computational budget.

Definition of the case study: impact of a jacket foundation

The semi-analytical solver proposed and implemented in [3] is used to generate datasets with the objective of assessing the global performance of polynomial response surfaces when predicting nonlinear responses resulting from collision events. The solver is based on closed-form solutions and allows a faster evaluation of collision scenarios, defined as a function of the ship velocity and impact angle, compared to high-fidelity numerical simulations, e.g., explicit nonlinear finite element simulations. The semi-analytical solver yields the dissipated energy and the resistance force given the plastic deformation of the substructure produced by the ship penetration. In order to explore the jacket structural performance under collision events, the solver is adjusted to sample output values given four input independent random variables. The lower and upper bounds of the design variables are defined considering the limitations of the semi-analytical simulator and listed in Table 1. Additionally, the diameter of the legs and braces of the jacket are included as input variables in order to assess the crashworthiness of the substructure for varying geometrical parameters.

The global metamodelling is based on polynomial response surfaces of 1, 2, 3, 4, and 5 degrees fitted over two strategies of stratified samples. Each strategy distributes batches of 10, 20, 30, 40, and 50 samples over the design space, as listed in Table 1. The first approach scatters datasets for all the batches following a Random Latin Hypercube technique (LHS), while for the second group of datasets, the samples follow a random uniform distribution (RND). An additional larger dataset of 1,000 samples is generated following RND sampling for the validation of the generated response surfaces based on the least square error (LSE) metric. Furthermore, the estimation of the failure probability is performed through Monte Carlo simulations (MCS). The failure event is defined through a threshold of 3 m maximum penetration. For comparison purposes, the conducted Monte Carlo simulations are computed with one million samples for all failure probability estimations. The geometry of the substructure is considered as $x_3 = 0.9$ m and $x_4 = 0.4$ m. The collision scenarios are sampled considering the velocity as a Gaussian distribution, $x_2 \backsim \mathcal{N}(\mu = 3, \sigma = 0.6)$ and the angle as a uniform distribution delimited by the values listed in Table 1.

Results and comparison of the surrogate-based reliability assessment

The prediction performance of the surrogate models derived from the combination of two stratification strategies is summarised in Figure 1 and Figure 2 for LHS and RND, respectively. For each strategy, the performance metric,

Design variable	Definition	Lower bound	Upper bound	units
$\mathbf{x_1}$	Impact angle	0.0	45.0	$deg.$
$\mathbf{x_2}$	Impact velocity	0.1	5.5	m/s
$\mathbf{x_3}$	Leg diameter	0.8	2.3	m
$\mathbf{x_4}$	Brace diameter	0.4	0.8	m

Table 1: Design variable boundaries considered in the numerical experiments.

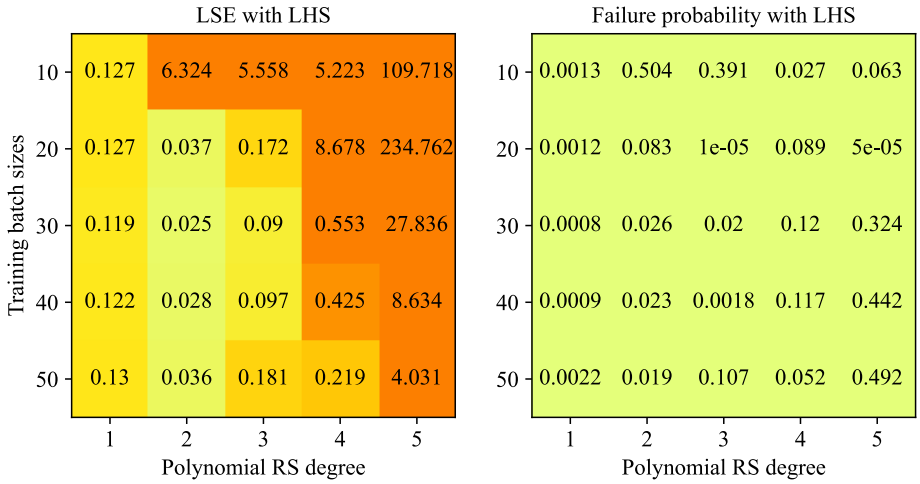


Figure 1: Global generalization error and failure probability estimation resulting from surrogate models trained via Latin hypercube sampling.

LSE, is illustrated as a heatmap for which higher generalization errors are intense colored cells inside a domain defined by the combination of different training batch sizes and the learning capacity controlled by the expansion of polynomial terms. Adjacent to the LSE representation, the failure probability estimation obtained with MCS is also plotted for its corresponding response surface. For the case of response surfaces trained via space-filling stratification strategy, showcased in Figure 1, the lower values of generalization error are obtained from lower degree polynomials. According to the LSE, the complexity of the retrieved nonlinear response is globally reproduced with an error below 20% from polynomials of 1, 2, and 3 degrees trained with a minimum of 20 observations. A set of degree 2 polynomial responses, outstanding among the local group, results in a global prediction error below 4%. The corresponding failure probability, on the other hand, is not categorized according to its magnitude given an expected poor failure estimation of polynomials with high LSE.
Figure 2 showcases the LSE and corresponding failure probability associated with polynomial response surfaces trained via random uniform distribution of samples. Similar to LHS, the global response performance of polynomials with different learning capacities is presented as a heatmap depicting cells with intense color for higher LSE values, before their corresponding failure probability estimation. The lowest global generalization error is found for polynomials of degree 2 with an estimation of failure probability at least 3 times higher than the same polynomial trained via LHS with 40 samples.

Discussion and concluding remarks

In this work, a surrogate-based reliability assessment is conducted for an offshore substructure with the aim of reducing the number of high-fidelity simulations. The computational budget needed to estimate the failure probability given a crash-worthiness performance function is constrained to the generation of only 50 simulations.

In the comparative study, described in the previous section, the results reveal that second-degree polynomial response surfaces are able to efficiently duplicate nonlinear responses with a generalization error below 3%. The models' learning capacity increases when more terms are added to the polynomial expansion, yet additional computational effort is needed for their adequate training. In the showcased study, second-degree polynomial surrogate models trained with 30 simulations are sufficient to yield global predictions. The estimation of the failure probability, however, is sensitive to the local prediction accuracy of the surrogate model around the imposed limit state. Second-degree polynomials associated with a low generalization error may result in inconsistent failure probability estimations. Quadratic polynomials trained with 40 LHS and RND samples result in LSE equal to 2.8%, while the failure probability is 2.3% and 7.8%, respectively. The stratification of samples influences significantly the structural reliability assessment results. A similar estimation is found on models trained via LHS for 30, 40, and

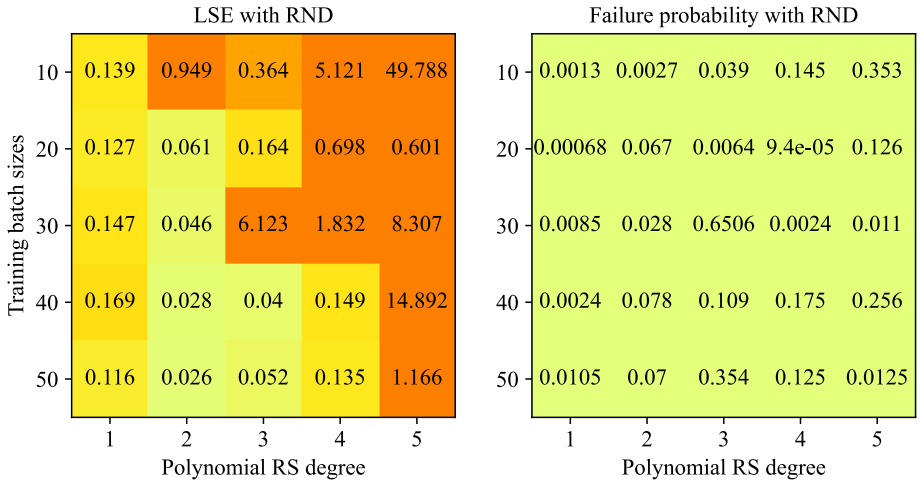


Figure 2: Global generalization error and failure probability estimation resulting from surrogate models trained via random uniform sampling.

50 samples. Even though space-filling techniques provide a more uniform distribution of samples, thus resulting in a reduction of the global generalization error, the computational effort can be dedicated to an improvement of reliability estimates near the limit state function, instead of only targeting global performance metrics. Retrieving information from costly high-fidelity simulations, the training procedure can be enhanced to progressively reduce the generalization error in areas of interest. Future research efforts might be devoted to the development of active learning approaches, specifically tailored to structural reliability analyses, based on surrogate models, e.g., Gaussian processes-based regressors, which are able to additionally provide variance predictions.

References

[1] Zhaokai Li, Qiang Yu, Xuan Zhao, Man Yu, Peilong Shi, and Cilei Yan. Crashworthiness and lightweight optimization to applied multiple materials and foam-filled front end structure of auto-body. *Advances in Mechanical Engineering*, 9(8), 2017.

[2] Nielen Stander, Willem Gabriel Le Roux, Mathias Giger, Marcus Redhe, N. P. Fedorova, and Johannes Haarhoff. Crashworthiness optimization in ls-opt : Case studies in metamodeling and random search techniques. 2003.

[3] T. Pire. *Crashworthiness of offshore wind turbine jackets based on the continuous element method*. PhD thesis, University of Liège, Allée de la Découverte 9, 2018.

[4] Georgios Gasparis, Wai Hou Lio, and Fanzhong Meng. Surrogate models for wind turbine electrical power and fatigue loads in wind farm. *Energies*, 13(23), 2020.

[5] Rui Teixeira, Alan O'Connor, Maria Nogal, Nandakumar Krishnan, and James Nichols. Analysis of the design of experiments of offshore wind turbine fatigue reliability design with kriging surfaces. *Procedia Structural Integrity*, 5:951–958, 2017. 2nd International Conference on Structural Integrity, ICSI 2017, 4-7 September 2017, Funchal, Madeira, Portugal.

[6] René M.M. Slot, John D. Sørensen, Bruno Sudret, Lasse Svenningsen, and Morten L. Thøgersen. Surrogate model uncertainty in wind turbine reliability assessment. *Renewable Energy*, 151:1150–1162, 2020.

[7] Martin J. Petersen. Dynamics of ship collisions. *Ocean Engineering*, 9(4):295–329, 1982.

[8] Preben Pedersen. Collision and grounding mechanics. *The Danish Society of Naval Architects and Marine Engineers*, pages 125–157, 01 1995.

[9] Hervé Sourne, Nicolas Couty, Fermín Besnier, Cyrille Kammerer, Hervé Legavre, and Principia Marine. Ls-dyna applications in shipbuilding. 01 2003.

[10] Ian J. Goodfellow, Yoshua Bengio, and Aaron Courville. *Deep Learning*. MIT Press, Cambridge, MA, USA, 2016. http://www.deeplearningbook.org.

[11] Ong YS. Cai J. Liu, H. A survey of adaptive sampling for global metamodeling in support of simulation-based complex engineering design. *Structural and Multidisciplinary Optimization*, 57:393–416, 2018.

[12] *Engineering Design via Surrogate Modelling, Constructing a Surrogate*, chapter 2, pages 33–76. John Wiley Sons, Ltd, 2008.

18th EAWE PhD Seminar on Wind Energy
2 – 4 November 2022
Bruges, Belgium

Fleet-wide model updating and virtual sensing for fatigue monitoring of offshore wind turbines

D.J.M. Fallais[a,b], W.Weijtjens[a,b]

[a] Vrije Universiteit Brussel, Pleinlaan 2, 1050 Brussels, Belgium
[b] OWI-lab, Offshore wind infrastructure laboratory

E-mail: dominik.fallais@vub.be

Keywords: Offshore wind, model updating, uncertainty quantification

1 Introduction

Despite big advancements in the design of offshore wind turbines the modal properties of as-designed offshore wind turbines do still show discrepancies with respect to the modal properties observed from as-built offshore wind turbines. Parts of these discrepancies are rooted in uncertain input parameters related to e.g. soil-structure interaction. Accurate finite element models, closely resembling the modal properties of the as-built structures, are required to extrapolate strain measurements at easily accessible locations to locations close to e.g. the mud-line. The latter would allow to effectively use virtual sensing approaches for fatigue monitoring at arbitrary locations on the support structure [1,2,3].

At the current stage, within the OWI-lab, finite element models are being prepared based on design documents to allow a wind farm wide assessment of discrepancies between base-line models and observed modal parameters from corresponding operational turbines which are obtained using in-house state of the art operational modal analysis tools.

The aim of this PhD project will be to a) validate virtual sensing methods for extrapolating reponses from easy accessible locations, to fatigue hotspots at inaccessible location, 2) device a strategy for calibrating wind farm wide finite element models. These models will be employed to facilitate response extrapolation for fatigue monitoring over the full range of operational and environmental conditions; the calibration will be based on a limited number of sparsely equipped turbines.

The first two years of this PhD project, will be devoted to the following topics:

1. Exploring model updating of simplified numerical and analytical engineering models using existing techniques and frameworks. The simplified surrogates will be calibrated such that the modal properties resemble observed values from operational modal analysis.

2. Exploring the effect of parameter changes on modelled natural frequencies, which will be compared to identified frequencies. Furthermore, the variability of identified frequencies will be investigated with the aim to map out discrepancies as function of the operational and environmental conditions.

3. In the next stage, updating strategies for single turbines will be investigated and verified. The focus will be on applying state of the art finite element model updating techniques on

engineering models over a wide range of operational and environmental conditions; With the aim to arrive at a strategy which efficiently can account for the latter variations.

4. As a first major result, several response extrapolation methods will be benchmarked on a individual turbines in order to assess the differences between these methods, as well as the effect of the model updating;

Acknowledgements

This project is part of the PhairyWind project: https://www.phairywind.be/.

Bibliography

[1] Weijtjens W, Iliopoulos A, Henkel M, and Devriendt C 2017 'Virtual Sensing on Offshore Wind Turbines: Long Term Experience'

[2] Iliopoulos, A. N. *et al.* (2015) 'Prediction of dynamic strains on a monopile offshore wind turbine using virtual sensors', *Journal of Physics: Conference Series*, 628, p. 012108. doi: 10.1088/1742-6596/628/1/012108.

[3] Maes, K. *et al.* (2016) 'Dynamic strain estimation for fatigue assessment of an offshore monopile wind turbine using filtering and modal expansion algorithms', *Mechanical Systems and Signal Processing*, 76–77, pp. 592–611. doi: 10.1016/j.ymssp.2016.01.004.

18th EAWE PhD Seminar on Wind Energy
2-4 November 2022
Bruges, Belgium

Grey-box modeling for data-based structural health monitoring

Sören Kai Möller[a], **Tanja Grießmann**[a], and **Raimund Rolfes**[a]

[a]Leibniz University Hannover, Institute of Structural Analysis, Appelstr. 9a, D-30167 Hannover, Germany

E-mail: s.moeller@isd.uni-hannover.de

Keywords: Structural Health Monitoring, Offshore-Megastructures, Grey-box modelling, Machine Learning

1 Introduction

To detect damage in structural and mechanical systems as early as possible structural health monitoring methods (SHM) are commonly used [8]. Especially for offshore megastructures, the associated concept of condition-based maintenance has primarily been driven by factors like minimizing downtime as well as operating and maintenance costs. In addition, the design life can be extended [1].
To infer the structural integrity, there exist, according to Farrar and Worden [8], two main approaches: The model-based and the data-based approach. The first one is usually implemented by building a physics-based model (white-box model) of the structure of interest [7]. The second one is based on machine learning (ML) methods. Therefore it relies on building a model on measured data to learn relationships from the data (black-box model) [7]. Due to the complexity of many modern structures and their environments, it is often difficult to define physically based engineering analysis procedures. And so, according to Worden [15], data-based SHM could be useful for several applications.
The data basis for the underlying methods often consists of measured system response data, such as acceleration or strain measurements [11]. At the same time, however, considering dynamic loads caused by varying environmental and operational conditions (EOCs), e.g., wind speed, rotational speed, and temperature, is of considerable importance for obtaining damage-sensitive features [9]. In this context, various data normalization forms need to be used in feature extraction to separate changes in measured response caused by different EOCs from changes caused by damage [6]. The extracted features can then be used to implement statistical models for quantifying the damage state of the structure [7].
As introduced at the beginning both, physically-based models, such as finite element (FE) models [7] and data-based models (e.g., artificial neural networks (ANNs) [15], support vector machines (SVMs) [15] and gaussian process (GP) regression [3]) are conceivable approaches in the field of SHM. Especially GP regression, as an ML method, is becoming common in several SHM applications [4]. Beneficial here are its nonparametric nature, the ability to work with a small number of training points, and the applicability within the Bayesian framework. In this context, instead of a single prediction point, a GP provides a predictive distribution.
In addition, it is also possible to combine the two approaches into a grey-box model [4]. Those models are about using prior knowledge about the system and estimating the unknown parts of the model based on measured data. In this respect, it is first stated that domain knowledge is available for many use cases, but this is often incomplete. It can prove helpful to pursue a model-building approach between white-box and black-box models. The result is a model with some elements given by physics and elements learned from data. In this context, different approaches are conceivable, which can be divided according to how prior knowledge is dealt with. Based on this, an approach for a grey-box model was developed by Alvarez et al.[2]. They combine data-driven modeling, in the form of a GP, with a physical model of the system based on differential equations to form a so-called Latent Force Model (LFM). Furthermore, Rogers et al.[12] present an approach to identifying structural systems in conjunction with estimating the inputs to the system. They show that it is possible to simultaneously estimate the parameters of a dynamical system and the unknown input from some output measurements. Moreover, GPs can be used as so-called GP-NARX (Nonlinear Auto-Regressive with eXogenous inputs) models to approximate dynamic processes

[16]. In this context, Jones et al.[10] show that it is possible to incorporate physical insight into a GP by using a kernel function that explicitly captures the evolution of dynamic systems in time.

2 Methodology

Within the scope of the ongoing research project, the combination of physics-based models and ML approaches will be investigated to determine how the resulting grey-box models could form a suitable basis for the structural monitoring of an offshore megastructure during operation.
Due to the wide range of applications of GP regression in SHM, this ML approach will serve as the black-box model. To incorporate prior knowledge into this model, hybrid modeling [13] is a possible branch. This approach reflects the possibility of splitting the model into a white-box part, modeled by first principles equations, and a black-box part, to be identified by measurement data. The combination can be done in either a serial or parallel manner. The serial method usually refers to models where a specific physical part of the underlying process is captured by a white-box model of the following form

$$y = g(x, w(x)), \tag{1}$$

where $g(\cdot)$ refers to the resulting grey-box-model and $w(\cdot)$ to the white-box model [13]. The parallel approach is used to extend an approximate physics-based model with a data-driven part that compensates for the simplifications in the approximated model. This approach includes the so-called residual models. This can be described with the general form [4]:

$$y = w(x) + b(x) + \varepsilon. \tag{2}$$

Here $w(\cdot)$ represents the output of the physical model and $b(\cdot)$ the black-box model to compensate for the difference between the physics-based model and measurements. In addition, ε represents the process noise.
To realize the proposed hybrid approach for a GP, on the one hand, a kernel function can be derived from prior knowledge about the underlying system [5]. This approach corresponds to the form from Equation 1. Second, prior knowledge can also be introduced using the mean function of the GP [4] and is comparable to Equation 2.
However, in addition to the selection of a grey-box model, the design of the GP is also important, as these are static mappings that learn the relationship between point inputs and point outputs. To learn the dynamical system behavior, a NARX framework according to [16] is a useful approach. Here the current value of the system output is predicted using a nonlinear function F and previous inputs and outputs, i.e.

$$y_i = F(y_{i-1}, \ldots, y_{i-n_y}; x_i, \ldots, x_{i-n_x+1}) + \varepsilon_i, \tag{3}$$

where the residual sequence ε_i is white Gaussian noise. The number of output (respectively input) lags is denoted as n_y (respectively n_x) and the function F can also be represented by a GP [16].
Using a linear single-degree-of-freedom (SDOF) oscillator (with mass, damping, and stiffness parameters m, c, and k, respectively) driven by a force $F(t)$:

$$m\ddot{y}(t) + c\dot{y}(t) + ky(t) = F(t), \tag{4}$$

it shall be shown that the NARX model based on a GP according to formula 3 can be used well for a regression task. To introduce prior knowledge into the GP, it is convenient to express Equation 4 using a finite difference approach corresponding to the form:

$$y_t = \alpha y_{t-1} + \beta y_{t-2} + \gamma F_t. \tag{5}$$

The coefficients α, β, and γ result from the type of finite difference scheme. For further investigations, a finite difference scheme based on backward differences was chosen, because the NARX model (Eq.3) relies on backward inputs and outputs.

3 Results

The SDOF system from Equation 4 was excited by white noise with $\sigma = 0.001$ over a period of 2.1638 seconds. To train the GP-NARX, 22 values from the first 1.0787 seconds were selected as shown in Figure 1. The past values

for mapping the dynamic behavior were also considered according to Equation 5. Furthermore, a mean function of zero was assumed for the GP and a squared exponential kernel was used for the kernel function.
As shown in Figure 1, the dynamic behavior of the SDOF system is very well reproduced by the GP-NARX model used. From time $t = 1.0787$ seconds on, it can also be observed that the model can extrapolate very well and has a mean squared error of 1.0575×10^{-7} in this range. Thus, apparently few training data are sufficient to achieve acceptable performance on unknown data as well. It is also noticeable that the 95% prediction intervals are very close to the expected value of the GP, which means that the prediction is also subject to a high degree of certainty.

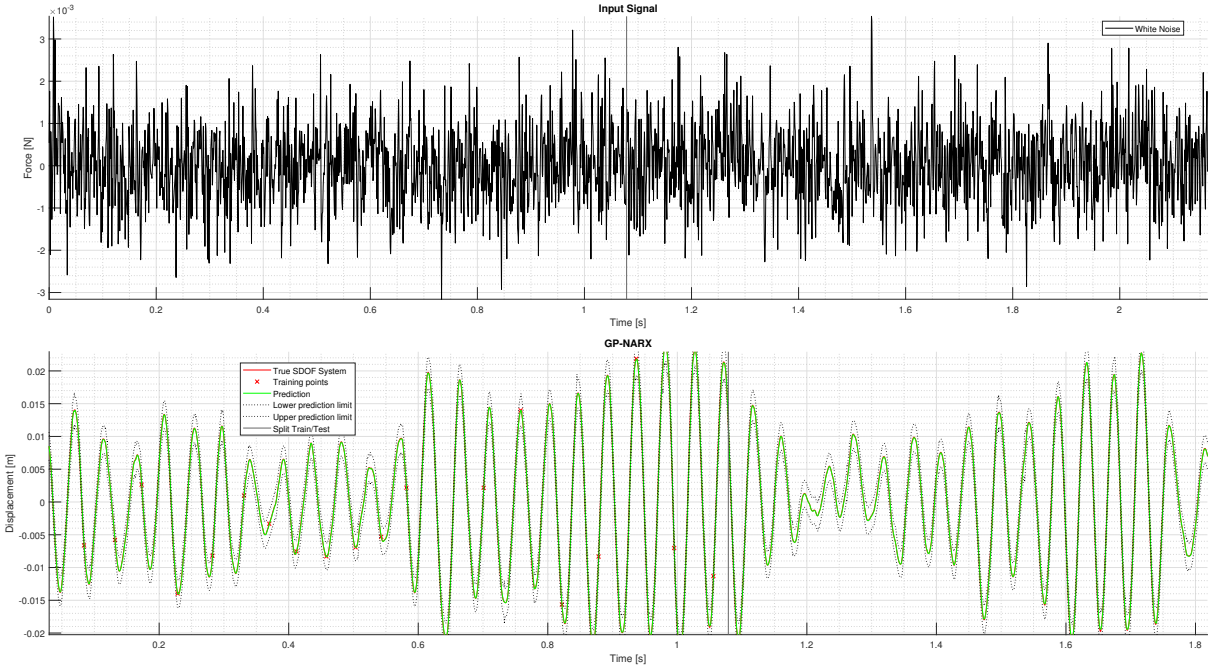


Figure 1: Fit of the SDOF system under random load

4 Conclusion and Outlook

It could be shown that the system behavior of the randomly excited SDOF system can be well identified using a GP-NARX approach based on a few data points. Thus, such a model seems to be well suited as a black-box part of a grey-box monitoring concept based on it. However, since black-box models strongly depend on the available data, the training data must therefore cover all relevant EOCs. Furthermore, such models cannot be guaranteed to adhere to fundamental physical laws on unknown data. To overcome these limitations, future work will explore the possibilities of incorporating prior physical knowledge using the mean function as well as the kernel function. In future steps it is also planned to test the proposed concept step by step and validated it on different databases, for example, the Leibniz University Test Structure for Monitoring (LUMO) [14]. Moreover, suitable training strategies and hypothesis tests will also be considered. They will be explored on synchronously recorded time series (acceleration, strain, temperature, wind speed, rotor speed, pitch angle, etc.) of the vibrating structure. For this purpose, the various system states must be learned under the changing operating and environmental conditions that occur, so that system changes are not mistaken for damage.

Acknowledgements

Funding was provided by Deutsche Forschungsgemeinschaft (DFG, German Research Foundation)-CRC1463, project C02. The authors would like to acknowledge the support gratefully.

References

[1] D. Adams, J. White, M. Rumsey, and C. Farrar. Structural health monitoring of wind turbines: method and application to a hawt. *Wind Energy*, 14(4):603–623, 2011.

[2] Alvarez, Mauricio and Luengo, David and Lawrence, Neil D. Latent force models. *12th International Conference-Artificial Intelligence and Statistics*, pages 9–16, 2009.

[3] L. D. Avendaño-Valencia, E. N. Chatzi, K. Y. Koo, and J. M. W. Brownjohn. Gaussian process time-series models for structures under operational variability. *Frontiers in Built Environment*, 3, 2017.

[4] E. J. Cross, S. J. Gibson, M. R. Jones, D. J. Pitchforth, S. Zhang, and T. J. Rogers. Physics-informed machine learning for structural health monitoring. 21(5):347–367, 2022.

[5] E. J. Cross and T. J. Rogers. Physics-derived covariance functions for machine learning in structural dynamics. *IFAC-PapersOnLine*, 54(7):168–173, 2021.

[6] C. R. Farrar, H. Sohn, and K. Worden. *DATA NORMALIZATION : A KEY FOR STRUCTURAL HEALTH MONITORING*. 2001.

[7] C. R. Farrar and K. Worden. An introduction to structural health monitoring. In G. Maier, F. G. Rammerstorfer, J. Salençon, B. Schrefler, P. Serafini, A. Deraemaeker, and K. Worden, editors, *New Trends in Vibration Based Structural Health Monitoring*, volume 520 of *CISM International Centre for Mechanical Sciences*, pages 1–17. Springer Vienna, Vienna, 2011.

[8] C. R. Farrar and K. Worden. *Structural health monitoring: A machine learning perspective*. Wiley, Chichester, West Sussex, U.K, 2013.

[9] M. W. Häckell, R. Rolfes, M. B. Kane, and J. P. Lynch. Three-tier modular structural health monitoring framework using environmental and operational condition clustering for data normalization: Validation on an operational wind turbine system. *Proceedings of the IEEE*, 104(8):1632–1646, 2016.

[10] M. R. Jones, T. J. Rogers, and E. J. Cross. Physical covariance functions for dynamic systems with time-dependent parameters. In P. Rizzo and A. Milazzo, editors, *European Workshop on Structural Health Monitoring*, volume 270 of *Lecture Notes in Civil Engineering*, pages 381–391. Springer International Publishing, Cham, 2023.

[11] F. L. Marques Dos Santos and B. Peeters. On the use of strain sensor technologies for strain modal analysis: Case studies in aeronautical applications. *The Review of scientific instruments*, 87(10):102506, 2016.

[12] T. J. Rogers, K. Worden, and E. J. Cross. On the application of gaussian process latent force models for joint input-state-parameter estimation: With a view to bayesian operational identification. *Mechanical Systems and Signal Processing*, 140:106580, 2020.

[13] B. Sohlberg and E. W. Jacobsen. Grey box modelling – branches and experiences. *IFAC Proceedings Volumes*, 41(2):11415–11420, 2008.

[14] S. Wernitz, B. Hofmeister, C. Jonscher, T. Grießmann, and R. Rolfes. A new open–database benchmark structure for vibration–based structural health monitoring. *Structural Control and Health Monitoring*, 2022.

[15] K. Worden. Structural health monitoring using pattern recognition. In G. Maier, F. G. Rammerstorfer, J. Salençon, B. Schrefler, P. Serafini, A. Deraemaeker, and K. Worden, editors, *New Trends in Vibration Based Structural Health Monitoring*, volume 520 of *CISM International Centre for Mechanical Sciences*, pages 183–246. Springer Vienna, Vienna, 2011.

[16] K. Worden, W. E. Becker, T. J. Rogers, and E. J. Cross. On the confidence bounds of gaussian process narx models and their higher-order frequency response functions. *Mechanical Systems and Signal Processing*, 104:188–223, 2018.

18th EAWE PhD Seminar on Wind Energy
2-4 November 2022
Bruges, Belgium

Higher-Order Cyclostationary approaches for Fault Detection of Wind Turbines Gearboxes

Marcello Nitti[a], **Cédric Peeters**[a], **Kayacan Kestel**[a], **Rebeca Marini**[a], and **Jan Helsen**[a]

[a]Vrije Universiteit Brussel - VUB, Department of Applied Mechanics, Brussels, 1050, Belgium

E-mail: marcello.nitti@vub.be

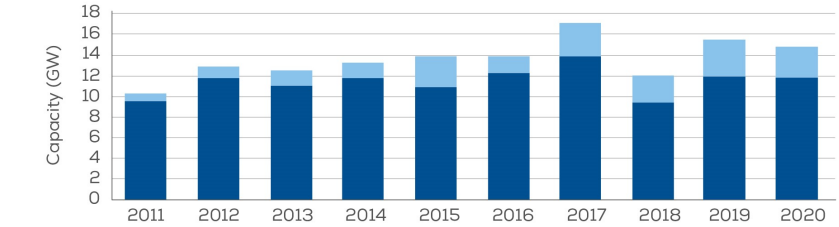
Keywords: Vibration signal processing, condition monitoring, higher-order cyclostationarity

1 Abstract

This paper investigates the scalar indicators for higher-order cyclostationarity faults detection in gear and bearings of rotating machines. The assumption for these indicators is that the faults of such components can be considered cyclostationary (first or second order). Moreover, the performance of these indicators can be hindered by interference from other vibration sources. To overcome this problem their performance is integrated with a blind deconvolution approach. The deconvolution step aims at increasing the signal-to-noise ratio of a potential fault signature. This goal is reached by optimizing a finite impulse filter based on the higher-order cyclostationarity indicators. Finally, the performance of the proposed methodology is validated on both simulated and experimental vibration data showing how these indicators are an effective way of tracking the faults with a cyclostationart signature.

2 Introduction

Wind energy is a rapidly growing source of green energy production. Figure 1 shows the additional capacity of onshore and offshore wind turbines over the past years.



	2011	2012	2013	2014	2015	2016	2017	2018	2019	2020
Offshore	0.8	1.2	1.5	1.5	3.0	1.6	3.2	2.7	3.6	2.9
Onshore	9.5	11.7	11.0	11.7	10.9	12.3	13.9	9.4	12.0	11.8
Total	**10.3**	**12.9**	**12.6**	**13.2**	**13.9**	**13.8**	**17.1**	**12.1**	**15.6**	**14.7**

Figure 1: Onshore and offshore wind energy installation capacity in Europe [3]

This green technology is rapidly evolving in terms of complexity and size, together with their essential rotating components such as gears, bearings, and shafts. Defects on rotating elements of machines can result in severe economic losses, especially if these are not fixed in time, leading to severe component failure. The typical failures of rotating machinery are caused by gears and bearings. A failure of one of these components will influence the machine's performance, influencing the power transmission or, in the worst case, leading to the shut-down of the entire machine [4].

To solve these issues, the fields of prognosis and health management have become more and more relevant in the industry over the past decades. The practice of collecting data and analyzing them for health monitoring is called Condition Monitoring (CM) and nowadays it is a crucial part of many industrial projects. CM can be applied via several methods and vibration analysis is generally very popular in both academia and industry thanks to its easy implementation and fast data analysis [11].

The most common faults of gears and bearing can be plastic deformation, local defects, distributed surface imperfections, cracks, fractures, corrosion, and wear [7].

An important concept in advanced vibration analysis for rotating machines is the theory of cyclostationarity, first proposed in 1958 [1]. Cyclostationary signals are a family of signals which include all waveforms with different periodicities by decomposing them into their periodic and random parts, it is possible to analyze different physical contributions. The vibrations of rotating components are typically non-stationary, but their signals have some statistical properties that repeat over the shaft rotation cycles. By analyzing changes in these properties, it is possible to detect faults. In the case of gears and bearings, their fault signatures can generally be considered as first- or second-order cyclostationary [12] [8] , even though they do have their differences with the former being considered deterministic and the latter stochastic.

The cyclostationary approach has proven particularly efficient to detect weak incipient faults and blindly extract signals of interest from strong background noise. For instance, [10] shows new indicators of cyclostationarity (ICS) from 1^{st} to 4^{th} order without the need of computing the nth-order polispectra for analyzing the data. They tested these indicators on two single-stage gear units mounted back-to-back with an equal number of teeth. Results showed how the first two indicators were suitable to detect gear faults in the frequency range below 16 kHz, while the last two worked well above 16 kHz. In another experiment with bearing rolling elements [5] shows how the third and fourth indicators were able to detect faults reliably.

However, one expected obstacle to the performance of these indicators is interference from other vibration sources. Blind deconvolution approaches can be applied in addition to the higher-order cyclostationary techniques in order to overcome this problem. Several approaches have been proposed in the literature, such as minimum entropy deconvolution (MED), maximum correlated kurtosis deconvolution (MCKD), optimal MED adjusted (OMEDA), multipoint OMEDA (MOMEDA), and cyclostationarity-based blind deconvolution (CYCBD). [16] The common objective of these methods is the aim of increasing the signal-to-noise ratio (SNR) of a potential fault signature hidden in the noise level. This goal is reached by finding a suitable filter that maximizes the SNR.

The goal of this research is to study the potential application of the indicators proposed in [10] in combination with a blind deconvolution approach explained in [2] and [9] for fault detection. Both simulated and real signals are measured on compelex industrial rotational machinery in order to test the indicators. Based on the research gaps identified in the literature, the following questions will be researched:

- What are good higher-order cylostationary indicators (HOCS) for faults detection?
- Can these HOCS be used as an effective fault detection mechanism?
- What is the frequency range where they work the best?
- Can they be used for both gear and bearing fault detection?
- How well do they perform in non-stationary operating conditions?
- Do we need to analyze for even higher orders (> 4) of cyclostationarity in particular cases?
- What order of cyclostationarity provides us with the most reliable machine health information?

These questions along with others that will surely follow whilst doing this research will be the focus of the research.

3 Methodology

The indicators are first derived starting from the definition given by [10] and later evaluate and validate on both simulated and real signals on compelex industrial rotational machinery. The simulated signals have different signal-to-noise ratio, while the experimental one are based on a fault of one bearing. The following section summarises the general expression of the indicator and their derivation.

The cyclostationary indicators are based on the use of cumulants, while the blind deconvolution approach is based on the one derived in [2]. In this work, the blind filtering technique is applied to maximize the indicators.

3.1 Indicators of cyclostationarity

A cyclostationary process can be considered such if there are some hidden periodicities in its statistical structure. More generally, it is cyclostationary if its nth statistical moment or cumulant contains some periodic components. The cyclostationary indicators are based on the cumulants of a noisy signal **x**. The advantage of using cumulants instead of moments is that the first are pure in the sense that no lower order cumulants are present in the nth order. The indicators applied in this paper are the one defined in [10] as follows:

$$ICS_n = \sum_{\alpha=\varpi,\alpha\neq 0} \frac{|C_n^\alpha(0)|^2}{|C_2^0(0)|^n} \tag{1}$$

where α is the frequency of interest of the cycling frequency ω.

3.2 Blind filtering tecnique

The ideal input signal **s** can be expressed in matrix form as follows:

$$\mathbf{s} = \mathbf{X} * \mathbf{h} \tag{2}$$

where **h** is the inverse finite impulse responce (FIR) filter of length L and * stands for the convolute product. Vectors are indicated in bold and matrix quantities in capitals and bold in order to distinguish them from scalars. The blind filtering method is based on the generalized Rayleigh quotient approach and it is used to maximize the eigenvector associated with the maximum eigenvalue. In this case the ICS values are assigned to the eigenvalue. Thus, maximising the first quantity means maximising the ICS for the given signal. As already shown in [2], eq. 1 can also be expressed as follows:

$$ICS_n = \frac{\sum_{k>0}|c_s^k|^2}{|c_2^0|^n} \quad \text{with} \quad c_s^k = \frac{\mathbf{E}^H(|\mathbf{s}|^n)^2}{L-N+1} \quad \text{and} \quad c_s^0 = \frac{\mathbf{s}^h\mathbf{s}}{L-N+1} \tag{3}$$

The superscript H indicates the Hermitian transpose, **E** is a Fourier matrix and L the signal length. Substituting the expression of c_s^k and c_s^0 in ICS_n and taking n=2, the ICS2 becomes:

$$ICS_2 = \frac{|\mathbf{s}|^{2H}\mathbf{E}\mathbf{E}^H|\mathbf{s}|^2}{|\mathbf{s}^H\mathbf{s}|^2} \tag{4}$$

Finally, substituting eq. 2 in eq. 4, the final expression of the ICS2 becomes the following:

$$ICS_2 = \frac{\mathbf{h}^H\mathbf{X}^H\mathbf{W}\mathbf{X}\mathbf{h}}{\mathbf{h}^H\mathbf{X}^H\mathbf{X}\mathbf{h}} = \frac{\mathbf{h}^H\mathbf{R}_{XWX}\mathbf{h}}{\mathbf{h}^H\mathbf{R}_{XX}\mathbf{h}} \tag{5}$$

where $\mathbf{R}_{XWX}$ and $\mathbf{R}_{XX}$ are the weighted correlation matrices. Eq. 5 is a generalized Rayleigh quotient problem. Maximizing it with respect to **h** is the same as maximizing the eigenvector associated with the maximum eigenvalue λ of the following problem:

$$\mathbf{R}_{XWX}\mathbf{h} = \mathbf{R}_{XX}\lambda \tag{6}$$

In this case, λ corresponds to the maximization of the ICS2 indicator. The way to proceed is the following:

1. Make an initial guess for **h**
2. Estimate $\mathbf{R}_{XWX}$ and $\mathbf{R}_{XX}$ given the input signal **X** and **h**
3. Solve eq. 6 in order to find the corresponding new value of **h** associated with λ
4. Return to the second step with the updated value of **h** until the convergence criteria is met or until the convergence is reached

Following a similar approach, ICS3 can be found with n=3 in eq. 3. The matrix form is the following:

$$ICS_3 = \frac{|\mathbf{s}|^{3H}\mathbf{E}\mathbf{E}^H|\mathbf{s}|^3}{|\mathbf{s}^H\mathbf{s}||\mathbf{s}^H\mathbf{s}|^2} = \frac{\mathbf{h}^H\mathbf{X}^H\mathbf{W}\mathbf{X}\mathbf{h}}{\mathbf{h}^H\mathbf{X}^H\mathbf{X}\mathbf{h}} = \frac{\mathbf{h}^H\mathbf{R}_{XWX}\mathbf{h}}{\mathbf{h}^H\mathbf{R}_{XX}\mathbf{h}} \tag{7}$$

Solving eq. 5 and eq. 7 allows for the maximization of the 2nd and 3rd order cyclostationarity.

4 Simulation data

To validate the developed approach the proposed indicators are tested on a simulated case and experimental one.

The simulated signals consist of impulses of a fault signal. These impulses have a Gaussian distributed amplitude. A Gaussian noise is added to the signal and it varies in signal-to-noise ratio (SNR) from -40 dB to 40 dB to assess the trending behavior of the indicators and of the filtering technique. The overall variance of the full signal is kept constant. Figure 2 shows the structure of the simulated fault signal, while the results of ICS2 and ICS3 with and without filter are depicted in Figure 3 and Figure 4.

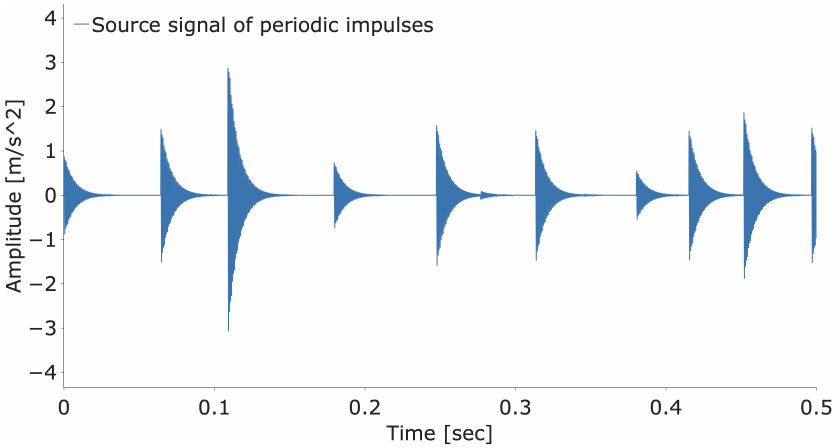


Figure 2: Input signals used for the simulation cases.

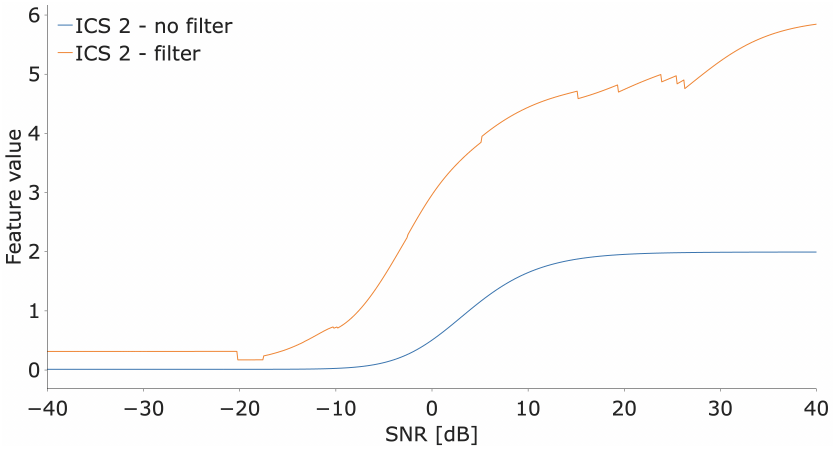


Figure 3: Evolution of the ICS2 indicator with and without filter on simulation data with increasing SNR from -40 dB to 40 dB.

The ICS2 without the filter is able to detect the development of the fault, but the filtering technique improves its trend, as clearly visible in Figure 3. Indeed, its absolute value not only increases but also the trend of the curve starts to go up around -15 dB, leading to early detection of the fault. This is in line with what was expected, since the fault exhibit 2nd order cyclostationarity behavior leading to a rise of the ICS2.

A similar trend occurs for the ICS3 as depicted in Figure 4. It has to be pointed out that even if the curve of ICS3 without filter seems a straight line, in reality, it is not. Its trend is the same as the ICS2 or the ICS3 with the filter. However, its value is so small compared to the filter case, that it appears as a straight line. Overall, the indicator without the filter is able to detect the fault, however the ICS3 values are so low that in a real case it would be difficult to say if there is a fault. By contrast, the situation improves with the filter application.

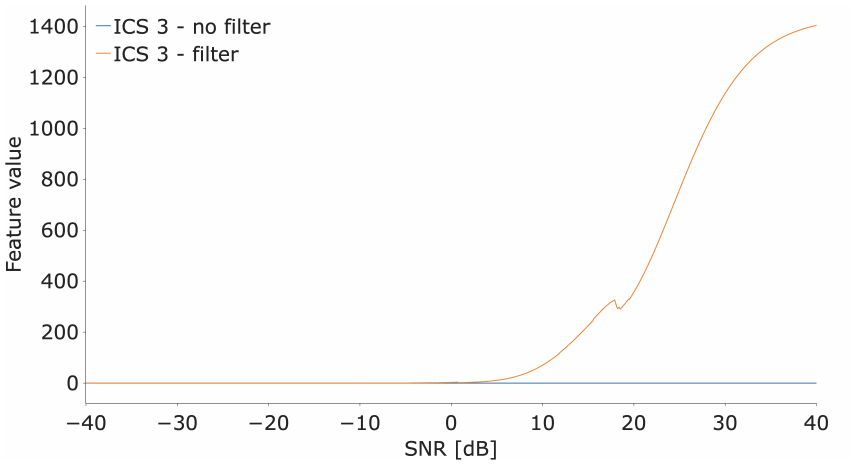


Figure 4: Evolution of the ICS3 with and without filter on simulation data with increasing SNR from −40 dB to 40 dB.

5 Experimental data

The experimental data used for the validation are taken from the Prognostics Data Repository of NASA as provided by the Center for Intelligent Maintenance Systems (IMS) of the University of Cincinnati [6]. The test rig consists of four bearings mounted on the same shaft. During the experiment, the shaft rotation speed is kept constant at a value of 2000 rpm and a radial load of 27.7 kN is applied on the second and third bearing. The bearings are equipped with accelerometers. The sampling frequency is 20.48 kHz. The experiment run continuously for seven days, and at the end of the experiment, the first bearing showed an outer race fault with a characteristic fault frequency of the outer race (BPFO) of approximately 236 Hz. The results of the ICS2 and ICS3 are showed in Figure 5 and Figure 6.

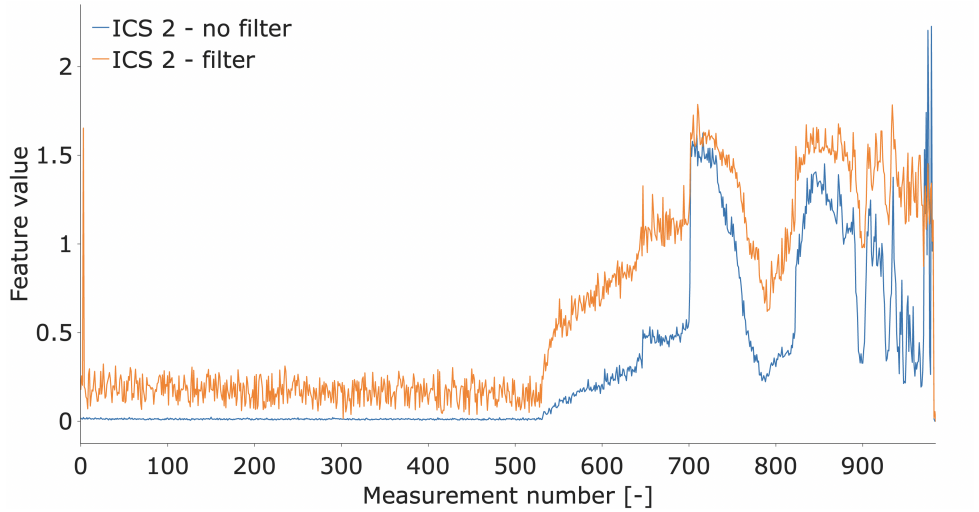


Figure 5: Evolution of the ICS2 indicator with and without filter on experimental data.

For what concerns the experimental case, as can be seen in Figure 5 and Figure 6, the trend of the indicators and filtering technique is similar to the simulated case. In general, the increase of the indicators can be associated with the impulsive patterns given by the fault present on the bearing. At every new completed turn, the fault hits the outer ring of the bearing enhancing its cyclostationarity behaviour. The rapid increase of the ICS2 and ICS3 can be considered a clear indication of a potential bearing fault.

As a side note, the early detection of the ICS2 is crucial for industrial applications because, condition mon-

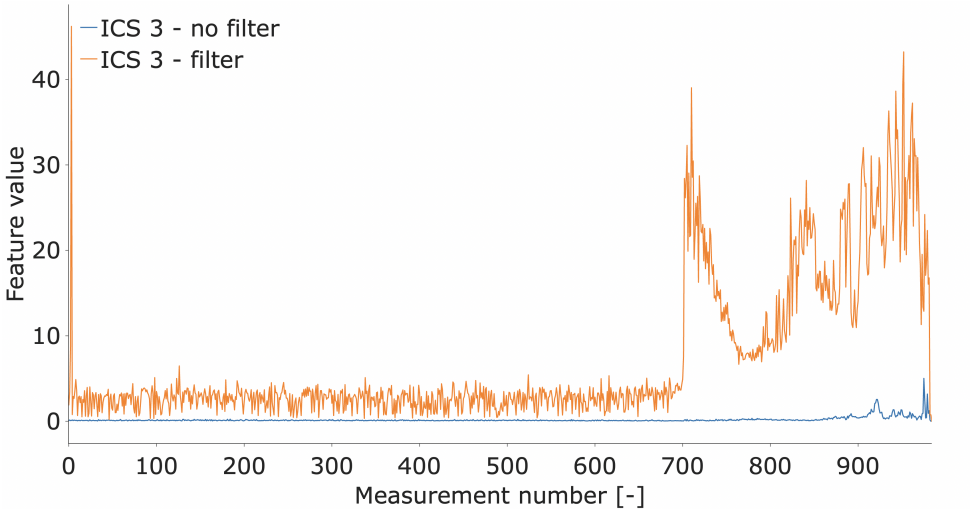


Figure 6: Evolution of the ICS3 indicator with and without filter on experimental data.

itoring is typically done in an automatic way, where fault detection requires a clear elevating trend exceeding a threshold. Thus, a small increase in the trend may not be considered a clear indication of a fault.

Some final remarks should be made about the blind filtering technique used in this paper. It should not be designated as blind deconvolution, blind signal separation, or denoising. This approach does not deconvolve the signal in order to recover the source signal. neither does it tries to separate signals from a mixture or remove noise from the signal without distorting it. This approach tries to maximize the selected indicator.
The earliest sudden increase in the level of the indicator (see ICS3) or the steep increase of the curve (see ICS2) can be attributed to the implemented blind filtering approach.

The simulation and experimental results show the potential for condition monitoring using a blind filtering approach of vibration signals.

Finally, the proposed approach shows an alternative way of combining blind filtering and the indicators of cyclostationarity. However, one main drawback is in selecting the filter length since it can significantly impact the results and the computation time. Longer filter lengths increase the computation time, leading to slower convergence or non-convergence in the worst-case scenario. For this reason, it is recommended to keep the filter length short.

6 Conclusions

This paper researches the application of scalar indicators for higher-order cyclostationarity for faults detection by analyzing the signature in vibration signals. The indicators are also combined with a blind filtering technique to improve their performances. The blind filtering approach is based on a generalized Rayleigh quotient problem. This helps for easy implementation in the code, as well as a fast computation. The evaluation of the indicators and blind filtering technique is tested on both simulated as well as experimental signals. Results show how the trend is the same for all the indicators when it comes to simulated signals. A similar trend occurs when tested on experimental dataset. The ICS2 performs better compared to the ICS3. The blind filtering approach improved a lot these last two indicators, having on lead still the ICS2.

The paper hopes to give insight and inspiration for further research with this blind filtering approach for vibration monitoring. Furthermore, the paper shows that the Rayleigh quotient iteration is the main tool for easily implementing the proposed filters.

Future work will focus on the improvement of the filter in order to have a better behaviour of the ICS3, as well as implement and test the ICS4.

Acknowledgements

Marcello Nitti, Cédric Peeters, and Jan Helsen received funding from the Flemish Government (AI Research Program). They would like to acknowledge FWO (Fonds Wetenschappelijk Onderzoek) for their support through the post-doctoral grant of Cédric Peeters (# 1282221N). The authors are also grateful to the FWO for the support through the SBO Robustify project (S006119N). They would also like to thank the Blue Cluster ICON Rainbow project for their support.

References

[1] W. Bennett. Statistics of regenerative digital transmission. *Bell System Technical Journal*, 37(6):1501–1542, 1958.

[2] M. Buzzoni, J. Antoni, and G. d'Elia. Blind deconvolution based on cyclostationarity maximization and its application to fault identification. *Journal of Sound and Vibration*, 432:569–601, 2018.

[3] W. Europe. Wind energy in europe 2020 statistics and the outlook for 2021-2025, 2020.

[4] Z. Feng and F. Chu. Cyclostationary analysis for gearbox and bearing fault diagnosis. *Shock and Vibration*, 2015, 2015.

[5] G. Ishak, A. Raad, and J. Antoni. Analysis of vibration signals using cyclostationary indicators. *Institute of Technology of Chartres: Chartres, France*, 2013.

[6] J. Lee, H. Qiu, G. Yu, and J. Lin. Rexnord technical services, bearing data set, ims, university of cincinnati. nasa ames prognostics data repository. *NASA Ames, Moffett Field, CA*, 2007.

[7] Z. Liu and L. Zhang. A review of failure modes, condition monitoring and fault diagnosis methods for large-scale wind turbine bearings. *Measurement*, 149:107002, 2020.

[8] Z. Ma, Y. Liu, D. Wang, W. Teng, and A. Kusiak. Cyclostationary analysis of a faulty bearing in the wind turbine. *Journal of Solar Energy Engineering*, 139(3), 2017.

[9] C. Peeters, J. Antoni, and J. Helsen. Blind filters based on envelope spectrum sparsity indicators for bearing and gear vibration-based condition monitoring. *Mechanical Systems and Signal Processing*, 138:106556, 2020.

[10] A. Raad, J. Antoni, and M. Sidahmed. Indicators of cyclostationarity: Theory and application to gear fault monitoring. *Mechanical Systems and Signal Processing*, 22(3):574–587, 2008.

[11] R. B. Randall. *Vibration-based condition monitoring: industrial, automotive and aerospace applications*. John Wiley & Sons, 2021.

[12] V. Sharma and A. Parey. Use of cyclostationarity based condition indicators for gear fault diagnosis under fluctuating speed condition. In *Cyclostationarity: Theory and Methods III*, pages 241–257. Springer, 2017.

18th EAWE PhD Seminar on Wind Energy
2-4 November 2022
Bruges, Belgium

Interpretation of offshore wind management policies identified via partially observable Markov decision processes

Nandar Hlaing[a], **Pablo G. Morato**[a], **Konstantinos G. Papakonstantinou**[b], **Charalampos P. Andriotis**[c], and **Philippe Rigo**[a]

[a]Naval & Offshore Engineering, ArGEnCo, University of Liege, 4000 Liege, Belgium
[b]Department of Civil & Environmental Engineering, The Pennsylvania State University, University Park, PA 16802, USA
[c]Faculty of Architecture & the Built Environment, Delft University of Technology, 2628 BL Delft, The Netherlands

E-mail: nandar.hlaing@uliege.be

Keywords: Offshore wind turbines; Inspection and maintenance planning; Markov decision processes.

1 Introduction

The installation of offshore wind turbines, profiting from available abundant and stable wind resources, has been steadily increasing in the last decade, yet preserving offshore wind structures in a good condition throughout their lifetime still remains a challenge. Structural components are exposed to deterioration mechanisms (e.g., fatigue, corrosion, among others), and far offshore, inspection and maintenance (I&M) operations can be complex and expensive. Hence the need for efficient optimal I&M planning methods has been increased in order to control the risk of structural failures by timely allocating inspection and maintenance interventions.

Identifying optimal I&M policies demands the solution of a complex sequential decision-making problem under uncertainty and imperfect information. Whereas time-, condition-, or heuristic-based strategies are conventionally followed in the offshore wind industry in order to alleviate the aforementioned computational difficulties, the resulting policies statically select inspection and maintenance actions and/or consist in predefined heuristic decision rules, e.g., equidistant inspections, repairs after detection inspection outcomes, which are optimized by exploring a subset out of the vast policy space. Instead, optimal management strategies can be identified via partially observable Markov decision processes (POMDPs), relying on mathematical principles conceived for planning under uncertainty [1]. POMDP policies, efficiently computed through point-based solvers, provide optimal adaptive I&M strategies that ultimately result in substantial cost benefits compared to their state-of-the-art counterparts [2], also demonstrated in offshore wind inspection and maintenance planning settings [3].

Even if recently reported results demonstrate the benefits of implementing POMDP-based adaptive policies for the management of offshore wind assets, the interpretation and execution of POMDP-based strategies by decision-makers (e.g., designers, operators, etc.) accustomed to calendar- and/or condition-based conventional I&M approaches might be initially challenging. In this work, we analyze and interpret POMDP-based policies with the objective of accelerating their practical implementation by offshore wind asset management decision-makers. Also, we showcase the inherent flexibility and adaptability properties offered by POMDP-based policies in a typical offshore wind inspection and maintenance planning setting, in which a decision-maker opts for an action other than the one suggested in the optimal POMDP policy.

2 Optimal I&M planning for offshore wind structures through POMDPs

A Markov decision process (MDP) is a 5-tuple $\langle S, A, T, R, \gamma \rangle$ controlled stochastic process for optimal planning under uncertainty and perfect information. At every decision step, the agent observes state $s \in S$ and takes an action $a \in A$, then the state randomly transitions to state $s' \in S$ according to a stochastic transitional model $T(s,a,s') =$

$P(s'|s,a)$, and finally the agent receives a reward $R(s,a)$. An MDP policy $(\pi : S \rightarrow A)$ prescribes actions as a function of the current state, with the main objective of identifying the optimal policy $\pi^*(s)$, resulting in the maximum expected rewards (or minimum expected cost).

A POMDP is a generalization of an MDP in which the agent only receives partial information about the current state. In this case, the agent reasons according to the current belief **b**, i.e., a probability distribution over states. A POMDP is defined as a 7-tuple $\langle S,A,O,T,Z,R,\gamma \rangle$ controlled stochastic process. While a POMDP transitional model corresponds to the underlying MDP, an observation model is additionally defined by specifying the probability $Z(o,s',a) = P(o \mid s',a)$ of collecting observation $o \in O$ after taking action a. After taking action a and collecting observation o, the belief **b** is updated via Bayes' rule:

$$b(s') \propto P(o \mid s',a) \sum_{s \in S} P(s' \mid s,a) b(s). \tag{1}$$

Since beliefs are dynamically updated, the current belief, **b** is a sufficient statistic of the past taken actions and collected observations. A POMDP policy therefore maps the current belief **b** to the action. As for an MDP, the goal is to identify the optimal policy $\pi^*(\mathbf{b})$ leading to the maximum expected reward.

The decision-making problem corresponding to the optimal inspection and maintenance planning for offshore wind structures can be adequately formulated as a POMDP, in which the agent reasons in a stochastic environment (i.e., probabilistic deterioration model) and under imperfect information (i.e., measurement uncertainty associated with inspection techniques). Once the optimal POMDP policy $\pi^*(\mathbf{b})$ is identified, the decision-maker (e.g., operator, designer, etc) selects inspection and/or maintenance actions according to the current belief state. As opposed to static decision rules, e.g., calendar- or condition-based maintenance approaches, POMDP policies are inherently adaptive since beliefs are dynamically updated, thus resulting in substantial cost benefits.

2.1 Solving POMDPs

The exact solution of a POMDP demands the identification of optimal actions for each belief state, which as mentioned before, is a continuous probability distribution over states, thus rendering the problem computationally challenging. Whereas value iteration algorithms or grid-based interpolation techniques might work well for solving very low-dimensional state space POMDPs, their application to higher dimensional state space POMDPs remains limited, also due to computational tractability problems. However, the recently developed point-based solvers, by executing Bellman backups only for a set of reachable belief points, have enabled the solution of medium to high dimensional state space POMDPs [4]. Since the value function is generally piece-wise linear and convex, it can be parametrized through a finite set Γ of α-vectors, each of them associated with an action [2]. At a certain belief state, the optimal action is, therefore, indicated by the α-vector that maximizes the value function. Point-based solvers are usually developed for the solution of infinite horizon settings, yet practical applications normally correspond to finite horizon problems, e.g., the operational lifetime of offshore wind structural components is often considered as 20 or 30 years. In that case, the infinite horizon POMDP can be transformed into a finite horizon POMDP through state augmentation techniques [1, 2].

3 Interpretation of POMDP-based management policies

With the objective of facilitating the interpretation of POMDP-based offshore wind management policies, we conduct hereafter an I&M planning case study for a fatigue-sensitive offshore wind structural component, inspired by [3]. The I&M decision problem is formulated as a POMDP, adequately defining the elements of the POMDP tuple, as follows:

- States: The structural component deterioration states correspond to the discretized fatigue crack size. In this study, the crack size is discretized into 40 deterioration states, with the last one indicating a failure state.
- Actions: Three action-observation combinations are considered, (i) Do-nothing/No-inspection (DN-NI), (ii) Do-nothing/Inspection (DN-I), and (iii) Perfect-repair/No-inspection (PR-NI).
- Observations: Inspections provide binary indications, resulting in either 'crack detection' or 'no crack detection'. If an inspection is not performed, no additional information is collected.
- Transition probabilities: The transitional model associated with a Do-nothing (DN) action is estimated through crack propagation Monte Carlo simulations, where the crack growth is computed according to Paris

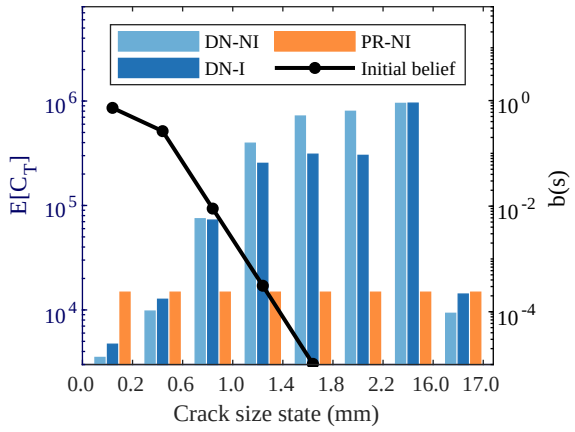
law. If a Perfect-repair (PR) action is undertaken, the structural component deterioration transitions to its initial belief condition state.

- Observation probabilities: The observation model is defined according to the detection probability curve that corresponds to eddy current inspection techniques [5].
- Rewards: At every decision step, the agent collects a reward, $R(\mathbf{b},a)$, which is a weighted sum of the belief probability $b(s)$ and state reward $R(s,a)$. A penalization of one million monetary units is charged at the last state, i.e., failure condition, whereas 1,000 and 10,000 thousand monetary units are assigned as inspection and repair costs, respectively.

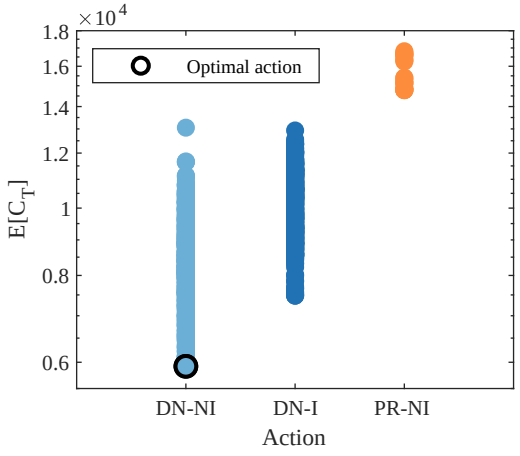
In this case study, the structural component lifetime is defined as 20 years and the corresponding finite horizon POMDP is computed via SARSOP point-based solver [6]. The resulting optimal policies are parametrized by a set of α-vectors, and as mentioned before, each α-vector is associated with a specific action. At each decision point, the decision-maker selects the α-vector (and corresponding action) that maximizes the value function $V^*(\mathbf{b})$ (minimizes the total expected cost):

$$V^*(\mathbf{b}) = \max_{\alpha\in\Gamma} \sum_{s\in S} b(s)\alpha(s). \tag{2}$$

The expected total cost associated with each α-vector can be simply computed as the weighted sum of the expected total cost corresponding to a specific deterioration state $\alpha(s)$ and the probability of being in that state $b(s)$. Figure 1a illustrates the expected total cost resulting from three α-vectors, indicating both the corresponding deterioration state values along with the representation of the initial belief $\mathbf{b}_0$. The key observation is that the actions recommended in POMDP-based policies are selected according to the current belief state $\mathbf{b}$, which is dynamically updated after each taken action and collected observation, as mentioned in Section 2. The expected costs associated with all α-vectors available at the initial decision step (i.e., $\mathbf{b}_0$) are additionally represented in Figure 1b. Logically, the optimal decision at this point is DN-NI, and its corresponding value function indicates the total expected cost $\mathbb{E}[C_T]$ for the considered 20-year decision horizon.



(a) Initial belief (black line) and state values of three α-vectors (colored bars).

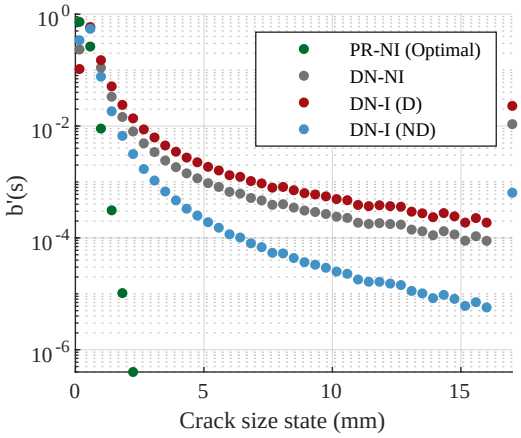


(b) Expected total cost associated with each α-vector (and corresponding action).

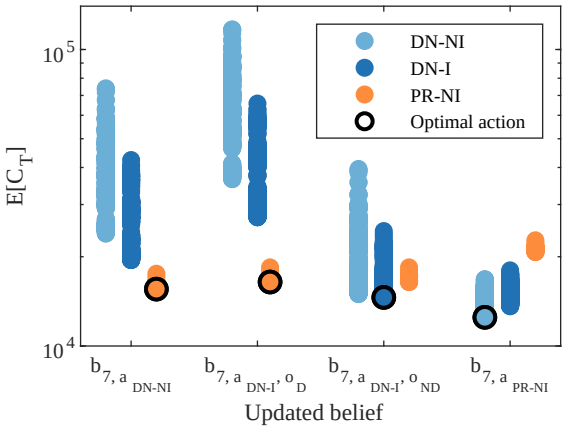
Figure 1: Initial probability distribution over deterioration states (i.e., initial belief, $\mathbf{b}_0$) and expected total cost resulting from each α-vector at the initial decision step.

3.1 What if the optimal policy is not strictly followed?

In this study, we investigate the effect of selecting an alternative action rather than the optimal one suggested in the POMDP policy. We consider that the optimal POMDP policy is followed up to year 7, and at that point, the decision-maker is evaluating the potential economic implications of avoiding a perfect repair maintenance intervention, which is the action suggested in the optimal POMDP policy, as showcased in Figure 2b. Previously, two crack detection inspection outcomes were reported at years 6 and 7, thus indicating a high structural failure risk, which could be effectively mitigated by conducting a repair action (Figure 3a). In that case, the structural condition



(a) Updated beliefs for all action-observation combinations.



(b) Total expected cost for all action-observation combinations.

Figure 2: Updated beliefs and corresponding total expected cost for all action-observation combinations at year 8.

will be restored, and the updated belief will transition to its initial deterioration condition, $\mathbf{b}_0$, as illustrated in Figure 2a with green markers. If the decision-maker opts, however, for an alternative action at year 8, the expected total cost and the regret, i.e. the extra cost associated with potentially suboptimal actions, can be straightforwardly computed through a Bellman backup operation, as:

$$V(\mathbf{b}_7) = \sum_{s \in S} b_7(s) R(s,a) + \gamma V(\mathbf{b}'_7), \tag{3}$$

where $\mathbf{b}$ and $\mathbf{b}'$ correspond to the current and updated beliefs, respectively, and $R(s,a)$ stands for the reward associated with the action taken. Specifically, the potential alternative actions at this decision point are:

- Do-nothing/No-inspection (DN-NI), in which the fatigue deterioration will naturally progress according to the defined transition model, as illustrated with grey markers in Figure 2a.
- Do-nothing/Inspection (DN-I), which can result in either a crack detection or no crack detection outcome. The corresponding updated beliefs are plotted in Figure 2a with red and blue markers, respectively. Since two inspection outcomes can be collected, in this case, the expected total cost estimated can be computed as:

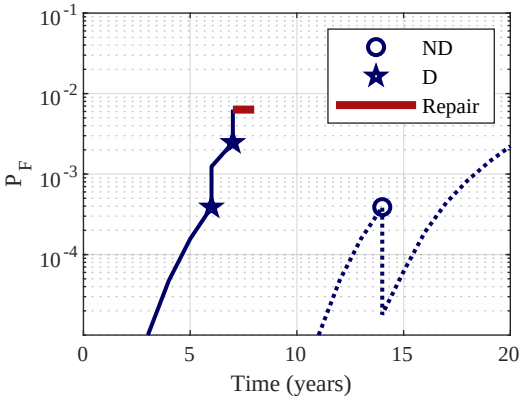
$$V(\mathbf{b}_7) = \sum_{s \in S} b_7(s) R(s, a_{DN-I}) + \gamma \left[\sum_{o \in O} p(o \mid \mathbf{b'}_{7,a_{DN-I}}) \cdot V(\mathbf{b}'_{7,a_{DN-I},o}) \right], \tag{4}$$

  where $p(o \mid \mathbf{b}')$ represents the probability associated with each inspection outcome.

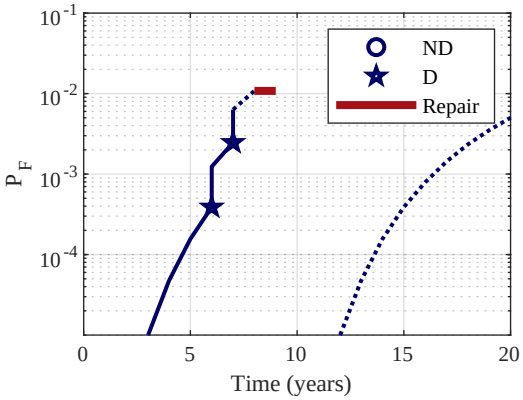
Gathering all action-observation combinations, Figure 2b illustrates the expected cost associated with each action. The suggested action and expected total cost corresponding to each updated belief, $\mathbf{b}'$, can be directly computed through the α-vectors included in the original POMDP policy, as indicated in Equation (2). For instance, if the decision-maker follows the optimal policy and opts for a perfect repair action at year 8, the suggested subsequent optimal action is DN-NI (Figure 3a). Instead, if the decision-maker selects a DN-NI action at year 8, the logical suggested action is an immediate repair action the following year. Note that in the reported results, the total expected cost, i.e., $V(\mathbf{b}')$, is computed from the original POMDP policy. In order to exactly evaluate the economic implication of selecting suboptimal actions, the formulated POMDP can be solved again, considering $\mathbf{b}'$ as the initial belief in a reduced finite decision horizon, which corresponds, in this particular example, to twelve time steps. However, only minor differences in the estimation of the expected total cost between the two aforementioned approaches are observed in this study.

Further examining all alternative action-observation combinations available at year 8, Figure 3 showcases typical resulting policy realizations. As one could expect, a perfect repair is suggested after a DN-NI action is selected at year 8 (Figure 3b), then the structural component condition is restored, and no additional future

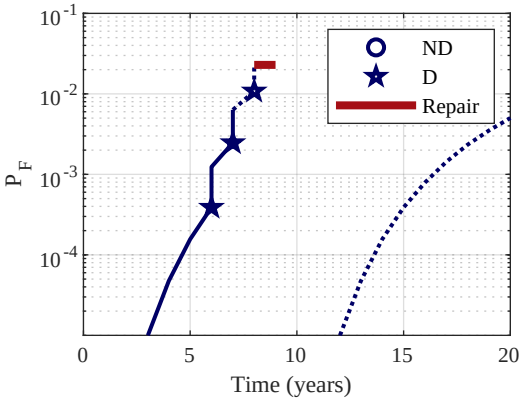
interventions are usually needed. If a DN-I action is taken at year 8, the POMDP policy suggests a subsequent repair action after a crack detection inspection outcome is observed (Figure 3c), whereas if the inspection results in a no detection outcome, a repair is not planned, and instead, the policy realization shows a series of inspections for the remainder of the horizon (Figure 3d).



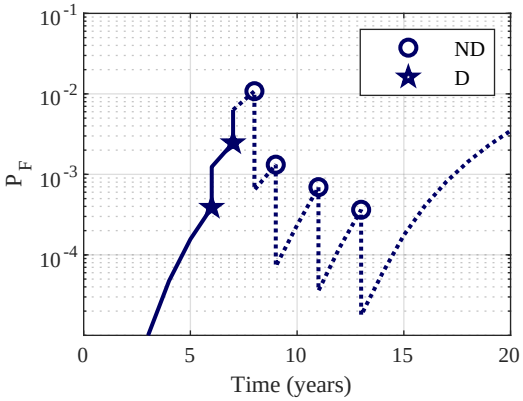
(a) Policy realization for a_{PR-NI} (following the original optimal POMDP policy).



(b) Policy realization for a_{DN-NI}. A repair action is immediately suggested the next year.



(c) Policy realization for a_{DN-I}, o_D. A repair action is immediately suggested the next year.



(d) Policy realization for a_{DN-I}, o_{ND}. A repair action is not subsequently suggested.

Figure 3: Representation of typical policy realizations for all action-observation combinations available at year 8.

In summary, Table 1 lists the expected total cost associated with all available actions at year 8 and their corresponding regret $\mathbb{E}[C_P]$. It can be observed that, in this study, the most suboptimal choice is a DN-NI action, as it results in a yet higher failure risk after year 8, while a repair still needs to be allocated the following year. Interestingly, a DN-I action is less suboptimal, in this case, since subsequent no detection inspection outcomes can still be observed, thus slightly reducing the need of a perfect repair action.

Action at year 8	$\mathbb{E}[C_T]$ (monetary units)	$\mathbb{E}[C_P](\%)$
PR-NI (Optimal)	12,493	-
DN-NI	15,552	24.5
DN-I $\begin{cases} p(o_{ND} \mid \mathbf{b}'_{7,a_{DN-I}}) = 0.5437 \\ p(o_D \mid \mathbf{b}'_{7,a_{DN-I}}) = 0.4563 \end{cases}$	15,428	23.5

Table 1: Regret incurred when selecting alternative actions other than the one suggested in the optimal original POMDP policy.

4 Conclusion

In an offshore wind inspection and maintenance (I&M) planning context, we describe the fundamentals of Partially Observable Markov Decision Processes (POMDPs) -based policies and showcase their inherent adaptive and flexible properties. Through a typical offshore wind I&M planning case study, we also demonstrate that decision-makers following POMDP-based strategies can efficiently and swiftly quantify the effect of selecting alternative actions rather than those suggested in the optimal POMDP policy. Based on the reported benefits offered by POMDP-based policies in terms of optimality [1, 7], adaptability [2, 8], and flexibility [3], along with the interpretability aspects introduced in this work, we encourage the adoption of POMDP-based I&M planning methods in the offshore wind industry.

Acknowledgements

This research is funded by the Belgian Energy Transition Fund (FPS Economy) through PhairywinD and MaxWind projects.

References

[1] K. G. Papakonstantinou and M. Shinozuka. Planning structural inspection and maintenance policies via dynamic programming and Markov processes. Part I: Theory. *Reliability Engineering & System Safety*, 130:202–213, 2014.

[2] P. G. Morato, K. G. Papakonstantinou, C. P. Andriotis, J. S. Nielsen, and P. Rigo. Optimal inspection and maintenance planning for deteriorating structural components through dynamic Bayesian networks and Markov decision processes. *Structural Safety*, 94:102140, 2022.

[3] N. Hlaing, P. G. Morato, J. S. Nielsen, P. Amirafshari, A. Kolios, and P. Rigo. Inspection and maintenance planning for offshore wind structural components: integrating fatigue failure criteria with Bayesian networks and Markov decision processes. *Structure and Infrastructure Engineering*, 18(7):983–1001, 2022.

[4] K. G. Papakonstantinou, C. P. Andriotis, and M. Shinozuka. POMDP and MOMDP solutions for structural life-cycle cost minimization under partial and mixed observability. *Structure and Infrastructure Engineering*, 14(7):869–882, 2018.

[5] DNV. DNV-RP-C210 Probabilistic methods for planning of inspection for fatigue cracks in offshore structures. Recommended practice, Veritasveien 1, 1363 Høvik, Norway, 2019.

[6] H. Kurniawati, D. Hsu, and W. S. Lee. SARSOP: Efficient point-Based POMDP planning by approximating optimally reachable belief spaces. In *Proceedings of Robotics: Science and Systems*, Switzerland, 2008.

[7] K. G. Papakonstantinou and M. Shinozuka. Planning structural inspection and maintenance policies via dynamic programming and Markov processes. Part II: POMDP implementation. *Reliability Engineering & System Safety*, 130:214–224, 2014.

[8] P. G. Morato, C. P. Andriotis, K. G. Papakonstantinou, and P. Rigo. Inference and dynamic decision-making for deteriorating systems with probabilistic dependencies through Bayesian networks and deep reinforcement learning. *arXiv preprint arXiv:2209.01092*, 2022.

18th EAWE PhD Seminar on Wind Energy
2 – 4 November 2022
Bruges, Belgium

Long-term damage effect of low-frequency loads of offshore wind turbines using SHM data

Negin Sadeghi[a], Pietro D'Antuono[a], Koen Robbelein[a], Nymfa Noppe[a], Wout Weijtjens[a], and Christof Devriendt[a]

[a] Offshore Wind Infrastructure-lab (OWI-lab) / Vrije Universiteit Brussel (VUB), Belgium

E-mail: Negin.Sadeghi@vub.be

Keywords: low-frequency fatigue dynamics (LFFD), fore-aft bending moments, strain measurements, Rainflow cycle counting, damage ratio

1 Introduction and objectives

Dynamic loads of offshore wind turbines (OWTs) contain cycles of diverse ranges, and the hysteresis of some cycles is within others. Rain flow is the most famous cycle-counting algorithm that provides the cycles' number and amplitude [1][2]. Eventually, the resulting cycle-count matrix from the Rain flow cycle counting will be used in the lifetime analysis, which shall be performed through a damage accumulation model. For example, DNV's suggestion is to use the Palmgren-Miner [3][4] linear damage accumulation rule (PM rule) [5].

Our study focuses on a specific long-term fatigue lifetime assessment method through real data stored in 10-min subsets. Performing cycle counting and damage analysis based on these short windows neglects the highly damaging effect of gradually varying loads, known as Low-Frequency Fatigue Dynamics (LFFD). The lifetime predictions with or without recovering the LFFD impact can be significantly different because the incomplete large cycles that span more than 10 min may not be considered as a whole but in smaller half cycles within 10 min. In previous work the authors implemented a practical LFFD recovery method based on the 10-min cycle count subsets introduced by Amzallag et al. [6] and Marsh et al. [7]. They have introduced an approach that significantly reduces calculation time without losing accuracy in the final spectrum histogram, as it can retrieve all the hysteresis cycles caused by LFFD without needing the signal concatenation. Using the rain flow counting method for each 10-min signal subset, we store a histogram with the cycles and half-cycles (residuals), their ranges, and the sequence of half cycles' start and end points. These time-ordered points are used to retrieve the LFFD [8]. Mainly, this contribution investigates how much data is necessary for the effect of LFFD to stabilize and if different periods/seasons of the year influence the result. This is done by calculating the damage ratio with and without considering the LFFD.

In the approach applied to include the LFFD effect, we need the time-ordered sequence of residuals to calculate the damage. In cases where only the short-term damages are calculated from 10-min cycle counted subsets and further analysis like binning is based on these damages, we cannot follow the same method to consider the long-term LFFD effect. So, in such cases, we miss the opportunity to resolve the residuals and consider the LFFD effect, because we only have the 10-min damages, and not the chronological order of the residuals. Therefore, we study the possibility of another method by applying a fixed LFFD factor to the damage/DEL (calculated from the primary cycle count histograms without considering the LFFD effect) to include the impact of LFFD. Finally, this impact is studied for different damage sources, like Fore-Aft and Side-to-Side (FA/SS) bending moments and individual strain sensors.

2 Measurement campaign and methodology

Three years of structural health monitoring (SHM) was available to OWI-lab including the strain and SCADA data on an offshore wind turbine installed on a monopile located in the Belgian North Sea. The turbine has six strain gauges (of which five provide reliable measurements) at the tower-transition piece interface.
The FA bending moments were used to display the study of the effect of LFFD, and finally, the SS bending moments and the signals of five individual strain gauges were also used to compare the LFFD factors from various damage sources.
We use the Palmgren-Miner (PM) rule for the damage calculation, as shown in Eq 1.

$$D = \sum_{i=1}^{k} \frac{n_i}{N_i} = \sum_{i=1}^{k} \frac{n_i}{\bar{a}\,(\Delta\sigma)_i^{-m}} = (\bar{a})^{-1} \sum_{i=1}^{k} n_i \cdot (\Delta\sigma)_i^{\,m} \quad (1)$$

Equivalently to Marsh et al. [7], we express the damage ratio before to after applying LFFD through Eq 2.

$$D_{RATIO} = \frac{D_{Before\ LFFD}}{D_{After\ LFFD}} = \frac{\sum_{i=1}^{K_{Before\ LFFD}} n_i \cdot (\Delta\sigma)_i^{\,m}}{\sum_{j=1}^{K_{After\ LFFD}} n_j \cdot (\Delta\sigma)_j^{\,m}} \quad (2)$$

Where $K_{Before\ LFFD}$ and $K_{After\ LFFD}$ are the number of load blocks composing the fatigue histogram (before and after LFFD recovery, respectively.
By taking the damage ratio, the term $(\bar{a})^{-1}$ cancels out, and the ratio is only affected by the Wöhler exponent from the SN curve. We used three SN curves in our analyses, with Wöhler exponents of m = 3, m = 4, and m = 5.

3 Results and Discussion

We have calculated the damage ratio for each SN curve as a cumulative merge of extended fatigue histograms. The results of our analysis are plotted in Figure 1 together with Marsh et al.'s, which we use as a reference.

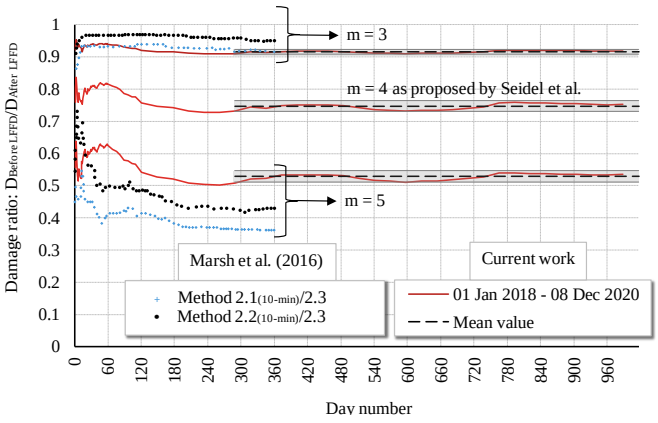


Figure 1. Results from Marsh et al.[7] – markers – versus Three-year long accumulated damage ratios – lines –. Marsh et al. analyzed the one-year accumulated damage ratios from corresponding stress data for a multi-megawatt OWT support structure. The black dashed line represents our analyses' converged average damage ratio ± two standard deviations after 300 days.

First, we observe some apparent similarities with the results obtained by [7]. As expected, they also received a lower ratio for m = 5 than for m = 3. As the LFFD contains cycles with very high stress ranges, the difference between before and after LFFD will be higher for m=5. Moreover, both Marsh et al.'s and our analyses present some significant variations in results for short durations, while the value of the ratio stabilizes after a reasonable duration. Nevertheless, the time-to-convergence does differ: Marsh et al.'s damage ratios converge after ca. 180 days, while the damage ratios from our case study stabilize after ca. 300 days. After convergence, we still see some variation, but it is contained within two standard deviations. This range is shown by the grey area and the average by the black dashed line in Figure 1. In the case of m=5, our result shows higher fixed ratios compared to Marsh et al. This might be because of the difference between onshore (Marsh et al.) and offshore (ours) wind turbines.
To study the seasonal impact as a refinement to the above, we have defined a series of 2-year-long time windows over the entire 3-year data with a step of three months in Figure 2. In the first months of every time window, damage ratios suffer profound influence from the starting season. During summer, the ratios are lower; thus, the LFFD effect is higher. This phenomenon occurs because summer fatigue cycles are, on average, of low amplitude and frequency. Therefore, storms can generate massive, slowly varying cycles, and the high-range residuals will have a higher impact on the damage ratio. In winter, the behavior is the opposite. Eventually, for a

long-enough observation time (> 300 days/~three seasons), all oscillations stabilize around the average damage ratio, and seasonality becomes negligible. Figure 2(b), having the day number on the x-axis instead of the actual date of the considered time window, demonstrates said observation after 300 days, all lines with the same m-value stabilize around the same damage ratio ± two standard deviations.

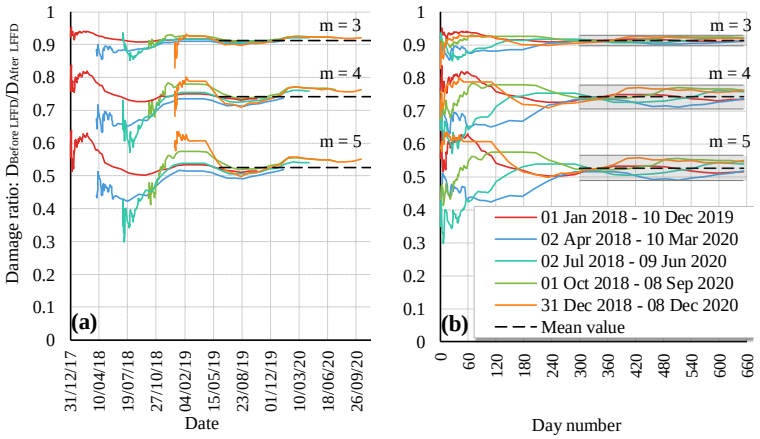


Figure 2. Two-year accumulated damage ratios over a three-year time window. Every time window slides by one season (3 months). In (a), the time windows are plotted in chronological order. In (b), the time windows are presented as if they all started at day zero. The black dashed line is the average converged damage ratio ± two standard deviations after 300 days.

After verifying that the damage ratio due to LFFD recovery converges to a constant value, we want to investigate whether scaling the damage before LFFD recovery by the average damage ratio (average of damage ratios after 300 days) instead of using LFFD recovery itself produces acceptable results (Figure 3). Figure 3 shows a close to perfect match between both methods of calculating the final damage. As mentioned, this factor is practical in cases where we do not deal directly with the cycle count histograms to resolve the LFFD residuals.

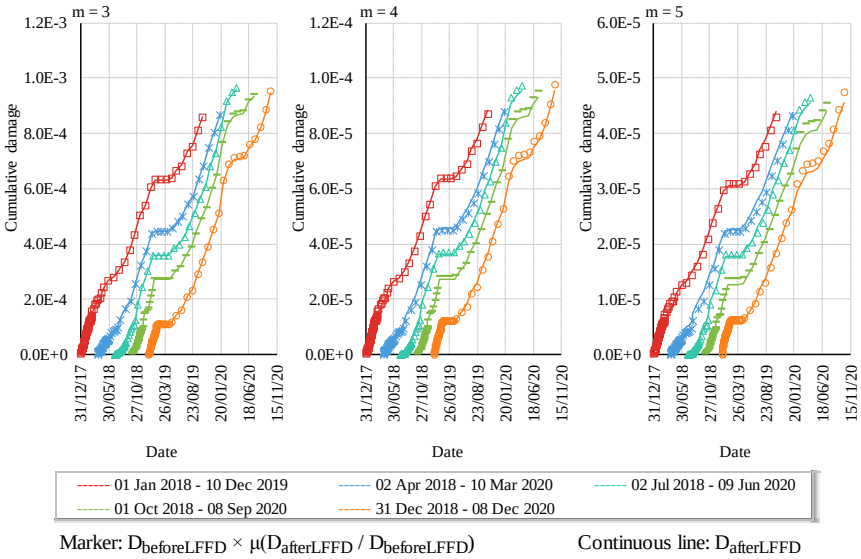


Figure 3. Accumulated damage calculated using LFFD recovery – continuous lines – versus accumulated damage without LFFD recovery scaled by the average damage ratio (μ) (average of damage ratios after 300 days) – markers –.

All the above results were obtained based on the damages calculated for FA. As a final analysis, we examined the effect of LFFD also on the SS bending moment. Moreover, the change of heading on the LFFD is investigated by performing fatigue analyses on fixed directions (the sensors' headings) instead of using FA/SS directions only. As the general trend of convergence was almost similar for all of them [8], we compared the stabilized damage ratios (after 300 days of observation) in Figure 4, where we show the scatter of the cumulative damage ratios from each damage source. We compared the boxplots of three linear SN curves with the slope of m=3, 4, and 5. The scatter of all the factors from the five strain sensors is also shown in Figure 4.

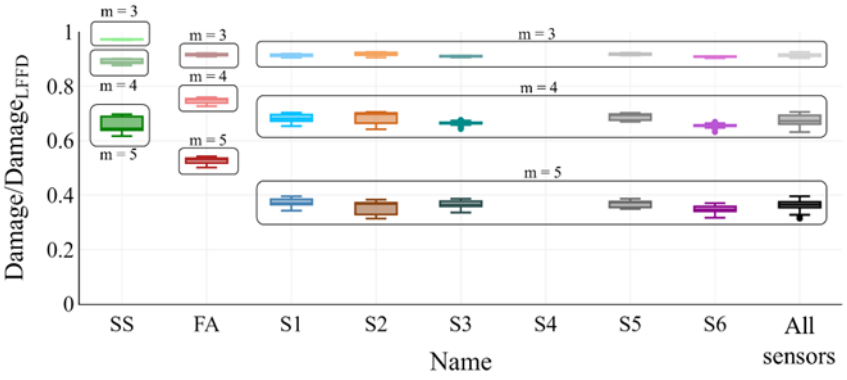


Figure 4. Comparison of fixed damage ratios (cumulative damage ratios from day 300 to day 1000) from FA/SS/different headings (sensors)) for SN curves with m = 3, 4, and 5. The boxplots for all the factors from the five strain sensors are shown in the right-most column.

Given this long-term damage assessment, Figure 4 shows that the long-term damage factor in FA is higher – thus less LFFD – compared to the factor derived from the individual strain gauges. We should notice that the gradual change in the wind direction might also cause LFFD. For example, if we have the wind with fixed speed but with a gradual shift in the direction, FA does not change because it turns with the change in the yaw angle, while a specific heading like a sensor, feels this gradual change and therefore, it will have more residuals than FA. This fact can explain why the ratios of sensors are less than FA.

4 Conclusions and future works

In this contribution, we have implemented an approach for long-term fatigue calculation based on [7]. The method can recover the effects of low-frequency fatigue dynamics by avoiding the time-consuming concatenation and processing of a high quantity of subsets of data. We validated the approach through three years of measured data and compared different time windows in terms of total duration and season of the year, as well as the possibility that the damage ratio eventually (after nine months) converges to a fixed value. In addition, considering the long-term fatigue damage with LFFD, we investigated the feasibility of applying a fixed factor (depending on the properties of the signal and on the SN curve) to the calculated damage by concatenating the histograms without taking into account the LFFD effect, instead of the primary method which corrects the residuals from the cycle count histograms. Finally, we compared the LFFD damage ratios calculated from either FA/SS bending moments or each sensor's strain signals. The results showed that the sensors' factors are more conservative than FA/SS; therefore, the authors recommend the average (- 2 standard deviation) of sensors' factors to be applied to the final accumulated damage without LFFD to consider the full LFFD effect. The same study will be performed on other wind farms and turbines within a wind farm to see if the factor and the needed duration to achieve the factor are the same.

Acknowledgments

This research is conducted within the project MAXWind, funded by the Belgian Energy Transition Fund (ETF).

References

[1] C. Amzallag, J. P. Gerey, J. L. Robert, and J. Bahuaud, 'Standardization of the rainflow counting method for fatigue analysis', International Journal of Fatigue, vol. 16, no. 4, pp. 287–293, Jun. 1994, doi: 10.1016/0142-1123(94)90343-3.
[2] ASTM International, Standard Practices for Cycle Counting in Fatigue Analysis, vol. 85. 2017. Accessed: Dec. 27, 2021.
[3] A. G. Palmgren, 'Die Lebensdauer von Kugellagern (Life Length of Roller Bearings. In German)', Zeitschrift des Vereines Deutscher Ingenieure (VDI Zeitschrift), ISSN, pp. 0341–7258, 1924.
[4] M. A. Miner, 'Cumulative Damage in Fatigue', . Journal of Applied Mechanics, vol. 3, pp. 159–164, 1945.
[5] 'DNVGL-RP-C203: Fatigue design of offshore steel structures', Recommended Practice DNV GL RP C203.

[6] C. Amzallag, J. P. Gerey, J. L. Robert, and J. Bahuaud, 'Standardization of the rainflow counting method for fatigue analysis', International Journal of Fatigue, vol. 16, no. 4, pp. 287–293, Jun. 1994, doi: 10.1016/0142-1123(94)90343-3.
[7] G. Marsh et al., 'Review and application of Rainflow residue processing techniques for accurate fatigue damage estimation', International Journal of Fatigue, vol. 82, pp. 757–765, Jan. 2016, doi: 10.1016/j.ijfatigue.2015.10.007.
[8] Sadeghi, N., Robbelein, K., D'Antuono, P., Noppe, N., Weijtjens, W., & Devriendt, C. (2022). Fatigue damage calculation of offshore wind 'turbines' long-term data considering the low-frequency fatigue dynamics. Journal of Physics: Conference Series, 2265 (3), 032063.

18th EAWE PhD Seminar on Wind Energy
2 – 4 November 2022
Bruges, Belgium

Model Updating for damage localisation and quantification using a deterministic optimiser and a damage distribution function

Niklas Dierksen[a], Clemens Hübler[a], Raimund Rolfes[a]

[a] Leibniz University Hannover, Institute of Structural Analysis, ForWind, Appelstr. 9a, D-30167 Hannover, Germany

E-mail: n.dierksen@isd.uni-hannover.de

- *Keywords*: model update, structural health monitoring, damage localization, optimisation, reliability, monitoring and sensing technology

1 Introduction

To reduce the maintenance costs of offshore wind turbines, precise and reliable structural health monitoring (SHM) methods are needed. This work presents a model updating method that can be used to detect, locate and quantify damage to mechanical structures. Apart from damage detection, model updating can improve the accuracy of a simulation model and realise the adaptation to long-term changes of the structure or the constraints. Saying this, model updating is suitable to realise the adaptation of a digital twin i.e. a digital copy of a real system, which is the main goal of the collaborative research centre 1463.

2 Method

Procedure:
The basic idea behind the method is that a structural change, for example a damage, is to be detected by a change in the modal quantities. [1] In this case, the first 20 mode shapes are used to identify different kinds of structural changes. This method was first presented by Bruns et al [2] and is visualised in Figure 1.

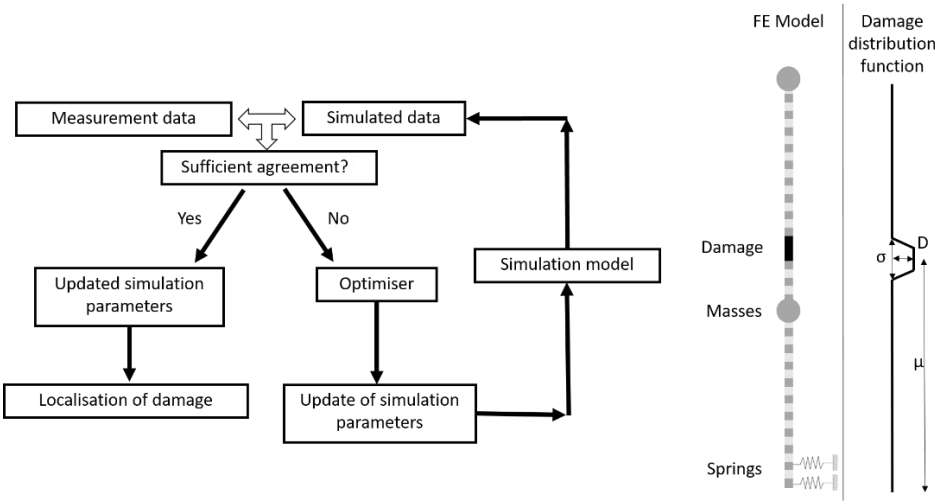


Figure 1: left, flow chart of the method; right, visualisation of the FE model and the damage distribution function

Measurement results and simulation results are compared with each other. In the case of an undamaged structure, the two results agree except for small differences resulting from model uncertainty. If the structure is damaged, the measurement result changes. Now an optimiser creates samples, which modify the stiffness of the simulation model. Here the global pattern search algorithm is used [3]. The results of the simulation are compared with the measurement data. As long as the measured data differ from the simulation results, new samples are generated. If the measurement results and the simulation results almost agree after several calculations, the damage or the change in the structure can be concluded from the optimised simulation parameters. There will always be a small difference between the results due to model uncertainty.
The damage is expressed by a reduction in the stiffness of individual elements. To avoid having to adjust each element individually, a damage distribution function with only three parameters is used that describes the stiffness reduction, which can be seen in Figure 1. μ defines the position of the damage, σ the width of the damage and D the intensity of the damage. Hence, the final, optimised value of μ describes the location of the damage.
In this work simulated "measurement" data is used. For that purpose, the stiffness of the initial simulation model is reduced using the same damage distribution function. The resulting mode shape vectors are treated like measurement data here.

Model:
The model used is shown in Figure 1. It is a 1205 mm long steel bar clamped vertically in the floor. The bar consists of beam elements with a constant rectangular cross-section and 59 elements. At the top and in the middle of the structure there are point masses and the last two nodes are fixed by 3 linear springs each. This structure is intended to be a very simplified representation of an offshore wind turbine substructure. The springs represent the clamping in the seabed and the point masses represent the marine growth and the mass of the RNA (rotor-nacelle-assembly). The model is calculated with the finite element, multi-body system software DeSiO (Design and Simulation Framework for Offshore Support Structures) [4].

3 Results

In the first example, the structure was damaged at one position in the upper part of the bar. The stiffness was reduced by 3% on a width of 50 mm and the damage was centred around the 750 mm position. Figure 2 shows the results of the optimiser. In the three subplots, the convergence of the individual values for μ, σ and D is shown. It can be clearly seen that the optimiser very quickly finds the correct parameters and converges after about 1500 model evaluations.

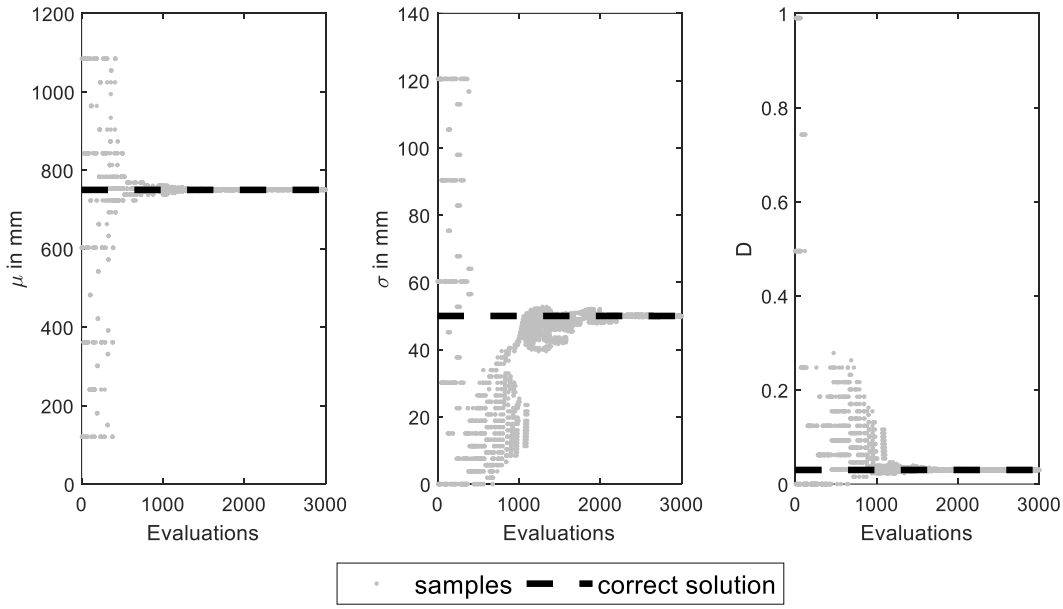


Figure 2: Convergence of optimisation results

In the second example measurement uncertainty is taken into as well. The first example is reused. Each value of the mode shape vector of the simulated measurement data, is multiplied with a random value between 0.99 and 1.01. This leads to a measurement uncertainty of ±1%. In the result in Figure 3 it can be seen that the optimiser also converges similarly fast, but it no longer correctly determines the damage. Although the position of the damage is still determined with sufficient precision, the intensity and width are no longer determined correctly due to the uncertain measurement data. Since the measurement uncertainty is calculated by random variables, results vary for various optimisation runs. A representative run is shown here.

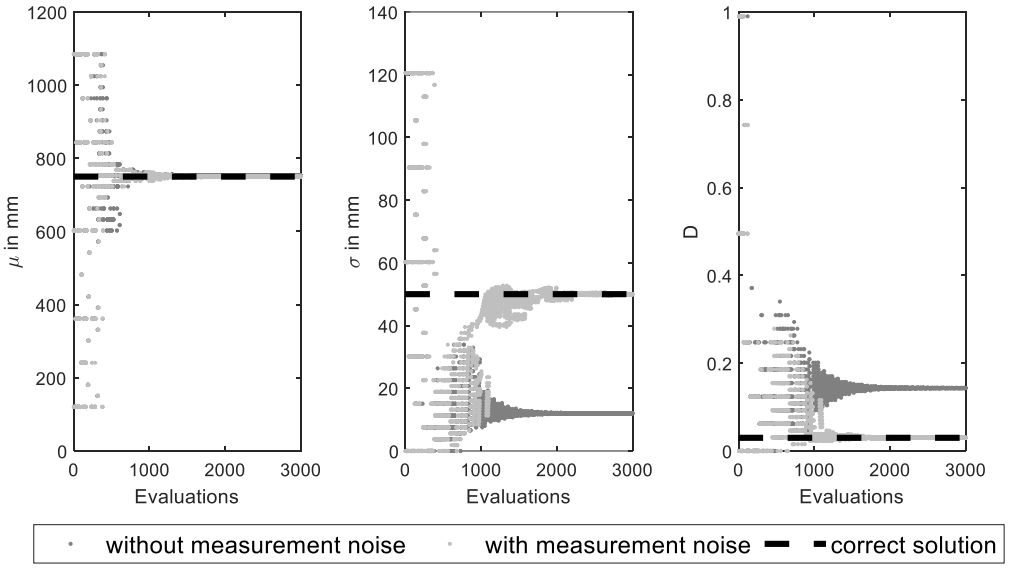


Figure 3: Convergence of optimisation results taking into account measurement uncertainty

4 Future work

As the determination of damage was less precise when taking measurement uncertainty into account, further work will be done on methods that explicitly take uncertainties into account. In addition, this was only an example of simulated damage and simulated measurement uncertainty. For this reason, experiments on a steel beam with a reversible damage mechanism are planned.

Acknowledgements

This work was Funded by the Deutsche Forschungsgemeinschaft (DFG, German Research Foundation) - SFB1463 – 434502799.

References

[1] S.W. Doebling, C.R. Farrar, M.B. Prime. A SUMMARY REVIEW OF VIBRATION-BASED DAMAGE IDENTIFICATION METHODS. *The Shock and Vibration Digest*, Vol. 30. 91-105, 1998

[2] M. Bruns, B. Hofmeister, D. Pache, R. Rolfes. Finite element model updating of a wind turbine blade—a comparative study. *EngOpt 2018 proceedings of the 6th international conference on engineering optimization*. 569–80. 2019.

[3] B. Hofmeister, M. Bruns, R. Rolfes. Finite element model updating using deterministic optimisation: A global pattern search approach. *Engineering Structures* 195. 373-381. 2019

[4] C. Gebhardt. Robust computational procedures for the nonlinear dynamic analysis of beam and shell structures, *habilitation dissertation*. 2019

18th EAWE PhD Seminar on Wind Energy
2-4 November 2022
Bruges, Belgium

Monitoring blade leading edge erosion with Graph Neural Networks and aerodynamic data

Gregory Duthé[a], **Imad Abdallah**[a], **Sarah Barber**[b], and **Eleni Chatzi**[a]

[a]ETH Zürich
[b]Eastern Switzerland University of Applied Sciences

E-mail: duthe@ibk.baug.ethz.ch

Keywords: leading edge erosion, computational fluid dynamics, graph neural networks

1 Introduction

As wind turbine blades are becoming larger and more elastic, it is becoming increasingly important to develop new blade condition monitoring approaches that may support operators in pursuing optimal maintenance strategies. Motivated by current efforts to construct a novel low cost MEMS-based [1] surface pressure and acoustic measurement system as a part of the Aerosense project [1], we aim to design aerodynamics-based data-driven Leading Edge Erosion (LEE) monitoring approaches. LEE is a key topic in the wind energy industry today as it can lead to reductions on the order of 5% of the Annual Energy Production of a MW-scale wind turbine [4]. Typically, LEE monitoring is performed via visual inspection, although recent work has shown that aerodynamic signals could also be of interest [2]. Aeroacoustic methods have the potential to disrupt traditional blade condition monitoring techniques, particularly when the retrieved data are fused with well-established physics-based computational tools, such as Computational Fluid Dynamics (CFD) simulations. We propose to apply a data-driven deep graph-based method [9] for monitoring LEE, utilizing synthetic data emulating an Aerosense system installed on blade undergoing this degradation. This data will be generated via calibrated CFD simulations of an eroded 2D blade cross-section, with the end goal being to generalize to real Aerosense measurements. While CFD modelling of LEE is not a new concept [6], it is not trivial to accurately calibrate computational models to match slowly evolving LEE, a process which may take place over decades. Minor increases in the level of erosion only marginally increase the roughness of the leading edge, which has a small impact on airfoil aerodynamics. Although the impact on 2D aerodynamics may be small, when accumulated over the span of the blade, it can lead to significant power production losses. Thus, being able to monitor and detect minor changes is a net gain for owners/operators of wind farms as it allows for more optimal maintenance intervention schemes. As a means of monitoring LEE from aerodynamic signals, we frame our task as graph node regression problem. Graphs are an attractive form for modeling and representing relational dependence in complex data, such as simultaneous measurements from multiple sensors placed at different locations along the span or cross-section of a blade. Graph Neural Networks (GNNs) are flexible deep learning methods unconstrained by a tabular format, which can therefore be trained on graphs with different number of nodes and edges. Indeed, GNNs are well suited for mesh-based physics problems [7], allowing us to avoid issues stemming from array-based representations (aliasing, pixelation, etc.). By training a GNN to use the aerodynamic signals emanating from an Aerosense node, we aim to provide operators with a disruptive blade monitoring solution unlike any existing method.

2 Objectives

The three main objectives of this work are: (1) develop an accurate CFD simulation pipeline with OpenFOAM [10] that is representative of actual leading edge erosion, (2) use the pipeline to produce a synthetic training dataset of pressure distributions of airfoils affected by various LEE scenarios, which is then parsed into graph structure, and (3) exploit the generated graphs to train a GNN model for LEE severity node classification. We

[1]Micro-electromechanical systems

aim to deliver a prediction tool which can accurately model incremental changes in severity; this requires an appropriately calibrated CFD model and pertinent boundary conditions which incorporate sufficient amounts of uncertainty.

3 Methodology

We model the flow around airfoils with eroded leading edges [6] using OpenFOAM, a 2D Reynolds-Averaged Navier–Stokes (RANS) turbulent CFD solver. In particular, the Langtry-Menter k-omega Shear Stress Transport [5] RANS model with modified rough wall functions is utilized, as it better accounts for boundary layer transition effects [6]. We choose to simulate the increase in leading edge roughness through the use of rough wall functions applied to specific patches of the airfoil and not through geometrical modifications, as it avoids mesh-dependency issues. The simulation setup is calibrated so that aerodynamic polars of degraded airfoils match those gathered in [8], under different stages of erosion. Once calibration is complete, a dataset of CFD simulations is generated under diverse random, yet physical, inflow conditions mimicking the operational conditions of a 5 MW turbine. The pressure distribution of each simulated airfoil is then parsed into graph format, with nodes constructed from the surface airfoil cells and edges formed between adjacent cells. Pressure values are gathered at each node, while edge features are constructed based on geometrical properties. The GNN used to classify erosion severity at each node has an Encoder-Processor-Decoder structure, similar to [7]. The Encoder projects the input edge and node features into a higher-dimensional latent space of size L. The Processor network then updates the encoded graph by performing N successive Message-Passing [3] steps, and finally the updated graph is used by the Decoder to output the predicted erosion status at each node. This process is summarized in Figure 1.

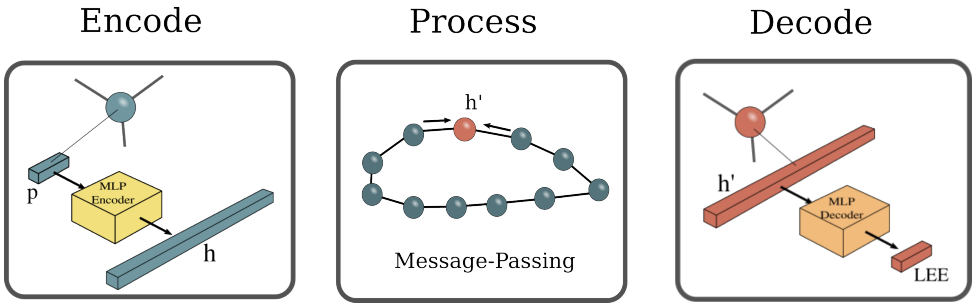


Figure 1: Workflow of the graph learning LEE monitoring method. In the first step, the input feature vector of each node is encoded into a latent space, yielding a latent vector h. The latent vectors are then updated through N Messaging-Passing layers, resulting in updated latent vectors h'. Finally, each latent vector is decoded back into physical space in order to assess the degradation severity at each node.

4 Results

Figure 2 displays the results of preliminary CFD calibrations, where numerical values of the roughness height used in the wall functions were selected in order to match with aerodynamic polars of the DU-96-W-180 airfoil, reported for different stages of LEE in [8]. This figure also highlights the challenge in differentiating between the various LEE severities at low angles of attack, based on integrated pressure quantities. This justifies our decision to use simultaneous surface pressure measurements at multiple locations along the airfoil surface in our diagnostics algorithm, and not integrated pressure values.

5 Conclusions

We propose an approach that adopts GNN to predict the state of the surface condition of the leading edge of airfoils, based on CFD training data. The CFD simulation setup is first calibrated in order to model degradation of the leading edge of wind turbine blades in a realistic manner. Then, an Encoder-Processor-Decoder GNN is trained on a dataset of airfoils to detect and classify erosion at each airfoil surface node. The graph-based method will be fully developed and compared against other approaches, such as those based on point clouds. Moreover,

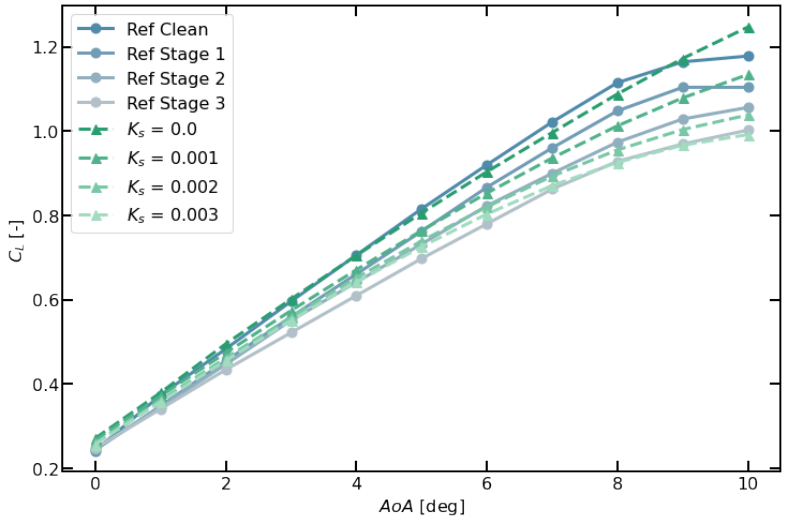


Figure 2: Results of preliminary CFD calibration, used to associate numerical roughness height values with real LEE severities as reported in [8], for the DU-96-W-180 airfoil for Re=1'500'000.

the structure of the network will be tuned for robustness (i.e., resistant to missing, perturbed data and noise) and studies of its limitations will be discussed.

Acknowledgement

This work is funded by the BRIDGE Discovery Programm of the Swiss National Science Foundation and Innosuisse, project number $40B2-0_187087$.

References

[1] S. Barber, J. Deparday, Y. Marykovskiy, E. Chatzi, I. Abdallah, G. Duthé, M. Magno, T. Polonelli, R. Fischer, and H. Müller. Development of a wireless, non-intrusive, mems-based pressure and acoustic measurement system for large-scale operating wind turbine blades. *Wind Energy Science*, 7(4):1383–1398, 2022.

[2] G. Duthé, I. Abdallah, S. Barber, and E. Chatzi. Modeling and monitoring erosion of the leading edge of wind turbine blades. *Energies*, 14(21):7262, 2021.

[3] J. Gilmer, S. S. Schoenholz, P. F. Riley, O. Vinyals, and G. E. Dahl. Neural message passing for quantum chemistry. In *International conference on machine learning*, pages 1263–1272. PMLR, 2017.

[4] C. M. Langel, R. Chow, O. F. Hurley, C. C. P. Van Dam, D. C. Maniaci, R. S. Ehrmann, and E. B. White. Analysis of the impact of leading edge surface degradation on wind turbine performance. In *33rd Wind Energy Symposium*, page 0489, 2015.

[5] R. B. Langtry and F. R. Menter. Correlation-based transition modeling for unstructured parallelized computational fluid dynamics codes. *AIAA journal*, 47(12):2894–2906, 2009.

[6] D. C. Maniaci, E. B. White, B. Wilcox, C. M. Langel, C. Van Dam, and J. A. Paquette. Experimental measurement and cfd model development of thick wind turbine airfoils with leading edge erosion. In *Journal of Physics: Conference Series*, volume 753, page 022013. IOP Publishing, 2016.

[7] T. Pfaff, M. Fortunato, A. Sanchez-Gonzalez, and P. W. Battaglia. Learning mesh-based simulation with graph networks. *arXiv preprint arXiv:2010.03409*, 2020.

[8] A. Sareen, C. A. Sapre, and M. S. Selig. Effects of leading edge erosion on wind turbine blade performance. *Wind Energy*, 17(10):1531–1542, 2014.

[9] F. Scarselli, M. Gori, A. C. Tsoi, M. Hagenbuchner, and G. Monfardini. The graph neural network model. *IEEE transactions on neural networks*, 20(1):61–80, 2008.

[10] H. G. Weller, G. Tabor, H. Jasak, and C. Fureby. A tensorial approach to computational continuum mechanics using object-oriented techniques. *Computers in physics*, 12(6):620–631, 1998.

18th EAWE PhD Seminar on Wind Energy
2-4 November 2022
Bruges, Belgium

Optical corrosion detection techniques for offshore wind turbines.

Thomas De Kerf[a], **Steve Vanlanduit**[a], and **Paul Scheunders**[b]

[a]InViLab, Faculty of Applied Engineering, University of Antwerp, Belgium
[b]Imec-VisionLab, Physics Department, University of Antwerp, Belgium

E-mail: thomas.dekerf@uantwerpen.be

Keywords: Corrosion, Hyperspectral Imaging, Infrared Imaging

Offshore wind turbines are constantly exposed to conditions that can induce corrosion. The salty water, large temperature differences and the breaking of the waves on the structure are the main factors for the development of corrosion. Once the structure's coating is breached, corrosion progresses and can potentially cause dynamic structural problems due to the localised loss of material from the corrosion attack. Frequent inspections are required to detect and locate these corrosion sites. [3, 5]. However, these interventions are costly (special equipment and personnel are needed), dangerous (inspectors must board the turbine and then rappel down), and not objective (depending on the experience and training of the inspector). Therefore, an automated inspection method is highly recommended.

There are several methods to identify corrosion that are described in the literature: FTIR (fourier transfor infrared spectroscopy), XRD (X- Ray Diffraction) , Raman, SEM (Scanning electron microscopy), UT (Ultrasonic Testing) ,... An overview of these methods can be found in Figure 1 or in more detail in [4]. However, the most common methods have several flaws, such as: they are time-consuming, point-based methods, they need to be in direct contact with the surface or are limited to the laboratory. Scanning an entire structure remotely would be very cumbersome. Imaging methods such as camera inspection, thermography or hyperspectral imaging can be a solution to this problem.

Using **RGB** cameras presents the following issues:

- Since corrosion products are very similar in the visual spectrum, detection can only occur if the coating is clearly distinguishable from the actual corrosion products. e.g.: No brown/yellow/red hues may be present, otherwise false positive results will be obtained.
- Due to corrosion run-off (where the corrosion products form streaks on the coating), false positive results occur and it is difficult to locate the actual corrosion site.
- To achieve the highest accuracy, neural networks are often the right choice. The drawback is that these neural networks are very data hungry and the relevant data for offshore corrosion is expensive to obtain.

Hyperspectral imaging is an optical imaging technique that typically measures more than 100 specific wavelengths, as opposed to the three wavelengths (red, green, and blue) in a normal camera. Previous research by the same authors [1, 2] shows that a hyperspectral camera in the shortwave infrared region (900-1700nm) is capable of identifying the various corrosion minerals. In figure 2 the different spectra are displayed.

Infrared imaging uses a thermal infrared camera to measure temperature differences on a given object. These temperature differences can be enhanced by using an external heating source. This technology allows us to examine deeper than just the surface and measure the loss of material due to the corrosion process. However, implementing this technology in a mobile platform is a major challenge. To produce a meaningful temperature difference, a large pulse of energy must be applied to each measurement. And this pulse should remain focused on exactly the same spot so as not to influence the measurement.

In summary, there is no single sensor that meets the following criteria: Time effectiveness, low cost and accuracy. Hyperspectral imaging is time efficient and initial testing has shown it to be accurate in a laboratory setting, but it is not a low cost sensor. It may be beneficial to further explore custom multispectral imaging to lower the cost of the sensor. Accuracy also needs further analysis for in situ processes. As for infrared imaging, the sensor has a lower cost, compared to the HS sensor but the measuring process and processing takes longer, compared to the HSI method.

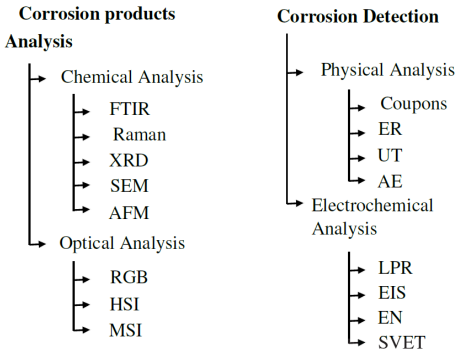


Figure 1: Overview of commonly used corrosion detection methods. Modified from [4]

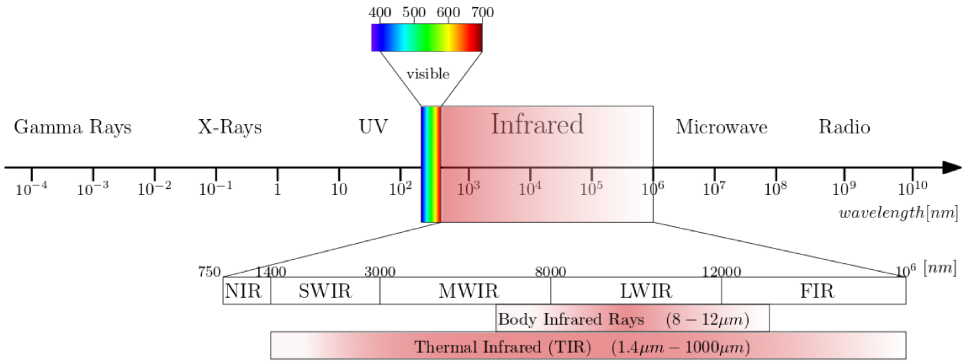


Figure 2: Overview of the electromagnetic spectrum, taken from [6].

References

[1] T. De Kerf, N. Hasheminejad, J. Blom, and S. Vanlanduit. Qualitative comparison of 2d and 3d atmospheric corrosion detection methods. *Materials*, 14(13), 2021.

[2] T. De Kerf, G. Pipintakos, Z. Zahiri, S. Vanlanduit, and P. Scheunders. Identification of corrosion minerals using shortwave infrared hyperspectral imaging. *Sensors*, 22(1), 2022.

[3] P. Hevia-Koch and H. K. Jacobsen. Comparing offshore and onshore wind development considering acceptance costs. *Energy Policy*, 125:9–19, 2019.

[4] M. S. B. Reddy, D. Ponnamma, K. K. Sadasivuni, S. Aich, S. Kailasa, H. Parangusan, M. Ibrahim, S. Eldeib, O. Shehata, M. Ismail, and R. Zarandah. Sensors in advancing the capabilities of corrosion detection: A review. *Sensors and Actuators A: Physical*, 332:113086, 2021.

[5] J.-Y. Soh, M.-W. Lee, S.-K. Kim, and D. H. Kim. Corrosion monitoring for offshore wind farm's substructures by using electrochemical noise sensors. *KEPCO Journal on Electric Power and Energy*, 2(4):615–618, 2016.

[6] J. Verstockt, S. Verspeek, F. Thiessen, W. A. Tjalma, L. Brochez, and G. Steenackers. Skin cancer detection using infrared thermography: Measurement setup, procedure and equipment. *Sensors*, 22(9), 2022.

18th EAWE PhD Seminar on Wind Energy
2-4 November 2022
Bruges, Belgium

System Structural Reliability Modelling for Offshore Wind Welded Connections

Jose Mishael[a], **Felipe Giro**[a], **Pablo G. Morato**[a], and **Philippe Rigo**[a]

[a]ANAST, ArGEnCO, University of Liege, Liege, Belgium

E-mail: jmjoseph@uliege.be

Keywords: System modelling, k-out-of-n systems, Probability of failure, OWT monopile foundations

1 Introduction

Most engineering systems such as jacket structures, ships, etc. can be represented by the combination of many interdependent components. The failure of one of these components can influence the performance of other components which in turn can alter the reliability of the structural system. The reliability of a system depends on the reliability of its components, their number, and their mutual arrangements. A suitable arrangement of components may enhance the reliability estimation of the structural system. Therefore, the representation of a system and the inter-dependencies among its components play a crucial role in the system's structural reliability assessment.

The offshore wind turbine (OWT) support structure can itself be considered as a complex system comprising multiple interdependent components. For instance, the fatigue hotspots located at the joints between braces or columns of an OWT jacket foundation or the fatigue hotspots along the circumferential welds of an OWT monopile foundation. The OWT support structures are exposed to combined cyclic loading of wind, waves, and currents throughout their lifetime and are subjected to fatigue and corrosion deterioration limiting their operational life and increasing their failure probability. The optimal representation of components in the support structures may increase the system's reliability by reducing the risk of failure. This work aims to investigate different system modeling approaches suitable for representing an OWT support structure.

2 Fatigue deterioration and system structural reliability modelling

2.1 Deterioration modelling

The modeling of fatigue deterioration is associated with significant uncertainties arising from manufacturing processes, loading, etc., and can be properly treated through probabilistic approaches. These uncertainties can be represented by using probability distribution functions. Usually, fatigue cracks in steel structures initiate from weld defects induced during their manufacturing process and grow under the cyclic loads experienced by the structures.

The crack growth can be modeled using Paris law as recommended by standards such as [1].

$$\frac{da}{dN} = C\,(\Delta K)^m \tag{1}$$

where a is the crack depth growing through the thickness of the structural member, N is the number of stress cycles, ΔK is the stress intensity factor (SIF) range, and C, as well as m, are crack growth parameters accounting for material and environmental effects. The stress intensity factor range (ΔK) for a crack growing in the thickness direction of the structural member can be written as:

$$\Delta K = \Delta S\, Y_a \sqrt{\pi a} \tag{2}$$

where ΔS denotes the long-term stress range, which is usually represented by a two-parameter Weibull distribution following industrial guidelines [1] and Y_a is the geometry factor which theoretically depends on the geometry of the

component, welded joint detail and time-varying crack depth for a crack growing through the thickness direction. If it is assumed that the geometry factor (Y_a) does not depend on the time-varying crack depth and remains a constant over the lifetime, an explicit solution for the crack growth can be obtained as in [2]:

$$a(t) = \left[\left(1 - \frac{m}{2}\right) C Y_a^m \pi^{m/2} (\Delta S)^m N + a_{t-1}^{1-m/2}\right]^{(1-m/2)^{-1}} \tag{3}$$

Usually, the thickness of an offshore structural member is smaller than the other dimensions. Therefore, fatigue cracks initiated at the surface of the structural member will likely penetrate through the thickness first. The failure of such members can be defined using the through-thickness failure criterion in which the failure occurs as soon as the crack depth reaches the thickness of the member. The limit state function for through-thickness failure criteria can be formulated as [2]:

$$g(t) = a_{crit} - a(t) \tag{4}$$

where a_{crit} stands for the critical crack depth and is equal to the thickness of the member. The probability of failure (P_f) of the component can be calculated as the probability of the limit state being negative [3]:

$$P_f = P\{g(t) \leq 0\} \tag{5}$$

2.2 System structural reliability

There are multiple simplified system modeling approaches exist in the literature. The most simple system configuration can be obtained by arranging different components in series. The system will not work if any one of its components fails, thereby limiting the maximum attainable system reliability to the reliability of its weakest component and becoming the least redundant system. Another approach is to arrange the components in a parallel manner. The feature of parallel systems is that at least one component in working condition allows the system to work, resulting in increased system reliability than series systems and becoming the most redundant system configuration. The parallel system improves the overall reliability of the system even more than the reliability of individual components. Another configuration is a k-out-of-n system in which one or more components need to work for the system to work. In other words, if there are n components in a system, at least k components should be functional for the system to be functional. Both series and parallel arrangements are special cases of the k-out-of-n system; when k equals n, it becomes a series system whereas when k equals 1 and n is greater than 1, it becomes a parallel system. The reliability of a k-out-of-n system (R_S) formed by n identical components with individual reliability, R is given by;

$$R_{Sys} = \sum_{m=0}^{n-k} \binom{n}{m} R^{n-m}(1-R)^m \tag{6}$$

where the individual component reliability (R) can be computed from the probability of failure (P_f) of the component. Barlow and Heidtmann [4] presented an efficient algorithm to compute the reliability of k-out-of-n systems which has been used in the numerical experiments for computing the system reliability. The probability of failure of a system can be calculated from it's reliability using,

$$P_{FSys} = 1 - R_{Sys} \tag{7}$$

3 Numerical experiments

Most of the installed OWTs in Europe are supported by monopile foundations [5]. They are fabricated by rolling and welding thick structural steel plates in the longitudinal direction to produce cylindrical sections, which are then circumferentially welded together to obtain their full length [5]. The circumferential weld rings are fatigue crack-prone locations due to the variations in the material properties at the BM-HAZ-WM (Base Metal-Heat Affected Zone-Weld Metal) interface resulted from the submerged arc welding process [6].

Two monopile circumferential weld connections located above mean sea level and exposed to air are considered for modeling different systems. The first circumferential weld has 8 components or fatigue hotspots and later one has 4 fatigue hotspots. Due to the cyclic loads from wind and waves, the cracks grow over time and it is assumed that the cracks grow independently without influencing each other. Different system arrangements were considered in the numerical experiments by varying the value of k in the k-out-of-n system of 8 components and 4 components circumferential welds. Each weld connection is treated as a separate k-out-of-n system to see the influence of the total number of components on the system's reliability.

Table 1: Parameters for modelling the fatigue crack growth

Variables	Distribution	Mean (Median)	Std (CoV)
a_0 [mm]	Exponential	1	-
Y_a	Lognormal	(1)	(0.1)
log (C) [1]	Normal	-27.8890	0.1928
m	Deterministic	3	-
q [2]	Normal	6.0357	(0.25)
h [2]	Deterministic	0.8	-
N [cycles]	Deterministic	$3.5 \ .10^7$	-
a_{crit} [mm]	Deterministic	60	-

[1] The corresponding unit of da/dN is mm/cycle and ΔK is MPa$\sqrt{mm}$

[2] The scale parameter (q) and shape parameter (h) of Weibull distribution to define long-term stress range.

The initial crack size distribution (a_0) is assumed to be the same for all fatigue hotspots as they are located on the same circumferential weld of the monopile formed by the continuous submerged arc welding process. The monopile is fabricated by rolling and welding together 60 mm thick structural steel plates. The probabilistic fatigue crack growth of the components is calibrated based on the structural reliability obtained from SN curves in the air as the components are considered to be located in the air. The stress range (ΔS) parameters for the Weibull distribution are also obtained from the same SN curves. The detailed procedure for the calibration can be seen in [2]. It is assumed that the offshore wind support structure has a service life of 20 years. All the relevant parameters for modeling the crack growth based on Paris law can be seen in Table 1.

4 Results and discussion

The probability of failure of different system configurations over their service life is shown in Fig. 1 for welded connections with 8 and 4 fatigue hotspots. As expected, the probability of failure of the system increased with the increase in the number of components for a series system (8-out-of-8 and 4-out-of-4) and decreased with the increase of components for a parallel system (1-out-of-8 and 1-out-of-4). Since the 1-out-of-8 system is more redundant than the 1-out-of-4 system, the probability of failure of the 1-out-of-8 system is 10^3 times smaller than that of the 1-out-of-4 system at the end of service life. It has been found that the probability of failure of an 8-out-of-8 system is only 1.45 times higher than that of a 4-out-of-4 system at the end of 20 years. It is also interesting to note that the probability of failure of the k-out-of-n system increased with the increase in k. For example, the probability of failure of the 8-out-of-8 system is approximately 10^6 times higher than that of the 1-out-of-8 system at the end of service life. Similarly, the probability of failure of the 4-out-of-4 system is 500 times higher than that of the 1-out-of-4 system.

It can be seen in Fig. 1 that the probability of failure evolution curves for all k-out-of-n systems falls inside the curves of parallel and series systems for both the circumferential weld rings considered here as the parallel system being the most redundant system and the series system being the least redundant system out of all configurations. Therefore, a lower bound probability of failure curve has been created by the parallel system (1-out-of-8 system) and an upper bound curve by the series system composed of 8 fatigue hotspots.

It is important to emphasize that the system probability of failure is computed under the assumption that failure of the components in k-out-of-n systems does not affect the functional ones, thereby ensuring the independent nature of the component. However, in practice, the failure of a component affects the efficiency of the functional ones in a system with multiple components. For instance, the failure of a fatigue hotspot will increase the stress experienced by the other fatigue hotspots closer to the failed one. Therefore, rational system models considering inter-dependencies among components are required for representing realistic structures.

5 Concluding remarks

The system reliability of OWT monopile foundation circumferential weld connections has been investigated by representing them in k-out-of-n system configurations. However, real-life structures are complex systems, therefore,

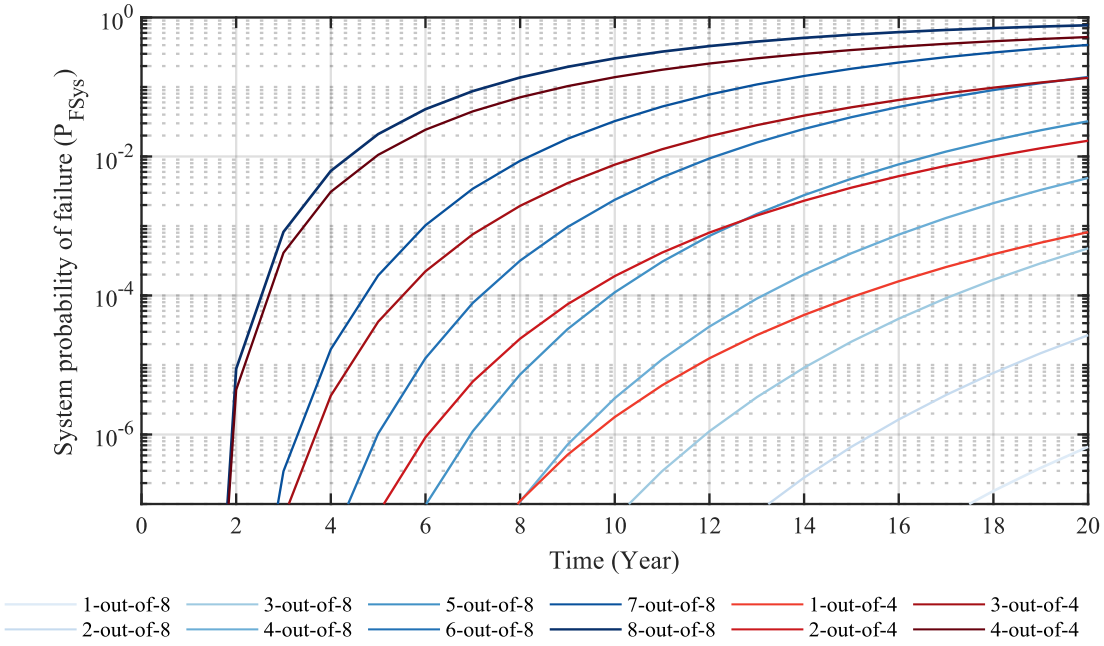


Figure 1: Probability of failure for different system representations of weld connections with 8 and 4 fatigue hotspots over the service life of the structure.

a more rational representation of the system is required for obtaining higher accuracy in the reliability analyses. A rational system for modeling the OWT monopile foundation circumferential welds with fatigue hotspots is under development.

Acknowledgements

The authors gratefully acknowledge the financial support provided by the Belgian Energy Transition Fund (ETF) through the MAXWind project.

References

[1] DNVGL. DNVGL-RP-C203 Fatigue design of offshore steel structures. (Recommended Practice). Veritasveien 1, 1363 Høvik, Norway. 2016.

[2] N. Hlaing, P. G. Morato, J. S. Nielsen, P. Amirafshari, A. Kolios, and P. Rigo. Inspection and maintenance planning for offshore wind structural components: integrating fatigue failure criteria with bayesian networks and markov decision processes. *Structure and Infrastructure Engineering*, 18(7):983–1001, 2022.

[3] P.G. Morato, K. G. Papakonstantinou, C. P. Andriotis, J. S. Nielsen, and P. Rigo. Optimal inspection and maintenance planning for deteriorating structural components through dynamic bayesian networks and markov decision processes. *Structural Safety*, 94:102140, 01 2022.

[4] R. E. Barlow and K. D. Heidtmann. Computing k-out-of-n system reliability. *IEEE transactions on reliability*, R-33(4):322–323, 1984.

[5] A. Jacob and A. Mehmanparast. Crack growth direction effects on corrosion-fatigue behaviour of offshore wind turbine steel weldments. *Marine Structures*, 75:102881, 2021.

[6] R. Biswal, A. Al Mamun, and A. Mehmanparast. On the performance of monopile weldments under service loading conditions and fatigue damage prediction. *Fatigue and Fracture of Engineering Materials and Structures*, 44:1–15, 2021.

18th EAWE PhD Seminar on Wind Energy
2 – 4 November 2022
Bruges, Belgium

Measurement Uncertainty in Structural Health Monitoring Systems for Offshore Wind Turbines

Jan-Hauke Bartels[a], **Steffen Marx**[a]

a TU Dresden, Institute of Concrete Structures, Helmholtzstr. 10, Dresden, Germany

E-mail: jan-hauke.bartels@tu-dresden.de

Keywords: Initial Measurement Uncertainties, Temperature compensation, Laser Triangulation Sensors, Transfer Function, Structural Health Monitoring Systems

1 Introduction

In the condition assessment of infrastructures such as offshore wind turbines (OWT), the use of continuous monitoring systems has become increasingly important in recent years [1]. With regard to the advancing digitalization, research is being conducted in the building industry on the digital twin [2,3]. The digital twin is essentially based on the link between real subcomponents of the building and digital representatives and must represent the real structure as accurately as possible [3,4]. The essential information for this must be obtained via monitoring systems that ensure a lifelong link between the real and virtual systems. The problem is that with large structures, the changes in condition due to aging are very small [5,6]. Typical sensors for monitoring the structures are e.g. laser triangulation sensors (LTS). These can be used, for example, to monitor the horizontal joints between the tower segments of an OWT. The range of values for the elastic deformation or the joint gap in prestressed tower segments due to a bending moment is between 0.05 and 0.1 mm [7]. However, the measurement system also has initial measurement uncertainties, so that it is often not possible to distinguish between measurement errors and changes in the condition of the structure [8]. The measuring system basically consists of the components sensor, measuring cable and measuring amplifier. This connection of the components is called the measurement chain. The difficulty in evaluating measurement results is that the true value of the measurand cannot be determined or is unknown if there is no comparison variable, such as a reference measurement.
The aim of this work is therefore to determine measurement uncertainty for sensors which are typically used for monitoring OWT. With the help of the time-invariant and temperature-dependent transfer function, the temperature influence on the measurement signal is to be compensated. With this compensation, known systematic measurement errors are eliminated and the measurement uncertainty of the measurement system can be calculated based on experimental data.

2 Determination of temperature-dependent transfer function

Laser triangulation sensors (LTS) will be investigated as an example to determine the time-invariant and temperature-dependent transfer function. The experimental setup is shown in Figure 1. In the left subfigure the climate chamber is shown, in which the test setup (right subfigure) is installed. The test setup consists of a base plate with an upstand made of the material Alloy 36 fixed by screws. Alloy 36 is a nickel-iron alloy with low thermal expansion. The coefficient of thermal expansion is calculated to be approx. $\alpha_{T,\text{Alloy 36}} = 0.50 \cdot 10^{-6}\ 1/K$ for the used temperature range of $T = -10°\text{C}... + 50°\text{C}$ and is therefore almost smaller by a factor of 10 than for steel ($\alpha_{T,\text{Steel}} = 13.0 \cdot 10^{-6}$ 1/ K).

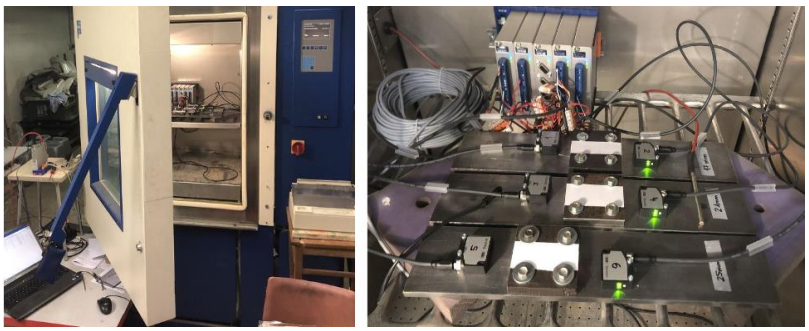


Figure 1: Experimental setup for Laser Triangulation Sensors within the climate chamber

The used sensor from BAUMER company has a measuring range of 10 mm, which is defined in a measuring distance of 16 mm...26 mm. Three specimens with three fixed distances were prepared. The selected distances d_{sel} are chosen to be approx $d_{sel,1}$ = 17 mm, $d_{sel,2}$ = 21 mm and $d_{sel,3}$ = 25 mm, in order to be able to describe a wide measuring range of the sensor with the help of the transfer function. In the climate chamber, different temperature levels are hold constant for a longer period of time (see Figure 2), so that the temperature dependence of the measurement signal, which occurs during monitoring of OWT, can be investigated.

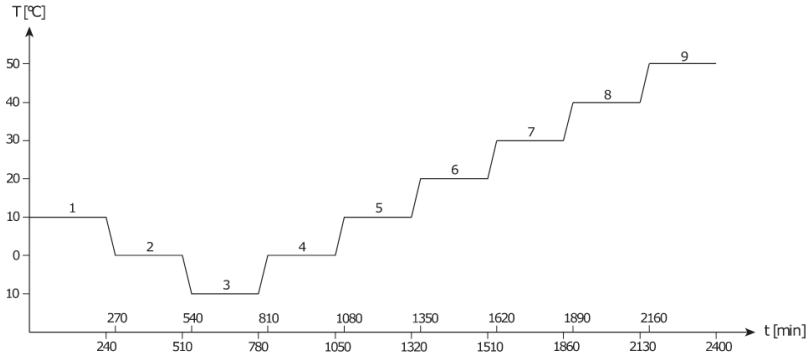


Figure 2: Temperature curve

The predefined value d_{sel} change with a different temperature, since both the base plate with upstand and the components inside the sensor are exposed to thermal expansion. The raw data signal of one LTS is shown in Figure 3. In the figure it becomes obvious that the measurement signal depends on the temperature simulated in the climate chamber.

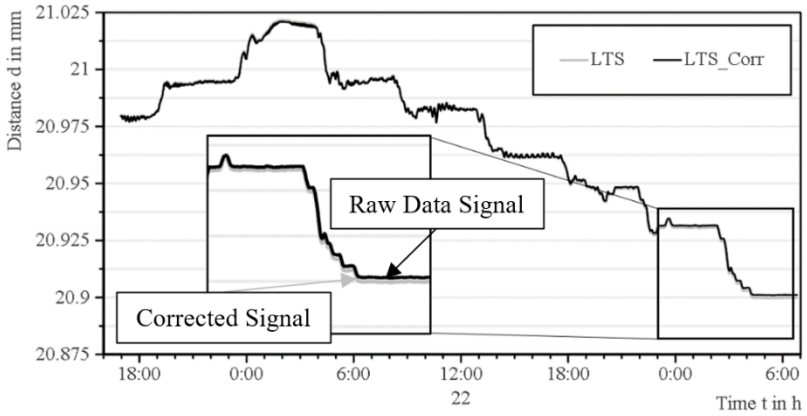


Figure 3: Raw data signal of the LTS (material expansion corrected)

In the diagram, the time *t* is shown on the x-axis and the measured distance *d* is shown on the y-axis. Comparing with the temperature curve in Figure 2, it can be seen that for the considered LTS, the measured distance *d* becomes larger when the temperature decreases and *d* becomes smaller when the temperature increases. To eliminate the influence of the used specimen material Alloy 36 from the measurement signal (grey solid line in Figure 3), the raw data signal need to be corrected in a first step for the influence of temperature-dependent specimen expansion (black solid line in Figure 3).
To determine the temperature-dependent transfer function $\hat{h}(T)$, the arithmetic mean value for each trimmed temperature level and the associated transfer factor *H(T)* are determined. After averaging the measurement signal at constant temperature levels, the transfer function can be plotted as in Figure 4.

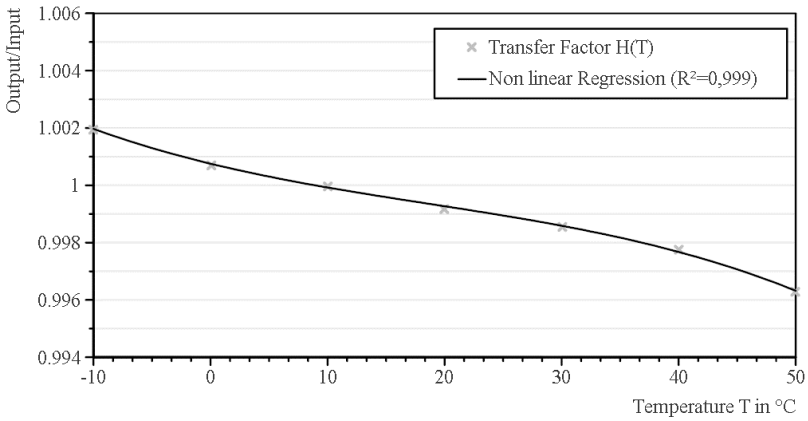


Figure 4: Temperature-dependent transfer function for one LTS

3 Analysis of measurement uncertainty for LTS

In the next step, the acquired raw data signal (cf. Figure 3) must be cleaned of any known systematic measurement errors due to temperature influences. For this purpose, the determined transfer function (cf. Figure 4) is used. With the equation

$$d_{comp}(t) = d(t,T) \cdot [1 - \hat{h}(T)] \quad (1)$$

the known systematic measurement errors are compensated. Due to this compensation the compensated measurement signal has less measurement errors than the non-temperature compensated measurement signal. This temperature compensation was performed for three different sensors with three different distances. For this purpose, nine sub-tests were carried out (cf. Table 1).

Table 1: Absolute measurement uncertainty in 10^{-3} µm

	17 mm	21 mm	25 mm
LTS 1	±0.313996	±0.423199	±0.591017
LTS 2	±1.235300	±3.884654	±2.948856
LTS 3	±0.484918	±1.632574	±2.549844

It can be seen that the measurement uncertainty is lower at an initial distance of 17 mm than at initial distances of 21 mm and 25 mm. For LTS2 (21mm), the measurement uncertainty is the largest at about $\pm 3.884654 \cdot 10^{-3}$µm, while for LTS1 (17 mm) it is the smallest at about $\pm 0.313996 \cdot 10^{-3}$µm. In all cases, the repeatability of $\pm 1{,}000 \cdot 10^{-3}$µm is clearly undercut, so that the three investigated LTS can be assumed to have reliable sensors at their start of use, which would ensure a robust measurement at the beginning of a OWT's lifetime. Furthermore, the measurement chain components were examined separately and it was found that the temperature influence on the measurement amplifier and the measurement cable on the measurement uncertainty is significantly smaller than the influence on the sensor.

4 Conclusion

In this work, the temperature dependence of laser triangulation sensors was investigated over the entire measuring range of the sensor. For this purpose, the entire measurement system, consisting of LTS, measurement cable and measurement amplifier, was exposed to different temperatures inside a climate chamber. The measurement result shows a clear temperature dependence of the measurement system. Based on these investigations, a temperature-dependent transfer function was calculated, which varies from sensor to sensor. With the temperature-dependent transfer function, it was possible to compensate for the temperature of the measurement signal, so that only unknown systematic and random measurement errors are present. The compensated signal could be evaluated with regard to its measurement uncertainty and compared with the specified measurement uncertainty in the sensor manufacturer's data sheet. This showed that the measurement uncertainty of the sensor determined in the experiment is smaller than the one given in the data sheet, so that reliable measurement signals can be expected at the beginning of the service life of a structural health monitoring system for OWT. This ensures reliable and continuous condition monitoring for OWT.

Acknowledgements

This research was funded by the German Research Foundation (DFG), as part of the Collaborative Research Centre 1463 (SFB 1463) “Integrierte Entwurfs- und Betriebsmethodik für Offshore-Megastrukturen”/”Integrated Design and Operation Methodology for Offshore Megastructures” (subproject C01, project number 434502799).

References

[1] C.R. Farrar, K. Worden, An introduction to structural health monitoring, *Philosophical Transactions of the Royal Society A: Mathematical, Physical and Engineering Sciences 365* 303–315. https://doi.org/10.1098/rsta.2006.1928, 2007

[2] M. Grabe, C. Ullerich, M. Wenner, M. Herbrand, smartBridge Hamburg – prototypische Pilotierung eines digitalen Zwillings, *Bautechnik 97* 118–125. https://doi.org/10.1002/bate.201900108, 2020

[3] D. Schuster, C. Hente, C. Hübler, R. Rolfes, Integrierte Entwurfs- und Betriebsmethodik für Offshore-Megastrukturen, *Bautechnik 98*, 563–570. https://doi.org/10.1002/bate.202100044, 2021

[4] R. Rolfes, C. Hübler, Strukturüberwachung zur Schaffung Digitaler Zwillinge bei Infrastrukturbauwerken, *Bautechnik 99*, 423–424. https://doi.org/10.1002/bate.202270603, 2022

[5] M. Herbrand, M. Wenner, C. Ullerich, T. Rauert, G. Zehetmaier, S. Marx, Beurteilung der Bauwerkszuverlässigkeit durch Bauwerksmonitoring, *Bautechnik 98* (93–104). https://doi.org/10.1002/bate.202000094, 2021

[6] J.-H. Bartels, H. Naraniecki, S. Marx, Schadenspriorisierungsanalyse bei Eisenbahnbrücken: Priorisierung von Brückenschäden bei der Deutschen Bahn nach dem Prinzip der FMEA, Bautechnik

[7] F. Klein, F. F¨urll, T. Betz, S. Marx, Experimental Study on the Joint Bearing Behavior of Segmented Tower Structures Subjected to Normal and Bending Shear Loads, Structural Concrete (2022)

[8] F. Wedel, S. Marx, Application of machine learning methods on real bridge monitoring data, *Engineering Structures 250*, 113365. https://doi.org/10.1016/j.engstruct.2021.113365, 2022

18th EAWE PhD Seminar on Wind Energy
2-4 November 2022
Bruges, Belgium

Wind Turbine Blades Defect Detection using Fibre Bragg Grating Distributed Sensing

Aananthalakshmy Sihivahana Sarma[a]

[a]Department of Electronic Engineering, University of Hull

E-mail: a.sihivahana-sarma-2019@hull.ac.uk

Keywords: Defect Detection, Fibre Optic Sensors, Wind Turbine Blades

1 Introduction

Fiber Bragg Grating (FBG) sensors for structural health monitoring (SHM) for wind turbine blades (WTB) is a mature and highly developed technique [1]. While a typical SHM system has its own benefits and features, defect or damage detection in blades come with a lot of challenges as damage is not a physical parameter, rather a local change in the material's properties or at the structure boundaries (for e.g., a crack is simply a new boundary) that degrades structural performance [2]. These defects or small variations in parameters such as strain which lead to defects are much harder to detect with present SHM systems with limited resolution and sensitivity/ functionalities. Improving the resolution of measurements and to investigate the use of these sensors at different points along the blade (distributed sensing) is important to WTB-SHM research. To investigate this ultimately on large scale, geometrically complex structure, such as a blade, a simple and direct way of testing experimentally would be to first use a cantilever beam setup. From a numerical calculations perspective, the blades can be viewed as beam-like structures. Some of the main concerns in utilising FBGs or any fibre optic sensors for this are the sensitivity to change in strain due to the presence of defect, resolution of measurements, sensing length/ no of sensors and suitable data interrogation technique. The objective of this study is to focus on increasing sensitivity to damage for in-situ strain with improved data interrogation techniques for damage detection. Since most defects in blades have a localised variation in strain, it is also important to determine the spatial resolution and positioning of the sensors. Having developed a data acquisition system (DAQ) for wavelength division multiplexed (WDM) FBGs and a peak detection-Gaussian fit data processing algorithm, preliminary investigations of a static-transversely loaded cantilevered beam with a known defect present were conducted with the aid of surface bonded FBGs at multiple locations. Further details of experiments conducted along with results, analysis, limitations and future work are discussed in sections below.

2 Simulations and Experiment Methods

In order to characterise the FBGs under static loading experimentally, a series of simulations were conducted using the finite element analysis (FEA) tool ANSYS Workbench/ Mechanical v.19.2 (ANSYS Inc., United States), so that the experimental results can be compared with the numerical/ analytical results. The first set of simulations were conducted for a uniform Aluminium beam, (without defects) which was 550 mm long; 50 mm of it was fixed and 500 mm was free. The material Aluminium was characterised with homogeneous, isotropic and linear elastic properties; with a Young's modulus (E) value of 7.1 GPa and a Poisson's ratio (ν) of 0.33. Additional construction geometry paths were created to accurately predict the elastic strain and directional deformation of the beam along that path. These paths were created so that they coincide with the FBG mounting locations. Static loads of upto 3.2 kg or 31.392 N was applied transversely by hanging weights at 35 mm from the tip. The second set of simulations were conducted for the same beam specimen with a known defect present. The known defect in this case was a 2 mm deep, 2 mm wide 'V' notch on top of the beam at 30 mm from the fixed end as depicted in the Figure 1 below. Based on the FBG Equation 1 shown, where λ_B is the Bragg or the peak/centre wavelength of the grating, $\Delta\lambda_B$ is the amount of wavelength shift, p_e is the strain optic coefficient and ε is the applied strain. When the grating is subjected to strain, the reflected wavelength shifts proportional to the applied strain and shifts left or right

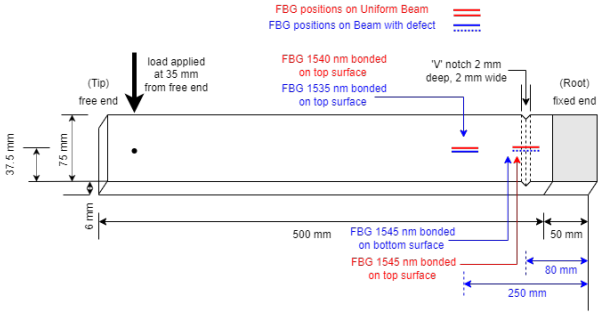


Figure 1: FBGs bonded to the top and bottom surface of the beam with defect

depending on the compression/tension. This equation was used to estimate the experimental strain based on the wavelength shift determined by the Gaussian fitting algorithm developed in MATLAB based on the (Equation 2).

$$\frac{\Delta\lambda_B}{\lambda_B} = (1 - p_e)\,\varepsilon \tag{1}$$

For the experiments, the 10 mm FBGs are bonded at 15 mm at either sides of the grating to the beam's surface using Cyanoacrylate at various lengths along the beam as depicted in Figure 1. A S-LED, centred at a wavelength of 1550 nm, with a built-in optical circulator was used as the broadband light source. For the static loading tests, measurements of the Bragg wavelengths were performed at a low frequency of 100 Hz and a resolution of 0.2 nm using Anritsu MS9740B Optical Spectrum Analyser (OSA). An automated LabVIEW based DAQ system was developed and used to record the FBG Reflected spectra. Sampling points were taken as 1000 for 2 nm spectral span for each FBG. For each load applied, measurements were taken for 3 minutes and then later averaged. The measurement campaign started with zero strain without weights/ transverse loads applied on the beam. The second loading case was conducted with just an aluminium rod secured to the beam's tip. The third and the rest of the measurements were taken by hanging weights off this rod one by one (increasing in load) attached to the beam. Th reverse was also performed where the loads were taken off one by one while measuring the strain response. This was done to check for any hysteresis effect present. This was done for both the uniform beam without any defect as well as the beam with a defect present and were repeated thrice to ensure repeatability.

3 Results and Discussion

The results were analysed with the assumption that the reflected spectra of a single FBG may be modelled as a 1st order Gaussian function with amplitude corresponding to the peak/centre wavelength and arbitrary amplitude and bandwidth [3]. Due to the low-res limitations of the OSA at 0.07 nm, the minimum detectable strain (MDS) thus becomes 58.3 $\mu\varepsilon$ for FBGs with a calibrated sensitivity of 1.2 pm/ $\mu\varepsilon$ [4]. This sensitivity can also be found in numerous strain FBG measurements in [5-6]. Due to this limit of detection posed by the OSA as the optical interrogator, small changes in wavelength shifts corresponding to tiny variations in FBG strain needs to be improved in post-processing. For this, an automatic Gaussian fitting function developed in MATLAB was used to accurately calculate the centroid wavelength shift with an increase/ high resolution which is needed for the accurate strain estimation. Equation 2 was used to represent the FBG peak; where a is the amplitude, b is the centre (location) or the mean, c is related to the peak width, i.e. standard deviation and n is the number of peaks to fit, in this case of a single grating, n=1 representing single peak. By using this approach, he resolution of the spectra was increased to 1 pm, i.e., wavelength shifts of upto 1 pm were detectable which roughly corresponds to 1-2.5 $\mu\varepsilon$. Finally, with the sensitivity and the wavelength shift, the experimental strain were calculated.

$$y = \sum_{i=1}^{n} a_i e^{\left[-\left(\frac{x-b_i}{c_i}\right)^2\right]} \tag{2}$$

Looking at the results for the strain measurements taken by the FBGs vs predicted ANSYS strain for the uniform beam in Figure 3, both FBG (1) at 1545 nm and FBG (2) at 1540 nm mounted on beam-top experience tensionas expected when the beam is transversely loaded. The simulated strain shows relatively good agreement with the experimental results of both FBG 1545 nm which was mounted close the root and as well as with FBG 1540 nm.

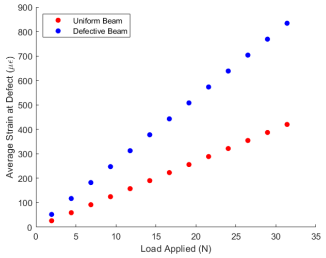


Figure 2: Expected Strain for Uniform Beam vs Defective Beam

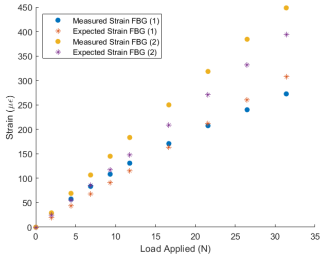


Figure 3: Measured vs Expected Strain on Uniform Beam

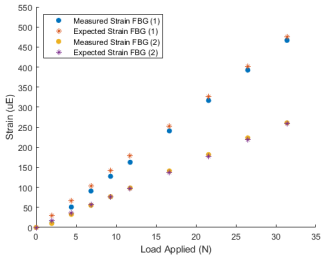


Figure 4: Measured vs Expected Strain on Defective Beam

For the defective beam, in Figure 5 it can be seen that FBG (1) 1545 nm which was bonded directly under the defect experienced compression under transverse loading and the reflected peak shifts to the left. As for the FBG (2) 1535 nm which was mounted on the top surface, it was subjected to tension as the strain/ load increased and this can be seen in Figure 6 showing a right shift of the FBG reflected peak.

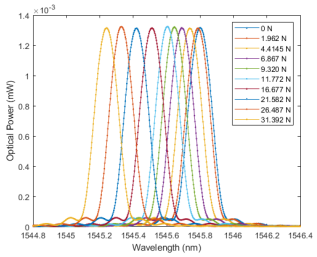


Figure 5: 1545 nm FBG under compression

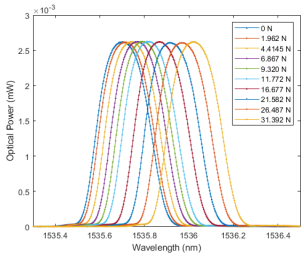


Figure 6: 1535 nm FBG under tension

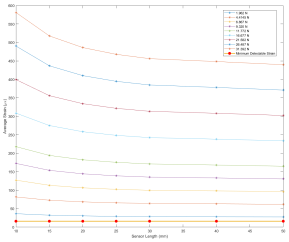


Figure 7: Average Strain estimated for different FBG sensing lengths

For the beam with the defect, the experimental vs expected strain are shown in Figure 4. It may be seen that the estimated Bragg wavelength for both FBG 1545 nm and FBG 1535 nm from the measurements is proportional to the applied strain. It is also worth noticing that in comparing Figure 4 and Figure 3, both 1545 nm FBGs which were mounted at the same distance from the root, the strain sensed by the FBG 1545 nm on the beam with the defect was higher than the uniform vs defect-less beam case as expected when there is a structural defect present. Due to the distributed measurements, it can be observed that the strain sensed by the FBGs mounted at different locations measure different strain and show good agreement with the expected strain for that specific mounting locations.

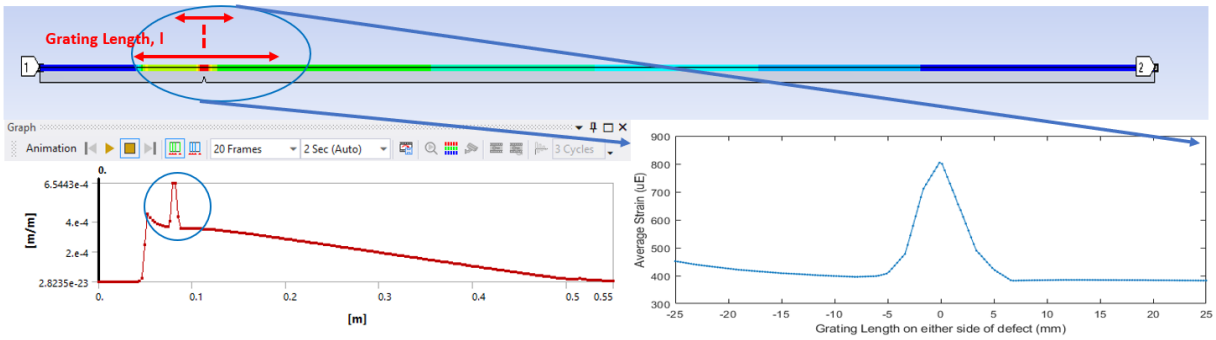


Figure 8: FEA for Defective Beam with Different FBG sensing lengths

For the investigation of sensor position and length, the results from the FEA under different load cases were considered. As mentioned before for the experiments, the sensing lengths (bonded) were considered as 30 mm. Figure 8 shows the various simulated sensing lengths underneath the defect and the average strain expected for the

entire beam as well as at the defect and a sharp rise in strain was observed at the defect location. Figure 2 clearly shows that strain at the defect location is high enough to be distinguished form the uniform beam in increasing load cases. Figure 7 shows the average strain expected by the sensors from FEA with different grating/ sensing lengths. It can be seen that experimental minimum detectable strain is lower than the strain expected by different sized sensors, which is useful for further experimental validation by bonding FBGs with different grating lengths. This analysis also gives some initial insight into determining the minimum sensing length and the spacing of the sensor for a given defect and load case. As FBGs are sensitive to both strain and temperature changes, the ambient temperature variations were monitored and measured for this investigation using a k-type thermocouple as well as a strain-insensitive FBG. Results from these were will be included for cross sensitivity analysis and active temperature compensation later. The residuals relative to a linear fit to the data show $\simeq$6 root mean square error for all sensors used.

4 Conclusions and Remarks

This work has demonstrated a method of utilising FBGs to characterising defects based on strain measurements using precise mounting while also studying the response of FBGs in other locations. An FEA was carried out in simulation to investigate the load–strain relationship, strain distribution along the beam as well as determining the optimum FBG sensor length for a given defect. A suitable FBG peak-fitting automated Gaussian algorithm has been developed as well as a LabVIEW based DAQ for the OSA. This offers an opportunity to expand the number of sensors using WDM which can be utilised to study the distributed strain variation along the beam. This FBG-defect characterisation approach is reliant on good estimates of the peak reflected wavelength of each grating and has exhibited good agreement between simulated vs experimental strain results especially for the beam with defect. Preliminary analysis indicate that the approach can be successfully further expanded to composite cantilevered beam as well as scaled wind blades with and without defects of various sizes to study the effects of defect using FBG strain measurements at difference points of measurements. This will serve as a direct-way of understanding structural damages/ defect characteristics on blades using FBG-strain measurements and significance of distributed sensing and trade-off between sensor position, length, sensitivity with resolution. This will be explored in future work.

Acknowledgements

The author would like to thank Prof. James M Gilbert, Dr. Kaushal Bhavsar of the University of Hull and the wider community of SuperGen ORE Hub and EPSRC Prosperity Partnership ‘A New Partnership in Offshore Wind’ (EP/R004900/1, 2017-2022).

References

[1] Glavind, L., Olesen, I. S., Skipper, B. F., and Kristensen, M. V. (2013). “Fiber-optical grating sensors for wind turbine blades: a review”. In: *Optical Engineering* 52.3, p. 030901.

[2] Güemes, A., Fernández-López, A., Dıaz-Maroto, P. F., Lozano, A., and Sierra-Perez, J. (2018). “Structural health monitoring in composite structures by fiber-optic sensors”. In: *Sensors* 18.4, p. 1094.

[3] Lee, H.-W., Park, H.-J., Lee, J.-H., and Song, M. (2007). “Accuracy improvement in peak positioning of spectrally distorted fiber Bragg grating sensors by Gaussian curve fitting”. In: *Applied optics* 46.12, pp. 2205–2208.

[4] Technica (n.d.). “Customized FBG Sensor Datasheet”. URL: https://technicasa.com/wpcontent/uploads/2017/01/T10-Customized-FBG-Sensor-1.pdf.

[5] Di Sante, R. (2015). “Fibre optic sensors for structural health monitoring of aircraft composite structures: Recent advances and applications”. In: *Sensors* 15.8, pp. 18666–18713.

[6] Eum, S., Kageyama, K., Murayama, H., Ohsawa, I., Uzawa, K., Kanai, M., and Igawa, H. (2006). “Process and Health Monitoring Using Fiber Optic Distributed Sensors for Wind Turbine Blades”.

Support structures and geotechnics

18th EAWE PhD Seminar on Wind Energy
2 – 4 November 2022
Bruges, Belgium

A Numerical Investigation on the Pitting Corrosion in Offshore Wind Turbine Substructures

F. Mehri Sofiani[a], S. A. Elahi[a], S. Chaudhuri[a] , W. De Waele[a]

[a] Soete Laboratory, EMSME Department, Faculty of Engineering and Architecture, Ghent University, 9000 Ghent, Belgium.

E-mail: farid.mehrisofiani@ugent.be

Keywords: offshore wind turbines; fatigue; pitting corrosion;phase-field modelling; stress concentration factor

Pitting corrosion is a common cause of concern for steel structures in an offshore environment. As geometric stress concentrating features, corrosion pits can potentially act as fatigue crack initiation sites. The current study is a part of the MAXWind project which, amongst others, aims to develop numerical tools for a more accurate estimate of the remaining lifetime of in-service wind turbines. UGent is responsible for developing an advanced corrosion-fatigue model which will be used to build "smart S-N curves". The smart S-N curve is a novel concept that takes the level of corrosion into account. To this end, the entire evolution of corrosion fatigue is divided into three major phases including pitting corrosion, short fatigue crack propagation, and long fatigue crack propagation, see Figure 1.

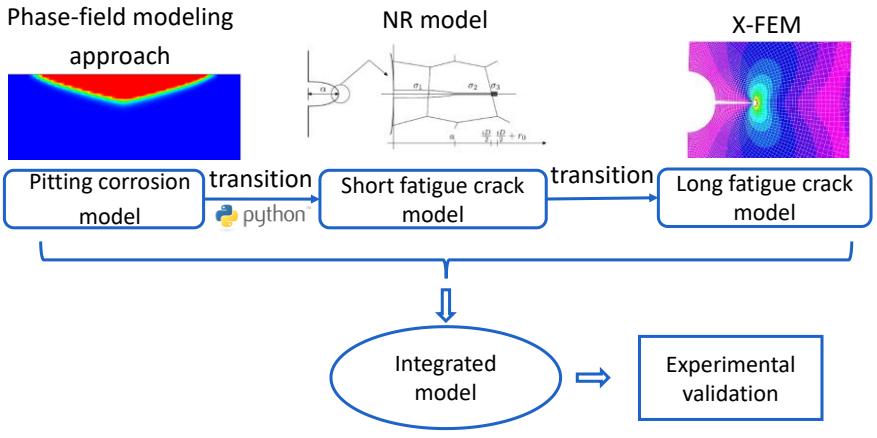


Figure 1: Overview of the numerical approach to model the corrosion fatigue process.

The main focus of this work is on pitting corrosion and its transition to short fatigue crack propagation. A phase-field modelling approach [1],[2] is used to simulate the autonomous growth of a corrosion pit. The corrosion phenomenon - pitting corrosion in particular – is a complex electrochemical process that is influenced by various environmental factors such as temperature, dissolved oxygen, pH, salinity, etc. [3]. Phase-field modelling is a robust technique that is capable to incorporate a vast range of influential parameters. In essence, in a phase-field model, each phase (here, metal and electrolyte) possesses a constant value in the bulk (0 for

electrolyte and 1 for steel), with a continuous interpolation between the bulk values across the interface between phases. The evolution of the system is a result of constrained minimization of free energy for which the advective Cahn-Hilliard equation is used. The Nernst-Planck equation is used to describe the diffusion of ions within the electrolyte, and the Butler-Volmer-type kinetic expression is used to calculate the reaction current density throughout the process. For more information and formulations see [1].

First, an electrochemical characterization was performed for structural steel grade S355 in an environment that is representative of the North Sea. This study is crucial to evaluate the electrochemical behaviour of this steel grade and will support further studies towards predicting pit dimensions in offshore wind turbine support structures in the North Sea. To this end, potentiodynamic polarization tests were implemented for S355 steel. An Ag/AgCl electrode was used as reference electrode in the tests and potential values are obtained against this electrode. The corresponding corrosion potential and current density were obtained as -711 mV vs. Ag/AgCl and 0.1534 A/m^2, respectively. For a metal, the more negative the corrosion potential is, the more susceptible it will be to corrosion [4]. In practice, corrosion protection systems and coatings will be applied to the metal structure, which will increase the value of corrosion potential [5].

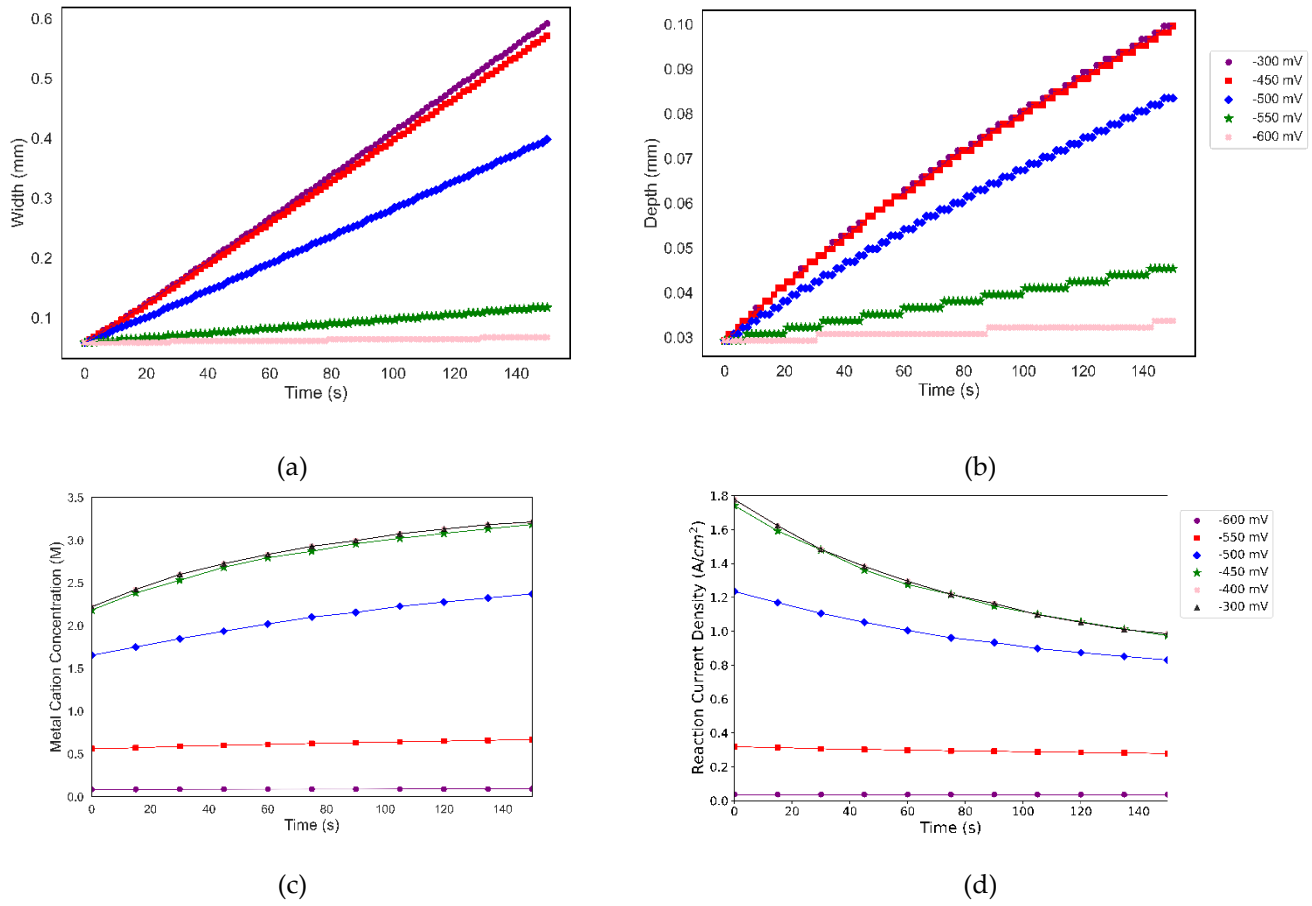


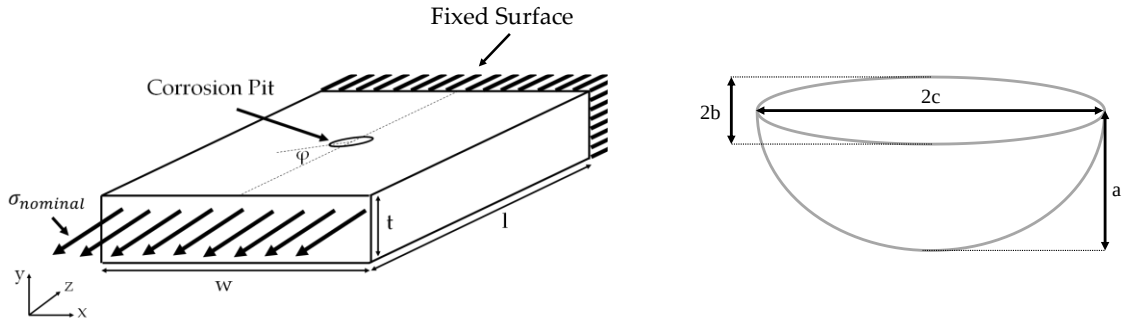
Figure 2: For a range of applied potentials: evolution of (a) pit width vs. time. (b) pit depth vs. time. (c) metal cation concentration vs. time. (d) reaction current density vs. time.

Using the output of the experiments as input to the phase-field model, a parametric study was performed to assess the effect of the applied potential on geometrical parameters (pit width and depth) and electrochemical parameters associated with pit growth rate (metal cation concentration and reaction current density), see Figure 2. It was found that for an applied potential of -600 mV vs. Ag/AgCl, the corrosion process stays in the activation-controlled regime throughout the simulation time (150 seconds). Applied potentials of -550 to -500 mV vs. Ag/AgCl take the system to the current-resistance-controlled regime where the metal cation concentration does not reach the saturation. The higher the applied potential is, the more pitting corrosion is accelerated until it reaches to the point where any additional increase in applied potential will not have any

additional influence on pit growth rate. As it is easier for the metal ions to diffuse into the bulk electrolyte near the pit mouth in bare steel, pit width increases with a higher velocity in comparison to the pit depth. All numerical results will be validated with dedicated experiments.

Any changes in temperature will cause changes in electrochemical parameters such as ionic diffusivity, corrosion potential and corrosion current density. As future work, a parametric study will be conducted on the effect of temperature on the corrosion pit growth rate. Ultimately, pit dimensions extracted at every time step will serve as input to a short fatigue crack propagation model [7].

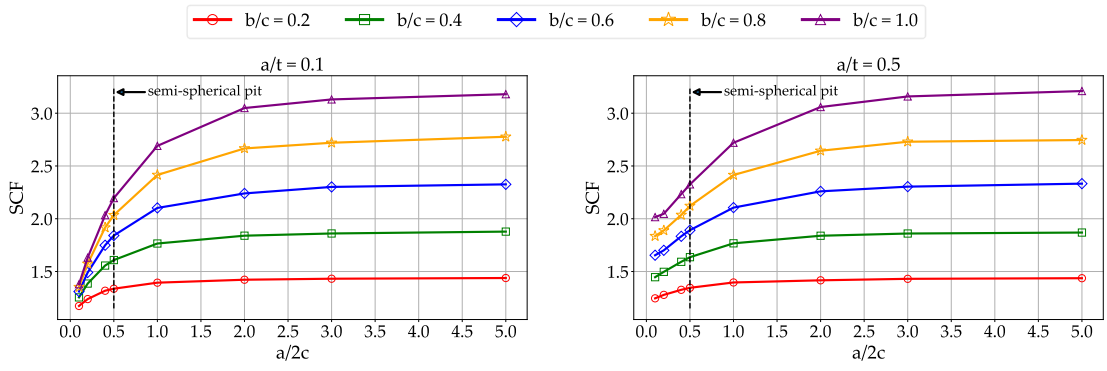
Once a corrosion pit nucleates, the local stress in the material increases at the discontinuity. Therefore, in parallel to the pitting corrosion study, a finite element analysis was performed to assess the stress concentration factor (SCF) of corrosion pits and to identify the effect of different normalized geometrical parameters on SCF, see Figure 3. According to [8], a crack will initiate from a pit under the following conditions: (a) the pit size must pass a critical value, and (b) the crack growth rate must be higher than the pit growth rate. The concept of SCF can assist to address the first criterion. A pit becomes susceptible to transit to a crack as soon as it causes a considerable increase in the local stress.



(a) (b)

Figure 3: Schematic representation of (a) 3D pitted plate dimensions and boundary conditions, and (b) Semi-ellipsoidal corrosion pit.

Results show that an increase in a/2c or b/c leads to enhanced SCF when the loading is oriented parallel to the pit's major axis (i.e., $\varphi = 0$), see Figure 4 (a) and (b).



(a) (b)

Figure 4: (a) SCF variation vs. a/2c for a range of b/c values and a/t = 0.1 and (b) a/t = 0.5.

Acknowledgements

The authors would like to acknowledge the financial support of the Belgian Federal Government through the Energy Transition Fund (ETF).

References

[1] A. F. Chadwick, J. A. Stewart, R. A. Enrique, S. Du, and K. Thornton, "Numerical Modeling of Localized Corrosion Using Phase-Field and Smoothed Boundary Methods," *J. Electrochem. Soc.*, vol. 165, no. 10, pp. C633–C646, 2018, doi: 10.1149/2.0701810jes.

[2] S. DeWitt, S. Rudraraju, D. Montiel, W. B. Andrews, and K. Thornton, "PRISMS-PF: A general framework for phase-field modeling with a matrix-free finite element method," *npj Comput. Mater.*, vol. 6, no. 1, pp. 1–12, 2020, doi: 10.1038/s41524-020-0298-5.

[3] Z. Ahmad, *Principles of Corrosion Engineering and Corrosion Control*, vol. 7, no. 1. Elsevier, 2006.

[4] X. Yu, S. Al-Saadi, X. L. Zhao, and R. K. S. Raman, "Electrochemical investigations of steels in seawater sea sand concrete environments," *Materials (Basel).*, vol. 14, no. 19, 2021, doi: 10.3390/ma14195713.

[5] S. Price and R. Figueira, "Corrosion Protection Systems and Fatigue Corrosion in Offshore Wind Structures: Current Status and Future Perspectives," *Coatings*, vol. 7, no. 2, p. 25, 2017, doi: 10.3390/coatings7020025.

[6]

[7] S. A. Elahi, "Numerical study on the effect of pitting corrosion on the fatigue strength degradation of offshore wind turbine sub-structures using a short crack model," 2022.

[8] Y. Kondo, "Prediction of fatigue crack initiation life based on pit growth," *Corrosion*, vol. 45, no. 1, pp. 7–11, 1989, doi: 10.5006/1.3577891.

18th EAWE PhD Seminar on Wind Energy
2 – 4 November 2022
Bruges, Belgium

Analysis of discrepancy between modelled and measured natural eigenfrequencies of offshore wind turbines

K. Winkler[a], C.S. Jurado[a], W. Weijtjens[a], B. Stuyts[b], C. Devriendt[a]

[a] Vrije Universiteit Brussel, OWI-lab, AVRG, Pleinlaan 2, 1050, Brussels, Belgium

[b] UGent, Geotechnical Laboratory, Technologiepark 68, Zwijnaarde, 9052, Belgium

E-mail: kristof.winkler@vub.be

Keywords: Finite element model updating, Parametrization, modelling error, design verification, model sensitivity, integrated modelling

1 Introduction

Offshore wind has the potential to be one of the major contributors towards a relatively clean and renewable energy future. To make this technology more (cost)efficient, OWI lab has spent the last few years collecting data from various wind farms and offshore wind turbine (OWT) designers. This has resulted in the creation of the OWI meta database [1] and an inhouse 1D finite element model which uses said database to construct models based on the real in situ situation. In addition, multiple measurement campaigns were held to determine the natural eigenfrequencies of all the studied OWTs. These are important because of their influence on the fatigue damage the structures will suffer over their lifetimes. As was found by other sources [2], these real-life measurements seem to deviate from the models used during design [3], leading to a discrepancy between the actual and calculated lifetime expectancy. The goal should thus be to better understand both reality and these models, to come to better predictions and designs. Furthermore, new findings can retroactively be applied to existing structures in attempt to extend their operational lifespan. In this presentation, the focus will be on the sensitivity of the models to specific environmental conditions as well as lessons learned from trying to fit in situ measurements. The goal is to define the current inconsistencies and propose potential fixes that will be explored in later publications.

2 Objectives

First, the basic assumptions of the OWI-lab 1D FE model will be presented as well as the method used to measure the natural eigenfrequencies. Second, will be an in-depth comparison for a specific wind farm between different design assumptions and real-life conditions. An example of this can be seen below (Fig 1). Next the focus will shift to certain individual parameters such as, soil stiffness, RNA mass and inertia, sea water level, …etc. Their sensitivity with regards to the model will be checked as well as if they can be held responsible for the discrepancies between calculated and measured natural eigenfrequencies (Fig 2). Finally, there will be some specific attention for the effects scour protection has on the structures. More specifically a method to model this layer will be presented as well as how it relates to a better fit for, not only the frequencies, but bending moments as well. [4] [5]

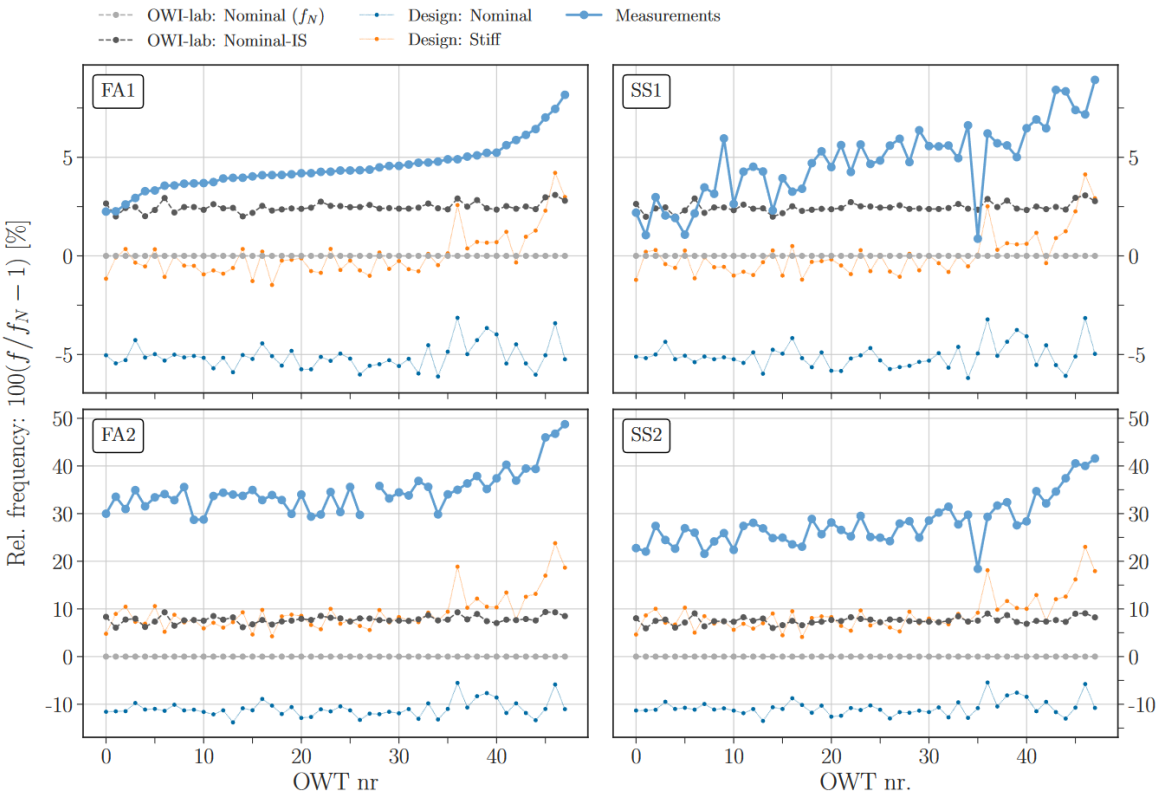


Figure 1: Comparison of measured frequencies, as-designed frequencies and frequencies computed with the integrated OWI-lab FE model. All frequencies are expressed relative to the corresponding nominal frequencies (f_N) computed with the OWI-lab: Nominal model, and have been sorted such that the error between the measured first fore-aft frequency and the corresponding nominal frequencies are in ascending order. Upper half: first order fore-aft (FA1) and side-side (SS1) frequencies. Lower half: second order fore-aft (FA2) and side-side (SS2) frequencies. [3]

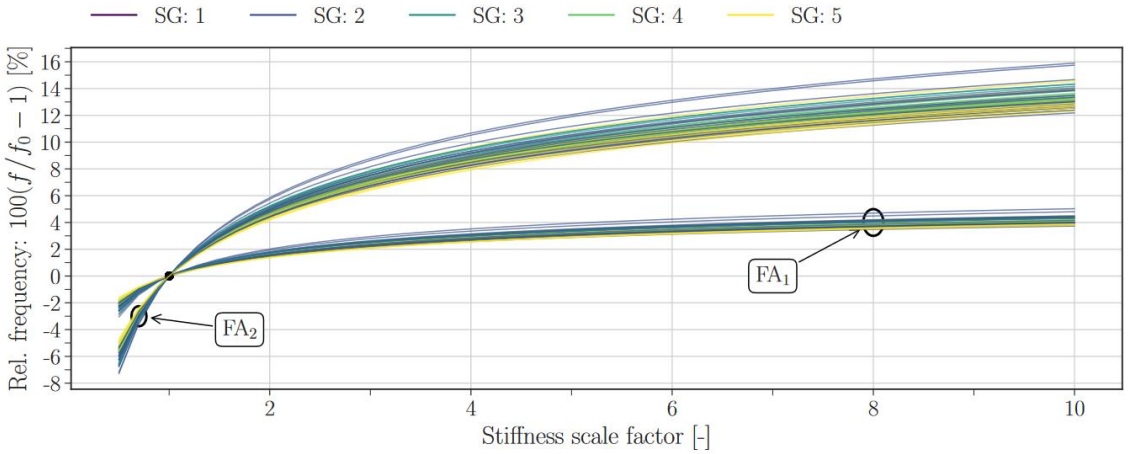


Figure 2: Sensitivity of the first and second order natural frequencies in fore-aft direction with respect to a scaling of the soil spring stiffness values. With SG being 5 distinct soil groups which are defined by the design documentation based on soil properties and monopile slenderness (L/D) [3]

3 Results

Most results have already been generated over the past year and can be presented as shown in the objectives. Right now, the most important aspects about design that we are aware of are:

- Soil parameters, both linearization and calculation method seem to have a big impact. Furthermore, it might be necessary to implement isotropic properties to account for the for-aft and side-side direction of the OWT. [3] [5] Although more recent inhouse testing suggest a better, more detailed, modelling of the rotor nacelle assembly (RNA) is required.
- Seawater level has a big impact on the second order eigenfrequencies and can result in uncertainties if not measured/modelled properly. [3]
- Scour protection seems to have an actual impact on soil properties as well as second order eigenfrequencies. Not taking this layer into account makes it impossible to get a good fit for the bending moments as well. [5] [4]

4 Conclusions

At this moment it is possible to approximate the first order eigenfrequencies up to less than 2% of the measured value. Minimal finetuning for specific OWTs can decrease this threshold even further. The second order frequencies are more difficult to calculate, and the gab between model and reality can go upwards of more than 30%. This can be lowered by taking into account scour protection and deviations between the real insitu vs design mudlines. Also, taking into account the seawater level and other sea properties allows for a better fit. But even in our more current best estimates, a gab of 8% still remains. It is suspected that more detailed modelling of the RNA might be part of the cause for this discrepancy. To this end, different stages of construction will be looked at in the future. Example of this are instances without tower and/or RNA installed, as to eliminate for-aft and side-side dependencies and potential modelling errors. Others will be comparing values before and after the rock armour has been dumped around the foundation to isolate the exact effects on changes in natural eigenfrequencies of the owt's.

5 References

[1] B. Stuyts, "OWI-Lab metadatabse api demonstration," 2021. [Online]. Available: https://github.com/OWI-Lab/owimetadatabase_demo.

[2] D. Kallehave, "Optimization of monopiles for offshore wind turbines," *Philosophical Transaction of the Royal Society A: Mathematical, Physical and Engineering Sciences,* 2015.

[3] D. Fallais, "Farm wide sensitivity assessment of resonant frequencies of integrated offshore wind turbine finite element models," in *Torque 2022*, Delft, 2022.

[4] B. Stuyts, "Monopile lateral response calibration from in situ monitoring data.," in *Proceedings of the Fourth International Symposium Frontiers in Offshore Geotechnics*, Austin, 2020.

[5] C. S. Jurado, "Impact of calibrated soil-monopile-interaction model on resonance frequencies," in *Torque 2022*, Delft, 2022.

18th EAWE PhD Seminar on Wind Energy
2 – 4 November 2022
Bruges, Belgium

Current and wave patterns in the nearfield of an offshore jacket structure

Mareile Wynants[a], Alexander Schendel[a], Mario Welzel[a],

Nils B. Kerpen[a], Torsten Schlurmann[a]

[a] Leibniz University Hannover, Ludwig-Franzius-Institute
E-mail: wynants@lufi.uni-hannover.de

Keywords: Water waves, Laboratory tests, Offshore Hydrodynamics, Offshore engineering, Wave-Current-Interaction, Jacket Structure

1. INTRODUCTION AND MOTIVATION

In order to meet renewable energy targets and reach a climate-neutral European economy by 2050, the capacity of offshore wind energy must be significantly expanded. For this, an integrated design process and sustainable operation of offshore wind turbines in the susceptible marine environment is essential. Understanding the complex current- and wave-induced impacts and interactions with the sub-structures of offshore wind turbines in experimental set-ups is key to improving design parameters and developing guidelines (Hildebrandt & Schlurmann 2012).

2. BACKGROUND

The foundation for understanding the influence of future structures increased dimensions is the comprehension of how current- and wave patterns develop and ultimately interact with each other around the structure. For monopiles, the individual aspects of current-structure-interaction (Sumer & Fredsoe, 2006) and wave-structure-interaction both in and outside of the diffraction regime (MacCamy & Fuchs, 1954; Morison et al., 1950) are well understood and have been experimentally investigated. For jacket structures, research is much less developed yet. Besides scarce investigations specifically aimed at jacket structures, pile groups of four piles as the closest approximation of jacket structures present a wider range of existing research.

In terms of the current-structure interaction, research specified to jackets is mainly limited to scour development (Welzel et al., 2020). Transferring knowledge from pile groups, (Lam et al., 2003) and (Yang et al., 2021) suggest complex depth dependent interactions of the individual wakes induced by each main pile and their respective gap ratio.

Regarding wave-structure interaction, jackets are classified as hydraulically transparent with regard to the resulting force on the structure (Morison et al., 1950). Existing investigations are mainly focussed on slamming impacts from breaking waves (Sruthi & Sriram, 2017). In research on pile groups, further focus is set on local and global diffraction (Cong et al., 2015) as well as resonance phenomena like near-trapping (Evans & Porter, 1997).

Ultimately, the interaction of waves and currents in the nearfield of a jacket structure has been considered with regard to current blockage (Santo et al. 2017) and scour development (Welzel et al., 2019).

3. OBJECTIVE

In the context of offshore megastructures, increasing pile diameters as well as increasing relative geometrical densities raise the question to which extent a mega-jacket can still be classified as hydraulically transparent. The exploration of this research question has been set as the superordinate objective of the entire study. To investigate the influence of increasing jacket sizes on the interaction with surrounding waves and currents, in-depth understanding of the underlying wave-current-structure interactions has to be available as the basis. The here-in presented partial study will be limited to addressing this aspect, to provide the foundation for future work on the influence of structure scale.

It needs to be questioned, which concepts investigated in the context of pile groups can be transferred towards jacket structures. Commonly, literature on pile groups is focussed on gap (G) to pile diameter (D) ratios between $G/D = 1$ and 6 and thus deviates from an accurate representation of a jacket structure, commonly with ratios of $G/D > 12$ (Welzel et al., 2019; Rudolph et al., 2004).

Therefore, the need for a systematic parameter study on the interaction of a jacket structure with currents, waves and their combination has been identified. Within this context, the objective of the experimental study has been set as the identification of characteristic phases in the progression of the following influences around a jacket structure:

a) A temporally and spatially uniform current.
b) Regular, monochromatic, long-crested waves.
c) The combination of both a) and b) in a 90° angle.

A focus is set on the thorough documentation of the individual processes in the jacket nearfield as well as the temporal development of depth resolved current profiles and the development of the wave shape in the interaction regime of wave and current.

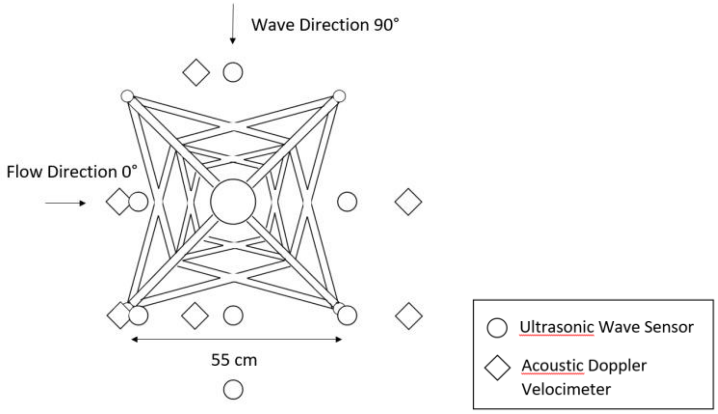


Figure 1: Schematic view of the jacket model plan view with grid positions of the wave gauges (circle) and Acoustic Doppler Velocitmeters (diamond).

4. METHODOLOGY

Hydraulic model tests were carried out in a scale of 1:45 in the 3D wave-current-basin of the Ludwig-Franzius-Institute, Hannover, Germany. A 4-legged jacket structure (prototype base width $bw = 25$m) with inclined legs is investigated in a prototype water depth of 45 m. Gap to pile diameter ratios range over the water depth from $G/D = 4$ to 13 due to the inclination of the main piles.

In the first phase of the tests (current only), velocities have been ranged from $Re = 4.8 \cdot 10^3$ to $Re = 9.7 \cdot 10^3$ (subcritical, completely turbulent wake). In the second test phase (wave only), $KC = uT/D$ with u defined as the orbital velocity has been ranged from 6.3 (a pair of asymmetric vortices) to 23.6 (vortex shedding). In the third phase (wave plus current) the combined influence of waves and a current perpendicular to the wave direction has been investigated for these ranges of Re and KC, varying the flow regime accordingly (Sumer, 2006).

Information and data on the development of current patterns have been acquired in a raster of 7 grid points around the jacket structure by the use of an acoustic Doppler velocimeter (ADV) in three different depths along all three coordinate axes. Information on the wave characteristics in the nearfield of the structure has been acquired by ultrasonic wave gauges following the same grid. Documenting vortex development and wave patterns has been supported through imaging techniques utilizing consumer-grade cameras and a fluorescent tracer.

5. PRELIMINARY RESULTS

Preliminary results of the described model test aspects have been derived mainly with focus on the current-structure-interaction. A high dependency of the vorticity on the water depth due to the inclination of the jacket main piles as well as the presence of the X-braces has been documented.

As a first indicator for this, videos of the fluorescent tracer distribution have been utilised. For the current only tests, the tracer has been injected in a depth of 0.1 m, focus is set on the tracer injection at the upstream pile. The development of the vortex street along the outside face of the jacket has been analysed as a first indication of the transferability of a four-pile configuration to a jacket structure. At the injection depth of the tracer, the main piles are spaced with a gap ratio of $G/D = 6.35$, indicating co-shedding behaviour in a comparable tandem pile setting ($G/D > 5$; Sumner, 2010).

In figure 2, a representative excerpt of the video sequence from a current with $Re = 4.8 \cdot 10^3$ is given and supplemented with schematic sketches indicating the vortex street development. Corresponding to $Re = 4.8 \cdot 10^3$, vortices shed from the pile with an approximate frequency closely matching the expected vortex shedding frequency of $fv = 0.2$ (function of Re; Sumer, 2006) at position (1). The first structural aspect to differ from a tandem pile setting is observed at position (2), where the vortex strikes the X-brace. The chosen injection depth is located closely to the depth of the X-brace middle node. The vortex appears to swirl around the node, leading to a widening of its shape. At the location of the downstream pile, the vortex travels along the outside of the pile (3) and detaches from the pile with a further increase in extent (4).

A possible preliminary explanation for the observation could be found if the node of the X-brace as an interruption of the vortices travel path was to be interpreted as a further pile in terms of the gap ratio. The ratio would approximately decline to $G/D = 2.7$, indicating a reattachment regime (G/D ≈ 2-5; Sumner, 2010). What is described above as swirling around the X-brace could therefore be a form of reattachment, the same applies to the downstream pile. This would lead to a high depth-dependency of the structure-interaction regime, due to changing gap ratios not only being influenced by the inclination of the main piles but additionally by the relative position of the X-braces. Further systematic analysis of this aspect is necessary to examine this hypothesis.

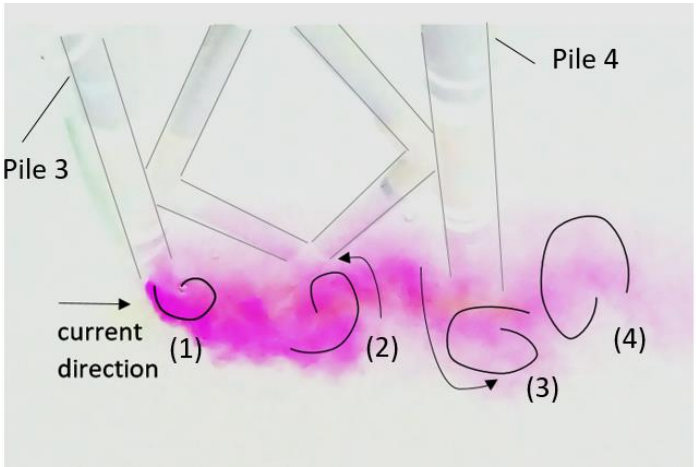


Figure 2: Temporal development of velocity profiles in current direction under current only influence directly downstream to the jacket structure over the representative time span of one second, averaged over 0.1s in each subplot.

In the development of the wave field, but especially under the combined influence of waves and currents, the introductions of asymmetry into the wave field is expected to result into a transformation of wave shape towards nonlinear characteristics, influencing both the pressure distribution on the structure and the marine environment.

Acknowledgements

Funded by the Deutsche Forschungsgemeinsschaft (DFG, German Research Foundation) – SFB1463 – 434502799

References

[1] A. Hildebrandt, T. Schlurmann. Breaking wave impact on offshore tripod structures – Comparison of large scale experiments, CFD simulations, and DIN recommended practice. *Bautechnik* 89:301 – 308, 2012
[2] B. M. Sumer, J. Fredsoe. Hydrodynamics around cylindrical structures. *World Scientific Publishing*, 2006
[3] R. C. MacCamy, R. A. Fuchs. Wave forces on piles: a diffraction theory. *U.S.C.E. Beach Erosions Board*., 69:1 – 17, 1954
[4] J.R. Morison, M.P. O'Brien, J.W. Johnson, S.A. Schaaf. The force exerted by surface waves on piles. *Journal of Petroleum Technology*, 189:149 – 154, 1950
[5] M. Welzel, A. Schendel, N. Goseberg, A. Hildebrandt, T.Schlurmann. Influence of structural elements on the spatial sediment displacement around a jacket-type offshore foundation. *Water,* 12:1651, 2020
[6] K. Lam, J.Y. Li, R.M.C. So. Force coefficients and Strouhal numbers of four cylinders in cross flow. *Journal of Fluids and structures*, 18:305 – 324, 2003
[7] Y. Yang, M. Qi, J. Li, X. Ma. Experimental study of flow field around pile groups using PIV. *Experimental Thermal and Fluid Science*, 120, 2021
[8] C. Sruthi, V. Sriram. Wave impact load on jacket structure in intermediate water depth. *Ocean Engineering*, 140:183 – 194, 2017
[9] P. Cong, Y. Gou, B. Teng, K. Zhang, Y. Huang. Model experiments on wave elevation around a four-cylinder structure. *Ocean Engineering*, 96:40 – 55, 2015
[10] D. V. Evans, R. Porter. Near-trapping of waves by circular arrays of vertical cylinders. *Applied Ocean Research,* 19:83 – 99, 1997
[11] H. Santo, P. H. Taylor, A. H. Day, E. Nixon, Y. S. Choo. Current blockage and extreme forces on a jacket model in focussed wave groups with current. *Journal of Fluids and Structures*, 78:24 – 35, 2017
[12] M. Welzel, A. Schendel, A. Hildebrandt, T. Schlurmann. Scour development around a jacket structure in combined waves and current conditions compared to monopole foundations. *Coastal Engineering*, 152, 2019
[13] D. Rudolph, K. J. Bos, A. P. Luijendijk, K. Rietema, J. M. M. Out. Scour Around Offshore structures – Analysis of Fiel Measurements. *Proceedings of the Second International Conference on Scour and Erosion, ICSE 2, Singapore, 14-17 November 2004*
[14] D. Sumner. Two circular cylinders in cross-flow: A review. *Journal of fluids and structures,* 26:849 – 899, 2010

18th EAWE PhD Seminar on Wind Energy
2-4 November 2022
Bruges, Belgium

Development of Bluff Body Benchmark at high Reynolds numbers

S Breitkopf[a], **A Sander**[b,c], and **C Hartz**[a]

[a]TU Dortmund University, Chair of Structural Design, August-Schmidt-Str. 6, 44227 Dortmund, Germany
[b]Bremen University, BIK, Badgasteinerstr. 1, 28359 Bremen, Germany

E-mail: sophie.breitkopf@tu-dortmund.de

Keywords: supporting structure, fidelity, CFD, wind tunnel, best practices, engineering problem

Abstract

The Reynolds number still poses a significant challenge regarding the realistic evaluation of wind effects on slender supporting structures such as wind turbine towers. Nowadays either scaled wind tunnel tests or advanced CFD simulations can be used in engineering practice. The latter could theoretically reproduce the full-scale Reynolds number, but are still limited due to the required computing power. Reliable predictions and precise simulations of the turbine tower aerodynamics become even more necessary with increasing hub heights, to prevent turbine oscillations during installation or severe weather events.
Towards a better understanding of the currently achievable fidelity of wind simulations we propose a new method agnostic benchmark. It should merge progress in different bluff body aerodynamics related disciplines to judge the accuracy of existing best practices. The benchmark is based on a real engineering problem, instead of common academic examples. Thereby the required and achieved fidelity of the actual engineering problem at hand is considered. Another difference to existing benchmarks is the reduction of constraints for the applied methods. While a reduction in constraints may lead to an accumulation of errors, it will give relevant insight regarding the range of results for a qualitative comparison. The result of this research is the Bluff Body Benchmark.

1 Introduction

With the dawn of human flight, investigations into aerospace engineering through wind tunnels and later computational fluid dynamics (CFD) simulations began more than a century ago. Wind energy engineering has a historic close link to classical aerodynamics engineering due to how similar wind turbine blades and aeroplane wings work regarding shape and construction. When looking at supporting structures of wind turbines, however, the occuring phenomena are more commonly found in civil engineering. In civil engineering it took until the industrialization enabled more slender structures, that the relevance of wind effects on buildings was discovered. More so, reproducing the atmospheric boundary layer in wind tunnels took until the 1960s. At that time aerospace engineering already included CFD simulations in their design process.
Due to wind tunnels providing the foundation for most scientific findings regarding wind, they are still the most accepted and trusted means to determine the probabilistic wind effects on structures. The necessity of scaled models in the unadjusted air leads to multiple similarity constraints (among others: the Reynolds number and Strouhal number) that cannot be fulfilled simultaneously.
For CFD simulations, full-scale investigations are technically feasible if required computing power is available or a modelling approach, such as Reynolds-Averaged Navier Stokes (RANS), is chosen. An inverse relationship between modelling complexity and required computational resources severely restricts the application of CFD. In everyday engineering problems mostly RANS-based simulations are applied. Further challenges are — apart from the obvious question of how to deal with turbulence – accurate representation of the atmospheric boundary layer and the highly complex fluid structure interactions. With these limitations in mind, the question as to the currently achievable quality arises, when adhering to the current CFD best practice guidelines.
Thus far, evaluation of CFD model performance through benchmarks mainly focused on the precise flow at low Reynolds numbers around infinite cylinders under well-defined conditions. To judge the applicability of a given

CFD model for the actual design process, a real world engineering problem is required. To bridge this gap and to include the various methods throughout different fields (e.g. wind energy and wind engineering), we propose a new engineering driven benchmark.

2 Literature Review

A wide range of benchmarks already exist. While they first focused on wind tunnel studies (gray, e.g. [9], [7], [5],[6]), they were later also adapted to CFD studies (blue, e.g. [13], [15], [11]). There are still only a few benchmarks that intend to compare both approaches (green, e.g. [4]). Another issue is the low Reynolds number that is commonly used in CFD benchmarks or the common downscaling in wind tunnels. It is gradually increased to see how precise results are at those lower numbers. Figure 1 displays existing benchmarks and their currently covered Reynolds numbers. The covered range is far outside the interesting range for wind energy and wind engineering. Often benchmarks are run for infinite bodies (2D or 3D) instead of wall-mounted structures (see [11], [4]). It also has to be considered that many benchmark cases deal with only laminar flow (e.g. [13]). Benchmarks are often applied to evaluate the influence of the chosen grid for the CFD simulation (e.g. [3], [1]).
To fully judge the application and accuracy of a chosen method (such as CFD simulations or wind tunnel measurements) for an engineering problem, we propose a blind benchmark at a high Reynolds number for a wall-mounted finite cylinder under a typical turbulent atmospheric boundary layer condition with three different cross-sections. The parameters to be evaluated have to be chosen by relevance for the engineering problem. Therefore we propose integral values such as force and moment coefficients. This benchmark is from here on referred to as the Bluff Body Benchmark.

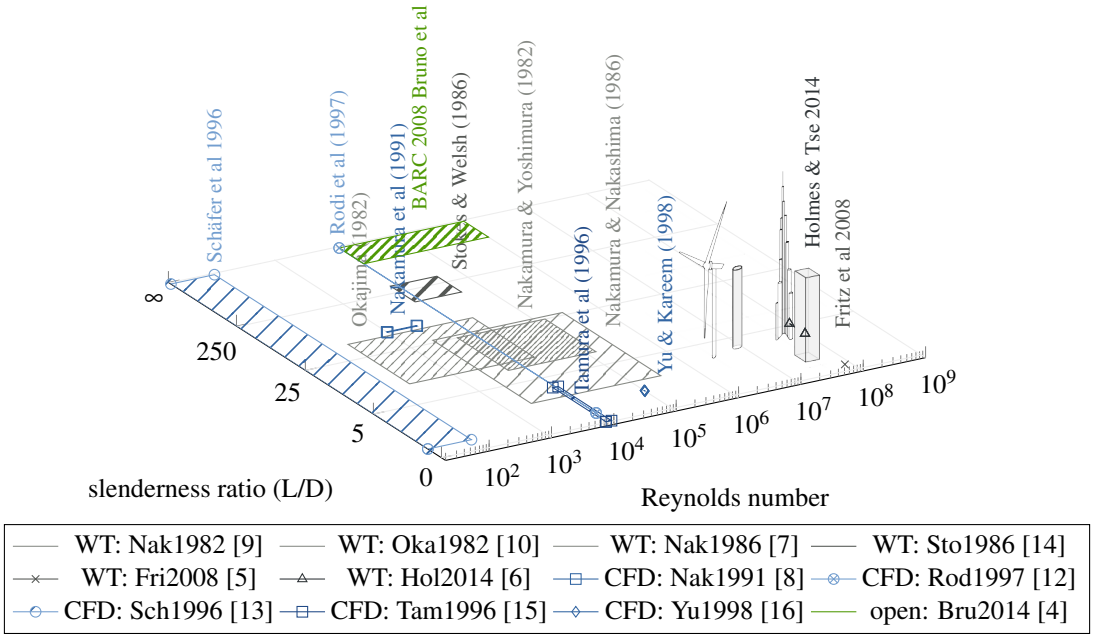


Figure 1: overview previous benchmarks for WT and CFD

3 Bluff Body Benchmark

The Bluff Body Benchmark was developed to test the range of results of available methods for a given engineering problem (see table 1). Representing a standard supporting structure (CAARC building), a freestanding building of 180 m height is chosen with a slenderness ratio of 6:1 (height:width). The relevant design factor are the horizontal wind loads. At the same time, the characteristics of the building are defined in such a way, that most codes can be covered. Three different cross-sections are compared: A square (1:1), a rectangle (2:1) and a circle. The wind conditions are based on a suburban terrain with a high 10-min-mean wind-speed (between zone III and IV for Japan, China, Europe, Canada, and Australia).
Simulations can be run for different levels of complexity, namely: the 2D cross-section of the building top or the

3D rigid model. As an outlook, a 3D aeroelastic model is included for the highly advanced participants. This allows to compare the accuracy and suitability of different methods for each level of complexity.
Table 1 also includes the recommended outputs based on typical values stated in wind tunnel reports for the design process. The values are obtained to the best of the knowledge of the participant, to display the qualitative range of results throughout current state-of-the-art approaches.

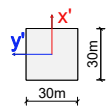
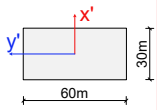
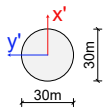
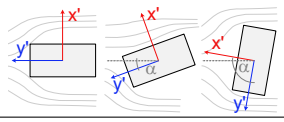
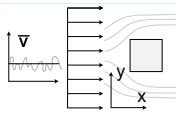
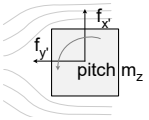
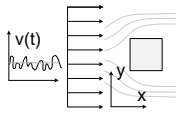
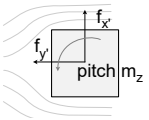
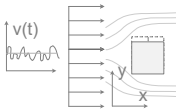
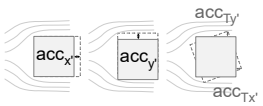
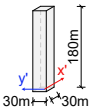
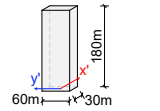
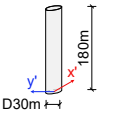
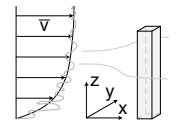
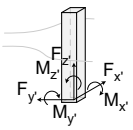
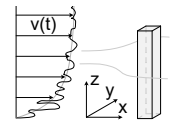
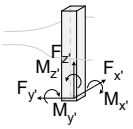
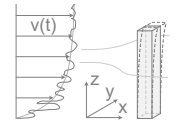
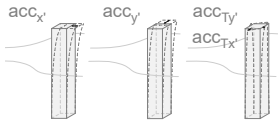
	INPUT	BLUFF BODIES			OUTPUT
2D	suburban ABL: $\bar{v}_{10}$= 27.5 m/s , z_0=0.3 m, ρ=1.25 kg/m^3 $\bar{v}(180m) = 40m/s$ $I_v(180m) = 0.148$				
	steady 				$\bar{x}$ 
	transient 				$\bar{x}$, peak, RMS 
	aeroelastic 				peak, RMS 
3D	suburban ABL: $\bar{v}_{10}$= 27.5 m/s , z_0=0.3 m, ρ=1.25 kg/m^3 $\bar{v}(z) = 0.77\bar{v}_{10}\left(\frac{z}{10}\right)^{0.22}$ $I_v(z) = 0.28\left(\frac{z}{10}\right)^{-0.22}$ $L(z) = 300\left(\frac{z}{300}\right)^{0.37}$				
	steady 				$\bar{x}$ 
	transient 				$\bar{x}$, peak, RMS 
	aeroelastic 				peak, RMS 

Table 1: Bluff Body Benchmark [2]

4 Conclusion

Existing benchmarks focus on specific methods in selected academic examples. This leaves little room to incorporate the participants' experience as the boundaries are defined in great detail. Also it lacks information regarding the current fidelity in applications for engineering problems.
We propose the Bluff Body Benchmark to compare the current best practices for the determination of wind loads

on bluff bodies on an international and interdisciplinary level. The authors believe that this new approach has to be undertaken to bridge the gap between wind tunnel and CFD simulations.

Acknowledgements

We want to thank all the people who already gave their valuable feedback on this benchmark idea. We also greatly appreciate the assured contributions.

References

[1] S. Breitkopf, C. Hartz, and S. Turek. On the influence of meshing regarding the accuracy of cfd simulations. In *17th EAWE PhD Seminar on Wind Energy*, pages 13–20, Porto, 2021. EAWE.

[2] S. Breitkopf and A. Sander. Bluff Body Benchmark. `https://bluffbodybenchmark.science/`, 2022. [Online; accessed 20.06.2022, 08:30].

[3] L. Bruno and D. Oberto. Effects of cell quality in grid boundary layer on the simulated flow around a square cylinder. *Computers & Fluids*, page 105351, 2022.

[4] L. Bruno, M. V. Salvetti, and F. Ricciardelli. Benchmark on the aerodynamics of a rectangular 5: 1 cylinder: an overview after the first four years of activity. *Journal of Wind Engineering and Industrial Aerodynamics*, 126:87–106, 2014.

[5] W. Fritz, B. Bienkiewicz, B. Cui, O. Flamand, T. Ho, H. Kikitsu, C. Letchford, and E. Simiu. International comparison of wind tunnel estimates of wind effects on low-rise buildings: Test-related uncertainties. *Journal of structural engineering*, 134(12):1887–1890, 2008.

[6] J. D. Holmes and T. K. Tse. International high-frequency base balance benchmark study. *Wind and Structures*, 18(4):457–471, 2014.

[7] Y. Nakamura and M. Nakashima. Vortex excitation of prisms with elongated rectangular, h and [vdash] cross-sections. *Journal of Fluid Mechanics*, 163:149–169, 1986.

[8] Y. Nakamura, Y. Ohya, and H. Tsuruta. Experiments on vortex shedding from flat plates with square leading and trailing edges. *Journal of Fluid Mechanics*, 222:437–447, 1991.

[9] Y. Nakamura and T. Yoshimura. Flutter and vortex excitation of rectangular prisms in pure torsion in smooth and turbulent flows. *Journal of Sound and Vibration*, 84(3):305–317, 1982.

[10] A. Okajima. Strouhal numbers of rectangular cylinders. *Journal of Fluid mechanics*, 123:379–398, 1982.

[11] W. Rodi. Large-eddy simulations of the flow past bluff bodies: state-of-the art. *JSME International Journal Series B Fluids and Thermal Engineering*, 41(2):361–374, 1998.

[12] W. Rodi, J. Ferziger, M. Breuer, M. Pourquie, et al. Status of large eddy simulation: results of a workshop. *Transactions-American Society of Mechanical Engineers Journal of Fluids Engineering*, 119:248–262, 1997.

[13] M. Schäfer, S. Turek, F. Durst, E. Krause, and R. Rannacher. Benchmark computations of laminar flow around a cylinder. In *Flow simulation with high-performance computers II*, pages 547–566. Springer, 1996.

[14] A. Stokes and M. Welsh. Flow-resonant sound interaction in a duct containing a plate, ii: square leading edge. *Journal of Sound and Vibration*, 104(1):55–73, 1986.

[15] T. Tamura, T. Miyagi, and T. Kitagishi. Numerical prediction of unsteady pressures on a square cylinder with various corner shapes. *Journal of Wind Engineering and Industrial Aerodynamics*, 74:531–542, 1998.

[16] D. Yu and A. Kareem. Parametric study of flow around rectangular prisms using les. *Journal of Wind Engineering and Industrial Aerodynamics*, 77:653–662, 1998.

18th EAWE PhD Seminar on Wind Energy
2 – 4 November 2022
Bruges, Belgium

Development of a database of offshore substructures for evaluating and prognosing the design quality of the structures using machine learning methods

Han Qian[a], Steffen Marx [a]

[a] TU Dresden, Institute of Concrete Structures, August-Bebel-Straße 30/30A, D-01219 Dresden, Germany
E-mail: han.qian@tu-dresden.de

Keywords: offshore substructure, design quality, database, machine learning, data points

1 Introduction

In comparison with building structures, the substructures of Offshore Wind Turbines (OWT) are unifunctional structures whose main task is to transfer loads. The structural design of OWT is generally based on explicit theoretical and practical knowledge as well as on the engineers' intuition. Therefore, the calculation methods for Offshore Substructures (OSS) have been developed over the past decades. The conventional methods for designing OSS are based on the structural assessments in ultimate limit states (ULS), fatigue limit states (FLS) and accidental limit states (ALS) [1], which only consider a small aspect of the life process of OWT, i.e. the operation phase. With the higher demands of power classes of OWT, there are more influence factors throughout the life cycle that determine the quality of structural design of OSS. Apart from the operation phase, the boundary conditions in the life phases of production, transport and installation also have enormous influences on the feasibility, economic efficiency and approvability of OSS [2]. Therefore, large amounts of design data are required in the integrated design process, e.g. structural data, site conditions, information of transport and installation vessels, information of rotor-nacelle-assembly (RNA) and tower, etc.
With the rapid development of Artificial Intelligence (AI) technologies, Machine Learning (ML) algorithms shows advantages in handling large amounts of data in multi-dimensions and can identify the complex internal relationships between features [3]. In order to accumulate the design data and apply experience from existing OWT projects as well as the intuitions of engineers in the field of offshore wind industry, it is thus meaningful to develop a data-based ML model to evaluate the design quality of OSS. The current work focuses on the first step for developing the ML model, which is to create a database of existing OSS in different wind farms around the world and to augment the database with new realizations based on the existing design data of OSS. Furthermore, the data point for each OSS designs will be generated for holistic evaluations from experts and engineers in this field. The evaluation outputs should be in the form of quality level or score for each OSS design and used as labels in the database.

2 Overview of database and improvement

According to the systematic analysis of the life process of OSS, the main influence factors for designing OSS in different life phases are parameterized and classified. The basic structure of the database is represented in Table 1. The structural members consist of RNA, tower and OSS. The structural parameters are organized in the corresponding sections. In addition, all other features from different life phases are collected in the sections of additional info, which include environmental conditions, vessels of transport and installation, etc. In this case, the identical features existing in different life phases, such as environmental conditions, will be integrated into the same sections of additional info, which avoids oversized database that seriously impacts the computing efficiency in ML models.

Table 1: Basic structure of database

	Structure Member 1			Structure Member 2			...	Additional Info I			Additional Info II			…
	Feature 1.1	…	Feature 1.m	Feature 2.1	…	Feature 2.n	...	Feature I.1	…	Feature I.x	Feature II.1	…	Feature II.y	…
Dataset 1														
Dataset 2														
Dataset ...														
Dataset i														

Regarding the data resource used for populating the OSS database, there already exist several online platforms contributing to the creation of accessible OWT databases. A good reference database is from 4Coffshore, in which most of the relevant design inputs are involved. However, there are two main issues on reference database. On the one hand, the collected data are not full, especially the structural data of OSS, i.e. the datasets are incomplete due to the missing data. On the other hand, the data structure in reference database is usually imbalanced and doesn't consist many different or complete instances. The main reason is that the most common type of OSS in offshore wind industry is the monopile due to its sophisticated manufacturing and construction techniques. Then the jacket holds the second largest market share, but still well below the monopile.
In order to train and test ML models in next research stage, a new database with the structure shown in Table 1 should be developed and improved based on the raw data from reference database. To solve the first problem on the missing data, some ML methods can be leveraged to identify the correlations between features and missing data, and to fill in the missing data, e.g. Gaussian process regression (GPR), artificial neural network (ANN), etc. The general work flow is shown in Figure 1.

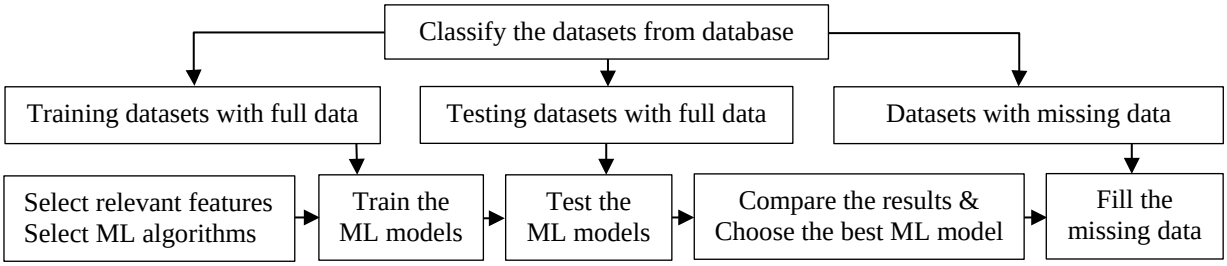


Figure 1: Work flow for filling the missing data

Regarding the second issue about the imbalanced data structure, the database will be extended with synthetic datasets, i.e. new realizations of OSS based on the existing designs of OSS. For this purpose, the generative AI algorithms can be used in the structural design and optimization of the structure [4]. In this work, a platform for generating new realizations is to be developed, and the non-dominated sorting genetic algorithm (NSGA-II) is used for multi-objective optimization [5].

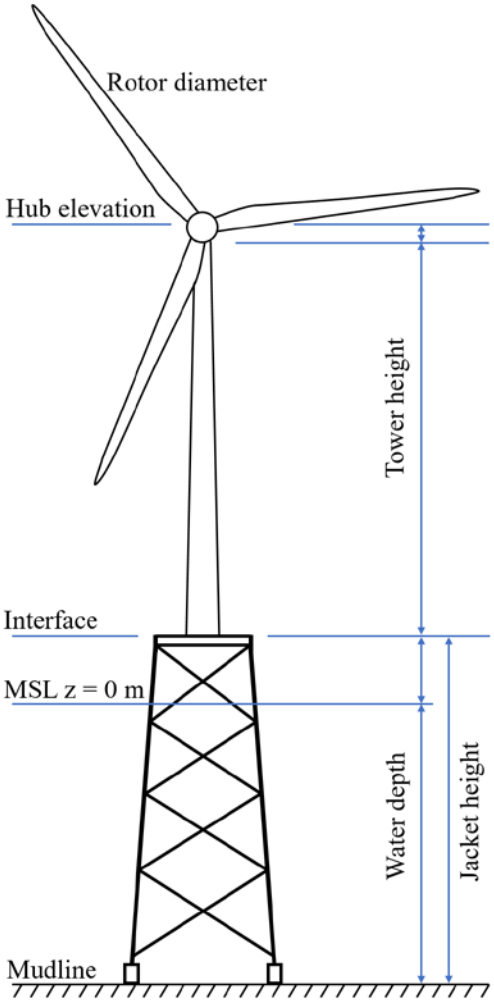
3 Creation of data points for evaluation

Due to the high number of realized and created OSS datasets as well as large amounts of features in each dataset, it is a challenging task for experts to perform holistic assessments for all datasets. In order to simplify the evaluated objects based on datasets and improve its visibility, the creation of data points is crucial for the generation of evaluation labels. The data point for each realization includes the representative features in sections of the corresponding dataset. The selection of features is determined with the help of expert knowledge in civil engineering and feature engineering [6]. In addition, a 2D schematic diagram of the OWT with necessary dimensions for each data point plays an important role in visualization of the realization. One sample of the data point is shown below:

RNA:
- Rated power [MW]
- Hub elevation [m]
- Rotor diameter [m]
- Rotor weight [t]
- Number of blades [-]
- Blade length [m]
- Blade type [-]
- Blade weight [t]
- Nacelle height [m]
- Nacelle length [m]
- Nacelle width [m]
- Nacelle weight [t]

Tower:
- Total weight [t]
- Total height [m]
- Top/base elevation [m]
- Top/base diameter [m]
- Wall thickness [m]
- Material [-]

Substructure, e.g. jacket:
- Total weight [t]
- Total height [m]
- Top/base width [m]
- Layer number [-]
- Cross-sections
- Material [-]



Site conditions:
- Water depth [m]
- Wind shear [m/s] (10 m – 200 m)
- Wind direction [°]
- Wave height [m] (wind & swell)
- Wave period [s] (wind & swell)
- Surface temperature [°C]
- 2-m air temperature [°C]
- Sea-level pressure [hPa]
- 2-m relative humidity [%]
- Total precipitation [mm]
- Scour depth [m]

Transport & installation:
- Port location [-]
- Vessel type [-]
- Vessel length [m]
- Operational limits:
  - Max. water depth [m]
  - Max. wind speed [m/s]
  - Max. wave height [m]
  - Max. tide [m/s]
- Jack-up capacities
- Lift capacities

Other additional info i:
- …
- …
- …
- …
- …
- …

Quality level	Very good						Very bad	Comments:

Figure 2: Sample of the data point for a realization

The experts will evaluate the realizations of OSS according to the data points and grade the design quality level for each OSS with their experiences and intuitions, as shown in the bottom block of Figure 2. The design quality levels will be extracted as labels for datasets. In this case, the entire database of OSS will be completed and utilized for further supervised learning modelling.

4 Future research

In the future research, several ML algorithms for classification will be implemented using the database with evaluation labels, e.g. logistic regression, Bayesian networks, support vector machine and decision tree [7]. The overall objective of the ML model is to predict the holistic design quality of new OSS with different design variants and to extend the design space to the entire life cycle of the structure.

Acknowledgements

This work was funded by German Research Foundation (Deutsche Forschungsgemeinschaft, DFG) – Collaborative Research Centre 1463 (CRC 1463) – Subproject B01. This financial support is gratefully acknowledged. The author would also like to thank the partners within the project.

References

[1] Veritas, D. N. 2014. DNV-OS-J101-Design of offshore wind turbine structures.
[2] Seidel, M. 2010. Design of support structures for offshore wind turbines–Interfaces between project owner, turbine manufacturer, authorities and designer. Stahlbau, 79(9), 631-636.
[3] Zaki, M. J., & Meira Jr, W. (2020). Data mining and machine learning: Fundamental concepts and algorithms. Cambridge University Press.
[4] Sbai, O., Elhoseiny, M., Bordes, A., LeCun, & Y., Couprie, C. (2019). DesIGN: Design Inspiration from Generative Networks. In: Leal-Taixé, L., Roth, S. (eds) Computer Vision – ECCV 2018 Workshops. ECCV 2018.
[5] Deb, K., Pratap, A., Agarwal, S., & Meyarivan, T. A. M. T. (2002). A fast and elitist multiobjective genetic algorithm: NSGA-II. IEEE transactions on evolutionary computation, 6(2), 182-197.
[6] Dong, G., & Liu, H. (Eds.). (2018). Feature engineering for machine learning and data analytics. CRC Press.
[7] Neelamegam, S., & Ramaraj, E. (2013). Classification algorithm in data mining: An overview. International Journal of P2P Network Trends and Technology (IJPTT), 4(8), 369-374.

18th EAWE PhD Seminar on Wind Energy
2 – 4 November 2022
Bruges, Belgium

Geological considerations for offshore wind foundations at "Sørlige Nordsjø II", Norwegian North Sea

Hannah E. Petrie [a], **Christian H. Eide** [a], **Haflidi Haflidason** [a]

[a] University of Bergen

E-mail: hannah.petrie@uib.no

Keywords: geology, geotechnics, offshore wind, North Sea

1. Introduction

A better understanding of how offshore wind turbine foundations interact with geological substrates is required to optimize their design and reduce costs. An important component of this will come from developing a more detailed geological and geotechnical understanding of the foundation substrates within new offshore wind areas. The Norwegian North Sea represents a new area for the development of offshore wind, with two >1000 km^2 sites announced in 2020 and a recent government announcement signalling plans to develop 30 GW of offshore wind capacity by 2040. In this study, we focus on the geological conditions at the Sørlige Nordsjø II (SNII) site, located 140 km offshore, along the southern border of the Norwegian North Sea. Here the water depths range from 50-70 m: extending beyond the maximum depth of any bottom-fixed offshore wind farm developed to date. For this reason, a detailed understanding of possible design challenges relating to the geological substrate will be particularly important at SNII. During the Quaternary period (<2.6 million years ago), the southern North Sea was occupied repeatedly by icesheets, glacial outwash plains, and a moving coastline dictated by changing sea level. As a result, the distribution, thickness, and geotechnical properties of the soil units present within the shallow subsurface (<50-100 m) can vary significantly from one foundation location to another. The aims of this contribution are therefore to 1) present the preliminary results from a newly acquired geological dataset from SNII, and 2) to define key geological units within the shallow subsurface and their implications for site survey planning, foundation design and installation at SNII.

2. Methods and Data

In this study we combine an overview of previous knowledge about the geological history of the southern North Sea with observations from bathymetric data, 2D and 3D seismic data, and sub-bottom profiles and shallow cores collected from SNII in June 2022 by the University of Bergen. The preliminary geological interpretations from these data are integrated to define a conceptual geological model for SNII, which divides the upper 50 m of the stratigraphy into geological units likely to have contrasting geotechnical properties and implications for foundation design.

2D and 3D seismic data were sourced from the Norwegian National Data Repository for Petroleum Data (surveys DG15001, MC3D-NDB2008 and ST99M1-AREA 3) and PGS Geophysical AS (survey MC3D-NDB2013) (Fig. 1b). The seabed reflection was interpreted, and depth converted using a seismic velocity of 1500 m/s (average P-wave velocity of seawater). The depth converted surfaces were then used to identify geomorphic features on the seabed and compared with the geomorphology of the wider region on bathymetric maps [1] (Fig. 1a). Seismic variance and amplitude attribute extractions were made for the seabed surface, and for time slices below seabed, to identify buried features and those with a subtle surface expression. The features identified on the seismic data were then targeted for further investigation during a University of Bergen marine geological cruise on the R/V G.O. Sars in June of this year. This included collecting parametric sub-bottom profiles with the Kongsberg TOPAS PS18 sonar system and vibro-cores collected with the Geo-Corer 6000 High Frequency Vibro Core System at various locations across the site (Fig. 1c). In total, 900 km of sub-bottom profiles and 13 vibro-cores (total combined length 67 m) were collected within the upper 6 m of the subsurface. These are currently undergoing sedimentological analysis, multisensor core-logging and planning for geotechnical analysis. The sub-bottom profiles are being interpreted in the seismic interpretation software Petrel to map out the distribution and thickness of the distinguishable seismic units (e.g., Figs. 2a, 2b). The sub-bottom profiles give an approximately ten-fold increase in resolution across the geomorphological features identified on the 3D seismic (25 cm vs~25 m), allowing a more thorough investigation of the stratigraphic architectures within the different features. During the cruise, each of the seismic units were sampled by the vibro-corer to investigate the sedimentological and geotechnical properties of the unit and thus the implications for offshore wind foundation design and site survey planning.

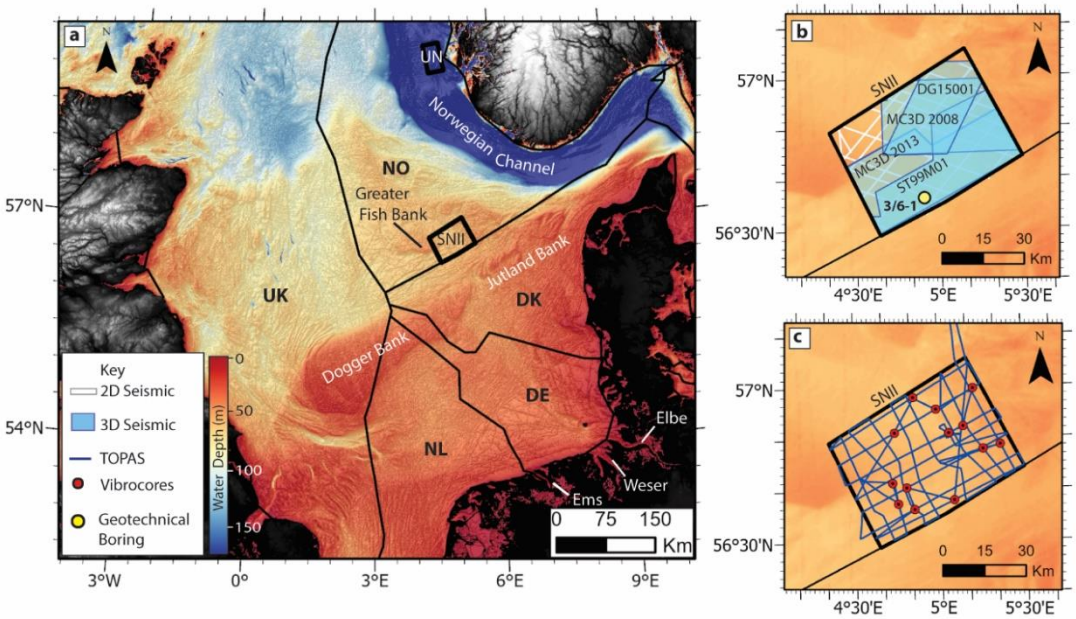


Figure 1: (a) Locations of announced Norwegian offshore wind sites Utsira Nord (UN) and Sørlige Nordsjø II (SNII). Bathymetry (seafloor depth map) [1], (b) existing 2D and 3D seismic data at SNII and geotechnical boring 3/6-1 [2], c) newly acquired vibro-core and sub-bottom profiler (TOPAS) data at SNII, collected by University of Bergen.

3. Results

SNII can be divided into two provinces (Fig. 2): a shallow (~ 50 m deep) eastern province characterized by mounded and ridge-like features on the seabed comprising mud, sand, gravel and boulders, and a 50-70 m deep western province with a smooth seabed consisting of sand to gravelly-muddy sand ([3]) (Fig. 2). The mounds and ridges in the eastern province are related to a chaotic seismic unit consisting of multiple generations of sediment deposition and valley incision (Unit 5, Fig. 2b), interpreted as a remnant glacial landscape comprising glacitectonized (glacially deformed) sediments. This unit is often exposed at the seabed in the eastern part of SNII but is locally covered by a transparent seismic unit with a smooth surface, interpreted as post-glacial marine sand (Unit 1a, Fig. 2b). In the western province, Unit 5 is overlain by several different seismic units whose thickness and distribution vary laterally. The oldest of these (Unit 4, Figs. 2a, 2d) is a flat-lying to deformed, layered unit which infills lows in Unit 5, which likely represents glacimarine to marine sands from the previous interglacial period (the Eemian). In the south-western part of the site, Unit 4 is locally incised and infilled by a transparent seismic unit (Unit 3, Fig. 2a) which likely correlates with the stiff to hard glacilacustrine clays assigned a Weichselian age (the last glacial period) within boring 3/6-1 (Fig. 1b, [2]). Within southern and central parts of the site, incisions, and depressions within Units 4 and 5 are infilled by a seismic unit with medium to high amplitude, inclined internal reflections (Unit 2, Figs. 2a, 2d), indicating a layered sedimentary deposit likely of fluvial origin. Along the boundary between the western and eastern provinces, Unit 2 sediments appear to have been disturbed by an overlying low to medium amplitude, layered, seismic unit (Unit 1b, Figs. 2b, 2d), interpreted as shallow marine sediments deposited as sea level began to rise after the last glaciation. Unit 1b is onlapped in turn by a transparent seismic unit (Unit 1a) interpreted as open marine sediments deposited as the area became fully submerged by the North Sea.

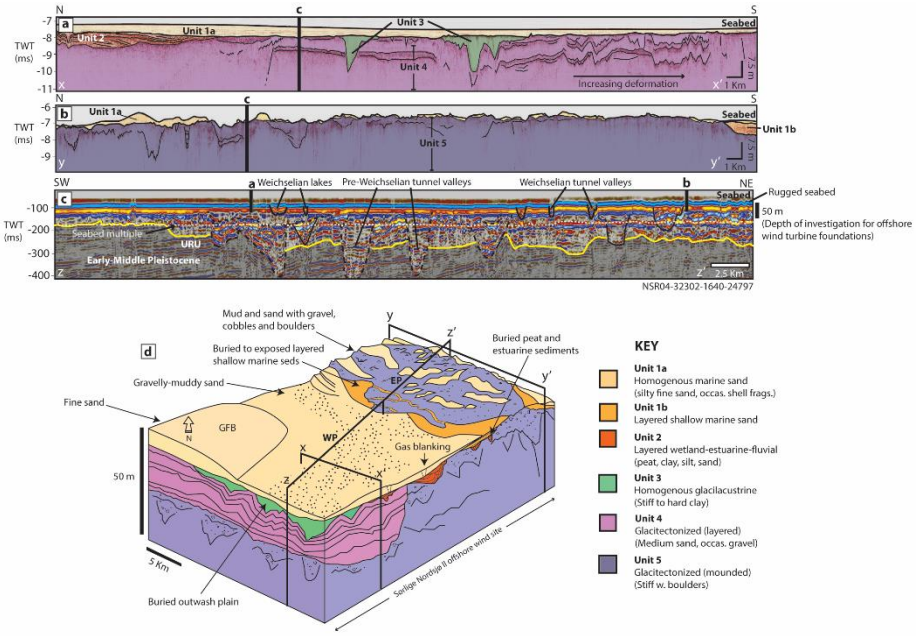


Figure 2: (a) Sub-bottom profile from western SNII, (b) Sub-bottom profile from eastern SNII, (c) 2D seismic section across SNII showing the deeper subsurface stratigraphy, (d) Conceptual geological model for SNII showing key geological units. GFB, Greater Fish Bank; WP, Western Province; EP, Eastern Province.

4. **Discussion**

The next phase of this project will focus on evaluating the sedimentological and physical properties of geological Units 1-5, and the implications of their distribution and thickness for offshore wind foundation design. Key factors to be investigated include: 1) the stiffness of glacitectonized Unit 5, given that it has likely been compressed by ice during both the Weichselian and Saalian glacial periods, 2) the geotechnical properties of sandy Unit 4, 3) the stiffness of localised Unit 3 and whether the contrasting properties of Units 3,4 and 5 are likely to cause any foundation challenges, 4) the sedimentology and geotechnical properties of estuarine Unit 2 and whether these deposits present any risks to site survey operations such as use of jack-up rigs. Remaining uncertainties which cannot be addressed in this study but are recommended as follow up topics for full-scale site surveying of SNII include 1) in-situ and geophysical investigation of Unit 5 to determine whether boulders are widespread or rare in occurrence, 2) soil scour evaluation for surficial sand Units 1a and 1b for the foundation type chosen.

5. **Conclusions**

The conceptual geological model presented in this study defines five geological units: 1) homogeneous and layered marine sands covering most of the site, with patchy distribution in the east, 2) buried estuarine channel deposits common within central and southern parts of the site, containing organic material and associated biogenic gas, 3) buried, stiff, glacilacustrine clay deposits, 4) buried, layered, glacitectonized glacimarine-marine sands and 5) mounded glacial tills/glacitectonized deposits containing boulders, exposed in the east. The next phase of the project will focus on investigating the sedimentological and geotechnical characteristics of the defined geological units through core analysis and comparison to correlatable units within other sectors of the southern North Sea.

Acknowledgements

This study is part of a PhD project funded by the Akademia Agreement at the University of Bergen. Many thanks to the scientific and technical crew who worked on the GS22-241 cruise on R/V G.O. Sars to collect the data for this project. Schlumberger is acknowledged for an academic license of Petrel, which was used for seismic interpretation.

References

[1] General Bathymetric Chart of the Oceans, 2020. GEBCO_2020 Grid. Available online: https://www.gebco.net/data_and_products/gridded_bathymetry_data/gebco_2020/ [last accessed 1 March August 2021].

[2] Fugro, 2000. Soil investigation and spud can penetration analysis, Transocean Nordic jack-up rig, Block 3/6, Norwegian Sector, North Sea. Report no. 03319-2.

[3] Norwegian Geological Survey, 2022. Marine Maps: Seabed sediments (grainsize). Available online: https://geo.ngu.no/kart/marin_mobil/ [last accessed 12 August 2022].

18th EAWE PhD Seminar on Wind Energy
2 – 4 November 2022
Bruges, Belgium

Numerical study on the effect of pitting corrosion on the fatigue strength degradation of offshore wind turbine sub-structures using a short crack model

S. A. Elahi, F. Mehri Sofiani, S. Chaudhuri, W. De Waele

Department of EMSME, Laboratory Soete, Faculty of Engineering and Architecture, Ghent University, Technologiepark 46, BE-9052, Zwijnaarde

E-mail: SeyedAhmad.Elahi@Ugent.be

Keywords: Offshore wind turbines; Corrosion-fatigue; Short crack model; Fatigue

Steel support structures of offshore wind turbines (jackets and monopiles) undergo both fatigue and corrosion damage, impacting their lifetime. Due to the time-variant uncertainties associated with environmental and mechanical loads, having reliable models that allow to predict the degradation due to corrosion and fatigue is necessary to accurately assess the structural integrity and to support decision making.

Three Belgian universities (UGent, ULiege and VUB) and a collective center (Sirris) work together in the context of the ETF-funded project MAXWind to enhance the corrosion-fatigue analysis of offshore wind turbine support structures. The following objectives have been assigned to UGent:

1 Development of an advanced corrosion-fatigue model to analyze the interactive effects of corrosion and fatigue load on the lifetime of offshore wind turbine sub-structures.
2 Development of smart S-N curves that take into account the level of corrosion damage to predict the remaining lifetime.

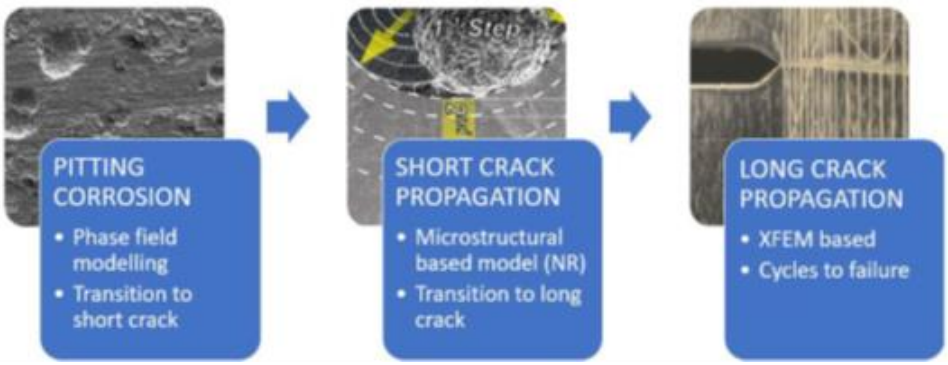


Figure 1: Workflow of an integrated corrosion-fatigue model

According to Figure 1, the first objective necessitates the development of models for pitting corrosion, short crack propagation and long crack propagation. Integrating the models at these three levels should allow the prediction of the total lifetime of a structure and to develop the aforementioned smart S-N curves.

In this particular research, a microstructure-based model based on the work of Navarro and de los Rios (NR model) [1] is used to simulate the short crack propagation regime. The NR model represents

the crack and microstructural barriers by means of the distributed dislocation technique. It uses the Kitagawa-Takahashi diagram [2] to account for the effect of the environment on the resistance of the material to crack propagation. The model is based on a 2D representation of the pit (its cross-section) and on the assumption that the short crack emanates from the bottom of the pit.

Available field data [3] of maximum pit depth in structural steel coupons exposed to North Sea conditions for 2.6, 4.0 and 7.2 years have been analysed to determine the pit depth growth rate. A second set of data [4] on pit shape and dimensions following 1.9 years of exposure of S355 steel coupons to the North Sea environment is utilized to define a relation between pit depth and pit width. According to these data, the cross-section of the corrosion pits have, on average, a semi-elliptical shape with a maximum depth growth rate of 0.409 mm/year. The derived relation between the pit depth (α in mm) and width (2β in mm) is $2\beta = 2.2\alpha + 1.062$. The following material parameters are needed as input to the model and have been derived from literature [5]: fatigue limit in air (200 MPa), threshold stress intensity factor (12 MPa$\sqrt{m}$), Young's modulus (210 GPa), Poisson's ratio (0.29) and grain size (10 μm).

Having the pit shape evolution during the exposure time to the sea environment and using the short crack model, the degraded fatigue strength of the material (i.e., the stress level below which there will be no propagating crack in the material) because of pitting corrosion is determined. Figure 2 shows the calculated decrease in fatigue strength of S355 steel due to corrosion pit evolution representative of the North Sea environment. It is observed that degradation occurs faster in the early years of exposure, with subsequent convergence of fatigue strength to around 40% of the initial fatigue strength value for the considered case.

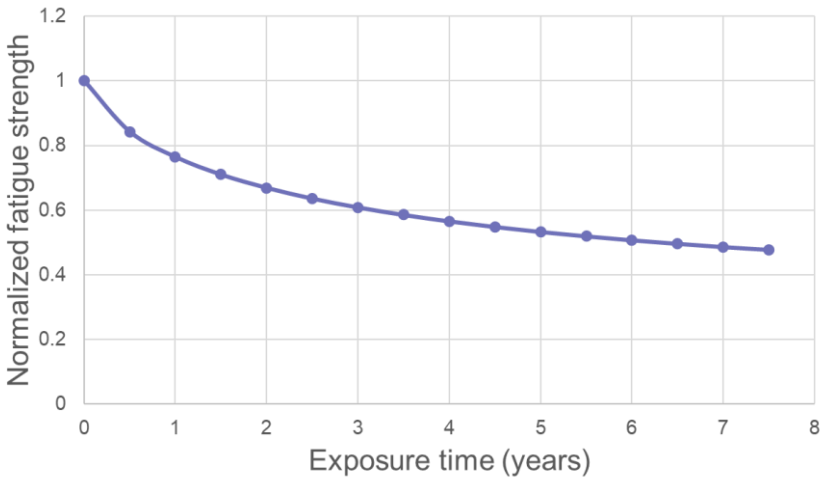


Figure 2: Fatigue strength degradation of structural steel S355 due to exposure to the seawater environment

Figure 3 shows the concept of the so-called smart S-N curve. The upper blue line shows the ultimate tensile strength (UTS) which is considered constant and therefore does not change as the exposure time increases. The fatigue strength degradation shown in Figure 2 corresponds to the lower blue line in Figure 3 where the knee-point of the red curve (no exposure) is taken at 10^7 cycles.

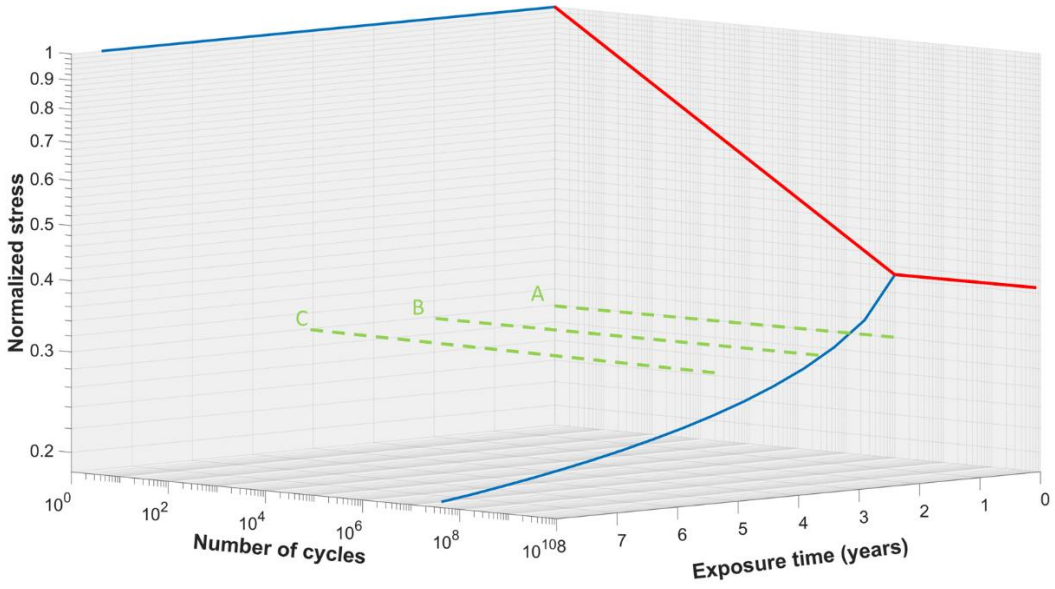


Figure 3: Smart S-N curve displaying the location of the fatigue strength line

A constant normalized applied stress value equal to 0.3 is considered as an example. For an exposure time equal to zero (line A), this value is less than the normalized fatigue limit value (which is around 0.4). This means that there will be no growing short cracks and consequently no damage accumulation in the structure. However, pitting corrosion causes the fatigue strength to degrade as the exposure time increases. As soon as the fatigue strength value reaches to the applied stress value (line B), which occurs in the given scenario after two years of exposure, the interaction of cyclic stress and pitting corrosion will result in damage accumulation. For even longer exposure times (line C), the level of degradation due to corrosion increases which leads to a larger amount of damage caused by each loading cycle.

In future work, the corrosion fatigue model will be enriched by also including crack growth. This will allow to estimate the remaining fatigue life of offshore wind turbine sub-structures after being exposed to the marine environment for a given amount of time using the novel idea of the smart S-N curve. It can support decision making activities, i.e., definition of optimized inspection and maintenance plans, and finally have an impact on reducing energy production expenses.

Acknowledgements

The authors would like to acknowledge the financial support of the Belgian Federal Government through the Energy Transition Fund (ETF).

References

[1] A. Navarro and E. R. De los Rios, “Short and long fatigue crack growth: A unified model,” *Philos. Mag. A*, vol. 57, no. 1, pp. 15–36, 1988, [Online]. Available: https://www.tandfonline.com/doi/abs/10.1080/01418618808204496.

[2] H. Kitagawa and S. Takahashi, “Applicability of fracture mechanics to very small cracks or cracks in the early stage,” in *Proceeding of the second international conference on mechanical behavior of materials*, 1976, pp. 627–631.

[3] F. Blekkenhorst, G. M. Ferrari, C. J. Van Der Wekken, and F. P. Ijsseling, “Development of

high strength low alloy steels for marine applications : Part 1 : Results of long term exposure tests on commercially available and experimental steels," *Biritish Corros. J.*, vol. 21, no. 3, pp. 163–176, 1986, doi: 10.1179/000705986798272136.

[4] C. Vanden Haute and P. Thibaux, "Quantification of pitting and stress concentration factors on steel coupons exposed to seawater in the north sea," in *Proceedings of the ASME 2022, 41st International Conference on Ocean, Offshore and Arctic Engineering OMAE2022*, 2022, pp. 1–7.

[5] S. Anandavijayan, A. Mehmanparast, J. Braithwaite, F. Brennan, and A. Chahardehi, "Material pre-straining effects on fatigue behaviour of S355 structural steel," *J. Constr. Steel Res.*, vol. 183, p. 106707, 2021, doi: 10.1016/j.jcsr.2021.106707.

18th EAWE PhD Seminar on Wind Energy
2 – 4 November 2022
Bruges, Belgium

Sensitivity of Monopile Response to Scour: a laboratory case study

A Fernandes[a], **C Sastre Jurado**[ab], **W Weijtjens**[a], **B Stuyts**[ab], **C Devriendt**[a]

[a] Vrije Universiteit Brussel (VUB)/Offshore Wind Infrastructure-lab (OWI-lab)
[b] UGent, Geotechnical Laboratory, Technologiepark 68, Zwijnaarde, 9052, Belgium

E-mail: Adelmo.Fernandes@vub.be

Keywords: instrumentation, piles, soil-structure interaction, scour

1. Introduction

Inside the scope of the BOPTIC and Soiltwin projects, the Offshore Wind Infrastructure-lab (OWI-lab) is conducting research on offshore wind foundation behaviour to understand what is causing the mismatch between the design resonance frequencies values and in field measured resonance frequencies of offshore wind structures supported by monopiles. A better understanding of the bending strains along the monopile is also a concern of these two projects. In order to tackle these objectives, OWI-Lab has developed a testbed in order to test monopile models instrumented by state-of-the-art sensors that can perform dynamic and quasi-static tests. The testbed consists of an 1x1x1m box made by acrylic filled with sand from North Sea and supported by aluminium profiles. The testbed can perform quasi-static tests by applying loads using weights, Figures 1(a). The monopile was instrumented by optical strain sensors, displacement laser sensors, load cells, temperature sensors, and LVDTs. Some preliminary results of a quasi-static test campaign of bending moment measurements of various scour configurations are also presented. Figure 1(b) presents one of the local scour configuration and Figure 1(c) presents a global scour configuration.

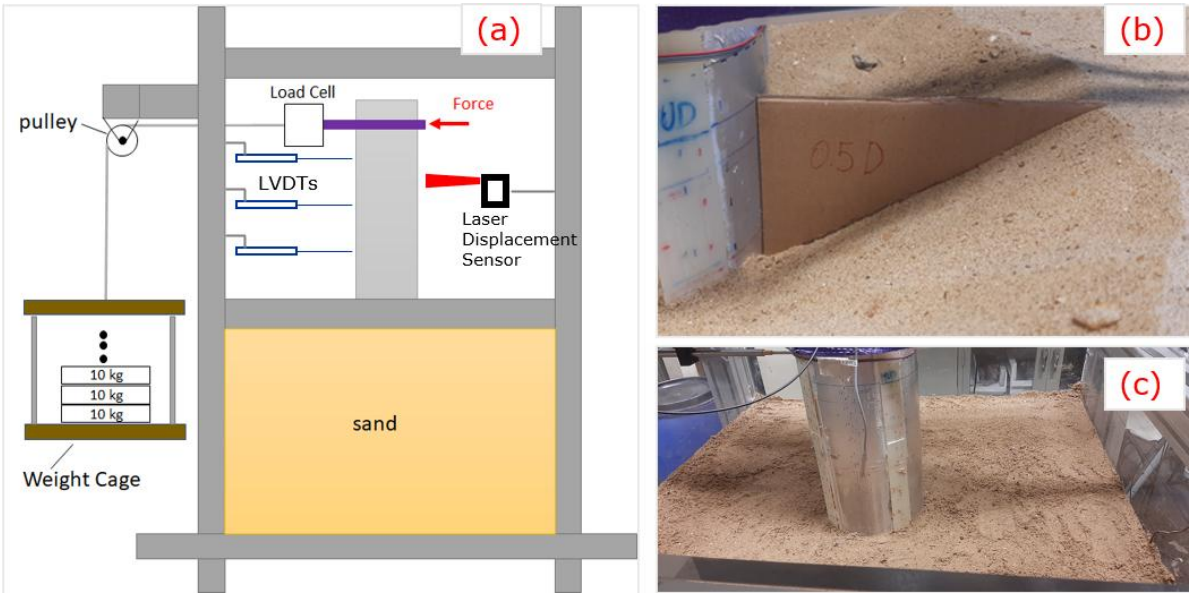


Figure 1 (a) Illustration of the testbed in quasi-static configuration. (b) 0.5D local scour configuration. (c) 0.75D global scour configuration.

2. Methodology

An aluminium pipe of 200mm (outer diameter), 5mm in wall thickness and 1.800mm length was used as the monopile model. It was instrumented with two types of fibre optics strain sensors (FBG and OFDR) along its length in four different heads 90º apart from one another. The monopile model was driven into the sand by hammering it on top. The total embedded length was 800mm. The force was applied on the top of the monopile with gradual increasing by adding weight disks, and measured by a loadcell, see Figure 1(a). Three conventional displacement sensors (LVDTs), as well as one laser displacement sensor, were installed along the monopile model's length left out of the sand. Table 1 presents a summary of the test protocol used in the test campaign. In total, there are 9 configurations of scour, 6 local scour (LS), 1 global scour (GS) and 1 global plus local scour (GLS). Apart from these configurations, there are one configuration named no scour which represents the virgin mud line configuration.

Table 1 summary of the test protocol used during the test campaign.

Scour Config.	Load Duration (min)					# of Tests
	200N	300N	400N	500N	600N	
No scour	1	2	4	6	15	3
0.2D LS	1	2	4	6	15	3
0.3D LS	1	2	4	6	15	3
0.4D LS	1	2	4	6	15	3
0.5D LS	1	2	4	6	15	3
0.6D LS	1	2	4	6	15	3
0.75D LS	1	2	4	6	15	3
0.75D GS	1	2	4	6	15	3
0.75D GLS	1	2	4	6	15	3

3. Results and Discussion

Figures 2(a) and 2(b) present the bending moment profiles due to a 600N force for various scour configurations measured by the FBG and OFDR DAQ systems, respectively. It was noticed, for this configuration, a variation on the bending moment profile for scour configuration as shallow as 0.2D for the FBG strain sensors. Figure 2 (c) presents the displacement on the top of the monopile model where it can be noticed an exponential increase of the displacement as we increase the scour depth. In the same Figure, it can also be noticed an increase of variation in the measurements as we increase the scour depth. Figure 2 (d) presents an attempt to quantify thresholders, in terms of percentage, for different amount of scour. The big variation is explained by the fact that all sensors were considered, and as can be noticed from Figures 2(a) and 2(b), there are sensors more sensitive than others.

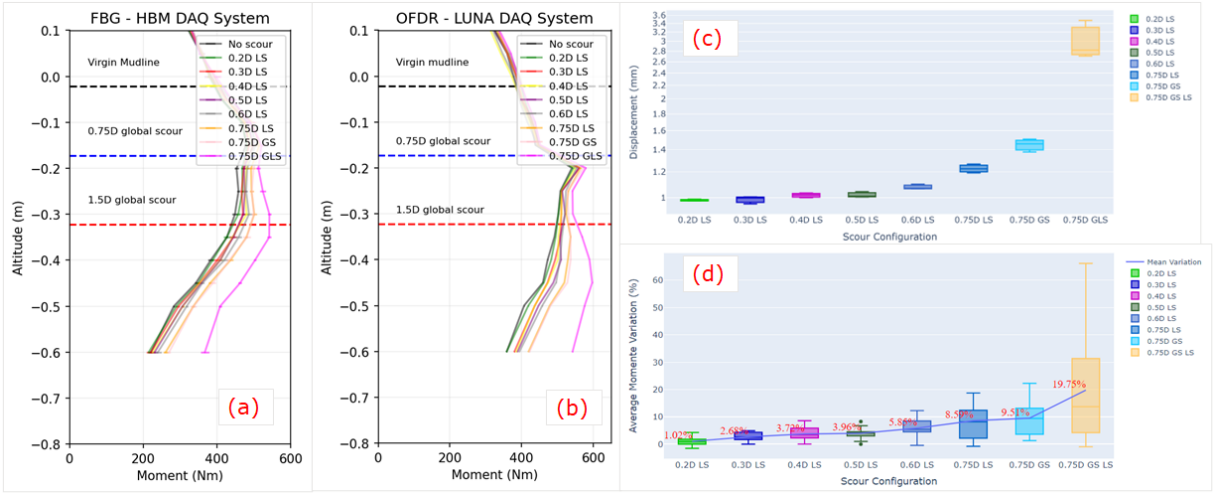


Figure 2 (a) Test of the pneumatic actuator in the reaction frame. (b) Simulate test of a monopile model.

4. Conclusion

This paper presented the testbed used to perform dynamic and quasi-static tests and its major characteristics. The mains focus was to show and discuss the preliminary results of a bending moment measuring campaign for various scour configurations. The experiment was able to detect variation on the bending moment profile for a minimum local scour configuration of 0.2D for a load of 600N. Measured pile displacements also incresed with scour. Finally, an attempt to define thresholders for different amounts of scour was presented.

Acknowledgements

The current research is conducted in the frame of the "*cSBO SOIL-TWIN: data driven design optimization and smart monitoring of monopile*" and "BOPTIC".

Bibliography

[1] Abadie, C. N., B. W. Byrne, and S. Levy-Paing. 2015. "Model pile response to multi-amplitude cyclic lateral loading in cohesionless soils." In Int. Symp. on Frontiers in Offshore Geotechnics, 681–686. London: CRC Press

[2] Albiker, J.; Achmus, M.; Frick, D. 1 g Model tests on the Displacement Accumulation of Large Diameter Piles under Cyclic Lateral Loading. Geotech. Test. J. 2017, 40, GTJ20160102

[3] Roesen HR, Ibsen LB, Andersen LV. "Experimental testing of monopoles in sand subjected to one-way long-term cyclic lateral loading."In: Proceedings of the 18th International Conference on Soil Mechanics and Geotechnical Engineering. Paris: Presses des Ponts; 2013. p. 2391–4.

[4] Mayall, R. O., et al. "Experimental modelling of the effects of scour on offshore wind turbine monopile foundations." Physical Modelling in Geotechnics. CRC Press, 2018. 726-730.

[5] Li, Q., Li, Q., Prendergast, L. J., Askarinejad, A., Chortis, G., & Gavin, K. (2020). "Centrifuge modeling of the impact of local and global scour erosion on the monotonic lateral response of a monopile in sand." Geotechnical Testing Journal, 43(5), 20180322.

18th EAWE PhD Seminar on Wind Energy
2-4 November 2022
Bruges, Belgium

The Effect of Varying Soil Properties on the Probability of Unsatisfactory Performance of Offshore Monopile Foundations

Olgu Orakci[a], **Nejan Huvaj**[b,c], **Stijn François**[d], and **George Anoyatis**[a]

[a]KU Leuven, Department of Civil Engineering, Spoorwegstraat 12, Sint-Michiels, Campus Bruges, 8200,Belgium
[b]Middle East Technical University, Department of Civil Engineering, Ankara, 06800, Turkey
[c]Middle East Technical University Center for Wind Energy Research (RÜZGEM/METUWIND), Ankara, 06800, Turkey
[d]KU Leuven, Department of Civil Engineering, Campus Arenberg, Leuven, 3001, Belgium

E-mail: nejan@metu.edu.tr

Keywords: offshore wind turbines, probabilistic, uncertainty, monopiles, sand

Renewable energy gains importance against the increasing population and limited energy sources [13], and plays a role to meet clean energy targets. According to Wind Europe [8], Europe now has 220 GW of wind energy capacity. Besides, The EU Offshore Renewable Energy Strategy estimates offshore wind to grow from 12 GW today to 300 GW by 2050 [6]. Monopile is the most widely employed foundation type for offshore wind turbines around the world placed at shallow to intermediate water depths [10]. According to Wind Europe [11], monopiles have a ratio of 80.5% of all wind turbine foundations installed in 2020. The remarkable simplicity in design and production stages is believed to be the reason for this prevalence [7].

The most widely known and used 1D (beam-spring) method is the p-y method, where independent Winkler springs are attached to the 1D beam element to account for the soil-structure interaction throughout the pile length. The current design practice for monopiles is based on this method according to American Petroleum Institute (API) [1] and Det Norske Veritas - Germanischer Lloyd (DNV-GL) [5] guidelines. In such methods, the spring properties for lateral (p-y) and axial load (t-z, Q-z) are assigned based on the idealized soil layers based on the average soil material properties. Uncertainty on soil properties may result in possible unsatisfactory foundation performance causing repair or demolition-decommissioning.

In offshore wind turbine applications, probabilistic analysis is necessary due to three reasons. First, soil conditions may vary considerably in offshore wind farm sites, such as the case in Sheringham Shoal Wind Farm in the UK [9]. Second, offshore site investigation programs are more expensive than the ones onshore, and site investigations should be conducted over large areas compared to offshore oil and gas platforms [9]. Conducting one Cone Penetration Test (CPT) for each turbine is not possible. The soil variability may not be captured accurately since a low number of geotechnical field tests are applied in offshore environments usually. Third, the recent trends suggest new offshore wind farms be built further offshore, which increases the uncertainty in knowledge on soil conditions as the empirical correlations that can significantly differ from offshore conditions [12].

The research question of this study is "how to account for uncertainty in estimating soil parameters in offshore monopile design". In order to answer this question, the main aim is set to estimate the probability of unsatisfactory performance (unsatisfactory performance = unsatisfactory cases of analyses / all cases of analyses %), taking into account variations in soil material properties. An analysis method is developed to check whether the system shows satisfactory performance or not. These performance measures include shear, combined, overload, soil bearing, and service checks. If all these checks are satisfied, the system is evaluated as satisfactory. Monte Carlo Simulation is used to generate random fields for probabilistic analyses by assigning Coefficient of Variation (COV) values to mechanical soil properties.

The Probability of Unsatisfactory Performance (PUP) of monopiles is examined for: (Case A) a study presented in the literature using published COV values [3, 10], and (Case B) a design exercise for which site specific COV for the Belgian coast are proposed. Case A is used to verify the proposed model based on an existing design in Denmark, which is used next to design a monopile in Case B for North Sea soil conditions in Belgium. For

this case, a Siemens SWT-3.6-120 OWT is adopted from [2]. Additionally, the effect of select COV values and different distribution functions (normal distribution, lognormal distribution, and uniform distribution) are studied.

The considered load cases are kept limited to: 1) normal operational conditions, 2) extreme wave load conditions, 3) extreme wind load conditions, and 4) cut-out wind speed and extreme operating gust conditions following [2, 4]. Geotechnical information is obtained from CPT data available by the *Databank Ondergrond Vlaanderen* [14] in a selected location in the North Sea.

The methodology can be summarized in the following steps:

- Decide on probabilistic analysis properties of friction angle and the unit weight such as the select COV values, distribution functions, and the coefficient which correlates these two parameters based on the site,
- Create random soil layers by Monte Carlo simulation,
- Analyze each simulation having random soil layers and evaluate either satisfactory or unsatisfactory,
- Calculate PUP.

The outcomes of the study aim to display the effects of seabed soil variability on the probability of unsatisfactory performance depending on the specific soil conditions represented in the study as case A and case B with select probabilistic distributions.

References

[1] API. *RP2A-WSD: Recommended Practice for Planning, Designing and Constructing Fixed Offshore Platforms – Working Stress Design*. American Petroleum Institute, 2014.

[2] L. Arany, S. Bhattacharya, J. Macdonald, and S. Hogan. Design of monopiles for offshore wind turbines in 10 steps. *Soil Dynamics and Earthquake Engineering*, 92:126–152, 2017.

[3] A. H. Augustesen, K. Brødbaek, M. Møller, S. P. H. Sørensen, L. B. Ibsen, T. S. Pedersen, and L. Andersen. Numerical modelling of large-diameter steel piles at horns rev. In *Proceedings of the Twelfth International Conference on Civil, Structural and Environmental Engineering Computing*. Civil-Comp Press, 2009.

[4] S. Bhattacharya. *Design of foundations for offshore wind turbines*. John Wiley & Sons, 2019.

[5] DNV-GL. Support structures for wind turbines. *Offshore Standard DNVGL-ST-126*, 2016.

[6] F. Investment and Trade. Belgium is global 4th in offshore wind energy production. https://www.flandersinvestmentandtrade.com/invest/en/news/belgium-global- 4th-in-offshore-wind-energy-production, 2021. Accessed: 2021-06-04.

[7] M. Karimirad. *Offshore energy structures: for wind power, wave energy and hybrid marine platforms*. Springer, 2014.

[8] I. Komusanac, G. Brindley, D. Fraile, and L. Ramirez. 2020 statistics and the outlook for 2021-2025. 2021.

[9] T. M. H. Le, G. R. Eiksund, P. J. Strøm, and M. Saue. Geological and geotechnical characterisation for offshore wind turbine foundations: A case study of the sheringham shoal wind farm. *Engineering geology*, 177:40–53, 2014.

[10] O. B. Leite. *Review of design procedures for monopile offshore wind structures*. 2015.

[11] L. Ramirez, D. Fraile, and G. Brindley. Offshore wind in europe: Key trends and statistics 2020. 2021.

[12] C. Reale, J. Tott-Buswell, and L. Prendergast. Impact of geotechnical uncertainty on the preliminary, design of monopiles supporting offshore wind turbines. *ASCE-ASME J Risk and Uncert in Engrg Sys Part B Mech Engrg*, 2021.

[13] X. Sun, D. Huang, and G. Wu. The current state of offshore wind energy technology development. *Energy*, 41(1):298–312, 2012.

[14] D. O. Vlaanderen. https://www.dov.vlaanderen.be/portaal/?module=verkenner, 2021. Accessed: 2021-11-16.

Floating wind turbines

18th EAWE PhD Seminar on Wind Energy
2-4 November 2022
Bruges, Belgium

Design Optimization of Multi-used Components for Floating Offshore Wind Turbine Substructures

Victor Benifla[a] and **Frank Adam**[a, b]

[a]Lehrstuhl für Windenergietechnik, Universität Rostock, Albert-Einstein-Str. 2, 18059, Rostock, Germany.
[b]Großmann Ingenieur Consult GmbH, Tiergartenstr. 48, 01219, Dresden, Germany.

E-mail: victor.benifla@uni-rostock.de

Keywords: Floating Offshore Substructures, Buoyancy Body, Structural Analysis, Design Optimization, Machine Learning

1 Introduction

Offshore Wind Turbines (OWT), mainly bottom fixed, have thrived worldwide and more particularly in Europe due to the Levelized Cost of Energy (LCoE) of the technology which has dropped over the past decades [1]. However, a significant part of the world's offshore wind resource cannot be harvest by conventional bottom fixed OWT for technical and economical reasons. Floating foundations have a great potential for offshore wind farms in water depths greater than 40m, and could tap this newly accessible wind resource. The LCoE for floating offshore wind must decrease significantly to be competitive with fixed offshore wind technologies or even with onshore wind projects.

A Floating Offshore Wind Turbine (FOWT) is a complex system and optimization can concern its many different components such as the blades of the rotor, the tower, the foundation or the mooring system just to name a few. One of the FOWT's most relevant component in terms of cost is the floating substructure [2], therefore it is important to consider, in the early phase of its development, an optimized design in terms of production, transport and maintenance costs. In addition, design optimization studies are often focused on the floating foundation as it is an area which shows the most potential for cost reduction [3].

The design of FOWT substructures takes advantage of the knowledge from ship, oil & gas , and more recently from the fixed offshore wind industry, and was first done using insights from these industries. This lead to the three well known main floating substructure types: Spar, semi-submersible and Tension Leg Platform (TLP). Recently, different substructure concepts and modular components have been developed with the aim of reducing the production costs by serializing their fabrication procedure, leading to cost reduction for floating offshore wind energy. FOWT substructures are now designed so they are easy to build, like Legos and fast to produce as the industry is serializing its manufacturing chain like the automotive and other industries a few decades ago.

2 Objectives

The main focus of this study is on the design optimization of multi-used components for FOWT substructures. The majority of current floating platforms are mainly made out of steel and/or concrete, and their designs often involve cylindrical shaped bodies. Spar platform designs consist of long and slender cylinder, whereas TLPs and semi-submersible designs usually include different cylindrical bodies linked by bracing.

In 2009, the GICON group and their partners started a research project regarding a floating platform for offshore wind turbines, eventually leading to the evolving design of the so called GICON-TLP. The latest design of this TLP consists of a steel and concrete substructure with four buoyancy bodies that are arranged in a rectangle shape, connected to each other by horizontal bracing tubes and to the wind turbine transition piece by vertical and diagonal tubes. Details regarding the development of the GICON-TLP and the major design modifications it has undergone can be found in [4, 5], and is shown in Figure 1.

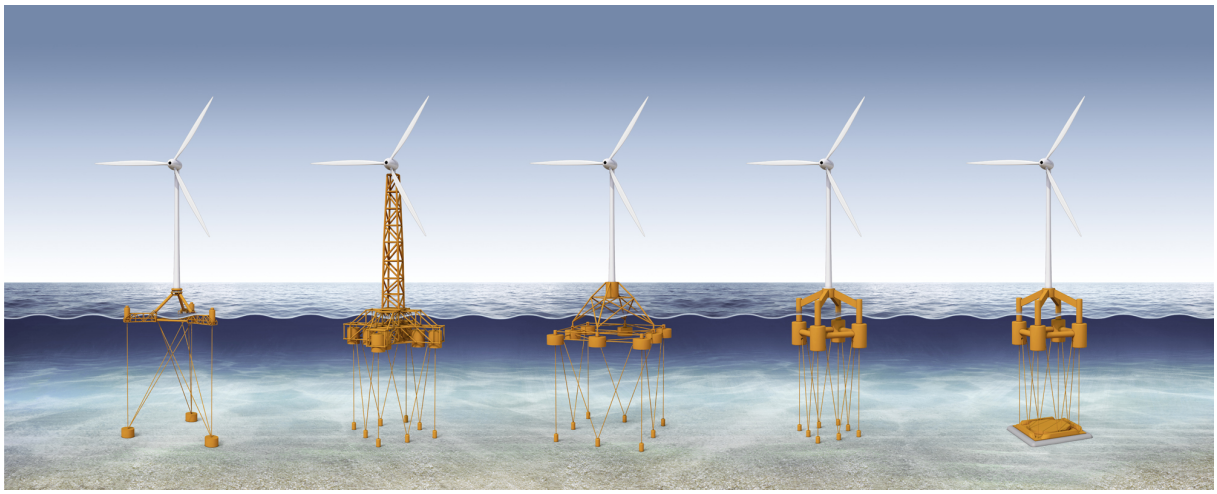


Figure 1: The development of the GICON®-TLP, from [5].

Many floating substructures involve cylindrical buoyancy bodies in their configuration, which have similarities particularly for TLPs and semi-submersible platforms. The design of floating substructure is usually similar to classical ship design, which are produced at yard and requires a large number of stiffeners and welds to ensure the strength and stability of the structure. This approach leads to high manufacturing time and costs, and therefore to high LCoE. With the development of the GICON-TLP globally aiming to reduce the cost of floating offshore wind, a particular cylindrical buoyancy body design was proposed in [6]. The Universal Buoyancy Body (UBB) is characterized by a simple design inspired by wind turbine tower and monopile designs, which enables a relatively fast manufacturing process and could fit into different floater concepts.

In the previous study [7], an optimization framework using a particular Genetic Algorithm (GA) is developed to parameterize the cylindrical geometry of the UBB and optimize its design in terms of cost, considering loads acting on the structure as well as manufacturing and floater specific dimension restrictions. The optimization process (implemented in Python) couples the the Cumulative Multi-Niching Genetic Algorithm (CMNGA), originally developed and described in [8], and the validated Finite Element Analysis (FEA) tool Ansys Mechanical. Figure 2 gives an overview of this design optimization process, highlighting the structure of the framework as well as the different files and modules which are at stake. Preliminary results for a given study case are obtained leading to a cost optimized UBB design with conical covers that respect the buoyancy and structural strength constraints defined. The particular design of this UBB and its fabrication process shows a great potential to significantly reduce manufacturing and material costs up to 30 %.

3 Outlooks

As the work discussed previously presented the first step of developing an optimization framework for the design of floating substructures, further improvements are planned to be presented in this study. Indeed, the design loads were derived using a multi-body load simulation (FLEX5) from which the extreme values for the mooring load and the maximum wave elevation were identified and used. This approach neglected any oscillation/temporal effects in the loading and therefore only a simple design verification, or sizing of the UBB was possible and no fatigue analysis could be performed. Comparably, only a simple model of the UBB's cylindrical geometry was used. The most important next step is to increase the design level of the UBB in order to consider the whole platform (transition piece, tubes, bracing, etc...) and eventually the whole FOWT (substructure, turbine, moorings, etc...) as well as all other more complex environmental loads, including oscillating wave loads for instance. In order to do so, state-of-the-art, open-source, and freely available time-domain simulation tool OpenFAST [9] is used to perform aero-hydro-servo-elastic coupled simulations of the FOWT mounted on the GICON-TLP, which will allow a more detailed structural analysis of the substructure and its components.

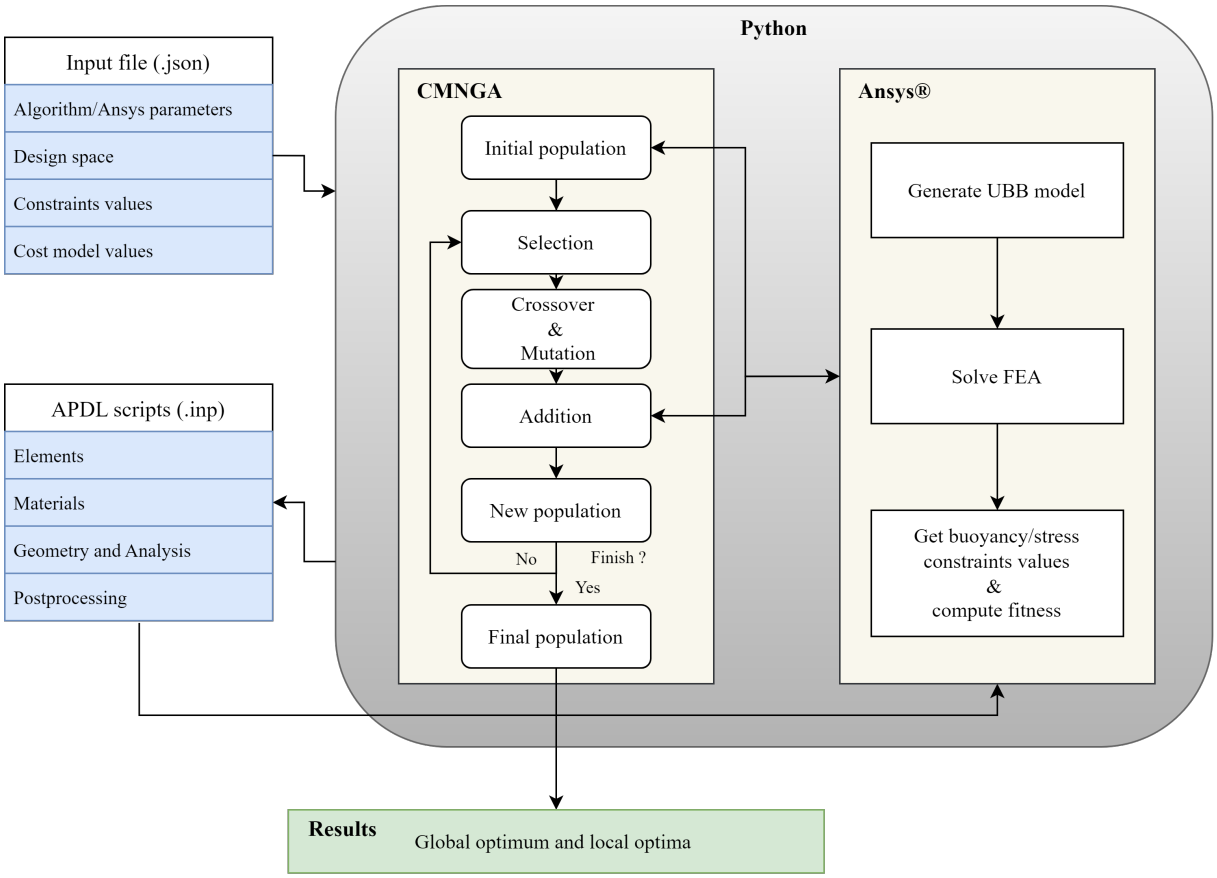


Figure 2: Framework for the design optimization of the UBB, from [7].

With regards to the optimization techniques used in the previous work discussed, there is also space for possible improvements. Evolutionary Algorithm (EA) and particularly GA, are often used in design optimization work dealing with FOWT [3], and it could be interesting to implement different algorithms with their different characteristics to compare their results, efficiency and behaviour. As for the particular GA used before, its parameters are fixed throughout the optimization process, and it could be interesting to adapt their values as generations go on. Also, different genetic operators and constraints handling techniques could be tested, studied and implemented. One of the major drawback of GA, is the computational time to evaluate the fitness function (quantifying the ”fitness” of the given potential design) which is often non negligible especially when dealing with complex, non linear and relatively long coupled simulations of FOWT. Surrogate model or machine learning techniques such as regression or prediction are more and more applied in the field of wind energy optimization. It is interesting to study those approaches to verify if they are applicable and implement them in order to obtain potential computation time savings. However, when dealing with FOWT design optimization specific challenges arise as they are exposed to a harsh environment, leading to different types of loads with sometimes non-linear effects complexifying the analysis [3]. This has to be taken into account because, for optimization work, proper balance between accuracy and computational efficiency needs to be found. Complex analysis will lead to slow optimization but with potentially more accurate results, as quick analysis using simpler models will be easier to repeat for optimization but will sometimes omit some important aspects of the modeling.

Finally, the cost model already implemented is quite simple and only includes experience values for manufacturing and material costs relative to TLPs. It could be improved including other type of costs depending on not only the mass of the substructure but also on other parameters related to life cycle of FOWT such as its installation process for example.

Acknowledgements

This research is made in the context of the European project FLOAWER, The FLOAting Wind Energy netwoRk. This project has received funding from the European Union's Horizon H2020 research and innovation program under the Marie Słodowska-Curie grant agreement N° 860579.





This project has received funding from the European Union's Horizon 2020 research and innovation programme under the Marie Skłodowska-Curie grant agreement N° 860879.

References

[1] J. Lee and F. Zhao. Global offshore wind report 2021. Technical report, Global Wind Energy Council, Brussels, Belgium, 2021.

[2] J. Rhodri and M. Costa Ros. Floating offshore wind: Market and technology review prepared for the scottish government. Technical report, The Carbon Trust, 2015.

[3] M. Muskulus and S. Schafhirt. Design optimization of wind turbine support structures — a review. *Journal of Ocean and Wind Energy*, 1(1):12–22, 2014.

[4] F. Adam, T. Myland, F. Dahlhaus, and J. Großmann. *GICON®-TLP for wind turbines – the path of development*, pages 24–26. 2014.

[5] F. Adam, C. Behr, D. Walia, U. Ritschel, and J. Großmann. A modular tlp floating substructure to maximize the flexibility within the supply chain. In *27th International Ocean and Polar Engineering Conference*, 2017.

[6] M. Lutz, D. Walia, and F. Adam. *Development of a universal useable and in series production manufacturable buoyancy body design for TLP and semi-submersible*, pages 709–716. Taylor & Francis Group, 2020.

[7] V. Benifla and F. Adam. Development of a genetic algorithm code for the design of cylindrical buoyancy bodies for floating offshore wind turbine substructures. *TORQUE 2022 conference proceedings IOP Journal of Physics: Conference Series (JPCS)*, 2022.

[8] M. Hall. A cumulative multi-niching genetic algorithm for multimodal function optimization. *International Journal of Advanced Research in Artificial Intelligence*, 1:9, 2012.

[9] Jason Mark Jonkman. *Dynamics modeling and loads analysis of an offshore floating wind turbine*. University of Colorado at Boulder, 2007.

18th EAWE PhD Seminar on Wind Energy
2 – 4 November 2022
Bruges, Belgium

Development of a methodology for the analysis of tip vortices in floating horizontal axis wind turbines

Stefano Cioni[a], **Alessandro Bianchini** [a]

[a] Department of Industrial Engineering (DIEF), Università degli studi di Firenze, Via di Santa Marta 3, 50139 Firenze, Italy
E-mail: stefano.cioni@unifi.it

Keywords: Tip Vortices, PIV, Floating wind turbines

Floating horizontal axis wind turbines represent a crucial technology that could allow an increase in wind energy production, extending the available off-shore sites to regions where the depth of the sea precludes the installation of bottom-fixed wind turbines [1]. Many challenges are encountered when designing these systems since their behavior is a result of the interaction of wind turbine aerodynamics and platform motion [2]. In particular, the wake of a floating wind turbine, represents a topic of interest, since an accurate description of the wake is essential for wind farm planning. In this context, previous work has focused on characterizing the wake over a range of platform motions, frequencies, and amplitudes with the objective of identifying the differences with bottom-fixed wind turbines [3][4]. The different regimes of motion have been defined and the wake recovery has been characterized. However, the study of tip vortices has been limited to the qualitative analysis of their collapse and no in-depth characterization has been provided.

In this work, the development of a methodology for the analysis of tip vortices shed from a floating horizontal axis wind turbine is described. This approach can be used to estimate the effect of platform motion on several tip vortex metrics, such as position, convection velocity, core radius, and strength.
The input data are two-dimensional velocity fields acquired for an imposed platform motion. The velocity fields can be obtained either from wind tunnel experimental campaigns, using Particle Image Velocimetry (PIV), or from numerical simulations (such as free vortex wake or CFD), allowing the validation of numerical results with experimental data. The velocity snapshots are recorded when one of the blades, which is chosen as a reference, reaches a specified azimuth position. In this way, since the blade tip position is the same for subsequent platform cycles, it is possible to perform phase averaging, in order to eliminate possible cycle dispersion in the results or to carry out a statistical analysis of the data, which might be useful for experimental or LES results.

The methodology developed in previous work by the authors [5] has been applied to identify the tip vortices from the velocity fields. Graftieaux's method has been chosen to identify the vortices and locate their centers since it has been shown that this is the most stable approach [5]. The existing methodology has then been improved by including an algorithm that allows the distinction of multiple vortices within a single field of view. From the vortex center locations, it is possible to track the tip vortices during the platform motion and to evaluate the convection velocity, core radius, and strength of the vortex.
Then, the Fourier transform is applied to the results to underline the effect of platform motion on these metrics. This is achieved by analyzing the frequency spectrum and by extracting amplitude and phase shift at the frequency of platform motion (Figure 1).
By applying this methodology to multiple amplitudes and frequencies of platform motion the behaviour of the tip vortices can be characterized. The methodology is tested on velocity field data obtained from CFD, Actuator Line Model (ALM) simulations of a 1:75 scaled version of the DTU 10-MW RWT [6], for both surge and pitch test cases. Preliminary results (Figures 2 and 3) show how the methodology can be used to characterize the effect of platform motion on the tip vortices, verifying if the wake of the turbine is following quasi-steady conditions or if unsteady aerodynamic effects are present.

Figure 2 (left) shows the amplitude of the streamwise motion of the tip vortices for surge and pitch cases as a function of the streamwise amplitude of blade tip motion Δx_t (for the surge cases Δx_t is equal to the platform motion amplitude, while for the pitch cases $\Delta x_t = h_{tip}\sin(\beta)$, where β is the pitch amplitude and h_{tip} the height of the tip). The amplitude of motion of the tip vortices in the streamwise direction is almost identical to the streamwise amplitude of the blade tip. Hence the platform motion seems to have only a minimal effect on the position of the tip vortices for the considered cases.
Figure 2 (right) shows the phase shift, $\Delta\varphi$, of the streamwise oscillation of the tip vortices compared to the platform motion. If no unsteady effects are present, the streamwise position of the tip vortices should follow the oscillations of the platform motion, without any phase shift ($\Delta\varphi = 0°$). However, while the phase shift is close to zero for the highest amplitudes (and lower frequencies) of motion, some differences are observed at the higher frequencies for both surge and pitch cases, suggesting that the rotor might not be working in quasi-steady conditions.
The same approach is applied to the tip vortex strength (Figure 3). Assuming that the strength of the tip vortices is a function of the angle of attack α [7],

$$\Gamma = \Gamma(\alpha) = \Gamma(\omega_r, U_{rel}) \tag{1}$$

the circulation can be written as a function of the rotational speed of the rotor ω_r, and of the relative speed U_{rel}. Hence, if the rotational velocity is fixed and hypothesizing quasi-steady conditions, the expression can be linearized as, Eq. (2),

$$\Gamma \approx \Gamma_o + \left.\frac{\partial\Gamma}{\partial U}\right|_0 (U - U_o) \tag{2}$$

Where $(\cdot)0$ denotes the steady-state value of a quantity for a given turbine operating point. So, for the surge and pitch cases,

$$\Gamma \approx \Gamma_o - \left.\frac{\partial\Gamma}{\partial U}\right|_0 (U_p), \tag{3}$$

$$U_p = (2\pi f_m)\Delta x_t sin\left(2\pi f_m - \frac{\pi}{2}\right), \tag{4}$$

where U_p is the platform velocity, Δx_t is the streamwise amplitude of the blade tip motion and f_m is the frequency of motion. Substituting Eq. (4) into Eq. (3) the vortex strength amplitude can be written as, Eq. (5),

$$\Delta\Gamma/_A \approx K(2\pi f_m), \tag{5}$$

$$K = \left.\frac{\partial\Gamma}{\partial U}\right|_0, \tag{6}$$

which shows that the circulation amplitude should increase linearly with the frequency of motion if unsteady aerodynamic effects can be neglected. The simulation results analysed in this work follow the expected linear trend (Figure 3, left), which might indicate that quasi-steady theory can be used to predict the variations of tip vortex strength due to platform motion in the analysed test cases.
Furthermore, for a fixed free-stream velocity, the tip vortex strength should follow the velocity oscillations of the platform (Eqs. (1,4)), increasing when the turbine is moving upstream and decreasing when it is moving downstream, due to the variation in relative wind speed.
Hence, since the imposed platform motion for both pitch and surge cases follows a sinusoidal, the platform velocity is represented by a cosine function (i.e. the velocity is shifted by 90° with regard to platform motion, Eq. (4)). Therefore, if the rotor is working in quasi-steady conditions, the tip vortex circulation should be shifted by 90° compared to platform motion.
The results show high scattering from the expected trend both at high and low frequencies of motion. These differences might indicate that unsteady effects cannot be neglected when analysing the tip vortices shed from a floating wind turbine at the simulated frequencies and amplitudes. However, unsteady aerodynamic effects should be relevant only at higher frequencies of motion [6], in contrast to what is observed in Figure 3. Another hypothesis is that the ALM approach might not describe the tip vortex strength oscillations correctly. In order to verify this, future work will compare the results from both PIV data and other simulation approaches, such as Free Vortex Wake (FVW) methods.
Additionally, the results obtained from the presented methodology can be compared with thrust data or further aerodynamic parameters (such as wake deficit or wake recovery). For example, Fontanella et al. [6] have shown

that the thrust oscillations induced by platform motion can be analysed in terms of amplitude and phase shift. Hence, tip vortex strength and thrust results could be compared, providing further validation of simulation methods, and giving insight into the relationship between aerodynamic loads and tip vortex shedding and wake behavior.

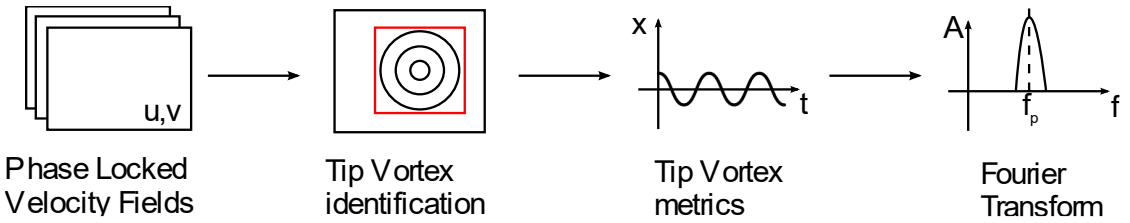


Figure 1: Summary of methodology

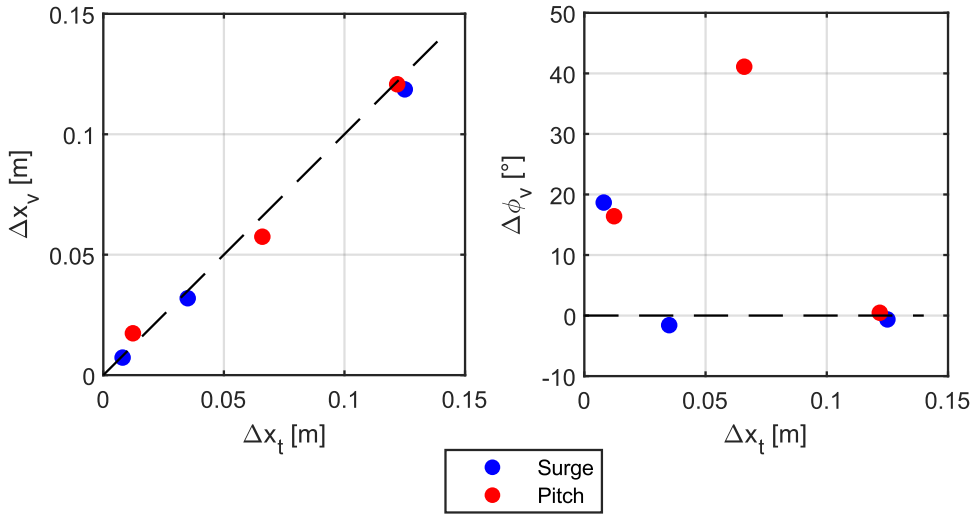


Figure 2: Tip vortex streamwise position amplitude (left) and phase shift with regard to plaftform motion (right). The results are shown for surge and pitch cases as a function of blade tip streamwise amplitude.

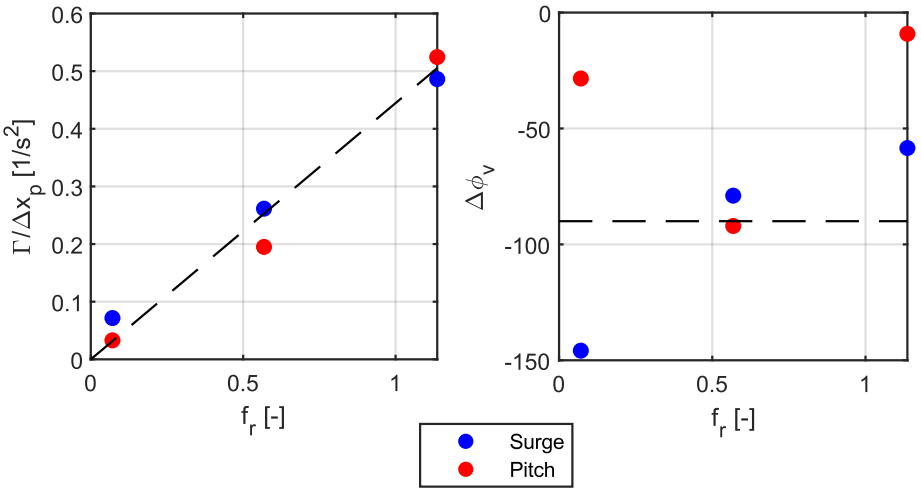


Figure 3: Tip vortex strength amplitude (left) and phase shift with regard to platform motion (right) as a function of reduced frequency. The tip vortex strength amplitude is normalized through the streamwise amplitude of blade tip motion.

Acknowledgements

The authors would like to thank Leonardo Pagamonci from Università degli studi di Firenze for providing the CFD data and Rodrigo Soto-Valle from TU Berlin for his help in the writing of some of the post- processing scripts.

References

[1] Chen P, Chen J and Hu Z 2020 Review of Experimental-Numerical Methodologies and Challenges for Floating Offshore Wind Turbines *J. Marine. Sci. Appl.* **19** 339–61

[2] Butterfield S, Musial W and Jonkman J 2007 Engineering Challenges for Floating Offshore Wind Turbines 13

[3] Cormier M, Caboni M, Lutz T, Boorsma K and Krämer E 2018 Numerical analysis of unsteady aerodynamics of floating offshore wind turbines *J. Phys.: Conf. Ser.* **1037** 072048

[4] Ramos-García N, Kontos S, Pegalajar-Jurado A, González Horcas S and Bredmose H 2022 Investigation of the floating IEA Wind 15 MW RWT using vortex methods Part I: Flow regimes and wake recovery *Wind Energy* **25** 468–504

[5] Soto-Valle R, Cioni S, Bartholomay S, Manolesos M, Nayeri C N, Bianchini A and Paschereit C O 2021 *Vortex identification methods applied to wind turbine tip vortices* (Aerodynamics and hydrodynamics)

[6] Fontanella A, Bayati I, Mikkelsen R, Belloli M and Zasso A 2021 UNAFLOW: a holistic wind tunnel experiment about the aerodynamic response of floating wind turbines under imposed surge motion *Wind Energy Science* **6** 1169–90

[7] Najarzadegan F 2019 Circulation Dependence of the Interaction Between a Wing-Tip Vortex and Turbulence

18th EAWE PhD Seminar on Wind Energy
2-4 November 2022
Bruges, Belgium

Experimental campaign of a floating offshore wind turbine: Preliminary results

Francisco Pimenta[a] and **Filipe Magalhães**[a]

[a]CONSTRUCT-ViBest, Faculty of Engineering of the University of Porto

E-mail: up200908672@edu.fc.up.pt

Keywords: Floating offshore wind turbine, semi-submersible, experimental data, operational modal analysis

Although offshore wind applications, and in particular floating solutions based on semi-submersible platforms, have been increasing over the years, the dynamic response characterisation or operating conditions influence on the experience fatigue damage of these type of structures are still poorly documented, or mostly relying on numerical simulations [1]. In this work, we propose to bridge this gap by presenting the preliminary results of an experimental campaign that is currently being conducted on a operating floating offshore wind turbine.

The instrumental layout includes 3 level of accelerometers and a single level of strain gauges and temperature sensors. From the strain gauges and temperature sensors we can reconstruct the bending moments time history at the instrumented section, that when combined with SCADA data can be used to identify environmental conditions that significantly impact the total fatigue damage the structure will experience during its lifetime. The 3 level of accelerometers can be used to identify both the platform low frequency response as well as the tower natural frequencies.

Acknowledgements

This work was financially supported by: PhD Grant SFRH/BD/138980/2018, Base Funding UIDB/04708/2020 of the CONSTRUCT-Instituto de I&D em Estruturas e Construções and the project PTDC/ECI-EST/29558/2017, funded by national funds through the FCT/MCTES (PIDDAC)

References

[1] F. Pimenta, C. Ruzzo, G. Failla, F. Arena, M. Alves, and F. Magalhães. Dynamic response characterization of floating structures based on numerical simulations. *Energies*, 13(21), 2020.

18th EAWE PhD Seminar on Wind Energy
2 – 4 November 2022
Bruges, Belgium

Multi-fidelity simulation of floating offshore wind turbine aerodynamics: are current tools ready for future challenges?

Francesco Papi[a], Alessandro Bianchini[a]

[a] Dept. of Industrial Engineering, University of Florence, via di Santa Marta 3, Firenze, Italy

E-mail: fr.papi@unifi.it

Keywords: aerodynamics, floating, FOWT

Floating Offshore Wind Turbines (FOWTs) are one of the most promising technologies for future development of offshore wind energy. By installing wind turbines on a floating foundation, they can be placed away from shorelines in deep water, tapping into previously unavailable and abundant wind resource. Levelized cost of energy (LCOE) of floating wind is considerable higher than bottom-fixed wind turbines, which are in turn still at a disadvantage with respect to onshore machines. To enable a widespread adoption of FOWTs and thus an increasing decarbonization of the energy grid, reducing LCOE is therefore key. The cost of FOWTs is envisioned to decrease in the coming decades due to economies of scale, standardization and optimization. Focusing on the latter aspect, more cost-effective designs are possible if the numerical tools used to design these increasingly large rotors are proven to be reliable.

In a FOWT the tower is not cantilevered to the ground and therefore the rotor can undergo relatively large motions. In current generation FOWT concepts such motions are caused by the combined loading effects of wind and wave loading [1]. Some authors are even attempting to exploit the rotor movements to improve LCOE of large wind farms by promoting wake mixing [2]. All these effects where not accounted for when formulating the aerodynamic models that are currently used to simulate and design wind turbine rotors.

Computational efficiency is also important in the wind turbine industry. Any new wind turbine design must undergo certification by international bodies before it can enter the market. This kind of exercise requires the simulation of the FOWT in every combination of environmental conditions and operating state that the system may encounter during it's design life, as specified by international design standards [3]. Although reliability-based methods for the evaluation of extreme and fatigue loads ae currently being screened, at the current state of the art, this mean performing thousands – sometime tens of thousands – of simulations. As noted in [4], this issue is further compounded by the fact that in an offshore environment, to obtain a long-term environmental representation of an installation site, one needs to account for not only the long-term wind speed distribution but also for the installation sea state, and thus also consider for instance, significant wave height, peak spectral period, wind-wave misalignment.

This work focuses on the validation of aerodynamic models for the simulation of FOWTs. The objective is to i) understand what aerodynamics effects are levant to accurately capture FOWT loads ii) provide modelling suggestions and find the right balance of computational cost and accuracy.

Starting simple to gain a basic understanding of the various aerodynamic modelling tool's capabilities to capture unsteady effects due to floating installation, a wind turbine rotor with imposed sinusoidal pitch or surge motion is analysed. The rotor that was tested in the Politecnico di Milano wind tunnel during the UNAFLOW project [5] is used. This allows for comparison not only between numerical codes but also to the experimental benchmark. Complete description of the testcase can be found in [5,6], only basic specifications will be reported here for brevity. The rotor is a 1:75 scale model of the DTU 10MW RWT [7], approximately 2.4 m in diameter. The carbon fibre blades are straight with no precone and can be considered rigid. Blade chord and twist as well as the airfoil used were chosen to preserve the thrust characteristics of the full-scale turbine at model scale, where Reynolds similarity cannot be maintained. The oscillation amplitudes and frequencies that were tested were chosen based on the response of the DTU 10MW rotor in floating conditions observed during the Lifes50+ project [6]. As for the oscillations, scaling was performed to match the reduced frequency of the full-scale model:

$$A_{ms} = A_{fs}/75$$

$$f_r^{ms} = f_r^{fs} = \frac{f * D}{U_\infty}, \quad D_{ms} = \frac{D_{fs}}{75}, U_\infty^{ms} = U_\infty^{fs}/3$$

Most of the numerical model tested were built within the OpenFAST framework. All models share the same blade definition in terms of chord distribution and airfoil coefficients, allowing us to clearly separate the effects of the various aerodynamic modelling theories. The models can be described as follows:

- *BEM*: Blade-Element-Momentum model to resolve the turbine wake with no correction for dynamic induction. Beddoes-Leishman unsteady aerodynamics modelling is considered. In the *BEM st* model the latter effect is not considered.
- *DBEM*: Blade-Element-Momentum theory to resolve aerodynamics with Oye dynamic inflow model and UA
- *LLFVW*: Lifting-Line Free Vortex Wake model to resolve the turbine wake, as descried in [8]. No blade-level unsteadiness is modelled.
- *ALM*: Actuator-Line model developed by the University of Florence. No UA are considered (i.e. dynamic stall). Wake is resolved using U-RANS CFD. The k-eps turbulence model is used. Automatic Mesh Refinement (AMR) ensures adequate resolution where velocity gradients are largest, such as in the wake sear-layer. More details can be found at [9].

Under imposed sinusoidal pitch and surge excitation rotor thrust response was found to also be sinusoidal and can therefore be described in terms of amplitude and phase shift to the imposed motion. Rotor torque also has shown a similar behaviour. All other rotor forces and moments are not significantly affected by the imposed motions and their response is approximately zero. Rotor thrust response is shown for surge excitation in figure 1, in terms of amplitude (1a) and phase shift (1b). Figures 1c and 1d are analogous but for pitch oscillation. The dashed trend line is obtained from a linear regression of the data at 0.125 Hz and by imposing the trendline to go through the origin. Experiments are performed up to 2 Hz (corresponding to a period of 12.5 s at full scale). Up to this mark the numerical simulations are very close to the linear trendline, indicating that the amplitude of thrust response normalized by the oscillation amplitude is linearly proportional to the apparent velocity. Simulations also appear to be able to capture the experimental trend well, although some differences appear at 2 Hz, especially for the pitch testcase. Where the non-linearities are more evident is in terms of phase shift. We will discuss Surge, but the same considerations are valid for the pitch DOF as well. BEM st predicts a phase shift of almost exactly -90° indicating that thrust force is perfectly in phase with the apparent wind and no dynamic effects are captured. BEM on the other hand shows a phase-shift smaller than -90° and decreasing a frequency increases. This indicates that blade-level unsteadiness is occurring, and it interest more and more parts of the blade as reduced frequency increases. DBEM shows even greater phase-lag as it also includes the effects of dynamic induction. In terms of phase-lag, LLFVW and ALM are similar to BEM as they also do not include UA. Increasing the surge oscillation amplitude tenfold – as shown in figure 1a and 1b – did not increase the relevance of unsteady aerodynamics significantly, and all models return very similar results both in terms of amplitude and phase-shift.

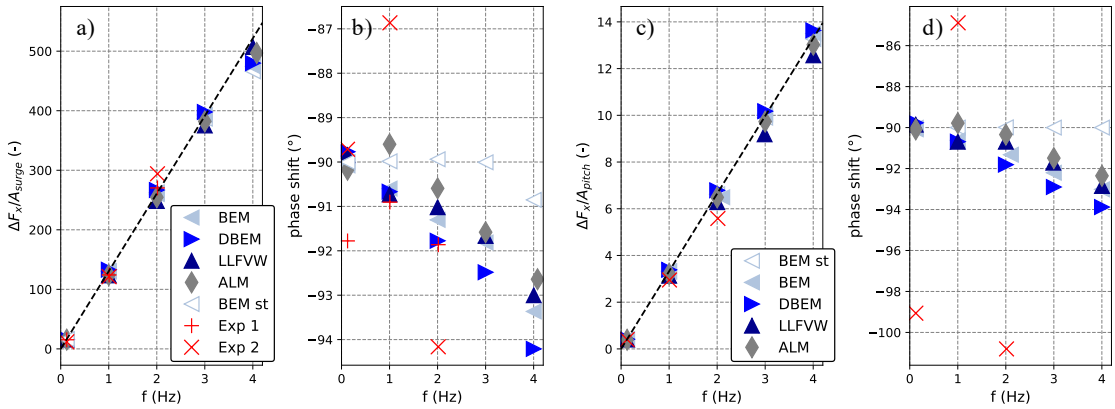


Figure 1: (a) amplitude and (b) phase shift of rotor thrust with respect to sinusoidal surge excitation with respect to sinusoidal pitch excitation (c and d) at different frequencies. Experimental data from the UNAFLOW test campaign [5] and OC6 phase III code-to-code comparison [10]

In an operating wind turbine however, rotor control is relevant. In general, a surge or pitch motion could result in variations in either rotor speed or blade pitch, as the controller reacts to the apparent different conditions. The magnitude of such variations depends on rotor inertia. To try to understand the differences between the codes, a variation in rotor speed of +-15% is imposed in Load Case 2.16 and a variation in blade pitch of +-1.5° is imposed in LC 2.17. This approach was proposed in [10]. These variations are supposed as in-phase with the rotor torque, and thus phase-lagged 90° respect to rotor motion. As shown in figure 2c and 2d, in this case differences between the modelling approaches start to emerge, especially in terms of amplitude of the response. In both cases BEM st is very similar to BEM, indicating that the differences are mostly driven by unsteady induction rather than UA. Using a dynamic induction model (DBEM) improves predictions if compared to a more sophisticated aerodynamic theory (LLFVW), however response amplitude seems to be overestimated when rotor speed is varied in LC 2.16.

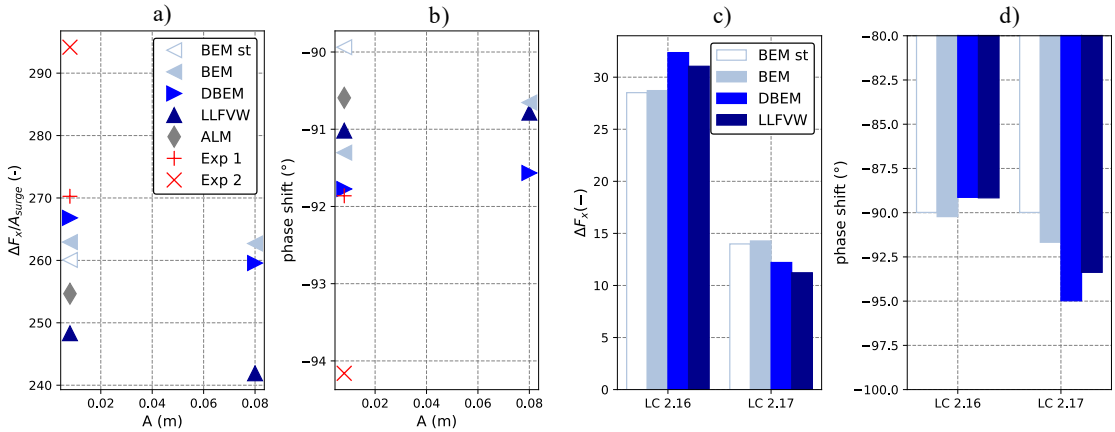


Figure 2: (a) amplitude and (b) phase shift of rotor thrust with respect to sinusoidal surge excitation at 2 Hz.

Another effect that could play a relevant role in accurate prediction of FOWT loading is flow misalignment. In fact, wind turbines often operate in moderate flow misalignment (+-8°/10°). In a FOWT, wind-wave misalignment can also be quite common, especially in low to moderate wind conditions, where waves driven by swell are more relevant. An investigation on model predictiveness for a pitching turbine in misaligned flow was performed by the author in [11]. Currently 20° inflow angle. results obtained with DBEM are compared to blade-resolved CFD simulations, but it is planned to also extend this comparison to BEM and LLFVW in the future. The testcase that was used in the comparison in the NREL 5MW RWT [12]. The rotor is oscillating in pitch, with a frequency of 0.1 Hz (wave frequency) and an amplitude of 1°. Full description of the simulated testcase and of the results can be found in [11]. A schematic representation of the testcase is shown in Figure 3. Results in terms of blade torque and thrust are shown in Figure 4a and 4b for no flow misalignment and for a flow misalignment of 20° is Figure 4c and 4d. When no flow misalignment is present, the DBEM model slightly overestimate thrust, but seems to adequately predict the amplitude of the thrust oscillation. Very good agreement in terms of power output is noted. When flow misalignment is introduced, both power and thrust decrease, as expected given the smaller rotor area normal to the flow. In these conditions, OpenFAST appears to overestimate the thrust amplitude oscillation and slightly underpredict the mean power. Overall notable decreases in both power and thrust are noted for OpenFAST respect to the CFD models.

In conclusion, the main takeaways can be reassumed as follows:

- Due to platform motion in pitch and in surge the rotor is subject to an apparent inflow velocity that causes cyclic loading on the structure. Under imposed cyclic excitation in pitch and surge the torque and thrust produced by the wind turbine rotor is also cyclic and can be descried by amplitude and phase of the load oscillation.
- Unsteadiness is driven mainly by reduced frequency, i.e., the higher the reduced frequency, the higher the unsteadiness, both in terms of induction and unsteady blade aerodynamics. On the other hand, increasing the relative velocity tenfold while maintaining reduced frequency did not yield an increase in unsteady phenomena in this testcase.
- All the tested aerodynamic models under imposed pitch and surge motion reproduce experimental behaviour well in terms of amplitude, while some non-linearities emerge at higher frequencies. In Terms of phase-shift it is important to include dynamic induction and UA in the simulations

- When oscillations in blade pitch or rotor speed, as a controller reaction to the rotor's motion are introduced, differences between the aerodynamic models appear. Modelling dynamic induction appears to be more important than accounting for UA. DBEM is able to improve agreement with LLFVW respect to BEM.

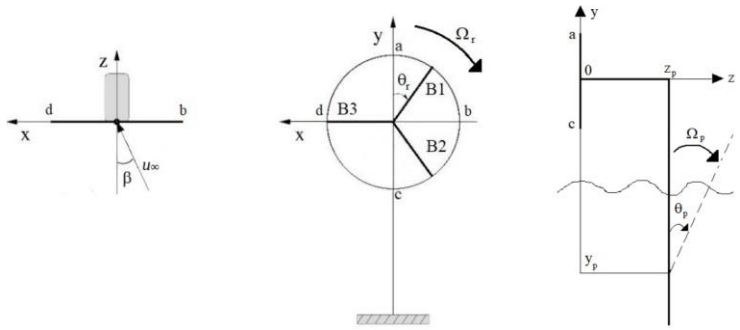


Figure 3: Schematic representation of the NREL MW as tested in [11] under imposed pitch motion

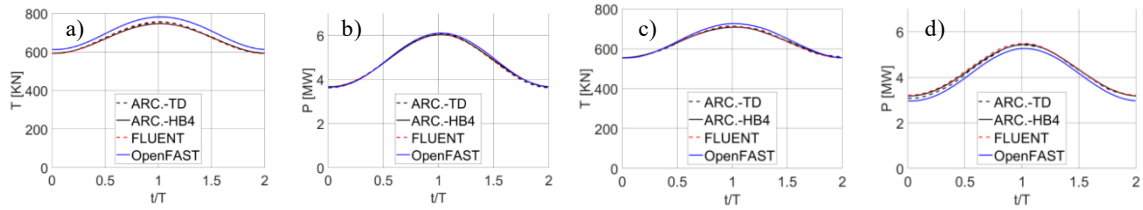


Figure 4: (a) Thrust and (b) Power of the NREL 5MW simulated using blade resolved CFD and DBEM at 0° flow misalignment and at 20° flow misalignment (c,d). [11]

References

[1] Papi F and Bianchini A 2022 Technical challenges in floating offshore wind turbine upscaling: A critical analysis based on the NREL 5 MW and IEA 15 MW Reference Turbines *Renewable and Sustainable Energy Reviews* **162** 112489

[2] Berg D van den, Tavernier D de and Wingerden J-W van 2022 Using The Helix Mixing Approach On Floating Offshore Wind Turbines *J. Phys.: Conf. Ser.* **2265** 042011

[3] International Electrotechnical Commission 2019 *IEC 61400-3: Wind energy generation systems. design requirements for floating offshore wind turbines Part 3-2 Part 3-2*

[4] Papi F, Perignong Y and Bianchini A 2022 Derivation of Met-Ocean Conditions for the Simulation of Floating Wind Turbines: a European case study (IOP - Conference Series)

[5] Fontanella A, Bayati I, Mikkelsen R, Belloli M and Zasso A 2021 UNAFLOW: a holistic wind tunnel experiment about the aerodynamic response of floating wind turbines under imposed surge motion *Wind Energy Science* **6** 1169–90

[6] Mancini S, Boorsma K, Caboni M, Cormier M, Lutz T, Schito P and Zasso A 2020 Characterization of the unsteady aerodynamic response of a floating offshore wind turbine to surge motion *Wind Energ. Sci.* **5** 1713–30

[7] Bak C, Zahle F, Bitsche R, Kim T, Yde A, Henriksen L C, Natarajan A and Hansen M 2013 *Description of the DTU 10 MW Reference Wind Turbine* (DTU Wind Energy)

[8] Branlard E, Brownstein I, Strom B, Jonkman J, Dana S and Baring-Gould E I 2022 A multipurpose lifting-line flow solver for arbitrary wind energy concepts *Wind Energy Science* **7** 455–67

[9] Papi F, Melani P F, et. al 2021 Development and Validation of an Advanced Actuator Line Model for Wind Turbines, *proceedings of 76° Congresso Nazionale ATI*

[10] Bergua R and et. al. 2022 OC6 Project Phase III: Validation of the Aerodynamic Loading on a Wind Turbine Rotor Undergoing Large Motion Caused by a Floating Support Structure *submitted to Wind Energy Science Journal*

[11] Ortolani A, Papi F, Bianchini A, Persico G, Drofelnik J and Campobasso M S 2022 Multi-fidelity Analyses of Rotor Loads of Floating Offshore Wind Turbines with Wind/Wave Misalignment *J. Phys.: Conf. Ser.* **2265** 042010

[12] Jonkman J, Butterfield S, Musial W and Scott G 2009 *Definition of a 5-MW Reference Wind Turbine for Offshore System Development*

18th EAWE PhD Seminar on Wind Energy
2 – 4 November 2022
Bruges, Belgium

Simulation models for the analysis of floating wind turbine wakes: a comparison between the Actuator Line and the Actuator Disk Models

Leonardo Pagamonci [a], Alessandro Bianchini [a]

[a] Dept. of Industrial Engineering, Università degli Studi di Firenze. Via di Santa Marta 3, 50139, Firenze, Italy

E-mail: leonardo.pagamonci@unifi.it

Keywords: Floating wind turbines, Actuator Line Model, Actuator Disk Model, Computational Fluid Dynamics

Floating Offshore Wind Turbines (FOWTs) have nowadays become one of the best options for spreading wind energy, potentially increasing the number of installation sites for wind turbines, especially in those contexts where the adoption of the monopile could not be possible or economically less feasible.

The introduction of the floating technology brings new aspects to be analysed during the design of the plant: one of the most important is the hydrodynamic effect of the waves on the platform, and by consequence on the turbine itself. From an aerodynamic point of view, this reflects on the effective wind velocity interacting with the blades, introducing an unsteady behaviour on the turbine performance and, by consequence, on the wake [1]. In a wind farm perspective, the in-depth evaluation of the impact of the upstream turbines on the downstream ones is fundamental for the design and optimization of the entire plant.

In order to perform this type of analysis in the industrial context, robust and quick design tools are required, which include both the analysis of the rotor and the behaviour of the wake. BEM-based design tools are by far becoming less suitable for this kind of analysis, and fully-resolved Computational Fluid Dynamics (CFD) is too much computationally expensive. Between these extremes, many approaches have been proposed to blend the calculation speed of the first with the accuracy of the latter: the result is the formulation of the so-called “hybrid models” [Figure 1], and two of the most promising of them are the Actuator Disk Model (ADM) [2] and the Actuator Line Model (ALM) [3].

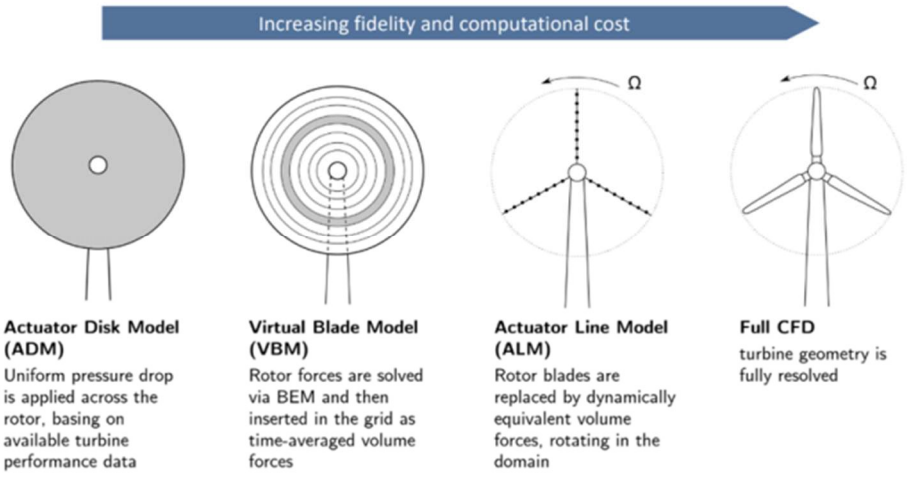


Figure 1 Overview of some available hybrid models, compared to full CFD

Both ADM and ALM hybridize the CFD resolution of the flow field with the BEM modelling of the rotor but, as can be seen in [Figure 1], while the first models the rotor as an actuator disk, the second splits the blade into multiple sections, and through a lumped parameters approach aerodynamic forces are calculated, usually referring to the Aerodynamic Centre of the airfoil.

In the case of the proposed study, the Rotational ADM, an advanced version of the ADM, is used: in this model, several AD nodes are defined, and a radial coordinate system is defined to represent the rotor area.

In this work, a comparative analysis was performed, in order to highlight the pros and cons of each model, either in terms of rotor quantities, wake resolution and computational cost, with particular focus on a potential wind farm application. The analysis started from the evaluation of a steady wind case to assess the basic differences between the two models, and then, moving to unsteady wind conditions, given by the imposition of a surge or pitch motion to the turbine, to investigate the further differences that these two models have in case of floating conditions.

The simulated turbine is a 1:75 scaled version of the DTU 10-MW RWT [4], and the simulated cases are the ones in Table 1 and Table 2.

Table 1 Steady wind case

Load Case	V_0 *(m/s)*	Ω *(rpm)*	Λ *(-)*	ϑ_P *(°)*
1	*4*	*240*	*7.5*	*0*

Table 2 Unsteady wind cases

Load Case	*Surge/pitch*	V_0 *(m/s)*	Ω *(rpm)*	$F_{surge/pitch}$ *(Hz)*	$A_{surge/pitch}$ *(m/deg)*
2	*Surge*	*4*	*240*	*1.0*	*0.035*
3	*Pitch*	*4*	*240*	*1.0*	*1.4*

Comparisons are performed in terms of medium values of rotor thrust and torque for the steady case, while for unsteady winds the trends of the indicated quantities over the period of platform movement are investigated. Regarding to wake analysis, contours of velocity at significant sections are available, as can be seen in Figure 2, and the velocity profile of the wakes are compared, extrapolating velocity data on a line crossing the wind at a certain distance from the rotor.

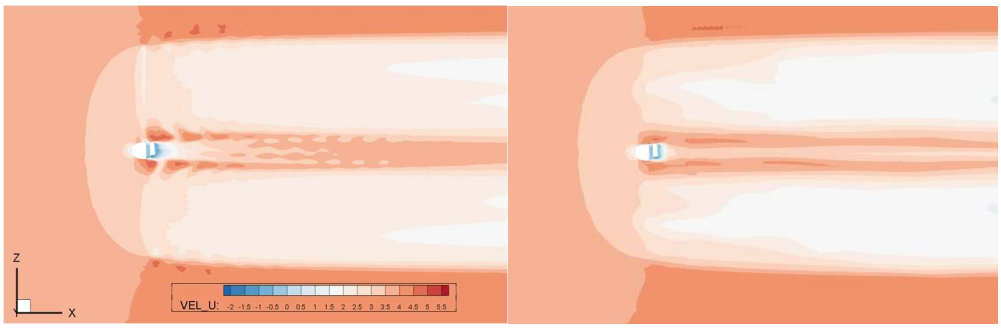


Figure 2 Axial velocity contour, comparisons between ALM (left) and RADM (right)

Acknowledgements

We thank the members of the REASE group of Unifi, with special thanks to Professor Giovanni Ferrara for leading the research group, and to Ph.D. Francesco Balduzzi, Ph.D Pier Francesco Melani and Dr. Francesco Papi for their experienced support during the activities on these themes.
We would also like to thank Convergent Science© for their technical support in order to perform, through their Converge® CFD software, the simulations presented in this paper. In particular, we thank Ph.D. Shengbai Xie for his ongoing and experienced support.

References

[1] I. Bayati, L. Bernini, A. Zanotti, M. Belloli, e A. Zasso, «Experimental investigation of the unsteady aerodynamics of FOWT through PIV and hot-wire wake measurements», *J. Phys. Conf. Ser.*, vol. 1037, pag. 052024, giu. 2018, doi: 10.1088/1742-6596/1037/5/052024.

[2] L. Martínez Tossas, S. Leonardi, M. Churchfield, e P. Moriarty, «A Comparison of Actuator Disk and Actuator Line Wind Turbine Models and Best Practices for Their Use», gen. 2012. doi: 10.2514/6.2012-900.

[3] J. N. Sørensen e W. Z. Shen, «Numerical Modeling of Wind Turbine Wakes», *J. Fluids Eng.*, vol. 124, n. 2, pagg. 393–399, giu. 2002, doi: 10.1115/1.1471361.

[4] C. Bak, F. Zahale, e al., «Description of the DTU 10 MW Reference Wind Turbine», DTU Wind Energy, 213d.C.

18th EAWE PhD Seminar on Wind Energy
2-4 November 2022
Bruges, Belgium

Wind tunnel investigation of the wake of a model floating wind turbine under imposed surge motion

T Messmer[a], **J Peinke**[a], and **M Hölling**[a]

[a]Institute of Physics and ForWind, University of Oldenburg , 26129 Oldenburg, Germany

E-mail: thomas.messmer@uni-oldenburg.de

Keywords: FOWT, wake, aerodynamics, wind tunnel experiment, model turbine

1 Introduction

A floating offshore wind turbine (FOWT) interacts with the incoming wind field and ocean waves resulting in additional complex motions of the turbine compared to a bottom-fixed machine. These added movements affect the turbine itself as well as the generated wake and its development with increasing distance to the turbine [1]. In a wind farm, the wake of a wind turbine is likely to be the inflow for turbines located downstream inside the farm and result again in additional dynamics which might lead to higher extreme loads, fatigue loads and power losses. Due to the lack of full scale data, either wind tunnel experiments or numerical investigations might help to better understand the wake of floating wind turbines. In this study, the wake features (recovery, turbulence properties, spectra, etc) of a model wind turbine submitted to harmonic motions in surge is investigated experimentally in the large wind tunnel of the University of Oldenburg (UOL). This research aims to contribute to answering the following questions: do the motions of a floating turbine improve the wake recovery in comparison with a fixed turbine? How does turbulence develop in the wake of a FOWT? What parameters are relevant for the investigation of the impact of motions on the wake of a moving wind turbine?

2 Methodology

2.1 Experimental set-up

For this research, wind tunnel testing were performed using the Model Wind Turbine Oldenburg (MoWiTO 0.6) mounted on a Stewart platform to mimic motions of a floating wind turbine [2]. The system is shown in the figure 1 (b). This set-up was installed in the closed-loop wind tunnel (3×3 m^2 inlet section) of the University of Oldenburg. All tests were performed with laminar inflow, with a background turbulence of around 0.3 %. The turbine was moved by the platform following harmonic motions in the surge Degree-of-Freedom (DoF). Various amplitudes and frequencies of motion were tested.

A total of 19 hot wire anemometers, arranged horizontally, were installed on an array to measure the wind speed in the wake of the turbine at different downstream positions ranging from 1.5D to 10D downstream, with D, the rotor diameter equal to 0.58 m. This set-up enabled to measure accurately horizontal wind profiles of streamwise velocity in the wake of the turbine with a high sampling frequency of 6 kHz.

2.2 Cases investigated

Surge is the most predominant DoF of a floating turbine, induced by both wind and waves. Amplitude of motions can be as high as 15 m for a multi MW floating turbine [2]. Surge motions can be idealised as sinusoidal motions, with a given frequency, f_p and amplitude, A_p. A graphical visualisation of such a motion can be seen in the figure 1 (b). Frequencies of motion from 0.2 Hz to 5 Hz were tested. Amplitudes

ranging from 4 mm to 70 mm were considered. A total of 3 wind speeds were tested: 3 m/s, 5 m/s and 7 m/s. To allow a direct comparison with a real scale floating wind turbine, two dimensionless parameters are used [3, 4]:

$$\begin{cases} f_{red} = f_p.D/U_0 \\ A^* = A/D \end{cases} \quad (1)$$

In equation (1), f_{red} is the so-called wake reduced frequency. It can be seen as a ratio of two characteristic times: period of one rotor oscillation to the time for an air particle to travel 1D. The higher f_{red}, the more the unsteadiness. A^* is the reduced amplitude with respect to the rotor diameter. Reduced frequencies from 0 to 1.0 and A^* from 0.7 % to 15 % were tested. These are typical values observed at full scale. The turbine was operated at various thrust coefficient by pitching its blades, C_T in [0.6, 1.0] were tested.

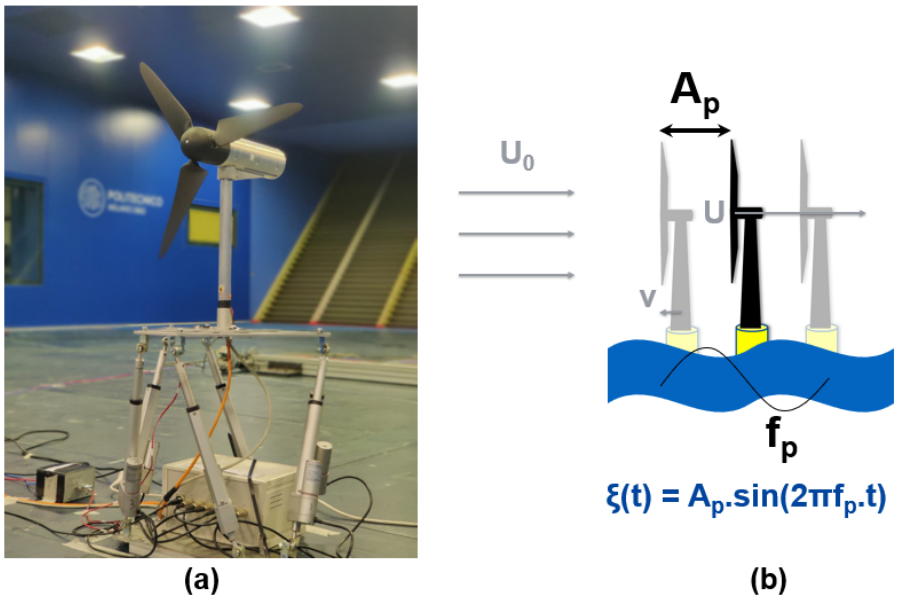


Figure 1: (a) MoWiTO 0.6 mounted on the Stewart platform of the UOL (b) Scheme of a floating wind turbine undergoing surge movement following harmonic motion

3 Results

At the conference, the impact of surge motions on the development of the wake of a floating turbine will be presented.. The figure 2 is a 2D map of the mean wind speed in the wake of the turbine for two cases: no motion and surge motion with $f_p = 0.39$, $A^* = 1\%$. The wake was measured every 0.5D from 1.5D to 10D. The impact of motions on the recovery is clearly visible on the plots, where the center of the wake shows the lowest wind speed around 5D for the moving turbine against around 7D for the fixed turbine. At 10D, the wake of the floating turbine contains about 20 % more energy than the wake of the fixed turbine. This reveals the great impact of motions on wake recovery, where motions are responsible for greater mixing with the outer flow.

In order to understand and explain the interesting results shown in figure 2, the development of turbulence in the wake will be depicted. The impact of various frequencies of motions on the recovery will be shown, where an optimum frequency of motions seems to exist. At the optimum, the wake shows the highest recovery.

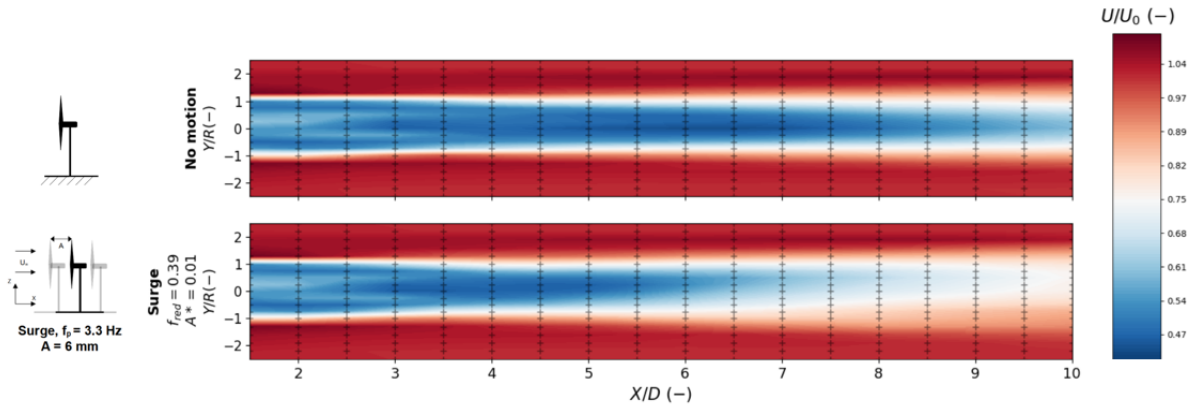


Figure 2: 2D color plot of the streamwise horizontal y-profile of the mean wind speed in the wake of the fixed turbine (top) and the surging turbine with $f_p = 3.3\ Hz,\ A = 6\ mm$ (bottom). For these cases: $U_0 = 5\ m/s,\ C_T \approx 0.8$

4 Conclusion

In this study, the wake of a floating wind turbine was investigated experimentally using a model wind turbine mounted on a 6-DoF motorised platform. The impact of imposed surge motions on the development of the wake was evaluated. The motions are responsible for a higher recovery compared to a fixed turbine. This interesting feature could be useful for the design of floating wind farms, where the triggering of specific motions of a floating turbine could help to improve the performance of a wind farm. Future studies will include more realistic cases, i.e. with turbulent wind and stochastic movements.

Acknowledgements

This project has received funding from the European Union's Horizon 2020 research and innovation programme under the Marie Sklodowska-Curie grant agreement N°860879 as part of the FLOAting Wind Energy netwoRk (FLOAWER) consortium. The authors would like to thank J. Jüchter for his valuable help with MoWiTO 0.6 and J. Puczylowski for his continuous support in the development of the experimental set-up.

References

[1] S. Fu, Y. Jin, Y. Zheng, L.P. Chamorro. Wake and power fluctuations of a model wind turbine subjected to pitch and roll oscillations. *Applied Energy*, 113605, 253. 2019

[2] T. Messmer, C. Brigden, J. Peinke, M. Hölling. A six degree-of-freedom set-up for wind tunnel testing of floating wind turbines. *J. Phys.: Conf. Ser.* 2265, 042015. 2022

[3] I. Bayati, M. Belloli, L. Bernini, A. Zasso. Wind Tunnel Wake Measurements of Floating Offshore Wind Turbines. *Energy Procedia*, 137, 214–222. 2017

[4] B. Schliffke, S. Aubrun Sandrine, B. Conan. Wind Tunnel Study of a "Floating" Wind Turbine's Wake in an Atmospheric Boundary Layer with Imposed Characteristic Surge Motion. *J. Phys.: Conf. Ser.*. 1618(6):062015. 2020

18th EAWE PhD Seminar on Wind Energy
2-4 November 2022
Bruges, Belgium

Wind tunnel study of the wake meandering of a floating wind turbines by a porous disk

Antonin Hubert[a], **Boris Conan**[a], and **Sandrine Aubrun**[a]

[a]Nantes Université, École Centrale Nantes, CNRS, LHEEA, UMR 6598, F-44000 Nantes, France
E-mail: antonin.hubert@ec-nantes.fr

Keywords: floating wind turbine, wake, meandering

Over the years, offshore wind farms are becoming an efficient energy solution thanks to the absence of obstacles, which allows a greater efficiency due to stronger and more constant winds. Indeed, the capacity factor is 23% on average for an onshore wind turbine and 35% for an offshore wind turbine (new models reach 30-35% for onshore and 42-55% for offshore [8]). Also, the development of floating wind turbines allows placement further from the coast, where the water depth is too important for bottom-fixed wind turbines, allowing even greater power. Moreover, in a wind turbine farm, it is important to know the wake generated by a wind turbine upstream in order to better understand its consequences on the one placed downstream. Indeed, the upstream wind turbine affects the wind by a velocity deficit and by an increase of the turbulence intensity which drops the energy efficiency and accelerates the fatigue of the blades of the downstream wind turbine. Thus, different studies have shown that in addition to these stationary mean wake characteristics, an unsteady component is responsible for the motion of the whole far wake at low frequency: the wake meandering [6, 9, 10, 14]. During their experiments on a floating wind turbine model, *Schliffke et al.* [13] presented the different characteristics of the velocity and turbulence intensity profiles downstream of a moving porous disk. The results show the possibility that the signature of the motion imposed on the wind turbine model can be detected in its far wake, implying that the motions of the floating wind turbine directly influence the dynamics of its far wake (at $4.6D$ distance from the porous disk in this case). Therefore, the objective here is to provide informations concerning the wake meandering of a floating wind turbine and to characterize different parameters of the wake according to the platform motion, such as the wake center position, the wake surface or the velocity deficit.

The various experiments are carried out in the atmospheric boundary layer wind tunnel of the Laboratoire de recherche en Hydrodynamique, Énergétique et Environnement Atmosphérique in Centrale Nantes (LHEEA). This wind tunnel has a $26m$ long test section and a $2 \times 2m$ test section. It has a centrifugal fan coupled to a $45kW$ electric motor which allows to reach speeds up to $10m/s$. A grid and spikes are installed at the entrance of the wind tunnel and perforated metal sheets are placed on the ground, over the $15m$ of the test section, to reproduce the model of a marine atmospheric boundary layer [5, 15]. The model used in the experiments represents the $2MW$ floating wind turbine of the FLOATGEN project installed at the Centrale Nantes SEM-REV offshore test site [4]. Using a geometric reduction scale of 1/500, the model is a $160mm$ diameter porous disk with a hub height of $120mm$ and a strength of 57%, which gives a drag coefficient $C_T \approx 0.65$ and a blockage ratio of 2% in the test section [1, 13]. Several studies have shown that the porous disk is an efficient tool that can represent very simply the physics of the far wake of a wind turbine ($x/D > 3-5$, with D the diameter of the wind turbine or its model) [2, 3, 12]. The model is placed in the wind tunnel test section and the three components of the velocity are measured in the plane normal to the mean flow at $x/D = 8$ using a SPIV system. In order to study the effects of the meandering of the wind turbine wake, several cases of float motion were tested: 1D motions with a single frequency (heave, surge and pitch), a realistic 1D surge motion with a range of amplitude and frequency and a real 3D motion with a multi-frequency heave-surge-pitch combination. In order to recover the parameters of the wake and of the meandering phenomenom, the algorithm utilised is a modified method Weighted Geometric-Center (WGC) already used in literature [6, 7, 11] and defined by the formula:

$$\forall \Delta u_i > \Delta u_{thresh} : \begin{cases} y_c = \dfrac{\sum_i e^{\Delta u_i} y_i}{\sum_i e^{\Delta u_i}} \\ z_c = \dfrac{\sum_i e^{\Delta u_i} z_i}{\sum_i e^{\Delta u_i}} \end{cases}$$

where (y_i, z_i) are the coordinates of the point, u_i the velocity and u_{thresh} the thresh value (here $u_{thresh} = 0.9u_{inlet}$).

As seen by *Schlifke et al.* [13], the results show that the motions of the floater do not modify mean fields. Figure 1 present the wake center distributions for the fixed case, a heave motion ($A = 10mm$ and $f = 6Hz$) and a pitch motion ($A = 8$ deg and $f = 2.5Hz$). The different distributions are very similar and have globally the same characteristics with a flattening along the y-axis and a concentration of wake centers inside the dashed line circle, which represent the position of the porous disk, where the density can reach its highest values. Same observations can be carried out for other mean fields like mean velocities, standard deviations, turbulent kinetic energy or Reynolds normal and shear stresses, not shown here. However, statistical graphics show responses of the mouvement on the wake, such as power spectral density on figure 2 where the PSD of the Z positions of the wake center in function of the Strouhal number are plotted for the different cases. The figure is separated into four graphics: the heave, the pitch, the surge and the 'realistic' motions. The black line represent the fixed case and the dashed vertical black lines indicate the Nyquist limit of the SPIV. Thus, the link between the heave and pitch motions and their respective far wake responses are clearly visible, especially for the pitch cases where the motion and wake Strouhal number are nearly the same. The surge mouvements do not seem to impose any response in the wake, or at least a smaller one than in the other studied cases, and the 'realistics' cases with a range of combinaisons amplitude/frequency show no specific response frequency.

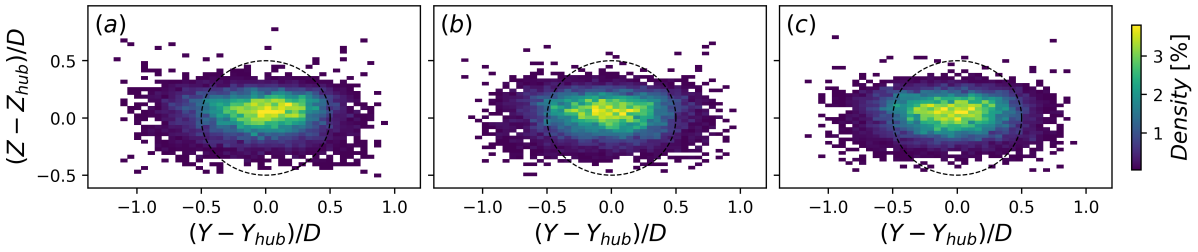


Figure 1: Wake center distribution for (a) fixed case, (b) heave $[A = 10mm, f = 2.5Hz]$ and (c) pitch $[A = 8, f = 2.5Hz]$. The dashed line circle represent the porous disk.

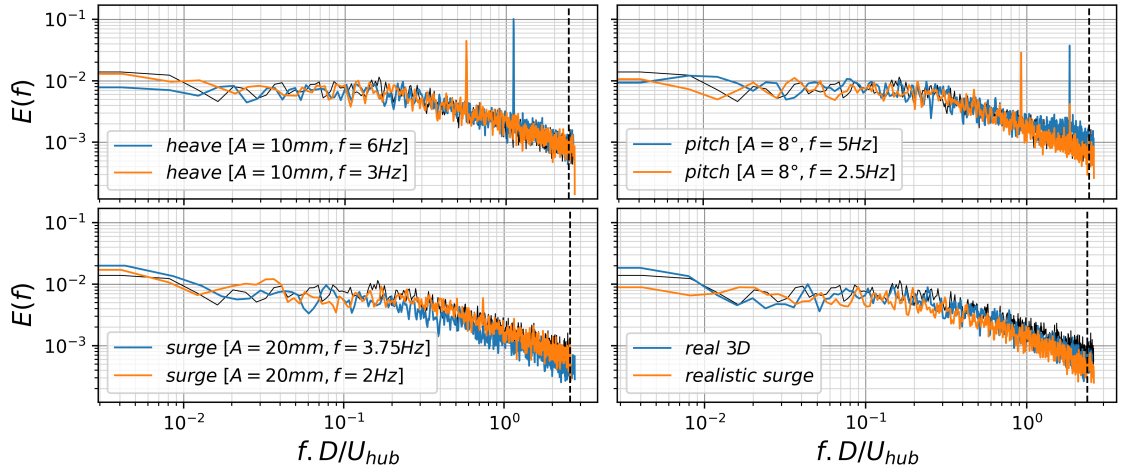


Figure 2: Z-wake center PSD for the different tested cases. The black line represent the fixed casea and the dashed vertical line is the Nyquist limit of the system.

References

[1] S. Aubrun, M. Bastankhah, R. Cal, B. Conan, R. Hearst, D. Hoek, M. Hölling, M. Huang, C. Hur, B. Karlsen, I. Neunaber, M. Obligado, J. Peinke, M. Percin, L. Saetran, P. Schito, B. Schliffke, D. Sims-Williams, O. Uzol, M. Vinnes, and A. Zasso. Round-robin tests of porous disc models. 1256(1):012004.

[2] S. Aubrun, S. Loyer, G. Espana, P. Hayden, and P. Hancock. Experimental study on the wind turbine wake meandering with the help of a non-rotating simplified model and of a rotating model.

[3] S. Aubrun, S. Loyer, P. Hancock, and P. Hayden. Wind turbine wake properties: Comparison between a non-rotating simplified wind turbine model and a rotating model. 120.

[4] T. Choisnet. Report on the requirements of the floating structure.

[5] EDSU. Characteristics of atmospheric turbulence near the ground. (85020).

[6] G. España, S. Aubrun, S. Loyer, and P. Devinant. Spatial study of the wake meandering using modelled wind turbines in a wind tunnel: Spatial study of the wake meandering. 14(7):923–937.

[7] M. F. Howland, J. Bossuyt, L. A. Martínez-Tossas, J. Meyers, and C. Meneveau. Wake structure in actuator disk models of wind turbines in yaw under uniform inflow conditions. 8(4):043301.

[8] I. Komusanac, G. Brindley, D. Fraile, and L. Ramirez. Wind energy in Europe - 2021 statistics and the outlook for 2022-2026.

[9] G. C. Larsen, Danmarks Tekniske Universitet, and Ris?? DTU. *Dynamic Wake Meandering Modeling*. Ris?? DTU - National Laboratory for Sustainable Energy : available from: Ris?? National Laboratory, Information Service Department.

[10] D. Medici and P. H. Alfredsson. Measurements on a wind turbine wake: 3D effects and bluff body vortex shedding. 9(3):219–236.

[11] Y.-A. Muller, S. Aubrun, and C. Masson. Determination of real-time predictors of the wind turbine wake meandering. 56(3):53.

[12] B. Sanderse. Review of CFD for wind-turbine wake aerodynamics. page 28.

[13] B. Schliffke, S. Aubrun, and B. Conan. Wind Tunnel Study of a “Floating” Wind Turbine’s Wake in an Atmospheric Boundary Layer with Imposed Characteristic Surge Motion. 1618(6):062015.

[14] J.-J. Trujillo, F. Bingöl, G. C. Larsen, J. Mann, and M. Kühn. Light detection and ranging measurements of wake dynamics. Part II: Two-dimensional scanning. 14(1):61–75.

[15] VDI-guideline. Physical modelling of flow and dispersion processes in the atmospheric boundary layer, application of wind tunnels. (3793/12).

Emerging technologies and special sessions

18th EAWE PhD Seminar on Wind Energy
2 – 4 November 2022
Bruges, Belgium

Analysis of stresses in a wind turbine composite adhesive using CT Scans and Deep Learning.

A. Wasay Khan[a], C. Balzani[a].

[a] Institute of Wind Energy Systems(IWES) Faculty of Civil Engineering and Geodetic Science Leibniz University Hannover Appelstraße 9A, 30167 Hannover, Germany
E-mail: abdul.wasay.khan@iwes.uni-hannover.de

Keywords: Deep Learning, Digital Transformation, CT Scans, Composites

In the context of digital transformation in computational solid mechanics, databases of material microstructures obtained from CT–Scans or other imaging techniques become extremely important. The need for quick and accurate prediction of mechanical behavior of structures is getting more popular with the developments in generative design and topology optimization. The work will explore and develop a deep learning based approach to predict stress fields in a 2D fibre reinforced composite(adhesive)used in wind energy blades using convolutional neural networks and generative adversarial networks.

Contrary to normal practice, the neural network will take as inputs arbitrary geometries, loads and boundary conditions in the form of different input channels and will predict the von Mises stress distributions. For this purpose, following tasks have to be addressed in the work: generation of image data sets using data obtained from CT Scans and synthetic stress distributions, designing and implementing the architecture of the planned neural network and then finally validating the predicted results with the FEM results. The geometry of fibres from the binarized images have to be obtained and meshed for the consequent FEM analysis so as to create a database for deep learning based framework.



Figure 1: Data Based Computational Mechanics (a) A binarized CT Scan image with boundary conditions (b)Stress prediction using FEA.

The work will also implement a deep convolutional generative adversarial network for generating realistic n-phase CT Scan image data from the available image data. A comparison between real and synthetic data will then be done based on volume fraction, surface areas and other properties to analyze the effectiveness of the

method. For this purpose the implementation of an algorithm which is based on GAN's for the generation of multi-phase 2D and 3D CT Scan data resulting in trained generators that are virtually representative of the CT Scan data has to be designed. Afterwards generated and real data need to be compared using stochastic approaches for validation.

References

[1] Aditya Khadilkar, Jun Wang, and Rahul Rai. Deep learning–based stress prediction for bottom-up sla 3d printing process. The International Journal of Advanced Manufacturing Technology, 102(5- 8):2555–2569, 2019.

[2] Grace X Gu, Chun-Teh Chen, and Markus J Buehler. De novo composite design based on machine learning algorithm. Extreme Mechanics Letters, 18:19–28, 2018.

[3] Imad Hanhan, Ronald F Agyei, Xianghui Xiao, and Michael D Sangid. predicting microstructural void nucleation in discontinuous fiber composites through coupled in-situ x-ray tomography experiments and simulations. Scientific Reports, 10(1):1–8, 2020.

[4] Sebahattin Tiryaki and Aytaç Aydın. An artificial neural network model for predicting compression strength of heat treated woods and comparison with a multiple linear regression model. Construction and Building Materials, 62:102–108, 2014.

[5] Xiaofang Hu, Jian Fang, Feng Xu, Bo Dong, Yu Xiao, and Luobin Wang. Real internal microstructure based key mechanism analysis on the micro-damage process of short fibre-reinforced composites. Scientific reports, 6:34761, 2016.

[6] Zhenguo Nie, Haoliang Jiang, and Levent Burak Kara. Stress field prediction in cantilevered structures using convolutional neural networks. Journal of Computing and Information Science in Engineering, 20(1), 2020.

[7] Zijiang Yang, Yuksel C Yabansu, Reda Al-Bahrani, Wei-keng Liao, Alok N Choudhary, Surya R Kalidindi, and Ankit Agrawal. Deep learning approaches for mining structure-property linkages in high contrast composites from simulation datasets. Computational Materials Science, 151:278–287, 2018.

18th EAWE PhD Seminar on Wind Energy
2 – 4 November 2022
Bruges, Belgium

High fidelity fluid-structure interaction simulation of a multi-megawatt airborne wind energy reference system in cross-wind flight

Niels Pynaert[a,b], Jolan Wauters[a,b], Guillaume Crevecoeur[a,b] and Joris Degroote[a,b]

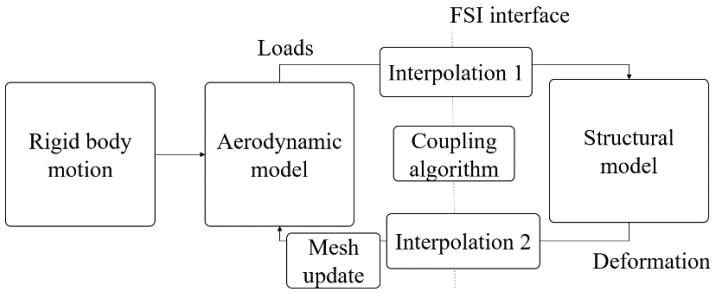
[a] Department of Electromechanical, Systems and Metal Engineering
Faculty of Engineering and Architecture
Ghent University
Sint-Pietersnieuwstraat 41, 9000 Gent, Belgium
[b] Core lab EEDT, Flanders Make, Belgium

E-mail: Niels.Pynaert@Ugent.be

Keywords: Airborne wind energy, Fluid-structure interaction, Chimera.

Airborne wind energy (AWE) is an emerging technology for the conversion of wind energy into electricity by flying crosswind patterns with a tethered aircraft connected to a generator either on board or on the ground. Having a proper understanding of the unsteady interaction of the air with the flexible and dynamic system during operation is key to developing viable AWE systems [1]. High fidelity simulation tools are needed to correctly predict these interactions, which will provide insights for the design and operation of advanced and efficient AWE systems. The research goal of this contribution is to simulate the time-varying fluid-structure interaction (FSI) of an AWE system in a cross-wind flight manoeuvre.

This research examines the multi-MW AWE reference system presented in [2]. The high fidelity FSI of the wing of this system is determined by means of a partitioned and explicit approach (Figure 1, left), using the open-source coupling tool CoCoNuT. This method couples an existing finite element method (FEM) model of the wing structure with a newly developed computational fluid dynamics (CFD) model of the wing aerodynamics. Moreover, a prescribed circular flight path of the AWE system is enforced and realized by overlaying the moving body-fitted mesh attached to the AWE aircraft's wing over a background mesh. By means of the chimera technique both meshes are connected, interpolating the solution at the overset boundary (Figure 1, right). An arbitrary Lagrangian-Eulerian (ALE) formulation is used such that the wing body-fitted mesh is able to update according to structural deformations. For comparison, a two-way and one-way FSI approach are considered. For the one-way coupling, the structural displacement is not fed back to the aerodynamic model as opposed to the two-way coupling.



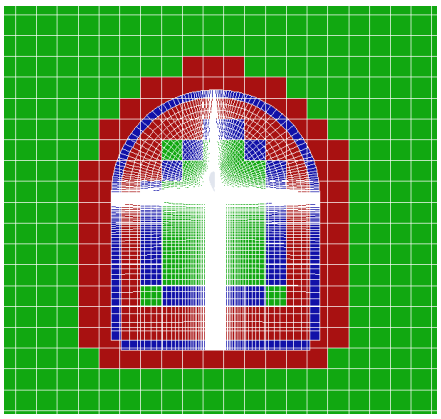


Figure 1: Partitioned FSI approach (left). Chimera mesh connectivity. Green: solved cells, red: donor cells, blue: receptor cells [3] (right).

The simulations are initialized with an unsteady CFD simulation by simulating the aircraft motion before t=0 as indicated in Figure 2 (left). The system is flying at 80 m/s and 0° angle of attack in a circular path with 265.5m radius. At t=0 the FSI simulation starts. On the right of Figure 2 the lift coefficient is plotted as a function of time. Due to the structural oscillation of the wing, the aerodynamic forces change. The oscillations die out after around 1.2 seconds. Hence, no aeroelastic instabilities are encountered. The results of the horizontal condition are plotted as well for comparison. The crosswind flight motion decreases the lift coefficient slightly compared to the horizontal motion. There is a reduction in lift coefficient of 1.4% for the FSI prediction, compared to the CFD prediction. This is due to a negative twist deflection of -0.45°.

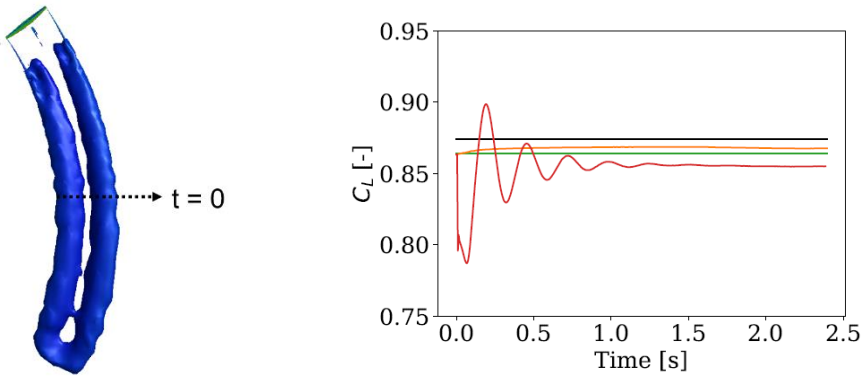


Figure 2: Visualization of wake and pressure contour (left). Lift coefficient vs time (right). Black: steady CFD (horizontal), green: steady FSI (horizontal), red: unsteady FSI (two-way), orange: unsteady FSI (one-way).

A contour plot of the magnitude of deformation is given in Figure 3 for the unsteady FSI simulation after the oscillations disappeared. The deflection and twist deformation at the tip versus time are plotted in Figure 4 for the steady and unsteady FSI simulation. Due to the circular motion there is a difference of 12.6% in tip deflection between the left and right wing. The right wing tip deforms more due to the higher experienced aerodynamic load.

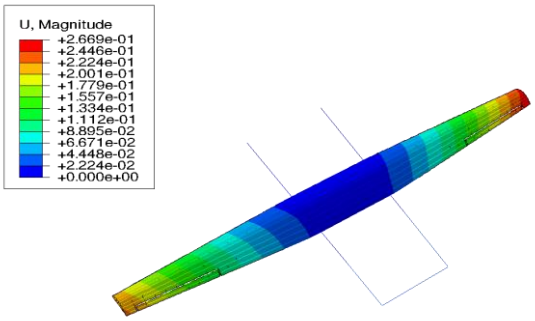


Figure 3: Magnitude of deformation for the unsteady FSI simulation after oscillations disappeared.

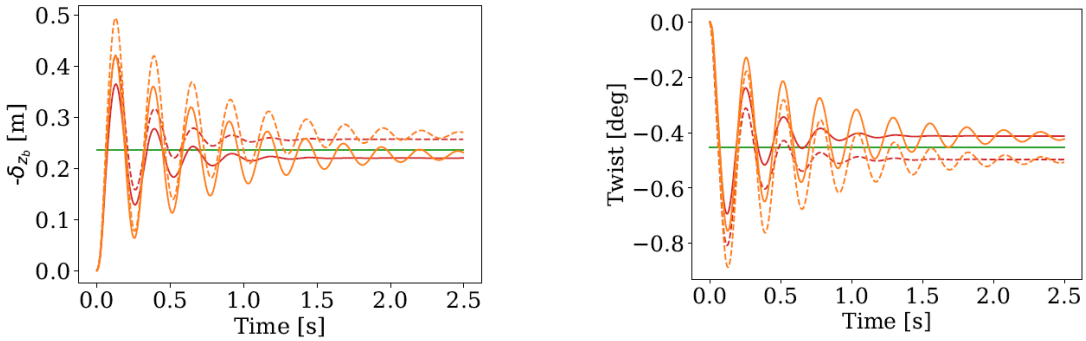


Figure 4: Deflection and twist deformation at tip vs. time. Green: steady FSI (horizontal), orange: unsteady FSI (one-way), red: unsteady FSI (two-way), solid line: left wing, dotted line: right wing.

The overset/Chimera technique has been proven to be a robust approach to simulate the motion of an AWE system in CFD simulations. This technique allows taking into account the large rigid body motion of the aircraft while maintaining a constant mesh quality. Ongoing research is directed towards coupling our high fidelity FSI model with the body dynamics model presented in [2] in pursuit of physically feasible flight prediction and the accurate simulation of power production.

References

[1] P. Echeverri, T. Fricke , G. Homsy and N. Tucker. The energy kite: selected results from the design, development and testing of Makani's airborne wind turbines, 2020.

[2] D. Eijkelhof, S. Rapp, U. Fasel, M. Gaunaa and R. Schmehl. Reference design and simulation framework of a multi-megawatt airborne wind energy system. *Journal of Physics Conference Series*, 2020.

[3] N. Pynaert, J. Wauters, G. Crevecoeur and J. Degroote. Unsteady aerodynamic simulations of a multi-megawatt airborne wind energy reference system using computational fluid dynamics. *Journal of Physics: Conference Series*, 2265 042060, 2022.

18th EAWE PhD Seminar on Wind Energy
2-4 November 2022
Bruges, Belgium

Modelling and control of Airborne Wind Energy Systems using lifting line/surface aerodynamics

Jean-Baptiste Crismer, **François Trigaux**, **Matthieu Duponcheel**, and **Grégoire Winckelmans**

Institute of Mechanics, Materials and Civil Engineering, UCLouvain,1348 Louvain-la-Neuve, Belgium

E-mail: jean-baptiste.crismer@uclouvain.be

Keywords: Airborne Wind Energy, Lifting Line, Lifting Surface

1 Introduction

Compared to wind turbines, airborne wind energy systems (AWES) are not rigidly supported by a tower and therefore need to stabilize themselves in turbulent wind fields and along various trajectories. The study of their behaviour in their environment, and the development of models, is therefore of primary importance. Much research was already achieved in the field, and various models were already developed. However, many models used for control applications are based on very simplified aerodynamics, such as empirical lift coefficient laws. Such models may not be accurate enough while thinking about the complex aerodynamics AWES can have. They indeed follow trajectories with sharp turns and rapid accelerations while operating at a high angle of attack. On top of that, the deformation of the wing has a huge influence on its aerodynamic properties.

In this work, we investigate the use of more advanced models such as lifting line (LL) and lifting surface (LS). They allow to better take into account the aerodynamics for the establishment of AWES models to study their performance and control them. The LL and LS methods are cheap computationally, yet they already provide a fair representation for fixed wing and soft kite aerodynamics in quasi-steady situations (i.e., with a time scale moderate relatively to b/U_∞). This study focuses on soft kite modelling, thus considering curved lines/surfaces, to investigate their steering behaviour.

2 Methodolgy

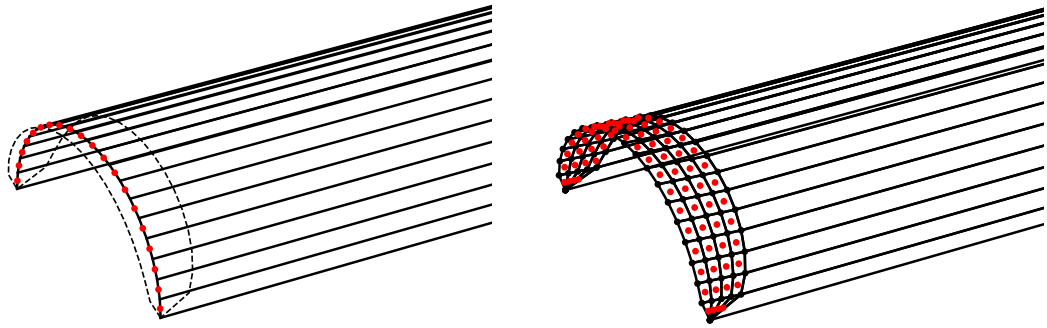
The lifting line/surface models are built using horseshoe vortices and vortex rings assemblies [4], as depicted in Figure 1, where the shed vortex sheet accounts for the influence of the wake. The induced velocity is evaluated for each vortex segment using the Biot-Savart law.

The implemented lifting line is a numerical extension of the Prandtl lifting line method [5]. It can be implemented in a non-linear way to allow the use of polar curves[1]. Kite airfoil polar curves (lift, drag and moment coefficients) are obtained from experiments or are generated using RANS. The effect of unsteady aerodynamics can also be implemented. The lifting surface best represents low aspect ratio wings (such as soft kites). The method also captures the chordwise load distribution. Polar curves cannot be used but geometrical complexities can be taken into account (such as large deformations, camber effects, etc.).

Simulations for different configurations are performed to better understand the steering mechanism. The results obtained with the curved lifting line and lifting surface methods are compared and discussed.

3 Soft wing deformation and steering

Two deformation modes are identified to be responsible for the steering of a kite in yaw [2]:

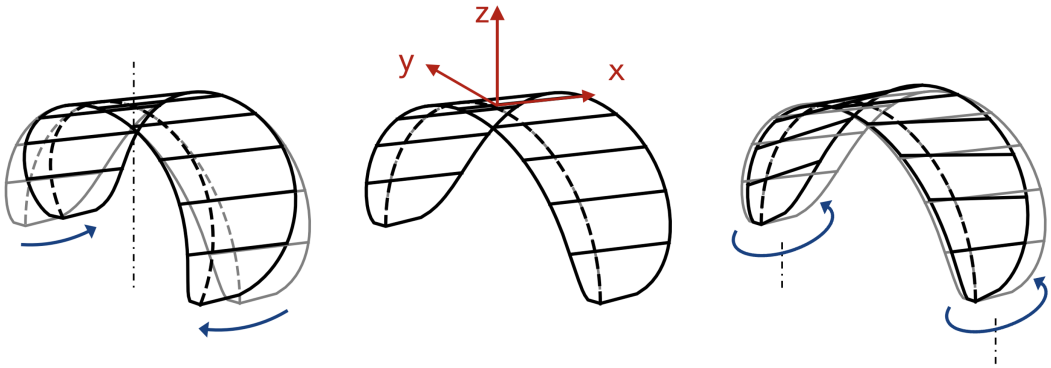


(a) (b)

Figure 1: Vortex assemblies for the lifting line (a) and lifting surface (b) methods. The red dots represent the control point.

- Twist of the airfoil profiles along the span;
- Deformation of the aerodynamic centerline;

They are shown in Figure 2. The difference in angle of attack along the span, due to the twist, induces a non-uniform repartition of the drag between the left and right side of the wing, thus producing a yawing moment. On the other hand, the displacement of the aerodynamic centerline creates a lever arm for the lift force that acts on the tip/vertical parts of the wing and also produces a yawing moment [2].



(a) (b) (c)

Figure 2: Schematic of the different configuration: deformation of the centerline (a); undeformed configuration (b); and twist of the airfoil along the centerline (c).

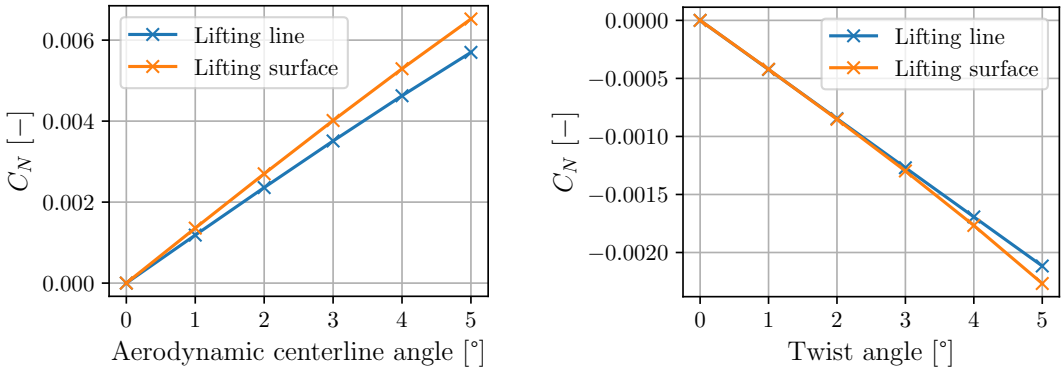
To understand how those two deformation modes contribute to steering, the yawing moment is evaluated for each of them. To be able to compare the LL and LS in a consistent way, all the 2D airfoils are flat plates perpendicular to the aerodynamic centerline. In the case of the LL it corresponds to choosing $a_0 = \frac{dC_L}{d\alpha} = 2\pi$. The deformation modes are applied linearly, as depicted in Figure 2, along the aerodynamic centerline. For the aerodynamic centerline deformation, it means that its angle with respect to the z-axis is given by

$$\theta_{a.c.}(s) = \theta_{a.c.,max}\frac{s}{b} \tag{1}$$

where s is the curvilinear abscissa and b the span of the wing (following the s). For the twist, the local 2D angles of attack are increased by

$$\alpha_t(s) = \alpha_{t,max}\frac{s}{b} \tag{2}$$

Then for each deformed configuration, the LL and LS method are used to evaluate the moment that results from the aerodynamic forces distribution obtained. The moment is computed at the centre of the straight line joining both tips. The induced yawing moment is plotted in Figure 3 as a function of $\theta_{a.c.,max}$ (a) and $\alpha_{t,max}$ (b).



(a) (b)

Figure 3: Yawing moment induced by aerodynamic centerline deformation (a) and twist along the aerodynamic centerline (b).

As it can be seen, for such small actuation, the response is nearly linear. A small difference between the LL and LS can be noted. Also, with our definitions of the actuation and the deformation, the magnitude of the yawing moment obtained from the aerodynamic centerline deformation is larger than the one obtained from twisting the wing. It means that this mode has a greater role in the steering of the kite.

4 Conclusion and perspectives

In this work, the steering capabilities of the two deformation modes were quantified. This is a first step towards the coupling of those models with the Julia kite power tools [3] to improve the current aerodynamic model. When coupled, a steady solution will be computed at each time step using the current inflow condition. It will then allow to investigate the behaviour and control of modelled AWES in different flow conditions. Various perturbed inflows are targeted such as the encounter with a system of contra-rotating vortices (as when crossing the wake of another wing or kite), with wind gusts, or being subjected to the whole spectrum of turbulent scales in atmospheric turbulent wind fields or wind turbine wakes, and generated using Large Eddy Simulation (LES).

The simple LL and LS models constitute a first step; yet they already allow to get insights into the dynamics of AWES at low computational costs, and investigate control strategies in various scenarios. The next level of modelling will use the actuator line model as implemented in our LES code (and which also allows for fast variations) for fixed wing concepts, and also a new flexible actuator curve model [6] for kite configurations. The model has already been used for aeroelastic simulations of large wind turbine blades in turbulent winds. Such LES will be useful to study AWES with fast and complex dynamics, and their turbulent wakes; which is not possible with the LL and LS models. First simulations for a rigid wing AWES were already run as test cases. Its wake can be visualized in Figure 4.

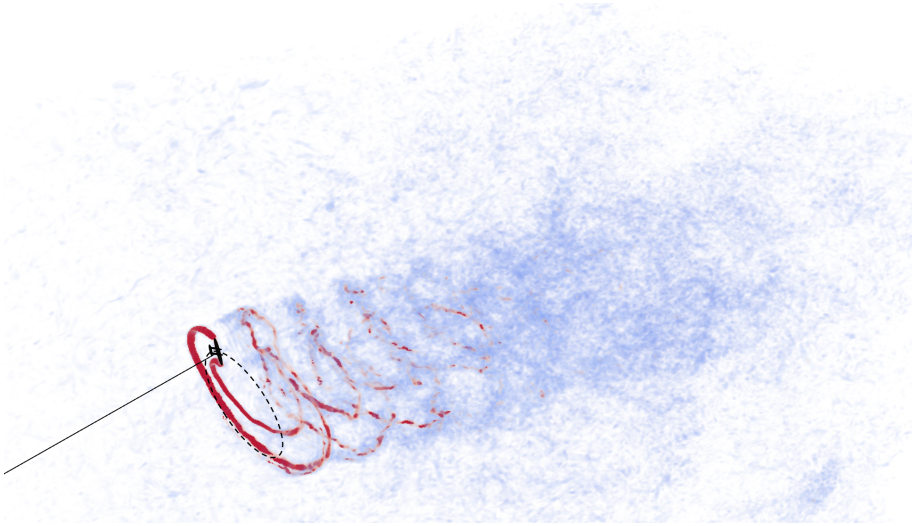


Figure 4: LES of a rigid wing AWES in a inflow at U_∞ = 10 m/s with 6% TI. Vorticity field.

Acknowledgements

This work is carried out as part of the BORNE project, funded by the Energy Transition Funds from the SPF Economy. BORNE (Belgian Offshore aiRborne wind Energy): Developing the tools and insight to expand the Belgian offshore wind farms with airborne wind energy systems.

Computational resources have been provided by the Consortium des Équipements de Calcul Intensif (CÉCI), funded by the Fonds de la Recherche Scientifique de Belgique (F.R.S.-FNRS) under Grant No. 2.5020.11 and by the Walloon Region.

References

[1] J. D. Anderson. *Fundamentals of aerodynamics*. McGraw-Hill, 5th edition, Feb. 2011.

[2] J. Breukels. *An engineering methodology for kite design*. PhD thesis, Delft University of Technology, 2011.

[3] U. Fechner. Julia kite power tools. https://github.com/aenarete/KiteSimulators.jl.

[4] J. Katz and A. Plotkin. *Low-Speed Aerodynamics*. Cambridge Aerospace Series. Cambridge University Press, 2 edition, 2001.

[5] R. Leloup, K. Roncin, G. Bles, J.-B. Leroux, C. Jochum, and Y. Parlier. *Estimation of the Lift-to-Drag Ratio Using the Lifting Line Method: Application to a Leading Edge Inflatable Kite*, pages 339,355. 09 2013.

[6] F. Trigaux, P. Chatelain, and G. Winckelmans. A flexible actuator curve model for aeroelastic simulations of wind turbines in atmospheric boundary layers. *Journal of Physics: Conference Series*, 2265(2):022050, May 2022.

18th EAWE PhD Seminar on Wind Energy
2-4 November 2022
Bruges, Belgium

Multi-objective substructure generation

Emmanouil Panagiotou[a]

[a]Freie Universität Berlin, Berlin, Germany

E-mail: emmanouil.panagiotou@fu-berlin.de

Keywords: Artificial Intelligence, Machine Learning, Multi-objective Optimization, Generative Design, Offshore Wind Turbines, Industrial Design.

Abstract

The design process of a offshore Wind Turbine (WT) structure depends on many parameters and boundary conditions. These are traditionally set by engineers, using complex and site-specific information. In recent years, (big) data and Artificial Intelligence (AI) are used to generate new realistic digital artifacts such as images, text, audio, or even molecules, based on existing training data. In this work, we investigate how to generate WT substructures using AI. As data regarding WT structures are sparse or non-existent, in this work we cannot follow a data-driven generative approach. Instead, we formulate a well-defined design space for substructures as 3D graphs based on domain knowledge and deploy a multi-objective genetic algorithm to create optimal designs. To demonstrate a use case for the generated data, we train a machine learning model that predicts the fitness of individual designs. To comprehend and trust the AI designs we employ explainable AI to evaluate the contribution of individual features to the goodness of a design.

1 Introduction

Our research focuses on the design of offshore Wind Turbines, and more specifically the supporting substructure, using AI. Recently, generative AI has had great success in producing novel data by learning to imitate distributions of existing datasets. However, existing substructure design databases are very unbalanced, containing mostly Monopile or X-brace Jacket structures, and often, missing detailed information about the exact topology. Therefore, we strive to use generative techniques that do not require real data, to create new designs that can be used to augment existing datasets.

While previous works maintain a simple predefined jacket structure, and try to optimize only certain parts of it [2, 4], in our process, we define a design space based on domain knowledge that can describe original designs, as well as, a multi-objective evaluation space.

2 Structure Formulation/Evaluation

Previous works on optimization of substructures are single-objective and have a specific design formulation. The main target for the optimization procedure are specific parts of a defined structure (e.g. thickness of the braces) [2]. Our goal is to create novel designs which can serve as inspiration for engineers, for augmenting existing datasets, and for training new models. Therefore, we define a more abstract design space, as well as multiple evaluation criteria, derived from domain knowledge.

Design Space

Our abstract definition of Wind Turbine substructures as 3D graphs, allows a parameterization through multiple Categorical and Continuous variables. An entire graph structure can be defined as follows.

$S = \{L, H, G_N, R_0, R_e, r, C\} \bigcup \{L_H, C_H\}$

Where:

- L is the number of layers

- H is the total height
- G_N is the normal *n-gon* of N nodes, that is maintained constant for each layer
- R_0 is the base radius
- R_e is the radius evolution (factor by which the radius decreases with each layer)
- r is the rotation in degrees between the bottom and top layer
- $C = \{C_0, C_1, ...\}$ are the different connection types between layers

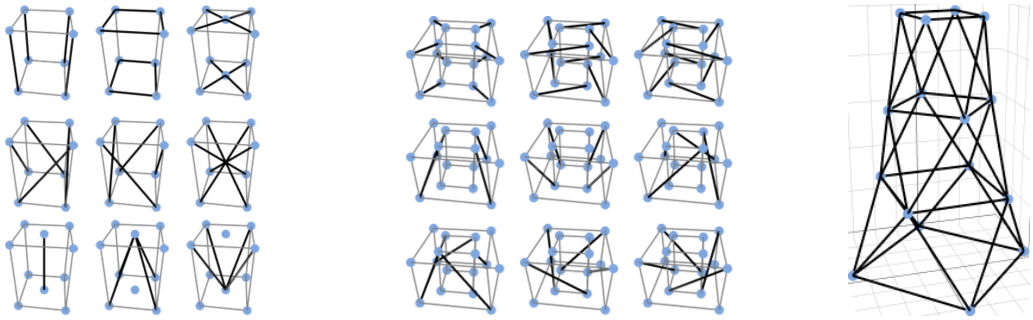
Additionally for horizontal layers:

- L_H is the number of horizontal layers
- D_H is a set of distances between the L_H horizontal layers
- $C_H = \{C_{H0}, C_{H1}, ...\}$ are the horizontal connection types

Because nodes of the n-gon belong to a circle, we can define a radius for each layer that controls the width of the structure. Similarly, nodes can be rotated uniformly using the rotation variable, to form *twisted structures* [1]. By expanding the structure horizontally, we can also define multiple horizontal layers which can serve for additional stability.

Connections between layers are well-defined both vertically and horizontally, and for all constant n-gon configurations. The choice of these specific connection types relies on domain knowledge. Particularly, our selection of connection types is based on typical *lattice structures* [5].

In Figure 1 connections for squares (4-gon) are presented, together with a sample structure.



(a) Vertical layer connection types (b) Horizontal layer connection types (c) Sample structure

Figure 1: Predefined layer connection types (examples for 4 nodes). A visualization of a sampled structure is also depicted.

Evaluation Space

In order to compare and optimize structures that belong to the abstract design space, multiple fitness indicators are used as different objectives. Ideally, we would want information from the entire life cycle of the structure to influence the decisions of the optimization algorithm, as well as an indicator of plausibility based on real data samples. Due to missing real data, for now, we rely on simulations to provide feedback on the stability of the structures, which should render them more plausible.

Three different stability tests are preformed by simulation using *OpenSeesPy*, an open-source finite element software framework in Python [7]. The *Compression* test applies a constant downward load among all top nodes (dividing the total load among all points). Similarly, the *Pushover* test, applies a constant load to one side of the structure (since the structures are symmetrical by definition). Lastly, we emulate a *Tortion* test by applying a twisting load. For all tests, we can calculate the maximum displacement among all edges, as seen in Figure 2. More advanced structural tests can be added as different objectives, but for now, we add the resulting displacements to form one unified *structural stability objective*. The second objective is the total mass of the structure, that is an estimate of its total material cost.

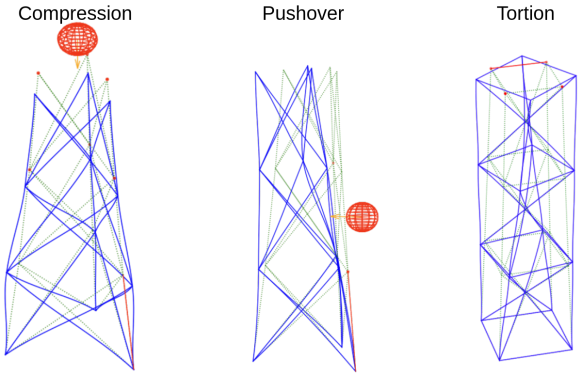


Figure 2: Visualizations of the structural tests. Highlighted with red is the edge with the highest displacement.

Future Directions

In future work, we would like to define an even more abstract formulation of the design space. A more general approach would eliminate the predefined connection types and layers by allowing arbitrary positions of nodes between the bottom and top layer, as well as any connection between them. This setup complicates the definition of structural (and other) tests, because of loss of symmetry. On a high note, it could facilitate more novel and interesting design ideas.

To ensure plausibility of the generated substructures, the objective space would have to include evaluation criteria learned from data-driven models, based on real data of the entire life-cycle of a structure, existing designs, and feedback/annotations from engineers.

3 Multi-objective optimization

Including multiple objectives to the problem, yields a multidimensional evaluation space. Therefore, the optimization procedure will return a set of alternative solutions, as some solutions might outperform others in one objective, but be inferior in another. We use NSGA-II, an evolutionary multi-objective algorithm, for the optimization process [3]. NSGA-II, is a genetic algorithm where best solutions in a population are selected, mutated and combined to create better offspring. The difference lies in the way solutions are ranked for multiple objectives. A solution is said to *dominate* another, when it is at least as good as the other for all objectives, but outperforms it for at least one objective. By computing dominated solution sets for all individuals in the population, they are sorted into different fronts. Using tournament selection, best ranked individuals are chosen for reproduction by crossover. This is performed by randomly exchanging genetic information between two parents. For example, when a solution with a triangle base is combined with a square one, the resulting structure has a 50 percent chance of being comprised of squares or triangles. This process continues for all features of the structures, until a new candidate is created. After a set number of generations, the algorithm converges to a final set of different solutions, that are optimal with regard to all objectives.

4 Statistics & Explanations

As solutions are evolved in a continuous process for many generations, we extract statistics which provide insight into the choices of the algorithm.

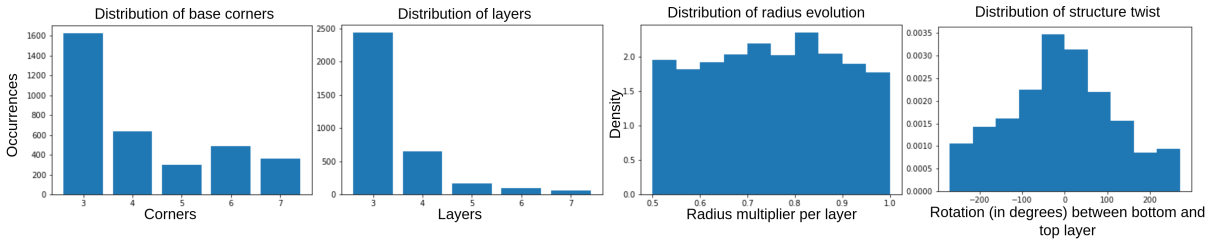


Figure 3: Population statistics of the Genetic algorithm

As seen in Figure 3, we observe that a low number of corners (nodes), and layers, are preferred. This relies mainly on the cost objective, as structures with lesser mass, are rewarded.

The ultimate goal of this generative approach is to augment existing datasets. To demonstrate this, we created a dataset of structures by sampling best solutions created by the genetic algorithm. Using this dataset, we trained a Neural Network that, given a structure's features as input, predicts its performance for only the structural objectives (all stability tests). In an attempt to explain the trained Neural Network, we deploy an idea from interpretable Artificial Intelligence to measure the importance of all the different features of the structures, for the outcome (prediction). Specifically, we compute the Shapley values [6] which can be used to estimate the importance of features as seen in Figure 4.

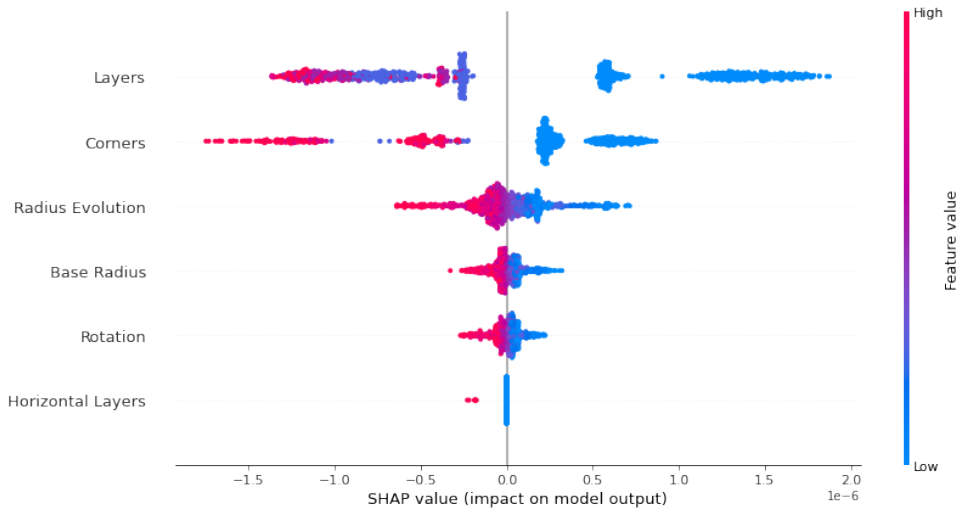


Figure 4: Feature importance (Shapley values) for the Compression test.

Acknowledgements

This project is Funded by the Deutsche Forschungsgemeinsschaft (DFG, German Research Foundation) - SFB1463 - 434502799. I gratefully acknowledge the assistance of Anton Kriese in developing the simulation & visualization environment for the 3D structures.

References

[1] I.-W. Chen, B.-L. Wong, Y.-H. Lin, S.-W. Chau, and H.-H. Huang. Design and analysis of jacket substructures for offshore wind turbines. *Energies*, 9(4):264, 2016.

[2] K.-H. Chew, K. Tai, E. Ng, and M. Muskulus. Analytical gradient-based optimization of offshore wind turbine substructures under fatigue and extreme loads. *Marine Structures*, 47:23–41, 2016.

[3] K. Deb, A. Pratap, S. Agarwal, and T. Meyarivan. A fast and elitist multiobjective genetic algorithm: Nsga-ii. *IEEE transactions on evolutionary computation*, 6(2):182–197, 2002.

[4] J. Häfele, C. G. Gebhardt, and R. Rolfes. A comparison study on jacket substructures for offshore wind turbines based on optimization. *Wind Energy Science*, 4(1):23–40, 2019.

[5] A. Panesar, M. Abdi, D. Hickman, and I. Ashcroft. Strategies for functionally graded lattice structures derived using topology optimisation for additive manufacturing. *Additive Manufacturing*, 19:81–94, 2018.

[6] L. S. Shapley. Stochastic games. *Proceedings of the national academy of sciences*, 39(10):1095–1100, 1953.

[7] M. Zhu, F. McKenna, and M. H. Scott. Openseespy: Python library for the opensees finite element framework. *SoftwareX*, 7:6–11, 2018.

18th EAWE PhD Seminar on Wind Energy
2-4 November 2022
Bruges, Belgium

Multidisciplinary Design, Analysis and Optimization of fixed wing Airborne Wind Energy Systems

Filippo Trevisi[a]

[a]Department of Aerospace Science and Technology, Politecnico di Milano, Via La Masa 34, 20156 Milano, Italy

E-mail: filippo.trevisi@polimi.it

Keywords: MDAO, AWE, flight stability

1 Introduction

Airborne Wind Energy (AWE) is the field of wind energy which aims at harvesting wind power throughout the use of airborne systems. Airborne Wind Energy Systems (AWES) are classified based on how electricity is generated and on the their flight operations. Power can be generated with a fixed or a moving ground station (Ground-Gen AWES) or on the flying device (Fly-Gen AWES). The flight operations can be additionally divided into crosswind, tether-aligned and rotational. This PhD work focuses on the AWES generating power by flying crosswind with fixed wings.

To enter the market successfully, AWES need to prove reliability and robust operations over long time frames, on top of being competitive in the energy market. These requirements shall be considered from the very first stages of an AWE project, when the system design is not fixed and modifications can impact system performances. Bearing this in mind, the present work introduces a new design approach where the AWES is designed based on market metrics, while ensuring good dynamic characteristics, which may enhance controllability and reliability. Based on the theory developed in [1], a multidisciplinary design, analysis and optimization framework: *T-GliDe* [2] (Tethered Gliding system Design) is been built with the aim of designing an AWES maximizing economics related objective functions, while satisfying constraints related to flight stability on top of conventional constraints. This approach differs from optimization approaches based on low-fidelity models or on approaches which focus on the aero-structural design for specific design load cases, which typically do not include flight dynamics, and from approaches which find power output and loads by running time simulations.

This abstract is organized as follows: In Section 2, the methodology and main results of the flight mechanics theory for AWES are summarized. In Section 3, the methodology and main results of a flight trajectory optimization are presented. In Section 4, an under-development reference economic model for AWE is introduced. Finally, in Section 5 how the aforementioned topics are included in the MDAO framework is presented.

2 Flight stability

The flight mechanics problem of AWES is fundamentally different from the one of conventional aircraft for mainly three reasons: the presence of the wind, needed for the power generation, the presence of the tether, which transfers all forces acting on the airborne unit to the ground, and the need for maneuvers to keep the aircraft in the correct trajectory and attitude. Therefore, a specific theory for AWES to evaluate flight stability is needed.

An analytical modelling approach to study flight stability is detailed in [1]. The six d.o.f. equations of motion are linearized about a fictitious steady-state motion of the AWES in the circular path. No real steady-state can be achieved during power generation because gravitational forces and aerodynamic forces related to the mean elevation angle act periodically on the kite ($V_w \sin(\beta)$ and $g\cos(\beta)$ in Figure 1). The fictitious steady-state motion is then computed by considering all the fluctuating terms as disturbances. The peculiarity of the selected flight path is that, if the fictitious steady-state is considered, centrifugal forces, induced by the constant turning maneuver, are balanced by the radial component of the force on the tether. In this way, lift is not used for the turn maneuver. The derivatives of external forces and moments are taken about the fictitious steady-state, to formulate the linearized

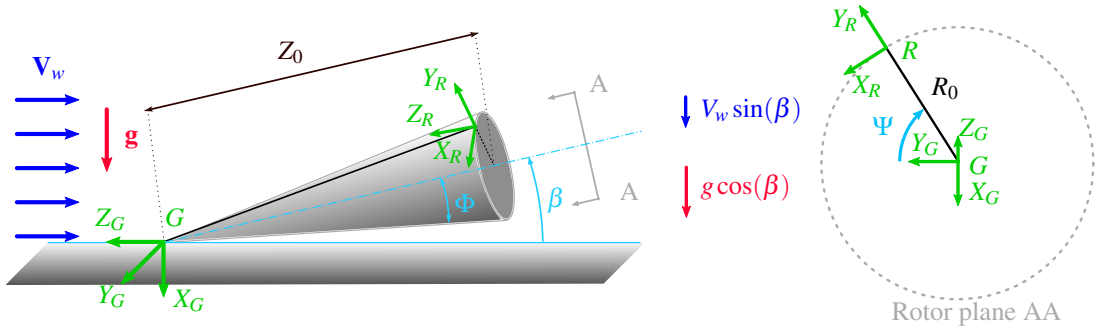


Figure 1: Coordinate systems needed for the flight mechanics theory [1].

problem. As the AWES performs a constant turning maneuver, the longitudinal and lateral equations of motion are coupled. Finally, the stability of the system can be studied by looking at the eigenvalues of the linearized problem

$$\dot{\mathbf{x}}(t) = \mathbf{A}\mathbf{x}(t). \tag{1}$$

Since the problem for AWES is space-dependent (it is not the case for conventional aircraft), new eigenmodes compared to aircraft are found. The procedure to study stability is summarized in Figure 2.

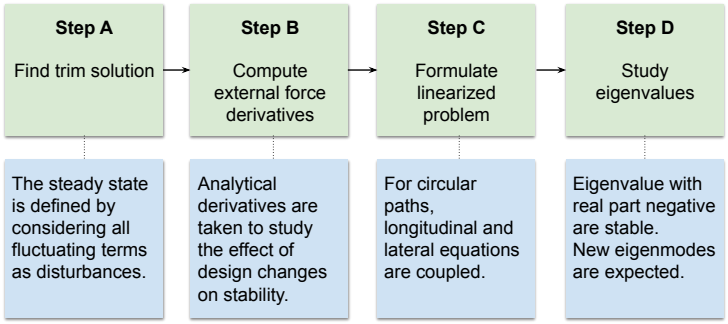


Figure 2: General procedure for the stability analysis of fixed wing AWES [1].

The linearized model allows for a simplified investigation of the influence of main wing geometry (position, area, aspect ratio, sweep, dihedral), main wing aerodynamics, control surfaces aerodynamics and geometry (area, aspect ratio, position), tether attachment position, tether mechanical and aerodynamic properties and mass properties of the AWES on flight stability. Also, since it does not primarily impact the dynamics of the flying craft, the power generation mechanism is not modeled. In this way, the model, with small modifications, to model both Ground-Gen and Fly-Gen AWES.

3 Flight trajectory optimization

Is the flight mechanics theory introduced in Section 2 representative of optimal flight trajectories? To answer this question and to study optimal trajectory physical characteristics, an optimal control problem is formulated in [3]. To approach the problem in a simplified way, a low-fidelity dynamic model for Fly-Gen AWES is selected. Instead of solving the dynamics $x(t)$ and the optimal control inputs $u(t)$ in time, the present approach models the periodic problem in the frequency domain, making use of a Harmonic Balance method, which expands the periodic solution $x(t)$ and the control inputs $u(t)$ as a Fourier series

$$x(t) \approx \frac{X_0}{2} + \sum_{k=1}^{N_x} X_{k,s}\sin(k\omega t) + X_{k,c}\cos(k\omega t), \quad u(t) \approx \frac{U_0}{2} + \sum_{k=1}^{N_u} U_{k,s}\sin(k\omega t) + U_{k,c}\cos(k\omega t). \tag{2}$$

Working with the Fourier coefficients and not with the time series themselves allows to reduce the problem size significantly, to look for periodic solutions implicitly and to study the solution in an intuitive way by looking

at the contribution of the different harmonics. Moreover, the analytical gradient of the objective function and the constraints with respect to the optimization variables can be provided to the solver. This methods may also be suitable to conventional wind energy. The procedure to formulate the optimal control problem in the frequency domain is presented in Figure 3.

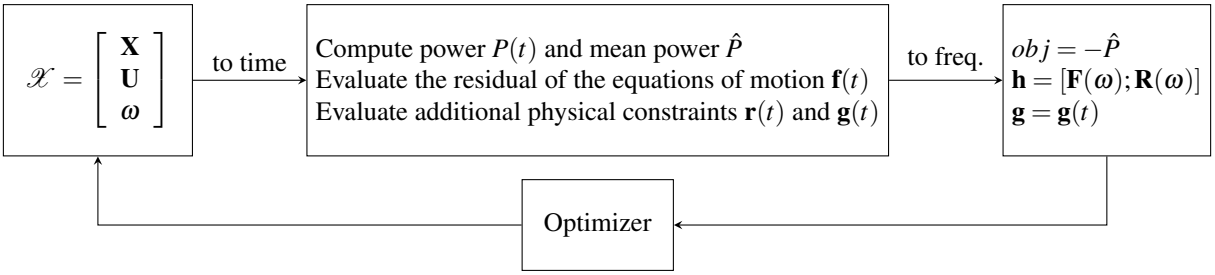


Figure 3: Graphical representation of the optimal control problem setup [3]. $\mathscr{X}$ are the optimization variables; **X** and **U** are the Fourier coefficient of the dynamics and the control inputs and ω is the main frequency. **h** and **g** are equality and inequality constraints.

Optimal control problems are solved with an incremental level of complexity and physical representation, allowing to understand results in a physical way and to give analytical approximations. Moreover, the optimal control inputs are modelled with the lowest number of harmonics, showing that they can be modelled with a sinus of period equal to the revolution period (or of frequency $f = 1P$). Optimal trajectories, for the analyzed case, are found to be within the linear bounds of the flight mechanics theory, introduced in Section 2.

4 Reference economic model for AWE

As for conventional wind turbines, the design of AWES will be driven by economics. Therefore, when developing a comprehensive design framework, focus should be given to both technological and economic aspects. A reference economic model for AWE [4] is being developed by collecting data from AWE companies. Economic metrics beyond LCOE are included, following trends in conventional wind energy. Moreover, reference business cases, representative of the energy markets of the future, are being defined.

5 Multidisciplinary Design, Analysis and Optimization

As the final aim of the PhD work is to develop an innovative methodology to perform an AWES design, the flight mechanics theory, the optimal control and the economic model are being incorporated in a MDAO framework [2]. The current architecture of T-GliDe (Tethered Gliding system Design) is shown in Figure 4. It features an uncertainty quantification module, to perform local and global sensitivity analyses, and an optimization module, to find optimal designs for given model parameters. Design variables can be divided into geometrical, defining the dimensions of the AWES, and operational, defining the working set-points as function of wind speed. The AWES design and operations are found to maximize an economic metric, while considering flight stability among the constraints (i.e. forcing the eigenvalues of **A** matrix in Eq. (1) to be stable).

An optimal control module, using the methods presented in Section 3, is currently under-development. It will make use of the linearized dynamic model, obtained with the flight mechanics theory

$$\dot{\mathbf{x}}(t) = \mathbf{A}\mathbf{x}(t) + \mathbf{B}\mathbf{u}(t) + \mathbf{d}(t). \tag{3}$$

Where **A** is considered to be constant and it is designed to be stable, **B** is the transfer function between control inputs $\mathbf{u}(t)$ (e.g. ailerons, rudder, reel-out velocity or on-board wind turbine thrust) and the dynamics and $\mathbf{d}(t)$ are the disturbances, which are the fluctuating terms in the flight stability theory. In this way, the AWES and its optimal control can be designed in a unique framework. The 6 d.o.f. dynamics and the optimal control are then characterized in frequency, enabling frequency-based control techniques which may relieve the controller, alleviate loads and improve power production in a turbulent environment.

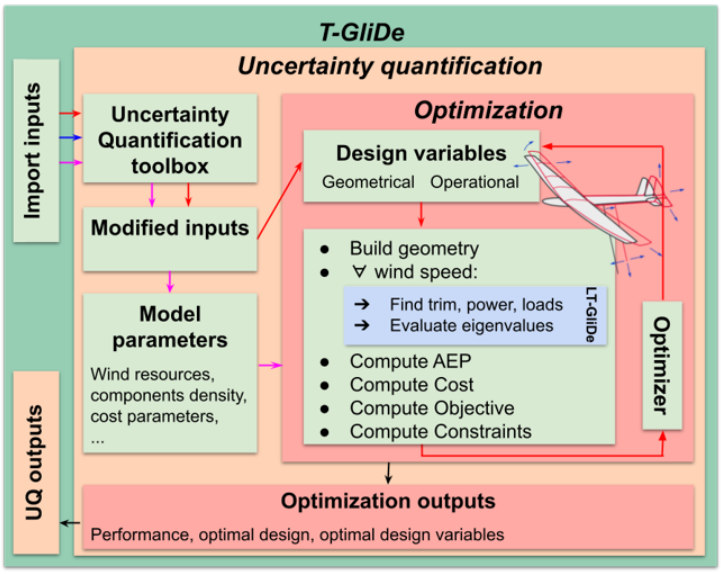


Figure 4: T-GliDe (Tethered Gliding system Design) architecture.

6 Future works

This abstract gives an overview of the present PhD work. The optimal control module in T-GliDe is currently under development. Modules related to AWES wakes and to the structural design are foreseen to be included. An improved aerodynamic solver (Vortex Step Method) is being included into a 6 d.o.f. simulator, to benchmark the outputs of linear flight mechanics theory with a nonlinear flight simulator. A small-scale prototype is being build to validate the flight mechanics theory and to test the new control scheme.

References

[1] F. Trevisi, A. Croce, and C. E. D. Riboldi. Flight Stability of Rigid Wing Airborne Wind Energy Systems. *Energies*, 14(22), 2021.

[2] F. Trevisi, C.E.D. Riboldi, and A. Croce. Sensitivity analysis of a Ground-Gen Airborne Wind Energy System design. *Journal of Physics: Conference Series*, 2265(4):042067, May 2022.

[3] F. Trevisi, I. Castro-Fernández, G. Pasquinelli, C. E. D. Riboldi, and A. Croce. Flight Trajectory Optimization of Fly-Gen AWE Systems through a Harmonic Balance Method. *Wind Energy Science Discussions*, 2022:1–29, 2022.

[4] R. Joshi, F. Trevisi, R. Schmehl, A. Croce, and Riboldi C.E.D. A Reference Economic Model for Airborne Wind Energy Systems. Presented at the Airborne Wind Energy Conference (AWEC 2021), Milan, 22-25 June 2022.

Legal aspects

Congestion management in an interconnected offshore grid

Angelo Goethals * [1]

[1] Universiteit Gent = Ghent University [Belgium] – Belgium

Keywords: Bidding zones, capacity allocation, congestion management, control area

*Speaker

18th EAWE PhD Seminar on Wind Energy
2 – 4 November 2022
Bruges, Belgium

Minimizing light pollution from wind turbines lighting

Yana Yakushina[a]

[a] University of Ghent; Department of European, Public and International Law, Campus Aula, Universiteitstraat 4, 9000 Gent, Belgium
http://www.ugent.be/re/epir

E-mail: ya.yakushina@gmail.com (alternative: Yana.Yakushina@UGent.be)

Keywords: wind turbines, light pollution, obstruction lighting, wind energy, aviation safety

1. Introduction

Global energy and environmental concerns have resulted in the development of renewable energy technologies, aiming at mitigation of climate change issues, as well as rapid environmental degradation. Among various innovative solutions, wind turbines became one of the most accessible, widespread, and increasingly stable renewable energy recourses. Despite significant sustainable benefits of wind energy, inter alia, carbon neutrality, investment attraction, and job creation, wind turbines have, however, notable impacts on the environment and local communities, in particular, they contribute to an increase in artificial light at night (ALAN) levels and, thereafter, increases light pollution. This paper discusses (1) the impacts of lighting emitted from wind turbines, (2) requirements for wind turbine lighting, (3) dark sky protection principles, and (4) the evolution of lighting requirements towards minimizing the negative effects of wind turbines ALAN. The main goal is to address the adverse impacts introduced by wind turbine lighting and suggest the implementation of dark sky protection principles to minimize these effects.

2. Light pollution: adverse impacts

Light pollution is one of the most fast-growing forms of environmental degradation that is caused by the increased amount of artificial light at night (ALAN). This new environmental problem started to be gradually recognized within the political and legal agenda due to broad research findings, indicating various adverse impacts of ALAN. Light pollution can be defined as every form of artificial light in the wrong place at the wrong time which creates a sky glow, glare, nuisance, and other relevant causes of environmental degradation including some properties of artificial light which emit non-environmentally friendly or inappropriate light [1].

The increased nighttime brightness is a concern in many areas. The most obvious negative effect of light pollution is the disappearance of the dark skies, leading to the inability to see the stars and starlight. Apart from that, light pollution causes serious health deterioration effects and contributes to further degradation of the environment. With regard to human health, scientific research has found that prolonged ALAN exposure can lead to the incidence of certain health issues, including insomnia, cardiovascular disease, obesity, hormone-dependent cancer, and various mental disorders [2],[3]. The adverse environmental impacts of ALAN are also well evident. To give some examples, light pollution contributes to climate change, has direct and indirect effects on different species, inter alia, migration birds, bats, and turtles, alters natural habitats, and harms ecosystem functioning [4]. In addition, increased nighttime lighting reduces public safety, creates a nuisance, and leads to inefficient energy consumption [5].

Turning to light pollution issues, researchers consider different types and sources of lighting. Light emitted from wind energy turbines has also received attention in terms of its negative effects. Wind turbines are not considered the main sources of light pollution, but nonetheless, they introduce additional light that can affect

local environments, causing further alteration of species behaviour and ecosystems, as well as worsening the well-being of the local population. Various bird species, for instance, are attracted to light emitted from wind turbines and as a consequence, such nighttime lighting influences the risk of mortality due to collisions with these energy structures [6]. Wind turbine lighting also contributes to the disorientation of different migratory species and the disturbance of habitats [7].

The most notable negative impact of wind turbine lighting is manifested in the disturbance of local communities. Wind turbine flashing lights became a serious obstacle to social acceptance of wind energy and, in some cases, have led to the cancellation of wind energy projects as a result of successful judicial proceedings initiated by locals. Research has shown that the annoyance caused by obstruction lights can have a significant effect on a number of residents, therefore, the reduction of the light nuisance may also reinforce a positive perception of wind energy [8]. In 2019, more than one hundred residents filed a complaint in the Supreme Court of New York against EDP Renewables, the developers of the Arkwright Wind Power, indicating the emergence of health issues and inability to properly enjoy their properties due to, in particular, increased nighttime lighting and constant flashing red lights [9]. One of the recent examples is the decision of the Toulouse Court of Appeal in 2021 [10]. The court granted a compensation of €110,000 for health deterioration linked to "wind turbine syndrome". The flashing light from wind turbines was mentioned among the factors that caused significant health deterioration, including insomnia and fatigue.

The adverse impacts of light pollution discussed above highlight the need to take into account the potential effects that may be introduced by turbine lighting during different stages of wind energy project development.

3. Lighting for wind turbines

The requirements for the installation of lighting for wind turbines stem from the need to ensure aviation safety. This type of lighting is called obstruction or warning lighting and is used to improve the visibility of structures or fixed obstacles that may impede safe aircraft flights. An obligation to install obstacle lights depends mainly on the height of the wind turbine and starts from 150 meters, which corresponds to a minimum flight altitude.

At the international level, the obligation for obstruction lighting is established by the regulations adopted by the United Nations International Civil Aviation Organisation (ICAO). ICAO was founded upon the adoption of the Chicago Convention on International Civil Aviation on 7 December 1944 (hereafter – *Convention*) and aims at ensuring international aviation safety [11]. Section 6.2.4. of Volume 1 of Annex 14 to the Convention is specifically dedicated to the recommendations on the lighting for wind turbines [12]. ICAO recommends using lights of medium or low intensity in accordance with the height. During the day and twilight conditions white, flashing lights with an intensity of 20,000cd should be used, while during the night, white or red flashing or red steady light of 2,000cd intensity are recommended. The ICAO recommendations specifically address the issues related to installations of lighting throughout wind farms. The latter includes several aspects to be considered, inter alia, the perimeter of the wind farm, requiring the illumination of wind turbines along the perimeter, simultaneous flashing requirements, and, depending on the height, additional lighting shall be installed. The same approach should be applied if the light is deemed necessary for a single wind turbine or short line of wind turbines. Despite providing all the necessary requirements needed for aircraft safety, the international recommendations, however, fail to address negative effects that may be introduced with obstruction light, thereby do not provide for any light mitigation measures.

National requirements for obstruction lighting for wind turbines are diverse, although several countries tend to adopt the recommendations developed by the ICAO. According to the USA requirements, for instance, wind turbines should have nighttime red flashing, strobe, or pulsed lighting of 2000cd [13]. The number of lights differentiates depending on the height of the structure. The US standards do not require any lights during the daytime and establish separate requirements for obstruction lights for offshore wind turbines. Canadian Aviation Regulations [14] require the installation of either red constant or flashing with the intensity of 2000cd or white flashing lights with the intensity of 20,000cd, depending on the part of the day and the height of the turbines. The wind farms should be illuminated around the perimeter with red flashing lights. Interestingly, the Canadian regulations do not define specific lighting configurations for onshore and offshore wind turbines. In addition, obstruction lighting is required throughout the whole day. Regarding European Union member states, the approaches to obstruction lighting are also different due to the absence of unified regulations at the EU level. A number of states, including Poland and the Netherlands, impose an obligation to install lighting on wind turbines throughout the whole day, while other states, such as Belgium, Germany, and Denmark, consider only nighttime lighting sufficient for safety purposes [15]. The intensity requirements vary between 2,000cd to 200,000cd in the

daytime and 100cd to 100,000cd in the nighttime. National regulations on obstruction lighting, in general, demand high illumination levels of wind turbines.

4. Light pollution mitigation principles

International recognition of light pollution as a global problem has led to the development of five dark sky protection principles, which aim to ensure the implementation of sustainable and responsible outdoor lighting practices [16]. These principles are directed to any type of outdoor ALAN, thereby their implementation can significantly improve wind turbine lighting requirements. The first principle is the purposeful use of any outdoor lights. Since obstruction lights have already clearly defined purpose, namely aviation safety, the requirements for wind turbine lighting comply with the first principle. The second principle is contained in the need to direct the lighting only where it is necessary. In a view of wind turbines, the implementation of this principle is rather difficult in terms of preventing collisions with aircrafts, however, attempts should be taken to prevent floodlighting. The principle of low light levels is the third dark sky protection principle. The amendments to the requirements should be related to minimizing the intensity of nighttime lighting to levels that will ensure aviation safety and simultaneously will not disturb local residents and the environment. Another responsible outdoor lighting principle requires control over the use of lights, in other words, lighting should be used only when it is necessary. To decrease light pollution levels from wind turbines, light mitigation technologies can be used, allowing the possibility of dimming or complete shutdown of ALAN when not needed. The last principle to be implemented wind turbines should be equipped with lights of warmer colours to limit the amount of shorter wavelength (blue-violet) light that is the most harmful to human health and biodiversity.

5. Evolution of lighting requirements

The increased awareness of the negative effects produced by wind turbine lighting has resulted in positive changes of obstruction light requirements. Several countries, such as the USA, Canada, Germany, Norway, The Netherlands, and Sweden, have attempted to minimize light pollution levels by adopting measures to introduce light mitigation technologies. The following technologies are commonly accepted: (1) aircraft detection lighting systems (ADLS) and (2) light intensity reduction systems (LIRS).

ADLS is a system designed to automatically activate obstruction lights upon detection of the approaching aircraft. Some countries provide for the establishment of warning zones for ADLS. The warning zone extends outward from the impact boundary to the detected aircraft, thus, determining the moment of the lighting activation. The USA, for instance, requires the lighting to be activated if an aircraft is at or below 1,000 feet above the tallest wind turbine and is approaching a three statute mile (4.8 kilometres) perimeter around the wind energy structures [13]. In other countries, the activation of ADLS is related to the speed of aircraft, e.g., in Canada. The installation of ADLS is subject to approval by authorized bodies. In addition, although in most cases ADLS for wind turbines is not obligatory, some countries establish a mandatory requirement for the installation of such systems. To give an example, Germany became the first European state that introduced the “on-demand” approach to warning lights and made ADLS compulsory for all wind turbines requiring obstruction markings: onshore until 12/31/2022 and wind farms offshore until 12/31/2023 [17].

LIRS is used to reduce the intensity of obstacle lighting with regard to visibility. The wind turbine is equipped with sensors to control visibility conditions. Light dimming can be allowed up to 30% with the visibility is 5 km and more and up to 10% less when the visibility is 10 km and more. LIRS is adopted across various jurisdictions, inter alia, the USA, Canada, Germany, France, Poland, and Belgium. Similar to ADLS, the possibility to install light dimming systems is subject to approval by authorized authorities.

With recent amendments to the existing wind turbine lighting requirements, some innovative measures for light pollution mitigation were introduced. Several countries, by opting for constant and stable ALAN, have prohibited flashing lights. Other improvements affected offshore wind turbines. Thus, direct lighting of surface water was prohibited while indirect lighting of surface water has to be minimized to prevent negative impacts on marine biodiversity. Moreover, some countries require to optimize the obstruction lighting so that they are directed only where it is needed. The latter should be determined for each project separately. In addition, several countries, including the Netherlands, are testing different light mitigation technologies in order to adopt regulatory changes in the near future.

6. Conclusions and recommendations

The current requirements for wind turbine lighting are focused on the need to ensure aviation safety, thereafter, they are highly demanding and result in significant illumination that causes light pollution. At the same time, however, there is a growing tendency to introduce light mitigation technologies for minimizing ALAN-induced impacts on communities and the environment, providing that such technologies do not diminish the necessary safety levels.

Newly introduces amendments are consistent with the main dark sky protection principles. The further incorporation of these principles, including through the implementation of light mitigation technologies, will contribute to the spread of wind energy due to greater public acceptance and reduction of the potential negative impacts of wind turbines caused by obstruction lighting. Nevertheless, it should be noted that the introduction of light mitigation solutions should be followed by the adoption of unified requirements for these technologies to prevent extensions of periods for project approval. In addition, light pollution mitigation measures should be also included in international and regional obstruction lighting regulations and recommendations.

References

[1] P. Youyuenyong. Comparative Environmental and Planning Law Relating to Light Pollution Control in England and Other Jurisdictions, Unpublished Ph.D. Thesis, School of Law De Montfort University, Leicester, UK, 2015.

[2] M. Hatori, C. Gronfier, , R.N.V. Gelder, P.S. Bernstein, J. Carreras, S. Panda, F. Marks, D. Sliney, C.E. Hunt, T. Hirota, T. Furukawa and K. Tsubota. Global rise of potential health hazards caused by blue light-induced circadian disruption in modern aging societies. npj Aging and Mechanisms of Disease, 3(1), 2017.

[3] H.S. Zahra, A. Iqbal, S.H. Hassan, H.A. Shakir, M. Khan, M. Irfan, C. Ara and S. Ali. Epigenetics: A bridge between artificial light at night and breast cancer. *Punjab University Journal of Zoology*, 34(2), 2019.

[4] H. Levente, F. Mics. Introductory Chapter: Ecological Effects of Light Pollution - A Review, Chapters in: Levente Hufnagel (ed.), Light Pollution, Urbanization and Ecology, *IntechOpen*, 2022.

[5] International Dark-Sky Association (IDA), Artificial Light at Night: State of the Science 2022, report, *IDA website*, 2022.

[6] A.T. Marques et al. Understanding bird collisions at wind farms: An updated review on the causes and possible mitigation strategies, *Biological Conservation* 179, 40–52, 2014.

[7] C.E. Reilly, J. Larson, A.M. Amerson, G.J. Staines, J.H. Haxel, P.M. Pattison. Minimizing Ecological Impacts of Marine Energy Lighting. *J. Mar. Sci. Eng.* 10, 354, 2022.

[8] J. Pohl, D. Rudolph, I. Lyhne, N.-E. Clausen, S.B. Aaen, G. Hübner, L. Kørnøv, J.K. Kirkegaard. Annoyance of Resi-dents Induced by Wind Turbine Obstruction Lights: A Cross-Country Comparison of Impact Factors. *Energy Policy*, 156, 112437, 2021.

[9] *Richard Alexander et al v. EDP Renewables et al*. New York State, Chautauqua County, Supreme Court, Sep. 24, 2019.

[10] *Christel Fockaert & Luc Fockaert v. S.A.S.U. Societe Margnes Energie et al*. France, Toulouse Court of Appeal. July 8. 2021.

[11] International Civil Aviation Organization (ICAO), Convention on Civil Aviation ("Chicago Convention"), 7 December 1944, (1994) 15 U.N.T.S. 295.

[12] ICAO Annex 14, Aerodromes, Volume 1 Aerodrome Design and Operations, Eighth Edition, July 2018.

[13] Federal Aviation Administration (FAA) of the USA AC 70/7460-1M - Obstruction Marking and Lighting, November 16, 2020.

[14] Canadian Aviation Regulations (CARs) Standard 621 - Obstruction Marking and Lighting T51-15/621-2011-1E-S, Amended November 2, 2021.

[15] H.T.H. van der Zee. Obstacle Lighting of Onshore Wind Turbines: balancing aviation safety and environmental impact. NLR-TR-2016-293, June 2016.

[16] International Dark-Sky Association (IDA) and Illuminating Engineering Society. Five Principles for Responsible Outdoor Lighting. April 17, 2020.

[17] General administrative regulation for the labeling of aviation obstacles, Decision of the Federal Council

of Germany N15/20, February 14, 2020; § 9 Abs. 8 S.1 EEG 2017 and Energy Collection Act ("Energiesammelgesetz") of December 27, 2018, Germany.

Economic and policy

18th EAWE PhD Seminar on Wind Energy
2 – 4 November 2022
Bruges, Belgium

A levelized cost of energy analysis of changing global commodity markets and the impact on floating offshore wind

Craig White[ab], José Cândido [ab]

[a] WavEC Offshore Renewables
[b] FLOAWER

E-mail: craig.white@wavec.org

Keywords: Economics, Floating offshore wind, Levelized cost of energy, Commodities, Costs

1. Introduction

Global warming pressure and a desire for energy security has driven a rapid rise in renewable energy generation. Among these, floating offshore wind (FOW) has demonstrated great potential thanks to strong and abundant winds, lower marine-use conflict, almost zero land-use conflict and less seabed impact when compared to conventional fixed-bottom offshore wind (FBOW).

FOW is currently at the precipice of a transition from pre-commercial arrays, due to the successful performance of early projects including Hywind Scotland [1] which boasted a capacity factor of 65%, Windfloat Atlantic adopting a tow-to-port (TTP) strategy [2] and Floatgen's innovative damping pool technology [3]. To transition to commercial status and make an impact on the European and Global energy mix, costs must be reduced whilst maintaining high capacity factors to reduce the levelized cost of energy (LCoE) and achieve commercial viability.

FOW capital expenditure (CAPEX) is one of the main driving factors in LCoE, alongside operational expenditure (OPEX) and energy generation. Floating Offshore Wind turbines (FOWTs) are extremely material dependant, relying on large quantities of steel, concrete, and rare earth metals. These prices can fluctuate heavily over time, impacting CAPEX, replacement components and vessel fuel costs, which can all impact LCoE and overall project viability.

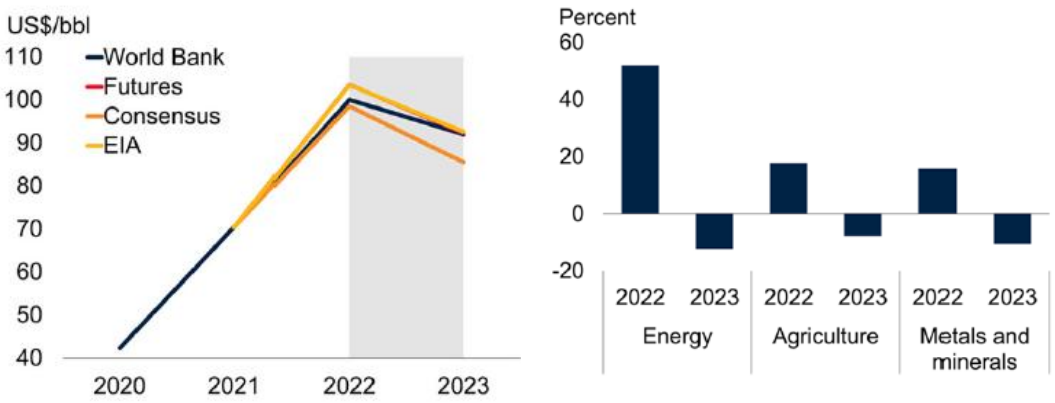


Figure 1: (a) Crude oil change from 2020-2023 (b) Commodity prices from 2022-2023

The past two and a half years have witnessed dramatic disruption and stress to supply chains, raw materials, energy costs and production outputs. Shown in Figure 1, crude prices have increased 42% in comparison to 2021, with the increases expected to remain high in the medium term outlook with prices to remain elevated in 2023-2024 in comparison to levels over the past five years. Energy is also greatly impacted, with prices forecast to rise by 50% in 2022, before settling at a higher level than previously predicted [4]. The current spikes in commodity prices directly impact FOW costs, with raw material costs affecting a third of the final cost of transmission cables [5].

To accurately cost FOW projects, and in turn produce reliable and ideally competitive LCoE values, these changes in commodities must be included in modelling scenarios. Raw data is both hard to find, especially at component level and static in time, with costs relating to a previous project not necessarily of relevance when comparing to a recent project. It is also important to understand the relative impact of commodity prices on cost data, as Fow components are often comprised of numerous materials which may not all be affected by commodity prices in the same way. A failure to accurately cost components in accurate 2022 levels could result in under-priced components and artificially low LCoE values, which would oversell a project's viability and cause major problems after the leasing rounds are awarded.

To address these problems, this research presents a new range of FOW-specific cost functions to accurately price FOW components, provide accurate project CAPEX values and generate reliable and robust LCoE calculations. The developed cost functions are flexible and not site or date specific, and so can be applied to a range of project criteria. The cost functions validity span from 2013 to 2035, which makes them suitable for FOW development over the next decade due to the long-range commodity forecasts used in their creation.

The overall aims of this research are as follows:

- Create a range of cost functions that are specific to FOW systems but flexible to be applied to a range of marine conditions
- Achieve an optimised LCoE value for a given year of project capital expenditure
- Link functions for integration into future techno-economic model to achieve an integrated FOW system design
- Reverse engineer cost functions to create a comprehensive cost database of FOW-specific components
- Provide a range of accurate FOW costs for use in the academic and wider community, to build confidence in economic modelling and LCoE analysis

The general structure of this paper is as follows:

- Method: Development of cost functions from raw cost data sources
- Method: Collection of commodity prices and integration into cost functions
- Method: Application of cost functions to FOW CAPEX
- Method: LCoE assessment of 50MW and 1GW reference floating offshore wind farm (FOWF)
- Results: Brief LCoE results yielding from early research stage.
- Results: CAPEX composition as a share of total project costs

2. Method

Cost functions were initially derived through cost data provided from previous research. Data was provided for key components including anchors, synthetic mooring lines, steel chains, static and dynamic array cables. Due to the comprehensive nature of the datasets, a wide range mathematical linear and non-linear relationships were established. As shown below with cost in Euros per unit on the y-axis, and the most useful independent variable on the x-axis, including weight (kg), apparent power (MVA), minimum breaking load (MBL) and megawatts (MW).

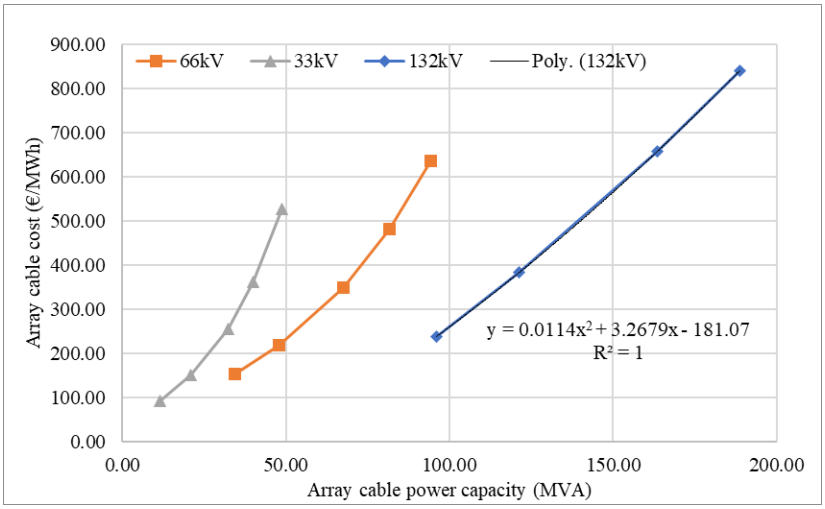


Figure 2: Example of cost functions for 33, 66 and 132kV array cables

Shown in Figure 2, data trends and the resulting equations were selected to maximise the R^2 value to best represent the raw data. As the final cost functions are complex with many parameters, simplistic linear, exponential, or power data trends were preferred, but if lower R^2 values were obtained then low order polynomial fits were used. These were not often required though, because of the strong correlation between the x and y values due to the relatively simple relationship between the x and y values. Also, the nature of the accurate manufacturer-supplied data, with few or zero errors and no outlier data points. Commodity price data is then added to the cost function as a percentage multiplier, usually consisting of metals, energy, and inflation indexes. This allows for the cost function to reflect the prices a FOWF developer would expect to pay for components, measuring the change in index between the initial cost data year) and the financial investment decision year. The resulting cost function will be in Euros per unit and can then be multiplied out to provide realistic CAPEX values in an energy cost model. Although this paper focuses on component costs, this approach has and can be applied to other areas of wind farm cost modelling, including installation vessel processes, O&M procedures, and the change in scrap rates for decommissioning.

3. Results

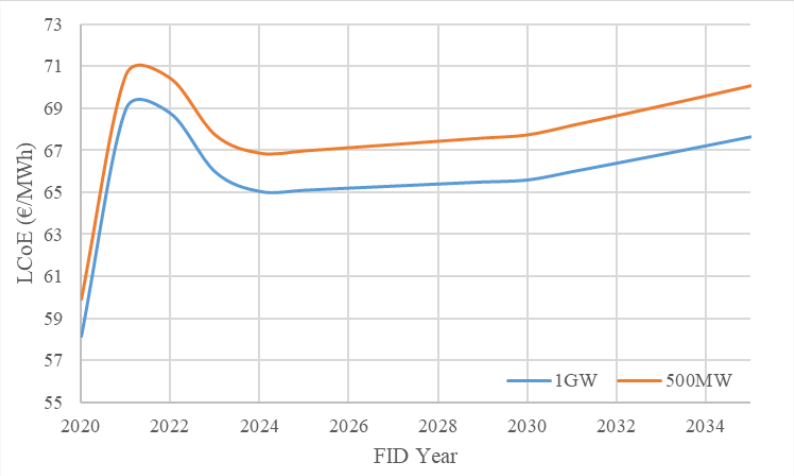


Figure 3 - LCoE change over 15 years FID for 500 and 100MW wind farm

Figure 3 shows early results after the set of cost functions were implemented into a techno-economic model for a reference wind farm, situated approximately 15km from shore. The increased commodity costs can be seen in the LCoE spike occurring from 2011-2012, followed by a dip in results. The gradual increase following this can be attributed to inflation.

4. Conclusion

Current events in Europe and beyond have sent shockwaves through commodity prices, but these have yet to be accurately costed and forecasted into energy cost models. This research presents a new range of cost functions for floating offshore wind that can accurately provide component-level costs data and predict future trends until 2035. Commodity changes have a large impact on project CAPEX and LCoE, resulting in an 18% increase in LCoE for a 1GW farm when comparing 2022 against 2020 results.

Such rises in LCoE must be accounted for using modern cost functions, and the aim of this research is to create a range of functions that can adapt to future commodity changes and be used as a valuable resource for the academic community for accurate FOW LCoE values.

Acknowledgements

This work is produced as part of the FLOAWER PhD Network of Early-Stage Researchers. This project has received funding form the European Union's Horizon 2020 research and innovation programme under the Marie Sklodowska-Curie grant agreement No 860879.

References

[1] P. Tisheva, "Hywind Scotland trumpets 65% capacity factor," Renewables Now, 15 02 2018. [Online]. Available: https://renewablesnow.com/news/hywind-scotland-trumpets-65-capacity-factor-601823/. [Accessed 13 03 2021].

[2] T. Duarte, S. Price, A. Peiffer and J. M. Pinheiro, "WindFloat Atlantic Project: Technology Development Towards Commercial Wind Farms," in *Offshore Technology Conference*, Houston, 2022.

[3] Y. P. T. C. R. B. U. R. H. Armando Alexandre, "Performance and mooring qualifications in Floatgen: The first French offshore wind project," in *ASME 2018 1st International Offshore Wind Technical Conference*, San Francisco, CA, 2018.

[4] International Bank for Reconstruction and Development / World Bank, "Commodity Markets Outlook: The Impact of the War in Ukraine on Commodity Markets, April 2022," World Bank Publications, Washington,

DC, 2022.

[5] J. Green, B. A, F. L.J. and Y. Wan, "Electrical Collection and Transmission Systems for Offshore Wind Power," in *2007 Offshore Technology Conference*, Houston, 2007.

[6] ORE Catapult, "Floating Offshore Wind: Cost Reduction Pathways to Subsidy Free," ORE catapult, 2021.

[7] C. Bjerkseter and A. Agotnes, "Levelized costs of energy for floating wind turbine concepts," 2013.

[8] L. Castro-Santos, E. Martins and C. Guedes Soares, "Cost assessment methodology for combined wind and wave floating offshore renewable energy systems," *Renewable Energy,* vol. 97, pp. 866-880, 2016.

[9] C. Maienza, A. Avossa, Ricciardelli, D. Coiro, G. Troise and C. Georgakis, "A life cycle cost model for floating offshore wind farms," *Renewable Energy,* vol. 66, pp. 41-48, 2014.

18th EAWE PhD Seminar on Wind Energy
2 – 4 November 2022
Bruges, Belgium

An integrated decision support system for offshore wind farm site selection in the Baltic Sea

Mojtaba Barzehkar[a], Matti Koivisto[b], Kevin E. Parnell[a], Tarmo Soomere[a,c]

[a] Department of Cybernetics, School of Science, Tallinn University of Technology, Tallinn, Estonia
[b] Department of Wind and Energy Systems, Technical University of Denmark, Frederiksborgvej 399, 4000, Roskilde, Denmark
[c] Estonian Academy of Sciences, 10130 Kohtu 6, Tallinn, Estonia

E-mail: mojtaba.barzehkar@taltech.ee

Keywords: Offshore wind farms, Decision support tools, Multi-criteria decision analysis, Baltic Sea

1. Introduction

The likely reduction of fossil fuel use along with population growth and industrial development has led to the growing demand for renewable energy (Emeksiz and Demirci, 2019). Renewable energy contributes to the mitigation of carbon dioxide emissions in the atmosphere, and assists with nature protection and increased energy independency (Kabak and Akalın, 2021).

Wind energy is one of the most crucial renewable energy sources (Noorollahi et al., 2016). It is environmentally sound and secure, for generating electricity (Baban and Parry, 2001; Latinopoulos and Kechagia, 2015). Winds in offshore locations are typically more stable than onshore areas, which leads to higher power production than onshore wind power plants (Bilgili et al., 2011; Wu et al., 2018). The development of offshore wind farms mitigate noise and aesthetic impacts (Bilgili et al., 2011). Site selection for offshore wind farms is a vital planning step, which is dependent on many environmental and socioeconomic criteria (Tercan et al., 2020). The application of decision support tools (DSTs) is used to identify suitable sites for the construction of renewable energy power plants (González and Connell, 2022).

2. Background

A variety of DSTs have been used over the years for offshore wind farm site selection. Geographical Information Systems (GIS) are commonly used as a decision support tool in wind farm site selection (Baban and Parry, 2001; van Haaren and Fthenakis, 2011; Rodman and Meentemeyer, 2006). The GIS approach provides a method for the processing and management of geographical data that makes it feasible to incorporate many factors into the analysis stage (Díaz-Cuevas et al., 2019). Another popular method is multi-criteria decision analysis (MCDA) for the combination of factors and prioritizing sites in the decision-making process (Mytilinou et al., 2018).

The combined use of GIS and MCDA has been employed for offshore wind farm site selection in numerous studies. Chaouachi et al. (2017) used GIS and analytical hierarchy process (AHP) for offshore wind farm site selection in the Baltic states. Gil-García et al. (2022) used fuzzy logic – GIS and AHP - The technique for order of preference by similarity to ideal solution (TOPSIS) in the Gulf of Maine, USA. Spyridonidou and Vagiona (2020) used GIS-AHP-TOPSIS for offshore wind farm location selection in Greece. Tercan et al. (2020) applied GIS and MCDA using fuzzy logic, AHP, and weighted linear combination (WLC) for offshore wind farm site selection in the Aegean Sea. Vagiona and Kamilakis (2018) undertook offshore wind farm site selection using GIS-AHP-TOPSIS in the South Aegean – Greece, providing a site selection hierarchy.

This study focuses on the application of an integrated decision support methodology for offshore wind farm site selection considering three goals. First, to promote the strengths and capability of decision support tools for offshore wind farm site selection. Second, to determine suitable sites for offshore wind power plants for the

optimization of power generation. Third, to select appropriate locations to ensure environmental protection while providing for electricity demands of communities.

3. Research questions

What decision support tools (DSTs) are available, and what data are required to enable their application?
Can combinations of DSTs in an integrated decision support system (DSS) enable experts to choose the appropriate locations for offshore wind power plants?
How to identify and prioritize the locations for offshore wind power plants in the Baltic Sea?

4. Materials and methods

4.1. The study area

The study area, the Baltic Sea (Figure 1), is a semi-enclosed sea in Northern Europe. It is surrounded by Finland, Estonia, Lithuania, Latvia, Denmark, Sweden, Germany, Poland, and Russia with an area of 392,978 km^2, an average water depth of 54 m and low salinity brackish water ecosystem (Leppäranta and Myrberg, 2009; Hordoir and Meier, 2010). The development of a wind power plant has impacts on marine ecosystems, coastal tourism, fisheries, and socioeconomic aspects (Reckermann et al., 2022). The sites suitable for offshore wind power plant must be evaluated with an aim to boost energy efficiency and reduce environmental concerns (Tercan et al., 2020).

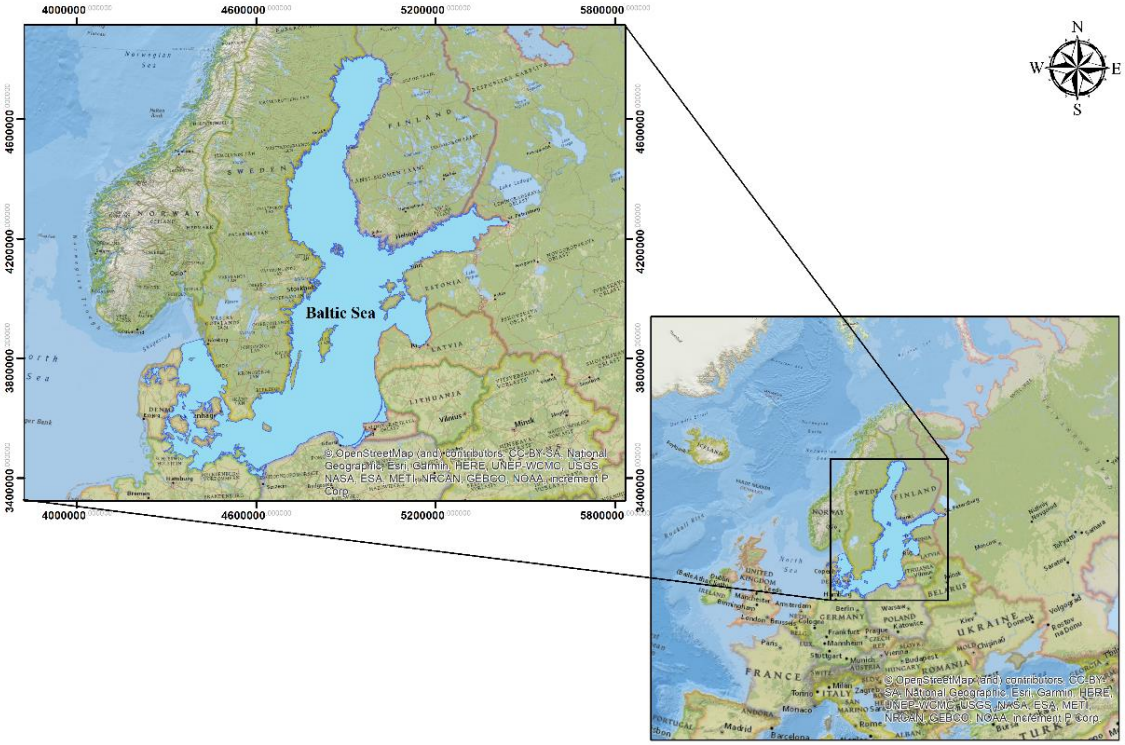


Figure 1: The Baltic Sea in Northern Europe

4.2. Methodology

A GIS-MCDA methodology that uses the integration of GIS with AHP, fuzzy logic, and WLC is used and organized in the following steps for wind farm location selection in the Baltic Sea. In the first step, data collection of the main environmental and socioeconomic parameters influencing the potential locations for offshore wind farm site selection is performed and these data are entered to GIS for raster mapping. The most

important factors for analysis are wind speed, water depth, distance from the shoreline, distance from ship navigation routes, distance from marine protected areas, distance from ports, distance from human activities and infrastructure. All these factors influence wind farm sites, the costs of installation and maintenance, and maritime safety (Tercan et al., 2020).

In the next step, fuzzy logic is used to normalize the pixels of the resulting raster maps in a range between 0 and 1 (Araya-Munoz et al., 2021). The value 1 represents very high value (Wu et al., 2018). There are various methods for standardization of raster maps, using minimum and maximum values (Barzehkar et al., 2020). For example, between the suitability ranges (minimum threshold *a* and maximum threshold *b*) (Table 1), the lower values are better for water depth, distance from ports, and distance from shoreline or the higher values are better for wind speed, capacity factor, distance from nature protection area, distance from seabed infrastructures, distance from military area, distance from shipping routes, and distance from fishing area.

Then, AHP is used to assess the relative importance that experts apply to each criterion to derive weights for each parameter (Mu and Pereyra-Rojas, 2018). The values for the weighting of parameters are based on a scale from 1 to 9 (Table 2) as recommended in the classic work by Saaty and Tran (2007). The validation of the results of the AHP uses a consistency ratio (Mu and Pereyra-Rojas, 2018). If the consistency ratio is less than or equal to 0.1 the result of weighting is acceptable (Saaty and Tran, 2007). After identification of the weight of each criterion, site suitability is calculated using the WLC method by multiplying the relative weight of the factor and normalized value of the factor (Díaz-Cuevas et al., 2019). Figure 2 shows the integration of GIS with MCDA using Fuzzy logic, AHP and WLC.

Table 1 Fuzzy standardization of raster layers for offshore wind farm site selection

Criteria	**Sub-criteria**	**Suitability**	**Reference**	**Threshold value**		**Type of the Fuzzy membership function**
				Minimum threshold value *a*	**Maximum threshold value *b***	
Wind resource	Wind speed	7–10 m/s	Danish Energy Agency (2016)	7	10	Increasing
Physical	Capacity factor	35–55 %	Wind Europe (2019)	35	55	Increasing
	Water depth	10–50 m	Danish Energy Agency (2016)	10	50	Decreasing
	Distance from nature protection area	≥2 km	European MSP Platform (2018)	2	5	Increasing
	Seabed geology	Finer sediments	European MSP Platform (2018)	0 (Rocks and boulders)	1 (Muddy)	User-defined
	Wave height	<10 m	Gil-García et al (2022)	< 10	> 10	Decreasing
Socioeconomic	Distance from ports	10–80 km	Based on the distance to shore (see below)	10	80	Decreasing
	Distance from seabed infrastructure	≥500 m	European MSP Platform (2018)	500	5000	Increasing
	Distance from shoreline	10–80 km	Danish Energy Agency (2016)	10	80	Decreasing
	Distance from military area	≥500 m	European MSP Platform (2019)	500	5000	Increasing
	Distance from shipping routes	≥3.7 km	European MSP Platform (2018)	3.7	5	Increasing
	Distance from fishing area	≥500 m	European Commission (2020)	500	5000	Increasing

Table 2 The priorities of experts for pairwise comparison of parameters

Priorities of experts	Numerical value
Extremely prioritized	9
Very strongly prioritized	7
Strongly prioritized	5
Moderately prioritized	3
Equally prioritized	1
Intermediate values between the two adjacent judgments	2, 4, 6, 8

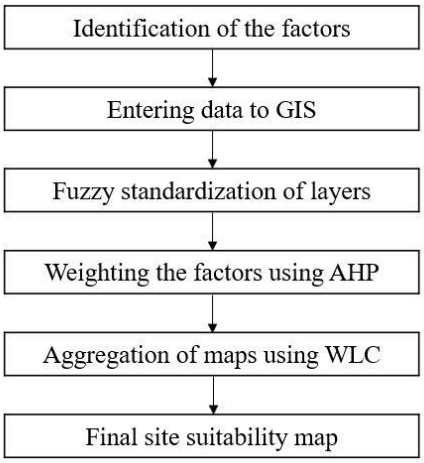


Figure 2: GIS - MCDA for offshore wind farm site selection in the Baltic Sea.

5. Initial results

A combination of GIS-MCDA using GIS, fuzzy logic, AHP, WLC has been employed for offshore wind farm site selection in the Baltic Sea. An integrated decision support system (DSS) has been used to prioritize the offshore wind farm locations in the Baltic Sea. This integrated methodology is a rational approach to integrate different tools to reduce uncertainty, and to incorporate experts' perspectives into the assessment and integration of multiple parameters into the analysis to strengthen knowledge-based decision-making. The generated outputs in map form are useful for environmental planners, consultants, and governmental organizations in consultation activities, which contribute to reliable marine spatial plans for offshore wind farm locations.

Experts consulted in this study considered (Figure 3) that the most significant factors that affect the offshore wind power plant site selection in the Baltic Sea are wind speed, capacity factor, water depth, followed by nature protection areas, wave height, seabed geology and distance from shipping routes. The calculated consistency ratio among experts' opinions for weighting of parameters was 0.045, thus the result of weighting is consistent.

For the site suitability map derived by an integrated GIS-MCDA (Figure 4, Table 3), the locations with highest site suitability (values between 0.80–0.92) (5.98 %) for the offshore wind farm development in the Baltic Sea, are areas close to shore, with high wind speeds, shallow water depths, far from nature protection areas, human infrastructure and activities, and are locations that have lower wave heights and finer seabed sediments. Sites determined by the analysis to have low site suitability (values between 0.34–0.46) (0.13 %) do not have all these characteristics. As ongoing research, the results shown in this study are being compared to the levelized cost of energy (LCOE) model, and the two methods seem to approximately agree.

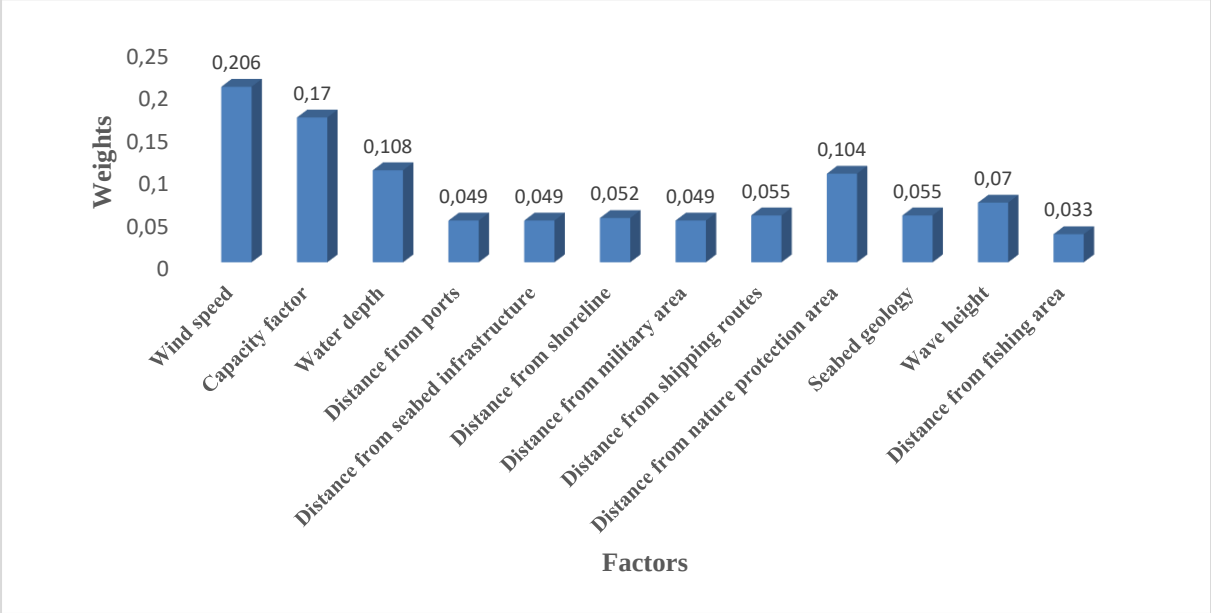


Figure 3: Final weights assigned to the factors using the AHP method

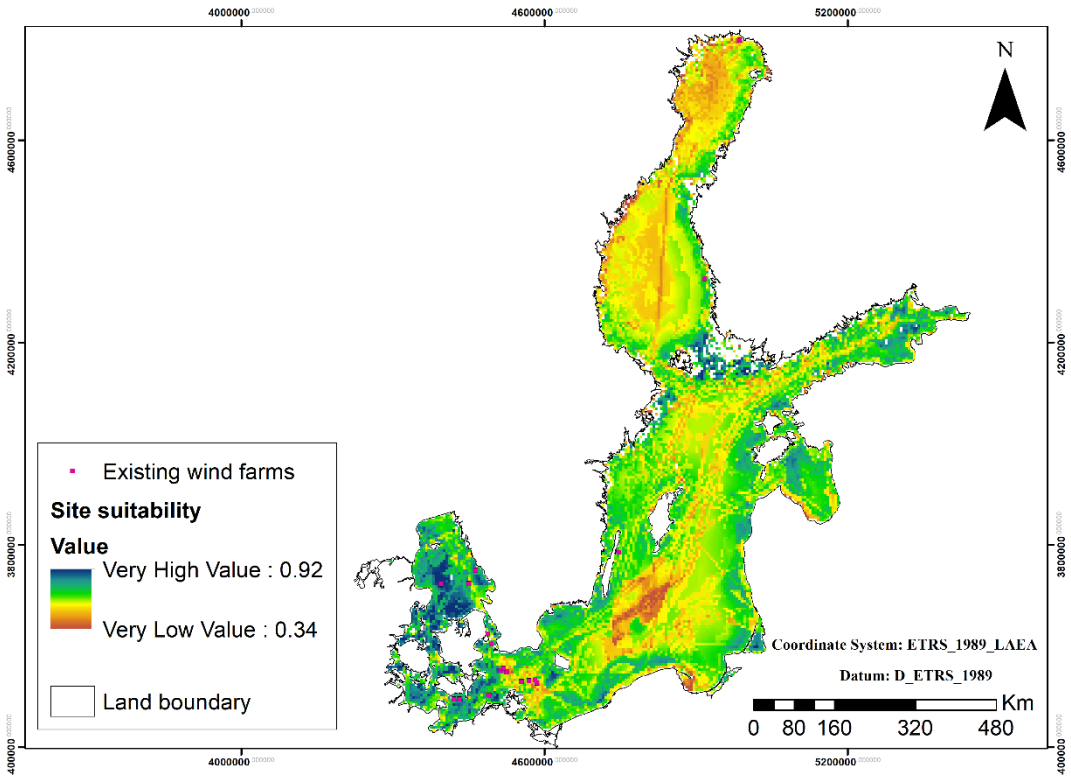


Figure 4: Offshore wind farm site suitability map

Table 3 Site suitability evaluation for offshore wind farm site selection

Suitability class	Area (Km^2)	Percent (%)
Very low (0.34 – 0.46)	500	0.13
Low (0.46 – 0.57)	12375	3.22
Moderate (0.57 – 0.68)	184975	48.21
High (0.68 – 0.80)	162900	42.46
Very high (0.80 – 0.92)	22925	5.98
Sum of classes	383675	100

6. Conclusions

An integration of decision support tools (DSTs) is a realistic approach to improve the functionalities of tools to obtain better outputs. The sites close to the shore are, as expected, more suitable than the sites far from the shore for wind power plant site selection in the Baltic Sea. GIS-MCDA method, is able to determine the most suitable sites based on the environmental protection and socio-economic constraints for power production. The distance from grid connection points is recommended to be considered in future studies to have a more accurate evaluation for wind farm site selection in the Baltic Sea.

Acknowledgements

Analysis and preparation of the paper were supported by the European Regional Development Fund program Mobilitas Plus, Estonian Research Council Top Researcher Grant MOBTT72, reg. no. 2014-2020.4.01.16-0024, the European Economic Area (EEA) Financial Mechanism 2014–2021 Baltic Research Programme, project SolidShore (EMP480) and Estonian Research Council Grant PRG1129. Matti Koivisto acknowledges support from the Nordic Energy Research BaltHub project (106840).

References

[1] Araya-Munoz, D., Metzger, M.J., Stuart, N., Wilson, A.M.W., Carvajal, D. A spatial fuzzy logic approach to urban multi-hazard impact assessment in Concepcion, Chile. *Science of the Total Environment*, 576:508–519, 2017.
[2] Barzehkar, M., Parnell, K.E. Mobarghaee Dinan, N., Brodie, G. Decision support tools for wind and solar farm site selection in Isfahan Province, Iran. *Clean Technologies and Environmental Policy*, 23(4):1179 – 1195, 2020.
[3] Baban, SMJ., Parry, T. Developing and applying a GIS-assisted approach to locating wind farms in the UK. *Renewable Energy*, 24(1):59–71, 2001.
[4] Bilgili, M., Yasar, A., Simsek, E. Offshore wind power development in Europe and its comparison with onshore counterpart. *Renewable and Sustainable Energy Reviews*, 15(2):905–915, 2011.
[5] Chaouachi, A., Covrig, C.F., Ardelean, M. Multi-criteria selection of offshore wind farms: Case study for the Baltic States. *Energy Policy*, 103:179–192, 2017.
[6] Díaz-Cuevas, P., Domínguez-Bravo, J., Prieto-Campos, A., Integrating MCDM and GIS for renewable energy spatial models: assessing the individual and combined potential for wind, solar and biomass energy in Southern Spain. *Clean Technologies and Environmental Policy*, 21(9):1855–1869, 2019.
[7] Danish Energy Agency (DEA) Technology Data - Energy Plants for Electricity and District heating generation. 1– 413, 2016.
[8] Emeksiz, C. Demirci, B. The determination of offshore wind energy potential of Turkey by using novelty hybrid site selection method. *Sustainable Energy Technologies and Assessments*, 36:100562, 2019.
[9] European Commission. Recommendations for positive interactions between offshore wind farms and fisheries. 1–26, 2020.
[10] European MSP Platform. Conflict fiche 3: Defence and other sea uses. 1–21, 2019.
[11] European MSP Platform. Conflict fiche 5: Offshore wind and commercial fisheries. 1–24, 2018.
[12] European MSP Platform. Conflict fiche 7: Maritime transport and offshore wind. 1–22, 2018.
[13] European MSP Platform. Conflict fiche 8: Offshore wind and area-based marine conservation. 1–20, 2018.
[14] European MSP Platform. Sector Fiche: Cables and Pipelines. 1–11, 2018.

[15] European MSP Platform. Maritime Spatial Planning (MSP) for Blue Growth. Final Technical Study. 1–307, 2018.
[16] Gil-García, I.C., Ramos-Escudero, A., García-Cascales, M.S., Dagher, H., Molina-García, A. Fuzzy GIS-based MCDM solution for the optimal offshore wind site selection: The Gulf of Maine case. *Renewable Energy*, 183:130–147, 2022.
[17] González, A., Connell, P. Developing a renewable energy planning decision-support tool: Stakeholder input guiding strategic decisions. *Applied Energy*, 312:118782, 2022.
[18] Hordoir, R., Meier, H.E.M. Freshwater fluxes in the Baltic Sea: A model study. *Journal of Geophysical Research*, 115:C08028, 2010.
[19] Kabak, M., Akalın, S. A model proposal for selecting the installation location of offshore wind energy turbines. *International Journal of Energy and Environmental Engineering*, 13:121–134, 2021.
[20] Latinopoulos, D., Kechagia, K. A GIS-based Multi-criteria evaluation for wind farm site selection. A regional scale application in Greece. *Renewable Energy*, 78:550–560, 2015.
[21] Leppäranta, M., Myrberg, K. Physical Oceanography of the Baltic Sea. *Springer Berlin, Heidelberg*, 378 pp, 2009.
[22] Mu, E., Pereyra-Rojas, M. Practical Decision Making using Super Decisions v3. An Introduction to The Analytic Hierarchy Process. *Springer*, 115 pp, 2018.
[23] Mytilinou, V., Lozano-Minguez, E., Kolios, A. framework for the selection of optimum offshore wind farm locations for deployment. *Energies*, 11(7):1855, 2018.
[24] Noorollahi, Y., Yousef, H., Mohammadi, M. Multi-criteria decision support system for wind farm site selection using GIS. *Sustainable Energy Technologies and Assessments*, 13:38–50, 2016.
[25] Reckermann, M., Omstedt, A., Soomere, T., Aigars, J., Akhtar, N., Bełdowska, M., Bełdowski, J., Cronin, T., Czub, M., Eero, M., Hyytiäinen, K.P., Jalkanen, J.P., Kiessling, A., Kjellström, E., Kuliński, K., Larsén, X.G., McCrackin, M., Meier, H.E.M., Oberbeckmann, S., Parnell, K., Pons-Seres De Brauwer, C., Poska, A., Saarinen, J., Szymczycha, B., Undeman, E., Wörman, A., Zorita, E. Human impacts and their interactions in the Baltic Sea region. *Earth System Dynamics*, 13:1–80, 2022.
[26] Rodman, L.C., Meentemeyer, R.K. A geographic analysis of wind turbine placement in Northern California. *Energy Policy*, 34:2137–2149, 2006.
[27] Saaty, T.L., Tran, L.T. On the invalidity of fuzzifying numerical judgments in the Analytic Hierarchy Process. *Mathematical and Computer Modelling*, 46:962–975, 2007.
[28] Spyridonidou, S., Vagiona, D.G. Spatial energy planning of offshore wind farms in Greece using GIS and a hybrid MCDM methodological approach. *Euro-Mediterranean Journal for Environmental Integration*, 5:24, 2020.
[29] Tercan, E., Tapkın, S., Latinopoulos, D., Dereli, M.A., Tsiropoulos, A., Ak, M.F. A GIS-based multi-criteria model for offshore wind energy power plants site selection in both sides of the Aegean Sea. *Environmental Monitoring and Assessment*, 192:652, 2020.
[30] Vagiona, D.G., Kamilakis, M. Sustainable site selection for offshore wind farms in the South Aegean — Greece. Sustainability, 10(3):749, 2018.
[31] van Haaren, R., Fthenakis, V. GIS-based wind farm site selection using spatial multi-criteria analysis (SMCA): evaluating the case for New York State. *Renewable and Sustainable Energy Reviews*, 15:3332–3340, 2011.
[32] Wind Europe. Wind energy in Europe in 2019. Trends and statistics. 1–24, 2019.
[33] Wu, B., Yip, T.L., Xie, L., Wang, Y. A fuzzy-MADM based approach for site selection of offshore wind farm in busy waterways in China. *Ocean Engineering*, 168:121–132, 2018.

18th EAWE PhD Seminar on Wind Energy
2-4 November 2022
Bruges, Belgium

Feasibility Study for Floating Offshore Wind in the Arabian Gulf

Orla Donnelly[a], **James Carroll**[a], and **Bassam AbuHijleh**[b]

[a]University of Strathclyde
[b]The British University in Dubai

E-mail: orla.donnelly@strath.ac.uk

Keywords: Floating wind, semisubmersible, tensioned leg platform, wind resource, cost breakdown, energy yield, LCOE

1 Introduction

The Arabian Gulf is a body of water that is surrounded by the countries of Iran, Saudi Arabia, United Arab Emirates (UAE), Oman, Kuwait, Qatar, Bahrain and Iraq. It connects into the Indian ocean and has a surface area estimated at 96,912 square miles with a mean depth of 50m [14]. With an established sense of the geographical features of the Gulf, it is important to understand the need for renewables in this region. Currently, the countries surrounding the Arabian gulf are some of the biggest exporters of crude oil and gas in the world. The UAE ranks 8th for the highest crude oil producing countries in the world; in 2021 the UAE was producing 3 million barrels per day [9]. From an environmental perspective, these production levels are detrimental to the planet's climate but on top of this, from an economic point of view, this creates a level of insecurity for the country's economy. The UAE have started to direct their attention to a more sustainable and diverse energy resource and potential export [1].

A feasibility study is an important starting point for a potential renewable project. The aim of this paper is to provide a thorough investigation into whether a floating offshore wind farm is both physically and economically feasible. Another area of interest in this project, and an indicator of feasibility, is the comparison of floating offshore wind to the other renewables that the UAE have invested in, with particular emphasis to solar PV. It has been the most successful and viable option for countries in this region so far, due to the abundance of sunlight they experience [12].

Currently, the topic of offshore wind in the UAE is sparse in terms of previous literature. There have been a few noteworthy works that have looked into the wind energy resource and also wind farm feasibility [3][4][5]. The annual wind power for the southern area of the Gulf was quoted at around 120 w/m^2 in [4], which is typically too low for large scale energy production. The criteria for a feasible offshore wind farm, according to [5], is that mean wind speed is above 5 m/s. Based on this limitation, there are areas, looking at the Global Wind Atlas, where a wind farm site would be suitable. The lower wind speeds in the Arabian Gulf mean that floating offshore wind could be a favourable option, as it has the ability to be deployed further offshore, which is a limitation of fixed offshore structures. Further from shore theoretically means higher wind speeds are present and thus a higher energy capture is possible. The location of a wind farm is a balancing act. On one hand, the further from the coast the site is located, the higher the wind energy density but the cost of the transmission system will be greater. Selecting various distances from shore will highlight how important this balance is.

The rationale to investigate floating wind structures as opposed to the traditional concrete monopile jacket structures is based on the environmental characteristics in the Arabian Gulf. Studies have found that saline sabhka soils and expansive clay, which are unsaturated, and the high presence of chlorides in the ground water of the gulf cause a greater rate of deterioration in concrete structures than their design life initially predicts [2] [13]. Furthermore, the durability of concrete tends to be lower due to the arid climate and hot temperatures in the Middle East. Previous concrete projects found their structures deteriorate and fail before reaching their predicted lifetime due to the heat. Cracks would appear during the manufacturing stage and the process of carbonation of the concrete was accelerated [13]. Floating offshore wind is a relatively new concept, but it is widely considered as a solution to installing wind farms in deep waters ($\geq$50m). Although Section 2 of this study found that the depth of

the water in the Arabian Gulf is 25-30m, not typical for a floating offshore case project, the case for floating wind is still physically possible. The question of feasibility is now pointed towards the financial case. The three main technologies for floating wind currently are Spar Buoy, Tensioned Leg Platform and Semi-submersible platform. Due to the shallow waters of the Arabian Gulf, spar buoy platforms would be unsuitable for a wind farm in this area, its large ballast is typically only considered for deep water sites that exceed 100m depths [15]. Therefore, the other two structures have been selected for this feasibility study.

2 Methodology

Using the Global Wind Atlas tool, four different locations in the Gulf were selected. The details of these locations are included in Table 1. An area of 200km^2 for each location was chosen as it covered a wide set of data points and is a suitable area of wind to study for a typical small offshore wind farm. The purpose of selecting different locations for this study was to see the variance in cost as a wind farm is located further offshore. Having extracted the mean wind speeds for four different locations, the annual energy yield for these areas need to be calculated. To do this, the type of turbine being used in the farm must be known. Two different sizes of turbines have been chosen

	S1	S2	S3	S4
Distance to shore (km)	30	60	90	140
Distance to port (km)	61.7	78.1	106	161
Depth (m)	25	25	25	30
Wind Farm Area (km^2)	200	-	-	-

Table 1: Site Location Details (S1= Site 1 etc.)

to analyse the impact that increasing turbine size has on the LCOE for the UAE. The turbines are the Vestas V136-3.45MW and Gamesa G132-5.0MW offshore turbines. The reason for selecting these relatively small turbines was based on previous literature suggesting that the capital cost of larger offshore wind turbines largely outweighed the energy yield the turbine was generating [8][5][7]. Once the turbines had been selected, the annual energy yield calculator from the Global Wind Atlas was utilised. Inputting the power curve data and turbine variables allowed a .tiff file to be compiled. Using QGIR software, the data in these files could be extracted and converted into the mean annual energy yield. The results of this are provided in Table 2 in Section 3.

Cost analysis for the project proved difficult as there is limited literature on this topic for the UAE, so in some aspects of the cost model, the inputs are based off of case studies for floating offshore wind in other parts of the world. These case studies often take place in deeper waters and rougher conditions, so it was assumed these inputs were a worst-case scenario for the UAE. The cost model that most calculations came from was the model by Maienza in 2020 [11]. The cost components can be split into three main categories: capital expenditures (CAPEX), operational expenditures (OPEX) and decommissioning expenditures (DECEX). Within CAPEX costs there are 8 components for this project: turbine, platform, mooring and anchoring, transmission and their associated installation costs. LCOE can be calculated using the equation found in [6].

3 Results

The first results from the project came from the wind resource. Table 2 illustrates the change in the energy yield both based on location and the turbine chosen. The energy yield increases for all sites when a 3.45MW turbine is replaced by the larger 5MW turbine. These results concur with the theory that the larger the capacity of these small turbines the larger the energy yield produced would be. The energy yield is expected to eventually plateau when larger turbines are used as there is only so much energy in the wind for the turbine to convert. It can be assumed that the relative improvement in energy yields reduces as turbine capacity increases.

Table 3 has been included to give a representative example of all of the cost estimates for the 5MW farm at site 1 for both TLP and semisubmersible platforms. As stated previously, these aren't exact values as many have been given worst case prices based on the lack of data for the UAE. The overarching capital cost comes from the mooring and anchoring which accounts for almost half the cost of the wind farm. This is an expected cost due to the complex nature of the mooring lines for the TLP, the number of these required and their associated drag anchors. The operation and decommissioning costs are a fifth of the overall cost for both site locations which is in agreement with other literature [10]. Using the values for each cost breakdown, like the ones shown in Table 3

Turbine Size	Energy Yield (10^8 kWh) Site 1	Site 2	Site 3	Site 4
3.45MW	1.59	1.58	1.61	1.70
5MW	1.86	1.85	1.89	2.01

Table 2: Energy Yield for the two different turbines in each site location

Cost Breakdown (M£)	TLP	Semisubmersible
Turbine	152.5	152.5
Platform	33.9	29.6
Mooring and Anchoring	583.9	846.0
Transmission System	39.0	39.0
Installation	194.2	40.5
OPEX	131.7	131.7
DECEX	134.3	26.6

Table 3: Cost breakdown for the whole wind farm at Site 1 using 5MW turbines with both TLP and semisubmersible platforms

and the annual energy yields in Table 2, an LCOE for each scenario can be calculated. These LCOEs are shown in Table 4. The most apparent trend is that the lowest LCOE for both turbine sizes and platform types is found at

3.45MW Turbine	Site 1	Site 2	Site 3	Site 4
TLP	208.98	213.20	210.80	202.68
SemiSub	208.37	212.58	210.19	208.19
5MW Turbine	Site 1	Site 2	Site 3	Site 4
TLP	192.92	195.80	192.79	182.12
SemiSub	192.40	195.27	197.81	186.77

Table 4: LCOE estimations for UAE wind farm using two turbines for the two different technologies at the various site locations

site location 4, furthest from shore. However, the cost difference is almost negligible for the 3.45MW turbine with only 18p difference between site 1 and 4.

Between the two technologies, for 3.45MW, the LCOE's are roughly the same for the two technologies with the TLP being slightly more expensive but the only significant difference in cost comes at site 4 where TLP is noticeably cheaper. For the 5MW, there is a similar observation. LCOE's are close to equal for sites 1 to 3, with semisubmersible being slightly cheaper in these scenarios. Again, at site 4 the LCOE gap is bigger with TLP being the cheaper option. The reason behind this may arise from the increased mooring costs associated with site 4 due to the deeper water which will have a bigger impact on the length of the semisubmersible steel mooring lines than the TLP rope.

4 Discussions and Conclusions

The cost of energy for the UAE in this case is much higher than typically expected for a floating offshore wind farm. For certain, it is much too high a cost for the project to be feasible or profitable for the wind farm developer. It is important to understand the root cause behind the large values for the LCOE. Placing the exact same wind farm with all the same inputs, into a different location provided the answer to this question. Using the Global Wind Atlas, as before, the wind farm area was selected off the coast of Scotland in the North Sea, where current fixed wind farms are located. Using the energy yield calculator, new values for the energy yield were input into the cost model. LCOE was more than halved for all scenarios. The large reduction in price reveals that the main cause that prevents a feasible offshore wind farm in the Arabian Gulf is directly linked to the low wind speeds experienced in the area. Overall, it is a fair statement to make that the UAE does not have a feasible floating offshore wind case at this current moment in time. One of the main contributors to this conclusion is the comparison of the LCOE's carried out in this project versus the main renewable energy source in the country, solar PV. In 2020 the price of

solar PV was as low as £11.24 per MWh. Offshore wind (fixed or floating) is not able to compete with these sort of prices in the current market.

The levelised cost of energy has been calculated for 16 different scenarios for a floating wind farm situated off the coast of the United Arab Emirates in the Arabian Gulf. The cost analysis looked at four different site locations for a wind farm of 200km^2 containing 25 wind turbines. There were two turbine sizes investigated for the wind farm, 3.45MW and 5MW. Finally, two different floating platform technologies were considered. The wind resource and bathymetry were utilised to find the annual energy production of the wind farm in the four locations. From the results, the cheapest LCOE was for a wind farm located 140km from shore that consisted of 25 5MW turbines with tensioned leg floating platforms, estimated at £182.12 per MWh. However, the overall consensus for the project is that this is a relatively high LCOE in comparison to other floating wind projects and in comparison to cheaper energy sources in the UAE (solar PV). Ultimately, at the present time the project is not feasible in financial terms due to the low energy yield provided by the low speed winds.

References

[1] H. Abdo. Opportunities, challenges and risks of transition into renewable energy: The case of the arab gulf cooperation council. *RERIC International Energy Journal*, 18:391–400, 12 2018.

[2] A. Al-Gahtani and M. Maslehuddin. Characteristics of the Arabian Gulf environment and its impact on concrete durability–an overview. In *The 6th Saudi Engineering Conference, KFUPM, Dhahran, December 2002*, 2002.

[3] A. A. Al Qubaisi, S. S. Dol, M. S. Khan, and A. A. Azeez. Feasibility study and design of floating offshore wind turbine farm in united arab emirates. In *2018 Advances in Science and Engineering Technology International Conferences (ASET)*, pages 1–5, 2018.

[4] K. Al-Salem, S. Neelamani, and W. Al-Nassar. Wind Energy Map Of Arabian Gulf. *Natural Resources*, 09:212–228, 2018.

[5] S. M. Baban and T. Parry. Developing and applying a GIS-assisted approach to locating wind farms in the UK. *Renewable Energy*, 24(1):59–71, 2001.

[6] M. Bruck, P. Sandborn, and N. Goudarzi. A Levelized Cost of Energy (LCOE) model for wind farms that include Power Purchase Agreements (PPAs). *Renewable Energy*, 122:131–139, 2018.

[7] L. Castro-Santos, A. Filgueira-Vizoso, C. Álvarez Feal, and L. Carral. Influence of Size on the Economic Feasibility of Floating Offshore Wind Farms. *Sustainability*, 10(12), 2018.

[8] L. Castro-Santos, D. Silva, A. Rute Bento, N. Salvação, and C. Guedes Soares. Economic feasibility of floating offshore wind farms in Portugal. *Ocean Engineering*, 207:107393, 2020.

[9] Government of Dubai. Dubai Statistics Centre, 2022.

[10] G. Katsouris and A. Marina. Cost modelling of floating wind farms. 2016.

[11] C. Maienza, A. Avossa, F. Ricciardelli, D. Coiro, G. Troise, and C. Georgakis. A life cycle cost model for floating offshore wind farms. *Applied Energy*, 266:114716, 2020.

[12] A. Mokri, M. Aal Ali, and M. Emziane. Solar energy in the United Arab Emirates: A review. *Renewable and Sustainable Energy Reviews*, 28:340–375, 2013.

[13] M. Samarai. Durability of Concrete in the Arabian Gulf. *Journal of Materials Science and Engineering A*, 5, 12 2015.

[14] V. . M. [U+FFFD] A. . a. O. . . United Nations Group of Experts on Geographical Names Working Paper No. 61 Archived 2012-10-03 at the Wayback Machine, 23rd Session. 2010.

[15] E. Uzunoglu, E. Oguz, and C. Guedes Soares. An overview of platform types used in floating wind energy. 09 2021.

Ecological aspects

18th EAWE PhD Seminar on Wind Energy
2-4 November 2022
Bruges, Belgium

Combined life cycle impact and cost assessment of wind energy generation in large-scale offshore wind farms

Samuel Kainz[a], **Adrien Guilloré**[a], **Helena Canet**[a], and **Carlo L. Bottasso**[a]

[a]Wind Energy Institute, Technical University of Munich, 85748 Garching bei München, Germany

E-mail: samuel.kainz@tum.de

Keywords: Life cycle assessment, Cost of energy, Wind farm design, Offshore wind energy

This work evaluates the economic and environmental performance of electricity generated in large-scale offshore wind farms and identifies potential room for improvement. An automatized holistic evaluation tool allows to calculate the two characteristic measures Impact of Energy (IoE) - quantifying the global warming potential expressed in g CO_2-eq/kWh - and Levelized Cost of Energy (LCoE) in €/MWh, related to one unit of electric energy produced offshore and transmitted to shore by nearly any European offshore wind farm. Subsequently, running the evaluation tool in loops commanded by genetic algorithms allows to conduct multi-objective optimization. Thereby, chosen design parameters can be optimized such that both IoE and LCoE are minimized. In this work, the evaluation tool is applied on four recently commissioned European offshore wind farms serving as case studies. One of the case studies is then used to demonstrate the potential of the optimization procedure which, however, is currently being further developed.

1 Introduction

Quantifying the IoE is crucial to evaluate the environmental performance of existing wind turbines and wind farms, to identify its main drivers, locate potential room for improvement, and design new facilities with minimized IoE while guaranteeing economic feasibility. Several life cycle analyses have been conducted on offshore wind energy generation (e.g. [15, 3, 16, 2, 14]). However, all studies are case-study specific, making the automatized evaluation tool as introduced in this extended abstract innovative. Furthermore, to the author's knowledge, no design tool focusing on both LCoE and IoE has been published or described in the scientific community so far.

2 Methodology

2.1 Evaluation tool

The evaluation tool consists of turbine- and plant-specific state-of-the-art mass, cost and logic models covering all wind farm components, a cradle-to-grave life cycle assessment model, and an energy harvest model.

The *turbine-specific model* assesses mass and costs of all wind turbine components, support structure, and scour protection. It is based on INNWIND's mass and cost model [10] for large-scale offshore wind turbines, NREL's ORBIT model for offshore balance-of-plant [13], and DNV's offshore standard for scour protection [6].

The *plant-specific model* calculates wind farm layout, mass and costs of off- and onshore substation, cabling and corrosion protection, and installation procedure for all wind farm components. It is based on the previously mentioned ORBIT model, a cabling model based on ABB cable data [1], and a corrosion protection model following the corresponding DNV recommended practices [7, 5].

The *life cycle assessment model* has been derived from scratch, following the standardized procedure for life cycle assessment as defined in ISO 14040 [8] and ISO 14044 [9]. The life cycle of the wind farm is modeled by means of more than 100 reference processes extracted from the ecoinvent database [17] and scaled to the applied case study, allowing to calculate the global warming potential related to each life phase, component and material of the wind farm.

Parameter	Unit	Horns Rev III	Wikinger	Hywind Scotland	Kincardine
		Specification			
Rated power	MW	8.3	5	6	9.5
Rotor diameter	m	164	135	154	164
Hub height	m	105	97.5	98	108
Number turbines	-	49	70	5	5
Turbine spacing	RD	7.92	5.96	8.7	9.47
Plant capacity	MW	406.7	350	30	48
Mean water depth	m	15.5	40	107.5	70
Support structure		Monopile	Jacket	Spar	Semisub.
Dist. to shore	km	33	90	30	15
Location		Denmark	Germany	Scotland	Scotland
		Results			
Aver. turbine AEP	GWh/a	28.88	16.67	22.45	33.56
Capacity Factor	%	39.71	38.05	42.70	40.32
LCoE	€/MWh	78.34	113.17	103.01	101.19
IoE	g CO_2-eq/kWh	19.00	40.34	33.97	33.18

Table 1: Specification and results of the case studies

The *energy harvest model* calculates the expected annual energy production (AEP) of the wind farm using the wake modeling utility FLORIS [12]. The power curve is based on a simple regulation trajectory where power is simply cut off above rated wind speed. The thrust curve is approximated via look-up tables taken from the DTU 10MW reference turbine [4].

2.2 Design tool

The design tool runs the evaluation tool in loops until configurations of input variables are found which deliver lowest values for IoE and LCoE. This procedure is directed by a genetic algorithm, implemented via the function *gamultiobj* provided by Matlab's 'Global optimization toolbox' [11]. In order to prevent unintended unequal weighting of the algorithm's in- and outputs, the predefined variable ranges and the model results as seen by the optimization algorithm are non-dimensionalized. To account for realistic results, constraints are set for specific power (200-600 W/m^2) and aspect ratio (0.55-1.2), the former being the ratio of rated power and rotor area, the latter the ratio of hub-height and rotor diameter.

3 Results

3.1 Evaluation results

The four case studies for IoE and LCoE evaluation have been chosen such that they represent differing design, technology, size, and siting in commissioned and planned real-life offshore wind farms. Horns Rev 3 and Wikinger are fixed-bottom large-scale wind farms, Hywind Scotland and Kincardine are full-scale pilot projects for floating wind turbine technology. The most characteristic parameters and main results of the four case studies are listed in Tab. 1. All results are preliminary.

The results for IoE and LCoE are visualized in Fig. 1. The indicated uncertainty bars refer to a best- and worst-case scenario where uncertainties in emission data, discount rate, water depth, lifetime, and measured distances are reflected as most optimistic and most conservative, respectively. Among the case studies, similar trends are observed for both IoE and LCoE, with variations being more pronounced for IoE. Interestingly, the results for the two floating wind farms are almost equal despite differing technological concepts.

To understand the differences of IoE and LCoE among the case studies, the results are broken down by life phases, components, and materials. The latter can only be applied on IoE results since the level of detail in the cost models is not allowing this analysis. The relative contribution of the life phases to IoE and LCoE is shown in Fig. 2. Similar trends are visible among the case studies, and for IoE and LCoE. Obviously, the component production is

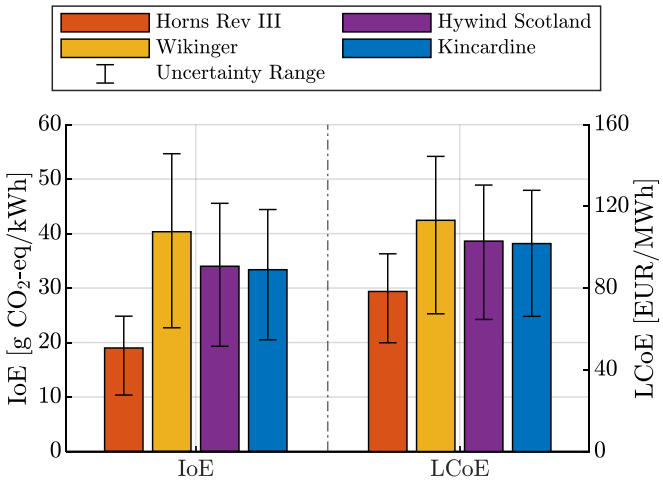


Figure 1: IoE (left) and LCoE (right) as evaluated for the four case studies, with corresponding uncertainty ranges

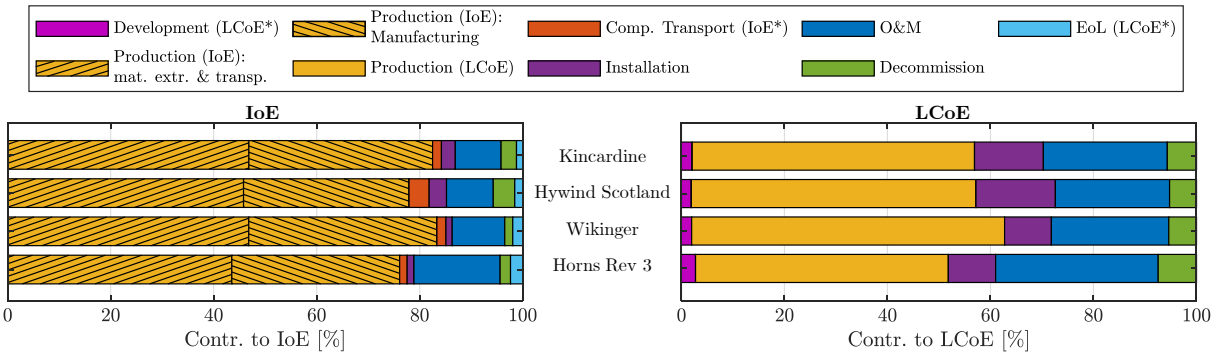


Figure 2: Relative contribution of the life phases to IoE (left) and LCoE (right). Note that the scope of the underlying models is different, phases that are evaluated for one model only are marked with a star (*).

causing most costs and - even more pronounced - most emissions, followed by operation & maintenance including component replacement, and installation. Conclusively, costs and emissions are mostly linked to their material-intensive components. This is especially pronounced for the Wikinger wind farm which is - considering its fixed-bottom concept - located in relatively deep water hence requiring massive support structures.

The breakdown of IoE and LCoE by component is shown in Fig. 3. All life-phases with respect to IoE can be allocated to the respective components, whereas the level-of-detail in the cost models is not allowing a completed allocation. Unallocatable costs are indicated as 'global'. For all case studies but Horns Rev 3, the support structures account for most of the emissions and allocatable costs, followed by the turbine components, the tower, and power cables. The substations are of minor importance. The impact of the support structure on IoE is significantly higher than on LCoE, highlighting the energy-intensive hence highly-emitting production of theses components. The trend among these case studies is similar. In contrast, the support structure of Horns Rev 3 has significantly lower contribution to the final IoE and LCoE, which can be explained by its location in shallow water resulting in the requirement of less massive support structures. Consequently, support structures are identified as significant drivers for IoE and LCoE, but dependent on water depth and applied support structure type.

Fig. 4 shows the breakdown of IoE by materials. Obviously, carbon steel - which is mainly used for the support structures - drives the IoE. Alloyed steel as applied in turbine components, copper in power cables and electric components, turbine electronics, and paint for corrosion protection are further significant carriers of global-warming-related burdens. Outstandingly, iron ore used as ballast material in the floating spar of Hywind Scotland turbines is a further significant driver of IoE.

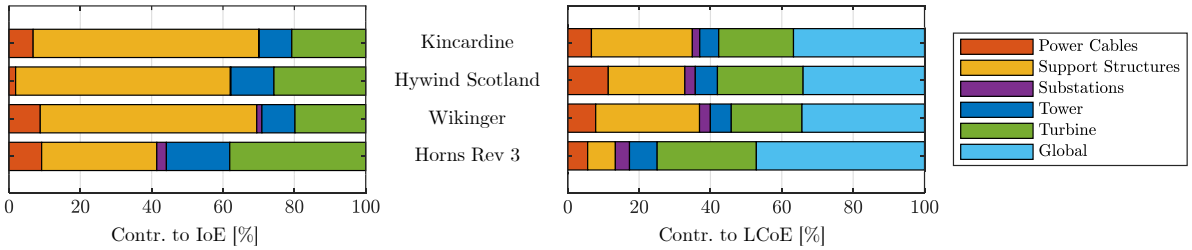


Figure 3: Relative contribution of the components to the results of IoE (left column) and LCoE (right column).

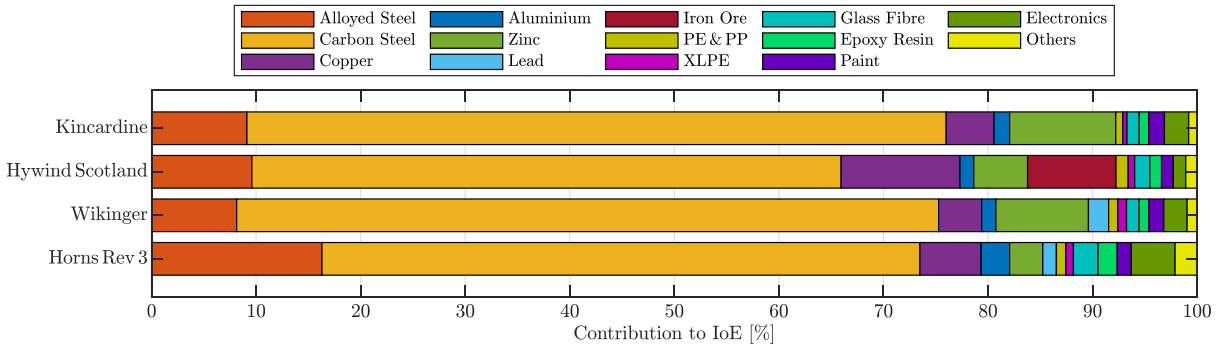


Figure 4: Relative IoE breakdown by materials.

3.2 Optimization results

Running the evaluation tool in loops by applying genetic algorithms allows to conduct multi-objective optimization such that both IoE and LCoE of wind farm design cases are minimized. Fig. 5 shows the optimization results for the case study Horns Rev 3. The first graph shows the assessed Pareto front in which every point represents an optimum design point, compromising the weighting of minimization objective between IoE (y-axis) and LCoE (x-axis). The underlying configuration of variable design parameters are presented in the other graphs, linked with the Pareto front via the x-axis. The dashed lines represent the allowed variation ranges, the chain lines mark the initial configuration. Apparently, both IoE and LCoE can be significantly reduced. With respect to the baseline, the optimized configuration favours smaller turbines, reduced hub-height, and increased turbine spacing. Within the optimization margin, prioritized IoE reduction is linked to increased nameplate capacity, whereas the other parameters are lower than in the case of focusing on minimized LCoE. However, all results are preliminary since the multi-objective optimization is currently undergoing further development. Furthermore, lowered IoE and especially lowered LCoE might only be achieved by neglecting unknown design constraints that had been applied when Horns Rev 3 was designed.

4 Conclusion

In a nutshell, this work describes a basic tool to evaluate the environmental and economic performance of existing European offshore wind farms with respect to IoE and LCoE, and to support decision-making processes in the design of new wind farm projects. By its holistic approach, variable evaluation possibilities and inclusion of design consideration, an identified gap in research is thereby closed. Evaluation of four case studies yields a range of IoE between 19.0 and 40.3 g CO_2-eq/kWh, corresponding LCoE is found between 78.3 and 113.2 €/MWh, with trends for IoE and LCoE among the case studies being similar but less pronounced for LCoE. The variation in results is mainly linked to different siting and design characteristics, of which water depth and support structure type are of particularly high influence. Generally, the support structure is identified as the main driver of both IoE and LCoE, followed by the turbine components. This results from the energy-intensive production processes of which massive steel-component production is particularly high-emitting. Multi-objective optimization of one case study supposes significant optimization potential with respect to both IoE and LCoE when varying main wind turbine and farm characteristics. However, method and evaluation are still undergoing further development.

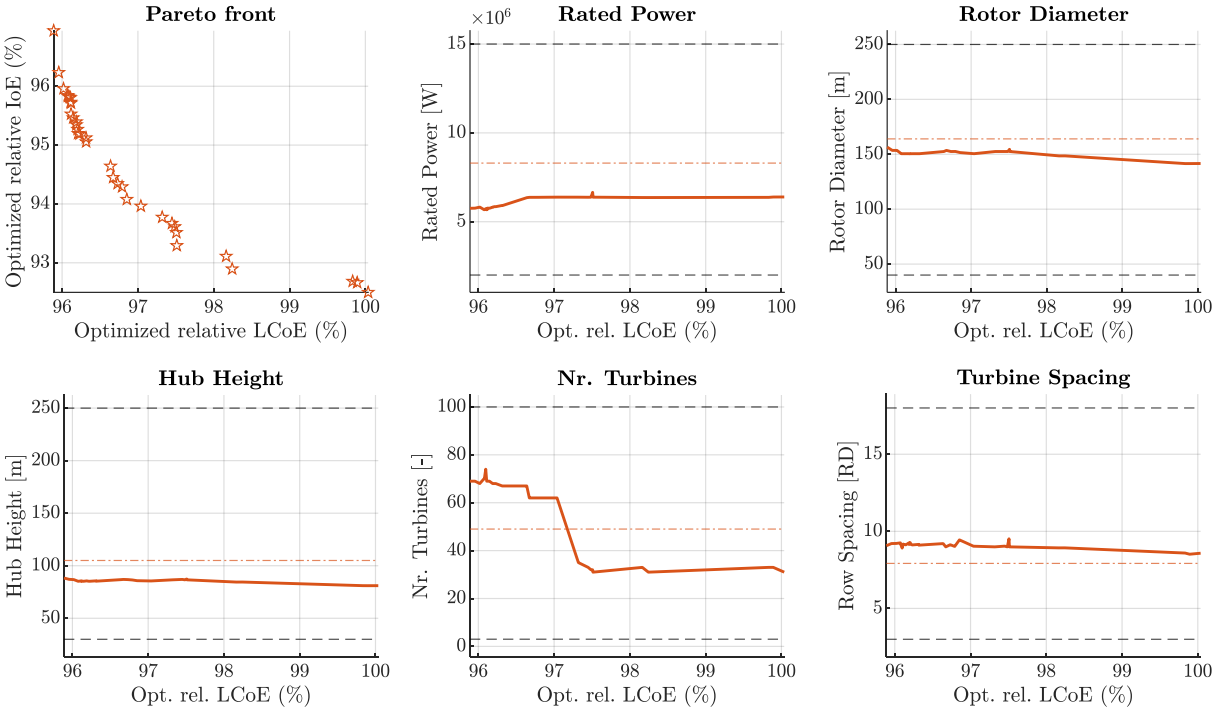


Figure 5: Multi-objective optimization results for Horns Rev 3.

References

[1] ABB. XLPE Submarine Cable Systems: Attachment to XLPE Land Cable Systems - User's Guide. *https://new.abb.com/docs/default-source/ewea-doc/xlpe-submarine-cable-systems-2gm5007.pdf*, 2010.

[2] J.-I. Bang, C. Ma, E. Tarantino, A. Vela, and D. Yamane. Life Cycle Assessment of Greenhouse Gas Emissions for Floating Offshore Wind Energy in California. *Bren School of Environmental Science & Management*, 2019.

[3] A. Bonou, A. Laurent, and S. I. Olsen. Life cycle assessment of onshore and offshore wind energy-from theory to application. *Applied Energy*, 180:327–337, 2016.

[4] P. Bortolotti, H. Canet Tarrés, K. Dykes, K. Merz, L. Sethuraman, D. Verelst, and F. Zahle. IEA Wind Task 37 on Systems Engineering in Wind Energy: WP2.1 Reference Wind Turbines, 2019.

[5] Det Norske Veritas. Cathodic Protection Design. *Offshore standard*, DNV-RP-B401, 2010.

[6] Det Norske Veritas. Design of Offshore Wind Turbine Structures. *Offshore standard*, DNV-OS-J101, 2014.

[7] Det Norske Veritas. Corrosion protection for wind turbines. *Offshore standard*, DNVGL-RP-0416, 2016.

[8] Deutsches Institut für Normung. Umweltmanagement - Ökobilanz: Grundsätze und Rahmenbedingungen, 2006.

[9] Deutsches Institut für Normung. Umweltmanagement - Ökobilanz: Anforderungen und Anleitungen, 2018.

[10] INNWIND. Deliverable 1.21. *http://www.innwind.eu/publications/deliverable-reports*, 2016.

[11] MathWorks. MATLAB: Global Optimization Toolbox: User's Guide, 2021.

[12] NREL. Floris version 2.4. *https://github.com/NREL/floris*, 2021.

[13] NREL. Offshore Renewable Balance-of-system Installation Tool. *https://github.com/WISDEM/ORBIT*, 2021.

[14] B. Poujol, A. Prieur-Vernat, J. Dubranna, R. Besseau, I. Blanc, and P. Pérez-López. Site–specific life cycle assessment of a pilot floating offshore wind farm based on suppliers' data and geo–located wind data. *Journal of Industrial Ecology*, 24:248–262, 2020.

[15] H. L. Raadal, B. I. Vold, A. Myhr, and T. A. Nygaard. GHG emissions and energy performance of offshore wind power. *Renewable Energy*, 66:314–324, 2014.

[16] L. Tsai, J. C. Kelly, B. S. Simon, R. M. Chalat, and G. A. Keoleian. Life Cycle Assessment of Offshore Wind Farm Siting: Effects of Locational Factors, Lake Depth, and Distance from Shore. *Journal of Industrial Ecology*, 20:1370–1383, 2016.

[17] G. Wernet, C. Bauer, B. Steubing, J. Reinhard, E. Moreno-Ruiz, and B. Weidema. The ecoinvent database version 3 (part I): overview and methodology. *The International Journal of Life Cycle Assessment*, 21:1218–1230, 2016.

Other topics

18th EAWE PhD Seminar on Wind Energy
2-4 November 2022
Bruges, Belgium

CFD model of a wind tunnel: making a digital twin

Rishabh Mishra[a], **Emmanuel Guilmineau**[a], **Ingrid Neunaber**[c], and **Caroline Braud**[a,b]

[a]LHEEA lab. - CNRS - Centrale Nantes, 1 rue de la Noë, 44100 Nantes
[b]CSTB, 11 Rue Henri Picherit, 44300 Nantes, France
[c]NTNU, Høgskoleringen 1, 7034 Trondheim, Norway

E-mail: rishabh.mishra@ec-nantes.fr

Keywords: Wind tunnel, transition model, lift coefficient, digital twin

1 Introduction

Multi-megawatt wind turbines typically have blades operating at Reynolds numbers ranging from 1 to 20 million [1] but many academic wind tunnel facilities, including the one at Research Laboratory in Hydrodynamics Energetics and Atmospheric Environment (LHEEA) can only reach Reynolds numbers of O(10^5)(see [4]). Therefore, it is necessary to create a digital twin of the wind tunnel to investigate the behaviour an airfoil at LHEEA which is validated against wind tunnel experiments performed at LHEEA. At low Reynolds number, flow transition from laminar to turbulent becomes an important phenomenon. Therefore, to simulate transition, a single equation Local Correlation Based Transition Model (LCTM), i.e., γ transition model [3] is incorporated, where $\gamma \in [0,1]$. When γ is 0, then the flow is considered to be laminar, and is considered turbulent when γ is 1. The γ transition model is chosen because it is the default transition model of the ISIS CFD solver and its applicability is well proven. During the validation process, by looking at the lift coefficient (C_l), we observed that the γ transition model does not work as well as it does at high Reynolds numbers.

2 Objectives

The main objectives of this work are to perform experiments, build a digital twin with focus on checking the suitability of the γ transition model, at low chord-based Reynolds number (Re_c) and compare results of experiments and simulations. In the present study we have chosen $Re_c = 1.7 \cdot 10^5$ for an airfoil with a chord length of $c = 0.125$m (see figure 1).

3 Methodology

First, experiments were performed in the aerodynamic wind tunnel of the LHEEA laboratory. To generate different turbulent inflow conditions, a regular grid could be installed at the inlet, and two inflow conditions were investigated with turbulence intensities (TI) of 0.3% (no grid) and 3.0% (with grid). A 2D blade section with the shape extracted from scans of the blade of an operated 2MW wind turbine (see figure 1) was installed on a force balance system to measure the aerodynamic forces for different angles of attack α, cf. figure 2.
Then, equivalent 2D Unsteady Reynolds Averaged Navier Stokes (URANS) simulations have been performed using $k-\omega$ SST menter tubulence model [2] (with and without γ transition model) integrated in ISIS-CFD incompressible flow solver developed by CNRS and ECN for $Re_c = 1.7 \cdot 10^5$. C_l curves obtained from experiments are compared with the simulations.

4 Main results

Figure 3 compares the C_l obtained from experiments with the results from simulations performed for the two cases labeled as 'with transition model' and 'without transition model' for $Re_c = 1.7 \cdot 10^5$ and TI = 0.3%. For the 'with

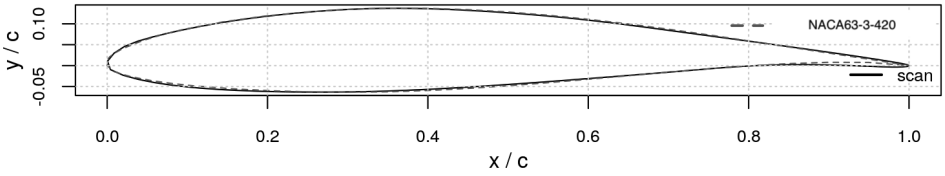


Figure 1: Blade section at 80% of the length of the blade of a 2MW wind turbine in comparison with a NACA63-3-620 profile with a modified camber of 4% instead of 2%.

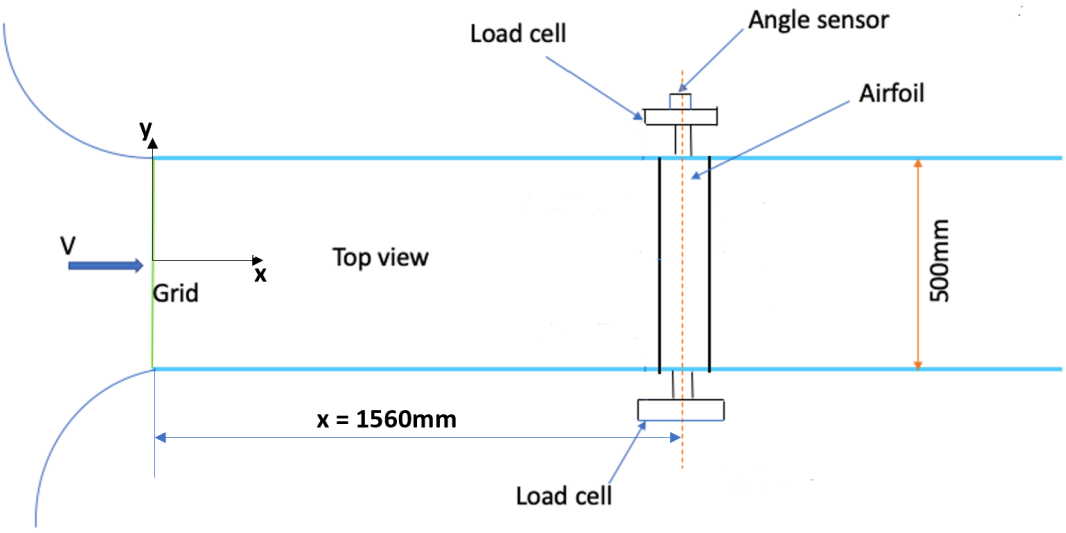


Figure 2: Illustration of the wind tunnel set-up with the airfoil mounted on a force balance system.

transition model' case for lower angles of attack (AOA) (up until 4°), the C_l values are found to be lower than the experimental results. For AOAs larger than 4° (up until 16°), the simulation follows the trend of the experiment. In the 'without transition model' case, the opposite happens: up until 4° AOA the simulation follows the experimental results but afterwards simulation results deviate from experimental values. This gives an indication that for lower AOAs at low Re_c, the use of a transition model is detrimental to the simulation results for lower AOAs, but for higher AOAs, transition model improves the results.
Figure 4 compares the C_l obtained from experiments with the results from simulations performed for the two cases labeled as 'with transition model' and 'without transition model' for $Re_c = 1.7 \cdot 10^5$ and TI = 3.0%. The trend seen in the 'without transition model' case is similar to what is seen in the case of TI = 0.3% 'without transition model' case. An increase in the TI is found to improve the performance of the transition model at lower AOAs except for a dip in C_l values seen at 6° and 8° AOA.

5 Conclusions

Observations made above clearly draw upon few important conclusions:

1. For the lower inflow TI (0.3%), the γ transition works well at higher AOAs ($> 6°$) but not for lower AOAs. It seems that for low Re_c and low TI inflow, simulations should be performed without γ transition model for lower AOAs and with γ transition model at higher AOAs to achieve a C_l curve that follows experiments best.

2. As the turbulence intensity of the inflow is increased, the γ transition model is found to improve the results

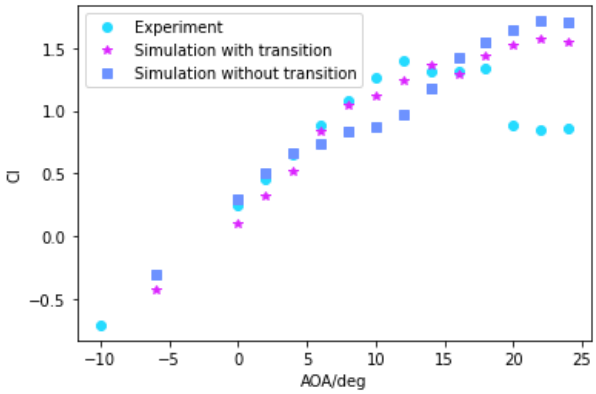


Figure 3: Comparison of C_l curves obtained from simulations performed with and without γ transition model against experiments for TI = 0.3% and $Re_c = 1.7 \cdot 10^5$

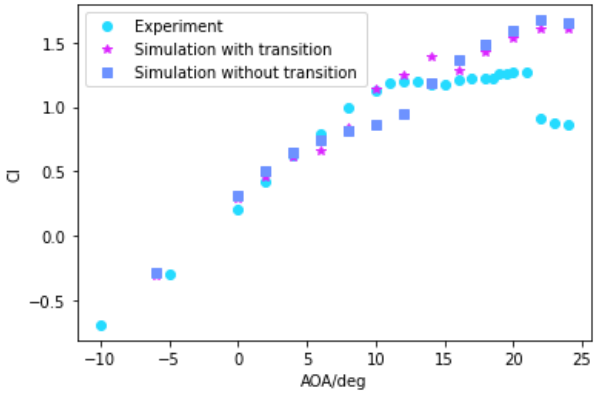


Figure 4: Comparison of C_l curves obtained from simulations performed with and without γ transition model against experiments for TI = 3.0% and $Re_c = 1.7 \cdot 10^5$

for lower AOAs.

6 Future works

3D simulations will be performed to include 3D flow effects known to occur especially at the higher AOAs. Experimentally, local pressure measurements will be performed and then it will be compared in detail.

Acknowledgements

The results presented here were obtained within the French national project **MOMENTA** (grant no. ANR-19-CE05-0034).

References

[1] E. Llorente, A. Gorostidi, M. Jacobs, W. A. Timmer, X. Munduate, and O. Pires. Wind tunnel tests of wind turbine airfoils at high reynolds numbers. *Journal of Physics Conference Series*, 1(524):012012, 2014.

[2] F. R. Menter, M. Kuntz, and R. Langtry. Ten years of industrial experience with the sst turbulence model. *Turbulence, heat and mass transfer*, 4(1):625–632, 2003.

[3] F. R. Menter, P. E. Smirnov, T. Liu, and R. Avancha. A one-equation local correlation-based transition model. *Flow, Turbulence and Combustion*, 95(4):583–619, 2015.

[4] K. Mulleners and M. Raffel. Dynamic stall development. *Experiments in Fluids*, 54(54):1469, 2013.

18th EAWE PhD Seminar on Wind Energy
2-4 November 2022
Bruges, Belgium

Description of the methodology for quantifying geometrically non-linear cross-sectional deformations of rotor blades

J Gebauer[a] and C Balzani[a]

[a]Leibniz University Hannover, Institute for Wind Energy Systems, Appelstr. 9A, 30167 Hannover, Germany

E-mail: julia.gebauer@iwes.uni-hannover.de

Keywords: Cross-Sectional Warping, Finite Element Method, Simulation, Wind Turbine

Abstract

Rotor blades of wind turbines are modelled as thin-walled, beam-like structures. Non-linear beam formulations are thus used in simulations of such structures. Though cross-sectional deformations are neglected therein. The deformation of cross-sections due to applied bending moments is also called cross-sectional warping. This effect is exemplarily shown in Figure 1 for a tubular beam under pure bending. The spar caps prevent the largest part of the cross-sectional deformation. Cross-sectional warping can affect the aerodynamic and structural properties of the blade. Especially with very large, more elastic blades, we assume that significant deformations can occur. Therefore, an investigation of this effect is necessary.
The rotor blade of the IEA 15 MW RWT [1] is used for this investigation. A Finite Element model was generated using the tool MoCA [2]. Simplified load cases were used for various simulations. The results of these simulations are the basis for this study.
In this work, two approaches to describe the cross-sectional deformation will be explained. In addition, the influence of different load cases on the deformation is shown.

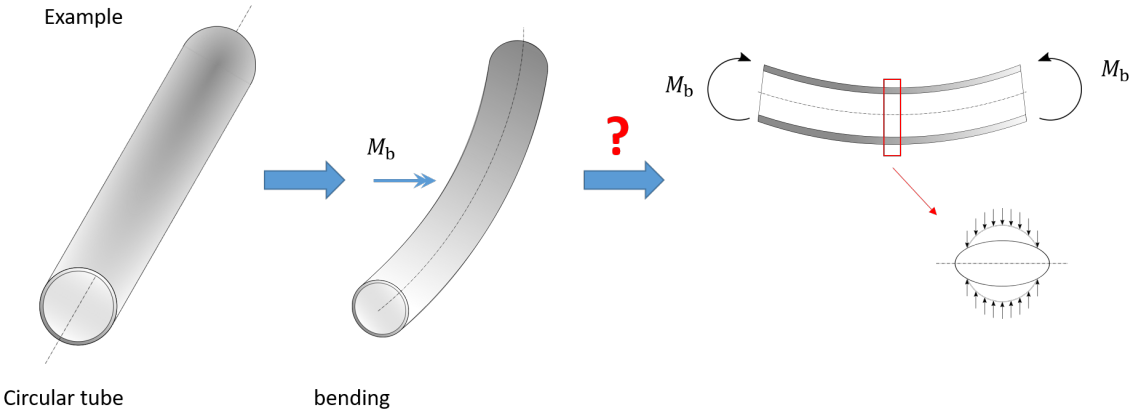


Figure 1: Cross-sectional warping in a tubular beam under pure uni-axial bending.

In order to be able to make a statement about the deformation of a single cross-section, the nodes have to be projected into a plane that is considered the cross-section plane in the deformed configuration. In this way, we fulfill the postulation of beam formulations that a plane cross-section remains plane during deformation. Hence, the out-of-plane displacement should be minimised in the projection procedure.

For first results, forces were applied individually in flap and edge directions. The resulting cross-sectional deformations can be seen in Figure 2. A cross-section close to the blade root was chosen, as the deformations are expected to be maximum in the maximum chord length region. The red arrows show the nodal deflection vectors.

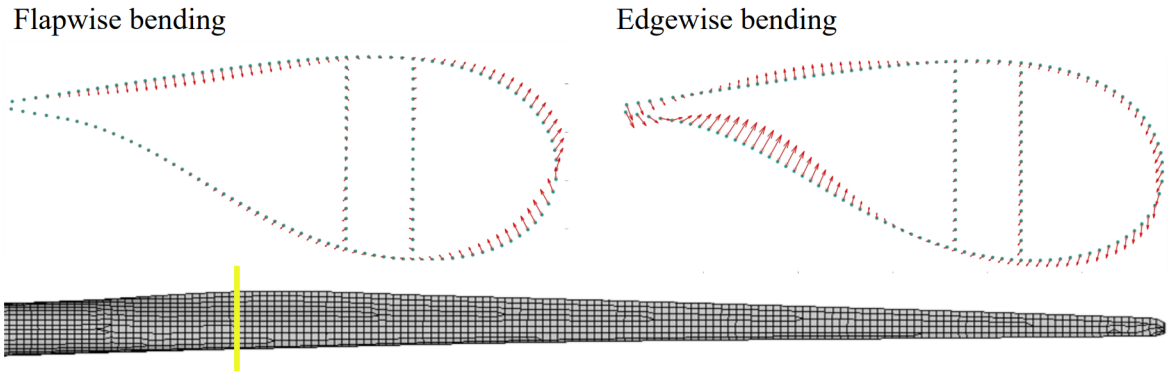


Figure 2: Cross-sectional deformation of the rotor blade under forces in flap and edge direction.

In order to further study the development of cross-sectional deformations, several positions along the blade under a variety of load cases and load distributions will be investigated in the future.

References

[1] E. Gaertner, J. Rinker, L. Sethuraman, *et al.* IEA wind TCP task 37: Definition of the IEA 15-megawatt offshore reference wind turbine. Technical Report No. NREL/TP-5000-75698, National Renewable Energy Lab. (NREL), Golden, CO (United States), 2020.

[2] P. Noever-Castelos, B. Haller, and C. Balzani. Validation of a modeling methodology for wind turbine rotor blades based on a full-scale blade test. *Wind Energ. Sci.*, 7, 105-127, `https://doi.org/10.5194/wes-7-105-2022`, 2022.

18th EAWE PhD Seminar on Wind Energy
2 – 4 November 2022
Bruges, Belgium

Experimental investigation of failure mechanism in cross-ply curved composite laminates under transverse loading

A Cevik[a], D Coker [a,b], D Yavas [c]

[a] Department of Aerospace Engineering, Middle East Technical University, Ankara, Turkey
[b] METU Center for Wind Energy, Middle East Technical University, Ankara, Turkey
[c] Mechanical Engineering, Lamar University, Beaumont, Texas 77710, USA

E-mail: coker@metu.edu.tr

Keywords: curved composite laminate, wind turbine blade, delamination, crack tip speed, digital image correlation

1 Introduction

In the aerospace and wind energy industries, composite materials are preferable due to their high specific stiffness and strength. The main load-carrying structures of airplanes and wind turbines, such as ribs and spars, are manufactured from composite materials. These structures are comprised of complex shaped components like curved parts. Curved region of these parts is exposed to high interlaminar tensile and shear stresses, and these interlaminar stresses lead to delamination type failure [1],[2]. In this study, an experimental investigation is carried out to elucidate the failure mechanism of cross-ply curved composite laminates under transverse loading. The in-house designed test fixture is used to apply shear load to the one of the arms of the curved beam while the other arm is clamped.

2 Method

Cross-ply curved composite laminates having a stacking sequence of $[(90/0)_4, \overline{90}]_s$ were manufactured from Hexply AST/8552 unidirectional (UD) prepregs with hand lay-up technique. The experimental setup is shown in Figure 1. The experiments were conducted with the universal electro-mechanical tensile testing machine Shimadzu. Photron SA5 high-speed camera is used to observe the dynamic failure event over the curved region. Dedocool light kit is used for better visualization of the crack propagation. In two of the experiments, Digital Image Correlation (DIC) technique is used to obtain the strain field over the curved beam, especially just before the failure. Fractography of the post-mortem specimens was also carried out with an optic microscope. Elastic Finite Element Analysis (FEA) is carried out to obtain the strain and stress fields over the curved region.



Figure 1: Test setup used in the experiments

3 Results and Discussion

In the experiments, cross-ply curved composite laminates lost their load-carrying capacity with multiple or single load drops. In the multiple load drop case, the crack tip travels in the sub-Rayleigh wave speed regime, whereas in the single load drop case, the crack tip speeds reach the intersonic speed. In Figure 2, through-the-thickness Mises strain distribution obtained from the experiment and finite element analysis are compared. Strain distributions are acquired at the center of the curved beam along the thickness direction, and it is presented in Figure 2a-d for four displacement values of 15 mm, 20 mm, 25 mm and 30 mm. It is observed that in the experiments, Mises strain is concentrated in the inner region of the curved beam just before the failure. Consequently, the strain concentration is attributed to the accumulation of the matrix cracks in the inner region.

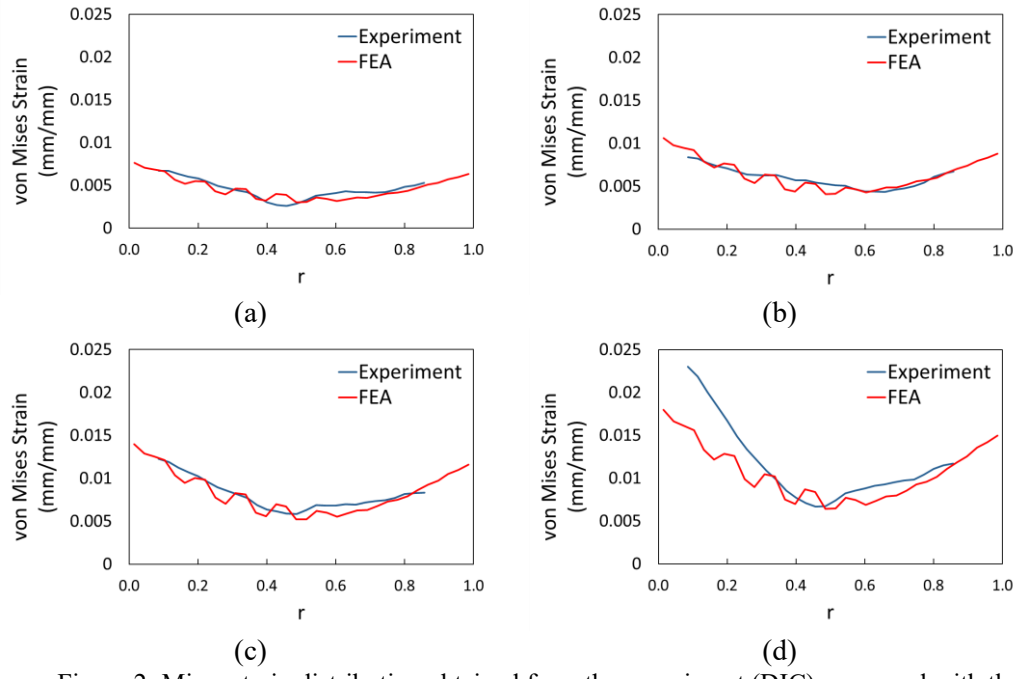


Figure 2: Mises strain distribution obtained from the experiment (DIC) compared with the finite element result for four displacement values of (a) 15 mm, (b) 20 mm, (c) 25 mm and (d) 30 mm

References

[1] F. Chang, G.-S. Springer. The Strengths of Fiber Reinforced Composite Bends. *The Journal of Composite Materials*, 20:30-45, 1986

[2] C.-T. Sun, S.-R. Kelly. Failure in Composite Angle Structures Part I: Initial Failure. *The Journal of Reinforced Plastics and Composites*, 7:220-232, 1988

18th EAWE PhD Seminar on Wind Energy
2 – 4 November 2022
Bruges, Belgium

Numerical investigation of impact-induced damage progression in composite wind turbine blade structures

O A Batmaz[a,b], M O Bozkurt[c], E Gurses[a], D Coker[a,b]

[a] Department of Aerospace Engineering, Middle East Technical University, Ankara, Turkey
[b] METUWind, METU Center for Wind Energy, Ankara, Turkey
[c] Department of Aeronautics, South Kensington Campus, Imperial College London, London, UK

E-mail: coker@metu.edu.tr

Keywords: Wind turbine blade, Composite damage, Low-velocity impact, Finite element analysis

1 Introduction

Wind turbine blades experience various impact events throughout their operational lifetime. These impact events can originate from environmental aspects such as bird strikes and hail storms, or from human mishandlings resulting in collisions with surroundings during transportation, assembling or maintenance [1,2]. These impact events may cause internal damages such as matrix/core cracks and delamination of composite layers that could not be identified easily with naked eyes and usually require sophisticated inspection methods [3]. The damage that occurred during such events leads to strength reduction of composite structures, which may result in the total collapse of the turbine blade unless proper care is not taken. Insight into damage mechanisms seen in the failure of composite blades after impact events can be obtained from virtual experiments accompanied by physical tests, either in coupon or component levels. This study aims to numerically investigate the matrix cracking and delamination damage progression in composite wind turbine blade structures subjected to low-velocity impact events in coupon-sized specimens. In this regard, the in-situ impact experiments of Bozkurt and Coker [4] on composite beam specimens are selected to simulate the progression of impact-induced damage numerically, and parameters affecting the dynamic behavior of delamination are investigated.

2 Method

3D Finite Element (FE) model for impact experiments of Bozkurt and Coker [4] is constructed using the commercial FE package ABAQUS/Explicit [5]. The composite ply damage and delamination of plies are two different damage mechanisms seen in experiments, therefore, separately modeled in the numerical simulations.

Plies of the composite laminate are modeled with single reduced-integration brick elements (C3D8R in ABAQUS). The initiation of matrix damage in composite plies is predicted with the LaRC05 criterion [6] and linear damage evolution scheme is applied via a user-defined subroutine. Delamination of composite plies is modeled with the cohesive zone method utilizing built-in cohesive elements (COH3D8 in ABAQUS) at the interfaces of plies having different orientations. A bilinear traction-separation law is specified for cohesive elements, where the quadratic nominal stress criterion predicts damage initiation. To consider multiaxial loading scenarios, the mixed-mode fracture toughness is defined by the Benzeggagh-Kenane criterion [7]. The schematic of the virtual test setup constructed in accordance with the reference experiments is depicted in Figure 2. The hemispherical steel impactor collides with the composite beam at a velocity of 3.13 m/s. To obtain an accurate global response of the composite beam, the experiment's boundary conditions are represented through the use of spring elements at the corresponding boundary regions. Each node residing on the boundary surfaces is connected to the ground by spring elements with a specific spring constant.

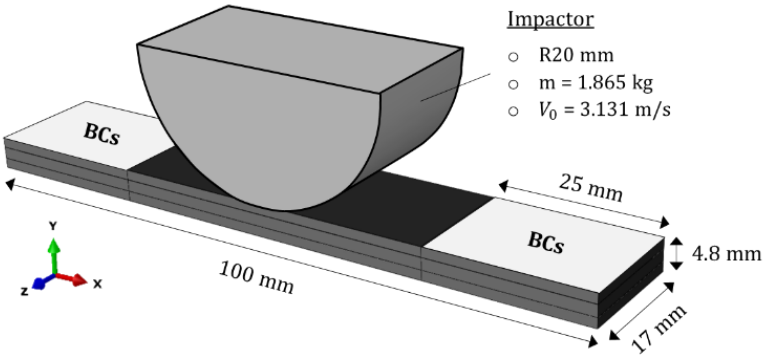


Figure 1: Geometries of $[0_5/90_3]_s$ CFRP beam and impactor for the FE simulation of a low-velocity impact event.

3 Results and Discussions

The damage progression captured in the in-situ impact experiment [4] is compared to the results of numerical simulations in Figure 4, where only the left half of the composite beam is presented in both experiments and simulations. Experiment photographs are taken with a high-speed camera at 525,000 frames per second and show the complete sequence of the damage progression. In both experiments and simulations, failure initiates as a matrix crack and propagates as delamination to the mid-section of the beam, where the impactor has collided. Numerical results are in agreement with the experiments in terms of damage form, sequence, and location. The total time elapsed for the crack to reach the mid-section of the beam is about 20 µs in the experiment, whereas it is under 10 µs in simulations. The reason for such discrepancy will be elucidated through the parametric studies on interface properties.

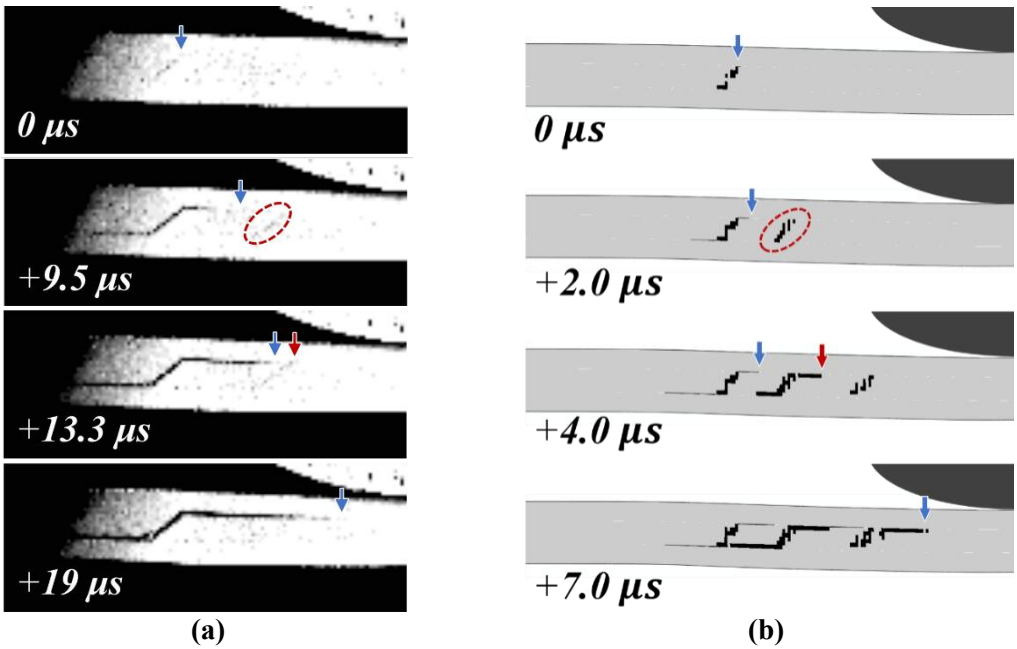


Figure 2: **(a)** Experiment photographs taken with a high-speed camera at 525,000 frames per second [4]. Failure initiates as a matrix crack and propagates as delamination. **(b)** FE simulation of the experiment in reference. Elements and thin lines in black correspond to fully damaged composite elements and delaminated interfaces, respectively.

Acknowledgements

The authors would like to thank METUWind, METU Center for Wind Energy for the use of their facilities.

References

[1] Verma A S, Haselbach P U, Vedvik N P and Gao Z 2018 A Global-Local Damage Assessment Methodology for Impact Damage on Offshore Wind Turbine Blades During Lifting Operations (American Society of Mechanical Engineers Digital Collection)

[2] Verma A S, Jiang Z, Vedvik N P, Gao Z and Ren Z 2019 Impact assessment of a wind turbine blade root during an offshore mating process *Engineering Structures* **180** 205–22

[3] Abrate S 1998 *Impact on Composite Structures* (Cambridge: Cambridge University Press)

[4] Bozkurt M O and Coker D 2021 In-situ investigation of dynamic failure in [05/903]s CFRP beams under quasi-static and low-velocity impact loadings *International Journal of Solids and Structures* **217–218** 134–54

[5] Hibbitt H, Karlsson B and Sorensen P 2016 Abaqus analysis user's manual version 6.10

[6] Pinho S, Darvizeh R, Robinson P, Schuecker C and Camanho P 2012 Material and structural response of polymer-matrix fibre-reinforced composites *Journal of Composite Materials* **46** 2313–41

[7] Benzeggagh M L and Kenane M 1996 Measurement of mixed-mode delamination fracture toughness of unidirectional glass/epoxy composites with mixed-mode bending apparatus *Composites Science and Technology* **56** 439–49

18th EAWE PhD Seminar on Wind Energy
2 – 4 November 2022
Bruges, Belgium

On the use of the Actuator Line Method to simulate the performance of twin Darrieus turbines

Omar Sherif Mohamed[a], Alessandro Bianchini[a]

[a] Università degli Studi di Firenze

E-mail: omar.sherif@unifi.it

Keywords: Actuator Line Method (ALM), Darrieus, Vertical Axis Wind Turbine (VAWT), Hydrokinetic Turbines, Computational Fluid Dynamics (CFD), Dynamic stall

1. Background and Motivation

Simulating the performance of Darrieus rotors and their flow field is a challenging topic, given the complexities associated with turbine kinematics. Conventional Reynolds-averaged Navier-Stokes (RANS) blade-resolved Computational Fluid Dynamics (CFD) can provide reliable results for performance and flow field, albeit with a high computational cost. On the other hand, installing Darrieus turbines in close proximity might lead to a significant power enhancement. Hence, it is vital to have a low-cost computational tool that is yet, capable of producing reliable results for the performance of closely-spaced Darrieus rotors and the influence of their flow interactions.

Counter-rotating configuration for twin Darrieus rotors has been extensively studied in the last few years with emphasise on the layout optimisation, e.g., spacing and oblique angle [1 - 4], as well as the physical mechanisms that lead to the performance augmentation [5 – 7]. In this work, the low-cost Actuator Line Method (ALM) is developed for twin rotors Darrieus turbines and validated against blade-resolved CFD.

2. Research Questions

Based on the above background, the following research questions were investigated:

- Is the ALM capable of predicting the performance of twin rotors Darrieus turbines?
- Can the ALM reproduce the wake flowfield of twin rotors Darrieus turbines?
- What are the limitations of the ALM when it is used to simulate pair of Darrieus rotors?

3. Research Method

In the ALM, lift and drag forces are projected into lines that represent the blades. Thus, no need to model the blade boundary layer. The aerodynamic forces are inserted into the computational domain of the CFD solver as a source term along the blade span. The main features of the ALM are as follows:

- *Velocity sampling*: The *LineAverage* method is used in this work to sample the local velocity through integral averaging of the undistributed inflow along a circular line around the hypothetical blade, this line has a radius r = 1c and a resolution N = 80 of equally spaced points along the sampling line.
- *Polar data*: The quality of the polar data plays a vital role in the capability of the ALM code to predict the rotor performance accurately, hence, proper modelling of the flow field around the rotor. The pre-stall aerodynamic coefficients were calculated with the viscid panel method software XFoil. Thereafter, these data have been extended over the deep stall region, i.e. up to AoA=±180°, via the Viterna-Corrigan model [8].
- *Berg dynamic stall model*: To consider the unsteadiness effect on the blade loads, the dynamic stall model from Berg [9] has been used in the ALM code. In brief, the Berg model involves the dynamic effects by introducing a delay in the measured angle of attack that is proportional to the flow reduced frequency via a coefficient γi. Lift and drag coefficients are eventually obtained as a linear interpolation between the static and dynamic ones, weighted over the constant A_M. In the present work, A_M was set to be 6 and γi to 1.5 based on the dedicated calibrations that were conducted in [10].

- *Pitching moment and BSC corrections*: To take the flow curvature phenomenon into account the tabulated polar data were derived for a virtually cambered airfoil, obtained by proper conformal mapping from the geometric one according to the rotor chord-to-radius ratio c/R, blade-spoke connection point (BSC) and TSR.
- Regularization kernel: To avoid non-physical discontinuities in the solution, the forces have to be projected into the CFD domain using a smearing function. In the current work, an isotropic Gaussian function was used to distribute the forces.

Further details on the ALM algorithm could be found in the dedicated study of Ref [11]. Figure 1 shows a schematic representation of the ALM for a straight-blade Darrieus turbine.

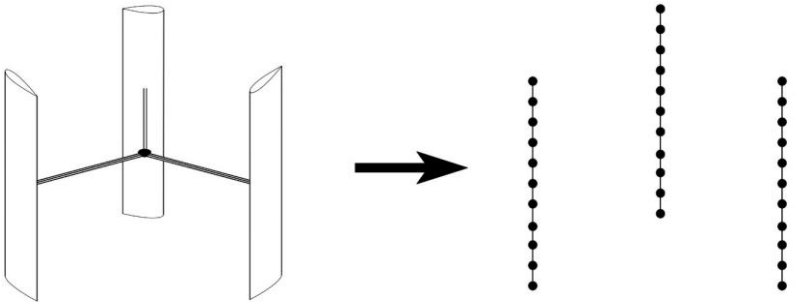


Figure 1: Schematic representation of the ALM for straight-bladed Darrieus turbine.

In the present work, the ALM has been developed to simulate the performance of twin Darrieus turbines. Two different pairs of Darrieus rotors were used as case studies to validate the ALM against blade-resolved CFD; Firstly, the Windspire rotor, a Vertical Axis Wind Turbine (VAWT) that has been used by Dabiri [12] to experimentally investigate the potential of installing two or more closely-spaced Darrieus rotors. In addition, twin rotors blade-resolved CFD results are available for this rotor in Ref. [5]. The latter results have been used in this work to validate the ALM. Secondly, the R1000 Hydrokinetic Turbine (HKT), for which multiple design configurations have been investigated in a previous work of Ref. [13]. It has been also studied in [10], where an investigation on a possible active pitch control strategy has been conducted using ALM. The operational and geometrical characteristics of the two turbine pairs are shown in table 1. A schematic representation of the twin rotors Darrieus turbine is shown in Figure 2.

Table 1: Operational and geometrical characteristics of the turbines pairs used in the present work

Variable	**WindSpire VAWT**	**R1000 HKT**
Airfoil shape	DU06W200	DU06W200 (reversed)
Number of blades [#]	3	2
Diameter [m]	1.6	2
Chord [m]	0.128	0.25
Solidity (nc/D) [-]	0.32	0.25
Tip Speed Ratio (TSR) [-]	2.7 – 3.2	2.5
Centre to centre spacing [-]	1.5D	2.5D
Wind/stream velocity [m/s]	8	2

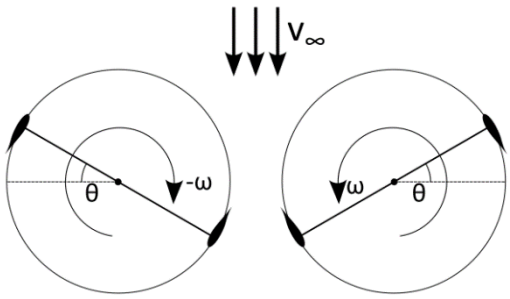


Figure 2: Schematic representation of the twin rotors Darrieus turbines.

4. Preliminary Results

4.1 WindSpire VAWT

Regarding the Windspire rotor, figure 3 shows the predicted instantaneous power coefficient (averaged for the two rotors) using the ALM and compared to that of the blade-resolved CFD [5]. As can be seen at TSR = 2.7, the use of the dynamic stall model in the ALM enhances the performance prediction accuracy during the upwind half, i.e., $0° < \theta < 180°$, on the contrary to the downwind half, i.e., $180° < \theta < 360°$, which overestimates the power coefficient if the dynamic stall model is used. At TSR = 3.2, where the dynamic stall phenomenon effect is negligible, the ALM without the inclusion of the dynamic stall model shows acceptable predictions of power coefficient compared to that of the blade-resolved CFD.

Generally, the mismatch in the ALM performance predictions could be attributed to the ALM intrinsic nature which does not account for the influence of blade-wake interactions, e.g., wake resulting from the blade during its upwind path that affects the performance of the blade during its downwind path. The latter issue could be noticed in the results of both TSRs, where the power coefficient is overestimated during the downwind half compared to that of the blade-resolved CFD.

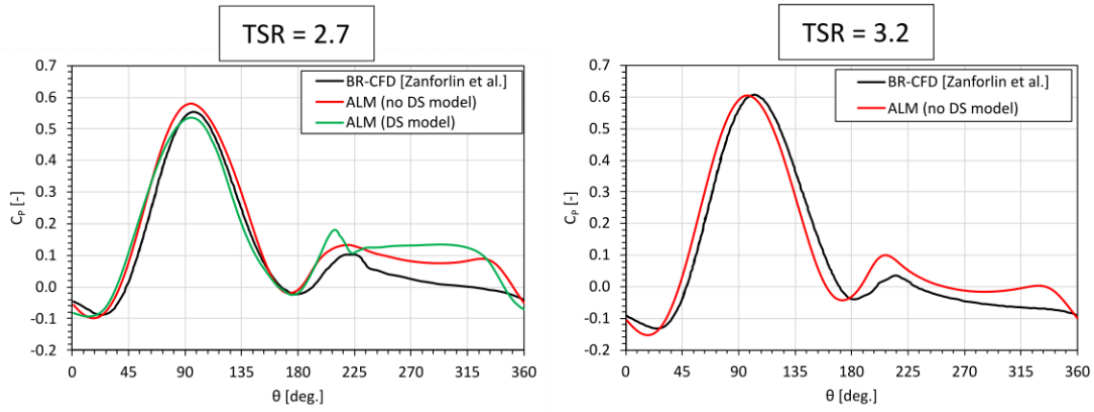


Figure 3: Instantaneous power coefficient results for WindSpire twin rotors.

4.2 R1000 HKT

Figure 4-(a) shows the instantaneous torque coefficient averaged for the twin rotors of R1000 using both ALM and blade-resolved CFD. The ALM results almost match that of the blade-resolved CFD during the first quarter, i.e., $0° < \theta < 90°$. On the other hand, one can notice that during the second quarter, i.e., $90° < \theta < 180°$, the ALM underestimates the power coefficient. During the downwind half, the ALM overestimated the power coefficient. In figure 4-(b), the results of the angle of attack sampling are presented for both the ALM and the blade-resolved CFD. Noting that the same settings for the LineAverage technique were used to sample the angle of attack in both simulations as discussed in section 3.

It can be observed that within the region where the blades of the two rotors are closer to each other, i.e., $90° < \theta < 270°$ (see figure 2), the ALM is not capable of capturing the complex flow interactions as accurate as the blade-resolved CFD, e.g., dAoA/dt. This issue significantly affects the estimation of the dynamic as described in the working principle of the Berg dynamic stall model in section 3.

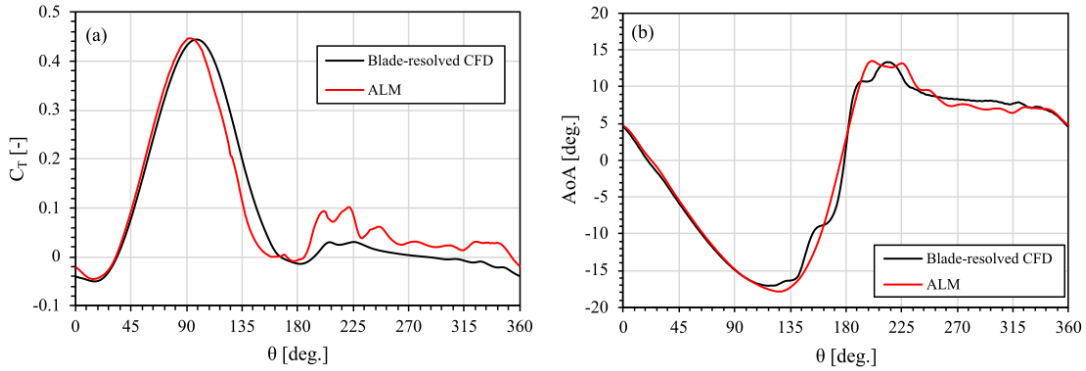


Figure 4: R1000 twin rotors results, a) instantaneous torque coefficient, b) angle of attack variation.

References

[1] O. S. Mohamed, A. Ibrahim, and A. M. R. El Baz, "CFD Investigation of the Multiple Rotors Darrieus Type Turbine Performance," presented at the ASME Turbo Expo 2019: Turbomachinery Technical Conference and Exposition, Nov. 2019. doi: 10.1115/GT2019-91491.

[2] H.-D. Zheng, X. Y. Zheng, and S. X. Zhao, "Arrangement of clustered straight-bladed wind turbines," *Energy*, vol. 200, p. 117563, Jun. 2020, doi: 10.1016/j.energy.2020.117563.

[3] P. Zhao, Y. Jiang, S. Liu, T. Stoesser, L. Zou, and K. Wang, "Investigation of fundamental mechanism leading to the performance improvement of vertical axis wind turbines by deflector," *Energy Conversion and Management*, vol. 247, p. 114680, Nov. 2021, doi: 10.1016/j.enconman.2021.114680.

[4] M. Hassanpour and L. N. Azadani, "Aerodynamic optimization of the configuration of a pair of vertical axis wind turbines," *Energy Conversion and Management*, vol. 238, p. 114069, Jun. 2021, doi: 10.1016/j.enconman.2021.114069.

[5] S. Zanforlin and T. Nishino, "Fluid dynamic mechanisms of enhanced power generation by closely spaced vertical axis wind turbines," *Renewable Energy*, vol. 99, pp. 1213–1226, Dec. 2016, doi: 10.1016/j.renene.2016.08.015.

[6] G. Jin, Z. Zong, Y. Jiang, and L. Zou, "Aerodynamic analysis of side-by-side placed twin vertical-axis wind turbines," *Ocean Engineering*, vol. 209, p. 107296, Aug. 2020, doi: 10.1016/j.oceaneng.2020.107296.

[7] A. S. Alexander and A. Santhanakrishnan, "Mechanisms of power augmentation in two side-by-side vertical axis wind turbines," *Renewable Energy*, vol. 148, pp. 600–610, Apr. 2020, doi: 10.1016/j.renene.2019.10.149.

[8] L. A. Viterna and D. C. Janetzke, "Theoretical And Experimental Power From Large Horizontal-Axis Wind Turbines," *NASA Technical Memorandum*, 1982.

[9] B. Massé, "Description de deux programmes d'ordinateur pour le calcul des performances et des charges aérodynamiques pour les éoliennes à axe vertical," technical report IREQ-2379, 1981.

[10] P. F. Melani, F. Balduzzi, G. Ferrara, and A. Bianchini, "Development of a desmodromic variable pitch system for hydrokinetic turbines," *Energy Conversion and Management*, vol. 250, p. 114890, Dec. 2021, doi: 10.1016/j.enconman.2021.114890.

[11] P. F. Melani, F. Balduzzi, and A. Bianchini, "Simulating tip effects in vertical-axis wind turbines with the actuator line method," *J. Phys.: Conf. Ser.*, vol. 2265, no. 3, p. 032028, May 2022, doi: 10.1088/1742-6596/2265/3/032028.

[12] J. O. Dabiri, "Potential order-of-magnitude enhancement of wind farm power density via counter-rotating vertical-axis wind turbine arrays," *Journal of Renewable and Sustainable Energy*, vol. 3, no. 4, p. 043104, Jul. 2011, doi: 10.1063/1.3608170.

[13] F. Balduzzi, P. F. Melani, G. Soraperra, A. Brighenti, L. Battisti, and A. Bianchini, "Some design guidelines to adapt a Darrieus vertical axis turbine for use in hydrokinetic applications," *E3S Web Conf.*, vol. 312, p. 08017, 2021, doi: 10.1051/e3sconf/202131208017.

18th EAWE PhD Seminar on Wind Energy
2-4 November 2022
Bruges, Belgium

UVLM-based aeroelastic simulation of large wind turbines

Daniel Schuster[a], **David Märtins**[a], **Christian Hente**[a], **Paula Krabbe**[a], **Franziska Müller**[a], **Clemens Hübler**[a], **Raimund Rolfes**[a], and **Cristian Guillermo Gebhardt**[b]

[a]Leibniz University Hannover, Institute for Structural Analysis, ForWind
[b]University of Bergen, Geophysical Institute (GIF) and Bergen Offshore Wind Centre (BOW)

E-mail: d.schuster@isd.uni-hannover.de

Keywords: aeroelasticity, fluid-structure interaction, mid-fidelity, vortex methods, simulation framework, offshore megastructures

Wind energy is expected to play a major role in the future energy supply given the recognized need to reduce the carbon emissions [5]. To be able to fulfil this potential, wind turbines have steadily grown in size over the past years and will continue to do so: future wind turbines will likely have a diameter of up to 400 m and a rated power of more than 20 MW [1]. Given the need to optimize the material use and weight, these new wind turbines will consist of large, slender structures which are more prone to large deformations than current generations of wind turbines [8]. Additionally, they will be subject to yet unknown loads, as they will reach further into the atmospheric boundary layer [2]. Nonlinear dynamic phenomena become more dominant and the interactions between the different components of the wind turbine as well as with their environment has to be considered in more detail.

Due to these factors, currently used simulation methods relying on low-fidelity methods such as Blade Element Momentum Theory and linear beam theories might not be sufficient to realistically approximate the behaviour of such large wind turbines [2]. High-fidelity methods like computational fluid dynamics of full three-dimensional finite element analysis are however too computationally expansive to be employed during the design process [8]. Instead, mid-fidelity methods seem to present an attractive alternative.

Our work concentrates on developing a mid-fidelity nonlinear aeroelastic approach, which combines the unsteady vortex lattice method (UVLM) and a flexible multi-body system approach. The multi-body system/finite elements - approach forms the structural model consisting of rigid bodies, geometrically exact beams and holonomic and non-holonomic constraints ([3], [4]). The aerodynamic forces are computed using the UVLM, which is a well-established tool to compute three-dimensional vortex-dominated flows of an ideal fluid around lifting as well as non-lifting surfaces [7]. This method offers an attractive compromise between computational effort and accuracy. The nonlinear structural and aerodynamic equations are coupled strongly using an approach based on the principle of virtual work.

After introducing the basic modelling ideas and governing equations, we discuss some details of the aerodynamic computation. While the structural computation is only considered briefly, the coupling between structural and aerodynamic computation is explained in more detail. We discuss the advantages and disadvantages of the used methods, especially in comparison with today's standard simulation tools, and present the results of some initial, academic verification and validation examples against literature as well some first comparisons of wind turbine simulation results against the solution of the commonly used program OpenFAST [6]. Finally, we give an outlook on our ongoing work and plans to expand our simulation tool towards a fully aerohydroservoelastic load computation suited for large offshore wind turbines.

Acknowledgements

This work was funded by the Deutsche Forschungsgemeinschaft (DFG, German Research Foundation) – Project-ID 434502799 – SFB 1463.

References

[1] T. Ashuri, J. R. R. A. Martins, M. B. Zaaijer, G. A. M. van Kuik, and G. J. W. van Brussel. Aeroservoelastic design definition of a 20 mw common research wind turbine model. *Wind Energy*, 19:2071–2087, 2016.

[2] K. Boorsma, F. Wenz, K. Lindenburg, M. Aman, and M. Kloosterman. Validation and accomodation of vortex wake codes for wind turbine design load calculations. *Wind Energy Science*, 5:699–719, 2020.

[3] C. G. Gebhardt, B. Hofmeister, C. Hente, and R. Rolfes. Nonlinear dynamics of slender structures: a new object-oriented framework. *Computational Mechanics*, 63:219–252, 2019.

[4] C. G. Gebhardt, I. Romero, and R. Rolfes. A new conservative/dissipative time integration scheme for nonlinear mechanical systems. *Computational Mechanics*, 65:405–427, 2020.

[5] IEA. World energy outlook 2019. Technical report, International Energy Agency, 2019.

[6] J. M. Jonkman and M. L. J. Buhl. Fast user's guide. Technical Report NREL/EL-500-38230, National Renewable Energy Laboratory, August 2005.

[7] J. Katz and A. Plotkin. *Low-Speed Aerodynamics*. Camebridge University Press, 2 edition, 2001.

[8] L. Wang, X. Liu, and A. Kolios. State of the art in the aeroelasticity of wind turbine blades: Aeroelastic modelling. *Renewable and Sustainable Energy Reviews*, 64:195–210, 2016.